

CONTENTS

	Page
Chapter 1: Introduction .....	1
1.1. Purpose of the investigation .....	1
1.2. Locality of the study area .....	1
1.3. The method of investigation.....	3
1.4. Acknowledgements.....	3
 Chapter 2: Geology of the Upington Terrane, Eastern Namaqua Province.....	 5
2.1. Introduction .....	5
2.2. Tectonic setting and regional geological succession .....	6
2.3. Regional metamorphism and tectonism .....	9
2.4. Regional data set .....	11
2.5. Local geology .....	12
2.5.1 Lithological succession at Areachap mine .....	12
2.5.2. Metamorphism in Areachap Mine .....	16
2.5.3. The sulphide minerals in defunct Areachap mine .....	16
2.5.4. Lithological succession of the Kantienpan deposit .....	17
2.6. Geomorphological evolution .....	19
2.7. Calcrete environments .....	22
2.7.1. Definition of calcrete .....	22
2.7.2. Calcrete classification .....	23
2.7.3. Mineralogy of calcretes .....	24
2.7.4. Mechanism of carbonate accumulation .....	25
2.7.5. Calcrete in the study area .....	26
 Chapter 3: Literature review of VHMS deposits and related lithogeochemical alteration	
3.1. Introduction .....	29
3.2. Classification and geological setting of VHMS deposits .....	29
3.3. Classification of metamorphosed massive sulphide deposits of the Namaqua Province .....	31
3.4. Hydrothermal Models for Formation of VHMS deposits .....	32
3.4.1. Convection cell model .....	32
3.4.2. Stratal aquifer model .....	32
3.4.3. Magmatic hydrothermal model .....	33
3.5. Mineral zonation in the alteration pipe and ore zone .....	33
3.5.1. Mineral variation in the ore zone .....	33
3.5.2. Wall rock alteration .....	35
3.5.3. Metamorphism of VHMS deposits and their alteration zones .....	37

3.6. Quantification of chemical changes in altered rocks .....	37
3.6.1. The isocon method .....	37
3.6.2. The alteration index and the Chlorite-Carbonate-Pyrite index .....	40
3.6.3. The mineralogical variation index (Pearce Element Ratio (PER) analysis) .....	43
Chapter 4: Lithogeochemical investigation .....	45
4.1. Introduction .....	45
4.2. Sampling, Sample preparation and analytical methods .....	47
4.3. Major element variation near the ore zone .....	48
4.3.1. Interpretation of major elements variation adjacent to the ore zone in borehole AP5 (Areachap) .....	48
4.3.2. Interpretation of major elements variation near the ore zone in borehole KN11 (Kantienpan) .....	52
4.4. Mineral chemistry near the ore zone .....	55
4.4.1. The retrograde chlorite .....	59
4.5. Identification of Peraluminous rocks close to the ore zone using normative calculations .....	60
4.6. Quantification of the degree of alteration in the precursor rocks .....	65
4.7. Development of alteration box plot for high-grade metamorphic rocks .....	73
4.7.1. The location of rock forming minerals in the box plot .....	74
4.7.2. Whole rock analysis and box plot .....	76
4.7.3. Combination of isocon results and the box plot .....	80
4.8. Refinement of chemical structure in the upper right corner of the box plot .....	81
Chapter 5: Lithogeochemistry as an exploration tool .....	84
5.1. Introduction .....	84
5.2. Lithogeochemical interpretation of borehole information .....	85
5.3. Economic element vectors of mineralization .....	86
5.4. Peraluminous, gneiss, and amphibolite factors .....	87
5.4.1. Peraluminous factors .....	87
5.4.2. Gneiss factors .....	89
5.4.3. Amphibolite factors .....	91
5.5. Application of factors to the regional data set .....	92
5.6. Prioritization of the anomalous samples in the regional data set .....	104
Chapter 6: Regolith geochemistry .....	117
6.1. Introduction .....	117
6.2. The concept of mobile metal ions and selective extraction techniques .....	118
6.2.1. Mobile Metal Ions (MMI) concept .....	119
6.2.2. Selective extraction techniques .....	121
6.3. Sampling programme .....	123
6.4. Selection of the most appropriate extraction reagent .....	124
6.5. Calculation of the threshold value for the anomalous population .....	124
6.5.1. The threshold value for NH <sub>4</sub> EDTA extraction .....	126
6.5.2. The threshold value for Ca(H <sub>2</sub> PO <sub>4</sub> ) <sub>2</sub> extraction .....	129
6.5.3. The threshold value for MMI-A analyses results .....	133
6.5.4. The threshold value for total analyses (XRF method) .....	134
6.6. Discrimination of concealed ore zones in the surface samples .....	140

6.6.1. Comparison of partial extraction techniques with total analysis method ...	140
6.6.2. Discrimination of the secondary dispersion haloes in other traverses .....	156
6.6.3. Discrimination of the secondary dispersion haloes (MMI results, Kantienganpan) .....	166
6.6.4. The comparison of NH <sub>4</sub> EDTA, MMI and XRF methods .....	169
6.7. Dispersion of the elements of the interest in the calcrete environment .....	170
6.7.1. Kantienganpan calcrete samples .....	171
6.7.2. Areachap calcrete samples .....	174
6.7.3. Comparison of calcretes close to the ore zone and further away .....	179
 Chapter 7: Discussion and conclusion .....	 182
7.1. Lithochemical characteristics of the hydrothermal alteration zones in VHMS deposits and vectors for further exploration .....	182
7.2. The Suitability a regolith geochemical survey of non-residual sand deposit cover for detecting concealed mineralization .....	186
7.3. Signature of the mineralization in the calcrete regolith .....	187
7.4. An integrated approach to geochemical exploration of arid areas .....	188
 References .....	 191
 Appendix A: Cross sections and extra figure .....	 209
Extra Figures .....	219
 Appendix B: Microprobe Analysis .....	 220
 Appendix C: Sample preparation and whole rock analysis .....	 232
C.1. Sample preparation for XRF Analysis .....	232
C.1.1. Calibration .....	233
C.3. XRF analytical precision and accuracy .....	233
C.4. Results of XRF analyses .....	233
 Appendix D: Analytical methods and results of regolith analyses .....	 261
D.1. Regolith samples .....	261
D.1.1. NH <sub>4</sub> NO <sub>3</sub> extraction .....	262
D.1.2. NH <sub>4</sub> OAC extraction .....	264
D.1.3. NH <sub>4</sub> EDTA extraction .....	266
D.1.4. Ca (H <sub>2</sub> PO <sub>4</sub> ) <sub>2</sub> extraction .....	270
D.1.5. XRF total analyses .....	273
D.1.6. Regolith data set of the Kantienganpan traverses .....	275
D.1.7. Regolith data set of the Areachap traverses .....	279
D.2. Calcrete samples .....	282
 Appendix E: XRD analyses results .....	 300
 Appendix F: Confidential agreement with Kumba Resources Limit.....	 306

List of Figures

	Page
Figure 1.1: Location map .....	2
Figure 2.1: The location of Namaqua-Natal Province (After Moen, 1999) and the study area .....	6
Figure 2.2: Geological map of the Areachap Group in the eastern part of Namaqua Sub-province .....	8
Figure 2.3: A cross-section of lithology at Areachap mine including the borehole AP5 .....	14
Figure 2.4: Geological map of the Areachap area (after Voet and King, 1986) .....	14
Figure 2.5: Geology map of the Kantienpan area (after Rossouw, 2003) (TDEM: Time domain electro-magnetic conductor) .....	18
Figure 2.6: Cross-section of borehole KN11 (after Rossouw, 2003) .....	18
Figure 2.7: The genetic calcrete classification (after Carlisle, 1980) .....	23
Figure 3.1: An isocon diagram for sample AP5/35 (least altered biotite-gneiss) and AP5/23 (altered biotite-gneiss) from drill hole AP5 in the Areachap area .....	40
Figure 3.2: Field for hydrothermal alteration described in the text (modified after Large et al., 2001) .....	41
Figure 3.3: Field for diagenetic alteration described in the text (after Large et al., 2001) .....	42
Figure 3.4: K/Ti versus Al/Ti PER diagram of Elura Zn-Pb-Ag deposit (adopted from Whitbread and Moore, 2004) .....	44
Figure 4.1: A cross-section of lithology at Areachap mine including the borehole AP5 (adopted from Voet and King, 1986) (Sil: sillimanite; Crd: cordierite and Hbl: hornblende) .....	49
Figure 4.2: Variation of CaO through the lithological successions adjacent to the ore zone, at the Areachap deposit (Gneiss1: normal quartzo feldspathic gneiss; Gneiss2: peraluminous rocks; Hbl: Hornblende; Crd: cordierite; Sil: sillimanite) .....	50

Figure 4.3: Variation of Na <sub>2</sub> O through the lithological successions hosting the ore zone, at the Areachap deposit (Gneiss1: normal quartzo feldspathic gneiss; Gneiss2: peraluminous rocks; Hbl: Hornblende; Crd: cordierite; Sil: sillimanite) .....	50
Figure 4.4: Variation of K <sub>2</sub> O through the lithological successions adjacent to the ore zone, at the Areachap deposit (Gneiss1: normal quartzo feldspathic gneiss; Gneiss2: peraluminous rocks; Hbl: Hornblende; Crd: cordierite; Sil: sillimanite) .....	51
Figure 4.5: Variation of MgO through the lithological successions hosting the ore zone, at the Areachap deposit (Gneiss1: normal quartzo feldspathic gneiss; Gneiss2: peraluminous rocks; Hbl: Hornblende; Crd: cordierite; Sil: sillimanite) .....	51
Figure 4.6: Cross-section of borehole KN11 in the Kantienpan area (Sil: sillimanite, Crd: cordierite and Hbl: hornblende) .....	52
Figure 4.7: Variation of CaO through the lithological successions adjacent to the ore zone (Hbl: Hornblende; Crd: cordierite; Sil: sillimanite) .....	53
Figure 4.8: Variation of Na <sub>2</sub> O through the lithological successions hosting the ore zone (Hbl: Hornblende; Crd: cordierite; Sill: sillimanite) .....	53
Figure 4.9: Variation of K <sub>2</sub> O through the lithological successions adjacent to the ore zone (Hbl: Hornblende; Crd: cordierite; Sil: sillimanite) .....	54
Figure 4.10: Variation of MgO through the lithological successions hosting the ore zone (Hbl: Hornblende; Crd: cordierite; Sil: sillimanite) .....	54
Figure 4.11: Variation of Na and Ca in plagioclase, Kantienpan (KN11) (Ab: albite and An: anorthite) .....	56
Figure 4.12: Variation of Mg, Fe and Ca in the pyroxene, Kantienpan (KN11), (En: enstatite and Fs: ferrosilite) .....	56
Figure 4.13: Variation of the Mg number in cordierite, Kantienpan, (KN11), (Hbl: Hornblende; Stri. Sulp.: stringer sulphide; Sil: sillimanite; Crd: cordierite) .....	57
Figure 4.14: Chemical components of garnet in the alteration and ore zones, Areachap (AP5), (FW: footwall) .....	58
Figure 4.15: Variation of Mg and Fe in mica at Areachap (A) and Kantienpan (B), (Ann: Annite and Phl: phlogopite) .....	58

Figure 4.15: The probability plot of peraluminous ratio based on AP5 and KN11 data set .....	63
Figure 4.16: The variation of peraluminous ratio near the ore zone in borehole AP5 (Gneiss1: normal quartzo feldspathic gneiss; Gneiss2: peraluminous rocks; Hbl: Hornblende; Crd: cordierite; Sil: sillimanite) .....	64
Figure 4.17: The variation of peraluminous ratio near the ore zone in borehole KN11 (Hbl: Hornblende; Crd: cordierite; Sil: sillimanite) .....	64
Figure 4.18: An isocon diagram between samples AP5/35, the least altered biotite-gneiss, and AP5/29, altered biotite-gneiss, from borehole AP5 in the Areachap area .....	67
Figure 4.19: An isocon diagram between samples AP5/35, the least altered biotite-gneiss, and AP5/30, altered biotite-gneiss, from borehole AP5 in the Areachap area .....	67
Figure 4.20: An isocon diagram for samples AP5/35 (the least altered biotite-gneiss) and AP5/32 (altered biotite-gneiss) from drill hole AP5 in the Areachap area .....	68
Figure 4.21: An isocon diagram between the least altered sample AP5/42 and altered sample AP5/25, altered biotite-gneiss, from borehole AP5 in the Areachap area .....	68
Figure 4.22: An isocon diagram for samples KN11/44 (the least altered biotite-gneiss) and KN11/40 (altered biotite-gneiss) from drill hole KN11 in the Kantienpan area .....	70
Figure 4.23: Box Plot of mineral compositions from Areachap (AP5 and AP2) .....	75
Figure 4.24: Box Plot of mineral compositions from Kantienpan (KN11 and KN12) .....	75
Figure 4.25: Box Plot of whole rock samples from Kantienpan (KN11, KN12 and surface outcrop) .....	77
Figure 4.26: The variation of AI and CCPI values in samples from Kantienpan (KN11). Massive sulphide zone indicated in black and alteration zone hatched .....	77
Figure 4.27: Box Plot of whole rock samples from Areachap (AP2 and AP5) .....	78

Figure 4.28: Inverted sequence see in drill hole AP5 (Areachap) showing the variation in the AI and CCPI values. Massive sulphide zone indicated in black and alteration zone hatched .....	79
Figure 4.29: Box plot with isocon and microprobe results (Kantienpan area, KN1) ..	80
Figure 4.30: Box plot with the isocon and microprobe results (Areachap area, AP5) .....	81
Figure 4.31: PER analysis for samples from drill holes KN11 and KN12, Kantienpan area. The Mn content of gahnite, cordierite and garnet from the ore zone is higher than in the identified footwall alteration zone. Pyroxene has lower Mn and Fe contents in the ore zone and altered footwall (11/43: borehole KN11/ sample number) .....	83
Figure 4.32: PER analysis of boreholes AP2 and AP5 in the Areachap area. The Mn content of Cordierite increases from the altered FW toward ore zone. The Mn content of garnets is higher in ore zone than in footwall alteration zone. No trend is evident in the composition of chlorite and chamosite (5/27: borehole AP5/ sample number) .....	83
Figure 5.1: The tree diagram of the peraluminous rocks .....	88
Figure 5.2: The tree diagram of the gneissic rocks .....	90
Figure 5.3: The tree diagram of the amphibolite rocks .....	91
Figure 5.4: The peraluminous factor (FPer) versus alteration factor (FAR), regional data set [189: Kantienpan (Boks); 92*: north west of Upington (UpUp); 426: south of Upington (BeUp)] .....	96
Figure 5.5: The pelitic factor (FPR) versus alteration factor (FAR), regional data set [189: south of Kantienpan (Boks); 903: south of Upington (BeUp)] .....	96
Figure 5.6: The peraluminous factor (FPer) versus amphibolite factor (FOrtho-Amp1) for the regional data set [189:south of Kantienpan (Boks); 903:south of Upington (BeUp); 196/: north west of Bokspuit (Kant)] .....	98
Figure 5.7: The para-amphibolite factor (Fpara-amp3) versus ortho-amphibolite factor (Fortho-amp1), regional amphibolite and peraluminous data set [196/: north west of Bokspuits (Kant); diamond filled: peraluminous and square filled: amphibolite] .....	99

Figure 5.8: The para-amphibolite factor (Fpara-amp3) versus general amphibolite factor (Famp2) for the regional amphibolite data set .....	99
Figure 5.9: Biotite-hornblende-gneiss factor (FHbl-Gn) versus peraluminous factor (FPer), combined data set of biotite-hornblende-gneiss and peraluminous samples, regional data set [diamond filled: peraluminous and square filled: biotite-hornblende-gneiss samples] .....	100
Figure 5.10: The leucogneiss factor (FLeu-Gn) versus peraluminous factor (FPer), mixed of peraluminous and leuco-gneissic samples, regional data set [diamond filled: peraluminous and square filled: leucogneiss samples] .	102
Figure 5.11: The probability plot of whole regional data set for the alteration factor (FAR) .....	105
Figure 5.12: The probability plot of anomalous values of the last stage for the alteration factor (FAR), regional data set .....	106
Figure 5.13: Box plot of the final results for the regional data set .....	109
Figure 5.14: The probability plot of Zn contents based on the data in Table 5.9, regional data set .....	110
Figure 5.15: The probability plot of Cu contents based on the data in Table 5.9, regional data set .....	110
Figure 5.16: The probability plot of Ni contents based on the data in Table 5.9, regional data set .....	110
Figure 5.17: Geology of the northern part of the Areachap Group, eastern Namaqua Province .....	114
Figure 5.18: The alteration factor versus sample number in-prioritised Traverses, rank one .....	115
Figure 5.19: The alteration factor versus sample number in-prioritised traverses, rank two .....	115
Figure 6.1: Schematic model of convection cell in connection with mobile metal ions in the secondary environment (after Mann et al., 1997) .....	119
Figure 6.2: Regolith traverses and geology map of the Kantienpan area (after Rossouw, 2003) .....	125

Figure 6.3: Regolith traverses and geology map of the Areachap area (after Voet and King, 1986) .....	125
Figure 6.4: Probability plot of the log values for Cu (A), Zn (B), Pb (C), Mn (D) and Ba (E), whole Kantienpan regolith data set (ICP-MS method, n=52 samples) .....	128
Figure 6.5: Probability plot of the log values for Cu (A), Zn(B), Pb(C), Mn (D) and Fe (E), whole Areachap regolith data set (ICP-MS method, n=61 samples) .....	130
Figure 6.6: Probability plot of S, Kantienpan (Ca (H <sub>2</sub> PO <sub>4</sub> ) <sub>2</sub> , shaking time of 120-minutes, ICP-MS method) .....	131
Figure 6.7: Probability plot of S, Areachap (Ca (H <sub>2</sub> PO <sub>4</sub> ) <sub>2</sub> , shaking time 120-minutes, ICP-MS method) .....	132
Figure 6.8: Probability plot of the normal and log values for Cu (A) and Zn (B) (MMI method, n=58 samples) .....	134
Figure 6.10: Probability plot of Zn based on the regolith traverse KP12 data, Kantienpan, XRF method .....	136
Figure 6.9: Probability plot of the normal and log values for Cu (A), Zn (B), Pb (C), MnO (D) and S (E), regolith traverse KP12, Kantienpan (XRF method, n=19 samples) .....	137
Figure 6.12: Probability plot of Zn, regolith traverse T2 (XRF method, n=25 samples) .....	138
Figure 6.11: Probability plot of the normal and log values for Cu (A), Zn (B), Pb (C), MnO (D), Fe <sub>2</sub> O <sub>3</sub> (E) and S (F), regolith traverse T2, Areachap (XRF method, n=21 samples) .....	139
Figure 6.13: Variation of Cu in regolith traverse KP12 based on ICP-MS (A, by using NH <sub>4</sub> EDTA and 180-minutes shaking times) and XRF analyses (B) .....	141
Figure 6.14: Variation of Zn in regolith traverse KP12 based on ICP-MS (A, by using NH <sub>4</sub> EDTA and 180-minutes shaking times) and XRF analyses (B) .....	142
Figure 6.15: Variation of Pb in regolith traverse KP12 based on ICP-MS (A, by using NH <sub>4</sub> EDTA and 180-minutes shaking times) and XRF analyses (B) .....	143
Figure 6.16: Variation of Mn in regolith traverse KP12 based on ICP-MS (A, by using NH <sub>4</sub> EDTA and 180-minutes shaking times) and XRF analyses (B) .....	144

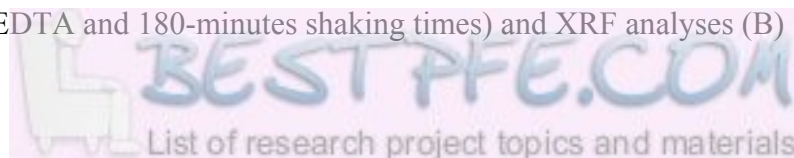


Figure 6.17: Variation of S in regolith traverse KP12 based on ICP-MS (A, by using NH <sub>4</sub> EDTA and 180-minutes shaking times) and XRF analyses (B) .....	145
Figure 6.18: Variation of Cu in the regolith traverse T2 based on ICP-MS (A) (NH <sub>4</sub> EDTA, 180-minutes shaking times) and XRF (B) analysis .....	148
Figure 6.19: Variation of Zn in the regolith traverse T2 based on ICP-MS (A) (NH <sub>4</sub> EDTA, 180-minutes shaking times) and XRF (B) analysis .....	149
Figure 6.20: Variation of Pb in the regolith traverse T2 based on ICP-MS (A) (NH <sub>4</sub> EDTA, 180-minutes shaking times) and XRF (B) analysis .....	150
Figure 6.21: Variation of Mn in the regolith traverse T2 based on ICP-MS (A) (NH <sub>4</sub> EDTA, 180-minutes shaking times) and XRF (B) analysis .....	151
Figure 6.22: Variation of Fe in the regolith traverse T2 based on ICP-MS (A) (NH <sub>4</sub> EDTA, 180-minutes shaking times) and XRF (B) analysis .....	152
Figure 6.23: Variation of S in the regolith traverse T2 based on ICP-MS (A) (NH <sub>4</sub> EDTA, 180-minutes shaking times) and XRF (B) analysis .....	153
Figure 6.24: Variation of Cu (A) and Zn (B) in the regolith traverse KP5 (Kantienpan) based on ICP-MS analysis (using NH <sub>4</sub> EDTA and 180-minutes shaking times) .....	157
Figure 6.25: Variation of Mn in the regolith traverse KP5 (Kantienpan) based on ICP-MS analysis (using NH <sub>4</sub> EDTA and 180-minutes shaking times) .....	158
Figure 6.26: Variation of Cu (A) and Zn (B) in the regolith traverse KP8 based on ICP-MS analysis (using NH <sub>4</sub> EDTA solutions and 180-minutes shaking times) .....	159
Figure 6.27: Variation of Mn in the regolith traverse KP8 based on ICP-MS analysis (using NH <sub>4</sub> EDTA solutions and 180-minutes shaking times) .....	160
Figure 6.28: Variation of Cu (A) and Zn (B) in the regolith traverse T1 based on ICP-MS analysis (NH <sub>4</sub> EDTA, 180-minutes shaking times) .....	161
Figure 6.29: Variation of Pb (A) and Mn (B) in the regolith traverse T1 based on ICP-MS analysis (NH <sub>4</sub> EDTA, 180-minutes shaking times) .....	162
Figure 6.30: Variation of Cu (A) and Zn (B) in the regolith traverse T3 based on ICP-MS analysis (NH <sub>4</sub> EDTA, 180-minutes shaking times) .....	164
Figure 6.31: Variation of Pb (A) and Mn (B) in the regolith traverse T3 based on ICP-MS analysis (NH <sub>4</sub> EDTA, 180-minutes shaking times) .....	165

Figure 6.32: Variation of Cu (A) and Zn (B) in the regolith traverse 7800NW, MMI method (Sil: sillimanite; Crd: cordierite and Hbl: hornblende) .....	167
Figure 6.33: Variation of Cu (A) and Zn (B) in the regolith traverse 7700NW, MMI method .....	168
Figure 6.34: The calcrete layer in an old excavation at Areachap. Calcrete profile Calc1 (A), Calc2 (B) and a gossan rock with malachite and calcrete-filled veinlets at the bottom of calcrete layer (C) .....	175
Figure 6.35: Major oxides variation versus depth in the Areachap (visually cleaned samples referred to as Calc1) .....	176
Figure 6.36: Variation of Cu, Zn, Pb and S versus depth in the calcrete layer, Areachap (visually cleaned samples referred to as Calc1).....	177
Figure 6.37: Major oxides variation versus depth (visually cleaned samples referred to as Calc2) in Areachap .....	178
Figure 6.38: Variation of Cu, Zn, Pb and S versus depth in the calcrete layer, Areachap (visually cleaned samples referred to as Calc2).....	179
Figure 6.39: Variation of trace elements (A and B) and major components (C) of calcrete samples close to ore deposit and further away from the mineralized zone .....	180
Figure A.1: Cross section includes borehole AP2 and sample locations .....	210
Figure A.2: Cross section includes borehole AP5 and sample locations .....	211
Figure A.3: Cross section includes borehole KN12 and sample locations .....	212
Figure A.4: Cross section of KN11 and location of samples .....	217
Figure A.5: Geology map of the Kantienpan area (after Rossouw, 2003) and locations of rock samples (TDEM: Time domain electro-magnetic conductor) ...	219
Figure A.6: Box plot of final results of regional data set (Figure 5.18) .....	219
Figure D.1: Optimization of the shaking times and concentrations for Zn (A and C), Cu (B and D) and Pb (E and F) within and outside of the halo, NH <sub>4</sub> EDTA method .....	269
Figure D.2: Optimization of the shaking times and concentrations of S for sample from inside of the halo, Ca (H <sub>2</sub> PO <sub>4</sub> ) <sub>2</sub> method .....	272
Figure D.3: Flow chart of the separation of magnetic and non-magnetic parts of calcrete samples [(in bracket): sample number for XRF analysis] .....	283
Figure E.1: XRD result for original sample KPR12/4 .....	301

Figure E.2: XRD result for sample Non-Mag 1 .....	301
Figure E.3: XRD result for sample Non-Mag 2 .....	302
Figure E.4: XRD result for sample Non-Mag 3 .....	302
Figure E.5: XRD result for sample Mag 1 .....	303
Figure E.6: XRD result for sample Mag 2.....	303
Figure E.7: XRD result for sample Mag 3.....	304
Figure E.8: XRD result for sample Mag 4.....	304
Figure E.9: XRD result for sample Mag 5.....	305

List of Tables

	Page
Table 2.1: Regional succession of Copperton Formation .....	7
Table 2.2: Regional succession of Jannelsepan Formation in Upington area .....	8
Table 2.3: Regional succession of Bokspits Formation in Van Wykspan area .....	9
Table 2.4: Summary of geomorphic events .....	20
Table 2.5: Classification of calcrete based on the weather conditions (after Khadkikar et al., 2000) .....	25
Table 2.6: Different Formations of the Kalahari Group. Data summarised from Malherbe (1984) .....	27
Table 4.2: Chemical composition of spinel grains from Kantienpan .....	59
Table 4.3: The chemical composition of chlorite grains near the ore zone from Areachap and Kantienpan .....	60
Table 4.4: Peraluminous ratio, normative corundum value and minerals present in AP5 and KN11 .....	62
Table 4.5: The number of population, percentage, and threshold value for peraluminous ratio .....	63
Table 4.6: Percentage of gains and losses in borehole AP5 and $\Delta$ values for Areachap samples. Sample AP5/35 is assumed to be the malted precursor for altered samples AP5/23, 29, 30, and 32 (Isocon line based on Zr) .....	69
Table 4.7: Percentage of gains and losses in borehole AP5 and $\Delta$ values for Areachap sample. Sample AP5/42 is assumed to be the malted precursor for altered sample AP5/25 (Isocon line based on Zr) .....	71
Table 4.8: Percentages of gains and losses in borehole KN11 and $\Delta$ values for Kantienpan samples. Sample KN11/44 is considered to be the malted precursor for altered sample KN11/40 (Isocon line based on Zr) .....	72
Table 4.9: The least altered and altered samples based on the isocon Analysis .....	80

Table 5.1: Sorted data set based on the peraluminous factor (FPer) for the regional data set .....	94
Table 5.2: Sorted data set based on the alteration factor (FAR) for the regional data set .....	95
Table 5.3: Sorted data set based on the pelitic factor (FPR) for the regional data set	95
Table 5.4: Sorted data set based on peraluminous factor and calculation of amphibolite factor for the regional data set .....	97
Table 5.5: Sorted the peraluminous factor (FPer) and calculation of biotite-hornblende-gneiss factor for the regional data set .....	101
Table 5.6: Sorted the peraluminous factor (FPer) and calculation of the leucogneiss for the regional data set .....	103
Table 5.7: The threshold value for each factor, regional data set (n= 2016 samples) .....	106
Table 5.8: The threshold value for peraluminous and alteration factors, regional data set (n= 975 samples) .....	107
Table 5.9: The sample numbers and localities for anomalous samples with selected chemical data .....	108
Table 5.10: The threshold value for Zn, Cu and Ni, regional data set (n= 57 samples) .....	111
Table 5.11: Ranking the anomalous values based on MgO & K <sub>2</sub> O contents, peraluminous ratio, AI, CCPI, FAR and FPer .....	113
Table 6.1: Different extractants classified by acidity (sequential leaching process and/or selective leaches) .....	122
Table 6.2: Some other extractants for selective leaching .....	122
Table 6.3: Selective extraction methods for Cu, Zn, Pb, Cd and S in the soil .....	123
Table 6.4: Results of the normality test for the data from Kantienpan (ICP-MS method, n = 52) .....	127
Table 6.5: The threshold values of elements in the Kantienpan data set (ICP-MS method, n=52 samples) .....	127

Table 6.6: The results of the normality test for the data set from Kantienpan (ICP-MS method, n = 52) .....	129
Table 6.7: The threshold values for whole Areachap data set (NH <sub>4</sub> EDTA method, n=61) .....	129
Table 6.8: The normality test of distribution of S in Kantienpan data set (ICP-MS method, n = 33 samples) .....	131
Table 6.9: S values for samples within and outside the halo and blank sample, Kantienpan and Areachap .....	131
Table 6.10: The threshold values of S for the Kantienpan data set (ICP-MS method, n=33 samples) .....	132
Table 6.11: The normality test for the distribution of S in the Areachap data set (ICP-MS method, n = 21 samples) .....	132
Table 6.12: The threshold values of S for the Areachap data set (ICP-MS method, n=21 samples) .....	133
Table 6.13: Results of the normality test (MMI method, n = 58 samples) .....	133
Table 6.14: The threshold values of Cu and Zn (MMI method, n=58 samples) .....	134
Table 6.15: Results of the normality test for regolith traverse of KP12 (XRF method, n = 19) .....	135
Table 6.16: Threshold values for regolith traverse KP12 (XRF method, n=19) .....	135
Table 6.17: The threshold value of Zn for regolith traverse KP12 (XRF analysis, n=19 samples) .....	136
Table 6.18: Results of the normality test for regolith traverse of T2 (XRF method, n = 25) .....	136
Table 6.19: Threshold values for regolith traverse T2 (XRF method, n=25) .....	138
Table 6.20: Threshold values for Zn, regolith traverse T2 (XRF method, n=25 samples) .....	138
Table 6.21: Anomaly to background ratio of different analytical methods for Cu, Zn, Pb, Mn and S .....	169

Table 6.22: The comparison of major and trace elements in original, magnetic and non-magnetic parts of calcrete sample KP12/4, Kantienpan (A: ampere) .....	172
Table 6.23: Mineralogical ratios of the more common minerals in magnetic and non-magnetic part of the calcrete .....	173
Table 6.24: The comparison of major oxides and trace elements of interest in visually cleaned parts of calcrete samples in the Kantienpan (A: ampere; *: semi-quantitative analyses) .....	174
Table 6.26: Chemical composition of visually cleaned calcretes near the ore zone (Calc1-3 and Calc2-3 at Areachap) and further away from the mineralized zone (Vcal2 and Vcal3) .....	180
Table A.1: Depth of samples in drill hole AP2, Areachap .....	210
Table A.2: Depth of samples in drill hole AP5, Areachap .....	211
Table A.3: Depth of samples in drill hole KN12, Kantienpan .....	212
Table A. 4: Lithological description of borehole KN12 (Rossouw, 2003) .....	213
Table A. 5: Lithological description of borehole KN7 (Rossouw, 2003) .....	214
Table A. 6: Lithological description of borehole KN3 (Rossouw, 2003) .....	215
Table A. 7: Lithological description of borehole KN2 (Rossouw, 2003) .....	216
Table A.8: Depth of samples in drill hole KN11, Areachap .....	217
Table A. 9: Lithological description of borehole KN11 (Rossouw, 2003) .....	218
Table B.1: Chemical composition of feldspar grains adjacent to the ore zone (Areachap and Kantienpan) .....	221
Table B.2: Chemical composition of pyroxene grains near the ore zone (Areachap and Kantienpan) .....	222
Table B.3: Chemical composition of cordierite grains close to the ore zone (Areachap and Kantienpan) .....	223
Table B.4: Chemical composition of garnet grains adjacent to the ore zone (Areachap) .....	224
Table B.5: Chemical composition of biotite grains near the ore zone (Areachap and Kantienpan) .....	224
Table B.6: Chemical composition of gahnite (spinel group) grains close the ore zone (Kantienpan) .....	225

Table B.7: Chemical composition of chlorite grains near the ore zone (Areachap and Kantienpan) .....	225
Table B.8: Chemical composition and unit formulae of plagioclase grains close to the ore zone (Areachap and Kantienpan) .....	226
Table B.9: Chemical composition and unit formulae of pyroxene grains close to the ore zone (Areachap and Kantienpan) .....	227
Table B.10: Chemical composition and unit formulae of cordierite grains near the ore zone (Areachap and Kantienpan) .....	229
Table B.11: Chemical composition and unit formulae of garnet grains near the ore zone (Areachap) .....	230
Table B.12: Chemical composition and unit formulae of biotite grains near the ore zone (Areachap and Kantienpan) .....	231
Table C.1: Standard deviation and detection limit of XRF analysis .....	234
Table C.2: XRF analytical results for samples from borehole AP5 (Areachap) .....	235
Table C.3: XRF analytical results for samples from borehole AP2 (Areachap) .....	241
Table C.4: XRF analytical results from surface (Kantienpan) .....	245
Table C.5: XRF analytical results for samples from borehole KN12 (Kantienpan) .....	247
Table C.6: XRF analytical results for samples from borehole KN11 (Kantienpan) .....	253
Table D.1: ICP-MS analytical results of wind blown sand samples (5 gram sample + 50 ml of 0.2 M NH <sub>4</sub> NO <sub>3</sub> solution, 30minute shacking times) .....	263
Table D.2: Results of statistical analysis on duplicate samples and the null hypothesis (0.2 M NH <sub>4</sub> NO <sub>3</sub> solution, 30 min shacking time, n=16) .....	264
Table D.3: ICP-MS analytical results of sand samples (2.5 gram sample + 45 ml of 1 M NH <sub>4</sub> OAC solution, different shacking times) .....	265
Table D.4: Results of statistical analysis on duplicate samples and null hypothesis (1 M NH <sub>4</sub> OAC solution, different shacking time, n=13) .....	266
Table D.5: ICP-MS analytical results of sand samples (2 gram sample + 50 ml of 0.02 M NH <sub>4</sub> EDTA solution, different shacking times) .....	267
Table D.6: Results of statistical analysis on duplicate samples and null hypothesis (1 M NH <sub>4</sub> EDTA solution, different shacking time, n=9) .....	268
Table D.7: ICP-MS analytical results of sand samples for sulphur (5 grams sample + 50 ml of 0.02 M Ca (H <sub>2</sub> PO <sub>4</sub> ) <sub>2</sub> solution, 120-minute shacking times) .....	271
Table D.8: Results of statistical analysis on duplicate samples and null hypothesis (0.02 M Ca (H <sub>2</sub> PO <sub>4</sub> ) <sub>2</sub> solution, different shacking times, n=12) .....	271

Table D.9: ICP-MS analytical results of sand samples for S for different shaking times (5 gram sample + 50 ml of 0.02 M Ca (H <sub>2</sub> PO <sub>4</sub> ) <sub>2</sub> solution) .....	272
Table D.10: XRF analytical results of regolith sampling traverse KP12 for the <75 μ size fraction .....	273
Table D.11: XRF analytical results of regolith sampling traverse T2 for the <75 μ finest size fraction .....	274
Table D.12: ICP-MS results of regolith sampling traverse KP12 (0.02 M Ca (H <sub>2</sub> PO <sub>4</sub> ) <sub>2</sub> solutions for S, shaking time: 120-minutes, and 0.02 M NH <sub>4</sub> EDTA solutions for the rest of the elements shaking time 180-minutes) .....	275
Table D.13: ICP-MS results of regolith sampling traverse KP5 (0.02 M NH <sub>4</sub> EDTA solutions for Cu, Zn, Pb, Ba, Mn and Fe, shaking time: 180-minutes) ..	276
Table D.14: ICP-MS results of regolith traverse KP8 (0.02 M NH <sub>4</sub> EDTA solutions for Cu, Zn, Pb, Ba, Mn and Fe, shaking time: 180-minutes) .....	277
Table D.15: MMI results of regolith traverses 7700NW and 7800NW for Cu and Zn (Rossouw, 2003) .....	278
Table D.16: ICP-MS results of regolith sampling traverse T1 (0.02 M NH <sub>4</sub> EDTA solutions for Cu, Zn, Pb, Ba, Mn and Fe, shaking time: 180-minutes; <75μ size fraction) .....	279
Table D.17: ICP-MS results of regolith sampling traverse T3 (0.02 M NH <sub>4</sub> EDTA solutions for Cu, Zn, Pb, Ba, Mn and Fe, shaking time: 180-minutes; <75μ size fraction) .....	280
Table D.18: ICP-MS results of regolith sampling traverse T2 (0.02 M NH <sub>4</sub> EDTA solutions for Cu, Zn, Pb, Ba, Mn and Fe, shaking time: 180-minutes; <75μ size fraction) .....	281
Table D.19: XRF results of the magnetic, non-magnetic and visually cleaned parts of the calcrete sample KPR12/4, Kantienpan (major elements: wt. %) .....	284
Table D.20: XRF results of calcrete samples and magnetic parts, Kantienpan (major elements: wt. %, A: ampere) .....	286
Table D.21: XRF results of calcrete samples and magnetic parts, Kantienpan (major elements: wt. %, A: ampere) .....	289
Table D.22: XRF results of calcrete samples and magnetic parts, Areachap (major elements: wt. %, A: ampere, Sample set Calc1) .....	291
Table D.23: XRF results of calcrete samples and magnetic parts, Areachap (major elements: wt. %, A: ampere, Sample set Calc2) .....	293

Table D.24: Chemical composition of calcretes near the ore zone (Calc1-3 and Calc2-3) and further away from ore zone (Vcal2 and Vcal3) .....	295
Table D.25: Chemical composition of magnetic parts of calcretes near the ore zone (Calc1-3) and further away from ore zone (Vcal2 and Vcal3) (A: ampere in) .....	297
Table D.26: Chemical composition of calcretes near and further away from ore zone analyzed by the XRF method (Vermaak, 1984) .....	299
TABLE E.1: Instrument and data collection parameters .....	300

# Chapter 1

## Introduction

### **1.1. Purpose of the investigation**

The principal purpose of this study is to characterise the primary and secondary geochemical halo's related to volcanic-hosted massive sulphide (VHMS) deposits in the highly deformed and metamorphosed rocks in the eastern part of the Namaqua Province. For this purpose two unexploited (largely), but well explored, VHMS deposits were selected namely the Areachap and Kantienpan deposits. Litho-geochemical characterization of the primary haloes is based on borehole samples of the footwall, ore zone and hanging wall successions, whereas the secondary dispersion haloes are studied in samples of the calcrete and sand cover.

The principal research questions could be phrased as follows:

- a) Could primary geochemical halo's that formed at the time of sulphide mineralization be identified in these rocks that suffered various phases of deformation and metamorphism?
- b) Are secondary dispersion halo's evident in wind deposited sand cover and the underlying calcrete regolith that formed in a semi arid environment?

The objective with this investigation is to show which geochemical methods could be used in future exploration programmes. The proposed litho-geochemical methods would be demonstrated utilizing a set of litho-geochemical samples collected in the region.

### **1. 2. Locality of the study area**

The area investigated in this study is located in the Northern Cape Province of the Republic of South Africa (Fig. 1.1). Within this area, the study focussed on the selected localities mentioned above.

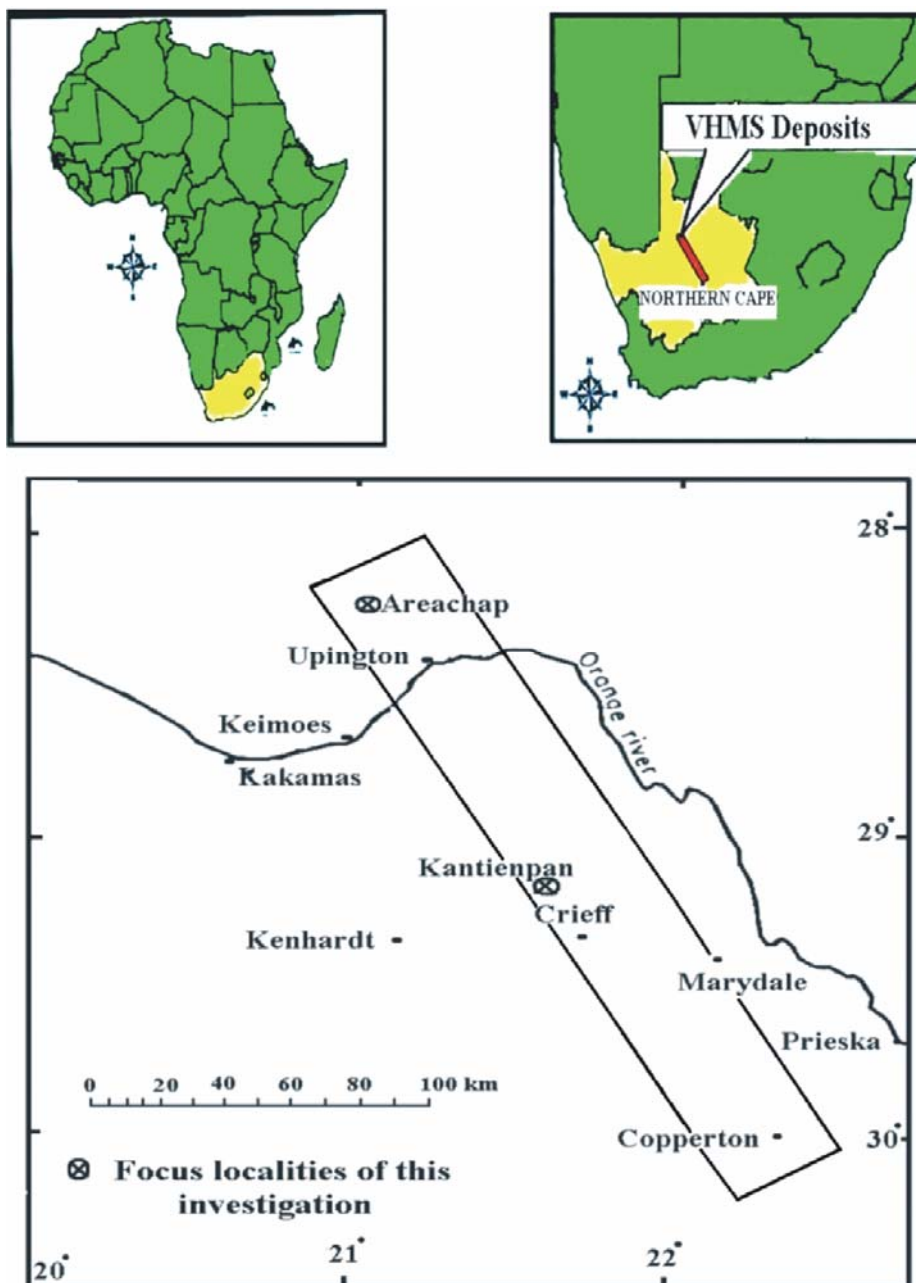


Figure 1.1: Location map

The defunct Areachap Cu-Zn mine is situated on the farm Areachap 426, 22 km northwest of Upington, in the Gordonia district. The area is flat, with an average height of 915 to 922 meter above sea level. The study area is readily accessible by gravel or sandy roads. A 12 km gravel road links the Areachap with Upington-Namibia national road.

The Kantienpan Cu-Zn deposit is situated on the farms Kantienpan 119 and Gemsbok Bult 120, about 85 km southeast of Upington in the Kenhardt district. The area is flat, with an

average height of 1060 meters above sea level. The study area is readily accessible by secondary sandy roads.

### **1.3. The method of investigation**

The method of investigation is divided into four sections. The first of these entails a comprehensive literature review of the geology of the Upington Terranes, eastern Namaqua Province where previously recognized VHMS deposits occurring in an area affected by deformation and high grade of metamorphism, weathering and erosion in a dry, semi arid climate could be studied to determine the effectiveness of modern geochemical exploration methods. The second section encompasses a literature review of the formation of the VHMS deposit focussing on the alteration features that characterise the sulphide mineralization event. Thirdly the lithogeochemical dispersion of the primary hydrothermal alteration is studied in rocks that have suffered various phases of deformation and metamorphism. This is done by considering both whole rock and mineral chemistry. Lastly, the secondary dispersion of geochemical halo's in the more recent soil and sand cover would be identified to determine the most appropriate geochemical exploration methodology for the discovery of similar deposits in areas affected by similar climatic condition.

In addition, a private company, Kumba Resources Limited, has kindly provided a set of rock sample results from this area to demonstrate the applicability of lithogeochemical exploration factors that could lead to the detection of sulphide mineralization.

### **1.4. Acknowledgements**

I would like to thank my supervisor, Prof H.F.J. Theart, for his support and effective guidance in this thesis. I am grateful to Prof S.A. de Waal for the financial support from the Centre for the Research of Magmatic Ore Deposits, University of Pretoria. Thanks are also due to Kumba Resources Limited for access to the borehole samples and field visits with Mr. D. Rossouw and for permission to use their regional lithogeochemical data base.

I am grateful to several people who helped during the course of this work. Mr. P.C. De Jager is thanked for his support and advice during the sand preparation and analysis. M

Classen and P Sibiya are thanked for their assistance with making of the thin sections. Thanks must also be given to Mrs. M. Loubser and Dr. S. Verryn for analyzing samples by XRF and XRD. Dr. S. Verryn is also so thanked for assistance in analysing the XRD results. I also wish to thank Mr. P. Graser for assistance during microprobe analyses and Miss. I. Chimeloa for drafting some of the geological maps.

I am extremely thankful to my wife, Jina, who left her relatives, friends and work to spend four years with me in South Africa. Without her support, patience, understanding and prayers during the long hours of working, this thesis would not have been possible.

## Chapter 2

# Geology of the Upington Terrane, Eastern Namaqua Province

### 2.1. Introduction

The Areachap Group in the eastern part of the Namaqua Province contains a number of volcanic hosted massive sulphide (VHMS) deposits such as the Copperton, Kantienpan, and Areachap ore bodies (Rossouw, 2003; Cornell et al., 1990a; Theart, 1985). In this chapter the crustal evolution of the eastern part of the Namaqua Metamorphic Province will be discussed to explain the metamorphism and deformation, which affected these deposits. This will be followed by a discussion of the regional geological succession and local geology of each of the areas mentioned above, focussing on the geological sequences near the ore body.

As this investigation also considers the secondary environment it is important to also discuss the evolution of the present erosion surface. For this, the different geomorphic events that affected the African earth's surface since the Mesozoic times till the present are considered. The calcretization process is particularly important because of its influence on the secondary dispersion of the ore forming elements.

## **2.2. Tectonic setting and regional geological succession**

The Kibaran Supercrustal Sequence (1600 to 1300Ma) was deposited on the Eburnian basement (2000 Ma) in the western Namaqua Terrane (Thomas et al., 1994a). The lithology of this sequence may indicate that there was an oceanic basin between the Kaapvaal and the older parts of the Namaqua Province at approximately 1600 Ma (Theart, 1985) (Fig. 2.1). The oceanic basin was affected by calc-alkaline and tholeiite volcanism until  $1285 \pm 14$  Ma (Cornell et al., 1990a) in the area now preserved in the east-central Namaqua-Natal Province. These extrusive rocks and associated sediments were preserved in the Areachap Group of the eastern part of the Namaqua Province and in the Mfongosi Group of Natal Province (Thomas et al., 1994a). During the period of volcanism, volcanogenic massive sulphide deposits formed on the sea floor due to reactions between the hydrothermal fluids and seawater (Cornell et al., 1990a). This was followed by plate convergence, thrusting, ductile transcurrent shearing, thickening of the crustal sequence, and intensive deformation from 1200 Ma to 1000 Ma due to a northwest-southeast-directed stress regime (Thomas et al., 1994a). The Koras and Sinclair Groups consisting of calc-alkaline volcanic and sedimentary rocks, were formed during the late syn-collision event at  $\sim 1150$ Ma (Jacobs et al., 1993). The collision of cratons and the related events led to high-grade metamorphism and widespread melting and generation of voluminous granitoid batholiths magma (I-type granites) between 1200 to 1000Ma (Geringer et al., 1994).

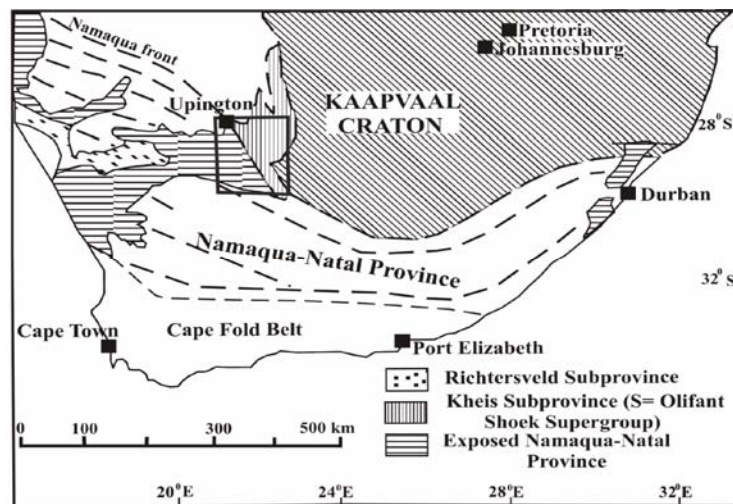


**Figure 2.1:** The location of Namaqua-Natal Province (After Moen, 1999) and the study area.

The study area considered here falls within the Gordonia Sub Province of the Namaqua Province (Fig. 2.2). Supercrustal rocks in this Sub Province belong to the Areachap Group comprising the Jannelsepan, Bokspuits and Copperton Formations (Barton et al., 1983; Cornell et al., 1990a; Rossouw, 2003). Middleton (1976) and later Geriner et al. (1994) suggested that the Copperton, Bokspuits and Jannelsepan Formations are time equivalents formed from separate volcanic centres.

Middleton (1976), Gorton (1981), Theart (1985) and Cornell et al. (1990a) suggested the volcanic precursors of the rocks related to deposits within the Copperton Formation. The major and trace elements geochemistry (Theart et al., 1989), and the zircon crystal form (Pupin, 1980) were interpreted as evidence for an igneous origin of the Smouspan Gneiss Member (Table 2.1), which forms the footwall to the Copperton VHMS deposit. It is suggested that this formed as dacitic lava (Theart, 1985; Cornell et al., 1992). The Copperton deposit itself is hosted within the Prieska Copper Mines Member (Theart, 1985) and this is overlain by the Volgelstruisbult Member (Theart, 1985; Theart et al., 1989; Cornell et al., 1992) (Table 2.1). The lithological succession of the Copperton Formation is summarized in Table 2.1.

**Table 2.1:** Regional succession of Copperton Formation

Member or Group	Lithological description [Reference]	Formation or sub-province
Volgelstruisbult Member	Interbanded amphibolites pelitic Gneiss, Hbl-and Bio-Gneiss and diopside-bearing calc-silicate <sup>[3]</sup>	Copperton Formation
Prieska Copper Mines Member	Peraluminous gneiss and schist including Metalliferous zone (massive sulphide) <sup>[2]</sup>	
Smouspan Member	Hornblende-biotite gneiss <sup>[1]</sup>	
Magazine Member	Interbanded calc-silicate quartzites and amphibolite <sup>[1]</sup>	
Doonerspan Leucogneiss Member	Leucocratic hornblende and biotite gneisses <sup>[4]</sup>	
Marydale Group	Amphibolites and quartzitic rocks <sup>[1]</sup>	Kheis sub-province

[1]: Geringer et al., 1994, [2]: Middleton, 1976; Theart et al., 1989; Cornell et al., 1990b

[3]: Humphreys et al., 1988a, [4]: Humphreys et al., 1988b

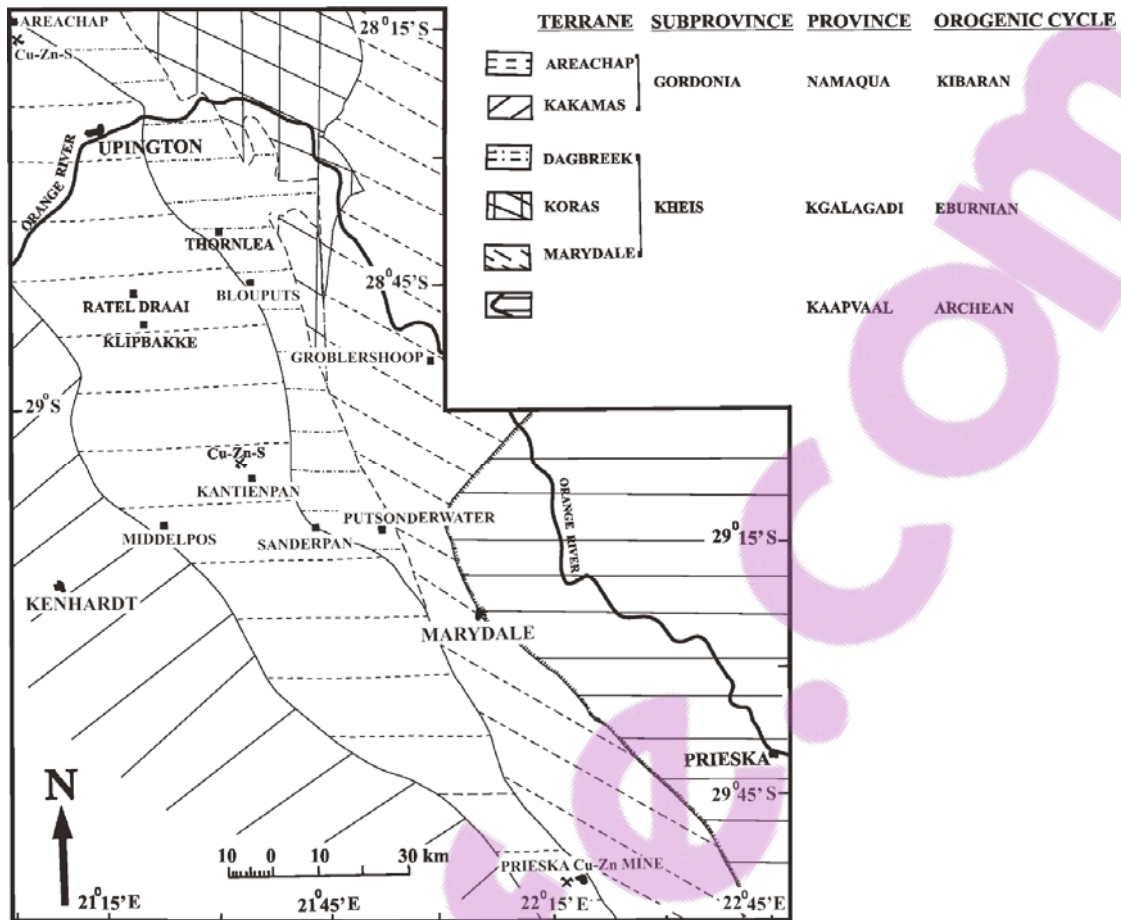


Figure 2.2: Geological map of the Areachap Group in the eastern part of Namaqua Sub-province.

The Jannelsepan Formation hosting the VHMS deposits at Areachap (Theart, 1985; Voet and King, 1986; Theart et al., 1989; Cornell et al., 1990a; Rossouw, 2003) comprise four members. These are the Swartkop, Quarry, Donkerkoekspruit and Skietbaan Members and a summary of the respective lithologies is given in Table 2.2.

Table 2.2: Regional succession of Jannelsepan Formation in Upington area

Member or Group	Lithological description [Reference]	Formation or sub-province
Swartkop Member	Porphyroblastic diopside bearing amphibolite with intercalated calc-silicate <sup>[2]</sup>	Jannelsepan Formation
Quarry Member	Banded biotite gneiss <sup>[1]</sup>	
Donkerkoekspruit Member	Hornblende-biotite gneiss, biotite-hornblende gneiss and massive amphibolite <sup>[1]</sup> including metalliferous zone	
Skietbaan Member	Quartzo-feldspathic gneiss <sup>[1]</sup>	
Micaceous schist (including quartz-feldspar gneiss, quartzites, amphibolite, and quartzitic conglomerate)		Sprigg Formation

[1]: Geringer, et al., 1994, [2]: Ludick, 1987

Geringer (1994) suggested that the Bokspuits Formation and Jannelsepan Formation are time equivalents. Rossouw (2003) described the Kantienpan deposit in the Bokspuits Formation, in the Van Wykspan area (see Table 2.3) as a VHMS deposit.

**Table 2.3:** Regional succession of Bokspuits Formation in Van Wykspan area

Lithological description [Reference]	Formation or sub-province
Diopside amphibolite <sup>[1]</sup>	Bokspuits Formation
Hornblende gneiss, massive amphibolite <sup>[1]</sup> and including metalliferous zone	
Quartzo-feldspathic gneiss <sup>[1]</sup>	

[1]: Geringer et al., 1994

### **2.3. Regional metamorphism and tectonism**

The rocks belonging to the Areachap Group were affected by a complex deformation and metamorphic history closely related to the accretion of tectonic terranes within the Namaqua metamorphic complex and the subsequent accretion of these terranes with the Kaapvaal Craton (Hartnady et al., 1985; Moor et al., 1990; Thomas et al., 1994a).

Cornell et al. (1992) proposed an empirical pressure-temperature-time (P-T-t) path explaining the metamorphic evolution of the Areachap Group rocks at the Prieska Cu-Zn mine. This evolution will be summarized and amended to relate to the entire Areachap Terrane. They proposed an original age of the rock succession of 1285 Ma, which most probably represent an early metamorphic age with the age of the succession closer to 1599 Ma (Theart, 1985; Theart et al., 1989; Schade et al., 1989).

Rocks of the Areachap Group were affected by the early collision events (Cornell et al., 1992) that lead to a rapid increase in pressure during thrust dominated, deep level deformation resulting in the early phase of isoclinal to shear folding (F1 and F2) and mineral parageneses reflecting upper amphibolite to granulite grade (M<sub>1</sub>) metamorphic conditions (Theart, 1985; Humphreys et al., 1988a) at a pressure of approximately 7Kbar and a temperature of approximately 525 to 600°C (Cornell et al., 1992). This event is most probably related to accretionary processes affecting the Areachap and Kakamas

Terranes as similar deformation and metamorphism are displayed by their supercrustal successions.

Thermal relaxation (Cornell et al., 1992) caused by the wide spread intrusion of granitic melts now seen as well foliated gneisses resulted in the pervasive high temperature (500°C) high pressure (7 Kbar) mineral parageneses largely replacing earlier metamorphic assemblages (Theart, 1985; Theart et al., 1989) giving rise to the predominant high grade M<sub>2</sub> metamorphic minerals assemblages reflecting upper amphibolite grade conditions. It is believed that these conditions also existed in the Kakamas Terrane. Uplift and erosion (Cornell et al., 1992) lead to a gradual decrease in pressure (5.5 Kbar) at almost the same temperature (500°C). Even through no discretely different mineral parageneses could be related to this time there is a marked difference in the style of deformation. Whereas the earlier isoclinal folds had predominantly sub horizontal axial cleavage foliation planes, deformation now resulted in a series of phases of folding where the axial planes are sub vertical and the folds themselves formed through a process of buckle folding (F3 and F4) (Theart, 1985). This deformation probably took place at higher tectonic levels during the assembly of the various terrains forming the Kibaran Namaqua Province. The folding, especially the later phase is directly related to the formation of shear zones responsible for the juxtaposition of the different terranes.

Cornell et al. (1992) referred to the next event as a thermal excursion, as its impact is seen in the development of grain boundary textures (M<sub>3</sub>) indicative of an influx of fluids at a high temperature (800°C) and slightly lower pressure (4 Kbar), resulting in the replacement of M<sub>1</sub> cordierite along grain boundaries by sillimanite phlogophite and almandine. This event is characterized by the replacement of hypersthene by anthophyllite and gedrite, and the invasion of feldspar grains by myrmekitic intergrowths of quartz and albite (Theart et al., 1989). Cornell et al. (1992) ascribed this to a contact metamorphic effect caused by the intrusion of the Plat Sambok Anorthosite Suite in the vicinity of the Prieska Cu-Zn mine. However as these features are also evident throughout the Areachap Group, the events influence must be assumed to have affected

all the supracrustal rocks from the Prieska Cu-Zn mine in the south to the Areachap mine in the north (Theart, 1985). This is far more pervasive than contact metamorphism related to a localized intrusion and it is suggested here that this thermal excursion resulted from the wide spread intrusion of the late tectonic Vaalputs or Keimoes Suite. These often show intrusions a metasomatic contact metamorphic halo' surrounding them. Rocks within these contact metamorphic halo's were described as kinzigites by (Stowe, 1983; Moen, 1988). The intrusions of these granites at 1100 Ma may be regarded as a stitching event after the accretion of the Kakamus and Areachap Terranes, as the intrusions cut across tectonic boundaries.

Following the intrusion of these large batholiths, the steady state geotherm is re-established (Cornell et al., 1992) and conditions returned to a temperature of approximately 500°C and a pressure of less than 4 Kbar. The Areachap Terrane now becomes the leading edge during the northward convergence of the Namaqua-Natal Province and the Kaapvaal Craton (Van Zyl, 1981; Stowe, 1983). This accretionary event also incorporated the Eburnian Dagbreek and Koras Terranes, and the Archean Marydale Terrane of the Kheis Subprovince (Thomas et al., 1994a), situated between rocks belonging to the Namaqua Province and the Kaapvaal Craton. Shear zones within the Namaqua Province recorded north ward shortening in excess of 400 km (Stowe, 1983) and reflects retrogressive metamorphism (M<sub>4</sub>) caused by ascending hydrothermal fluids (Theart et al., 1989). Cornell et al. (1992) suggested that this final accretionary event took place some 965 Ma ago and that the region reached surface at 550 Ma.

## **2.4. Regional data set**

Kumba Resources Limited sampled rock outcrops in a long traverses and large area. In total 59481 records are in Kumba's data file, but most of these records include zero values. In total 2016 rock samples of this data set, which does not have zero value, were used in this investigation.

The following elements were analyzed in the Kumba data set:

- 1) Major oxides: FeO, Fe<sub>2</sub>O<sub>3</sub>, MnO, TiO<sub>2</sub>, CaO, K<sub>2</sub>O, P<sub>2</sub>O<sub>5</sub>, SiO<sub>2</sub>, Al<sub>2</sub>O<sub>3</sub>, MgO, and Na<sub>2</sub>O;
- 2) Trace elements: Cl, S, Cu, Zn, Ni, Pb, As, Ba, Cd, Rb, and Sr; and
- 3) LOI and Total values were calculated.

Multivariate analyses were only used on these elements, although the following trace elements were analyzed in this research:

Co, Cr, F, Sc, V, As, Ga, Mo, Nb, Ni, Rb, Sr, Th, U, W, Y, Zr, Ba, La, and Ce.

For confidentiality reasons and to protect the company's interests, none of the sample coordinates, or maps indicating the locality of anomalous samples could be included here. The relevant information was however reported to Kumba Resources Limited and to Prof H F J Theart.

## **2.5. Local geology**

### **2.5.1 Lithological succession at Areachap mine**

The lithological variations near the ore zone at the defunct Areachap mine were examined by Voet and King (1986) and Theart (1985). In the current investigation, two boreholes were selected, sampled and the results were logged (boreholes AP5 and AP2, Appendix A). Samples were taken at sampling intervals of 2 to 5m in the ore zone and 10 to 15m away from the ore zone. Borehole AP5 was selected for studying rock successions southwest of the ore body and for constructing the cross-section of the area as this borehole intersects hangingwall, ore zone and footwall, thus providing a complete section (Fig. 2.3). The geological units near the massive sulphide deposit are also shown in the geological map of the Areachap deposit (Fig. 2.4). The major lithological rock types of the Jannelsepan Formation at the Areachap mine as identified by Voet and King (1986) are described in the following paragraphs. Voet and King (1986) are of the opinion that the succession display repetition due to isoclinal folding.

### **Banded biotite-garnet gneiss (AR3)**

The unit is composed of quartz, highly saussuritized plagioclase, microcline, biotite, garnet, cordierite, sillimanite and secondary minerals i.e., green biotite and chlorite, and greenish pinitite (Theart, 1985). The rocks have a foliation defined by quartz and biotite under the microscope. Voet and King (1986) named this unit banded and foliated biotite-gneiss to biotite-garnet gneiss (chloritized in part). On the geological map (Fig. 2.4) the unit is referred to as AR3.

### **Quartzo-feldspathic gneiss (AR4)**

Unit AR4 represented by quartzo-feldspathic gneiss may have originated either a rhyolite or arkose layer, but this was not investigated here.

### **Banded hornblende-biotite gneiss (AR5)**

The banding in this unit is caused by green hornblende alternating with plagioclase in amphibolite, and biotite layers alternating with plagioclase and quartz domains in biotite-rich gneisses. The mineralogy of amphibolites includes green hornblende, plagioclase (labradorite), and accessory sphene (Theart, 1985). The biotite-rich layers consist of quartz, plagioclase, biotite, hornblende, apatite and epidote. The mineralogy of the leucocratic zones comprise plagioclase, quartz and biotite accompanied by secondary minerals i.e., fine mica, chlorite and epidote (Theart,

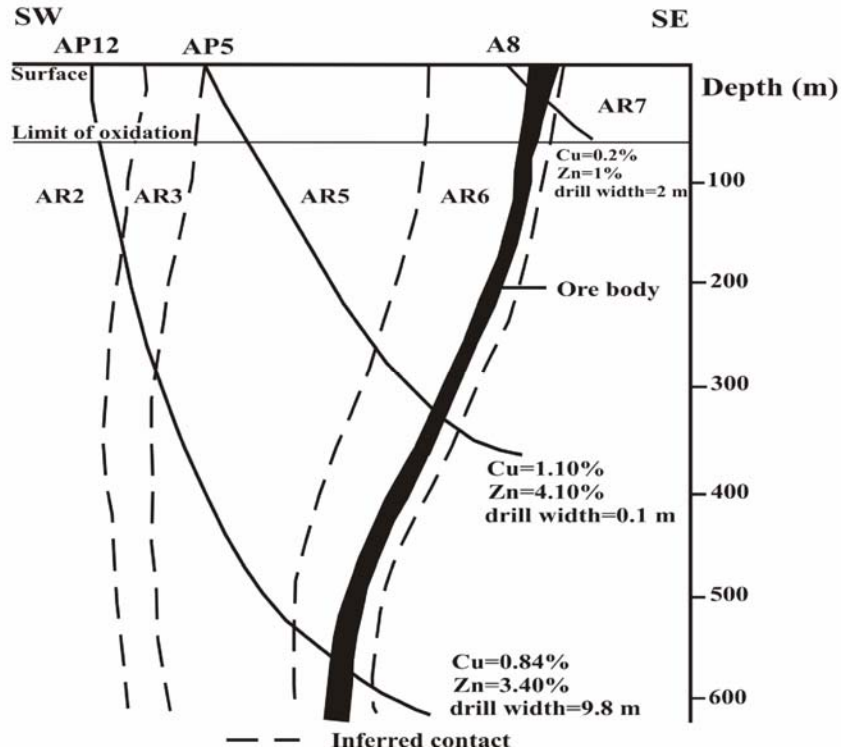


Figure 2.3: A cross-section of lithology at Areachap mine including the borehole AP5.

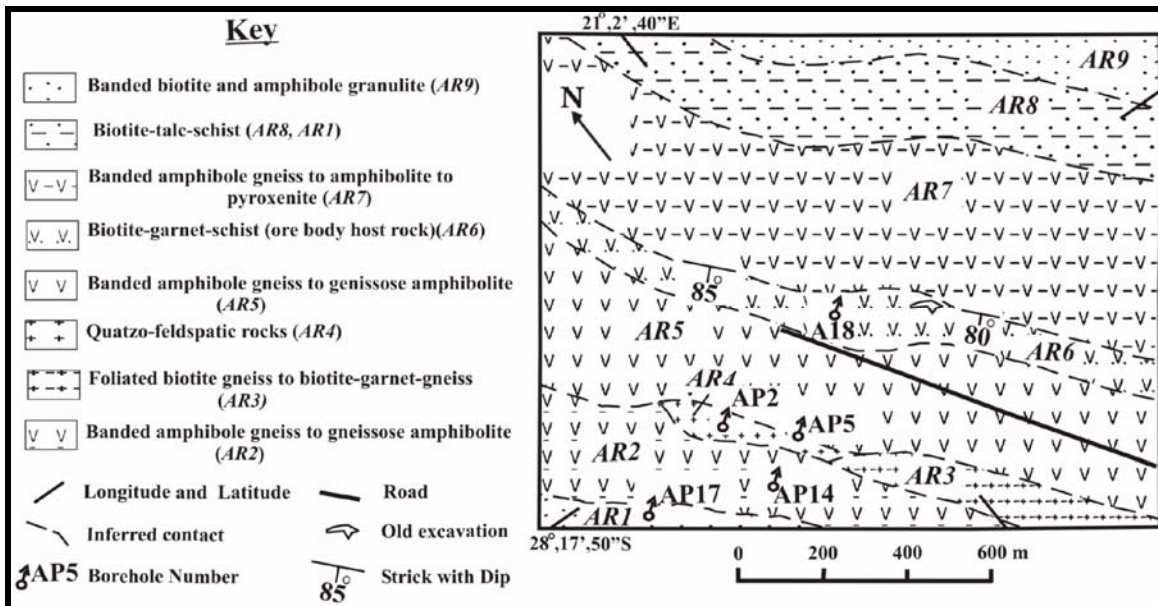


Figure 2.4: Geological map of the Areachap area (after Voet and King, 1986).

1985). Voet and King (1986) use the term grey green-banded amphibole gneiss for this unit which is referred to as AR5 on the map.

### **Banded amphibole gneiss to amphibolite (AR2)**

Units AR2 and AR5 indicated on the map of Voet and King (1986) were regarded as equivalent by Theart (1985) and these rocks may be seen as a correlate of the dacitic Smouspan Gneiss Member of the Copperton Formation. The Smouspan Gneiss Member represents the original footwall of the Prieska Cu-Zn mine (Theart, 1985).

### **Garnet-biotite-cordierite gneiss (AR6)**

This peraluminous unit forms the host rock of the massive sulphide deposit. The biotite is highly altered to chlorite. Cordierite rich rocks are more abundant on the southwestern side of the deposit compared to the northeastern side of the ore body (Theart, 1985).

The ore zone is characterised by two lensoid bodies (Voet and King, 1986). The massive sulphide layers include the sulphides pyrrhotite, pyrite, minor sphalerite, chalcopyrite and galena. Voet and King (1986) coined the name banded and foliated (amphibolitic) biotite-garnet schist (chloritized in part), AR6, for this unit.

### **A second unit of banded hornblende-biotite gneiss (AR7)**

This unit occurs adjacent to the garnet-cordierite-biotite gneiss on the northeastern side of the massive sulphide deposit (Theart, 1985). This unit when compared with the banded hornblende-biotite-gneiss on the southwestern side of the ore differs in that it is richer in garnet and amphibolite layers (Theart, 1985). The garnetiferous-biotite schist layers have a pelitic composition, with minerals quartz, biotite, plagioclase, garnet, sillimanite and pyrite. The mineralogy of the amphibolite layers includes hornblende, plagioclase, biotite, quartz, and sphene. Voet and King (1986) used the term AR7 or banded amphibolite gneiss for this unit.

### **Banded pelitic gneiss (AR8 and AR1)**

This unit is the only biotite-bearing gneiss in the area that does not have hornblende. The banded pelitic gneiss is similar to the host rocks of the sulphide ore body. Disseminated pyrite grains occur within some of the biotite schist bands of the unit (Theart, 1985). The mineralogy consists of quartz, plagioclase, biotite, fibrolitic

sillimanite, garnet, cummingtonite, and pyrite. Voet and King (1986) use the term garnet-biotite-talc schist, AR8 and AR1, for this unit.

### **Laminated biotite-gneiss (AR9)**

The unit occurs on the north-eastern side of the ore body. The mineralogy includes andesine, quartz, biotite and hornblende with no K-feldspar present (Theart, 1985). Voet and King (1986) refer to this unit as a banded biotite and amphibole granulite, AR9.

### **2.5.2. Metamorphism in Areachap Mine**

The mineral assemblages of the Areachap rocks i.e. feldspar, garnet, cordierite and sillimanite in AR6 unit and quartz-potassium feldspar-biotite-garnet or quartz-potassium feldspar-biotite-cordierite in AR3 unit are indicative of high-grade metamorphism (Theart, 1985). The rocks were then subjected to late-stage deformation as evidenced by the presence of a mylonitic fabric that is developed parallel to the lithological layering, and the large number of fractures present in the rocks. These fractures cause the rocks to be permeable resulting in aqueous fluids extensively altering the early mineral phases to muscovite, chlorite and epidote. These fluids were responsible for retrograde metamorphism, and partly destroyed the earlier metamorphic assemblages. These factors are related to M<sub>4</sub> conditions (Theart et al., 1989). Indicator minerals for this retrograde metamorphism could pinite after cordierite (in AR6), muscovite along late foliation planes (in AR5 and AR7 units) and chlorite after biotite (in AR5 and AR7 units) (Theart, 1985). The same sequences of tectono-metamorphic events have affected the Prieska Cu-Zn mine (Copperton Formation), Areachap mine (Jannelsepan Formation) and Kantienpan mine (Boksputs Formation) (Theart, 1985; Rossouw, 2003) of the Areachap Group (Wilson et al., 1998).

### **2.5.3. The sulphide minerals in the defunct Areachap mine**

The sulphide minerals described in the assumed footwall of this deposit include chalcopyrite, pyrite, and sphalerite. The ore zones comprise pyrite, sphalerite,

pyrrhotite, chalcopyrite, barite, anhydrite, and trace amounts of galena. Magnetite, pyrite and sphalerite are present in the assumed hanging wall successions at this deposit.

#### **2.5.4. Lithological succession of the Kantienpan deposit**

The geology of the ore zone at Kantienpan mine was described by Rossouw (2003). The geological map (Fig. 2.5) provided in Rossouw (2003) shows the local geology of the massive sulphide deposit. In the current investigation two boreholes were selected for sampling. Samples were taken at sampling intervals of 2 to 5m in the ore zone and 5 to 10m, away from the ore zone. The cross-section as drawn from borehole KN11 (Fig 2.6) was selected because this borehole intersects the hanging wall, ore zone and footwall. The major rock types of the Kantienpan deposit are described in the following paragraphs.

##### **Biotite-gneiss (Structural hanging wall)**

This unit consists of quartz, plagioclase, microcline, biotite, magnetite, and trace amount of hornblende and zircon suggesting that it's granitic in composition. The rock has interstitial magnetite and ilmenite, green hornblende and zircon. Rossouw (2003) described this unit as an orthogneiss.

##### **Hornblende-biotite-gneiss (Structural footwall)**

The principal minerals of this gneiss are quartz with minor amounts of plagioclase, biotite and minor to trace amounts of pyroxene, hornblende, and garnet. Magnetite is the main opaque mineral, with pyrite, pyrrhotite and very small amounts of chalcopyrite also present. This unit contains amphibolite layers, which are interpreted to represent the metamorphic equivalent of earlier dykes or sills (Rossouw, 2003).

Rossouw (2003) is of the opinion that this rock also represents an orthogneiss derived from a granite parent. But an alternative interpretation is that it was derived from a dacite layer (H.F.J. Theart, 2004, pers. Comm.).

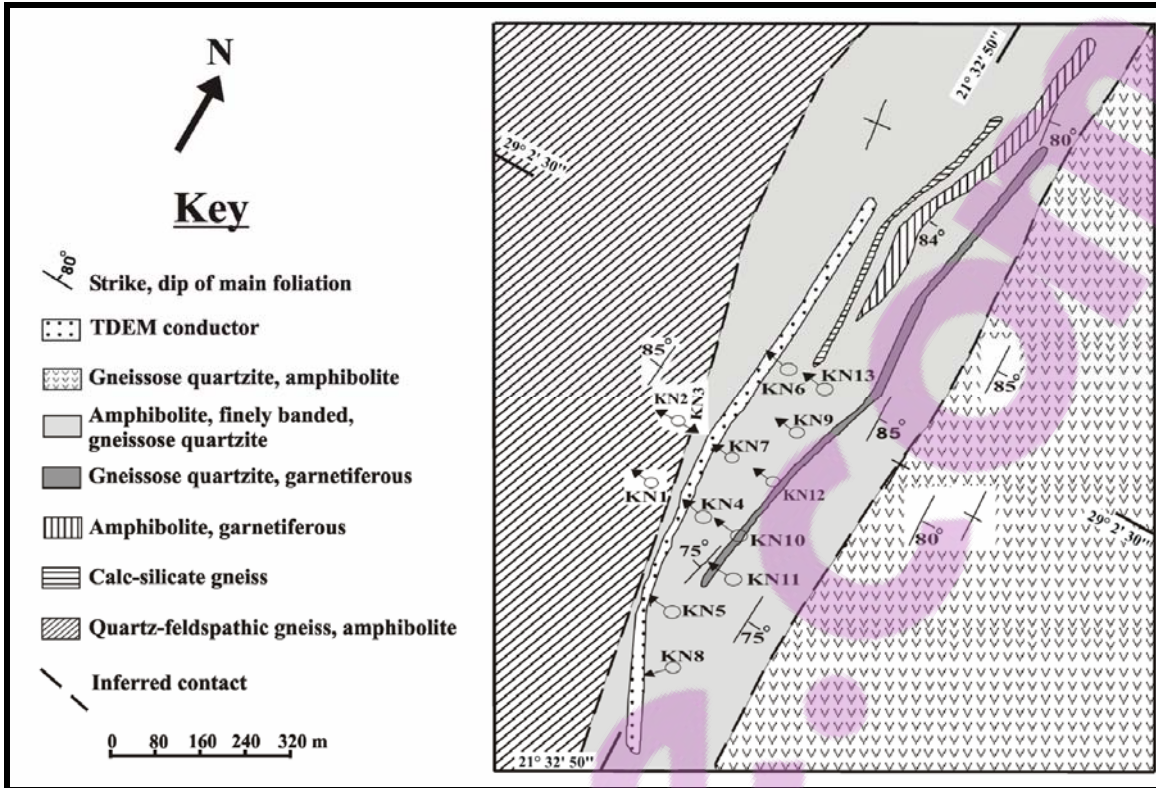


Figure 2.5: Geology map of the Kantienpan area (after Rossouw, 2003) (TDEM: Time domain electromagnetic conductor).

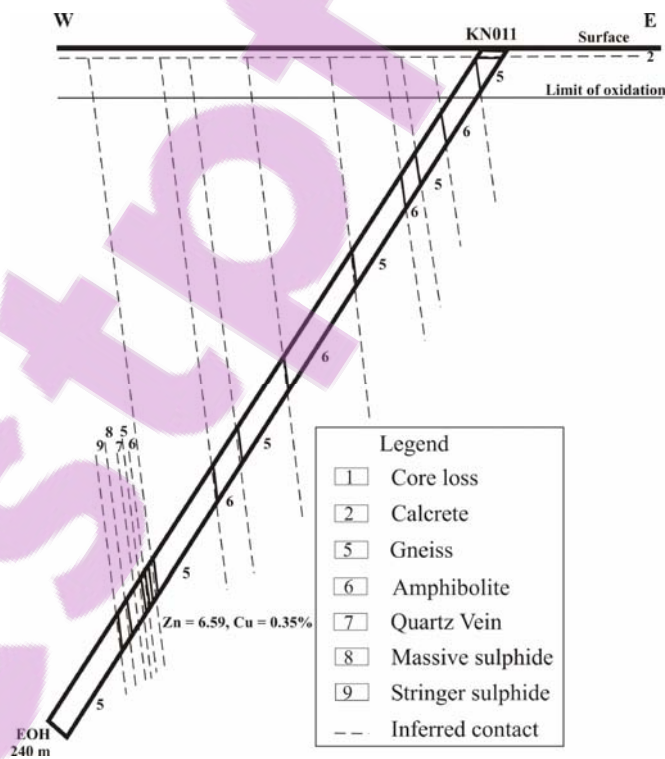


Figure 2.6: Cross-section of borehole KN11 (after Rossouw, 2003).

### **Mineralized zone**

The ore zone is dominated by pyrrhotite and sphalerite with minor amounts of chalcopyrite, pyrite and trace amounts of galena (Rossouw, 2003). The sulphide minerals occur as either patches of massive sulphides or disseminations in the host rock.

The sulphide minerals described in the assumed footwall of this deposit include pyrrhotite, chalcopyrite, and pyrite. Magnetite, pyrite and sphalerite are present in the assumed hanging wall successions at this deposit.

## **2.6. Geomorphological evolution**

Rocks belonging to the Areachap Group suffered repeated weathering and erosional events, since the first post metamorphic exposure to surface about 850 Ma ago (Cornell et al., 1992) prior to the Pan African sedimentation. In Table 2.4 a summary of geomorphological events is presented.

The earliest well-constrained geomorphological events coincided with the disintegration of Gondwanaland. This super-continent initially divided into east Gondwanaland and west Gondwanaland (Partridge et al., 1987; Moore, 1999). Although an earlier stage of separation dated at about 1150-1100 Ma were proposed by Partridge et al. (1987) this may coincide with the accretion of the Namaqua-Natal Province and the Kaapvaal Craton. More important is the second stage of Gondwana disintegration dated between 600-560 Ma (Cahen et al., 1984) as this follows on the first post metamorphic exposure of the Areachap Group discussed above. During this period the large parts of Africa were affected by convection generated orogenesis resulting in the formation of mobile belts during the Pan African episode (Cahen et al., 1984; Partridge et al., 1987). This was followed by denudation due to glaciation during the Dwyka times (300 Ma). Then a thick sedimentary cover belonging to the Karoo Sediment Group covered the entire region.

**Table 2.4:** Summary of geomorphological events

Era	Epoch	Age	Description	
Cenozoic	Middle Pleistocene		Ice age and cover the whole area by eolian sand <sup>1,2</sup>	
	Pliocene		Aridification <sup>1</sup>	
	Miocene			Uplift and Post-African II erosion cycle <sup>1</sup>
				Deformation of the post-African I surface by further uplift <sup>3</sup>
				Epirogenic uplift (Post-African I erosion cycle) <sup>4</sup>
	Oligocene			
	Eocene		Kaolinization and laterite duricrusts <sup>1</sup>	
Palocene		Calcretization in the Kalahari Group <sup>5</sup>		
Mesozoic	Cretaceous	~ 86-78 Ma	Second peak of sedimentation (basal Kalahari Group) <sup>3,6</sup>	
		~ 131-115 Ma	First peak of sedimentation <sup>3</sup>	
			African erosion cycle	
	Jurassic	~ 200-120 Ma	Separation of Africa from south America by a volcanic cycle (opening of the Atlantic basin and creating a Great Escarpment <sup>7</sup>	
The precipitation of Karoo sediments				
Paleozoic	Carboniferous	~ 300-289 Ma	Denudation due to glaciation during the Dwyka times <sup>1</sup>	
Neoproterozoic		~ 600-560 Ma	Secondary stage of Gondwana disintegration <sup>1</sup>	
Mesoproterozoic		~ 850 Ma	Post metamorphic exposure of the Areachap Group to surface <sup>8</sup>	
		~1150-1100 Ma	Disintegration of Gondwanaland into east and west Gondwana <sup>1,6</sup>	
		~ 1200-1050 Ma	Final stitching event of the different terranes belonging to the Namaqua-Natal Province <sup>9</sup>	
		~ 1600 Ma	VHMS deposits of Areachap Group in newly formed ocean floor <sup>9</sup>	
Palaeoproterozoic		~ 2000 Ma	Eburnian Basement currently to the west of the Areachap Terrane <sup>9</sup>	
Archaen		~ 3600 Ma	Kaapvaal Craton currently to the northeast of the Areachap Terrane <sup>10</sup>	

1. Partridge et al., 1987    2. Malherba, 1984    3. Dingle et al., 1983    4. Cogley, 1985    5. Netterberg, 1970    6. Moore, 1999    7. Summerfield, 1985    8. Cornell et al., 1992    9. Thomas et al., 1994a    10. de Wit et al., 1992

The African surface was formed when Africa was separated from South America by a volcanic cycle giving rise to the seafloor basalts separating the two continents from each other. This event resulted in the opening of the Atlantic basin from 200Ma to 120Ma, and created a Great Escarpment (Summerfield, 1985). The African erosion cycle proceeded at different levels above and below the Great Escarpment. There were two peaks of

sedimentation, the early-Cretaceous peak in Valanginian to Barremian times (131-115Ma) and a late-Cretaceous peak in Coniacian/Santonian times (86-78Ma) (Dingle et al., 1983).

The most important succession of the basal Kalahari Group sediments accumulated during the late Cretaceous, and directly overlies the African surface (Moore, 1999). Netterberg (1970) presumed a post-upper Cretaceous age or “pre-Pliocene” for calcretization in the Kalahari group, which indicates a semi-arid environment. The calcrete layer works as geochemical barrier and reduced the mobility of mobile elements. It is therefore an important part of this research because it affects the lateral extend of geochemical dispersion haloes. The advanced planation, deep weathering and kaolinization of the underlying rocks, and massive laterite duricrusts formed at end-Cretaceous to Eocene times (Partridge et al., 1987). The kaolinization is an indicator of a humid condition. The erosion removed an enormous thickness of material in different parts of the continent. The accumulation of the Kalahari sediments was continued during the Eocene and Oligocene. As this area is situated on the edge of the Kalahari Basin it could be assumed that erosion here was not that severe during this period.

Another epirogenic uplift of the subcontinent deformed the African surface, during a major episode of landscape evolution in Miocene times (Cogley, 1985). This event was confined to the northern and north-western Cape or the Griqualand-Transvaal axis. This was the beginning for the Post-African I erosion cycle, and major deposition in the Kalahari basin. In this relatively short time of erosion, there was no advanced weathering and kaolinization and the processes were limited to the development of duricrusts on the Post-African I surface (Partridge et al., 1987).

Further uplift in the Pliocene resulted in deformation of the Post-African I surface (Dingle et al., 1983). This movement had greater amplitude in some areas, confined to the same axes as in the Miocene. The Post-African II cycle began at the end-Tertiary uplift and warping of the subcontinent. Aridification and major climate deterioration were the most important changes (Van Niekerk et al., 1999), which began during the late Pliocene

(Partridge et al., 1987). These changes occurred together with major changes in the extent of the earth's ice caps.

The “ice age” began at the start of the middle Pleistocene, which was an important event of the Pleistocene period (Partridge et al., 1987). The sea level decreased due to increasing global ice volume, and then later rose due to warmer conditions. The changing conditions drove fluvial, colluvial, and aeolian processes, which results in sediment accumulation in the continental basins (Partridge et al., 1987).

Changes during the late Tertiary probably contributed most to the present landscape of southern Africa. This includes the two phases of uplifting during the Miocene and Pliocene accompanied by a period of weathering, aridification and deposition of the last member of Kalahari Group, i.e., sand dunes. The windblown sand covered the whole area during a very arid period (Malherbe, 1984). Fossil dunes formed during this period are still preserved in the study area and the area has undergone very little subsequent change due to the semi arid to desert climate conditions.

## **2.7. Calcrete environments**

### **2.7.1. Definition of calcrete**

Calcrete, also known as caliche, croutes, calcaires, nari and kunkar, is a predominantly calcium carbonate component that is accumulated near the surface. It is formed either through pedogenic (soil forming processes) or groundwater processes or a combination of both (Khadkikar et al., 1998; Ringrose et al., 1999; Jimenez-Espinosa et al., 2003). The source of the carbonate may be aeolian dust, rainwater, plants, sheet wash or weathering of calcareous parent material and shells (Vermaak, 1984; Dhir et al., 2004). Calcrete may form in arid (50-100 mm mean annual rainfall) to subhumid (500-700 mm mean annual rainfall) conditions (Khadkikar et al., 2000; Jimenez-Espinosa et al., 2003) and the existence of calcrete in an area is evidence for dry periods, where evaporation exceeds precipitation. Calcareous sediments with a prominence of SiO<sub>2</sub> (quartz) are known as calcareous sands or sandstones depending on the degree of diagenesis (Ringrose et al., 1999).

### 2.7.2. Calcrete classification

Khadkikar et al. (1997) classified calcretes into three groups based on the processes of formation. These are pedogenic calcrete (soil-forming), groundwater calcrete (groundwater processes) and calcrete conglomerate (reworking of both groups).

The groundwater or non-pedogenic calcrete is formed by carbonate-bearing groundwater circulating through sediments during dry seasons (Vermaak, 1984; Ringrose et al., 1999). During these dry periods, groundwater with dissolved carbonates rises through the host sediments by capillary action. As the groundwater reaches to the surface, evaporation will cause precipitation of carbonate close to or on surface resulting in the formation of calcrete (Fig. 2.8) (Vermaak, 1984; Ringrose et al., 1999). Alternatively, Ringrose et al. (1999) suggested that carbonate is precipitated in the capillary fringe of a fluctuating water table (Fig. 2.7).

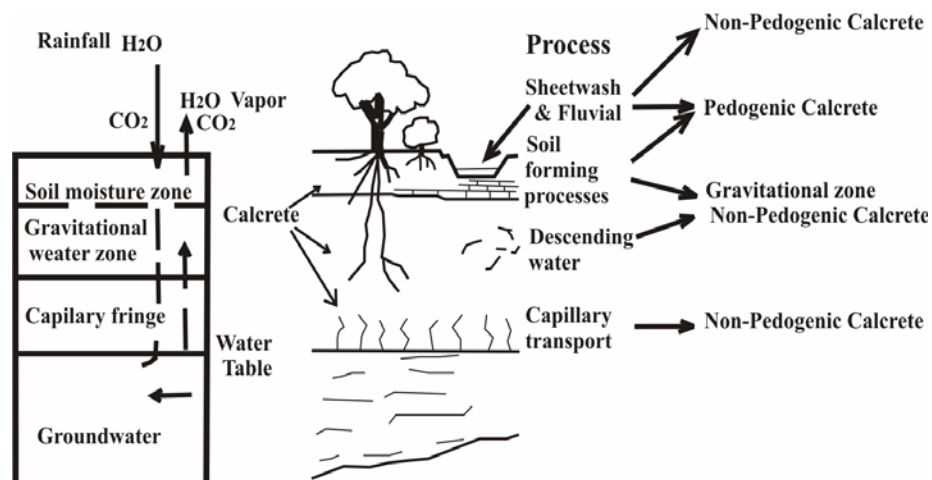


Figure 2.7: The genetic calcrete classification (after Carlisle, 1980).

Pedogenic calcrete develops in more arid areas where rainfall only moisturizes the soil and creates a soil moisture zone during wet seasons. The dissolved carbonates move through the soil moisture zone and are precipitated on the surface by evaporation during dry seasons (Fig. 2.7) (Vermaak, 1984; Ringrose et al., 1999). This type of calcrete is a residual product of weathering and soil forming processes (Vermaak, 1984). Khadkikar et al. (1998) subdivided pedogenic calcretes into two groups, the vertisols calcrete and red-soil-calcrete (Table 2.5). Vertisols calcrete is

formed in sub-humid conditions and is characterised by the presence of montmorillonite and illite (Khadkikar et al., 2000). Red-soil calcrete is formed in semi-arid conditions and is characterised by the presence of oxidised iron together with montmorillonite and illite (Khadkikar et al., 2000). Pedogenic calcretes are normally recognized by their laminar, highly indurated upper zones and a decrease in carbonate concentration with depth.

Calcrete conglomerates are formed by the reworking of both pedogenic as well as groundwater calcretes.

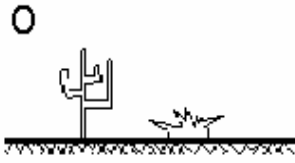
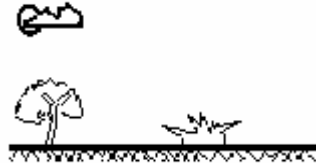
Calcrete may also form due to the interaction of plant root growth, water and the erosion-sedimentation processes (Jimenez-Espinosa et al., 2003). This type of calcrete is known as biogenic or  $\beta$ -calcretes and does not form layers. When water is available, high soil moisture may favour rapid plant colonisation. The plant would absorb the carbonate bearing groundwater via its roots (Jimenez-Espinosa et al., 2003). As the plant uses up the water, the carbonate is left behind to accumulate forming round micritic calcite particles. Khadkikar et al. (1998) introduced rhizogenic calcretes, which are calcretes formed by physiochemical processes in the root zone. The plant root uptakes the water causing the remaining soil water to be super saturated in  $\text{Ca}^{2+}$  ions (Khadkikar et al., 1998). These calcretes occur as sinuous cylindrical tubes (5-10 cm tubes), thus are referred to as calcrete tubes and are associated with both pedogenic and groundwater calcretes (Khadkikar et al., 1998).

### **2.7.3. Mineralogy of calcretes**

Calcretes are mostly composed of calcite, quartz and feldspar (Vermaak, 1984), with the silica content affecting the hardness of calcretes, i.e. the higher the silica content, the harder the calcrete. Aragonite and calcium carbonate-hydrate minerals may be present in the early stages of calcrete formation. Dolomite (dolocrete) may also occur together with calcite (Vermaak, 1984). Khadkikar et al. (1998); Khadkikar et al. (2000) reported on the presence of clay minerals and trace amount of gypsum and barite in some calcretes. In drier climates (50-100 mm average annual rainfall, Table 2.5), sepiolite and palygorskite are usually formed (Jimenez-Espinosa et al., 2003).

The absence of sepiolite-palygorskite and the presence of smectite and hematite associated with low Mg calcite are characteristics of calcretes formed in semi-arid climates (100-500 mm average annual rainfall, Table 2.5) (Jimenez-Espinosa et al., 2003). The formation of pedogenic hematite requires enough moisture to enable chemical weathering of primary minerals and low activity of water that would propel dehydration processes like in the tropical environments (Khadkikar et al., 2000; Jimenez-Espinosa et al., 2003).

**Table 2.5:** Classification of calcrete based on the weather conditions (after Khadkikar et al., 2000)

Groundwater calcretes	Pedogenic calcretes	Pedogenic calcretes
ARID (50-100 mm)	SEMI-ARID (100-500 mm)	SUB-HUMID (500-700 mm)
		
<b>Mineralogy of calcrete</b> Calcium carbonate, sepiolite and palygorskite. Hydromorphic features are absent.	<b>Mineralogy of calcrete</b> Calcium carbonate, oxidised iron, montmorillonite and illite. Hydromorphic features may be present (Red-soil-calcrete)	<b>Mineralogy of calcrete</b> Calcium carbonate, montmorillonite and illite. Hydromorphic and vertic features are present (Vertisols calcretes)

#### 2.7.4. Mechanism of carbonate accumulation

The calcium carbonate solubility is mainly controlled by pH (acidity of a solution) and the pH of the system is itself directly controlled by the CO<sub>2</sub>-pressure. In general for calcium carbonate to precipitate, a pH of 8.4 or more is required. Evaporation, CO<sub>2</sub>-loss, changes in temperature, pressure, grain size and mixing of solutions may also affect the pH of the solution leading to carbonate accumulation if favourable pH conditions are met.

During rainfall, acidic water percolates into the soil, and it carries with it dissolved CO<sub>2</sub> from river water as well as the aeolian dust. In the event that there is an ore body close to surface, the carbonate-bearing water will react with the ore body resulting in mobile elements in the ore body being dissolved. Later, evaporation processes take place and result in the solution rising to the surface by capillary action. H<sub>2</sub>O and CO<sub>2</sub> are lost and this increases the pH of the solution. The pH may reach favourable

conditions for the precipitation of calcium carbonate resulting in deposition of calcite together with dolomite, quartz, iron oxides and other dissolved elements on surface.

Large parts of the dryer central parts of North-West and Northern Cape Provinces of South Africa are covered by well developed calcrete layers concealing the underlying geology. These calcrete layers may be correlated with the Mokalanen Formation of the Kalahari Group described by Malherbe (1984).

The dispersion of ore-related elements in the calcrete environments, as a geochemical barrier, is an interesting process to look into in this current research.

#### **2.7.5. Calcrete of the study area**

The calcrete layers at the base of the Kalahari Group formed during a dry period that existed during the later part of the Tertiary Period (Thomas, 1981), more specifically during the late Miocene Epoch (23.8-5.3 Ma) (Ward et al., 1983). Different formations of the Kalahari Group were studied by Malherbe (1984) (Table 2.6). The Mokalanen Formation, which is the calcrete unit of the Kalahari Group, comprises of three units and two varieties of calcrete layers, namely nodular and hardpan calcretes. The hardpan calcrete is hard and impermeable and forms when the nodular calcrete is cemented by calcrete or silcrete. It provides evidence of the semi-arid environmental conditions during the formation of the Mokalanen Formation. The hardpan calcrete is an extremely weathering-resistant rock.

The calcrete layer developed near surface throughout the study area from Areachap in the North to Copperton in the South, is correlated with Malherbe's (1984) Mokalanen Formation.

Vermaak (1984) suggested a pedogenic process for the formation of the calcrete at Areachap, Copperton and Jacomynspan areas. A non-pedogenic, groundwater, processes was suggested by Nash and McLaren (2003) for the Kalahari valley calcrete in the capillary fringe zone of the groundwater table. Based on the semi-arid

**Table 2.6:** Different Formations of the Kalahari Group. Data summarised from Malherbe (1984)

<b>Name of the Formation</b>	<b>Lithologies in the Formation</b>
Gordonia Formation	Sand dune deposits and Fe-rich minerals such as magnetite, haematite and Ilmenite
Goeboe Goeboe Formation	Sand sediment
Lonely Formation	Clayey diatomaceous limestone
Mokalanen Formation	- Harden calcrete -Nodular calcrete -Sharpstone calc-conglomerate
Eden Formation	Sandstones and conglomerate
Budin Formation	Red clay
Wessels Formation	Gravel

environmental conditions proposed by Malherbe (1984) during the formation of the Mokalanen Formation, and the classification of calcrete by Khadkikar et al. (2000) and Table 2.5, a pedogenic origin may be accepted for these calcretes.

## Chapter 3

# Literature review of VHMS deposits and related Lithogeochemical alteration

### 3.1. Introduction

The objective of this chapter is to discuss hydrothermal alteration that could be associated with volcanic hosted massive sulphide (VHMS) deposits, that may be used related to the classification of VHMS deposits, their tectonic setting, and the related hydrothermal fluid models will be discussed. This will be followed by discussions on the mineral zonation in the ore zone and footwall, and the alteration products and the effect of subsequent metamorphism. Finally some geochemical alteration indexes will be introduced.

### 3.2. Classification and geological setting of VHMS deposits

Massive sulphide deposits consist of 60% or more sulphide minerals (Sangster and Scott, 1976). Two main groups were suggested for these deposits based on the host rock lithology. The first group is composed of sedimentary-exhalative (SEDEX) or shale-hosted stratiform massive sulphides (Lydon, 1998a; Goodfellow et al., 1993; Lott, 1999; Sangster, 2002; Canet et al., 2004) e.g. Sullivan, Broken Hill, Mt. Isa and Rammelsberg. The volcanic-hosted massive sulphide (VHMS) deposit forms the second group (Lydon, 1998a; Sanchez-Espana, et al., 2000; Ulrich et al., 2002; Ruiz et al., 2002; Tornos, 2006; Aftabi et al., in proof). The origin of the immediate host rocks of VHMS deposits are

thought to be either derived directly from volcanic activity such as lava or pyroclastic rocks, or have no direct volcanic affiliation e.g. shales or greywackes (Lydon, 1998a).

Sillitoe (1973) suggested that VHMS deposits dominated by Cu are related to spreading centre tectonic setting, whereas the Pb, Zn, Ag and Ba enriched deposits formed in island arc or continental margin environments. Hutchinson (1973) classified these deposits into the Zn-Cu-type which is associated with fully differentiated magmatic suites of tholeiitic and calc-alkaline affinities, predominately of Archean age. This may also be referred to as the primitive of Noranda type deposits (Lydon, 1998a). The second group of deposits are characterized by high Pb, Zn and Cu contents and are associated with intermediate to felsic calc-alkaline volcanic rocks of predominantly Phanerozoic age (Hutchinson, 1973). This group may collectively be referred to as the Kuroko type deposits (Lydon, 1998a). The third and last group are Cu deposits related to ophiolite of tholeiitic suites of Phanerozoic age (Hutchinson, 1973) also referred to as Cyprus type deposits (Lydon, 1998a).

Lydon (1998a) classified the VHMS deposits based on major ore metals instead of geological characteristics, into Cu-Zn and Zn-Pb-Cu types.

The location of massive sulphide lenses seem to be strongly related to structural controls of the ocean floor e.g. synvolcanic faults with vertical displacements (Knuckey, 1975). Hodgson and Lydon (1977) documented that most of VHMS deposits are related to the fracture systems produced by subvolcanic intrusions or resurgent calderas. This relationship shows that particular hydrologic, topographic and geothermal features of the ocean floor are required to form VHMS deposits (Lydon, 1998a).

It is important to note that the hydrothermal solutions responsible for the sulphide mineralization escapes onto the ocean floor at temperature of 300-400°C (Lydon 1998a). To prevent such solutions from boiling below surface, basin depths in excess of 2500 m are required (Ohmoto and Skinner, 1983).

### **3.3. Classification of metamorphosed massive sulphide deposits of the Namaqua Province**

The first massive and disseminated massive sulphide deposits exploited in Namaqualand are located within the Okiep copper district. These copper deposits are related to a late tectonic cross cutting group of mafic to intermediate intrusions collectively known as noritoids (Conradie and Schoch 1986; Lombaard and Schreuder, 1987). Theart (1985) suggested that the metamorphosed stratiform massive sulphide deposits of the Namaqua Province be divided into the SEDEX Aggeneys Group (Ryan et al., 1986; Thomas et al., 1994b) and the VHMS Copperton Group of deposits. This subdivision is based on lithological, compositional and isotopic characteristics. The VHMS deposits are confined to the Areachap Terran of the Namaqua Province and forms the focus of this investigation. The largest known deposit in this terran is the Prieska Cu-Zn deposit (47 mt @ 1.7% Cu and 3.8% Zn) located near the deserted mining town Copperton. This deposit was exploited during the 1970's and 1980's. Early workers in this region classified the Prieska Cu-Zn deposit and other small deposits in its immediate vicinity as VHMS deposits (Middleton, 1976; Gorton, 1981). Wagener and Van Schalkwyk (1986) opposed and suggested that it was a SEDEX deposit. Following further research (Theart, 1985; Theart et al., 1989; Schade et al., 1989) the VHMS nature of the ore body was established by the recognition of a metamorphosed and deformed equivalent of a chloritic footwall alteration zone and a sulphate-carbonate cap above the massive sulphide mineralization. The Areachap deposit (8.9 mt @ 0.4% Cu and 2.24% Zn) mined in the 1900's and further explored in the 1960's and 1970's was also classified as a VHMS deposit (Theart, 1985; Voet and King, 1986). Geringer et al. (1987) investigated small deposits in the Bokspuits area and classified these as VHMS deposits of the Besshi type. Rossouw (2003) discussed the financial viability of the latest discovery in this region on the farm Kantienpan (5 mt @ 0.49% Cu and 4.09% Zn). He provides a geological description of the deposit and classifies it as a VHMS deposit.

### **3.4. Hydrothermal Models for Formation of VHMS deposits**

There are three different models for the genesis of hydrothermal fluids and the source of energy for fluid circulation that are related to VHMS deposit formation. These are the *convection cell model*, the *stratal aquifer model* and the *magmatic hydrothermal model* (Lydon, 1998b). Two of these, the convection cell and the stratal aquifer models, are more common, but the third magmatic hydrothermal model, has little scientific support (Sangster, 1972; Solomon, 1976). These models are discussed below.

#### **3.4.1. Convection cell model**

Francheteau et al. (1979) suggested the presence of operating hydrothermal convection cells in VHMS deposit formation based on the presence of hydrothermal vents at mid-ocean ridges. There are different sources of heat for the formation of these vents such as cooling rhyolite domes or plugs (e.g., Ohmoto and Rye, 1974), sub-volcanic sills (e.g., Campbell et al., 1981), felsic plutons (e.g., Cathles, 1983), and spreading ridge magma chambers (e.g., Spooner, 1977; Lowell and Rona, 1985). The heat released from the roof of a vigorously convecting magma chamber would cause the circulation of subsurface waters in the overlying strata. When the strongly acidic fluids rise (~3.5 pH), they leach out the ore components of rocks along their flow path. The hydrothermal convection cell would remain active as long as the source of the heat is sustained. The principal source of water in these systems is the overlying ocean. Brauhart et al. (2000) and Scherdt et al. (2005) presents heat and fluid flow modelling results, developed for a relatively undeformed and unmetamorphosed VHMS deposits, indicating temperature gradients of 300<sup>0</sup>C to 400<sup>0</sup>C in the convection cells with flow velocities of approximately 1.8 m/s, that could have operated for up to 200, 000 yr.

#### **3.4.2. Stratal aquifer model**

This model assumes that the source of ore fluids is from the pore waters of a permeable rock capped by an impermeable rock. During sedimentation and diagenesis, the lithostatic pressure on the cap-rock increases and compacts the permeable rocks below resulting in an increase in the geothermal gradient and pore-

fluid pressure. When the lithostatic pressure and pore-fluid pressure are greater than the strength of the cap-rock, hydraulic or mechanical fracturing in the cap-rock occurs (e.g., Sibson et al., 1975). Due to the high pore water pressure, the water would escape via the fractures developed as a result of the mechanical fracturing described above. In this model, very large quantities of fluids move upward to the surface in a short time with minimal energy. The model is best applicable to the formation of SEDEX massive sulphide deposits (e.g., Walker et al., 1977; Badham, 1981; Lydon, 1983; Sawkins, 1984; Lydon, 1986).

### **3.4.2. Magmatic hydrothermal model**

In this model it is assumed that the ore fluids responsible for VHMS deposits are derived from the volatiles of magmas. Bryndzia et al. (1983) considered the source of ore fluids in Kourouko type deposits to be magmatic to explain the elevated salinities (up to 1.9 times greater than sea water) in fluid inclusions. This could be supported by the concept that VHMS deposits are products of a calc-alkaline magma (Solomon, 1979).

## **3.5. Mineral zonation within hydrothermal alteration pipes and ore zones**

### **3.5.1. Mineral variation in the ore zone**

Some of the evidences for VHMS deposits being precipitated by hydrothermal fluids include occurrence of massive sulphide lenses on the seafloor, sedimentary structures, the conformable contact between massive sulphide lenses and the hanging wall, and hydrothermal alteration pipes in the footwall (Lydon, 1998b). The high temperature fluids escape to the sea floor through structurally induced fracture systems. Within this fracture system reaction between the hydrothermal fluid and the rocks becomes more intense closer to the rock-ocean interface. Fluids escape through discrete chimney systems (Lydon, 1998a) or percolate through unconsolidated sediments at the sea floor (Lydon, 1998a). The reaction between the fluid and the surrounding wall rocks of the fracture system results in the formation of a footwall alteration zone containing disseminated sulphide mineralization below the massive sulphide lens that

can develop at the seafloor or within the sediments (Lydon, 1998a). The degree of alteration diminishes from the fracture system outwards into the wall rocks, and this depends on the permeability of the wall rocks and their composition (Lydon, 1998a). Sulphide mineralization varies from more Cu-rich, chalcopyrite dominated, to Zn and Pb-rich (sphalerite and galena dominated) disseminated fracture-controlled mineralization (Lydon, 1998b).

When the hydrothermal fluid mixes with seawater, the temperature of the hydrothermal fluids decrease rapidly leading to precipitation of anhydrite forming the walls of chimneys that develop. The physicochemical conditions inside the chimney are characterised by high temperature, acidic and reducing conditions, whereas alkaline, oxidising and low temperature conditions exist in the ocean water. The differences between the conditions inside and outside of the chimney lead to the formation of a variety of chemical phases that precipitate, and give rise to the mineral zonation observed within the chimney wall. The mineral zonation reflects the wide range of the physicochemical gradient between the mineralizing fluids and the seawater. This give rise to chalcopyrite (inside of the wall); pyrite, sphalerite and galena (toward the outside); anhydrite with minor sulphides, amorphous silica, and barite forms the exterior zone (Speiss et al., 1980; Haymon and Kastner, 1981; Oudin, 1981; Haymon, 1983; Oudin, 1983; Goldfarb et al., 1983; Tivey and Delaney, 1986). More further, the composition of the sulphide minerals depend on the temperature of the system. In high temperature systems, pyrrhotite forms first followed by chalcopyrite and sphalerite as the temperature decreases. At lower temperatures, galena or galena mixed with barite would precipitate. Pyrite could form in a wide range of temperatures and it accompanies all the other sulphide minerals mentioned above.

As the chimney grows, it becomes mechanically unstable and collapses. This could cause other chimneys to be formed due to rise in hydrothermal fluids via other permeable pathways. Eventually this process leads to formation of an impermeable mound, which causes an increase in the temperature and circulation of fluids inside

the mound. The circulation of the fluids may cause the replacement of previous sulphides by higher temperature minerals. Renewed episodes of fracturing (hydraulic or otherwise), on top of hydrothermal eruption create new channel ways for growing new chimneys and the mound (Lydon, 1998b).

One of the most important characteristics of VHMS deposits is the decrease in the Cu:Zn ratio upwards and outwards from the core of the massive sulphide lens. Computer modelling (Reed, 1983; Janecky and Seyfried, 1984; Bowers et al., 1985) shows that progressive local cooling of the solutions causes the Cu-dominant to Zn-dominant zonation (e.g., cf. Large, 1977).

The silica in hydrothermal fluids will precipitate to form quartz if the solution cools without any dilution (Janecky and Seyfried, 1984). When the temperature of seawater increases, if there is enough barium in the seawater, it would react with seawater sulphate and this would result in barite precipitation (e.g., Kowalik et al., 1981; Watanabe and Sakai, 1983). This occurs when a black smoker change (very fine-grained pyrrhotite with minor sphalerite and pyrite) to a white smoker (silica, barite and pyrite).

To prevent oxidation and of erosion the sulphide minerals, it would be necessary to insulate them from oxidising and erosive conditions by covering them with impermeable sediments or igneous rocks. The formation of iron oxide and manganese oxide might indicate oxidising conditions. These oxides could possibly precipitate in submarine brine pools (e.g., Pottorf and Barnes, 1983) or oxidation of a buoyant hydrothermal plume in a distal deposit (Kalogeropoulos and Scott, 1983; Large, 1977). A hydrothermal discharge system might produce these oxides contemporaneous with the sulphide mineralization or later, as well.

### **3.5.2. Wall rock alteration**

Chlorite and sericite are the two major alteration products that form due the reaction between the hydrothermal fluid and the wall rocks. The nature of the alteration assemblage does however also depend on the composition of the original wall rocks.

In most cases the primary calcium and sodium rich silicate minerals such as pyroxenes and feldspars are the first to be destroyed during alteration resulting in a depletion of Ca and Na which is removed from the system in the escaping hydrothermal fluid (Lydon, 1998b). The remaining rock becomes enriched in Al, Mg, and Fe, and in some cases K, since the conditions are favourable for formation of chlorite (Miyashiro, 1994). Silica released in the solution precipitates as soon as the temperature of the fluid decreases and this may commence in the zone immediately below the massive sulphide zone, and also trends to seal the conduit during the waning stages of the ore forming process. Other minerals that may also be formed within the alteration zone below the massive sulphide zone include tourmaline if the hydrothermal fluid was enriched in B (Jiang, 2000; Kawakami, 2001) and apatite or monazite if the fluid was enriched phosphates (Large et al., 1996).

If biotite is present as a primary mineral, the hydrothermal fluid will alter it to chlorite by removing potassium from the biotite i.e.



Mg could also be added to the system from seawater-basalt interaction (e.g., Hajash, 1975; Mottl and Holland, 1978; Seyfried and Bischoff, 1979). The fluids may also introduce iron derived from the seawater-basalt interaction (Lydon and Galley, 1986; Richards and Boyle, 1986).

The abundance of Al in the altered rocks results in them displaying a peraluminous character, which means that in these rocks the percentage of  $\text{Al}_2\text{O}_3$  is higher than the sum of  $\text{Na}_2\text{O}$ ,  $\text{CaO}$ , and  $\text{K}_2\text{O}$  (Humphreys, 1993).

Utilizing the isocon method of Grant (1986) it could be demonstrated that the footwall alteration zone of the Prieska Cu-Zn deposit became enriched in Al, Mg, Fe, Mn, K, Ti, V, Sc, Ni, Ba, Cu and Zn, whereas elements such as Si, Ca, Na and Sr were removed from the precursor rock during the alteration process (Theart et al., 1989).

### **3.5.3. Metamorphism of VHMS deposits and their alteration zones**

High grade metamorphosed VHMS deposits include the deposits of the Manitouwadge Camp in the Superior Province, Canada (the Geco, Nama Creek, Willray and Willecho deposits) which were metamorphosed to upper amphibolite grade (Cameron and Hattori, 1987; Pan and Fleet, 1995) and deposits of the Fennoscandian Shield, such as those in the Vihanti district of the Pyrite Belt and in the Aijala-Oryarvi region in Finland (Gaal, 1990; Tornos, 2006) and the deposits in the Skellfte district in Sweden (Sundblad, 1991).

The chlorite-rich rocks of the alteration zone are deformed to subparallelism with the massive sulphide layers and metamorphosed to cordierite-anthophyllite and cordierite-sericite assemblages.

Metamorphism of the massive sulphide rocks generally results in total recrystallization with a dramatic increase in grain size, the formation of granoblastic textures with foam texture triple grain junctions in monomineralic situations (Vokes, 1969; Theart, 1985). Theart et al. (1989) recognized textures of “Durchbewegung” in the ores of the Prieska Cu-Zn and Areachap deposits and suggested that the associated deformation was responsible for destruction of, and chemical, and isotopic variation that might have existed earlier across the ore body.

## **3.6. Quantification of chemical changes in altered rocks**

### **3.6.1. The isocon method**

The quantification of changes in the rock volume and elemental concentrations during hydrothermal alteration is an important component of lithogeochemical investigations of alteration zones. It is relatively easy to do the gain and loss calculations, when the altered rocks are distinguished as the least-altered equivalents or source rocks especially in relatively undeformed and unmetamorphosed rocks. Gresens (1967) presented equations for these calculations based on chemical analyses and specific

gravities of altered and unaltered rocks. Grant (1986) suggested a graphical solution to those equations, known as the isocon method. This contributes greatly to a more quantified approach in the study of these phenomena.

The Gresens's equations are based on mass rather than volume (Gresens, 1967). The mass of element after alteration ( $M_i^A$ ) is defined by the original mass ( $M_i^O$ ) plus any change in the mass ( $\Delta M_i$ ) of that element during the alteration (Grant, 1986):

$$M_i^A = M_i^O + \Delta M_i$$

Dividing throughout by  $M^O$  to get concentration units and multiplying by  $M^O/M^A$  to obtain the original concentration, one may derive the following equation:

$$M_i^A / M^A = M^O / M^A (M_i^O / M^O + \Delta M_i / M^O) \quad (1)$$

$M_i^A / M^A$  may be substituted for  $C_i^A$  and  $M_i^O / M^O$  for  $C_i^O$ , with C being an abbreviation for concentration and the equation (1) becomes:

$$C_i^A = M^O / M^A (C_i^O + \Delta C_i) \quad (2)$$

For an immobile element  $\Delta C_i = 0$ , and:

$$C_i^A = M^O / M^A \cdot C_i^O$$

This is a linear equation that passes through the origin with the slope of this line ( $M^O/M^A$ ), equal to  $(C_i^A / C_i^O)_{\text{immobile element}}$ . Therefore the final equation for an element in general is defined as:

$$C_i^A = (C_i^A / C_i^O)_{\text{Isocon line}} [C_i^O + \Delta C_i] \quad (3)$$

This is the general equation for the isocon line. If constant mass is assumed, then  $C_{\text{immobile element}}^A$  will be equal to  $C^O$  for an immobile element. If constant volume is assumed, then:

$$C_{\text{immobile element}}^A = (\rho^O/\rho^A) C^O$$

Recognition of the mobile and immobile elements is an important aspect of this method. If we know which elements would behave immobile during the alteration process, the isocon line will pass through the origin and the concentration of these immobile elements, when comparing the original and altered rocks. The gain and loss of the mobile elements may then be calculated and any volume change can easily be deduced.

Jenner (1996) defined the high field strength elements (HFSE) and REE as immobile elements. Those elements with low ionic potential, i.e. a ratio of ionic radius to ionic charge less than 0.2, are generally referred to as HFSE and these together with the REE are regarded as immobile (Jenner, 1996; Jiang, 2000). Trace elements such as Sc, Y, Th, U, Pb, Zr, Hf, Nb, Ta, and Ti belong to the HFSE group. Ti, Zr, Hf, Nb, Ta, and Y are generally immobile during alteration and metamorphism (Jenner, 1996; Piercey et al., 2001). The low field strength elements have a high ionic potential (> 0.2) and are generally regarded as mobile elements (e.g. Cs, Rb, K, Ba, Sr) under these conditions.

The isocon diagrams between least altered biotite-gneiss, Co, and altered biotite-gneiss, Ca, in Areachap are given in Figure 3.1 to demonstrate the concept of the isocon line, gain and loss. The isocon line passes through the origin and immobile elements and oxides i.e., TiO<sub>2</sub>, Al<sub>2</sub>O<sub>3</sub>, Zr, U, Th, Nb, Y, La, and Sc. Those elements, which plot in the upper part of isocon line, represent gain and those elements that plot below the isocon line represent loss. The delta value for each element is calculated based on the following formulae:

$$(\Delta \text{ value})_i = C_i^A - C_i^O \cdot (\text{Slope value of the isocon line}), \quad i: \text{the element of interest} \quad (4)$$

If the calculated delta value [(Δ value)<sub>i</sub>] of an element is positive it means that the concentration of that element in the altered rock is greater than in the least altered

rock (a gain). Where the calculated delta value for an element is negative it means that the concentration of the element in the altered rock is less than that of the least altered rock (a loss). The delta value can be converted to percentage based on the following formula:

$$\text{Percentage of gain or loss} = [(\Delta \text{ value})_i / C^O_i] \cdot 100 \quad (5)$$

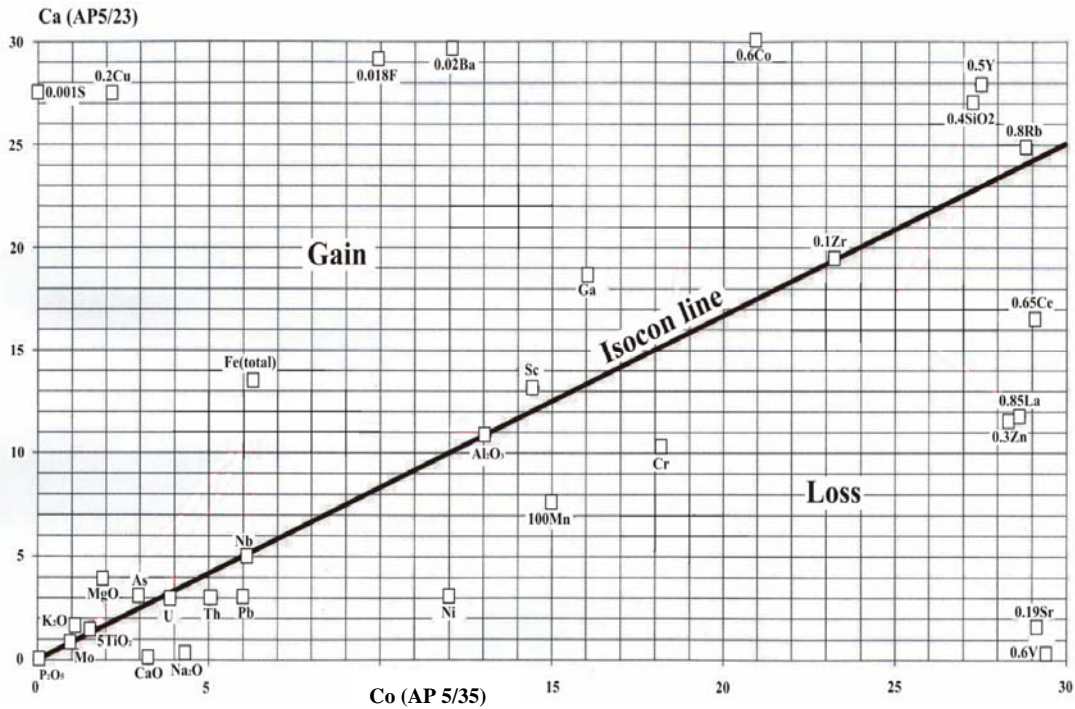


**Figure 3.1:** An isocon diagram for sample AP5/35 (least altered biotite-gneiss) and AP5/23 (altered biotite-gneiss) from drill hole AP5 in the Areachap area.

### 3.6.2. The alteration index and the Chlorite-Carbonate-Pyrite index

Ishikawa et al. (1976) defined the alteration index (AI) to measure the intensity of sericite and chlorite alteration in the footwall of VHMS deposits of the Kuroko type in Japan. The AI is defined as:

$$AI = 100 (K_2O + MgO) / (K_2O + MgO + Na_2O + CaO)$$

Large et al. (2001) used this index for calculating the intensity of sericitization and chloritization of plagioclase. Later Large et al. (2001) defined the Chlorite-Carbonate-Pyrite Index (CCPI) based on the following formula:

$$\text{CCPI} = 100 (\text{MgO} + \text{FeO}_{\text{total}}) / (\text{MgO} + \text{FeO}_{\text{total}} + \text{Na}_2\text{O} + \text{K}_2\text{O})$$

An increase in the AI and CCPI generally indicates a gain of MgO, FeO, and K<sub>2</sub>O and a depletion of Na<sub>2</sub>O and CaO. The box plot, an AI versus CCPI (Large et al., 2001) diagram, is a better way to demonstrate these variations. Other features that affect the CCPI ratio include Mg-Fe carbonate alteration, mineralization of pyrite and or hematite enrichments. These features are commonly present in the alteration zones of some of VHMS deposits.

The box plot is a useful method to separate hydrothermal alteration from diagenetic alteration (Large et al., 2001) (Fig. 3.2 and 3.3). If a diagonal line is drawn between epidote and K-feldspar, those samples plot above this line are hydrothermally altered and those samples that plot below the line reflect diagenetic alteration (Large et al., 2001).

In general, five fields can be demonstrated on the box plot (Fig. 3.2 and 3.3). Three of these trends are associated with hydrothermal alteration (after Large et al., 2001) (Fig. 3.2).

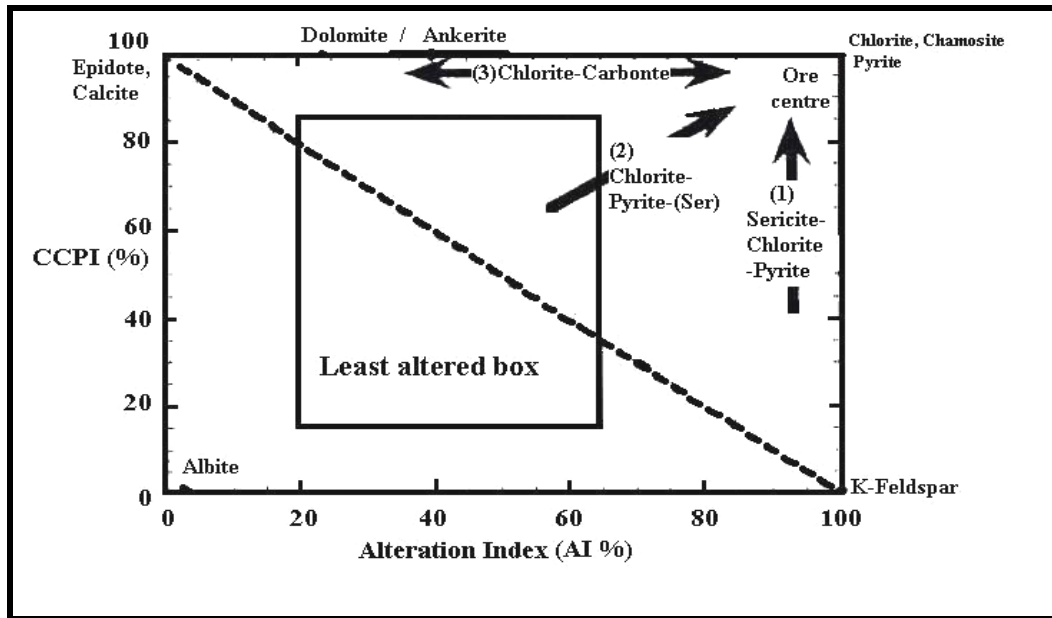


**Figure 3.2:** Field for hydrothermal alteration described in the text (modified after Large et al., 2001)

The fields that could be identified in the box plot are:

Field 1: Least altered rocks fall within a box bounded by an AI= 20 to 65% and a CCPI= 15 to 85%,

Field 2: Sericite-chlorite alteration in the footwall alteration close to the ore lenses, has AI>90% and CCPI>65%. This corresponds with trend 1 in Figure 3.2,

Field 3: Chlorite-pyrite (sericite) alteration typical of the footwall alteration system of the VHMS deposit corresponds with trend 2 in Figure 3.2,

Field 4: Chlorite-carbonate alteration typically developed in the ore zone and footwall alteration zone of massive sulphide. This corresponds with trend 3 in Figure 3.2.

The trend that could be related to diagenetic alteration (Large et al., 2001) is shown in Figure 3.3:

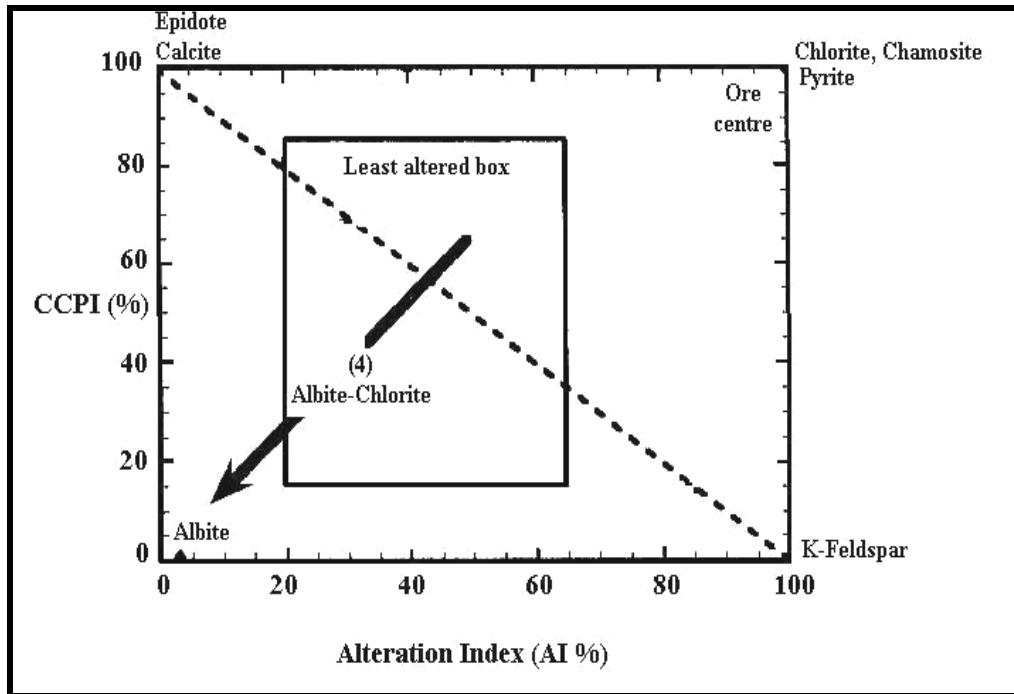


Figure 3.3: Field for diagenetic alteration described in the text (after Large et al., 2001)

Field 5: Albite-chlorite alteration (trend 4) is typical of seawater interaction at low temperatures (e.g., spilites and keratophysics; Hughes, 1972; Seyfried and Bischoff, 1979) (where albite  $\pm$  calcite  $\pm$  K-feldspar assemblages are absent in the mineralization) that has an AI < 57%, and occur below the epidote- K-feldspar join.

Albite, calcite, epidote, dolomite, ankerite, chlorite, chamosite and K-feldspar are located at the boundaries of the box plot (Large et al., 2001) (Fig. 3.2).

### 3.6.3. The mineralogical variation index (Pearce Element Ratio (PER) analysis)

This method was developed to avoid the effects of closure and/ or pre-existing lithological variations or background lithochemical trends in geochemical modelling during advanced geochemical investigations. In applied lithochemical methods, the major elements monitor mass balance and are used to identify relative or absolute variations in elements (Whitbread and Moore, 2004).

Variation in major element concentrations may be used as an index of mineralogical change, which is caused by alteration (Whitbread and Moore, 2004). The mineral changes are useful tools in exploration because the variations are process related. The PER analysis is based on mineral changes and uses the major element variations. This method presents a way to identify the hydrothermally altered rocks surrounding ore deposits. The weight percentage data is converted to molecular proportion in the PER diagrams. For this purpose the molar ratios, which is the molecular proportion of an element or a linear combination of elements divided by the molecular proportion of an immobile or conserved element, are used to plot the PER diagrams.

The PER diagram of an epigenetic Zn-Pb-Ag deposit (Elura ore deposit, 45 Mt @ 8.5% Zn, 5.3% Pb and 69 ppm Ag) is illustrated in Figure 3.4. The ore deposit is hosted within Devonian siltstone-sandstone turbidites of the Cobar Basin in central-west New South Wales, Australia (Whitbread and Moore, 2004). In this case, molar K/Ti versus Al/Ti diagram shows that the altered rock with the development of muscovite (boarder 1 and 2) are separated from the background rock, which has an illite  $\pm$  albite precursor (boarder 3 and 4).

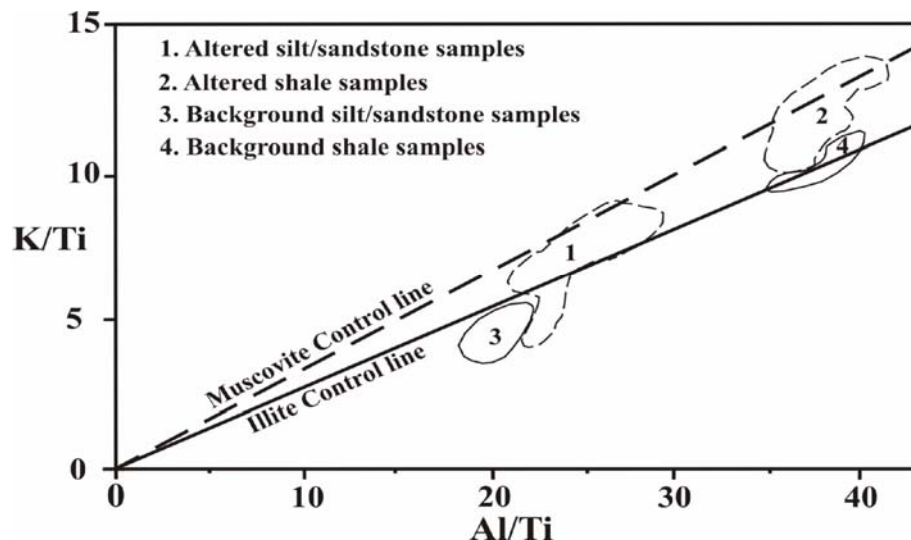


**Figure 3.4:** K/Ti versus Al/Ti PER diagram of Elura Zn-Pb-Ag deposit (adopted from Whitbread and Moore, 2004).

## Chapter 4

# Lithogeochemical investigation

### **4.1. Introduction**

Previous regional lithogeochemical investigations of the rocks related to massive sulphide ore bodies in the eastern part of the Namaqua Province were done by Middleton (1976), Wagener et al. (1986), Geringer et al. (1987), Cilliers (1987), Schade et al. (1989), Theart et al. (1989), Geringer et al. (1990), Moore et al. (1990), Cornell et al. (1990a), Cornell et al. (1990b), Cornell et al. (1992), Humphreys (1993), Geringer et al. (1994) and Thomas et al. (1994a,b). These investigations demonstrated:

- the presence of a volcano-sedimentary succession;
- the deposit is of volcanic hosted massive sulphide (VHMS) type; and
- that the rocks underlying the massive sulphide ore body at the Copperton mine experienced hydrothermal alteration (Theart et al., 1989).

The objective of this chapter is to find evidence of similar hydrothermal alteration in the other deposits and to quantify the degree of alteration, so that it could be shown to be useful in regional lithogeochemical exploration.

During the formation of metalliferous VHMS deposits, hydrothermal fluids leach from, or add some chemical elements into the host rocks. Primary lithogeochemical dispersion haloes refer to that part of the enclosing rocks that were affected by this process. Some of these elements may be considered typomorphic of specific ore deposits and they are interpreted as a direct index or vector indicating the existence of a specific ore body. The

leached elements would have precipitated somewhere else, or were removed out of the system at the time of ore formation (Beus and Grigorian, 1977; Sanchez-Espana et al., 2000; Bonnet et al., 2005; Dawood et al., 2005). Systematic sampling of ore bodies and their enclosing rocks is therefore an essential requirement in establishing the characteristic lithogeochemical features that could be used in exploration for undiscovered ore bodies. The analytical data thus obtained is processed and used to determine the chemical characteristics of the geochemical haloes. With this objective in mind, the boreholes which intersect the hangingwall, ore zone and the footwall successions, were selected in the present study area i.e. boreholes AP2 and AP5 from the Areachap Cu-Zn deposit, and boreholes KN11 and KN12 from the Kantienpan Cu-Zn deposit.

The following lithogeochemical parameters and methods were adopted and expanded to be used for identifying and characterizing the alteration haloes in the footwall and hangingwall lithologies that developed in the precursor rocks at the time of sulphide mineralisation:

- 1) variations in the relative abundance of major element concentrations throughout the rock successions;
- 2) microprobe analyses of silicates and spinels to confirm the identity of some minerals and investigate the chemical variation in rock forming minerals near the ore zone;
- 3) norm calculations mainly as a method to identify peraluminous rocks in the rock successions;
- 4) alteration index (AI) (Ishikawa, et al., 1976) and Chlorite-Carbonate-Pyrite Index (CCPI) (Large et al., 2001) to distinguish the alteration process affecting the ore zone in the precursors of high grade metamorphosed rocks, by means of the box plot (Large et al., 2001);

- 5) immobile and mobile elements to separate the least altered rocks from the altered rocks and compare them with each other utilizing the isocon approach (Grant, 1986). This method is also used to quantify the degree of alteration;
- 6) Pearce element ratio (PER) analysis to identify the effects of hydrothermal fluids and metamorphism on major elements in specific minerals near the ore zone (Whitbread and Moore, 2004).

#### **4. 2. Sampling, sample preparation and analytical methods**

With regard to the lithogeochemical investigation, a total of 160 rock samples which include 73 samples from Areachap (27 samples from borehole AP2 and 46 samples from borehole AP5) and 87 samples from Kantienpan (49 samples from borehole KN11 and 38 samples from borehole KN12) were collected from available core of diamond-drilled holes (Appendix A, Fig. A.1 to A.4). The sample selection was based on the lithological variation observed in the successions intersected. In addition, five samples were taken from the scarce outcrops on the farm, Kantienpan (Appendix A, Fig. A.5).

Each sample was cut by diamond saw into two halves. One half was used for thin or polished thin sections, and for chemical analyses and the other half was kept for future use and quality control. In total 185 thin sections were made of which 172 polished for microprobe work. The petrographic investigation of these sections was done systematically. This study also served as a basis for microprobe analyses after selected mineral grains were marked. Coordinates of the spots, where analyses were required, were recorded and later used during the microprobe analysis of the mineral grains (Appendix B, Tables B.1 to B.7).

An ARL 9400XP+Wavelength dispersive X-ray Fluorescence Spectrometer (XRF) was used for the determination of whole rock major and trace elements at the Geology Department Laboratory, University of Pretoria. The sample material was crushed in a jaw crusher and milled to a grain size of less than 63 micron. Powder pellets for trace elements analysis and fused beads for major elements analysis were made from the

powder (Appendix C, Tables C.2 to C.7).

### **4.3. Major element variation near the ore zone**

The variation of major element concentrations may be used as an index of compositional changes caused by alteration at the time of ore formation (Whitbread and Moore, 2004).

The diagram, which shows these variations, may be used to detect the presence of alteration pipes and the nature of the unaltered footwall lithologies.

The objective is to identify zones in the successions immediately enclosing the sulphide mineralization displaying compositional variation that is characteristic of hydrothermal alteration at the time of ore formation. It should be noted that in the case of the two study areas discussed below, the silicate rocks and associated ores, were metamorphosed and intensely deformed, and that no primary “way up” indicators survived these events.

For this purpose, two boreholes were selected, one from the Areachap mine (AP5) and the other from the Kantienpan mine (KN11). The variations of major element compositions are used in the paragraphs below to locate the alteration zones and to define their geochemical characteristics.

#### **4.3.1. Interpretation of major elements variations adjacent to the ore zone in borehole AP5 (Areachap)**

In AP5, the ore is hosted by biotite-gneiss or biotite-hornblende-gneisses (lithological zone AR6 in Fig. 4.1). The gneissic rocks structurally overlying the ore zone, is interpreted to represent the primary footwall in this particular case as explained below. These gneisses contain cordierite, sillimanite, garnet and biotite. The gneissic rocks structurally below the ore zone, which is interpreted to be the primary hangingwall in this particular case, contain more hornblende and biotite.

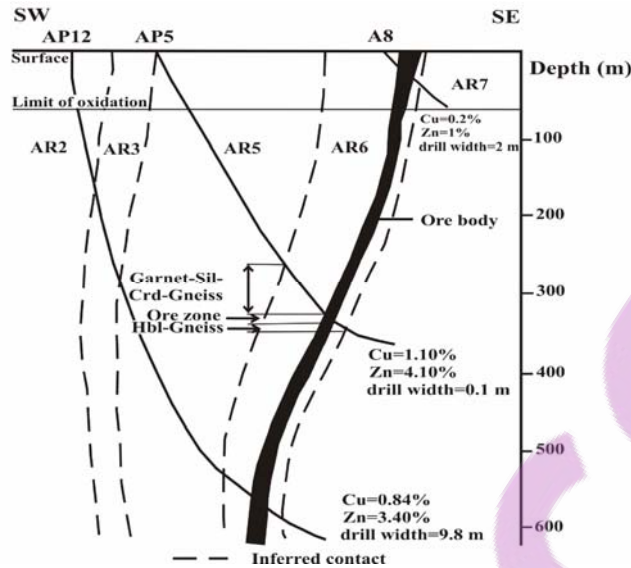


**Figure 4.1:** A cross-section of lithology at Areachap mine including the borehole AP5 (adopted from Voet and King, 1986) (Sil: sillimanite; Crd: cordierite and Hbl: hornblende)

The variations in CaO, Na<sub>2</sub>O, K<sub>2</sub>O and MgO (wt. %, all element concentrations are expressed as weight percent) in the lithological successions adjacent to the sulphide mineralisation are shown in Figures 4.2 to 4.5. The lowest CaO (0.01-1 %) and Na<sub>2</sub>O (0.2-1.5 %) contents in AP5 occur in samples depicted above the ore zone in Figures 4.2 and 4.3. Intervals with low CaO and Na<sub>2</sub>O are generally considered to represent a footwall alteration zone or an alteration pipe that characterizes VHMS deposits (Lydon, 1998b), therefore the interval described above probably represents the altered zone in the original footwall rocks of the deposit.

K<sub>2</sub>O contents (1-2.6 %) in AP5 are generally higher between samples AP5/21 and AP5/37 and decreases from AP5/37 (0.75-1.25 %) towards AP5/45 (Fig. 4.4).

The MgO contents (2.5-7 %) are on average higher between samples AP5/21 and AP5/37 when compared to samples from AP5/37 to AP5/45 (0.9-1.2 % MgO) in borehole AP5 (Fig. 4.5).

Intervals with high MgO and K<sub>2</sub>O are also generally considered to be characteristic of the footwall alteration zone of VHMS deposits (Lydon, 1998b), this therefore supports the interpretation that the above intervals (between AP5/21 and AP5/37)

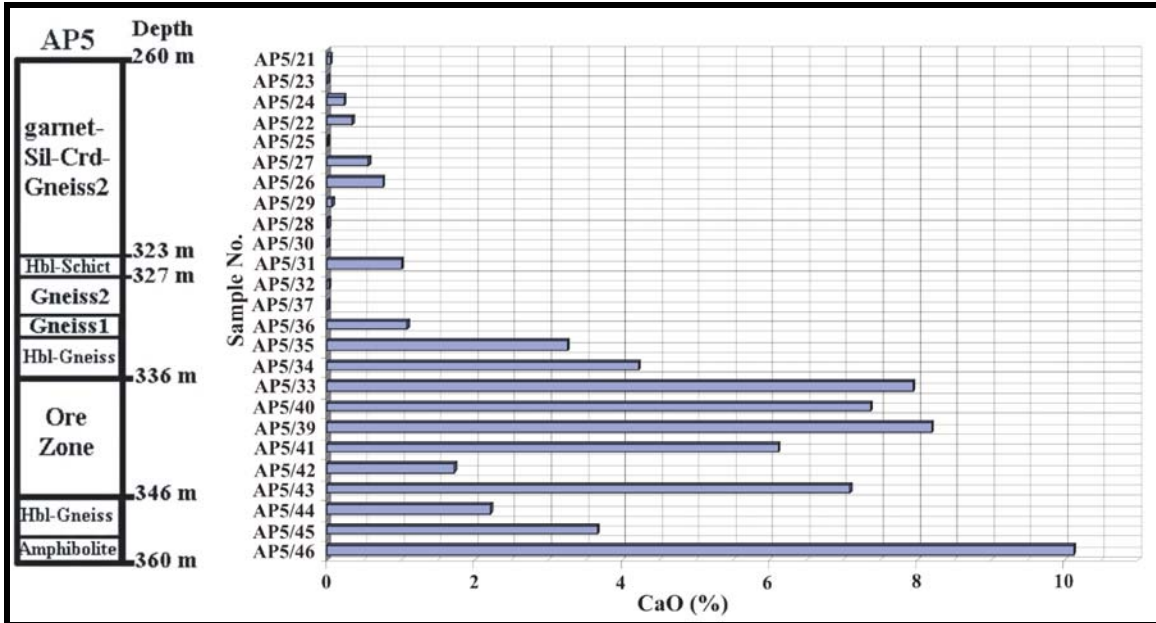


**Figure 4.2:** Variation of CaO through the lithological successions adjacent to the ore zone, at the Areachap deposit (Gneiss1: normal quartzo feldspathic gneiss; Gneiss2: peraluminous rocks; Hbl: Hornblende; Crd: cordierite; Sil: sillimanite).

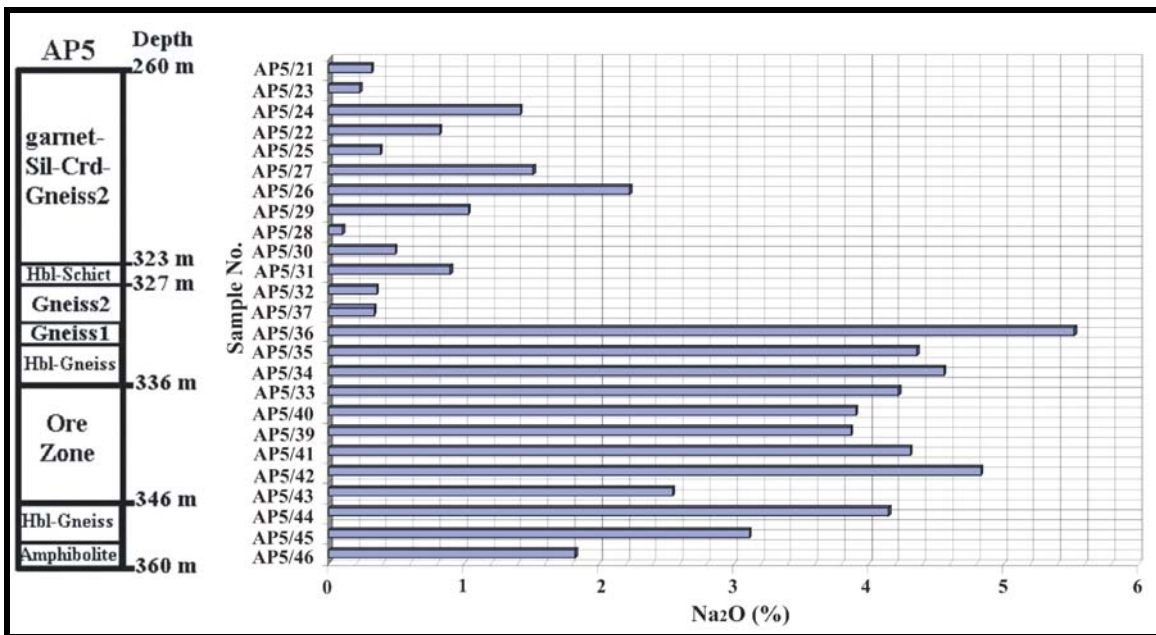


**Figure 4.3:** Variation of Na<sub>2</sub>O through the lithological successions hosting the ore zone, at the Areachap deposit (Gneiss1: normal quartzo feldspathic gneiss; Gneiss2: peraluminous rocks; Hbl: Hornblende; Crd: cordierite; Sil: sillimanite).

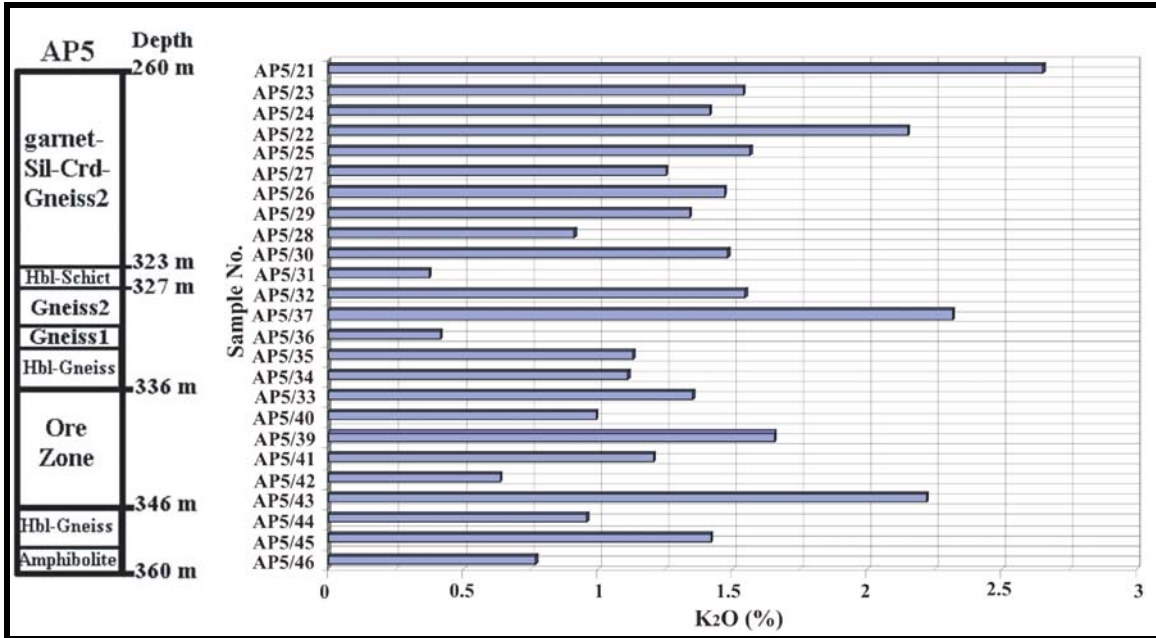


**Figure 4.4:** Variation of K<sub>2</sub>O through the lithological successions adjacent to the ore zone, at the Areachap deposit (Gneiss1: normal quartzo feldspathic gneiss; Gneiss2: peraluminous rocks; Hbl: Hornblende; Crd: cordierite; Sil: sillimanite).

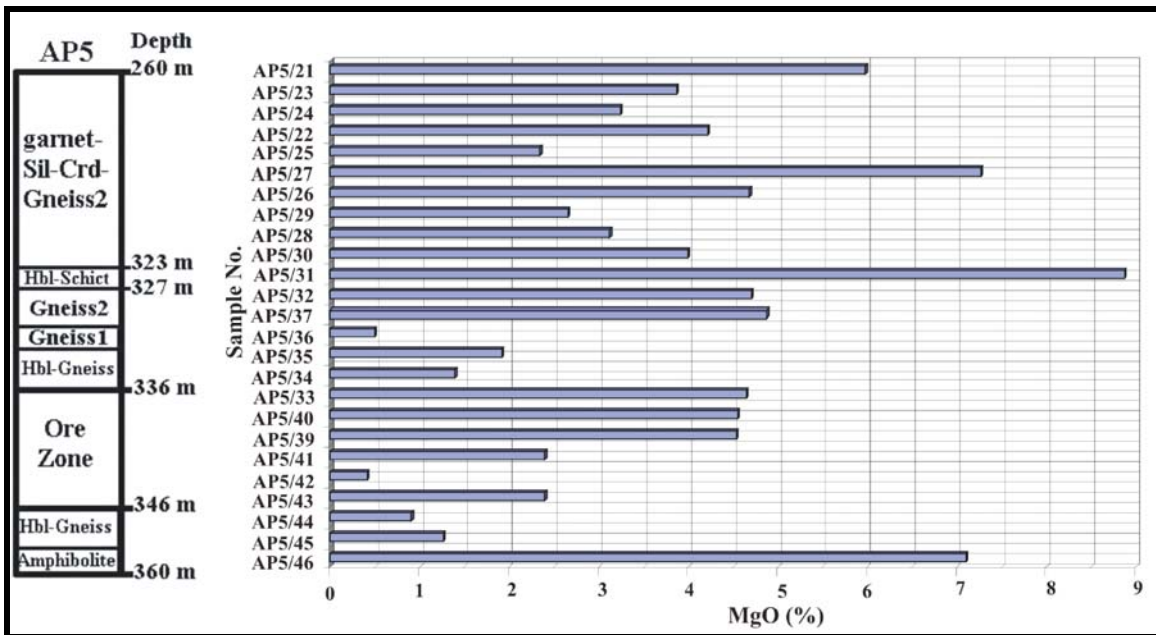


**Figure 4.5:** Variation of MgO through the lithological successions hosting the ore zone, at the Areachap deposit (Gneiss1: normal quartzo feldspathic gneiss; Gneiss2: peraluminous rocks; Hbl: Hornblende; Crd: cordierite; Sil: sillimanite).

probably represents the footwall alteration zone. This interpretation requires that the ore body must have been structurally turned over in acquiring its present habit.

#### 4.3.2. Interpretation of major elements variation near the ore zone in borehole KN11 (Kantienpan)

In KN11, the ore is overlain by biotite-gneiss or biotite-hornblende-gneiss (unit number 5 in Fig. 4.6). Whereas, the gneisses below the ore zone contain cordierite, sillimanite and biotite reflecting its peraluminous character, the gneisses intercalated with the massive sulphide towards the upper contact of the ore zone contain hornblende and biotite indicating the progressively more calcareous composition of the hangingwall rock succession.

The variations in CaO, Na<sub>2</sub>O, K<sub>2</sub>O and MgO (%) in the lithological successions hosting the sulphide mineralisation are shown in Figures 4.7 to 4.10. In KN11, the interval with the lowest CaO (0.01 %) and Na<sub>2</sub>O (0.1-0.25 %) contents occur between the samples KN11/38 and KN11/43, which are located at the bottom of the ore zone. Based on the depletion of CaO and Na<sub>2</sub>O, it is assumed that this interval represents the alteration pipe. This is also seen as evidence that the ore body has not been structurally over turned. This will be further demonstrated in subsequent sections.

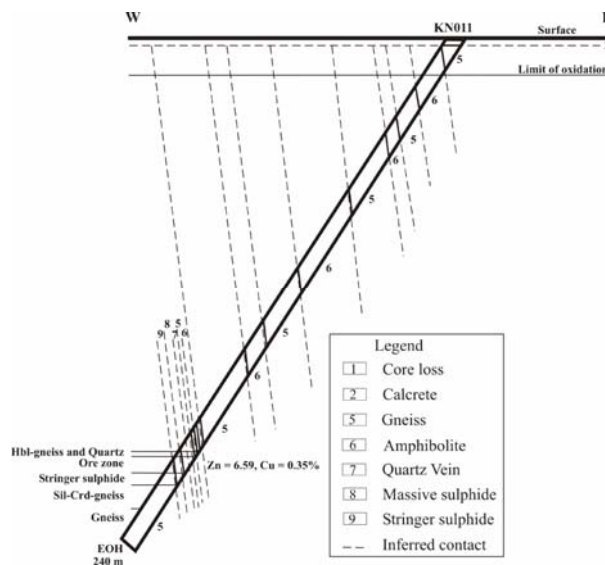


**Figure 4.6:** Cross-section of borehole KN11 in the Kantienpan area (Sil: sillimanite, Crd: cordierite and Hbl: hornblende).

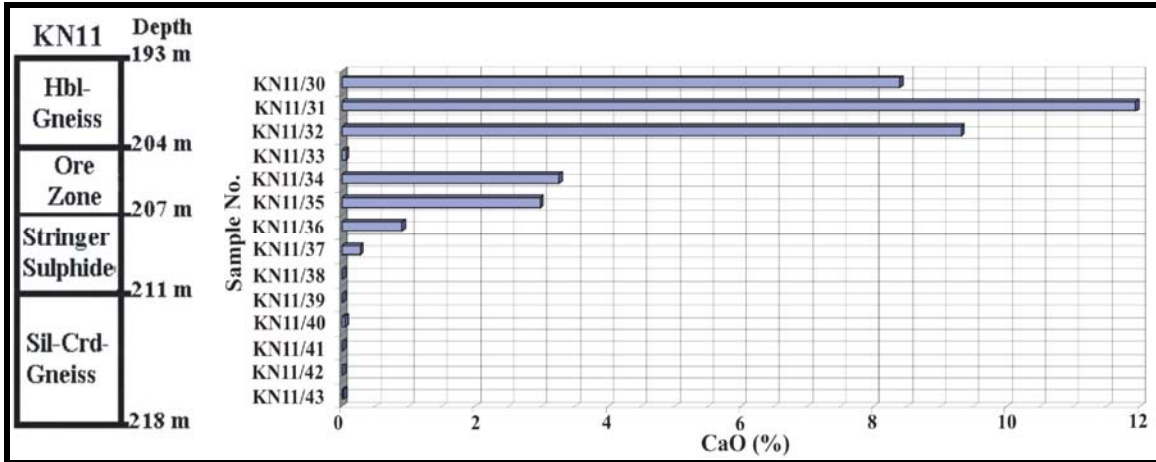


Figure 4.7: Variation of CaO through the lithological successions adjacent to the ore zone (Hbl: Hornblende; Crd: cordierite; Sil: sillimanite).

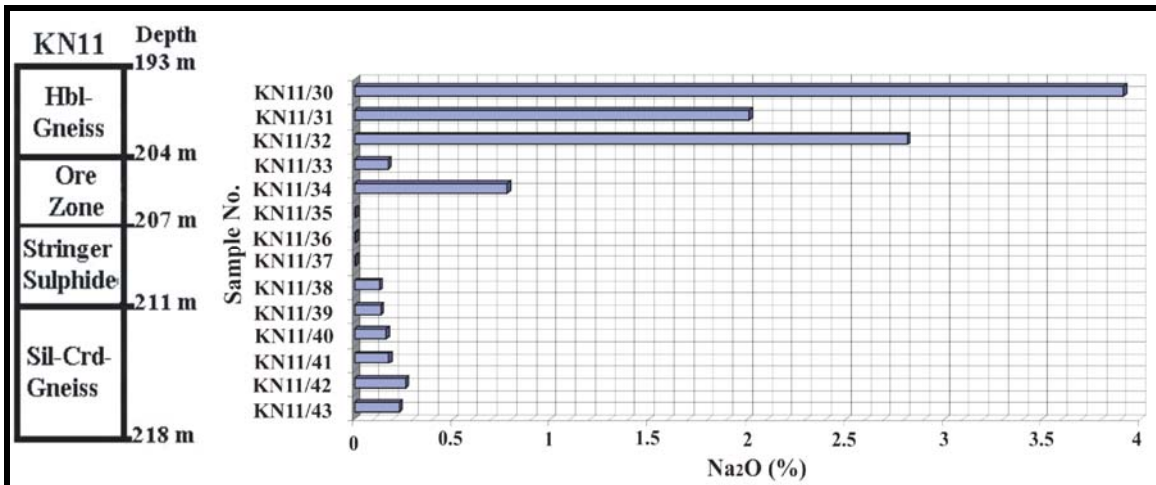


Figure 4.8: Variation of Na<sub>2</sub>O through the lithological successions hosting the ore zone (Hbl: Hornblende; Crd: cordierite; Sill: sillimanite).

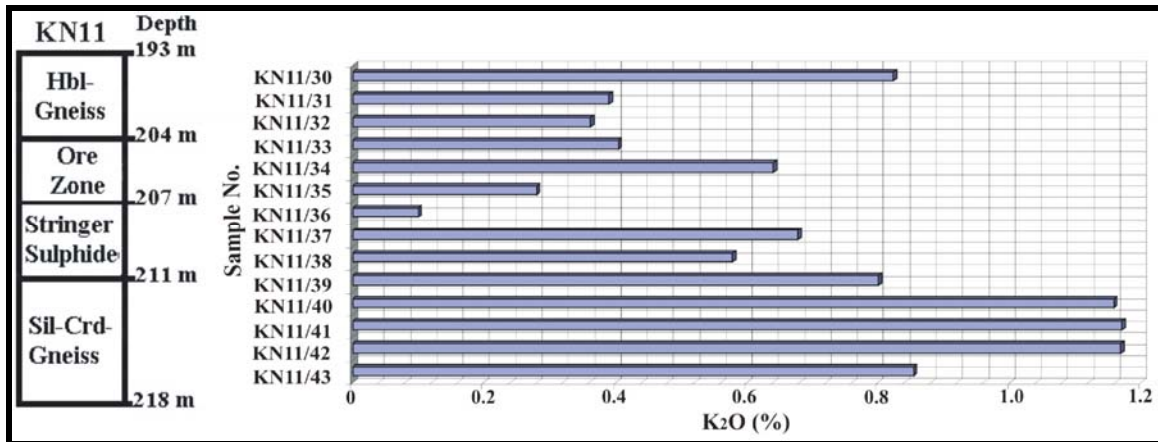


Figure 4.9: Variation of K<sub>2</sub>O through the lithological successions adjacent to the ore zone (Hbl: Hornblende; Crd: cordierite; Sil: sillimanite).

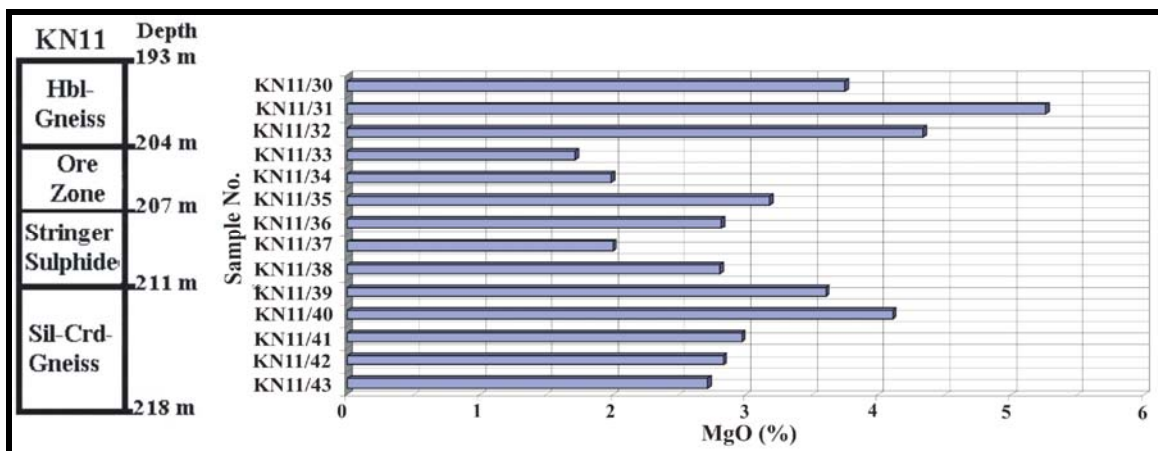


Figure 4.10: Variation of MgO through the lithological successions hosting the ore zone (Hbl: Hornblende; Crd: cordierite; Sil: sillimanite).

In borehole KN11, K<sub>2</sub>O contents (0.8-1.2 %) are higher between samples KN11/38 and KN11/43, and decreases from sample KN11/38 (0.35-0.81 %) towards KN11/30 (Fig. 4.9). Unlike in the case with Na and Ca (i.e. low contents), the high K<sub>2</sub>O bearing zones are ascribed to the footwall alteration zone.

The MgO contents are generally high (2.5-7 % MgO) between samples KN11/38 and KN11/43, when compared to samples from KN11/38 to KN11/30 (3.5-5.2 % MgO) in this borehole (Fig. 4.10). Samples KN11/30 to KN11/32 are biotite-hornblende-gneisses, which explain the high MgO contents in these samples.

#### **4.4. Mineral chemistry near the ore zone**

This section is intended to identify changes in the chemical composition of the rock forming minerals. These changes might be related to primary halo development and the minerals may supply additional evidence of the preservation of primary alteration features. For this purpose, the Na/Ca ratio in plagioclase,  $Mg / (Mg + Fe + Ca)$  ratio in pyroxene,  $Mg / (Mg + Fe)$  ratio in cordierite, the composition of garnet, the  $Mg / Fe$  ratio in biotite, and the composition of spinel are considered below. The  $Mg / (Mg + Fe)$  ratio of retrograde chlorite is also considered. Microprobe analysis was done on selected samples from the rock successions adjacent to the ore body. A CAMECA EPMA- SX 100 electron microprobe was used to analyse the minerals i.e., feldspars, pyroxenes, cordierite, garnets, biotite and chlorite (Appendix B, Tables B.1 to B.7).

Table B.8 (Appendix B) represents the chemical composition of plagioclase from Areachap (AP5) and Kantienpan (KN11). The variation of Na ( $100 * Na / (Ca + Na + K)$ ) and Ca values ( $100 * Ca / (Ca + Na + K)$ ) in plagioclase in the vicinity of the ore zone is shown in Figure 4.11 for KN11. The Na values have the lowest value in rocks collected from both sides of the ore zone ( $An_{40}$  to  $An_{77}$ ), reflecting that plagioclases are more Ca-rich close to the ore zone (samples KN11/32, KN11/40 and KN11/44). Plagioclases are more Na-rich further away from the ore zone ( $An_{19}$  to  $An_{33}$ , samples KN11/27 and KN11/28) in this intersection. A similar tendency has been noted in two samples from AP5 ( $An_4$  to  $An_{19}$ , sample AP5/22 in Table B.8).

The chemical composition of the Kantienpan pyroxenes are shown in Figure 4.12. The samples that are adjacent to the ore zone in the footwall alteration zone (KN11/39, KN11/40 and KN11/44) have the highest  $Mg^*$  ratio ( $100 * \text{cationic ratio of } Mg / (Mg + Fe + Ca)$ ). This value decreases in the stringer zone (KN11/38) and in the hangingwall (KN11/20) away from the ore zone. It is therefore suggested that the  $Mg^*$  ratios of pyroxenes reflects the compositional differences between the footwall and hangingwall lithologies.

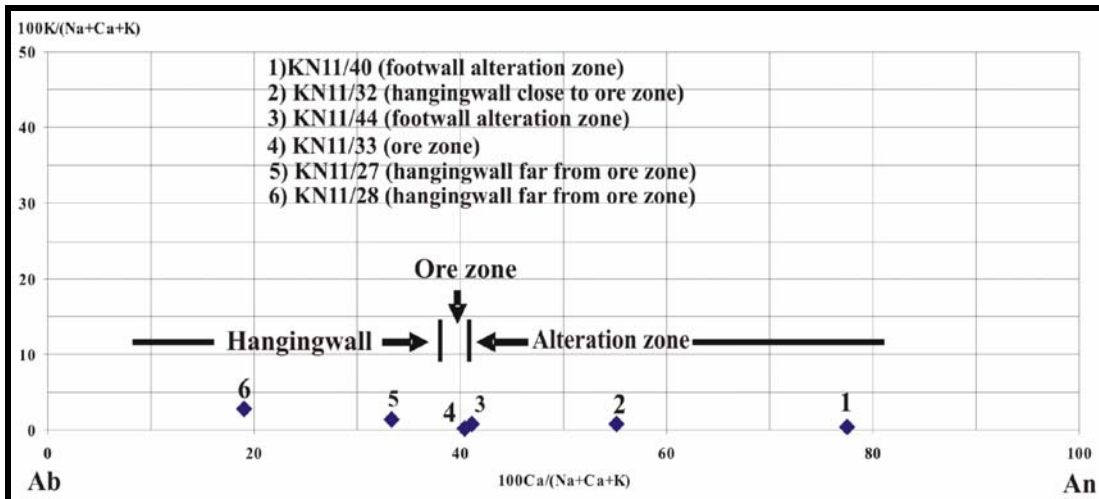


Figure 4.11: Variation of Na and Ca in plagioclase, Kantiengan (KN11) (Ab: albite and An: anorthite).

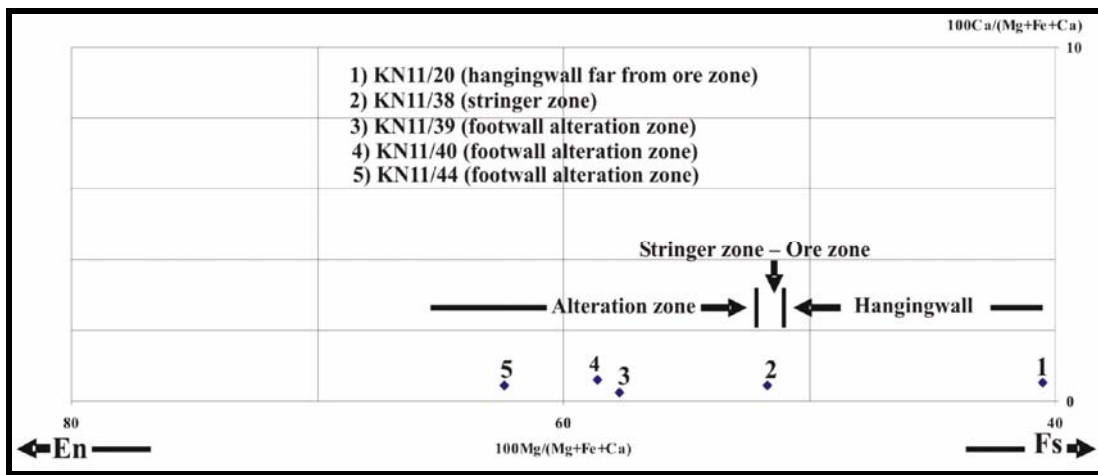
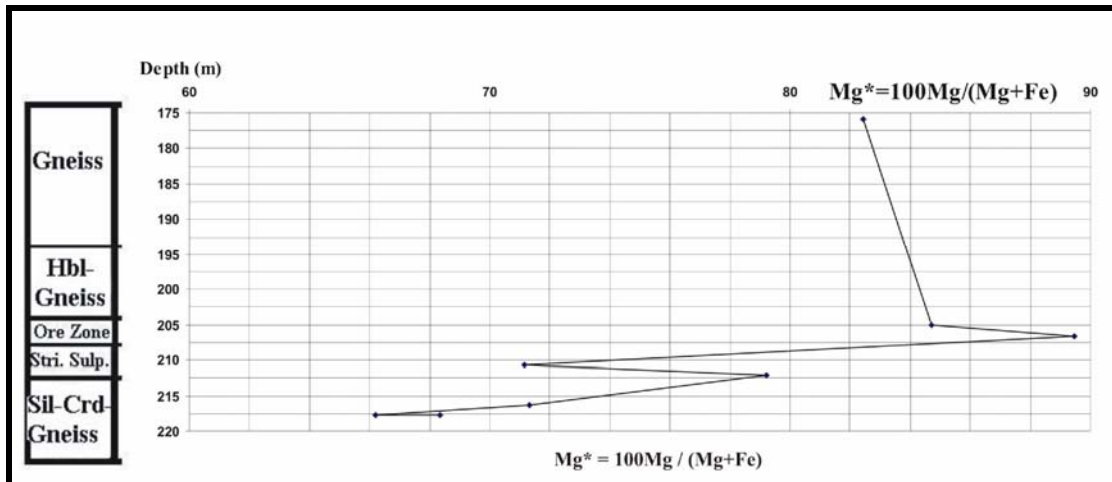


Figure 4.12: Variation of Mg, Fe and Ca in the pyroxene, Kantiengan (KN11), (En: enstatite and Fs: ferrosilite).

The variation in the magnesium number ( $Mg\# = 100 \cdot Mg / (Mg + Fe)$ ) of cordierite adjacent to the ore zone (for KN11) is shown in Figure 4.13. The  $Mg\#$  of cordierite in both footwall and hangingwall are generally high ( $>66.2$ ), but cordierites from the hangingwall have slightly higher  $Mg\#$  numbers ( $>82.5$ ), compared to those from the footwall (66.2-73.1). The  $Mg\#$  number of cordierite from the ore zone (89.4) is the highest, when compared to the hangingwall and footwall alteration zones.



**Figure 4.13:** Variation of the Mg number in cordierite, Kantienpan, (KN11), (Hbl: Hornblende; Stri. Sulp.: stringer sulphide; Sil: sillimanite; Crd: cordierite).

In the footwall alteration zone in the Areachap deposit (Appendix B, Table B.10, samples AP5/23, AP5/25, AP5/29 and AP5/32), the Mg number of cordierite changes from 42.19 to 77.67 and is lower than the maximum value (89.44) in the ore zone of KN11.

The chemical composition of garnet is given in Table B.11 (Appendix B). Variation in the composition of garnet in the footwall alteration zone and the ore zone at Areachap is shown in Figure 4.14. The almandine and pyrope components in garnet grains from the footwall alteration zone (samples AP5/22, AP5/23, AP5/25 and AP5/28) are high, whereas the spessartine and grossular components are low. The garnets in the ore zone (samples AP5/42 and AP5/43) have high Ca contents but low Mg contents.

The chemical composition of mica in the host rocks of the Areachap and Kantienpan ore body are shown in Figure 4.15. The Mg-rich variety, phlogopite, (samples AP5/22 to AP5/32 and KN11/37 to KN11/44) is more common adjacent to the ore zone in the footwall alteration zones in both boreholes. In sample AP5/35, the biotite is more Fe-rich and may be referred to as annite. This sample reflects the composition of mica in samples immediately below the ore zone that probably escaped the alteration processes, because its precursors were probably a distance away from the primary feeder zone. Theart (1985) reported that the Mg / (Mg + Fe) ratio of biotite decreases both vertically away from the ore zone at the Prieska Cu-Zn mine in the footwall succession, as well as laterally in the

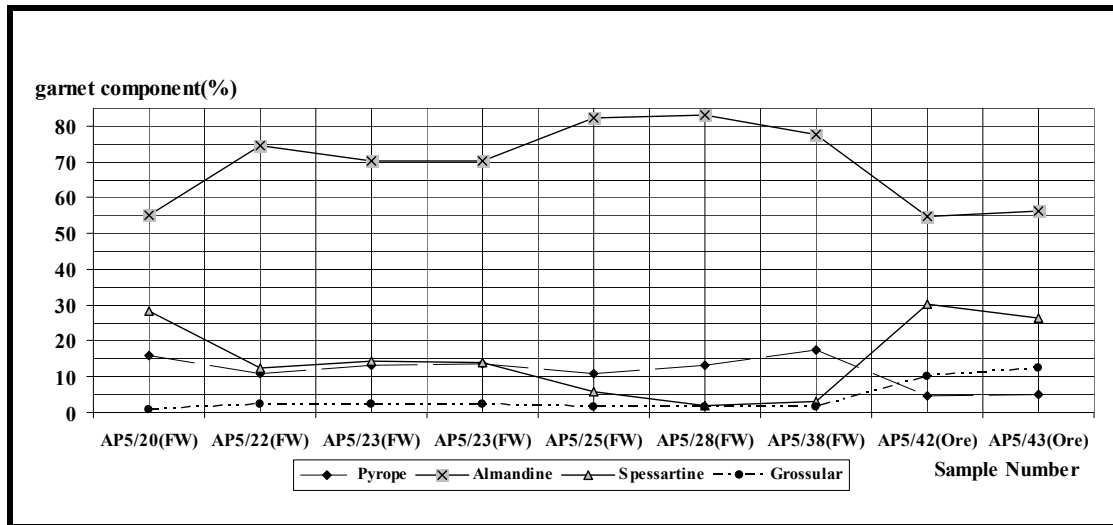


Figure 4.14: Chemical components of garnet in the alteration and ore zones, Areachap (AP5), (FW: footwall).

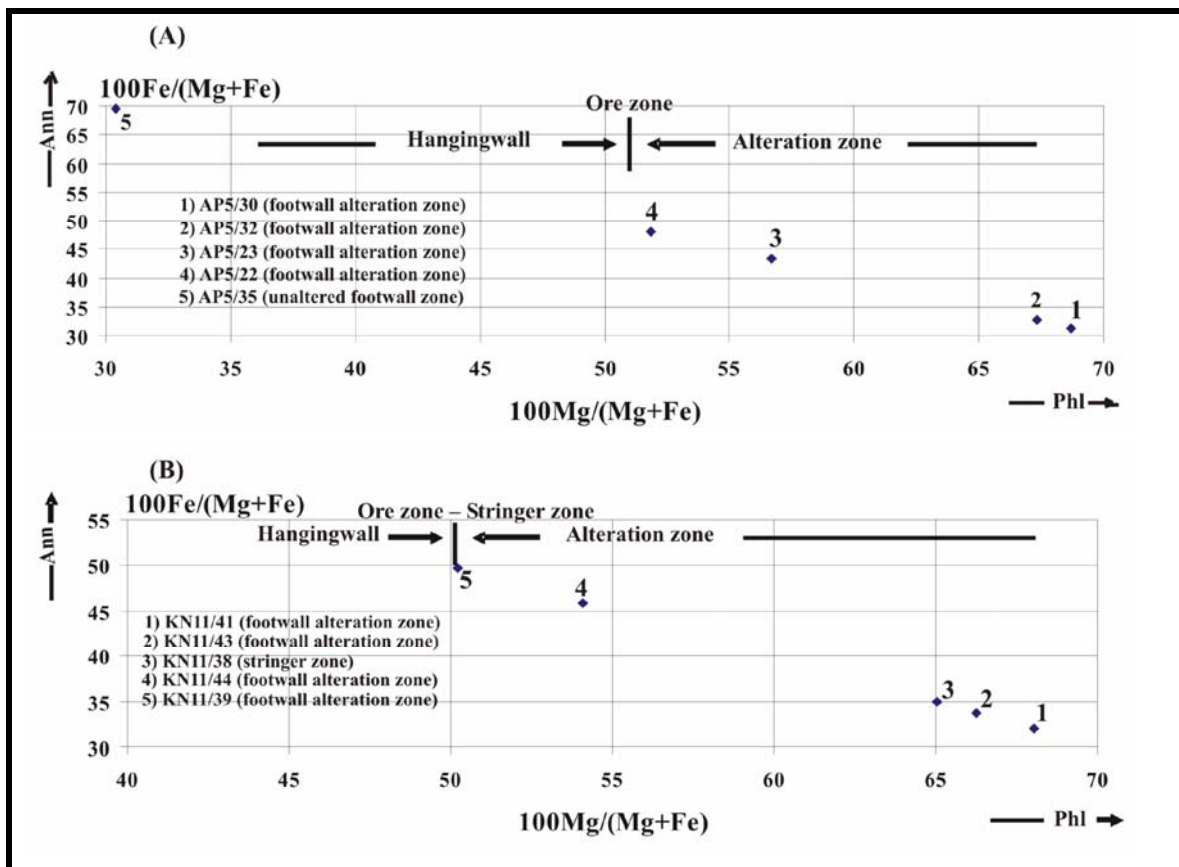


Figure 4.15: Variation of Mg and Fe in mica at Areachap (A) and Kantienpan (B), (Ann: Annite and Phl: phlogopite).

biotite schist on strike with the mineralization.

The chemical composition of spinel close to the ore zone at Kantienpan is given in Table 4.2. The high Al<sub>2</sub>O<sub>3</sub> content of these rocks confirms the peraluminous characteristic of the footwall alteration zone and ore zone. These spinels may therefore be regarded as metamorphic indicator minerals of the hydrothermal alteration that affected the precursor rocks. Spinel has a high Zn content in the ore zone and in the footwall alteration zone in KN11 (samples KN11/34, KN11/42 and KN11/43) suggesting that the spinel is of the gahnite type.

**Table 4.2:** Chemical composition of spinel grains from Kantienpan.

	Spinel Analyses					Based on 32(O)					
	KN11_34B [P5_Spin (Ore)]	KN11_42 [P1_Spin (FW)]	KN11_43 [P4_Spin (FW)]	KN12_32 [P2_Gah (Ore)]	KN12_35A [P3_Spin (Ore)]		KN11_34B [P5_Spin (Ore)]	KN11_42 [P1_Spin (FW)]	KN11_43 [P4_Spin (FW)]	KN12_32 [P2_Gah (Ore)]	KN12_35A [P3_Spin (Ore)]
	Gahnite	Gahnite	Gahnite	Gahnite	Zincianspinel		Gahnite	Gahnite	Gahnite	Gahnite	Zincianspinel
SiO <sub>2</sub>	0.03	0.21	0.23	0.42	0.01	Si	0.01	0.05	0.05	0.10	0.00
Al <sub>2</sub> O <sub>3</sub>	59.02	56.12	56.31	56.39	59.94	Al	15.86	15.76	15.71	15.67	15.76
Cr <sub>2</sub> O <sub>3</sub>	0.01	0.01	0.01	0.01	0.00	Cr	0.00	0.00	0.00	0.00	0.00
TiO <sub>2</sub>	0.00	0.01	0.01	0.00	0.02	Ti	0.00	0.00	0.00	0.00	0.00
FeO	5.39	13.71	12.04	9.50	16.60	Fe <sup>+2</sup>	1.03	2.73	2.38	1.87	3.10
MgO	6.26	2.30	2.47	4.28	8.56	Mg	2.13	0.82	0.87	1.50	2.85
MnO	0.46	0.23	0.23	0.22	0.39	Mn	0.09	0.05	0.05	0.04	0.07
ZnO	29.39	26.43	28.69	27.94	14.10	Zn	4.95	4.65	5.01	4.87	2.32
CaO	0.00	0.00	0.00	0.00	0.00	Ca	0.00	0.00	0.00	0.00	0.00
K <sub>2</sub> O	0.00	0.01	0.00	0.00	0.01	Note: FW: footwall; Spin: Spinel; Gah: Gahnite and [Lab number].					
Na <sub>2</sub> O	0.66	0.63	0.69	0.63	0.31						
F	0.00	0.06	0.00	0.02	0.00						
<b>Total</b>	101.27	99.73	100.68	99.41	99.94						

Note: KN11\_34B [P5\_Spin (Ore)] means borehole KN11\_ sample No 34B [analysis point No\_ in spinel (from the ore zone)].

Sample KN12/35A contains spinel with the highest Fe content and its Mg content is higher than that of Zn, but both Mg and Zn have lower molecular proportions than Fe. These spinels may be described as zincianspinel.

#### 4.4.1. The retrograde chlorite

The chlorite minerals observed at both localities is a product of retrograde metamorphism. The chemical composition of chlorite adjacent to the ore deposit is given in Table 4.3. Chlorites of the ore zone are characterised by the highest Mg# (Mg# = Mg/ (Mg + Fe), 0.93 in sample KN11/36) in KN11 when compared to the footwall (0.59 in sample KN11/41). The highest Mg# in AP5 (0.45 in sample

AP5/40) is also considered for the sample in the ore zone, and it has lower values in the hangingwall (samples AP5/44 and AP5/45). Based on the low Mg# value of chlorite in the hangingwall lithologies of AP5 (0.35 and 0.44 in samples AP5/44 and AP5/45) these chlorites are classified as chamosite.

**Table 4.3:** The chemical composition of chlorite grains near the ore zone from Areachap and Kantienpan.

	Chlorite Analyses						Based on 28(O)						
	AP5_40 [P3_Bio (Ore Zone)]	AP5_42 [P3_Bio (Ore Zone)]	AP5_44 [P2_Chlorite (HW)]	AP5_45 [P4_Bio (HW)]	KN11_36 [P2_alt(chlorite or pin) (Stringer Zone)]	KN11_41 [P4_Amp (FW)]		AP5_40 [P3_Bio (Ore Zone)]	AP5_42 [P3_Bio (Ore Zone)]	AP5_44 [P2_Chlorite (HW)]	AP5_45 [P4_Bio (HW)]	KN11_36 [P2_alt(chlorite or pin) (Stringer Zone)]	KN11_41 [P4_Amp (FW)]
	Fe-Mg Chlorite	Fe- Chlorite	Fe- Chlorite	Fe-Mg chlorite	Mg- Chlorite	Mg-Fe chlorite		Fe-Mg Chlorite	Fe- Chlorite	Fe- chlorite	Fe-Mg chlorite	Mg- Chlorite	Mg-Fe chlorite
SiO <sub>2</sub>	29.07	27	26.21	26.55	30.22	25.43	Si	6.18	6.03	5.75	5.76	5.86	5.29
Al <sub>2</sub> O <sub>3</sub>	16.9	17.01	18.46	18.23	12.57	23.09	Al	1.82	1.97	2.25	2.24	2.14	2.71
TiO <sub>2</sub>	0.39	0.79	0.04	0.17	0.00	0.03	Al	2.41	2.51	2.52	2.42	0.74	2.96
FeO	27.94	34.06	33.31	28.71	4.94	21.01	Ti	0.06	0.13	0.01	0.03	0.00	0.00
MgO	12.57	6.68	9.48	12.41	38.05	16.71	Fe <sup>+2</sup>	4.96	6.36	6.10	5.20	0.80	3.66
MnO	0.42	0.88	0.68	1.05	0.76	0.31	Mg	3.98	2.23	3.10	4.01	11.00	5.19
CaO	0.04	0.14	0.02	0.09	0.13	0.01	Mn	0.08	0.17	0.13	0.19	0.12	0.05
K <sub>2</sub> O	0.89	1.04	0.02	0.08	0.08	0.02	Ca	0.01	0.03	0.00	0.02	0.03	0.00
Na <sub>2</sub> O	0.05	0.04	0.01	0.01	0.02	0.01	K	0.24	0.30	0.01	0.02	0.02	0.01
F	0.13	0.00	0.05	0.05	0.00	0.12	Na	0.02	0.02	0.00	0.00	0.01	0.00
Total	88.48	87.72	88.31	87.45	86.82	86.81	Mg#	0.45	0.26	0.34	0.44	0.93	0.59

Note: Mg# = Mg/(Mg+Fe); Bio: Biotite; Chl: Chlorite; Pin: Pinite; alt: altered; Amp: Amphibole; FW: footwall, HW: hangingwall and AP5\_44 [P2\_Chlorite (HW)] means borehole AP5\_ sample No. 44 [analysis point No. in chlorite (from the hangingwall)].

It may be concluded that, notwithstanding the retrograde nature of the chlorite, the system behaved relatively closed during the retrograde stages of its evolution as the chlorite reflects the precursor bulk rock composition. It also indicates the addition of water, without major destruction of sulphide minerals.

#### **4.5. Identification of Peraluminous rocks close to the ore zone using normative calculations**

Normative calculations could be used to estimate the proportions of “standard or normative minerals” based on the chemical composition of the rock. The calculations assume that the crystallized assemblages could form from a magma of the same composition as the composition of the rock under ideal equilibrium conditions. An example is the Cross, Iddings, Pirsson and Washington (C.I.P.W.) method which is used here to determine the percentages of normative minerals. It should be noted that this method was developed for igneous rocks, but that the presence and abundance of

normative minerals may provide a holistic method to consider major element behaviour even in non-igneous rock types, given that it is not used to imply an igneous origin.

Normative corundum ( $\text{Al}_2\text{O}_3$ ) is one of the diagnostic standard minerals because it gives a direct indication of the peraluminous character of rocks. The Minpet software was used to calculate the normative minerals of each sample based on the chemical composition of the rock as determined by XRF (Table 4.4). Those samples with exceptionally high percentages of normative corundum ( $\geq 9$  wt. %) are listed in Table 4.4. Ten samples from AP5 and one from KN11 have exceptionally high percentages of normative corundum.

The peraluminous ratio ( $\text{Al}_2\text{O}_3 / (\text{Na}_2\text{O} + \text{K}_2\text{O} + \text{CaO})$ ) may also be used to define the peraluminous character of samples in the rock succession. The peraluminous ratio is listed for samples adjacent to the ore zone in boreholes AP5 and KN11 in Table 4.4.

The cumulative frequency versus probability behaviour of the peraluminous ratios in all of the samples (Fig. 4.15) identifies an anomalous sub-population. This principal is utilized in the Prob Plot software (Sinclair, 1976) to estimate the threshold values between different sub-populations within a polymodal distribution. These estimates are then entered into a maximum likelihood procedure to calculate a theoretical distribution of a mixture resulting from up to five different sub-populations. The resultant theoretical curve is compared with the original distribution and if the comparison is satisfactory, the threshold values of the underlying sub-population may be used in estimating the threshold value of the anomalous sub-population in the data set, as well as its mean and standard deviation (Sinclair, 1976). It is suggesting that there are three sub-populations in the peraluminous value data set depicted in Figure 4.15. The first of these sub-populations has a cumulative frequency of less than 37.4%, the second is between 37.4% and 83.8% and the third is located at higher than 83.8%. The statistical results of these calculations for anomalous values are summarized in Table 4.5. Based on the threshold value of the peraluminous ratio for the third sub-population ( $\geq 4$ ), 19 samples (AP5/21 to AP5/27, AP5/29 to AP5/37, KN11/33 and KN11/38 to KN11/43) were identified as anomalous (Table 4.4).

**Table 4.4:** Peraluminous ratio, normative corundum value and minerals present in AP5 and KN11

Sample No.	Depth (m)	Per. <sup>1</sup> Ratio	N.C. <sup>2</sup> Value	Minerals present	Sample No.	Depth (m)	Per. <sup>1</sup> Ratio	Minerals present
AP5/21	270	4	≥9%	Bt,Qtz,Pl(alt),Crd, sil, Grt	KN11/30	195.35	1	Pl, Hbl, Bt, Qtz
AP5/23	278	6	≥9%	Qtz, Bt, Sil, Crd (alt), Grt	KN11/31	196.85	1	Pl, Hbl, Cpx, Bt, Qtz
AP5/24	281	4	<9	Qtz, Bt, Sil, Crd (alt)	KN11/32	198.80	1	Pl, Hbl, Qtz
AP5/22	283	4	<9	Bt, Qtz, Grt, Pl	KN11/33*	205.00	6	Qtz, Crd, Sil, Bt
AP5/25	298	6	≥9%	Qtz, Bt, Sil, Crd, Grt	KN11/34*	206.57	3	Qtz, Crd, opaque min., Grt, Bt
AP5/27	306	4	≥9%	Hbl, Bt, Qtz, Crd	KN11/35*	206.95	1	opaque min., Qtz, Crd (alt.)
AP5/26	312	3	≥9%	Pl, Qtz, Ms	KN11/36*	208.25	1	opaque min., Qtz, Crd (alt.)
AP5/29	317	4	<9	Qtz, Bt, Pl, Crd (alt), Sil	KN11/37*	209.20	1	opaque min., Qtz, Crd (alt.)
AP5/28	318.8	15	14	Qtz, Bt, Crd, Sil, Grt	KN11/38*	210.66	12	Qtz, Crd, Bt
AP5/30	318.9	6	≥9%	Qtz, Bt	KN11/39	212.16	10	Qtz, Crd, Bt, Opx
AP5/31	322.7	6	≥9%	Hbl, Pl (alt), epidote	KN11/40	216.23	7	Qtz, Opx, Bt, Crd
AP5/32	326.8	6	≥9%	Bt, Qtz, Crd (alt)	KN11/41	217.73	8	Qtz, Crd, Sil, Bt
AP5/37	328.4	5	≥9%	Qtz, Bt, Crd (alt), Sil	KN11/42	217.80	7	Qtz, Bt, Hercynite, Crd, Sil
AP5/36	331.3	2	<9	Pl, Qtz, Chl	KN11/43	218.19	7	Qtz, Crd, Sil
AP5/35	334.2	1	<9	Pl, Qtz, Chl, Bt	1. Per.: Peraluminous 2. N.C.: Normative corundum  - Bt=biotite; Chl: chlorite; Pl=plagioclases; Qtz=quartz; Crd=cordierite; Sil=sillimanite; Opx= ortho-pyroxene; Cpx= clino-pyroxene; Hbl=hornblende; alt=altered; Kfs= k-feldspar; Grt=garnet; Ms=muscovite; Min=mineral  - AP5/33*, KN11/35*: Samples in the ore zone			
AP5/34	335.7	1	<9	Pl, Hbl, Qtz, Bt				
AP5/33*	337	1	<9	Hbl, Pl, Chl, opaque min				
AP5/40*	338	1	<9	Hbl, Qtz, Pl, Bt, opaque min				
AP5/39*	339	1	<9	Hbl, Kfs, Pl, Qtz, Chl, opaque min				
AP5/41*	341	1	<9	Pl, Hbl, Qtz, opaque min				
AP5/42*	344	2	<9	Pl, Qtz, Bt, Grt, opaque min				
AP5/43*	345	1	<9	Pl, Qtz, Bt, Grt, Hbl, opaque min				
AP5/44	349	2	<9	Hbl, Qtz, Pl				
AP5/45	354.8	2	<9	Pl, Qtz, Bt, Chl, Hbl				
AP5/46	360.1	1	<9	Hbl, Pl, Qtz				

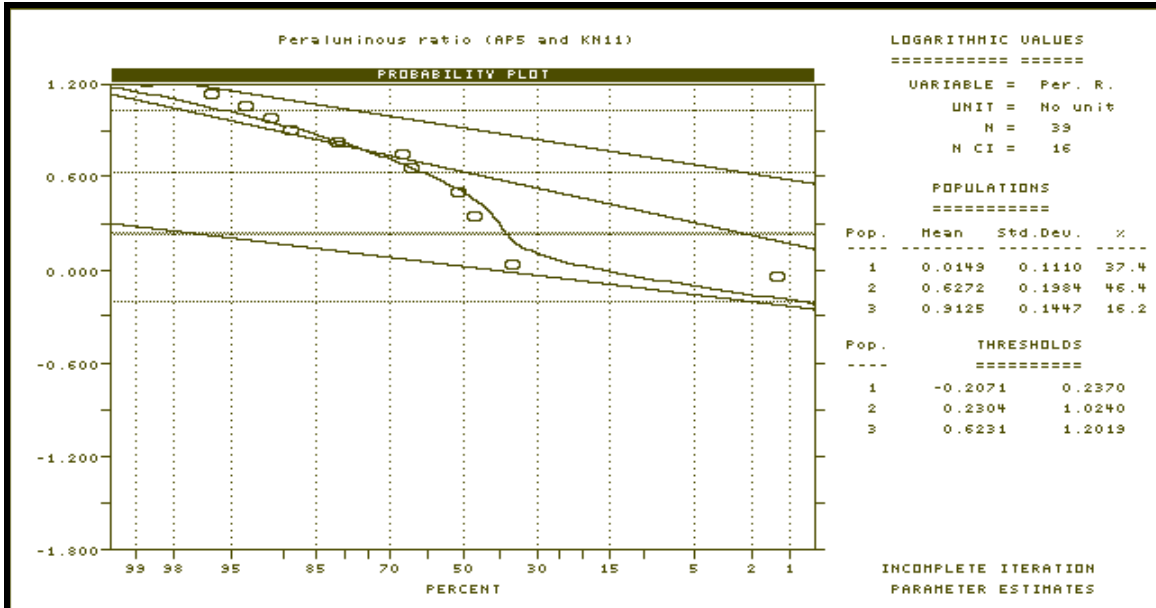


Figure 4.15: The probability plot of peraluminous ratio based on AP5 and KN11 data set

Table 4.5: The number of population, percentage, and threshold value for peraluminous ratio

Variable	No. of popul.	Means (M)	Stan. Dev. (SD)	%	Threshold values
Peraluminous Ratio	1	1	-0.80 1.34	37.4	0.6 1.7
	2	4	-2.68 6.69	46.4	1.7 10.6
	3	8	-5.86 11.41	16.2	4.2 15.9

Note: No. of popul.: Number of population, SD: Standard deviation

Mineralogically and lithologically all these samples (except sample KN11/33 from the ore zone of borehole KN11) belong to the garnet-sillimanite-cordierite-gneiss that has been identified as the rock type reflecting a hydrothermal footwall alteration zone in previous sections.

The variation of peraluminous ratio is plotted versus depth near the Areachap ore zone in borehole AP5 in Figure 4.16. As could be expected those samples with high peraluminous ratios (>3, between 270 to 330 meter depth) are situated above the ore zone in this borehole reflecting the inverted sequence. This depth interval may be described as the footwall alteration zone (Krishnakant Singh, et al., 2006). Those samples with low peraluminous values (<2) may be assumed to be located in the original hangingwall of the ore deposit.

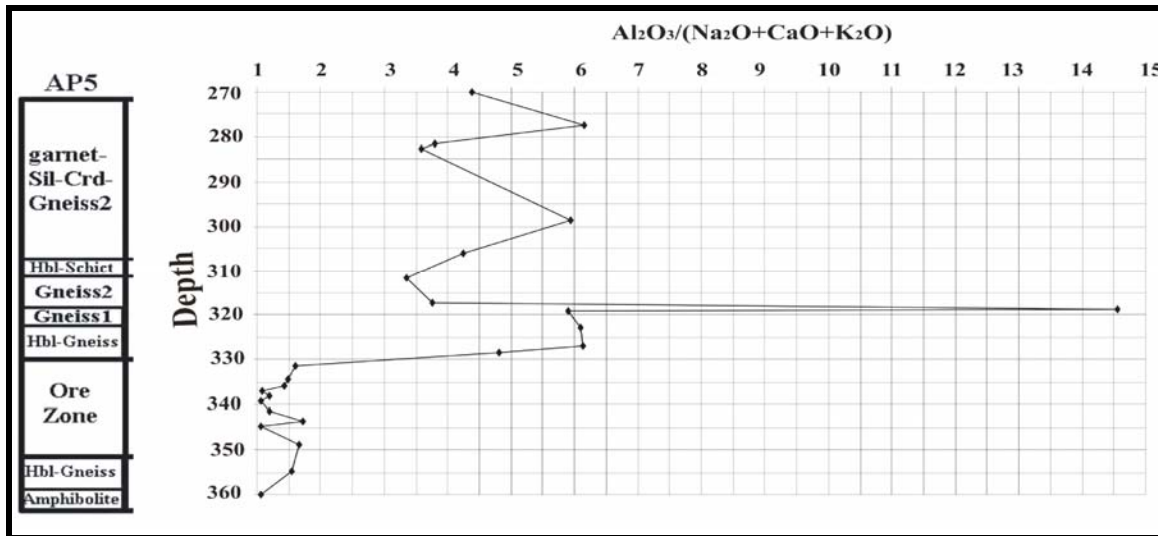


Figure 4.16: The variation of peraluminous ratio near the ore zone in borehole AP5 (Gneiss1: normal quartzo feldspathic gneiss; Gneiss2: peraluminous rocks; Hbl: Hornblende; Crd: cordierite; Sil: sillimanite)

In Figure 4.17, the variation in the peraluminous ratio is demonstrated versus depth near the Kantienpan ore zone in borehole KN11. In this graph, those samples with high peraluminous values (>6.7, between 212 to 218 meter depth) also belong to the gneissic rocks, which contain cordierite and sillimanite. It is suggested that this depth interval represents the footwall alteration zone of the Kantienpan deposit. Samples with low peraluminous values (<2) are assumed to be located in the original hangingwall of the ore deposit.

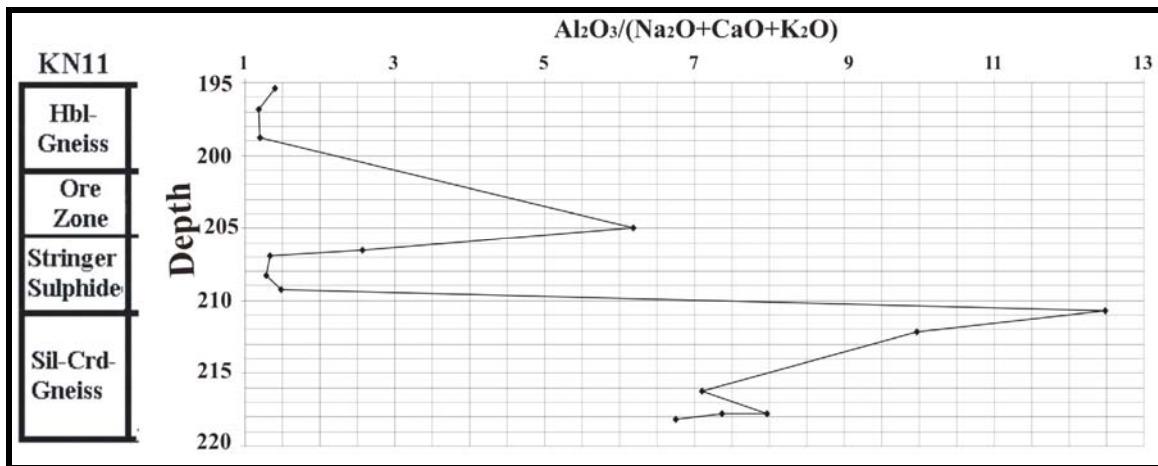


Figure 4.17: The variation of peraluminous ratio near the ore zone in borehole KN11 (Hbl: Hornblende; Crd: cordierite; Sil: sillimanite)

#### **4.6. Quantification of the degree of alteration in the precursor rocks**

In this section it would be attempted to quantify the degree of alteration in the precursor system, as seen in variation of the chemical composition of samples collected from the alteration zones identified above by using the isocon method, as proposed by Grant (1986).

Comparison between the rocks in the alteration zone and a similar rock that was not affected by the alteration event (known as a source rock or least altered precursor rock) is used to identify elements that remained in the rock during the alteration process (immobile) and those that were depleted from the rocks (mobile). Further more, these changes could be quantified using the isocon method.

In the isocon method, the percentage of gain and loss is calculated based on the slope of the isocon line. The isocon line is a line, which is extrapolated through the immobile elements and the origin-coordinate. Zr is an example of an element that has been found to behave immobile during hydrothermal alteration (Jenner, 1996). The distribution of this element is also not affected during metamorphism. For this reason Zr will be used here as an immobile element in the explanation given below. But, knowing that Zr could be expected to behave immobile, other elements plotting on or close to the isocon line could now also be identified that behaved relatively immobile during the specific alteration process.

The percentage of variation for each element or delta value is calculated as the residual value above or below the isocon line. The slope of the isocon line is calculated based on the immobile element (Zr) by the following formula:

$$\text{Slope of the isocon line} = (C^A / C^O)_{Zr}$$

$C^A$ : the concentration of immobile element, Zr, in the altered rock, and

$C^O$ : the concentration of immobile element, Zr, in the original or the least altered rock.

The  $\Delta$  value of an immobile element, Zr, is calculated as follows and would be equal to zero based on the definition of immobile element in the isocon method (Grant, 1986):

$$\Delta (\text{value})_{\text{Zr}} = (C^{\text{A}} - C^{\text{O}})_{\text{Zr}} * (\text{Slope of the isocon line}) = \Delta C_{\text{Zr}} \quad (1)$$

Where  $\Delta C_{\text{Zr}}$  = The change in concentration for an inspected element based on the Zr isocon line.

If there exists a direct relationship between the two samples where the one represents an altered variety of the other or the precursor prior to alteration, one may expect that the other elements that behaved immobile will plot on or close to the isocon line and will therefore display a small delta ( $\Delta$ ) value. As a corollary of this, one may also use this principle in identifying a suitable precursor composition.

The  $\Delta C$  of each element based on the isocon line through Zr could now be calculated (formula 4 in chapter 3). The percentage of gain and loss is estimated based on formula (5) in chapter 3.

The isocon diagrams comparing the least altered biotite-gneiss,  $C_o$ , and altered biotite-gneiss,  $C_a$ , in the succession at Areachap is presented in Figure 3.1 and 4.18 to 4.20. The isocon line passed through the origin and immobile elements such as  $\text{TiO}_2$ ,  $\text{Al}_2\text{O}_3$ , Zr, U, Th, Nb, Y, La, and Sc. The calculated  $\Delta$  values for oxides and trace elements for borehole AP5 in the Areachap area are given in Table 4.6. These calculations were based on Zr as an immobile element, where AP5/35 (biotite-gneiss) is selected as the least altered sample. It should be noted that the alteration process affected the protoliths to a variable degree and to illustrate that, Table 4.6 lists both the minimum and maximum concentration changes. Based on these figures and this table, the rocks in the alteration zone are depleted in CaO and  $\text{Na}_2\text{O}$ , but enriched in  $\text{K}_2\text{O}$ , MgO and FeO.  $\text{P}_2\text{O}_5$ , Cr, Y and Ce usually behave immobile during the weathering (Ohlander et al., 1996), but in the case of hydrothermal alteration Cr and Ce may be enriched or depleted.  $\text{P}_2\text{O}_5$  and Y behave immobile, enriched or depleted during the alteration. The mineral forming or mineral destruction processes may be a reason for these behaviour, especially the formation of phosphate minerals. The alteration zone is generally enriched in S, Pb and

Ba. Gain and losses of Zn and Cu can be observed in different samples. This most probably reflect formation of sulphides in fractures and the leaching of these elements during the destruction of the primary rock forming minerals by the hydrothermal fluids.

Figure 4.21 shows an isocon diagram comparing an alternative original rock namely sample AP5/42 and altered sample AP5/25, both biotite-gneisses, in the Areachap succession. The calculated  $\Delta$  values based on the Zr isocon line is given in Table 4.7. This confirms CaO and Na<sub>2</sub>O depletion and K<sub>2</sub>O and MgO enrichment in the alteration zone. In addition, Cr and Y are relatively enriched and P<sub>2</sub>O<sub>5</sub> and Ce are depleted. In this sample Cu, Zn, Pb and S are depleted whereas Ba is enriched.

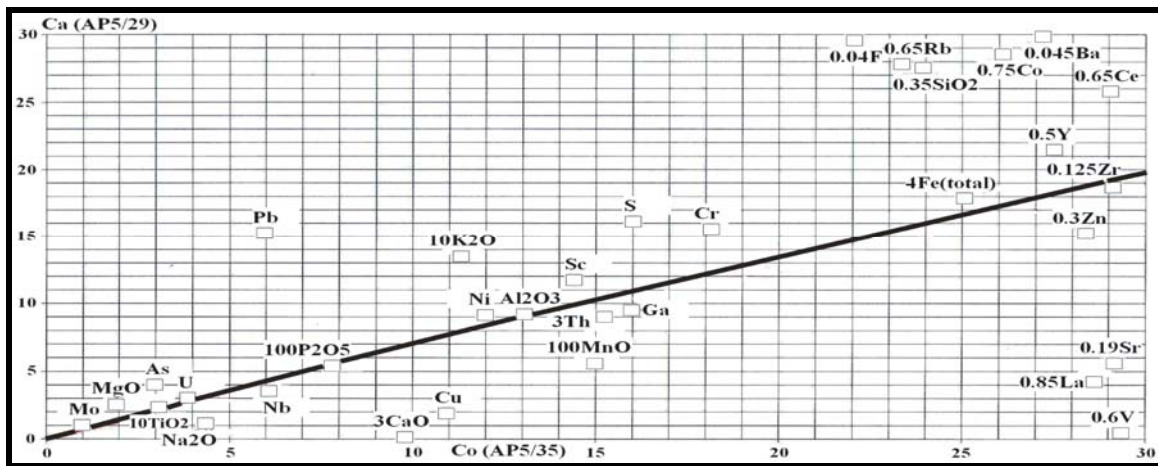


Figure 4.18: An isocon diagram of samples AP5/35, the least altered biotite-gneiss, and AP5/29, altered biotite-gneiss, from borehole AP5 in the Areachap area.

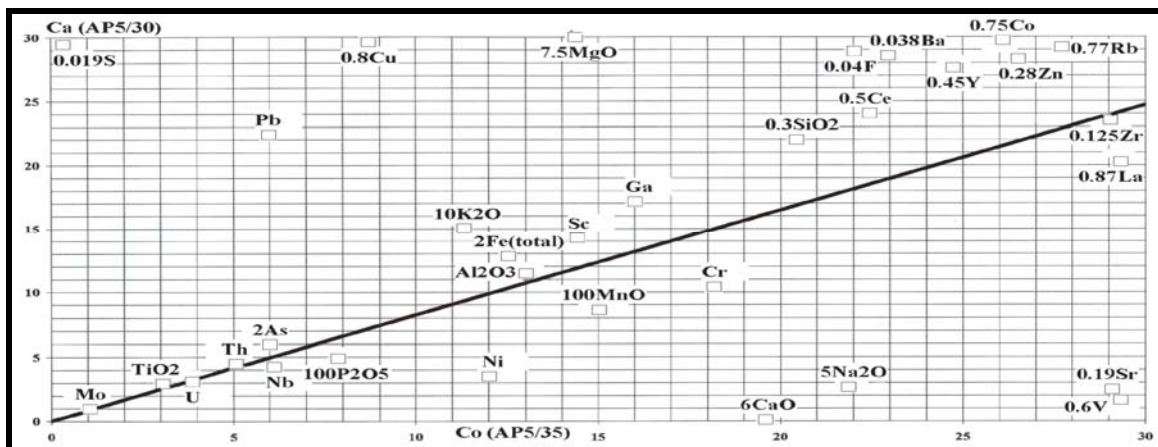


Figure 4.19: An isocon diagram of samples AP5/35, the least altered biotite-gneiss, and AP5/30, altered biotite-gneiss, from borehole AP5 in the Areachap area.

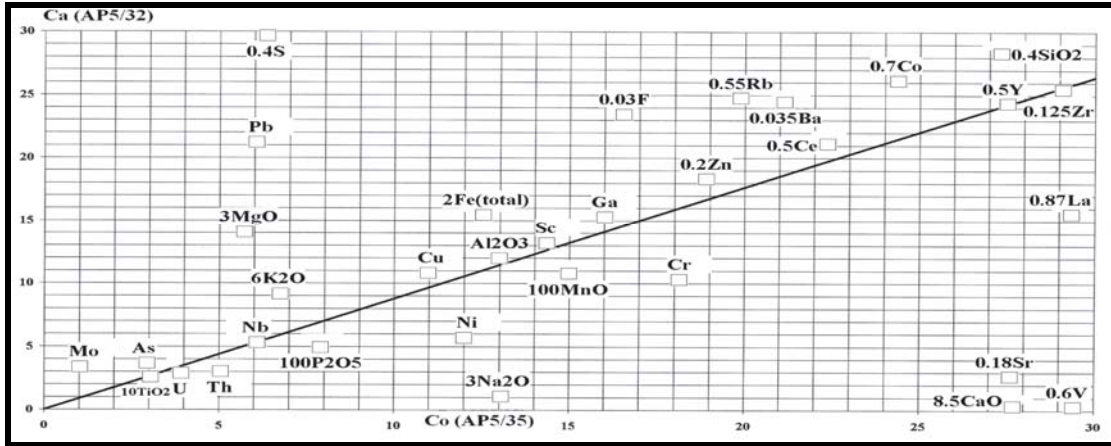


Figure 4.20: An isocon diagram for samples AP5/35 (the least altered biotite-gneiss) and AP5/32 (altered biotite-gneiss) from drill hole AP5 in the Areachap area.

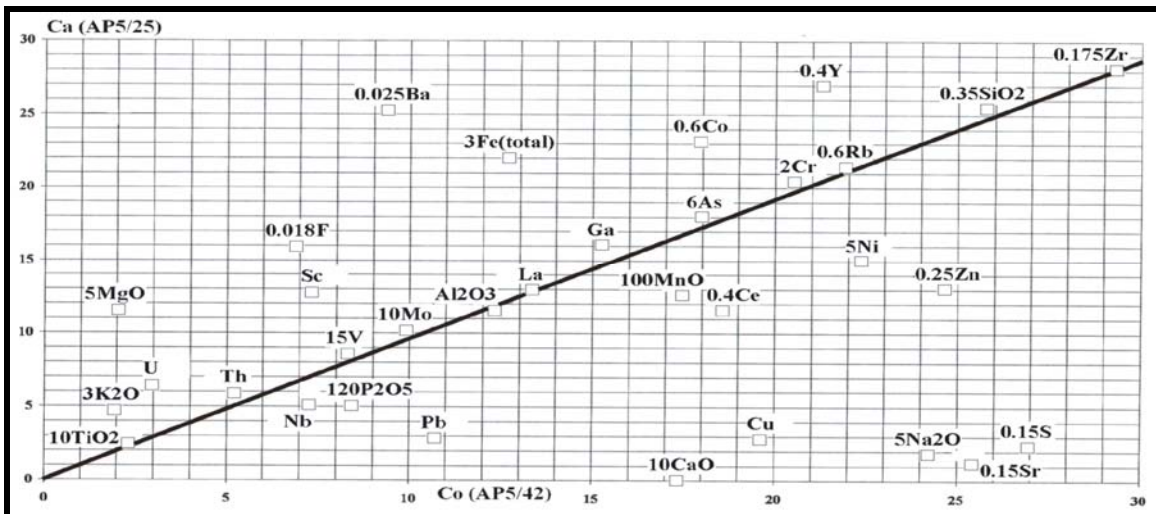
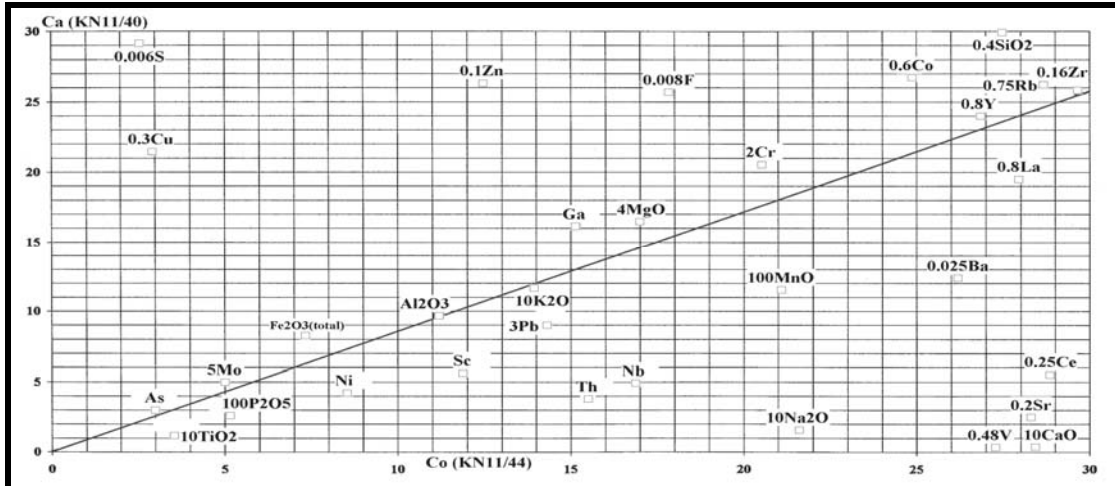


Figure 4.21: An isocon diagram for the least altered sample AP5/42 and altered sample AP5/25, altered biotite-gneiss, from borehole AP5 in the Areachap area.

**Table 4.6:** Percentage of gains and losses in borehole AP5 and  $\Delta$  values for the Areachap samples. Sample AP5/35 is assumed to be the unaltered precursor for altered samples AP5/23, 29, 30, and 32 (Isocon line based on Zr).

Element	Min $\Delta$ Value	Max $\Delta$ Value	Composition AP5/35	% Gain or Loss	Gain/Loss
CaO	-2.82	-2.03	3.26	-62 to -87	Loss
Na <sub>2</sub> O	-3.45	-1.78	4.36	-41 to -79	Loss
K <sub>2</sub> O	0.56	0.61	1.13	50 to 54	Gain
MgO	1.42	3.03	1.92	74 to 158	Gain
FeO	0.44	8.28	6.28	7 to 132.2	Gain
SiO <sub>2</sub>	10.15	33.98	68.26	15 to 50	Gain
Al <sub>2</sub> O <sub>3</sub>	-0.06	1.12	13.05	-0.5 to 9	Gain & Loss
TiO <sub>2</sub>	-0.03	0.04	0.31	-10 to 13	Gain & Loss
MnO	-0.05	-0.02	0.15	-13 to -33	Loss
P <sub>2</sub> O <sub>5</sub>	-0.03	0.00	0.08	-38 to 0	Loss
Ga	-0.82	5.19	16	-5 to 32	Gain & Loss
Rb	0.69	19.59	36	2 to 54	Gain
Sr	-119.80	-69.13	153	-45 to -78	Loss
As	0.48	2.05	3	16 to 68	Gain
Ba	177.47	966.44	604	29 to 160	Gain
Cu	-5.06	128.28	11	-46 to 1173	Gain & Loss
Pb	-2.04	17.54	6	-34 to 292	Gain & Loss
S	5.67	27633.37	16	35 to 172709	Gain
Zn	-41.21	24.55	95	-44 to 26	Gain & Loss
Ce	-12.09	11.75	45	-27 to 26	Gain & Loss
Cr	-5.57	3.85	18	-31 to 21	Gain & Loss
Co	7.20	20.57	35	21 to 59	Gain
Ni	-7.08	1.19	12	-59 to 10	Gain & Loss
Sc	0.46	2.51	14	3 to 17	Gain
F	272.25	1152.13	551	49 to 209	Gain
Nb	-0.70	0.02	6	-11 to 1	Gain & Loss
La	-14.39	-3.98	34	-43 to -12	Loss
Th	-1.44	0.45	5	-28 to 9	Gain & Loss
V	-42.17	-31.08	49	-86 to -63	Loss
U	-0.38	0.50	4	-10 to 13	Gain & Loss
Y	0.78	16.93	55	1 to 31	Gain

The isocon diagram comparing the least altered biotite-gneiss, C<sub>o</sub>, and altered biotite-gneiss, C<sub>a</sub>, from the assumed alteration zone identified in borehole KN11, in the Kantienpan area, is shown in Figure 4.22. The calculated  $\Delta$  values are given in Table 4.8. The least altered sample identified as precursor is sample KN11/44. CaO, Na<sub>2</sub>O and K<sub>2</sub>O are depleted, and MgO enriched in the alteration zone. Cr and Y are relatively enriched



**Figure 4.22:** An isocon diagram for samples KN11/44 (the least altered biotite-gneiss) and KN11/40 (altered biotite-gneiss) from drill hole KN11 in the Kantienpan area.

and P<sub>2</sub>O<sub>5</sub> and Ce are depleted during the alteration. Cu, Zn, and S are enriched, but Pb and Ba are depleted from the altered rocks.

**Table 4.7:** Percentage of gains and losses in borehole AP5 and  $\Delta$  values for the Areachap sample. Sample AP5/42 is assumed to be the unaltered precursor for altered sample AP5/25 (Isocon line based on Zr).

Element	$\Delta$ Value	Composition AP5/42	% Gain or Loss	Gain/Loss
CaO	-1.65	1.73	-95	Loss
Na <sub>2</sub> O	-4.26	4.83	-88	Loss
K <sub>2</sub> O	0.95	0.64	148	Gain
MgO	1.94	0.41	473	Gain
FeO	3.25	4.23	78	Gain
SiO <sub>2</sub>	1.65	73.83	2.2	Gain
Al <sub>2</sub> O <sub>3</sub>	-0.21	12.32	2	Gain
TiO <sub>2</sub>	0.03	0.23	13	Gain
MnO	-0.04	0.17	-24	Loss
P <sub>2</sub> O <sub>5</sub>	-0.03	0.07	-43	Loss
Ga	1.57	15	10	Gain
Rb	0.47	37	1.3	Gain
Sr	-155.04	169	-92	Loss
As	0.12	3	4	Gain
Ba	647.35	376	172	Gain
Cu	-15.90	20	-81	Loss
Pb	-7.31	11	-68	Loss
S	-156.98	180	-87	Loss
Zn	-42.28	99	-43	Loss
Ce	-15.10	46	-33	Loss
Cr	0.40	10	3.9	Gain
Co	10.16	30	34	Gain
Ni	-1.30	5	-29	Loss
Sc	5.71	7	78	Gain
F	517.90	384	135	Gain
Nb	-1.86	7	-26	Loss
La	0.17	13	1	Gain
Th	0.99	5	19	Gain
V	0.02	~1	4	Gain
U	3.53	3	118	Gain
Y	16.43	53	31	Gain

**Table 4.8:** Percentages of gains and losses in borehole KN11 and  $\Delta$  values for the Kantienpan samples. Sample KN11/44 is considered to be the unaltered precursor for altered sample KN11/40 (Isocon line based on Zr).

Element	$\Delta$ Value	Composition KN11/44	% Gain or Loss	Gain/Loss
CaO	-2.43	2.84	-85.6	Loss
Na <sub>2</sub> O	-1.72	2.16	-79.6	Loss
K <sub>2</sub> O	-0.05	1.39	-3.6	Loss
MgO	0.41	4.25	9.6	Gain
FeO	1.87	7.34	25.5	Gain
SiO <sub>2</sub>	15.47	68.55	22.6	Gain
Al <sub>2</sub> O <sub>3</sub>	-0.07	11.19	-1	Loss
TiO <sub>2</sub>	-0.19	0.36	-53	Loss
MnO	-0.07	0.21	-33	Loss
P <sub>2</sub> O <sub>5</sub>	-0.02	0.05	-40	Loss
Ga	2.99	15	20	Gain
Rb	1.71	38	5	Gain
Sr	-110.60	142	-78.1	Loss
As	0.39	3	13	Gain
Ba	-417.36	1048	-40	Loss
Cu	62.95	10	648	Gain
Pb	-1.15	5	-24	Loss
S	447.60	430	104	Gain
Zn	154.86	125	124	Gain
Ce	-78.24	116	-68	Loss
Cr	1.33	10	13	Gain
Co	8.52	42	21	Gain
Ni	-3.20	9	-38	Loss
Sc	-4.87	12	-41	Loss
F	1270.73	2228	57	Gain
Nb	-9.90	17	-59	Loss
La	-6.01	35	-17	Loss
Th	-10.02	16	-65	Loss
V	-48.67	57	-86	Loss
U	0.39	3	13	Gain
Y	0.79	34	2	Gain

It is possible to identify alteration zones in the original footwall lithologies of the massive sulphide ore bodies at Kantienpan and Areachap as Theart (1985) has done for the Prieska Cu-Zn deposit. The rocks least affected by the alteration process may be identified by utilization of major element comparison diagrams and iterative isocon calculations. These potential precursor rocks are used in identifying and quantifying the geochemical changes caused by the hydrothermal process related to the ore formation. In

general the alteration zones at Areachap and Kantienpan are enriched in Mg, Fe, S, Zn, Si, Co and F and depleted in Na, Ca, Sr, Ni, V and La. Ba is enriched in the footwall alteration zone at the Areachap and at the Prieska Cu-Zn deposits (Theart, 1989), but depleted at the Kantienpan deposit. Elements that behaved relatively immobile include Zr, Ti, P, Mn, Al, Y, and U. A notable feature is the enrichment in F at both of these deposits, but note that the F and S interpretations are based on semi-quantitative analyses. Theart (1989) reported a relatively enrichment of Mg, K, V, Sc, Ni, Ba, Cu and Zn and depletion of Si, Ca, Na and Sr in the alteration zone of the Prieska Cu-Zn deposit.

The  $\Delta$  values may also be used as an indication of proximity to the ore zone.

Unfortunately the samples collected from these deposits for the current investigation are not suitable for demonstrating this aspect. Proximity indicators in theory should be useful in the footwall and hangingwall lithologies as well as for lithologies on strike of the deposit.

#### **4.7. Development of alteration box plot for high-grade metamorphic rocks**

In order to understand the collective mineral processes responsible for the whole rock composition, Large et al. (2001) proposed a box plot that attempts to illustrate the various mineral processes that affects the composition of rocks subjected to common geological processes and discriminate them from those related to hydrothermal alteration. Large et al. (2001) concentrated on the primary reactions and minerals that form at the time of ore formation. The challenge addressed here is to identify the high-grade metamorphic minerals, formed during isochemical metamorphism, that now represent the original mineral processes and to determine if retrograde minerals such as chlorite would preserve these features.

The successful identification of characteristic lithogeochemical characteristics and metamorphic mineral assemblages that could be related to primary ore forming processes could lead to the discovery of new ore bodies. Lithogeochemical investigations are usually based on chemical analyses and this data have limited meaning on its own (Large

et al., 2001). In the box plot the typical mineralogical reaction trends are shown by plotting AI against the CCPI (Large et al., 2001).

#### **4.7.1. The location of rock forming minerals in the box plot**

The location of the rock forming minerals in the box plot may help to demonstrate the dominant mineral processes. Mineral compositions determined by microprobe are used for this purpose. The AI and CCPI calculated for each mineral composition are plotted in the box plot.

Figures 4.23 and 4.24 show the positions based in mineral compositions determined by some of the samples from boreholes AP2, AP5, KN11 and KN12. The location of albite, calcite-epidote, chlorite, biotite, k-feldspar were determined in the box plot by Large et al. (2001). In order to use the box plot for the present study area, the high-grade metamorphic minerals (hornblende, clinopyroxene, gahnite, cordierite, orthopyroxene, garnet), and retrograde minerals (chlorite, pinite and muscovite) have to be also plotted in this diagram. The top of the box plot is characterized by the chlorite carbonate trend defined by Large et al. (2001) for unmetamorphosed sequences. Under the metamorphic conditions reflected in the rocks of the study area, the minerals with a high CCP index (trend 2 in Fig. 4.23) display the following alteration sequences:

- a) Augite to enstatite and clinoenstatite.
- b) Hornblende to gedrite.
- c) Grossular-rich garnet to almandine/pyrope-rich garnet.
- d) Fe rich cordierite to Mg rich cordierite.

The minerals showing a high alteration index defining the right side of the box plot shows the following sequence related to the primary alteration process (trend 1 in Fig. 4.24):

- a) Biotite (annite) to phlogopite.

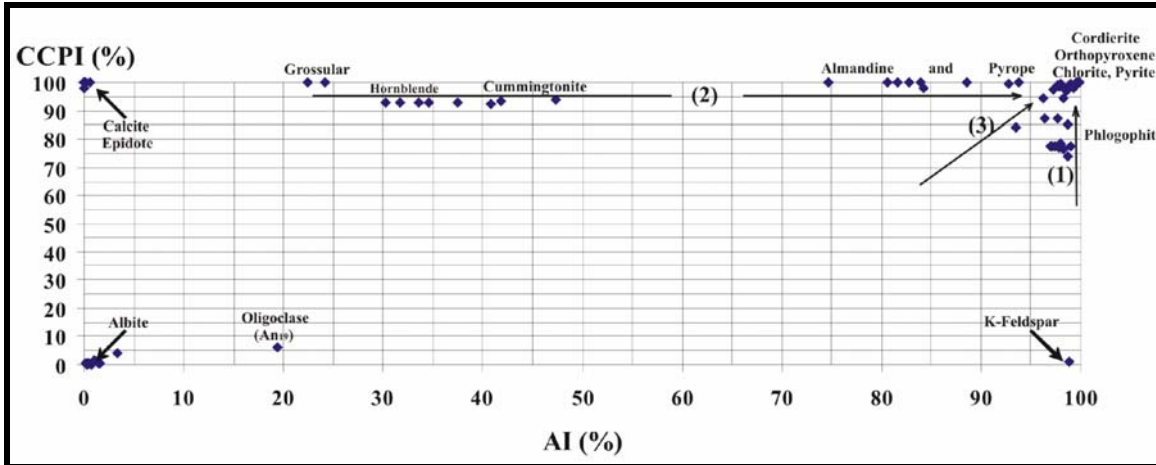


Figure 4.23: Box Plot of mineral compositions from Areachap (AP5 and AP2).

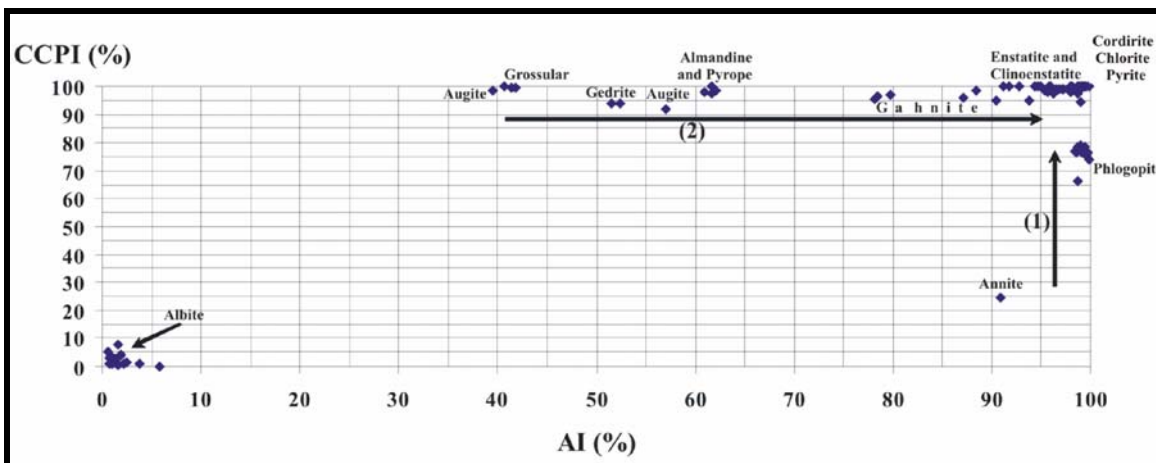


Figure 4.24: Box Plot of mineral compositions from Kantienpan (KN11 and KN12).

Cordierite, pinite and chlorite analysed in these rocks are located in the same place at the right-top corner of the box plot. Orthopyroxene plots very close to these minerals. Two groups of garnets are present in these rocks, grossular with low AI value (Ca-rich and low in Mg), which plots to the left, and the almandine and pyrope with high AI values (low in Ca and Mg-rich), plotting to the right (Fig. 4.23 and 4.24). Amphiboles of this trend include, hornblende with lower AI values (high Ca content), and cummingtonite and gedrite with higher AI values (high Mg contents).

#### 4.7.2. Whole rock analysis and box plot

The Kantienpan deposit consists of stratiform Zn-Cu bearing massive sulphide lenses hosted by quartzo feldspathic gneiss, biotite-gneiss, hornblende-gneiss and biotite-hornblende-gneiss (Rossouw, 2003). The AI and CCPI values were calculated based on the whole rock XRF analyses, of samples from two boreholes KN11 and KN12. The lithochemical data are plotted in Figure 4.25. The data can be grouped into two major fields in the diagram, which are related to the alteration zones (shown in Fig. 3.2):

Field 1: The least altered rocks fall within a area bounded by an AI= 15 to 65% and a CCPI= 15 to 85%,

Field 2: All the samples identified by means of other lithochemical considerations (such as by the presence of normative corundum), as having been affected by hydrothermal alteration, plot in a field bounded by AI values that exceed 67, and CCPI values greater than 60.

The samples of rocks that were originally affected by diagenetic alteration display AI values of less than 57% and plots below the epidote-K feldspar join.

Samples from KN11 are used to demonstrate the variation of AI and CCPI in the lithological successions adjacent to the sulphide mineralisation at Kantienpan (Fig. 4.26). The figure shows that the highest values of the AI and CCPI (CCPI>90 and AI>90) correspond to the previously identified altered footwall near the ore zone.

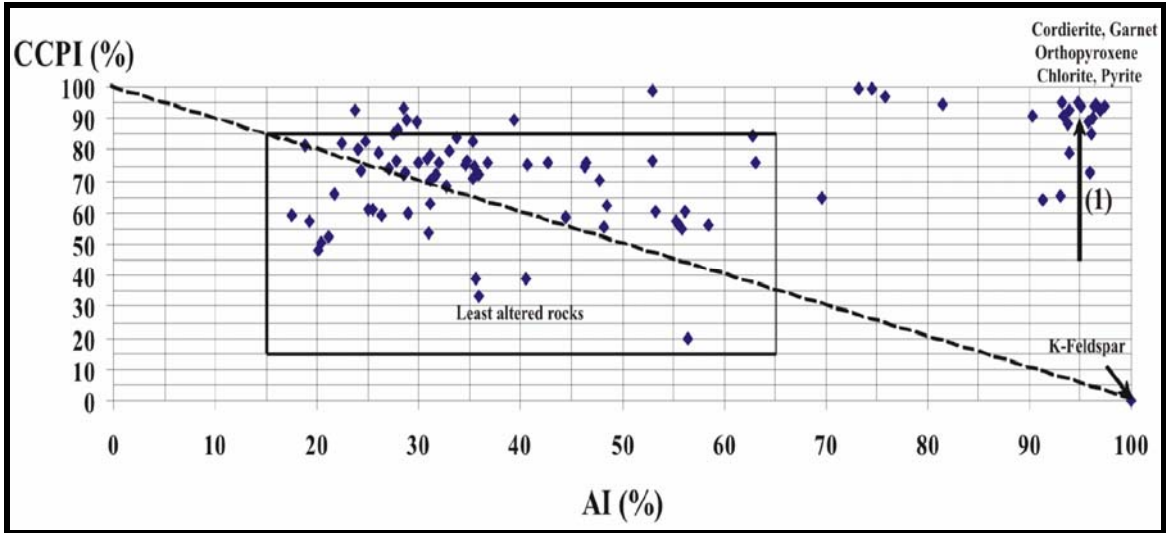


Figure 4.25: Box Plot of whole rock samples from Kantienpan (KN11, KN12 and surface outcrop).

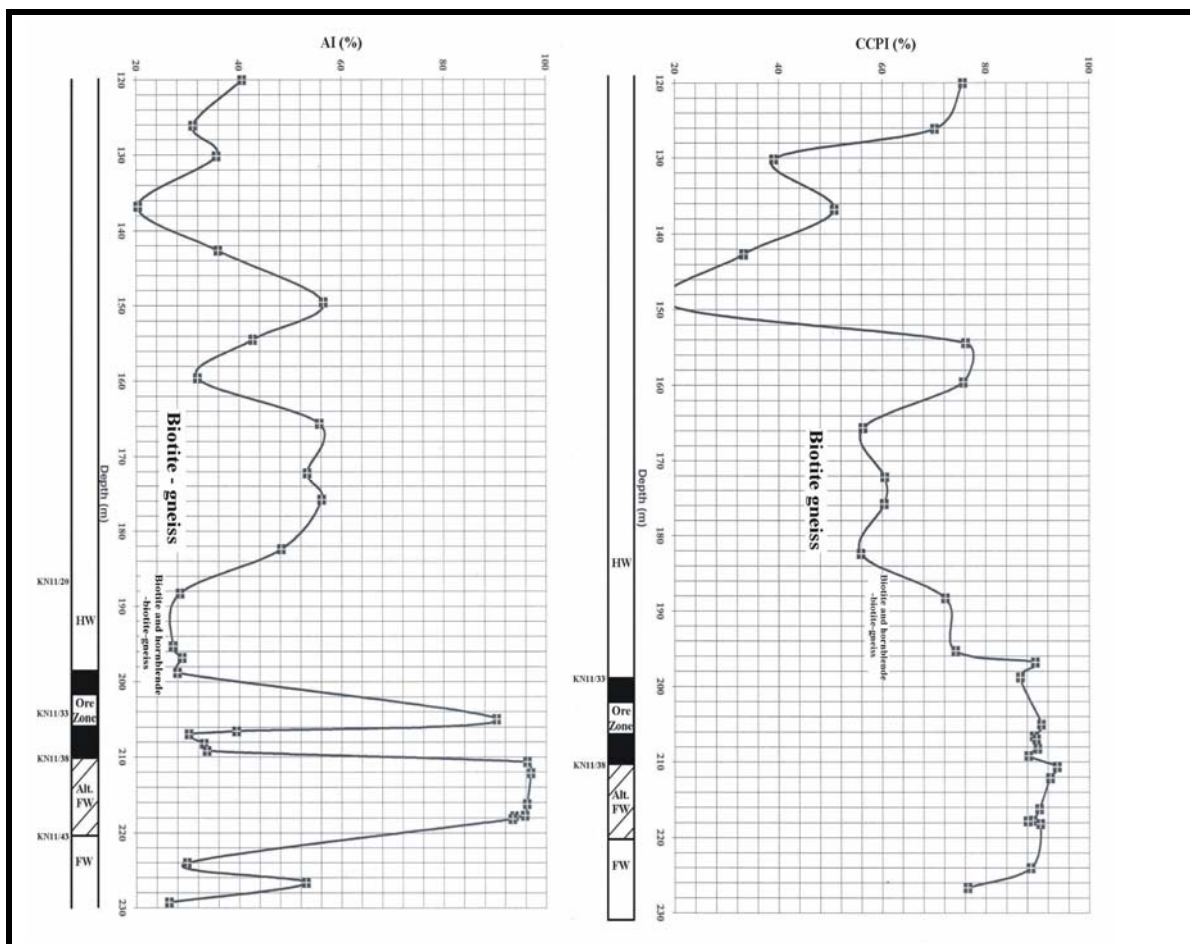


Figure 4.26: The variation of AI and CCPI values in samples from Kantienpan (KN11). Massive sulphide zone indicated in black and alteration zone hatched.

The ore body at the defunct Areachap Cu-Zn mine consists of discontinuous massive sulphide lenses. Locally, two layers of massive sulphide are intersected, separated by disseminated sulphides. Elsewhere only one massive and one disseminated layer were described (Vote and King, 1986). The total thickness of the mineralized zone ranges from 0.1 to 24.2 m.

The AI and CCPI calculated for the whole rock XRF analyses of samples from boreholes AP2 and AP5 and plotted in a box plot presented as Figure 4.27.

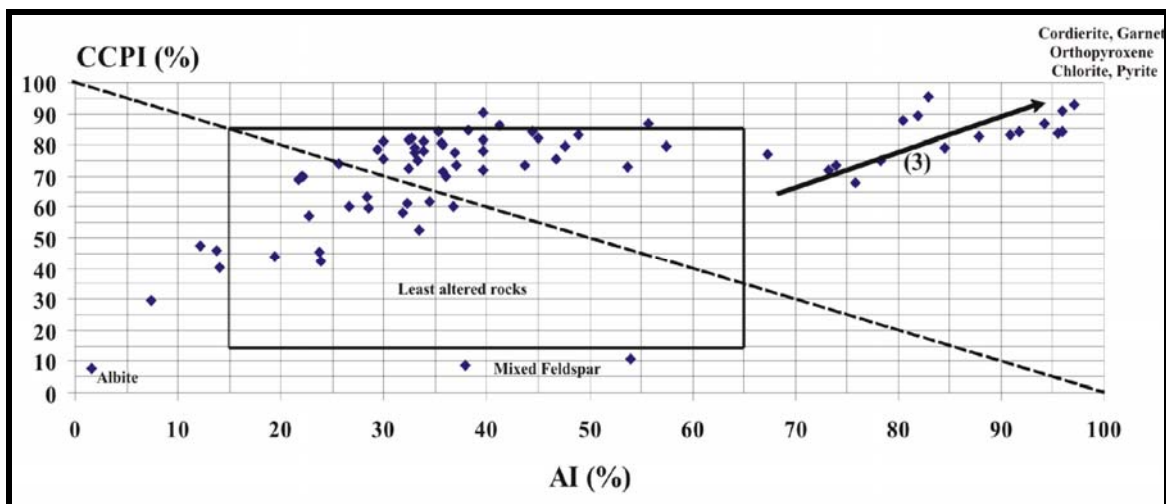


Figure 4.27: Box Plot of whole rock samples from Areachap (AP2 and AP5).

The data can be ascribed to three major fields in the diagram, which are related to the alteration zones described above (and in Figure 3.2 and 3.3), namely:

Field 1: The least altered rocks fall within the area bounded by an AI=15 to 65% and a CCPI= 15 to 85%,

Field 2: Samples assumed to have been affected by hydrothermal alteration have AI values in excess of 70 and the CCPI values greater than 70 (trend 3).

Field 3: Samples plotting outside the least altered field of Large et al. (2001). It is interesting to note that these samples are from rocks that could have had chemical sedimentary precursors, enriched in quartz, carbonate and sulphate minerals

(calcite, dolomite, barite and anhydrite) directly related to the sulphide ore zone, but since they are not believed to have formed during the primary alteration process itself, they will not be further considered here.

In order to demonstrate the variation of AI and CCPI in the lithological successions hosting sulphide mineralisation at Areachap, the variation with depth in borehole AP5 is demonstrated in Figure 4.28. This borehole intersects the footwall, ore zone and hangingwall successions. The figure shows that the highest values of AI and CCPI (AI>70 and CCPI>75) correspond to the previously identified footwall alteration zone.

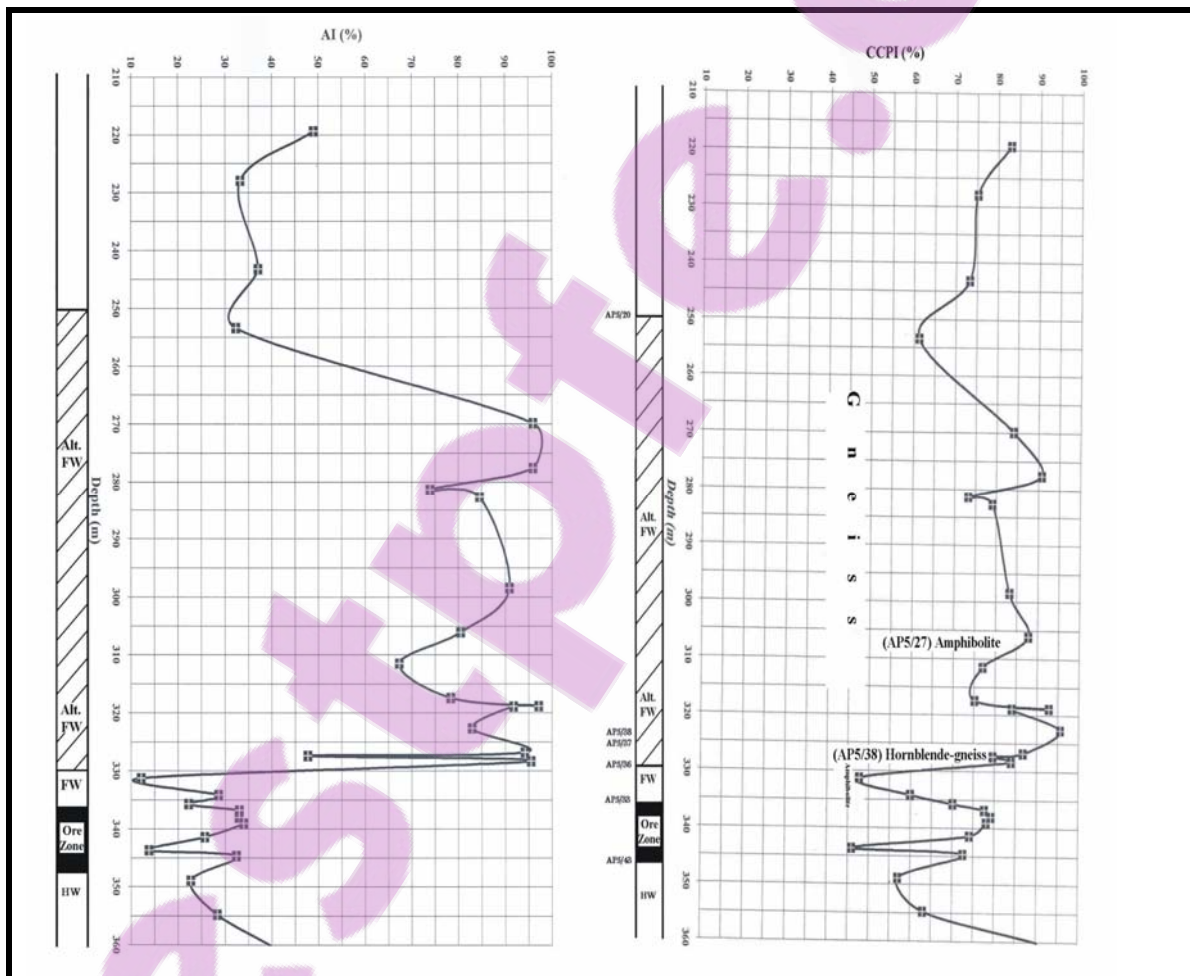


**Figure 4.28:** Inverted sequence seen in drill hole AP5 (Areachap) showing the variation in the AI and CCPI values. Massive sulphide zone indicated in black and alteration zone hatched.

### 4.7.3. Combination of isocon results and the box plot

As the source rock composition of the altered samples in the alteration zones has been independently determined using the isocon method, it can now be compared with the results of the box plot. For this purpose, the positions of the least altered and altered samples are highlighted in the box plot.

The results of isocon analyses are summarized in Table 4.9. The locations of source rock (KN11/44 and KN11/28) and altered products (KN11/40, 39 and 33) at Kantienpan are marked in the box plot (Fig. 4.29). In Figure 4.30 the source rock (AP5/35 and AP5/42) and altered products (AP5/23, 25, 29, 30 and 32) at Areachap are shown. Based on these two figures, it may be concluded that the results of the two methods confirm one another.

**Table 4.9:** The least altered and altered samples based on the isocon Analysis.

Borehole NO	Source rock (least altered)	Altered Equivalent for source rock <sup>(1)</sup>
AP5	AP5/35	AP5/29, 30, 32 [and 23]
AP5	AP5/42	AP5/25
KN11	KN11/44	KN11/40 [and 39]
KN11	[KN11/28 and 46]	[KN11/33]

(1): From footwall of the ore body

[ ]: Might be source rock or altered equivalent

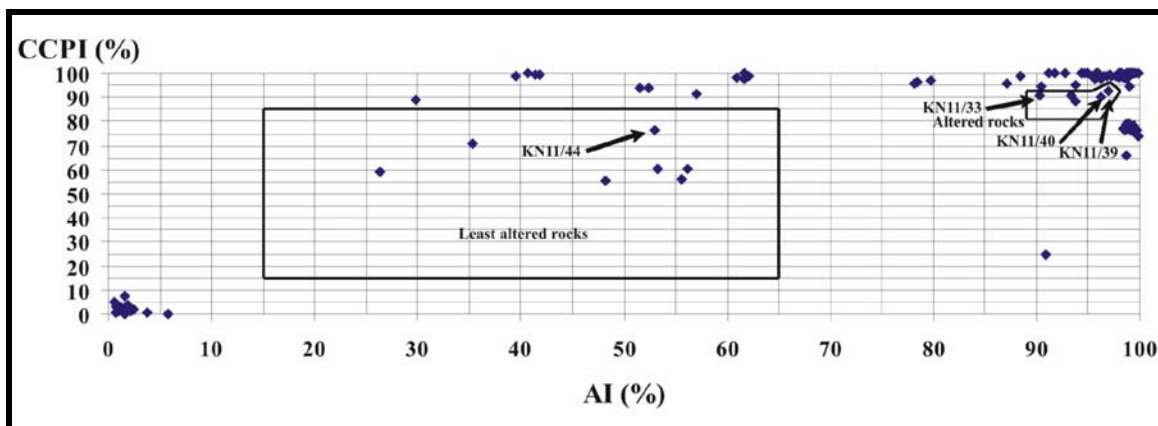


**Figure 4.29:** Box plot with isocon and microprobe results (Kantienpan area, KN1).

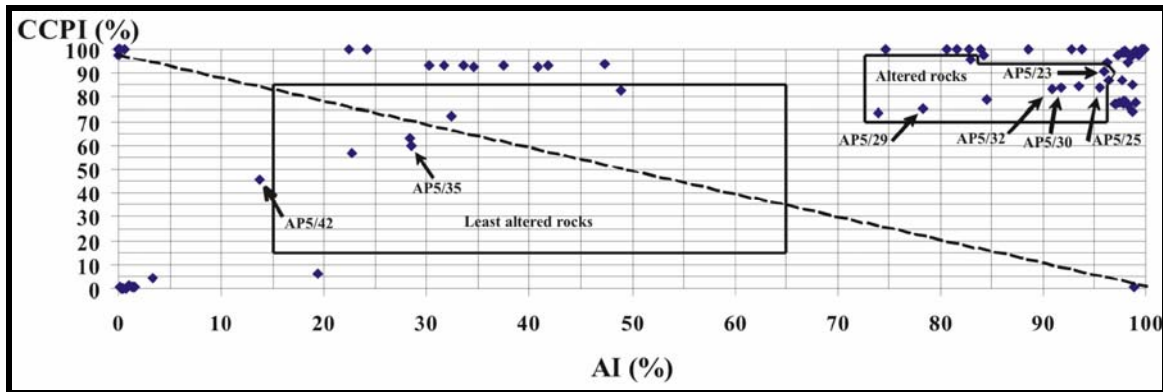


Figure 4.30: Box plot with the isocon and microprobe results (Areachap area, AP5).

Based on Figure 4.30, the least altered sample AP5/42 were more affected by the diagenetic alteration than sample AP5/35, which is close to the diametric line that is separating the hydrothermal alteration from diagenetic alteration.

Original complexities in the alteration zones are further shown by the variation in composition evident from the scatter of points in the box plot.

The value of the box plot lies in the fact that the composition of samples collected during regional lithogeochemical surveys of comparable rock types may be plotted to identify potential alteration zones.

#### **4.8. Refinement of chemical structure in the upper right corner of the box plot**

An alternative way to distinguish the mineralogical changes is to use the molar ratio or Pearce Element Ratio analysis (PER), based on the molecular proportion of major elements over the molecular proportion of an immobile element. A linear combination of major elements could remove the effect of some minerals and add the effects of others. These minerals might occur only in altered rocks where the new minerals formed as result of the alteration process. The method was introduced by Whitbread and Moore (2004).

In this research, the PER analysis is used to find out if it is possible to separate the mixed minerals at the upper right corner of the box plot (Fig. 4.23 and 4.24) and clarify this diagram. For this purpose, different molar ratios are calculated and the best ratio, which gives a better mineral separation, namely the molecular proportion ratio of Fe / Al versus Mn / Al, is plotted (Fig. 4.31 and 4.32).

Figure 4.31 is a log scale PER plot of the Kantienpan samples from KN11 and KN12. The figure shows that the Mn content of gahnite, cordierite and garnet in the ore zone is higher than in the footwall alteration zone. The Mn and Fe content of pyroxenes near the alteration pipe and ore zone is lower than those in pyroxenes that are further away from these zones. This trend was not observed in retrograde chlorite and chamosite an observation that may be ascribed to the redistribution and oxidation of Fe and Mn.

Similarly, Figure 4.32 is a log scale PER plot of the Areachap samples from boreholes AP2 and AP5. The Mn content of cordierite increases from the altered footwall towards the ore zone. The Mn content of garnets is higher in the ore zone than in the footwall alteration zone. Again, this trend was not observed in retrograde chlorite and chamosite.

This application of the PER analysis has clearly succeeded in resolving the upper right corner of the box plot and provided an added method that could be used as a proximity indicator for the identification of massive sulphide mineralization.

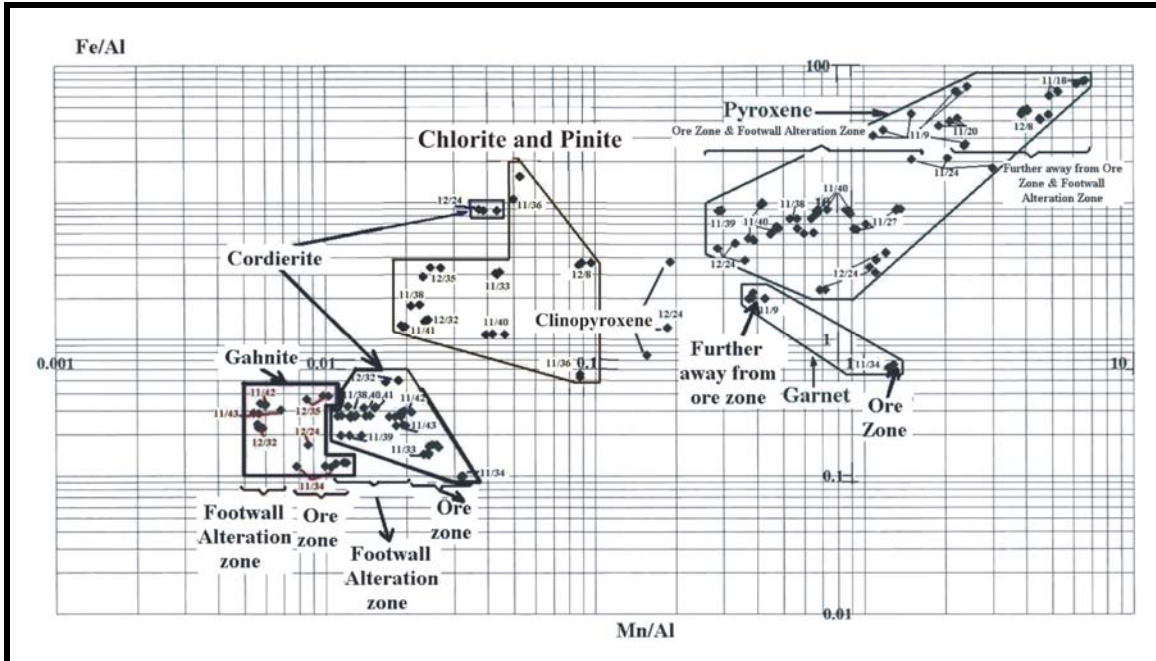


**Figure 4.31:** PER analysis for samples from drill holes KN11 and KN12, Kantiapan area. The Mn content of gahnite, cordierite and garnet from the ore zone is higher than in the identified footwall alteration zone. Pyroxene has lower Mn and Fe contents in the ore zone and altered footwall (11/43: borehole KN11/ sample number).

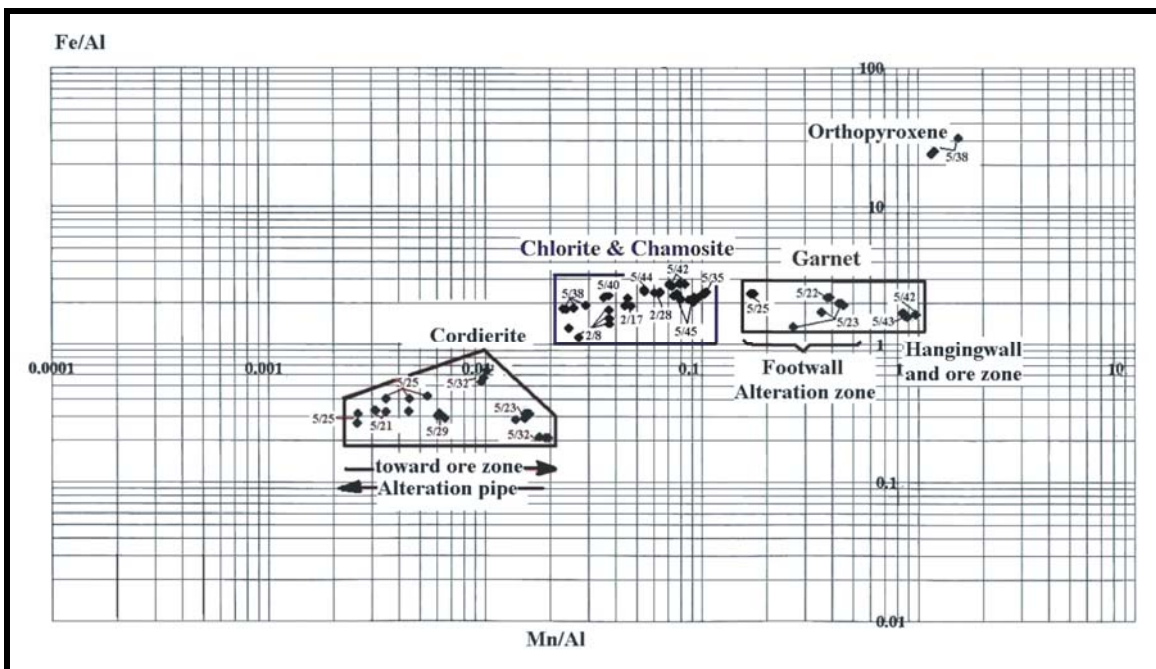


**Figure 4.32:** PER analysis of boreholes AP2 and AP5 in the Areachap area. The Mn content of Cordierite increases from the altered FW toward ore zone. The Mn content of garnets is higher in ore zone than in footwall alteration zone. No trend is evident in the composition of chlorite and chamosite (5/27: borehole AP5/ sample number).

## Chapter 5

# Lithogeochemistry as an exploration tool

### **5.1. Introduction**

The lithogeochemical characteristics were presented in the previous chapter of metamorphic rocks that formed from precursor rock types that suffered hydrothermal alteration at the time of sulphide mineralization in a VHMS system, as identified at Areachap and Kantienpan. In this chapter, those characteristics are used to formulate geochemical vectors that may be used in regional exploration. These vectors are applied to a regional data set to identify and prioritise anomalous areas. The geochemical vectors are based on multivariate statistical methods.

For this purpose, XRF analyses from the current work on the Areachap and Kantienpan areas in combination with analysis from the Prieska Cu-Zn deposit reported by Theart (1985) are used. This is then compared to a regional data set supplied by Kumba Resources. The objective is to identify a factor that represents the hydrothermal overprint related to the original sulphide mineralization event. Statistical methods used for this include cluster and canonical analysis. The values of the identified multivariate factors are analyzed utilizing maximum likelihood procedure to identify different sub-populations in the data set.

## **5.2. Lithogeochemical interpretation of borehole information**

A database was compiled of whole rock analyses from the three known VHMS deposits in the area. There are principally three main rock types in this data set, namely peraluminous gneiss and schist, quartzo-feldspathic gneiss, and amphibolite, based on the available petrographic descriptions of the individual samples. Three different codes are used to classify these rocks. Code “A” represents peraluminous rocks, code “B” quartzo-feldspathic gneisses, and code “C” for amphibolites.

The dominant lithogeochemical features of the alteration zones at the Areachap, Kantienpan, and Copperton ore deposits are their common peraluminous, Na and Ca depleted, and K and Mg enriched nature. The enrichment of K together with Mg may suggest that the source rock was pelitic, but that has been affected by alteration processes. An unaltered pelitic source rock will display only K-enrichment. The chemical characteristics of the alteration zone may therefore be defined as having high values of  $\text{Al}_2\text{O}_3$ , MgO, and/or  $\text{K}_2\text{O}$  and low  $\text{Na}_2\text{O}$  and CaO contents.

The quartzo-feldspathic gneissic rocks have high  $\text{SiO}_2$ ,  $\text{Na}_2\text{O}$ , and  $\text{K}_2\text{O}$  and low CaO and MgO contents. They could be subdivided into two subgroups i.e., the biotite-gneisses or leucogneisses and biotite-hornblende-gneisses. The leucogneisses are characterised by lower CaO and MgO, and higher  $\text{SiO}_2$ ,  $\text{Na}_2\text{O}$  and  $\text{K}_2\text{O}$  contents, relative to biotite-hornblende-gneisses.

In general, the amphibolites have high CaO, MgO and  $\text{Fe}_2\text{O}_3$  contents and very low  $\text{SiO}_2$ ,  $\text{K}_2\text{O}$  and  $\text{Na}_2\text{O}$  contents. Two types of amphibolites are distinguished based on the source rocks (Theart, 1985). These are ortho-amphibolites, derived from igneous basic rocks, and para-amphibolites, derived from marlstones or calcareous shales. Ortho-amphibolites have high Mg, Cr, Ni and  $\text{TiO}_2$  contents and displays a positive correlation between Mg and Cr; and Ni and  $\text{TiO}_2$  (Leake, 1964). Para-amphibolite rocks have low Cr, Ni, and  $\text{TiO}_2$  contents and show negative correlation when Mg is plotted against Cr and Ni and a low positive to slightly negative correlation between MgO and  $\text{TiO}_2$  (Leake, 1964). Only the correlation between MgO and Ni could be used here to discriminate between these

rock types, as the regional data set used in the study does not include analyses for Cr. TiO<sub>2</sub> does not show a distinct correlation with MgO in this data set.

A number of multivariate statistical methods were used to calculate geochemical factors that would distinguish these rock types. The statistical methods include principal component analysis (Rao, 1964; Morrison, 1976), principal factor analysis (Mardia et al., 1979; Geweke et al., 1980) and canonical correlation analysis (Kshirsagar, 1972; Mardia et al., 1979). The canonical correlation method provides the best discriminatory results. In the canonical correlation method, the relationships between two sets of variables are analyzed (Kshirsagar, 1972; Mardia et al., 1979). The canonical coefficients or canonical weights are coefficients of the linear combinations of variables. If the variables are not measured in the same units, the standardized coefficients could be used instead of raw coefficients. This latter technique also decreases the influence of closure effects due to the summing up of major elements to 100% (Kshirsagar, 1972; Mardia et al., 1979).

The statistical analyses were done, using SAS software (SAS<sup>®</sup> version 8.2). The input data file may include all the variables determined, but in the canonical analysis, the user determines the two sets of variables for analysis.

### **5.3. Economic element vectors of mineralization**

There are two vectors based on the economic element composition of known ore bodies in the area that may be used as vectors of mineralization (Theart, 1985; Attridge, 1986; Rossouw, 2003). Elements that characterized the two ore types present in this area include:

- a) Zn, Cu, Ba and B
- b) Ni and Cu

The first vector is related to VHMS mineralization in the region, which is the focus of the current study, whereas the second relates to the Jacomynspan type Ni-Cu mineralization described by Attridge (1986). The distributions of Zn, Cu and Ni in the regional data set

were investigated by means of the probability plot procedure (Sinclair, 1976). The anomalous subpopulations were identified and will be used in the subsequent discussion.

#### **5.4. Peraluminous, gneiss, and amphibolite factors**

It is important to utilize the known geochemical relationships between various major and trace elements during canonical multivariate analysis. Each of the two sets of variables required for canonical analysis should consist of those variables that have an underlying positive geochemical correlation with each other (Kshirsagar, 1972; Mardia et al., 1979; Tauson, 1999; Shpak et al., 2003 ). Cluster analysis is used to confirm the relationship between different variables in a data set (Harman, 1976), and this helps to separate the two sets of variables. In the following sections, various additional statistical methods are applied to the pre-defined data sets of each rock type in order to identify the two sets of variables for later use in cluster analysis.

##### **5.4.1. Peraluminous factors**

The results of cluster analysis of major and trace elements in peraluminous rocks are shown in Figure 5.1. There are two main groups in this tree diagram. The first set includes  $\text{Al}_2\text{O}_3$  (+), MgO (+),  $\text{K}_2\text{O}$  (+),  $\text{Na}_2\text{O}$  (-), CaO (-), Sr (-) and the other includes Cu (+), Zn (+), Pb (+), S (+), Ba (+). The first set consists of those oxides that are enriched or depleted in the host rocks of the ore deposit, which may now be regarded as the variables defining the peraluminous factor. Rb might be replaced by K, and Sr could be replaced by Ca. The second set comprises the ore forming elements and these may be regarded as the variables defining an ore factor.

As could be expected, it was found that the log transformed values of elements that display a strongly log normal distribution gives better results than the raw values when compared with elements displaying a normal distribution. This was done by

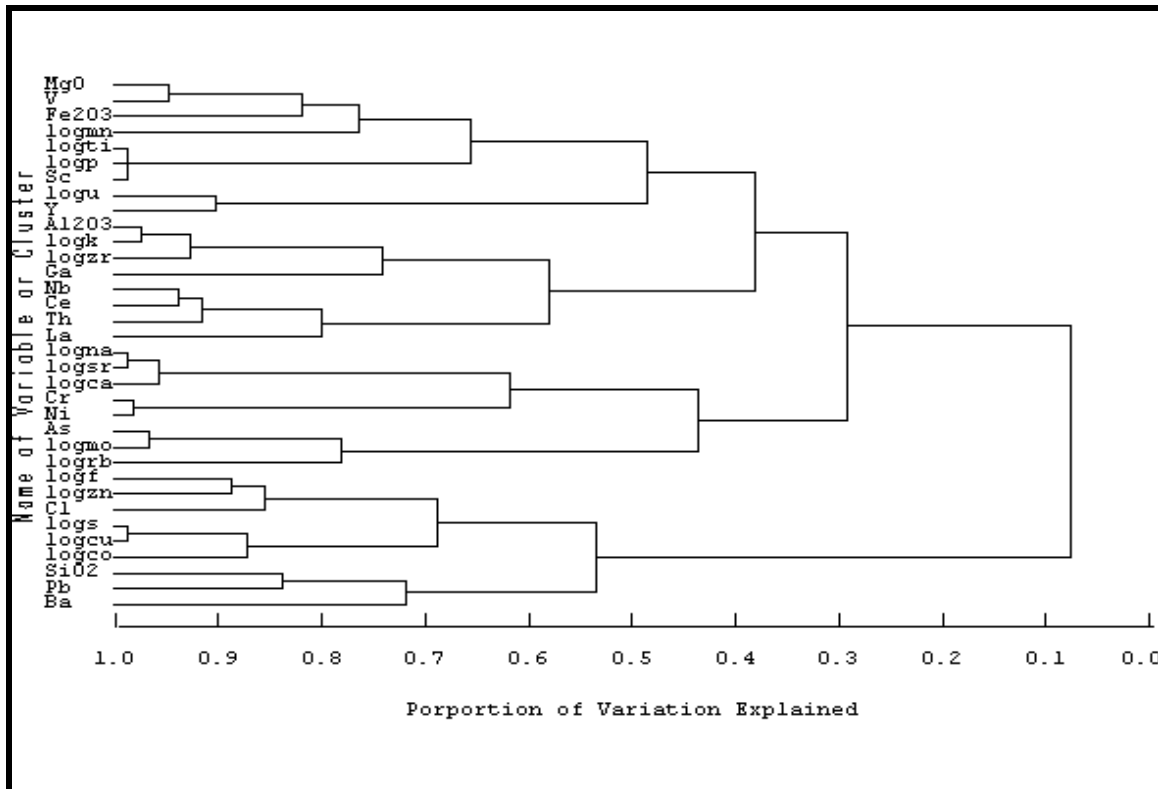


**Figure 5.1:** The tree diagram of the peraluminous rocks.

multiple inspections of the regression statistics between any two variables, and correlation coefficients.

The peraluminous factor may then be calculated by using canonical analysis of the peraluminous data set. The following factor formula was obtained:

$$F_{\text{peraluminous}} = 0.8375 \cdot \log \text{Al}_2\text{O}_3 + 0.8877 \cdot \log \text{Rb} + 0.7687 \cdot \log \text{MgO} + 0.1230 \cdot \log \text{K}_2\text{O} - 0.7069 \cdot \text{Na}_2\text{O} - 0.5433 \cdot \text{CaO} - 0.1923 \cdot \log \text{Sr} = \text{FPer}$$

When this factor is applied to the combined data set of the Areachap, Kantiengan, and Copperton samples, and the results sorted, the factor values effectively separated a very high percentage (>95 %) of independently identified peraluminous samples from the combined set. However, some peraluminous samples in the Copperton data set have high CaO and/or Na<sub>2</sub>O contents and the factor failed to separate them as peraluminous.

The common pelitic rocks have high Al<sub>2</sub>O<sub>3</sub>, K<sub>2</sub>O and low MgO contents (Fig. 5.1). When the canonical analysis was applied on a data set containing samples that were independently identified as metapelitics by petrographic analysis, utilizing as first set of variables Al<sub>2</sub>O<sub>3</sub>, K<sub>2</sub>O, and Rb, which was compared to the second set containing Na<sub>2</sub>O, CaO, Sr, and MgO, the following pelitic factor is suggested:

$$F_{\text{pelitic}} = 0.8961 * \text{Al}_2\text{O}_3 + 0.2027 * \log \text{Rb} + 0.0842 * \log \text{K}_2\text{O} - 0.8675 * \text{MgO} - 0.5195 * \log \text{Na}_2\text{O} - 0.0808 * \log \text{Sr} - 0.0161 * \log \text{CaO} = \text{FPR}$$

The assumed hydrothermally altered peraluminous rocks have high Al<sub>2</sub>O<sub>3</sub> and MgO and low K<sub>2</sub>O contents (Fig. 5.1). The canonical analysis between variables Al<sub>2</sub>O<sub>3</sub>, Fe<sub>2</sub>O<sub>3</sub>, and MgO with K<sub>2</sub>O, CaO, Na<sub>2</sub>O, Rb, and Sr gives the following alteration factor:

$$F_{\text{Alteration}} = 1.1113 * \text{Al}_2\text{O}_3 + 0.2169 * \text{Fe}_2\text{O}_3 + 0.1707 * \text{MgO} - 0.8618 * \log \text{K}_2\text{O} - 0.3372 * \log \text{CaO} - 0.1913 * \log \text{Rb} - 0.1443 * \log \text{Sr} - 0.0951 * \log \text{Na}_2\text{O} = \text{FAR}$$

It is suggested that samples displaying high values for both the peraluminous and alteration factors should be prioritized as probably related to a massive sulphide bearing lithological unit.

#### 5.4.2. Gneiss factors

A cluster analysis was done of the quartzo-feldspathic gneiss data set to determine the relationship between major element oxides and trace elements (Fig. 5.2). This analysis highlights the two different rock types in the data set. One subgroup of data set has high SiO<sub>2</sub>, Na<sub>2</sub>O and K<sub>2</sub>O contents whereas the other has high MgO, CaO, Fe<sub>2</sub>O<sub>3</sub>, Cr and Ni contents. These two types of gneisses may also be identified in the tree diagram (Fig. 5.2). Rocks with high SiO<sub>2</sub>, Na<sub>2</sub>O, and K<sub>2</sub>O and low CaO, MgO, and Fe<sub>2</sub>O<sub>3</sub> contents might be classified as leuco-gneisses and the other type is the biotite-hornblende-gneiss. The general canonical factor obtained for the entire gneiss data set is:

$$F_{\text{Gneiss}} = 0.8896 * \text{SiO}_2 + 0.2247 * \log \text{K}_2\text{O} + 0.1753 * \text{Na}_2\text{O} - 0.3978 * \text{CaO} - 0.3714 * \log \text{MgO} - 0.3534 * \text{Fe}_2\text{O}_3$$

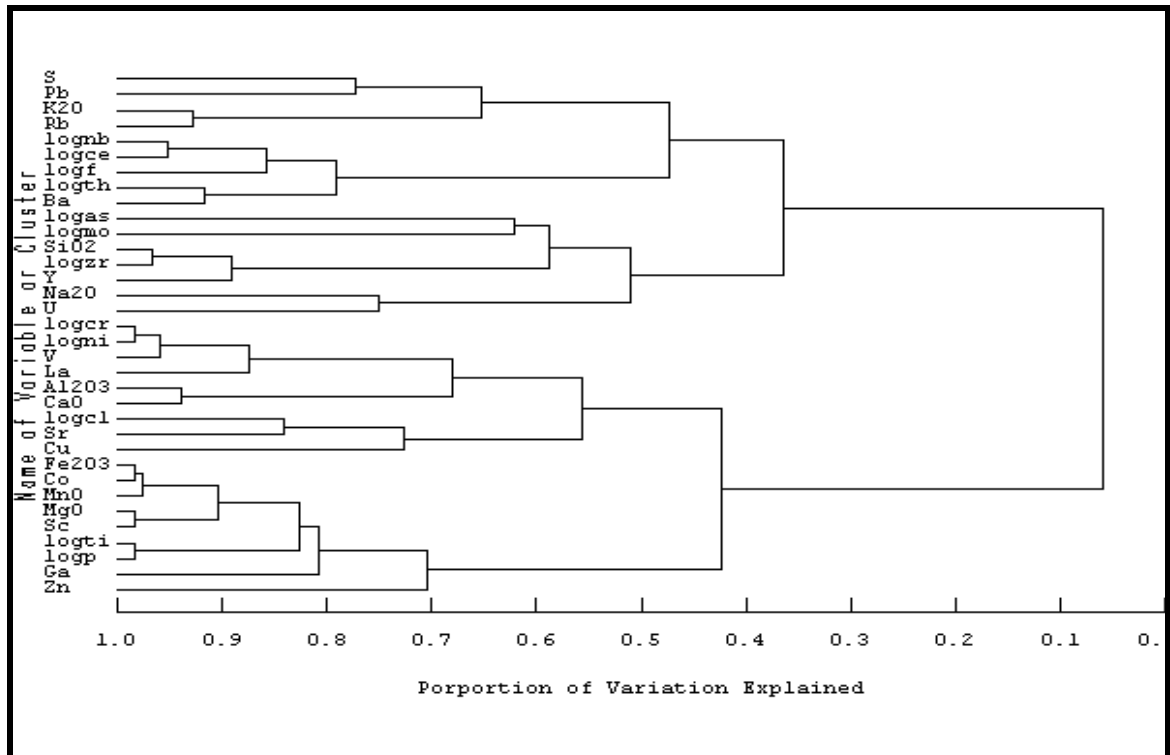


Figure 5.2: The tree diagram of the gneissic rocks.

This factor was tested using the combined data set, and it was found that some of the peraluminous samples returned high values for the gneissic factor. The reason for this is because these samples have very high SiO<sub>2</sub> (85-72%) and minor Na<sub>2</sub>O or K<sub>2</sub>O (1-2%) contents.

In the canonical analysis, where variables SiO<sub>2</sub>, Na<sub>2</sub>O, K<sub>2</sub>O, and Rb are compared with CaO, MgO, Al<sub>2</sub>O<sub>3</sub>, and Sr, the following factor for leuco-gneiss is derived:

$$F_{\text{Leu-Gn}} = 0.955 * \text{SiO}_2 + 0.1246 * \text{Na}_2\text{O} + 0.081 * \text{K}_2\text{O} + 0.0264 * \text{Rb} - 0.5633 * \text{MgO} - 0.4371 * \text{CaO} - 0.1627 * \text{Al}_2\text{O}_3 - 0.0225 * \text{Sr}$$

Canonical analysis gives the following factor for the biotite-hornblende-gneiss rocks:

$$F_{\text{Hbl-Gn}} = 0.5633 * \text{MgO} + 0.4371 * \text{CaO} + 0.1627 * \text{Al}_2\text{O}_3 + 0.0225 * \text{Sr} - 0.955 * \text{SiO}_2 - 0.1246 * \text{Na}_2\text{O} - 0.081 * \text{K}_2\text{O} - 0.0264 * \text{Rb}$$

In subsequent sections the code “B<sub>1</sub>” will be used for biotite-hornblende-gneiss.

### 5.4.3. Amphibolite factors

The results of a cluster analysis of the amphibolite data set are shown in Figure 5.3. There are good correlations between Fe<sub>2</sub>O<sub>3</sub>, TiO<sub>2</sub>, MgO, CaO, Ni, and Cr on one side and SiO<sub>2</sub>, K<sub>2</sub>O, Na<sub>2</sub>O, and Al<sub>2</sub>O<sub>3</sub> on the other side. In other words, the canonical analysis has to be calculated with a set of variables including CaO, MgO, Fe<sub>2</sub>O<sub>3</sub>, TiO<sub>2</sub>, and Ni and a set with SiO<sub>2</sub>, Al<sub>2</sub>O<sub>3</sub>, and K<sub>2</sub>O. A general amphibolite factor is then defined by:

$$F_{\text{Amphibolite}} = 0.72223 * \text{CaO} + 0.6584 * \text{Fe}_2\text{O}_3 + 0.4469 * \log \text{MgO} + 0.2729 * \text{TiO}_2 + 0.1774 * \log \text{Ni} - 0.6444 * \log \text{K}_2\text{O} - 0.4952 * \text{SiO}_2 - 0.2891 * \log \text{Al}_2\text{O}_3 - 0.2594 * \log \text{MnO}$$

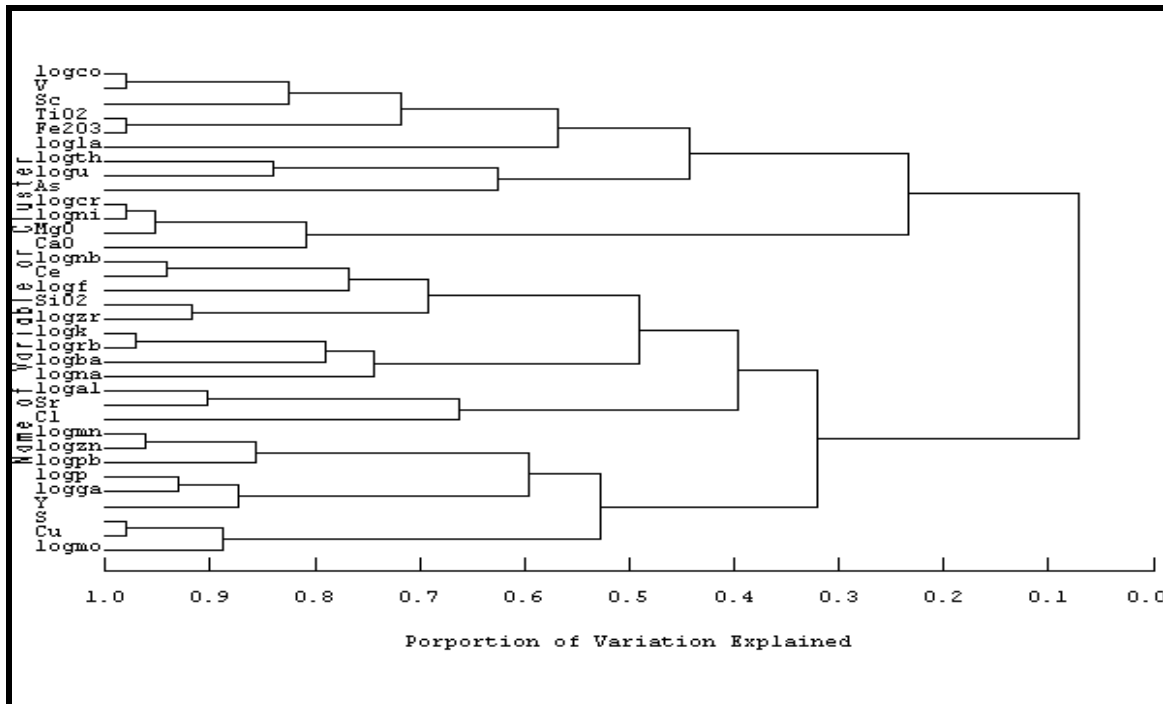


Figure 5.3: The tree diagram of the amphibolite rocks.

This factor when used for the combined data set, results in some of the gneissic samples returning high values. This may be explained by their low SiO<sub>2</sub> contents (45-54%) and low K<sub>2</sub>O contents (1-5%), and because these samples are rich in hornblende.

If a canonical analysis is done using CaO, MgO and Ni in the first set of variables and Na<sub>2</sub>O, SiO<sub>2</sub>, K<sub>2</sub>O and Rb in the second set, the following factors are derived to identify the ortho-amphibolites:

$$F_{\text{Ortho-Amp1}} = 0.6685 * \text{CaO} + 0.4981 * \text{MgO} + 0.0247 * \log \text{Ni} - 0.7536 * \log \text{Na}_2\text{O} - 0.2958 * \log \text{SiO}_2 - 0.1458 * \log \text{Rb} - 0.1177 * \log \text{K}_2\text{O}$$

$$F_{\text{Ortho-Amp2}} = 0.7588 * \text{CaO} + 0.37 * \log \text{Ni} - 0.7236 * \log \text{Na}_2\text{O} - 0.2982 * \log \text{K}_2\text{O} - 0.2399 * \log \text{SiO}_2 - 0.0008 * \log \text{Rb}$$

MgO in the para-amphibolite has a negative correlation with Ni and TiO<sub>2</sub>. The canonical factors derived for the para-amphibolite are:

$$F_{\text{Para-Amp1}} = 0.6173 * \text{CaO} + 0.5771 * \text{MgO} + 0.0756 * \text{Fe}_2\text{O}_3 - 0.5101 * \log \text{Na}_2\text{O} - 0.3706 * \log \text{Ni} - 0.2678 * \log \text{SiO}_2 - 0.2085 * \log \text{Rb} - 0.0321 * \log \text{K}_2\text{O}$$

$$F_{\text{Para-Amp2}} = 0.5619 * \text{CaO} + 0.6306 * \text{MgO} - 0.7001 * \log \text{Ni} - 0.2568 * \log \text{SiO}_2 - 0.2292 * \log \text{K}_2\text{O} - 0.2101 * \log \text{Rb}$$

$$F_{\text{Para-Amp3}} = 0.7382 * \text{MgO} + 0.439 * \text{CaO} - 0.9459 * \log \text{Ni} - 0.2358 * \log \text{TiO}_2$$

As there are some missing values for Ni in the regional data set, a general factor for amphibolite, which does not include Ni, has been derived as:

$$F_{\text{Amp2}} = 0.8404 * \text{CaO} + 0.4546 * \text{Fe}_2\text{O}_3 + 0.2584 * \log \text{MgO} + 0.196 * \log \text{TiO}_2 - 0.7205 * \log \text{K}_2\text{O} - 0.4869 * \log \text{SiO}_2 - 0.1964 * \log \text{Al}_2\text{O}_3;$$

In subsequent sections the code “C<sub>1</sub>” will be used for para-amphibolite, and the code “C<sub>2</sub>” for ortho-amphibolite.

## **5.5. Application of factors to the regional data set**

The peraluminous, alteration, and pelitic factors are the most important factors for the identification of peraluminous rocks that might be related to VHMS style alteration zones. To discriminate altered rocks from rocks containing both high MgO and K<sub>2</sub>O contents and probably had a pelitic precursor the pelitic factor values are also analysed. SAS software was used to calculate these factors for the whole regional data set. The

values calculated for each of the three factors were sorted and a maximum likelihood procedure was used to define the samples with anomalously high factor values. These samples are listed in tables below (Table 5.1, 5.2 and 5.3). Table 5.1 is sorted based on the peraluminous factor. For Table 5.2 the data is sorted based on the alteration factor, and, Table 5.3 gives anomalous samples based on the pelitic factor. The probable anomalous samples are ranked and marked by one or two stars in these tables based on their relative priority.

As shown in Table 5.1 and 5.2, samples 4, 189, 192 and 221 have the highest MgO (10.7-15 %), Al<sub>2</sub>O<sub>3</sub> (15.5-16.5 %), very low K<sub>2</sub>O (0.02-0.97 %), Na<sub>2</sub>O (0.3- 0.6 %) and CaO (0.32-0.84 %), low Ni (24-88 ppm) and slightly high Zn (177-349 ppm) contents. In these tables, there are two samples (232 and 903) with extremely high Al<sub>2</sub>O<sub>3</sub> contents (45.5-47.3 %) and high K<sub>2</sub>O contents (2.76-5.19 %), but low MgO contents (1.1-1.41 %) associated with Zn concentrations of 134 and 174 ppm respectively.

The peraluminous factor (FPer) is plotted versus alteration factor (FAR) in Figure 5.4. These two samples (232 and 903, in the first field) have the highest values for both factors. The diagram also shows seven samples that have high values for the alteration factor and these includes samples 92, 426, 430, 189,192, 221 and 222. These samples, which are located in the third field, may be related to an alteration zone.

The alteration factor (FAR) is plotted versus pelitic factor (FPR) in Figure 5.5. The same two samples (232 and 903, in the first field) have the highest values of both the alteration and pelitic factors. These samples probably represent unusual aluminous, pelitic precursors. Four samples have the highest values for the alteration factor (i.e. sample 4, 189, 192, and 221 in the third field) and lowest values for the pelitic factor. These samples are interesting in that they may represent the equivalents of rocks that were affected by ore forming alteration processes.

**Table 5.1:** Sorted data set based on the peraluminous factor (FPer) for the regional data set

No.	Code	Ranking	Al <sub>2</sub> O <sub>3</sub>	MgO	K <sub>2</sub> O	CaO	Na <sub>2</sub> O	SiO <sub>2</sub>	Cu	Zn	Ni	Ba	FPer	FPR	FAR
232	A		47.3	1.1	5.19	0.1	0.7	36.3	11	134	22	206	18.71	43.75	53.41
21	A		27.1	3.9	4.52	0.22	0.3	47.9	18	112	67	771	18.36	23.38	36.71
453	A		21.5	2.59	3.97	0.18	0.4	54.9	21	106	56	653	18.25	19.44	28.68
903	A		45.5	1.41	2.76	0.78	0.1	37.7	12	175	28	401	18.15	42.67	53.88
82	A		22.9	3.07	5.06	0.25	0.4	53.6	16	160	59	902	18.04	20.20	30.64
407	A		25.1	2.99	4.45	0.42	0.5	51.7	15	160	57	599	17.94	22.10	32.81
18	A		22.5	3.03	3.65	0.28	0.1	57.5	18	180	49	647	17.86	20.49	29.60
338	A		36.7	0.74	7.68	0.22	0.8	42.2	19	40	14	472	17.85	34.40	39.95
19	A		23.2	2.56	4.44	0.26	0.4	56.1	18	152	40	593	17.81	20.88	30.13
55	A		22.6	3.32	3.71	0.5	0.6	52.5	19	171	76	580	17.53	19.40	30.92
4	A	**	16.5	15	0.97	0.32	0.3	48.5	15	177	50	49	17.52	3.90	31.52
56	A		22.2	3.34	3.26	0.49	0.5	55.5	70	154	69	591	17.48	19.09	30.29
466	A		19.8	2.46	3.2	0.2	0.1	59.4	40	127	53	504	17.46	18.53	27.72
908	A		21.8	1.9	4.24	0.24	0.6	55.7	90	168	62	724	17.43	19.99	29.36
256	A	*	23.1	4.27	2	0.45	0.6	53	74	159	75	324	17.36	18.91	33.86
255	A	*	23.4	3.6	2.51	0.42	0.6	51.1	7	180	64	571	17.34	19.79	32.87
20	A		24.6	3.02	3.94	0.49	0.9	52.9	10	177	43	590	17.31	21.24	32.14
54	A		22.4	3.34	3.71	0.55	0.7	56.4	32	134	72	605	17.30	19.09	29.42
58	A		20.8	3.17	2.8	0.42	0.6	57.4	22	171	78	483	17.23	17.86	28.23
74	A		28.4	2.97	3.67	0.56	0.8	48.4	21	207	53	766	17.17	24.67	37.06
77	A	*	29.1	3.94	1.51	0.31	0.6	47.9	29	225	56	106	17.16	24.51	39.60
257	A	*	24.9	3.35	1.91	0.41	0.7	54.4	20	187	50	291	17.13	21.23	34.06
258	A	*	25.2	4.13	1.99	0.55	0.9	52.2	11	270	61	270	17.09	20.67	34.35
79	A		18.6	2	3.71	0.48	0.5	63.4	41	633	30	752	17.02	17.05	23.61
422	A		21	2.96	3.72	0.71	0.6	53.9	8	141	69	818	17.00	18.20	28.91
531	A		21.9	3.57	2.21	0.22	0.5	55.7	80	204	69	874	17.00	18.46	31.81
424	A		18.1	2.99	2.93	0.63	0.4	60.9	13	154	63	667	16.98	15.78	25.42
367	A		18	3.51	1.25	0.87	0.5	63.2	341	167	55	318	16.93	15.07	24.27
109	A		23.2	4.03	1.54	0.84	0.2	51.5	16	216	82	575	16.90	19.64	34.12
57	A		19.9	3.14	3.16	0.31	0.8	58.2	63	168	65	637	16.81	16.86	27.40
81	A		15.5	1.35	3.51	0.25	0.4	68.4	8	84	30	476	16.75	14.97	20.51
53	A		21.6	2.87	3.85	0.29	0.9	56.7	25	151	57	846	16.74	18.55	29.34
212	A		20	3.35	3.08	0.63	0.9	54.3	4	209	99	761	16.69	16.71	28.08
110	A		12.6	0.97	1.59	0.62	0.4	76.6	25	83	29	250	16.67	12.76	15.86
58	A		18.6	2	2.83	0.62	0.9	62.4	9	105	39	300	16.67	16.74	24.86
206	A	*	23.7	3.11	1.12	0.18	0.2	58.5	20	127	81	892	16.63	20.79	33.36
421	A		21.2	2.87	3.02	0.73	0.7	53.2	13	173	67	855	16.60	18.31	30.37
420	A		20.2	2.91	3.28	1.04	0.8	58.7	12	120	50	811	16.53	17.33	25.81
80	A		17.1	1.84	3.48	0.52	0.8	64.9	26	152	44	709	16.50	15.56	21.83
425	A		17.1	2.69	2.46	0.9	0.6	63	4	139	49	640	16.36	14.84	23.83
229	A		11.5	1.93	1.6	0.07	0.4	75.3	n.d.	77	n.d.	1131	16.06	10.73	17.77
184	A		19.5	0.46	4.45	0.15	0.7	69.3	6	81	1	1696	15.92	19.03	21.99
170	A		10.4	3.52	0.87	0.14	0.4	75.1	7	116	n.d.	806	15.80	8.16	16.90
75	A		10.6	1.15	1.89	0.43	0.5	78	18	78	27	178	15.68	10.49	13.64
172	A		9.4	2.13	1.71	0.23	0	81.7	1	49	n.d.	1354	15.67	10.43	12.06
221	A	**	16.6	10.7	0.07	0.45	0.6	45.8	14	167	88	76	15.65	6.91	36.91
192	A	**	16.2	11.7	0.24	0.43	0.3	43	17	178	24	10	15.55	6.01	37.95
426	A	*	28	4.81	0.38	0.68	0.7	44.1	46	249	94	107	15.53	22.20	43.85
189	A	**	15.5	13.7	0.23	0.84	0.6	41	12	349	25	30	15.32	3.29	36.67
92	A	*	17.3	3.03	0.19	0.68	0.2	64.3	24	137	102	2	15.20	14.83	27.15
430	A	*	24	3.63	0.25	0.57	0.5	53.7	32	190	68	87	15.10	19.74	36.75
717	A		11.7	0.27	8.37	0.26	0.8	74.8	9	11	12	1118	15.01	12.19	11.30
390	A		10.1	2.59	1.24	0.44	0.7	80.7	6	49	n.d.	215	14.99	8.36	12.78
222	A	*	13.3	2.81	0.32	0.34	0.3	69.9	12	60	3	305	14.98	11.27	23.31

Note: Ranking: anomaly ranking (\*= high to moderately high and \*\*= very high) and n.d.: Not detected

**Table 5.2:** Sorted data set based on the alteration factor (FAR) for the regional data set

No.	Code	Ranking	Al <sub>2</sub> O <sub>3</sub>	MgO	K <sub>2</sub> O	CaO	Na <sub>2</sub> O	SiO <sub>2</sub>	Cu	Zn	Ni	Ba	FAR	FPer	FPR
903	A		45.5	1.41	2.76	0.78	0.1	37.7	12	175	28	401	53.88	18.15	42.67
232	A		47.3	1.1	5.19	0.1	0.7	36.3	11	134	22	206	53.41	18.71	43.75
426	A	*	28	4.81	0.38	0.68	0.7	44.1	46	249	94	107	43.85	15.53	22.20
482	A	*	25.7	3.67	0.07	0.24	0.6	52.2	27	198	80	1	40.68	14.40	20.91
338	A		36.7	0.74	7.68	0.22	0.8	42.2	19	40	14	472	39.95	17.85	34.40
77	A	*	29.1	3.94	1.51	0.31	0.6	47.9	29	225	56	106	39.60	17.16	24.51
192	A	**	16.2	11.7	0.24	0.43	0.3	43	17	178	24	10	37.95	15.55	6.01
74	A		28.4	2.97	3.67	0.56	0.8	48.4	21	207	53	766	37.06	17.17	24.67
221	A	**	16.6	10.7	0.07	0.45	0.6	45.8	14	167	88	76	36.91	15.65	6.91
430	A	*	24	3.63	0.25	0.57	0.5	53.7	32	190	68	87	36.75	15.10	19.74
21	A		27.1	3.9	4.52	0.22	0.3	47.9	18	112	67	771	36.71	18.36	23.38
189	A	**	15.5	13.7	0.23	0.84	0.6	41	12	349	25	30	36.67	15.32	3.29
258	A	*	25.2	4.13	1.99	0.55	0.9	52.2	11	270	61	270	34.35	17.09	20.67
109	A	*	23.2	4.03	1.54	0.84	0.2	51.5	16	216	82	575	34.12	16.90	19.64
257	A	*	24.9	3.35	1.91	0.41	0.7	54.4	20	187	50	291	34.06	17.13	21.23
256	A	*	23.1	4.27	2	0.45	0.6	53	74	159	75	324	33.86	17.36	18.91
206	A	*	23.7	3.11	1.12	0.18	0.2	58.5	20	127	81	892	33.36	16.63	20.79
255	A	*	23.4	3.6	2.51	0.42	0.6	51.1	7	180	64	571	32.87	17.34	19.79
407	A		25.1	2.99	4.45	0.42	0.5	51.7	15	160	57	599	32.81	17.94	22.10
20	A		24.6	3.02	3.94	0.49	0.9	52.9	10	177	43	590	32.14	17.31	21.24
531	A	*	21.9	3.57	2.21	0.22	0.5	55.7	80	204	69	874	31.81	17.00	18.46
4	A	**	16.5	15	0.97	0.32	0.3	48.5	15	177	50	49	31.52	17.52	3.90
55	A		22.6	3.32	3.71	0.5	0.6	52.5	19	171	76	580	30.92	17.53	19.40
82	A		22.9	3.07	5.06	0.25	0.4	53.6	16	160	59	902	30.64	18.04	20.20
421	A		21.2	2.87	3.02	0.73	0.7	53.2	13	173	67	855	30.37	16.60	18.31
56	A		22.2	3.34	3.26	0.49	0.5	55.5	70	154	69	591	30.29	17.48	19.09

Note: Ranking: anomaly ranking (\*= high to moderately high and \*\*= very high)

**Table 5.3:** Sorted data set based on the pelitic factor (FPR) for the regional data set

No.	Code	Al <sub>2</sub> O <sub>3</sub>	MgO	K <sub>2</sub> O	CaO	Na <sub>2</sub> O	SiO <sub>2</sub>	Cu	Zn	Ni	Ba	FPR	FPer	FAR
232	A	47.3	1.1	5.19	0.1	0.7	36.3	11	134	22	206	43.75	18.71	53.41
903	A	45.5	1.41	2.76	0.78	0.1	37.7	12	175	28	401	42.67	18.15	53.88
338	A	36.7	0.74	7.68	0.22	0.8	42.2	19	40	14	472	34.40	17.85	39.95
74	A	28.4	2.97	3.67	0.56	0.8	48.4	21	207	53	766	24.67	17.17	37.06
77	A	29.1	3.94	1.51	0.31	0.6	47.9	29	225	56	106	24.51	17.16	39.60
21	A	27.1	3.9	4.52	0.22	0.3	47.9	18	112	67	771	23.38	18.36	36.71
426	A	28	4.81	0.38	0.68	0.7	44.1	46	249	94	107	22.20	15.53	43.85
407	A	25.1	2.99	4.45	0.42	0.5	51.7	15	160	57	599	22.10	17.94	32.81
20	A	24.6	3.02	3.94	0.49	0.9	52.9	10	177	43	590	21.24	17.31	32.14
257	A	24.9	3.35	1.91	0.41	0.7	54.4	20	187	50	291	21.23	17.13	34.06
482	A	25.7	3.67	0.07	0.24	0.6	52.2	27	198	80	1	20.91	14.40	40.68
19	A	23.2	2.56	4.44	0.26	0.4	56.1	18	152	40	593	20.88	17.81	30.13
206	A	23.7	3.11	1.12	0.18	0.2	58.5	20	127	81	892	20.79	16.63	33.36
258	A	25.2	4.13	1.99	0.55	0.9	52.2	11	270	61	270	20.67	17.09	34.35
18	A	22.5	3.03	3.65	0.28	0.1	57.5	18	180	49	647	20.49	17.86	29.60
82	A	22.9	3.07	5.06	0.25	0.4	53.6	16	160	59	902	20.20	18.04	30.64
908	A	21.8	1.9	4.24	0.24	0.6	55.7	90	168	62	724	19.99	17.43	29.36
255	A	23.4	3.6	2.51	0.42	0.6	51.1	7	180	64	571	19.79	17.34	32.87
430	A	24	3.63	0.25	0.57	0.5	53.7	32	190	68	87	19.74	15.10	36.75
109	A	23.2	4.03	1.54	0.84	0.2	51.5	16	216	82	575	19.64	16.90	34.12
453	A	21.5	2.59	3.97	0.18	0.4	54.9	21	106	56	653	19.44	18.25	28.68
55	A	22.6	3.32	3.71	0.5	0.6	52.5	19	171	76	580	19.40	17.53	30.92
56	A	22.2	3.34	3.26	0.49	0.5	55.5	70	154	69	591	19.09	17.48	30.29
54	A	22.4	3.34	3.71	0.55	0.7	56.4	32	134	72	605	19.09	17.30	29.42
184	A	19.5	0.46	4.45	0.15	0.7	69.3	6	81	1	1696	19.03	15.92	21.99

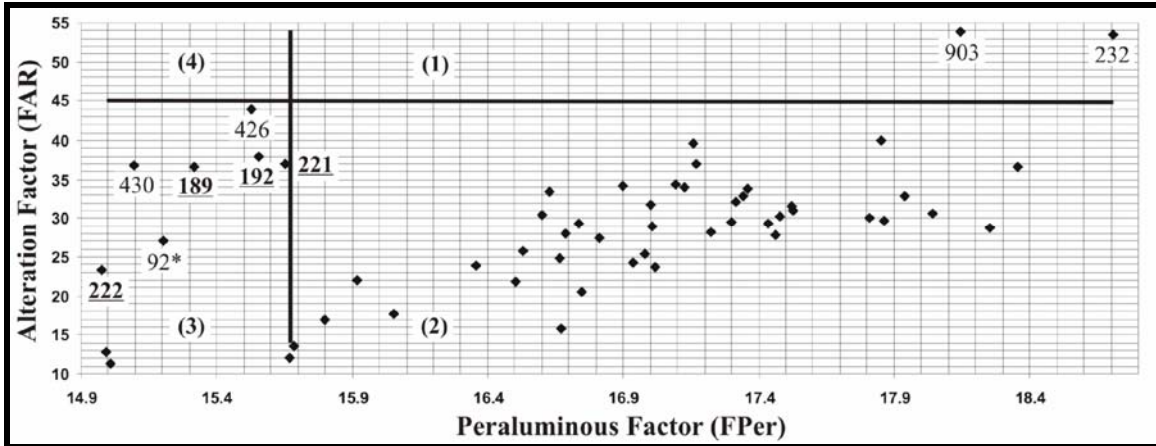


**Figure 5.4:** The peraluminous factor (FPer) versus alteration factor (FAR), regional data set [189]:  $MgO \gg K_2O$ ; 92\*, 426 and 430:  $MgO > K_2O$  from different areas; 903 and 232: very high  $Al_2O_3$ .

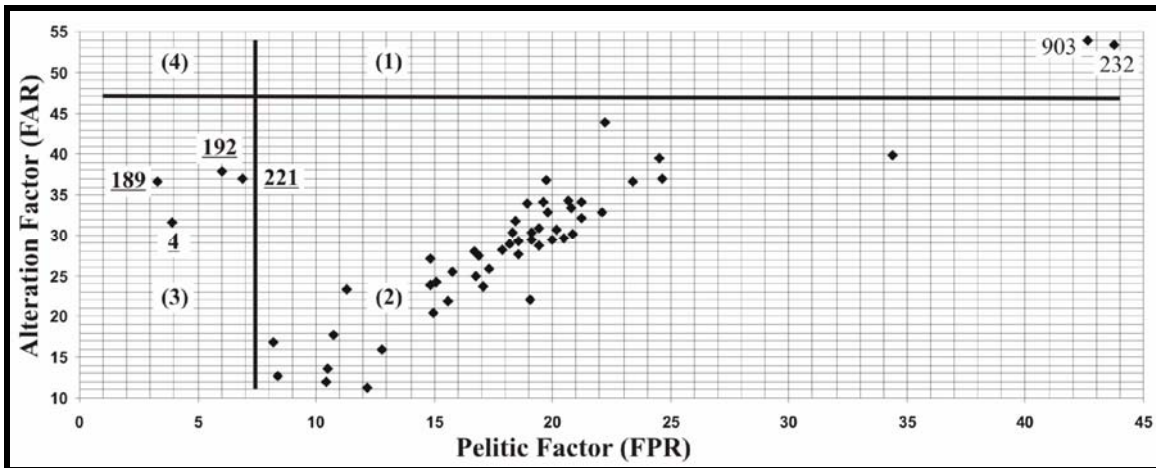


**Figure 5.5:** The pelitic factor (FPR) versus alteration factor (FAR), regional data set [189]:  $MgO \gg K_2O$ ; 903: very high  $Al_2O_3$ .

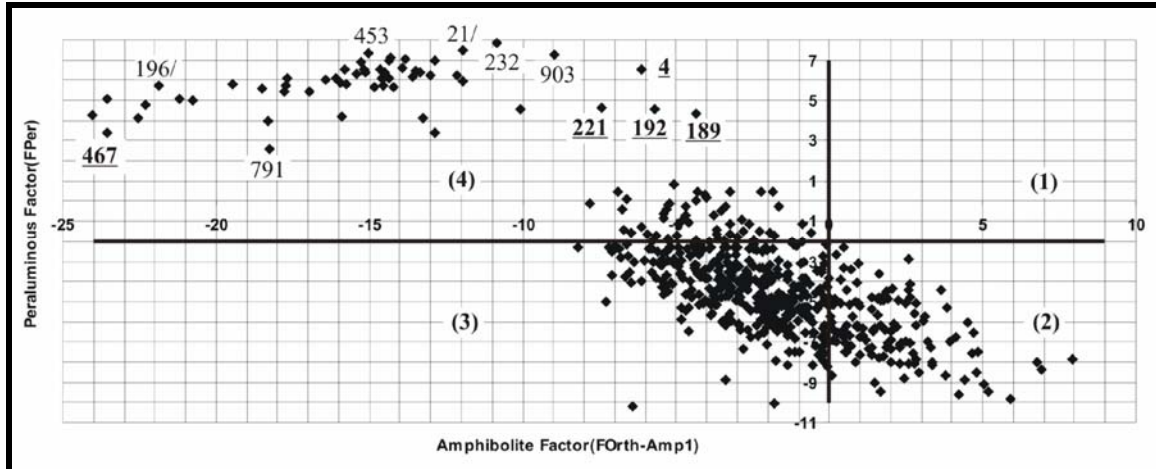
The amphibolite and peraluminous data set are ranked based on peraluminous factor (FPer) values, and the results are given in Table 5.4. In order to identify amphibolite samples that were possible affected by the alteration process and thereby attaining peraluminous characteristics, the variation of the peraluminous factor versus amphibolite factor is shown in Figure 5.6. All the peraluminous rocks are located in the fourth quarter of the figure and have peraluminous factor values  $> 3$ , and amphibolite factor values  $< 2.5$ . Four samples (232, 903, 453 and 21) have the highest values for the peraluminous factor ( $> 7$ ). Amphibolite samples are situated in the second, third and fourth quarter. Only one of these samples (sample 791), which plot in the fourth quarter, has a slightly

**Table 5.4:** Sorted data set based on peraluminous factor and calculation of amphibolite factor for the regional data set.

No.	Code	Ranking	Al <sub>2</sub> O <sub>3</sub>	MgO	K <sub>2</sub> O	Na <sub>2</sub> O	CaO	SiO <sub>2</sub>	Zn	Cu	Ni	Ba	Foa1	Foa2	Fpa1	Fpa2	FPer	FPR	FAR
232	A		47.3	1.1	5.19	0.7	0.1	36	134	11	22	206	-10.9	-7.7	-10.3	-10.5	7.7	42.7	53.4
21	A		27.1	3.9	4.52	0.3	0.22	48	112	18	67	771	-12.0	-9.4	-9.6	-11.4	7.4	22.4	36.7
453	A		21.5	2.6	3.97	0.4	0.18	55	106	21	56	653	-15.0	-11.3	-13.1	-14.1	7.3	18.4	28.7
903	A		45.5	1.4	2.76	0.1	0.78	38	175	12	28	401	-9.0	-5.9	-8.2	-9.1	7.1	41.7	53.9
82	A		22.9	3.1	5.06	0.4	0.25	54	160	16	59	902	-14.3	-11.0	-12.1	-13.4	7.0	19.2	30.6
407	A		25.1	3	4.45	0.5	0.42	52	160	15	57	599	-13.8	-10.5	-11.7	-13.0	6.9	21.1	32.8
18	A		22.5	3	3.65	0.1	0.28	58	180	18	49	647	-14.3	-10.9	-12.7	-13.5	6.9	19.5	29.6
338	A		36.7	0.7	7.68	0.8	0.22	42	40	19	14	472	-12.9	-9.4	-12.2	-12.0	6.9	33.4	39.9
19	A		23.2	2.6	4.44	0.4	0.26	56	152	18	40	593	-15.3	-11.7	-13.2	-14.2	6.8	19.9	30.1
55	A		22.6	3.3	3.71	0.6	0.5	53	171	19	76	580	-13.9	-10.6	-11.6	-13.1	6.5	18.4	30.9
4	A	**	16.5	15	0.97	0.3	0.32	49	177	15	50	49	-6.1	-9.1	-1.8	-4.2	6.5	2.9	31.5
56	A		22.2	3.3	3.26	0.5	0.49	56	154	70	69	591	-14.6	-11.2	-12.3	-13.7	6.5	18.1	30.3
466	A		19.8	2.5	3.2	0.1	0.2	59	127	40	53	504	-15.2	-11.3	-13.2	-14.4	6.5	17.5	27.7
908	A		21.8	1.9	4.24	0.6	0.24	56	168	90	62	724	-15.8	-11.7	-13.6	-14.9	6.4	19.0	29.4
256	A		23.1	4.3	2	0.6	0.45	53	159	74	75	324	-13.5	-10.6	-10.5	-12.6	6.4	17.9	33.9
255	A	*	23.4	3.6	2.51	0.6	0.42	51	180	7	64	571	-13.3	-10.3	-10.8	-12.5	6.3	18.8	32.9
20	A		24.6	3	3.94	0.9	0.49	53	177	10	43	590	-14.5	-11.3	-12.2	-13.4	6.3	20.2	32.1
54	A		22.4	3.3	3.71	0.7	0.55	56	134	32	72	605	-15.1	-11.7	-13.0	-14.1	6.3	18.1	29.4
58	A	*	20.8	3.2	2.8	0.6	0.42	57	171	22	78	483	-15.4	-11.8	-13.3	-14.4	6.2	16.9	28.2
74	A		28.4	3	3.67	0.8	0.56	48	207	21	53	766	-13.0	-9.9	-10.7	-12.2	6.2	23.7	37.1
77	A	*	29.1	3.9	1.51	0.6	0.31	48	225	29	56	106	-12.1	-9.5	-9.7	-11.3	6.2	23.5	39.6
257	A	*	24.9	3.4	1.91	0.7	0.41	54	187	20	50	291	-14.5	-11.2	-12.0	-13.4	6.1	20.2	34.1
258	A	*	25.2	4.1	1.99	0.9	0.55	52	270	11	61	270	-0.6	-10.7	-11.1	-12.5	6.1	19.7	34.4
79	A		18.6	2	3.71	0.5	0.48	63	633	41	30	752	-17.7	-13.5	-15.8	-16.2	6.0	16.1	23.6
422	A		21	3	3.72	0.6	0.71	54	141	8	69	818	-14.3	-10.9	-12.0	-13.5	6.0	17.2	28.9
531	A		21.9	3.6	2.21	0.5	0.22	56	204	80	69	874	-14.6	-11.4	-11.9	-13.6	6.0	17.5	31.8
424	A	*	18.1	3	2.93	0.4	0.63	61	154	13	63	667	-16.1	-12.3	-13.8	-14.9	6.0	14.8	25.4
367	A	*	18	3.5	1.25	0.5	0.87	63	167	341	55	318	-16.5	-12.6	-14.6	-15.1	5.9	14.1	24.3
109	A	*	23.2	4	1.54	0.2	0.84	52	216	16	82	575	-12.0	-9.1	-9.4	-11.5	5.9	18.6	34.1
57	A		19.9	3.1	3.16	0.8	0.31	58	168	63	65	637	-16.0	-12.4	-13.6	-14.7	5.8	15.9	27.4
81	A		15.5	1.4	3.51	0.4	0.25	68	84	8	30	476	-19.5	-14.7	-17.4	-17.8	5.7	14.0	20.5
53	A		21.6	2.9	3.85	0.9	0.29	57	151	25	57	846	-15.8	-12.2	-13.3	-14.5	5.7	17.5	29.3
212	A		20	3.4	3.08	0.9	0.63	54	209	4	99	761	-14.6	-11.1	-12.2	-13.7	5.7	15.7	28.1
110	A		12.6	1	1.59	0.4	0.62	77	83	25	29	250	-21.9	-16.1	-20.3	-20.0	5.7	11.8	15.9
58	A		18.6	2	2.83	0.9	0.62	62	105	9	39	300	-17.7	-13.4	-15.4	-16.2	5.7	15.7	24.9
206	A	*	23.7	3.1	1.12	0.2	0.18	59	127	20	81	892	-14.8	-11.1	-12.8	-14.1	5.6	19.8	33.4
421	A		21.2	2.9	3.02	0.7	0.73	53	173	13	67	855	-14.2	-10.7	-11.5	-13.3	5.6	17.3	30.4
80	A		17.1	1.8	3.48	0.8	0.52	65	152	12	50	709	-18.5	-14.0	-16.6	-17.0	5.5	14.6	21.8
169	A		10.6	4	1.4	0.3	0.12	75	113	26	44	537					5.4	7.2	16.3
425	A		17.1	2.7	2.46	0.6	0.9	63	139	4	49	640	-17.0	-12.9	-14.6	-15.6	5.4	13.8	23.8
405	A		16.6	2.3	3	1	0.85	63	133	11	58	660	-17.8	-13.4	-15.6	-16.4	5.3	13.6	22.3
229	A		11.5	1.9	1.6	0.4	0.07	75	77	0	0	1131					5.1	9.7	17.8
1031	A		12.2	0.9	3.43	0.7	0.37	72	98	25	29	469	-21.2	-15.9	-19.3	-19.2	5.0	11.1	15.6
196	A		7.85	0.1	6.24	0.1	0.39	83	0	7	19	115	-23.6	-17.4	-23.0	-21.5	5.0	9.3	6.5
184	A		19.5	0.5	4.45	0.7	0.15	69	81	6	1	1696	-20.8	-16.7	-18.2	-17.6	4.9	18.0	22.0
170	A		10.4	3.5	0.87	0.4	0.14	75	116	7	0	806					4.8	7.2	16.9
75	A		10.6	1.2	1.89	0.5	0.43	78	78	18	27	178	-22.3	-16.9	-20.6	-20.2	4.7	9.5	13.6
172	A		9.4	2.1	1.71	0.01	0.23	82	49	1		1354					4.7	9.4	12.1
221	A	**	16.6	11	0.07	0.6	0.45	46	167	14	88	76	-7.4	-7.8	-2.4	-6.4	4.7	5.9	36.9
192	A	**	16.2	12	0.24	0.3	0.43	43	178	17	24	10	-5.7	-7.5	0.6	-4.2	4.6	5.0	37.9
426	A	*	28	4.8	0.38	0.7	0.68	44	249	46	94	107	-10.1	-7.8	-6.4	-9.7	4.5	21.2	43.9
189	A	**	15.5	14	0.23	0.6	0.84	41	349	12	25	30	-4.4	-7.2	1.9	-2.6	4.3	2.3	36.7
467	A		7.9	0.7	1.91	0.5	0.17	82	91	34	13	428	-24.1	-18.4	-22.1	-21.4	4.2	7.5	10.4
92	A	*	17.3	3	0.19	0.2	0.68	64	137	24	102	2	-15.9	-11.5	-14.1	-15.1	4.2	13.8	27.2
430	A	*	24	3.6	0.25	0.5	0.57	54	190	32	68	87	-13.3	-10.0	-10.4	-12.5	4.1	18.7	36.8
717	A		11.7	0.3	8.37	0.8	0.26	75	11	9	12	1118	-22.5	-17.3	-21.2	-20.0	4.0	11.2	11.3
390	A		10.1	2.6	1.24	0.7	0.44	81	49	6		215					4.0	7.4	12.8
222	A	*	13.3	2.8	0.32	0.3	0.34	70	60	12	3	305	-18.3	-14.9	-14.5	-15.7	4.0	10.3	23.3
482	A	*	25.7	3.7	0.07	0.6	0.24	52	198	27	80	1	-12.8	-9.6	-10.0	-12.2	3.4	19.9	40.7
791	C		17.4	0.8	4.57	2.7	2.69	64	122	22	12	1564	-18.2	-13.5	-16.2	-16.2	2.5	15.1	19.7

Note: Ranking: anomaly ranking (\*=high to moderately high and \*\*= very high); Foa1=Fortho-Amp1; Foa2=Fortho-Amp2;

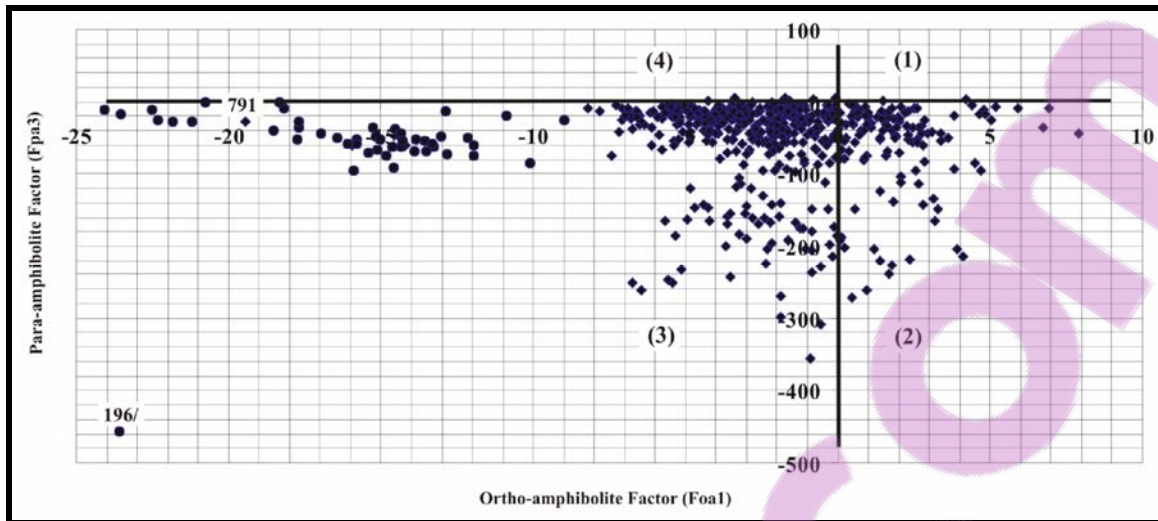
Fpa1=Fpara-Amp1; Fpa2=Fpara-Amp2; blank fields of factors is because of missing values for Ni.



**Figure 5.6:** The peraluminous factor (FPer) versus amphibolite factor (FOrth-Amp1) for the regional data set [**189**:  $MgO \gg K_2O$ ; 196/, 453 and **467**:  $K_2O > MgO$  from different areas; 903 and 232: very high  $Al_2O_3$ ; 791: high  $Na_2O$  and  $CaO$  contents].

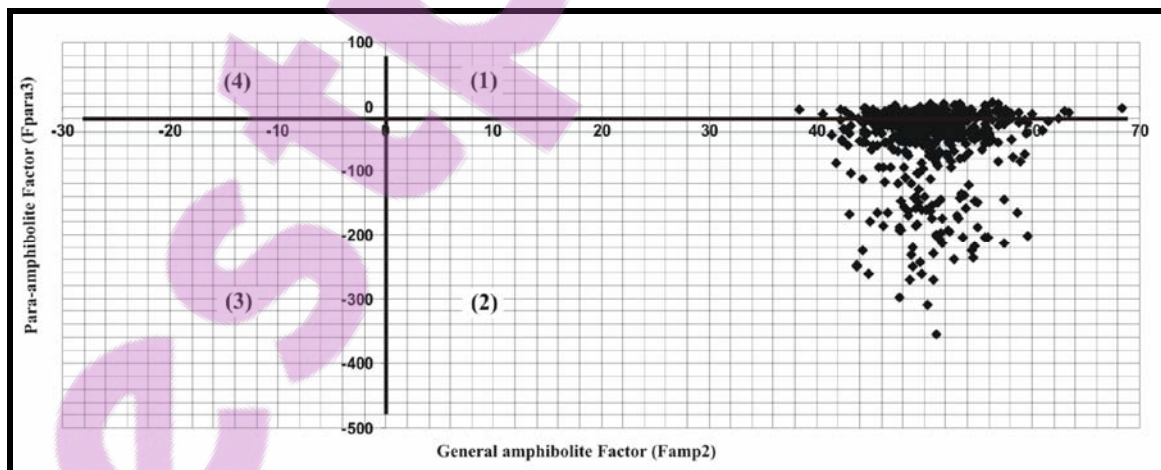
higher peraluminous value (2.5). The remained amphibolite samples display low peraluminous factor values ( $<1$ ).

The variations of ortho-amphibolite factors (Foa1) versus para-amphibolite factors (Fpa3) are plotted in Figure 5.7. In general, the para-amphibolites have a para-amphibolite factor similar to the peraluminous rocks. This is because the precursors of the para-amphibolites represent a sedimentary mix of shale and carbonate material. Ortho-amphibolites have para-amphibolite factor values lower than  $-100$ . Peraluminous samples are shown together with amphibolite samples in this diagram. The peraluminous rocks in this figure are situated in the third quarter and have an ortho-amphibolite factor of less than  $-8.5$ . Again only sample (791), which plots in the peraluminous field, has a slightly higher peraluminous values (2.5). There is an amphibolite sample (196), which has a very low para-amphibolite factor value ( $<-300$ ), with an ortho-amphibolite factor value of less than  $-8.5$ . This sample is completely separated from peraluminous field. The rest of the amphibolite samples have para-amphibolite factors higher than  $-8.5$  and are located in the first, second, third and fourth field.



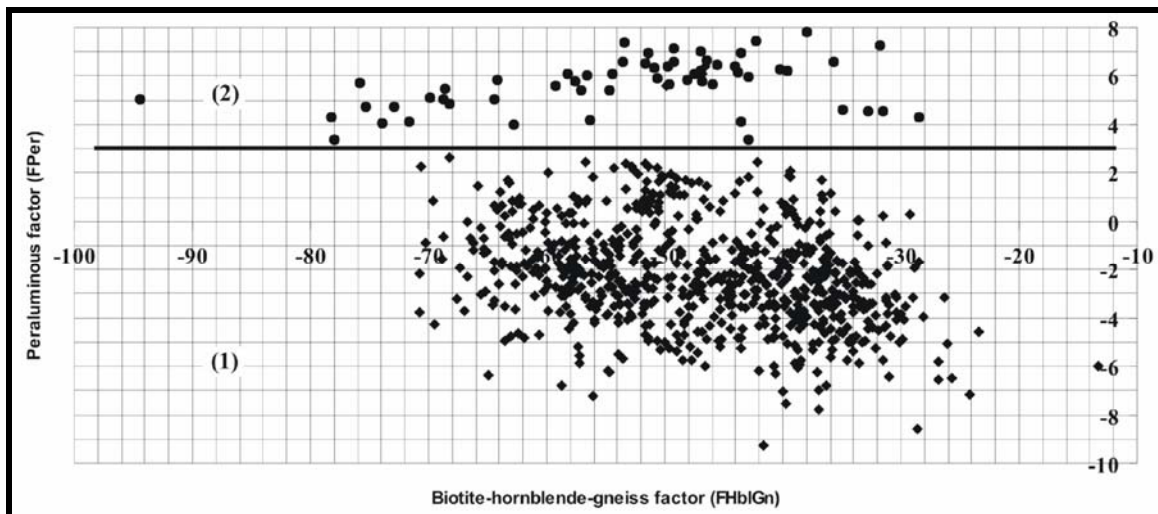
**Figure 5.7:** The para-amphibolite factor ( $F_{para-amp3}$ ) versus ortho-amphibolite factor ( $F_{ortho-amp1}$ ), regional amphibolite and peraluminous data set [diamond filled: peraluminous and square filled: amphibolite].

Figure 5.8 shows the variation of the general factor for amphibolite ( $F_{Amp2}$ ) versus the para-amphibolite factor ( $F_{Para-Amp3}$ ) for amphibolite samples. Assumed para-amphibolite samples have higher values of the para-amphibolite factor and the assumed ortho-amphibolite samples have low values of para-amphibolite factor. Amphibolite samples in this diagram are situated in the first and second field. It is expected that the discrimination between these amphibolite types could be improved if samples were also analysed for Ni (Leake 1964) and Sc (Theart 1985).



**Figure 5.8:** The para-amphibolite factor ( $F_{para-amp3}$ ) versus general amphibolite factor ( $F_{amp2}$ ) for the regional amphibolite data set.

Similarly, to identify biotite-hornblende-gneiss samples that were potentially affected by the alteration process, the biotite-hornblende-gneiss factor values are compared with values for the peraluminous factor. Values calculated for the biotite-hornblende-gneiss and peraluminous factors are listed in Table 5.5. These values were calculated for a combined data file consisting of biotite-hornblende-gneiss and peraluminous samples. The variation in the biotite-hornblende-gneiss factor versus peraluminous factor is shown in Figure 5.9. All the biotite-hornblende-gneiss samples plot outside the field defined by the peraluminous samples and no distinctly anomalous samples could be identified. However, a large number of the biotite-hornblende-gneiss samples plots close to the peraluminous dividing line of 3, based on the peraluminous factor.



**Figure 5.9:** Biotite-hornblende-gneiss factor (FHbl-Gn) versus peraluminous factor (FPer), combined data set of biotite-hornblende-gneiss and peraluminous samples, regional data set [diamond filled: peraluminous and square filled: biotite-hornblende-gneiss samples].

**Table 5.5:** Sorted the peraluminous factor (FPer) and calculation of biotite-hornblende-gneiss factor for the regional data set

No.	Code	Ranking	CaO	SiO <sub>2</sub>	MgO	Al <sub>2</sub> O <sub>3</sub>	Na <sub>2</sub> O	K <sub>2</sub> O	Zn	Cu	Ni	Ba	FPer	FPR	FAR	FGn	FHblGn
232	A		0.1	36.3	1.1	47.3	0.7	5.19	134	11	22	206	7.7	42.7	53.4	27.9	-37.9
21	A		0.22	47.9	3.9	27.1	0.3	4.52	112	18	67	771	7.4	22.4	36.7	29.2	-42.3
453	A		0.18	54.9	2.59	21.5	0.4	3.97	106	21	56	653	7.3	18.4	28.7	38.2	-53.4
903	A		0.78	37.7	1.41	45.5	0.1	2.76	175	12	28	401	7.1	41.7	53.9	25.2	-31.8
82	A		0.25	53.6	3.07	22.9	0.4	5.06	160	16	59	902	7.0	19.2	30.6	36.0	-49.2
407	A		0.42	51.7	2.99	25.1	0.5	4.45	160	15	57	599	6.9	21.1	32.8	34.5	-47.0
18	A		0.28	57.5	3.03	22.5	0.1	3.65	180	18	49	647	6.9	19.5	29.6	41.0	-51.4
338	A		0.22	42.2	0.74	36.7	0.8	7.68	40	19	14	472	6.9	33.4	39.9	34.6	-43.6
19	A		0.26	56.1	2.56	23.2	0.4	4.44	152	18	40	593	6.8	19.9	30.1	39.7	-51.4
55	A		0.5	52.5	3.32	22.6	0.6	3.71	171	19	76	580	6.5	18.4	30.9	33.9	-46.5
4	A	**	0.32	48.5	15	16.5	0.3	0.97	177	15	50	49	6.5	2.9	31.5	24.0	-35.6
56	A		0.49	55.5	3.34	22.2	0.5	3.26	154	70	69	591	6.5	18.1	30.3	37.2	-49.2
466	A		0.2	59.4	2.46	19.8	0.1	3.2	127	40	53	504	6.5	17.5	27.7	41.3	-53.5
908	A		0.24	55.7	1.9	21.8	0.6	4.24	168	90	62	724	6.4	19.0	29.4	38.0	-51.6
256	A	*	0.45	53	4.27	23.1	0.6	2	159	74	75	324	6.4	17.9	33.9	31.7	-45.5
255	A	*	0.42	51.1	3.6	23.4	0.6	2.51	180	7	64	571	6.3	18.8	32.9	31.8	-44.1
20	A		0.49	52.9	3.02	24.6	0.9	3.94	177	10	43	590	6.3	20.2	32.1	35.8	-46.6
54	A		0.55	56.4	3.34	22.4	0.7	3.71	134	32	72	605	6.3	18.1	29.4	39.5	-49.7
58	A	*	0.42	57.4	3.17	20.8	0.6	2.8	171	22	78	483	6.2	16.9	28.2	40.0	-50.9
74	A		0.56	48.4	2.97	28.4	0.8	3.67	207	21	53	766	6.2	23.7	37.1	30.7	-40.3
77	A	*	0.31	47.9	3.94	29.1	0.6	1.51	225	29	56	106	6.2	23.5	39.6	29.7	-39.6
257	A	*	0.41	54.4	3.35	24.9	0.7	1.91	187	20	50	291	6.1	20.2	34.1	35.9	-46.9
258	A	*	0.55	52.2	4.13	25.2	0.9	1.99	270	11	61	270	6.1	19.7	34.4	33.7	-43.8
79	A		0.48	63.4	2	18.6	0.5	3.71	633	41	30	752	6.0	16.1	23.6	48.2	-58.2
422	A		0.71	53.9	2.96	21	0.6	3.72	141	8	69	818	6.0	17.2	28.9	35.3	-46.9
531	A	*	0.22	55.7	3.57	21.9	0.5	2.21	204	80	69	874	6.0	17.5	31.8	35.6	-47.5
424	A		0.63	60.9	2.99	18.1	0.4	2.93	154	13	63	667	6.0	14.8	25.4	42.5	-54.4
367	A	*	0.87	63.2	3.51	18	0.5	1.25	167	341	55	318	5.9	14.1	24.3	47.0	-56.5
109	A	*	0.84	51.5	4.03	23.2	0.2	1.54	216	16	82	575	5.9	18.6	34.1	30.1	-42.9
57	A		0.31	58.2	3.14	19.9	0.8	3.16	168	63	65	637	5.8	15.9	27.4	40.5	-50.6
81	A		0.25	68.4	1.35	15.5	0.4	3.51	84	8	30	476	5.7	14.0	20.5	52.7	-64.1
53	A		0.29	56.7	2.87	21.6	0.9	3.85	151	25	57	846	5.7	17.5	29.3	38.7	-48.1
212	A		0.63	54.3	3.35	20	0.9	3.08	209	4	99	761	5.7	15.7	28.1	35.6	-46.9
110	A		0.62	76.6	0.97	12.6	0.4	1.59	83	25	29	250	5.7	11.8	15.9	62.4	-75.9
58	A		0.62	62.4	2	18.6	0.9	2.83	105	9	39	300	5.7	15.7	24.9	45.5	-57.6
206	A	*	0.18	58.5	3.11	23.7	0.2	1.12	127	20	81	892	5.6	19.8	33.4	39.9	-49.6
421	A		0.73	53.2	2.87	21.2	0.7	3.02	173	13	67	855	5.6	17.3	30.4	33.0	-45.9
420	B1		1.04	58.7	2.91	20.2	0.8	3.28	120	12	50	811	5.5	16.3	25.8	42.8	-49.9
80	A		0.52	64.9	1.84	17.1	0.8	3.48	152	26	44	709	5.5	14.6	21.8	49.7	-59.2
169	A		0.12	75.4	4.02	10.6	0.3	1.4	113	11	n.d.	537	5.4	7.2	16.3	59.5	-68.7
425	A		0.9	63	2.69	17.1	0.6	2.46	139	4	49	640	5.4	13.8	23.8	44.8	-54.7
405	A		0.85	63.3	2.27	16.6	1	3	133	11	58	660	5.3	13.6	22.3	46.3	-57.1
229	A		0.07	75.3	1.93	11.5	0.4	1.6	77	n.d.	n.d.	1131	5.1	9.7	17.8	58.6	-69.9
1031	A		0.37	72.3	0.91	12.2	0.7	3.43	98	25	29	469	5.0	11.1	15.6	57.9	-68.8
196	A		0.39	82.9	0.1	7.85	0.1	6.24	n.d.	7	19	115	5.0	9.3	6.5	73.9	-94.4
184	A		0.15	69.3	0.46	19.5	0.7	4.45	81	6	1	1696	4.9	18.0	22.0	58.4	-64.5
170	A		0.14	75.1	3.52	10.4	0.4	0.87	116	7	n.d.	806	4.8	7.2	16.9	58.3	-68.3
75	A		0.43	78	1.15	10.6	0.5	1.89	78	18	27	178	4.7	9.5	13.6	64.0	-72.9
172	A		0.23	81.7	2.13	9.4	0.01	1.71	49	1	n.d.	1354	4.7	9.4	12.1	69.3	-75.3
221	A	**	0.45	45.8	10.7	16.6	0.6	0.07	167	14	88	76	4.7	5.9	36.9	15.2	-34.9
192	A	**	0.43	43	11.7	16.2	0.3	0.24	178	17	24	10	4.6	5.0	37.9	9.2	-31.6
426	A	*	0.68	44.1	4.81	28	0.7	0.38	249	46	94	107	4.5	21.2	43.9	18.6	-32.7
189	A	**	0.84	41	13.7	15.5	0.6	0.23	349	12	25	30	4.3	2.3	36.7	8.1	-28.5
467	A		0.17	82.4	0.67	7.9	0.5	1.91	91	34	13	428	4.2	7.5	10.4	69.1	-78.3
92	A	*	0.68	64.3	3.03	17.3	0.2	0.19	137	24	102	2	4.2	13.8	27.2	45.3	-56.3
430	A	*	0.57	53.7	3.63	24	0.5	0.25	190	32	68	87	4.1	18.7	36.8	32.0	-43.6
717	A		0.26	74.8	0.27	11.7	0.8	8.37	11	9	12	1118	4.0	11.2	11.3	65.8	-71.7
390	A		0.44	80.7	2.59	10.1	0.7	1.24	49	6	n.d.	215	4.0	7.4	12.8	68.1	-73.9
222	A	*	0.34	69.9	2.81	13.3	0.3	0.32	60	12	3	305	4.0	10.3	23.3	49.3	-62.8
482	A	*	0.24	52.2	3.67	25.7	0.6	0.07	198	27	80	1	3.4	19.9	40.7	30.0	-43.0
699	A		0.9	83.6	1.3	5.53	0.7	0.56	49	7	484	10	3.3	4.4	9.0	68.3	-77.9
446	B1		1.23	72.1	0.31	13.6	2.7	4.99	47	9	4	473	2.5	12.2	13.4	62.6	-68.3
184	B1		22.6	57	0.38	13.6	0.3	0.39	17	17	10	130	-9.3	12.6	17.6	36.0	-41.7

Note: Ranking: anomaly ranking (\*= high to moderately high and \*\*= very high) and n.d.: not detected

In the same way, to identify leucogneiss samples that were potentially affected by the alteration process, the leucogneiss factor values are compared with values for the peraluminous factor. Values calculated for the leucogneiss and peraluminous factors are listed in Table 5.6. Figure 5.10 shows the variation of the leucogneiss factor versus peraluminous factor in a data file that includes both peraluminous and leucogneiss rocks. Leucogneiss samples are located in the second field and their peraluminous factor is less than 4. The leucogneiss factor values for these samples are higher than peraluminous samples and vary from 40 to 90. Peraluminous samples in this diagram are located in the first field, where the peraluminous factor is greater than 4. The leucogneiss factor values of peraluminous rocks vary from 7 to 72. However, some of the leucogneiss samples plot close to the peraluminous dividing line of 4, defined above.

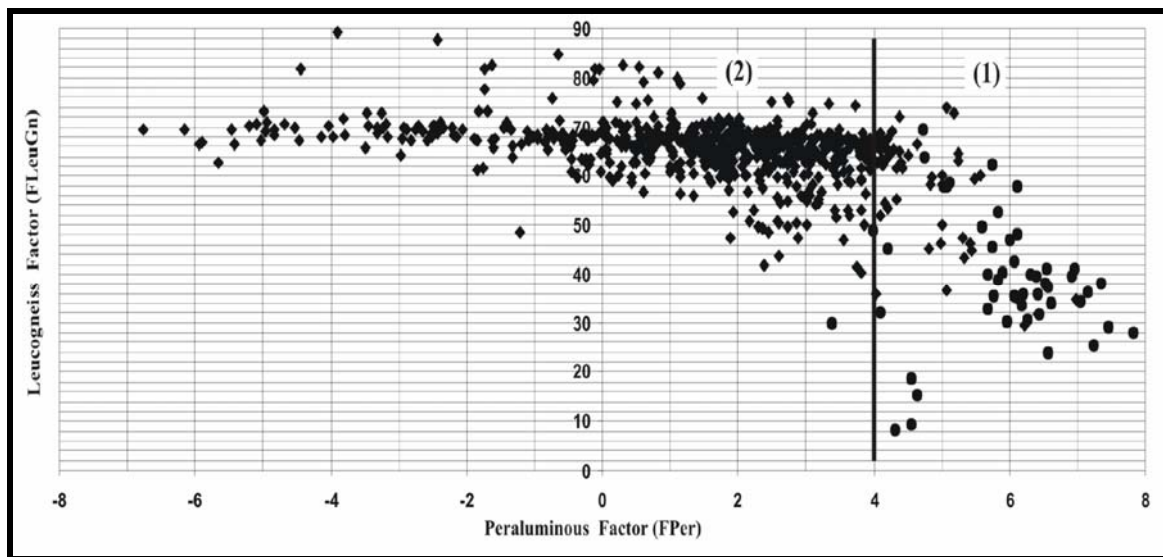


**Figure 5.10:** The leucogneiss factor (FLeu-Gn) versus peraluminous factor (FPer), mixed of peraluminous and leuco-gneissic samples, regional data set [diamond filled: peraluminous and square filled: leucogneiss samples].

**Table 5.6:** Sorted the peraluminous factor (FPer) and calculation of the leucogneiss for the regional data set.

No.	Code	SiO <sub>2</sub>	K <sub>2</sub> O	Na <sub>2</sub> O	CaO	Al <sub>2</sub> O <sub>3</sub>	MgO	Zn	Cu	Ni	Ba	FPer	FPR	FAR	FGn	FLeuGn
232	A	36	5.19	0.7	0.1	47.3	1.1	134	11	22	206	7.7	42.7	53.4	27.9	37.9
21	A	48	4.52	0.3	0.22	27.1	3.9	112	18	67	771	7.4	22.4	36.7	29.2	42.3
453	A	55	3.97	0.4	0.18	21.5	2.59	106	21	56	653	7.3	18.4	28.7	38.2	53.4
903	A	38	2.76	0.1	0.78	45.5	1.41	175	12	28	401	7.1	41.7	53.9	25.2	31.8
82	A	54	5.06	0.4	0.25	22.9	3.07	160	16	59	902	7.0	19.2	30.6	36.0	49.2
407	A	52	4.45	0.5	0.42	25.1	2.99	160	15	57	599	6.9	21.1	32.8	34.5	47.0
18	A	58	3.65	0.1	0.28	22.5	3.03	180	18	49	647	6.9	19.5	29.6	41.0	51.4
338	A	42	7.68	0.8	0.22	36.7	0.74	40	19	14	472	6.9	33.4	39.9	34.6	43.6
19	A	56	4.44	0.4	0.26	23.2	2.56	152	18	40	593	6.8	19.9	30.1	39.7	51.4
55	A	53	3.71	0.6	0.5	22.6	3.32	171	19	76	580	6.5	18.4	30.9	33.9	46.5
4	A	49	0.97	0.3	0.32	16.5	15	177	15	50	49	6.5	2.9	31.5	24.0	35.6
56	A	56	3.26	0.5	0.49	22.2	3.34	154	70	69	591	6.5	18.1	30.3	37.2	49.2
466	A	59	3.2	0.1	0.2	19.8	2.46	127	40	53	504	6.5	17.5	27.7	41.3	53.5
908	A	56	4.24	0.6	0.24	21.8	1.9	168	90	62	724	6.4	19.0	29.4	38.0	51.6
256	A	53	2	0.6	0.45	23.1	4.27	159	74	75	324	6.4	17.9	33.9	31.7	45.5
255	A	51	2.51	0.6	0.42	23.4	3.6	180	7	64	571	6.3	18.8	32.9	31.8	44.1
20	A	53	3.94	0.9	0.49	24.6	3.02	177	10	43	590	6.3	20.2	32.1	35.8	46.6
54	A	56	3.71	0.7	0.55	22.4	3.34	134	32	72	605	6.3	18.1	29.4	39.5	49.7
58	A	57	2.8	0.6	0.42	20.8	3.17	171	22	78	483	6.2	16.9	28.2	40.0	50.9
74	A	48	3.67	0.8	0.56	28.4	2.97	207	21	53	766	6.2	23.7	37.1	30.7	40.3
77	A	48	1.51	0.6	0.31	29.1	3.94	225	29	56	106	6.2	23.5	39.6	29.7	39.6
257	A	54	1.91	0.7	0.41	24.9	3.35	187	20	50	291	6.1	20.2	34.1	35.9	46.9
258	A	52	1.99	0.9	0.55	25.2	4.13	270	11	61	270	6.1	19.7	34.4	33.7	43.8
79	A	63	3.71	0.5	0.48	18.6	2	633	41	30	752	6.0	16.1	23.6	48.2	58.2
422	A	54	3.72	0.6	0.71	21	2.96	141	8	69	818	6.0	17.2	28.9	35.3	46.9
531	A	56	2.21	0.5	0.22	21.9	3.57	204	80	69	874	6.0	17.5	31.8	35.6	47.5
580	B	64	13.3	1.1	0.5	18.5	0.45	6	21	8	145	6.0	17.3	16.9	57.8	73.3
424	A	61	2.93	0.4	0.63	18.1	2.99	154	13	63	667	6.0	14.8	25.4	42.5	54.4
367	A	63	1.25	0.5	0.87	18	3.51	167	341	55	318	5.9	14.1	24.3	47.0	56.5
109	A	52	1.54	0.2	0.84	23.2	4.03	216	16	82	575	5.9	18.6	34.1	30.1	42.9
57	A	58	3.16	0.8	0.31	19.9	3.14	168	63	65	637	5.8	15.9	27.4	40.5	50.6
81	A	68	3.51	0.4	0.25	15.5	1.35	84	8	30	476	5.7	14.0	20.5	52.7	64.1
53	A	57	3.85	0.9	0.29	21.6	2.87	151	25	57	846	5.7	17.5	29.3	38.7	48.1
212	A	54	3.08	0.9	0.63	20	3.35	209	4	99	761	5.7	15.7	28.1	35.6	46.9
110	A	77	1.59	0.4	0.62	12.6	0.97	83	25	29	250	5.7	11.8	15.9	62.4	75.9
58	A	62	2.83	0.9	0.62	18.6	2	105	9	39	300	5.7	15.7	24.9	45.5	57.6
206	A	59	1.12	0.2	0.18	23.7	3.11	127	20	81	892	5.6	19.8	33.4	39.9	49.6
421	A	53	3.02	0.7	0.73	21.2	2.87	173	13	67	855	5.6	17.3	30.4	33.0	45.9
80	A	65	3.48	0.8	0.52	17.1	1.84	152	26	44	709	5.5	14.6	21.8	49.7	59.2
978	B	71	6.91	1.4	0.54	14	1.1	31	6	12	782	5.5	12.4	14.7	60.0	71.4
425	A	63	2.46	0.6	0.9	17.1	2.69	139	4	49	640	5.4	13.8	23.8	44.8	54.7
405	B	63	3	1	0.85	16.6	2.27	133	11	58	660	5.3	13.6	22.3	46.3	57.1
229	A	75	1.6	0.4	0.07	11.5	1.93	77	n.d.	n.d.	1131	5.1	9.7	17.8	58.6	69.9
52	B	56	2.68	1.3	1.36	19.7	3.72	193	4	87	520	5.0	14.9	27.6	36.8	47.7
184	A	69	4.45	0.7	0.15	19.5	0.46	81	6	1	1696	4.9	18.0	22.0	58.4	64.5
423	B	64	1.79	0.8	1.25	16.6	2.54	152	2	52	524	4.9	13.3	22.7	46.4	55.5
170	A	75	0.87	0.4	0.14	10.4	3.52	116	7	n.d.	806	4.8	7.2	16.9	58.3	68.3
323	B	70	4.13	1.9	0.69	14.8	0.95	54	30	13	202	4.8	13.0	15.7	59.7	69.3
75	A	78	1.89	0.5	0.43	10.6	1.15	78	18	27	178	4.7	9.5	13.6	64.0	72.9
172	A	82	1.71	0.01	0.23	9.4	2.13	49	1	n.d.	1354	4.7	9.4	12.1	69.3	75.3
221	A	46	0.07	0.6	0.45	16.6	10.7	167	14	88	76	4.7	5.9	36.9	15.2	34.9
192	A	43	0.24	0.3	0.43	16.2	11.7	178	17	24	10	4.6	5.0	37.9	9.2	31.6
426	A	44	0.38	0.7	0.68	28	4.81	249	46	94	107	4.5	21.2	43.9	18.6	32.7
1006	B	73	9.14	1.3	0.1	14.8	0.26	1	3	5	216	4.5	13.9	13.6	66.5	72.6
189	A	41	0.23	0.6	0.84	15.5	13.7	349	12	25	30	4.3	2.3	36.7	8.1	28.5
353	B	73	5.95	1.8	1.13	12.3	0.52	53	18	2	310	4.3	11.3	12.7	61.6	75.0
92	A	64	0.19	0.2	0.68	17.3	3.03	137	24	102	2	4.2	13.8	27.2	45.3	56.3
1011	B	72	8.82	1.3	0.25	15.5	0.19	1	6	1	436	4.2	14.5	14.3	65.3	71.0
430	A	54	0.25	0.5	0.57	24	3.63	190	32	68	87	4.1	18.7	36.8	32.0	43.6
892	B	65	7.3	1.8	1.71	16.3	0.96	58	8	6	1142	4.1	14.3	17.3	53.3	60.2
717	A	75	8.37	0.8	0.26	11.7	0.27	11	9	12	1118	4.0	11.2	11.3	65.8	71.7
390	A	81	1.24	0.7	0.44	10.1	2.59	49	6	n.d.	215	4.0	7.4	12.8	68.1	73.9
222	A	70	0.32	0.3	0.34	13.3	2.81	60	12	3	305	4.0	10.3	23.3	49.3	62.8
44	B	75	3.16	3.1	1.27	13.2	0.31	20	33	n.d.	750	1.3	11.5	13.1	65.7	67.7
162	B	78	0.35	5.1	2.16	10.9	0.01	n.d.	3	3	151	-6.2	8.7	12.5	69.6	69.6

Note: n.d.: not detected

Factor analyses were used in the above paragraphs to identify rocks from the regional data set that were possibly affected by hydrothermal processes related to sulphide mineralization processes. In the following section various techniques will be used to prioritize potential target areas for follow-up exploration.

### **5.6. Prioritization of the anomalous samples in the regional data set**

The objective with an initial geochemical exploration survey is to identify anomalous areas or probable mineralized zones for follow up exploration. When there is more than one such anomalous area, these should be ranked based on the calculated relative potential for all the samples. For this purpose, a data file composed of the peraluminous, pelitic and alteration factor values was used in a maximum likelihood procedure to identify anomalous sub-populations.

A cumulative frequency probability plot of the alteration factor values is used to identify estimates of the anomalous sub-population. The probplot software requires positive variable values, and for this reason a constant value was added to all factors returning same negative values. This results a shift in the data without any influence on the underlying distribution of the values.

The cumulative frequency probability plot of the regional data set is shown in Figure 5.11 for the alteration factor. The observed distribution may be described as a mixture of three sub-populations. The first represents less than 1.2% of the values, the second represent between 1.2% and 53.7% of the values and the third comprise more than 53.7% of the values. The anomalous sub-population has a lower threshold for the alteration factor values of 17.82 (Table 5.7), and 975 samples return of greater than this. These samples were separated from the whole data set (2016 samples in total), and the alteration factor values were recalculated using the SAS software. The resulting subset was again inspected and the probability plot results are shown in Figure 5.12. Again three sub-populations are identified based on this diagram. 1% of the data belongs to the first, the

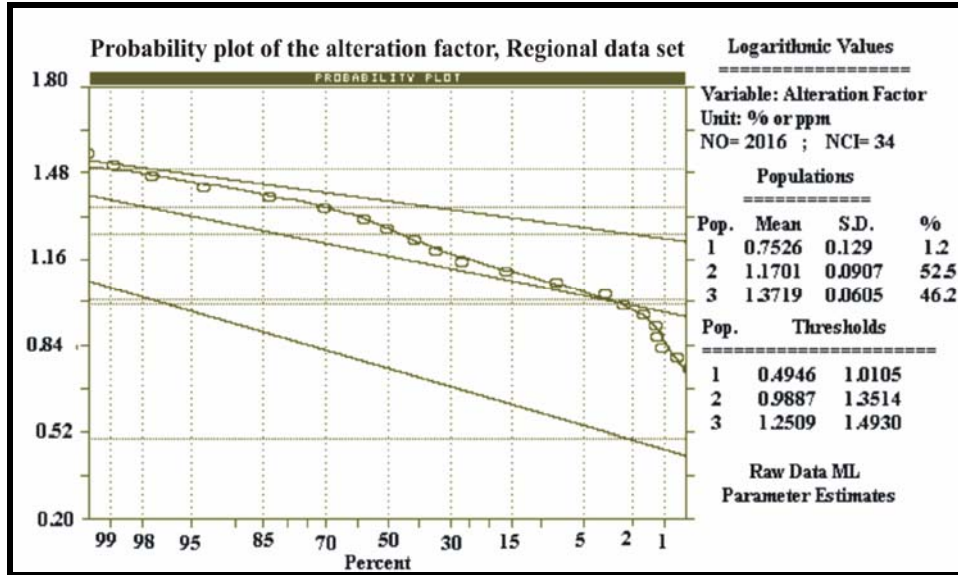


Figure 5.11: The probability plot of whole regional data set for the alteration factor (FAR).

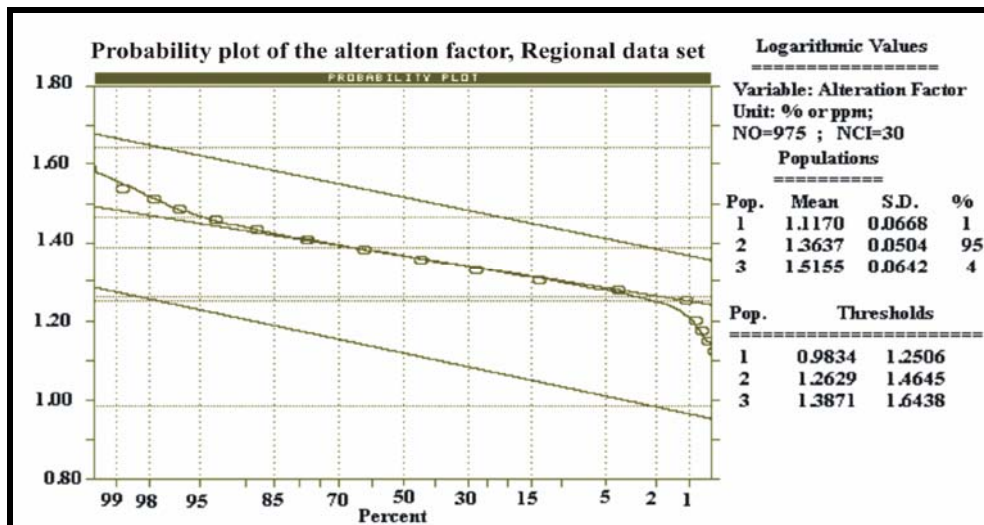


Figure 5.12: The probability plot of anomalous values of the last stage for the alteration factor (FAR), regional data set.

second consists of between 1 and 96%, and the third contains the upper 4% of the data. The descriptive statistics of the anomalous sub-populations thus identified are listed in Table 5.8. Based on the new threshold value of the alteration factor (29.1), 57 samples are identified as anomalous and are listed with their respective coordinates in Table 5.9.

**Table 5.7:** The threshold value for each factor, regional data set (n= 2016 samples).

Factor	No. of popul.	Means (M)	Std. Dev. (SD)	%	Threshold values
FPer	1	5.9	-4.6 +7.6	16.5	3.6 9.9
	2	9	-7.7 +10.5	44.6	6.6 12.3
	3	13.8	-12.2 +15.7	39	10.8 17.8
FAR	1	5.7	-4.2 +7.6	1.3	3.1 10.2
	2	14.8	-12 +18.2	52.5	9.7 22.5
	3	23.5	-20.5 +27.1	46.2	17.8 31.1
FPR	1	7.1	-3.9 +13.1	9.8	2.1 24.1
	2	12.956	-10.7 +15.7	90.2	8.8 19
FAmp <sub>2</sub>	1	14.3	-10 +20.5	40.2	6.9 29.5
	2	32.600	-27 +39.3	25.5	22.4 47.4
	3	48.3	-43.3 +53.8	34.3	38.8 60
FGn	1	28.2	-22.4 +33.9	36	19.4 40.8
	2	51.1	-41.7 +62.6	38.7	34.1 76.7
	3	66.2	-63.2 +69.4	25.3	60.3 72.7

Note: No. of popul.: Number of population, Std. Dev.: Standard deviation (SD)

**Table 5.8:** The threshold value for peraluminous and alteration factors, regional data set (n= 975 samples).

Factor	No. of population	Means (M)	Std. Dev. (SD)	%	Threshold values
FAR	1	13	-11.2 +15.3	1	9.6 17.8
	2	23	-20.6 +25.9	95	18.3 29.1
	3	32.8	-28.3 +38	4	24.4 44
FPer	1	4.5	-3.4 +6	7.7	2.5 8.1
	2	8.3	-6.6 +10.6	85.7	5.2 13.4
	3	16.9	-15 +17	6.6	13.3 21.5

Note: No.: Number, Std. Dev.: Standard deviation (SD)

Samples identified in the previous sections showing features that could be related to the hydrothermal alteration, are identified by the Code “A” in Tables 5.1 to 5.6 and 5.9. As can be seen, most of the samples in Table 5.9 were given the Code “A”. However, some of these may now be excluded where the samples returned K<sub>2</sub>O contents higher than the MgO contents, as these rocks probably had common shale precursors. It was also shown in section 5.5 that para-amphibolites show high peraluminous factors values. These samples could be discarded using their high CaO and K<sub>2</sub>O and low MgO contents. Para- and ortho-amphibolites are identified with the Codes “C1” and “C2” respectively in Table 5.9. The remaining 15 samples from the original 57 samples in this subset (Table 5.9) may be regarded as highly anomalous and should be given priority for follow-up exploration.

The high priority samples include four samples (4, 189, 192, and 221) which have extremely high MgO and low K<sub>2</sub>O contents, eleven samples (482, 430, 426, 206, 255, 256, 257, 258, 77, 109 and 531) with MgO higher than K<sub>2</sub>O. In addition, some of these samples have anomalous Zn concentrations (180-349 ppm).

**Table 5.9:** The sample numbers and localities for anomalous samples with selected chemical data.

No.	Code	Pr.	CaO	Na <sub>2</sub> O	Al <sub>2</sub> O <sub>3</sub>	MgO	K <sub>2</sub> O	SiO <sub>2</sub>	Cu	Zn	Ni	%AI	%CCPI
54	A		0.55	0.7	22.4	3.34	3.71	56.4	32	134	72	84.94	88.18
55	A		0.5	0.6	22.6	3.32	3.71	52.5	19	171	76	86.47	89.98
56	A		0.49	0.5	22.2	3.34	3.26	55.5	70	154	69	86.96	90.76
74	A		0.56	0.8	28.4	2.97	3.67	48.4	21	207	53	83.00	89.34
77	A	*	0.31	0.6	29.1	3.94	1.51	47.9	29	225	56	85.69	94.91
82	A		0.25	0.4	22.9	3.07	5.06	53.6	16	160	59	92.60	86.76
109	A	*	0.84	0.2	23.2	4.03	1.54	51.5	16	216	82	84.27	96.38
232	A		0.1	0.7	47.3	1.1	5.19	36.3	11	134	22	88.72	71.30
903	A		0.78	0.1	45.5	1.41	2.76	37.7	12	175	28	82.57	89.50
908	A		0.24	0.6	21.8	1.9	4.24	55.7	90	168	62	87.97	87.82
338	A		0.22	0.8	36.7	0.74	7.68	42.2	19	40	14	89.19	55.87
407	A		0.42	0.5	25.1	2.99	4.45	51.7	15	160	57	89.00	87.64
255	A	**	0.42	0.6	23.4	3.6	2.51	51.1	7	180	64	85.69	93.01
256	A	**	0.45	0.6	23.1	4.27	2	53	74	159	75	85.66	94.71
257	A	**	0.41	0.7	24.9	3.35	1.91	54.4	20	187	50	82.57	93.55
258	A	**	0.55	0.9	25.2	4.13	1.99	52.2	11	270	61	80.85	93.09
421	A		0.73	0.7	21.2	2.87	3.02	53.2	13	173	67	80.46	91.95
426	A	**	0.68	0.7	28	4.81	0.38	44.1	46	249	94	79.00	88.25
206	A	**	0.18	0.2	23.7	3.11	1.12	58.5	20	127	81	91.76	96.47
482	A	**	0.24	0.6	25.7	3.67	0.07	52.2	27	198	80	81.66	98.60
430	A	**	0.57	0.5	24	3.63	0.25	53.7	32	190	68	78.38	98.38
68	B		1.1	1.2	18.7	3.52	0.62	58	14	177	82	64.29	96.16
443	C <sub>1</sub>		23.3	0.2	23.6	1.12	0.07	38.9	14	41	21	4.82	98.68
785	C <sub>1</sub>		16.6	0.9	22	1.42	0.29	46.2	70	40	19	8.90	96.54
896	C <sub>1</sub>		13.3	1.7	22.6	2.79	0.87	48.2	45	132	33	19.61	91.71
18	A		0.28	0.1	22.5	3.03	3.65	57.5	18	180	49	94.62	89.25
19	A		0.26	0.4	23.2	2.56	4.44	56.1	18	152	40	91.38	86.58
20	A		0.49	0.9	24.6	3.02	3.94	52.9	10	177	43	83.35	87.70
21	A		0.22	0.3	27.1	3.9	4.52	47.9	18	112	67	94.18	89.57
326	C <sub>2</sub>		11.5	0.5	16	3.4	0.12	47.6	12	44	28	22.68	99.01
365	C <sub>2</sub>		17.4	0.7	23.4	2.25	0.17	45.3	17	72	20	11.79	97.13
461	C <sub>2</sub>		16.5	0.9	23.5	0.77	0.1	48.8	26	13	9	4.76	95.94
495	C <sub>2</sub>		13.1	0.7	22.4	4	0.26	44.5	12	10	71	23.59	97.79
506	C <sub>2</sub>		15.5	1	23.4	3.7	1.03	40.6	15	46	34	22.28	95.06
526	C <sub>1</sub>		15.9	0.9	21.5	3.56	0.73	44.8	12	61	261	20.34	95.70
536	C <sub>2</sub>		21.5	0.4	25	1.8	0.19	37.6	17	52	22	8.33	98.32
586	C <sub>2</sub>		13.7	2.5	19.4	2	0.62	44.5	10	138	21	13.92	93.66
624	C <sub>2</sub>		12.9	0.7	20.2	5.3	0.23	48.7	100	58	29	28.91	97.50
641	C <sub>2</sub>		21.2	0.4	23.7	2.5	0.05	42.3	21	22	33	10.56	98.36
737	C <sub>2</sub>		19	0.6	22.7	1.4	0.34	43.7	14	39	21	8.15	96.96
748	C <sub>2</sub>		15.2	1.8	23.7	1.63	0.23	47.2	22	49	14	9.86	93.02
750	C <sub>2</sub>		15.8	1.3	21.1	2.9	0.19	44.6	40	79	14	15.30	96.28
88	C <sub>2</sub>		15.9	0.7	19.2	5.92	0.62	41.5	21	161	91	28.26	97.15
4	A	***	0.32	0.3	16.5	15	0.97	48.5	15	177	50	96.26	98.11
531	A	*	0.22	0.5	21.9	3.57	2.21	55.7	80	204	69	88.92	93.98
53	A		0.29	0.9	21.6	2.87	3.85	56.7	25	151	57	84.96	88.31
221	A	***	0.45	0.6	16.6	10.7	0.07	45.8	14	167	88	91.12	99.15
189	A	***	0.84	0.6	15.5	13.7	0.23	41	12	349	25	90.63	99.08
192	A	***	0.43	0.3	16.2	11.7	0.24	43	17	178	24	94.24	99.40
20	C <sub>2</sub>		9.96	1.1	16.9	7.08	0.18	45.9	28	99	22	39.63	97.72
157	C <sub>1</sub>		20.8	0.6	24.7	0.41	0.8	43.2	14	0	9	5.35	94.99
226	C <sub>1</sub>		13.8	1.2	24.9	1.38	1.77	45.1	6	20	5	17.36	89.17
290	C <sub>2</sub>		10.6	1.4	15.5	5.03	0.37	46.3	71	107	22	31.03	97.12
381	C <sub>1</sub>		22.2	0.4	23.2	1.8	0.2	41.6	7	42	8	8.13	97.49
468	C <sub>2</sub>		13.3	1.8	22.1	3.95	0.28	48.5	198	46	34	21.88	93.43
523	C <sub>2</sub>		14.2	0.8	23.2	5.79	1.38	41.1	7	70	37	32.34	94.35
526	C <sub>1</sub>		18.3	1.5	22.5	0.49	0.2	46.4	1	12	4	3.37	94.09

Pr.: Prioritised anomaly (\*=moderately high; \*\*=high and \*\*\*= very high)

The alteration index and CCPI were calculated in Table 5.9, and the box plot is shown in Figure 5.13 (see Appendix A, Figure A.6 for more detail). Peraluminous samples with high Mg ( $MgO > K_2O$ ) have  $AI > 64\%$  and  $CCPI > 93\%$ , but peraluminous samples with high K ( $K_2O > MgO$ ) have  $55\% < CCPI < 93\%$  with the same amount of AI. The rest of the samples have  $AI < 40\%$  and  $CCPI > 88\%$ .

The probability plot based on data in Table 5.9 for Zn, Cu and Ni contents is shown in Figures 5.14 to 5.16. The distribution of the data as can be seen in the probability plots can best be modelled as a mixture of three sub-populations by using maximum likelihood procedure. Three sub-populations are identified for Zn (Fig. 5.14). 50.2% of the data belong to the first, the second consists 14.7% of the data and the third contains 35.1% of the data. The anomalous sub-population has Zn values higher than approximately 240 ppm (Table 5.10, two times the lower level of the threshold of the last sub-population).

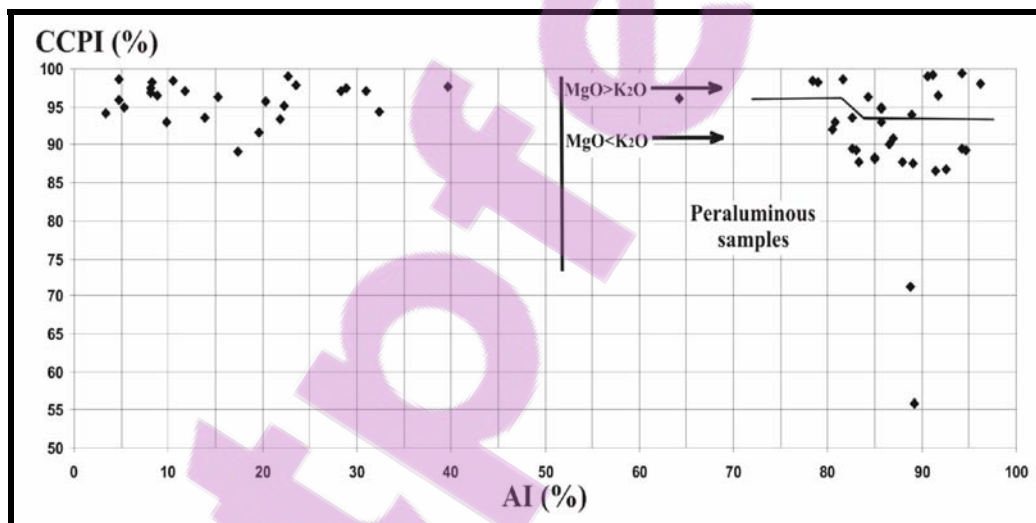


Figure 5.13: Box plot of the final results for the regional data set.

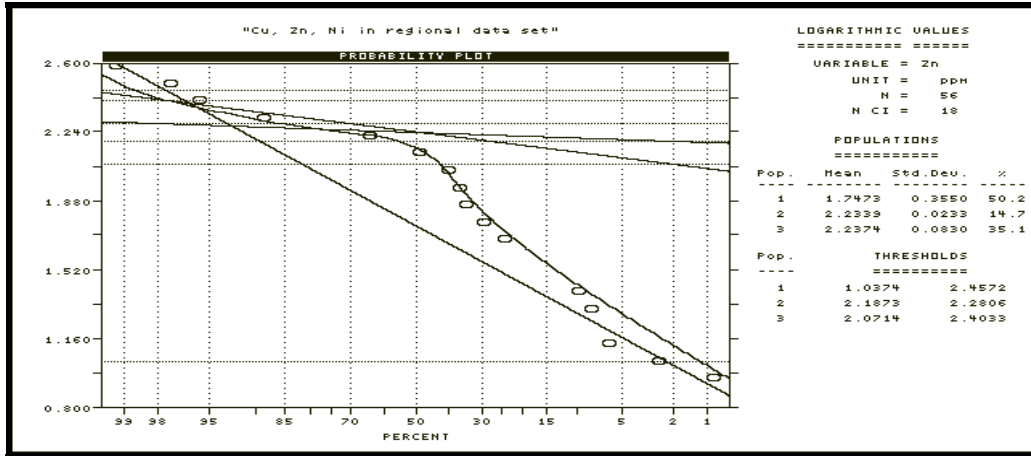


Figure 5.14: The probability plot of Zn contents based on the data in Table 5.9, regional data set.

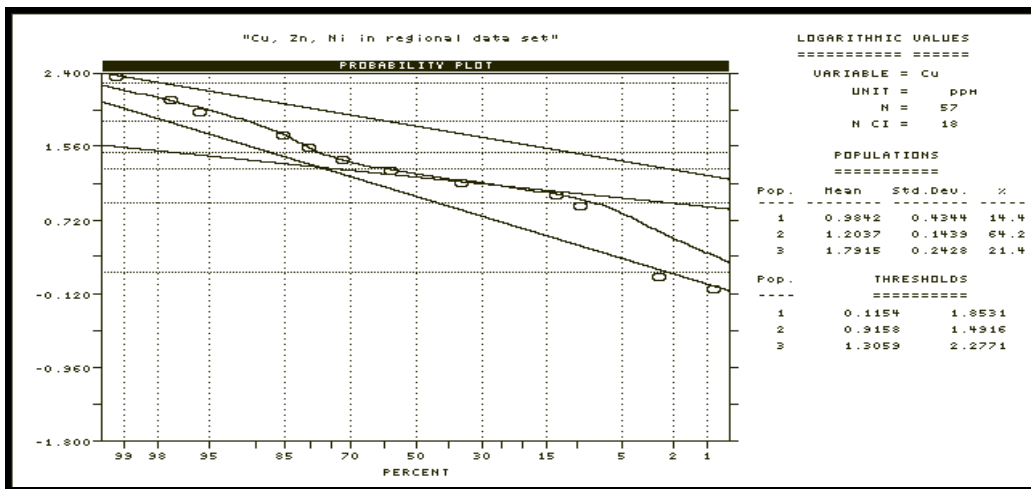


Figure 5.15: The probability plot of Cu contents based on the data in Table 5.9, regional data set.

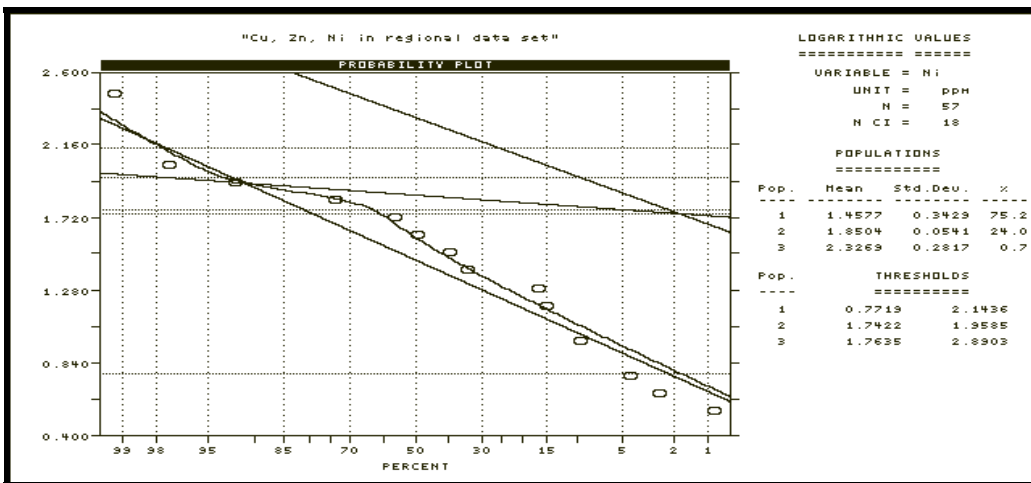


Figure 5.16: The probability plot of Ni contents based on the data in Table 5.9, regional data set.

**Table 5.10:** The threshold value for Zn, Cu and Ni, regional data set (n= 57 samples).

Factor	No. of population	Means (M)	Std. Dev. (SD)	%	Threshold values
Zn	1	56	-24.7 +126.6	50.2	11 287
	2	171	-162.4 +180.8	14.7	154 191
	3	173	-142.7 +209.1	35.1	118 253
Cu	1	10	-3.6 +26.2	14.4	1 71
	2	16	-11.5 +22.3	64.2	8 31
	3	62	-35.4 +108.2	21.4	20 189
Ni	1	29	-13 +63.2	75	6 139
	2	71	-62.6 +80.3	24	55 91
	3	212	-111 +406.1	1	58 777

Note: No.: Number, Std. Dev.: Standard deviation (SD)

Three sub-populations are identified for Cu (Fig. 5.15). The first of these sub-populations contains less than 14.4% of the samples, the second between 14.4% and 78.6% and the third 21.4% of the data. The anomalous sub-population has Cu concentrations higher than 40 ppm (Table 5.10, two times the lower level of the threshold of the last sub-population).

Three sub-populations are identified for Ni (Fig. 5.16). The first includes 75% of the data, the second consists 24% of the data and the third 1% of the data. The anomalous sub-population has Ni contents higher than 116 ppm (Table 5.10, two times the lower level of the threshold of the third sub-population).

Based on the threshold values for Zn, Cu and Ni and Table 5.9, Ni distributions were found to be not as diagnostic as is that of Zn and Cu, which may be used as a vector in the prioritization of anomalous areas.

MgO and K<sub>2</sub>O contents, peraluminous ratio, AI, CCPI, FPer and FAR are used to rank the anomalous values in Table 5.11. The rocks in the alteration zone of VHMS metamorphic deposits are peraluminous or the peraluminous factor has the highest values. This zone may be recognized by MgO higher (to extremely higher) than K<sub>2</sub>O or the highest alteration factor values. Alteration index and CCPI have the highest values in the alteration pipes of VHMS deposits. These characteristics are used with the data in Table 5.11 and to prioritize the anomalous values. In the last column of this table, the anomalies are ranked.

The geology of the northern part of the Areachap Group, of the eastern Namaqua Metamorphic Province is given in Figure 5.17. Four Cu-Zn-Pb mineralized occurrences are indicated to the south of Upington on the geological map by the Council for Geoscience (2820 Upington 1:250000 Geological Series).

Four anomalous areas identified during this study in the research area. Two of these anomalies are prioritized as rank one on the anomaly map, which has extremely high MgO and low K<sub>2</sub>O contents. The other two anomalies are prioritized as rank two, which have MgO>K<sub>2</sub>O. Anomalies that are prioritized as rank three and have MgO>K<sub>2</sub>O include of only one sample.

The variation of the alteration factor for some of these prioritised areas, rank one and two, may now be represented in traverses. The traverse of the anomalous area of rank one is shown in Figure 5.18 and that of rank two in Figure 5.19. These two traverses show the location of values higher than threshold value, determined with the probe plot procedure (Sinclair, 1976).

**Table 5.11:** Ranking the anomalous values based on MgO & K<sub>2</sub>O contents, peraluminous ratio, AI, CCPI, FAR and FPer

No.	Code	PR	MgO	K <sub>2</sub> O	CaO	Na <sub>2</sub> O	Al <sub>2</sub> O <sub>3</sub>	Zn	Cu	Ni	%AI	%CCPI	FPer	FPR	FAR	Number	R
54	A	4.52	3.34	3.71	0.55	0.7	22.4	134	32	72	84.94	88.18	17.30	19.09	29.42	UpSHG228	
55	A	4.70	3.32	3.71	0.5	0.6	22.6	171	19	76	86.47	89.98	17.53	19.40	30.92	UpSHG229	
56	A	5.22	3.34	3.26	0.49	0.5	22.2	154	70	69	86.96	90.76	17.48	19.09	30.29	UpSHG230	
74	A	5.65	2.97	3.67	0.56	0.8	28.4	207	21	53	83	89.34	17.17	24.67	37.06	UpSHG314	
77	A	12.02	3.94	1.51	0.31	0.6	29.1	225	29	56	85.69	94.91	17.16	24.51	39.60	UpSHG317	3
82	A	4.01	3.07	5.06	0.25	0.4	22.9	160	16	59	92.6	86.76	18.04	20.20	30.64	UpSHG322	
109	A	8.99	4.03	1.54	0.84	0.2	23.2	216	16	82	84.27	96.38	16.90	19.64	34.12	UpSHG919	3
232	A	7.90	1.1	5.19	0.1	0.7	47.3	134	11	22	88.72	71.3	18.71	43.75	53.41	TrN452	
903	A	12.50	1.41	2.76	0.78	0.1	45.5	175	12	28	82.57	89.5	18.15	42.67	53.88	kaNU44	
908	A	4.29	1.9	4.24	0.24	0.6	21.8	168	90	62	87.97	87.82	17.43	19.99	29.36	kaNU49	
338	A	4.22	0.74	7.68	0.22	0.8	36.7	40	19	14	89.19	55.87	17.85	34.40	39.95	TrN638	
407	A	4.67	2.99	4.45	0.42	0.5	25.1	160	15	57	89	87.64	17.94	22.10	32.81	TrN822	
255	A	6.63	3.6	2.51	0.42	0.6	23.4	180	7	64	85.69	93.01	17.34	19.79	32.87	TrN515	2
256	A	7.57	4.27	2	0.45	0.6	23.1	159	74	75	85.66	94.71	17.36	18.91	33.86	TrN516	2
257	A	8.25	3.35	1.91	0.41	0.7	24.9	187	20	50	82.57	93.55	17.13	21.23	34.06	TrN517	2
258	A	7.33	4.13	1.99	0.55	0.9	25.2	270	11	61	80.85	93.09	17.09	20.67	34.35	TrN518	2
421	A	4.76	2.87	3.02	0.73	0.7	21.2	173	13	67	80.46	91.95	16.60	18.31	30.37	TrN836	
426	A	15.91	4.81	0.38	0.68	0.7	28	249	46	94	79	98.25	15.53	22.20	43.85	TrN841	2
206	A	15.80	3.11	1.12	0.18	0.2	23.7	127	20	81	91.76	96.47	16.63	20.79	33.36	TrN426	2
482	A	28.24	3.67	0.07	0.24	0.6	25.7	198	27	80	81.66	98.6	14.40	20.91	40.68	TrNJ229	2
430	A	18.18	3.63	0.25	0.57	0.5	24	198	32	68	78.38	98.38	15.10	19.74	36.75	TrN845	2
68	B	6.40	3.52	0.62	1.1	1.2	18.7	177	14	82	64.29	96.16	16.00	14.87	29.53	TrN220	
443	C1	1.00	1.12	0.07	23.3	0.2	23.6	41	14	21	4.82	98.68	2.19	21.61	30.48	TrN858	
785	C1	1.24	1.42	0.29	16.6	0.9	22	40	70	19	8.9	96.54	6.06	19.40	30.42	kaNU153	
896	C1	1.42	2.79	0.87	13.3	1.7	22.6	132	45	33	19.61	91.71	7.22	18.34	29.17	kaNU340	
18	A	5.58	3.03	3.65	0.28	0.1	22.5	180	18	49	94.62	89.25	17.86	20.49	29.60	TrST618	
19	A	4.55	2.56	4.44	0.26	0.4	23.2	152	18	40	91.38	86.58	17.81	20.88	30.13	TrST619	
20	A	4.62	3.02	3.94	0.49	0.9	24.6	177	10	43	83.35	87.7	17.31	21.24	32.14	TrST620	
21	A	5.38	3.9	4.52	0.22	0.3	27.1	112	18	67	94.18	89.57	18.36	23.38	36.71	TrST621	
326	C2	1.32	3.4	0.12	11.5	0.5	16	44	12	28	22.68	99.01	8.21	12.26	31.03	KINP35	
365	C2	1.28	2.25	0.17	17.4	0.7	23.4	72	17	20	11.79	97.13	4.77	19.68	31.71	KINW58	
461	C2	1.34	0.77	0.1	16.5	0.9	23.5	13	26	9	4.76	95.94	4.65	21.01	31.13	KINP289	
495	C2	1.59	4	0.26	13.1	0.7	22.4	10	12	71	23.59	97.79	8.66	17.60	33.03	KINP413	
506	C2	1.33	3.7	1.03	15.5	1	23.4	46	15	34	22.28	95.06	8.54	18.94	31.76	KINP424	
526	C1	1.23	3.56	0.73	15.9	0.9	21.5	61	12	261	20.34	95.7	6.66	17.03	29.72	KISP718	
536	C2	1.13	1.8	0.19	21.5	0.4	25	52	17	22	8.33	98.32	3.53	22.00	34.29	KISP64	
586	C2	1.15	2	0.62	13.7	2.5	19.4	138	10	21	13.92	93.66	6.34	15.99	29.57	KINP13	
624	C2	1.46	5.3	0.23	12.9	0.7	20.2	58	100	29	28.91	97.5	8.24	14.34	29.40	KISP55	
641	C2	1.09	2.5	0.05	21.2	0.4	23.7	22	21	33	10.56	98.36	3.37	20.04	32.46	KISP522	
737	C2	1.14	1.4	0.34	19	0.6	22.7	39	14	21	8.15	96.96	4.78	20.19	30.26	KINW340	
748	C2	1.38	1.63	0.23	15.2	1.8	23.7	49	22	14	9.86	93.02	5.98	20.28	31.13	KINW351	
750	C2	1.22	2.9	0.19	15.8	1.3	21.1	79	40	14	15.3	96.28	4.54	16.60	31.32	KINW353	
88	C2	1.11	5.92	0.62	15.9	0.7	19.2	161	21	91	28.26	97.15	6.36	12.86	29.16	KINP14	
4	A	10.38	15	0.97	0.32	0.3	16.5	177	15	50	96.26	98.11	17.52	3.90	31.52	KSKP63	1
531	A	7.47	3.57	2.21	0.22	0.5	21.9	204	80	69	88.92	93.98	17.00	18.46	31.81	KSHP1111	3
53	A	4.29	2.87	3.85	0.29	0.9	21.6	151	25	57	84.96	88.31	16.74	18.55	29.34	KSKP655	
221	A	14.82	10.7	0.07	0.45	0.6	16.6	167	14	88	91.12	99.15	15.65	6.91	36.91	KSME144	1
189	A	9.28	13.7	0.23	0.84	0.6	15.5	349	12	25	90.63	99.08	15.32	3.29	36.67	KSME112	1
192	A	16.70	11.7	0.24	0.43	0.3	16.2	178	17	24	94.24	99.4	15.55	6.01	37.95	KSME115	1
20	C2	1.50	7.08	0.18	9.96	1.1	16.9	99	28	22	39.63	97.72	9.70	9.59	29.82	KSKP620	
157	C1	1.11	0.41	0.8	20.8	0.6	24.7	0	14	9	5.35	94.99	2.97	22.90	31.06	KSME335	
226	C1	1.48	1.38	1.77	13.8	1.2	24.9	20	6	5	17.36	89.17	9.59	22.47	29.78	KSME149	
290	C2	1.25	5.03	0.37	10.6	1.4	15.5	107	71	22	31.03	97.12	9.88	10.47	29.49	KSME233	
381	C1	1.02	1.8	0.2	22.2	0.4	23.2	42	7	8	8.13	97.49	2.41	20.28	30.13	KSRP235	
468	C2	1.44	3.95	0.28	13.3	1.8	22.1	46	198	34	21.88	93.43	6.44	16.57	29.95	KSRP144	
523	C2	1.42	5.79	1.38	14.2	0.8	23.2	70	7	37	32.34	94.35	9.78	17.09	30.62	KSHP1103	
526	C1	1.13	0.49	0.2	18.3	1.5	22.5	12	1	4	3.37	94.09	4.10	20.38	29.72	KSHP1106	

PR=Al<sub>2</sub>O<sub>3</sub>/(Na<sub>2</sub>O+K<sub>2</sub>O+CaO) R: Anomaly Ranking (1: very high, 2:high, 3: moderately high) Anomalous values: Zn>240, Cu>40 & Ni>116

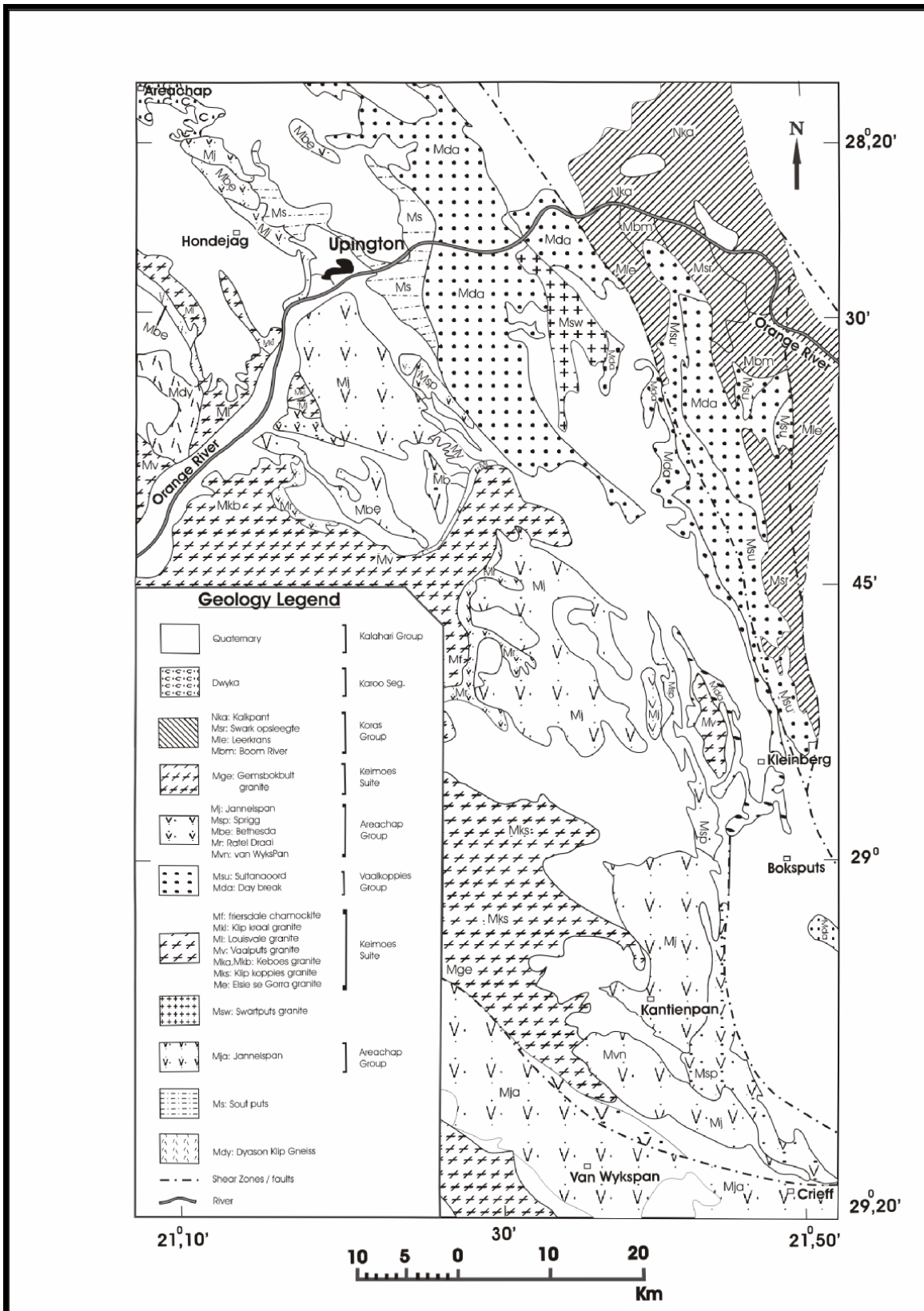


Figure 5.17: Geology of the northern part of the Areachap Group, eastern Namaqua Province.

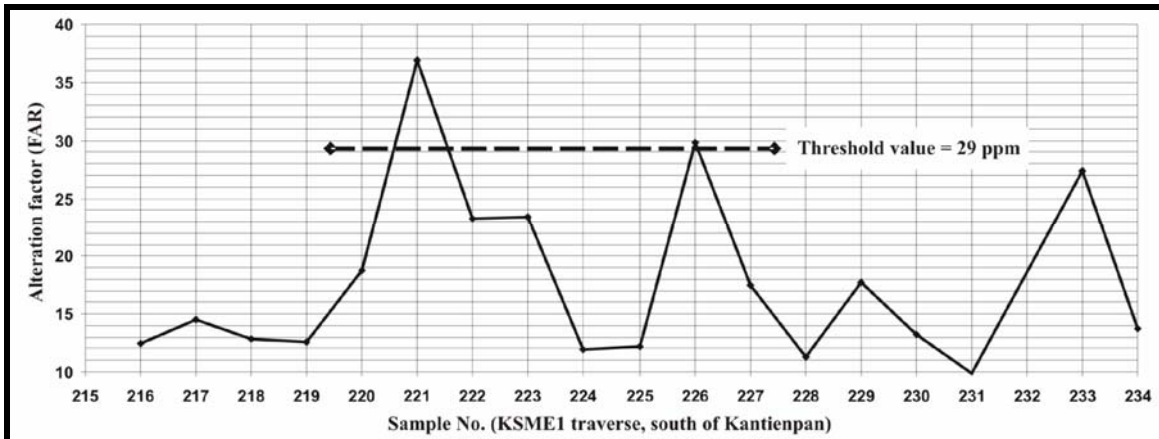


Figure 5.18: The alteration factor versus sample number in-prioritised Traverses, rank one.

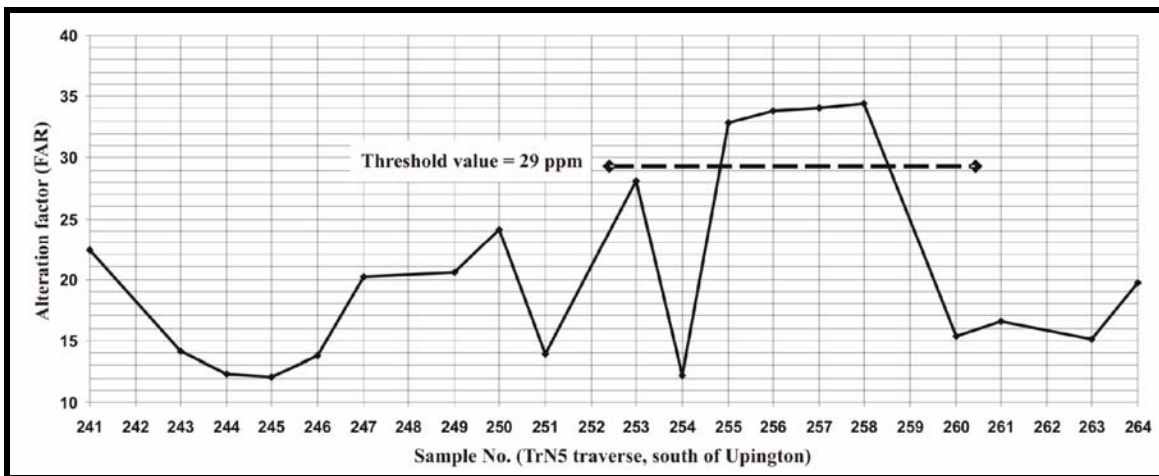


Figure 5.19: The alteration factor versus sample number in-prioritised traverses, rank two.



## Chapter 6

### Regolith geochemistry

#### **6.1. Introduction**

Selective leaching or selective extraction analysis of soil samples is one of the more frequently applied geochemical methods in the identification of buried mineral deposits (Xueqiu, 1998; Gray et al., 1999; Cameron et al., 2004). This is a partial extraction method, which only dissolves part of the weakly absorbed and, or adsorbed elements of interest in a particular solution. This method is also effective in identifying highly soluble new mineral phases that may form in the secondary environment including phosphates, chlorides and carbonates. The soluble part of the sample represents the “mobile” phases, referred to as mobile metal ions (MMI) (Mann et al., 1998; Cameron et al., 2004; Mann et al., 2005), which could have been derived from a weathering ore deposit. In nature, the water cycle and secondary processes cause the metal ions to be leached from the rock and ore deposit and to become precipitated in the soil.

The secondary soil forming processes may form a gossan at the top of massive sulphide deposits by reduction and oxidation weathering processes and a calcrete layer near the surface by evaporation of soil moisture during the diurnal cycle (under arid to semi-arid conditions). In the study area, a layer (of variable thickness ranging from zero to several meters) of wind blown sand covers this calcrete layer that in itself varies from zero to 6 m or more.

The main objective of this chapter is to investigate nature's ability to impart a secondary geochemical dispersion halo to a non-residual wind blown sand cover above a massive sulphide ore body and to determine to what extent the intermediate calcrete layer acted as

a geochemical barrier to this process. For this, wind blown sand (Kalahari sand) samples were collected along regolith sampling traverses in the research areas. Different types of selective leach methods and total analyses are used to determine if an anomaly related to the mineralization may be detected, and which method is the most appropriate for this. The results of selective extraction methods are also compared to total analysis by x-ray fluorescence (XRF) results to identify the method which gives the highest anomaly to background ratio and widest dispersion.

The calcrete layer, as part of the secondary environment, is investigated by samples collected from surface and at different depths in the calcrete layer to investigate the variation in the concentration of some trace elements in this potential barrier to geochemical dispersion. The objective with this is to determine whether a lithochemical survey of calcrete samples would be successful in detecting underlying massive sulphide mineralization.

The principal aspects that would be addressed in this chapter are:

- a) An experiment to determine the most appropriate reagents to use for detecting the concealed ore bodies in the sand cover at surface.
- b) A comparison of the best reagent partial extraction method with a total analysis method (XRF).
- c) The distribution of the elements of interest in the calcrete layer.

## **6.2. The concept of mobile metal ions and selective extraction techniques**

In theory, it could be argued that partial extraction or selective extraction methods, when applied to soil geochemistry in exploration programmes, may provide a better selection of "true" anomalies and also result in a better definition of the secondary dispersion haloes related to concealed massive sulphide ore bodies (Levinson, 1974). Such definition may be defined by larger peak to background ratios and, or a larger anomalous area (dispersion area) that could be detected. Initially these methods were hampered by the relatively high (ppm) lower limits of detection of the standard analytical methods

commonly used (mostly atomic absorption techniques). But since the advent of inductively coupled plasma, optical emission spectrometry (ICP-OES) and especially with the introduction of inductively coupled plasma mass spectrometry (ICP-MS) the detection of very low concentrations of various elements in solution (ppb range) has become a viable method for exploration geochemical application. Simultaneous advances in total analytical techniques such as XRF has also lowered the detection limit of this technique although still much less sensitive than the ICP techniques. These two methods would be compared in the following sections.

### 6.2.1. Mobile Metal Ions (MMI) concept

“Mobile Metal Ions” is a term that describes ions that have migrated into the weathering zone, and are only weakly or loosely attached to the surfaces of the soil particles (Mann et al., 1998; Cameron, et al., 2004; Mann et al., 2005). These ions have the ability to disperse through un-mineralized rock e.g. hundreds of meter vertically upwards (Genalysis Laboratory Services Pty Ltd, 20th January, 2005) possibly by poorly understood micro-bubbles, vapor, ground-water flow, capillary rise or electrochemical processes (Cameron et al., 2004; Mann et al., 2005). The convection cells set up by rainfall and evaporation during the rainfall and dry periods, respectively, are also contributing to the movement of mobile ions into the soil traverses (Figure 6.1).

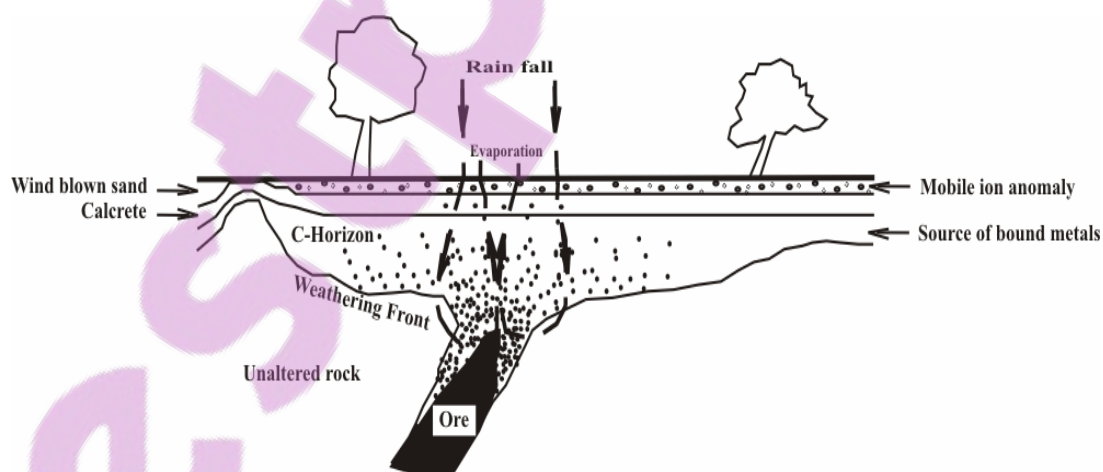


**Figure 6.1:** Schematic model of convection cell in connection with mobile metal ions in the secondary environment (after Mann et al., 1997)

Mann et al. (1995) and Mann et al. (1997) carried out experimental work to determine the vertical movement of mobile elements and the effect a calcium carbonate layer would have on the movement of these mobile ions. In the first experiment (without

addition of calcium carbonate), coarse silica sand was added to a flower pot partially filled with a solution containing base metals. The metals in the solution were shown to move vertically upwards through the silica sand in a very short period (Mann et al., 1995; Mann et al., 1997). In the second experiment, varying quantities of calcium carbonate were added as a single layer to a pot with a solution and coarse silica sand as in the first experiment. In both experiments i.e. with or without carbonate added, a surface accumulation of mobile metals was observed. Thus it suggests that carbonate, a known precipitant of base metals, has not inhibited the surface response or the movement of the base metals (Mann et al., 1995; Mann et al., 1997).

The elements that have migrated due to soil forming processes may be derived from two sources, i.e., from an endogenic or exogenic source. Elements from an endogenic source are derived from primary minerals, which are not directly related to the mineralization. These elements are referred to as bound elements as they are not dissolved by digestant or selective extractants (Bardshaw et al., 1974; Leinz et al., 1993). Elements from an exogenic source are derived from the disintegration of the ore minerals (sulphides) related to the mineral deposits, due to natural oxidation processes (Cameron et al., 2004). The term unbound elements are used for these metals as they can be extracted by a digestant or detached from soil. Mobile ions are therefore unbound elements, which are concentrated in the A horizon of a soil profile. Bound elements originate from the C-horizon and get concentrated in the B-horizon in the event of low rainfall and infiltration (Mann et al., 1995; Mann et al., 1997). In this investigation, Cu, Zn, Pb, Fe, Mn, Ba and S are considered elements of interest, as they are directly related to the ore and it will be attempted to determine if they behave mobile and are detectable in the Kalahari sand overlying the deposit.

According to Goldberg (1998), mobile metal ions may occur in surface environments in one of the following forms:

- aqueous forms e.g. ionic, colloidal, etc;
- adsorbed onto the mineral surfaces or soil colloids;
- adsorbed onto organic matter, certain metal-organic complexes;
- as soluble sulphates, carbonates, phosphates, etc; or
- adsorbed onto oxides and hydroxides of Fe and Mn.

Unfortunately major rainfall events or periodic flooding in soils are accompanied by loss of such mobile metal ions, because these events have the capacity to remove weakly bound metals from soils (Genalysis Laboratory Services Pty Ltd, 20th January, 2005). This is the reason for not sampling soon after major rainfall events unless data to the contrary exists. The samples for this study were collected during the dry season (winter) of 2003.

### **6.2.2. Selective extraction techniques**

The purpose of selective extraction is to leach only the mobile metal ions of the sample matrix. These methods are designed to attack specific components within a sample. Some methods dissolve precipitated carbonates or other salts, while others attack Mn-oxides, amorphous Fe-oxides, or extract metal ions held in organic complexes. The base of these extractants is an acidic solution, but the intensity of pH determines which elements will be leached from the sample. Weaker acid affects the exogenic phase and in order to dissolve the endogenic phase, a stronger acid has to be used. In general, most metals become more soluble at low pH values (Maes, 2003).

In Table 6.1, different extractants are classified based on their chemical power or acidity. These extractants may be used in a sequential leaching process from the top to the bottom of this table i.e. starting with the weakest solutions. Other extractants are given in Table 6.2, which may be used for selective leaches. Some of the selective extraction methods for Cu, Zn, Pb, Cd and S in soil samples are listed in Table 6.3.

The ions in the extraction solution generally occur in very low, typically parts per billion (ppb) concentrations and this require a low detection technique such as ICP-MS to determine the mobile metal content (Wang, 1997). The ICP-MS technique is also used here to determine the concentration of the elements of interest in the various solutions prepared.

**Table 6.1:** Different extractants classified by acidity (sequential leaching process and/or selective leaches)

Extractant	Effects	Classification	Examples	References
Deionized water	does not attack any minerals, but removes elements loosely adsorbed on mineral surfaces	This solution dissolves water-soluble salts and elements loosely adsorbed on mineral surfaces.		Cameron et al., 2004
Enzyme leach (dilute glucose solution)	Removes the MnO coating found on all clay crystals. It forms oxidation halo anomalies.	This leach dissolves little more than deionized water, but gives better analytical reproducibility (Electrically migratable atoms)	To detect reduced mineral deposits such as porphyry Cu, Oil and gas reservoirs	Clark and Russ, 1992; Clark, 1997; Cameron et al., 2004
Mobile Metal Ions (MMI)	Dissolves secondary minerals	1. MMI-A (acidic) 2. MMI-B (Basic) 3. MMI-C (Carbonate) 4. MMI-D (diamonds) 5. MMI-E 6. MMI-F 7. MMI-G (granophiles)	1. Base metals (Cu, Pb, Zn, Cd) 2. Precious metals (Au, Ag, Ni, Co, Pd [Pt]) 3. Base metals (Cu, Pd, Zn, Cd) 4. Kimberlites (Ni, Nb, Cr, Mg, Fe, Mn) 5. Major mineral sands (Ti, Fe, Si, Mg, Ca, Th, Zr, Sc) 6. Path finders (As, Sb, Mo, W) 7. Pegmatophiles (U, Pb, Th, Sn, Li, Ta)	Cameron et al., 2004
Ammonium acetate	Dissolves carbonate minerals (pH= 5)	Use a leach that dissolves one or more secondary minerals that contain a favourable ratio of exogenic/endogenic material		Cameron et al., 2004
Hydroxylamine hydrochloride (HX)	For oxide minerals (It affects two phases: Carbonate and water-soluble minerals)	1. Cold Hydroxylamine 2. Hot Hydroxylamine	1. {pH=1.5, room temperature}(HX Mn) : carbonate and water-soluble minerals 2. {pH= more strongly acidic, T=60°C}(HX Fe) : carbonate and water-soluble	Cameron et al., 2004
Aqua-regia (HCl + HNO <sub>3</sub> )	Most of the secondary minerals and some of the silicates	It is not a selective leaching analysis.	Gold reacts only with the concentrated acid mixture which is referred to as aqua regia (royal water)	Cameron et al., 2004
HF+HClO <sub>4</sub> + HNO <sub>3</sub> +HCl	Silicates, residual crystalline fraction	It is not a selective leaching analysis.	Refractory minerals could remain in the final residual	Cameron et al., 2004

**Table 6.2:** Some other extractants for selective leaching

Extractants	Effects	Classification	Examples/ (References)
Sodium pyrophosphate	Dissolves large amounts of endogenic metals or those unrelated to the mineralization	Organic material, humus	
Regoleach	Dissolves metal ions adsorbed on clay surfaces, those attached to organic material, and those combined with amorphous Fe and Mn oxides	Strongly attack most metals	Moderate-strength leach Au, pathfinder and indicator (W, U, REE, et.) in a wide range of sample materials and base metal
Ethylene Diamine tetraacetic acid (EDTA)	To extract metals freshly adsorbed onto organic matter, metals from Fe-oxide or Fe-hydroxide species and to release metals by dissolution of carbonates		(Luoma and Jenne, 1976; Miller et al., 1986; Miller and McFee, 1983; Stover et al., 1976)
Ammonium citrate	To attack metals adsorbed on organic and clay particles		
Ammonium citrate and dilute hydrochloric acid	To attack some of the metals bound on Mn oxide		

**Table 6.3:** Selective extraction methods for Cu, Zn, Pb, Cd and S in the soil

Element	Form	Method of extraction
Cu and Zn in soil <sup>1</sup>	-As free and complexed ions, adsorbed cations (exchangeable cations), ions occluded mainly in soil carbonates and hydrous oxides; in biological residues and living organisms and in the lattice structure of primary and secondary minerals. -These elements are absorbed by carbonates, soil organic matter, phyllosilicates, and hydrous oxides of Al, Fe, and Mn. Cu and Zn are more concentrated in silty or clayey soils than in sandy soils	-Diethylenetriaminepentaacetic acid-Trithanolamine (DTPA-TEA) and Diethylenetriaminepentaacetic acid-NH <sub>4</sub> HCO <sub>3</sub> (DTPA-AB) Method: To identify near-neutral and calcareous soils with insufficient levels of available Cu, Fe, Mn and Zn; -Mehlich-I (double acid) Method: The EDTA result for Zn has a high correlation with the result of this method; and - Mehlich-I Method: Solution includes EDTA to extract the available Cu, Mn, and Zn.
Pb and Cd in soil <sup>2</sup>	The content is quite low except in areas where the parent material has high levels of these elements or air pollution and land disposal of industrial and municipal wastes occur.	-Exchangeable phase: NH <sub>4</sub> OAc (pH=7, buffered salts) -Carbonate-bound metals: NaOAc (pH=5, 1M) NH <sub>4</sub> OAc (pH=4.5, 1M) -Organic matter and metal oxides: NaOCl; Na <sub>4</sub> P <sub>2</sub> O <sub>7</sub>
Cu, Zn and Pb in soil <sup>3</sup>	-As adsorbed, exchangeable metals and dissolution of phases.	-20 g of soil sample + 50 ml of 1 M NH <sub>4</sub> NO <sub>3</sub> <sup>3</sup> (to determine concentrations of Ag, As, Bi, Co, Cr, Cu, Hg, Mn, Mo, Ni, Pb, Sb, Tl, U, V and Zn in soil).
S (sulfur) in soil <sup>4</sup> (Most soils contain 100 -500 mg kg <sup>-1</sup> )	1) Inorganic S (SO <sub>4</sub> <sup>2-</sup> , S <sup>2-</sup> , Sn <sup>2+</sup> , SO <sub>3</sub> <sup>2-</sup> , S <sub>2</sub> O <sub>3</sub> <sup>2-</sup> ): They may occur as water-soluble salts (in arid regions), adsorbed by soil colloids (on kaolinite clay, Fe and Al oxides), or insoluble form (include Ba and Sr sulfates, sulfate coprecipitate with CaCO <sub>3</sub> , and basic Fe and Al sulfates) in soils 2) Organic S: >.95 % of the total S in humid and semi humid regions is organic sulfur.	1-a) Soluble sulfate: extractable with H <sub>2</sub> O and salt solutions containing NaCl, LiCl, or CaCl <sub>2</sub> 1-b) Adsorbed sulfate shaking with NaHCO <sub>3</sub> , CaCO <sub>3</sub> suspensions, NH <sub>4</sub> OAc (1M, pH=7), acidic NH <sub>4</sub> OAc, Morgan's solution and Ca(H <sub>2</sub> PO <sub>4</sub> ) <sub>2</sub> (0.01 M). 2) In this investigation is not important.

1-Liang et al., 1991; Soltanpour, 1991; Kabata-Pendia and Pendias, 1991; Neilsen et al., 1986; Mehlich, 1984; Soltanpur et al., 1982; Iyengar et al., 1981; Schnitzer, 1978; Lindsay and Norvell, 1978; Wear and Evans, 1968.

2-Adriano, 1986; Miller et al., 1986; Salomons and Forstner, 1984; Chao, 1984; Shuman, 1983; Tessier et al., 1979.

3-Hall, et al., 1998 4-Tabatabai and Lafren, 1976a, b; Almore et al., 1967; Fox et al., 1964; Stanford and Lancaster, 1962; Williams and Steinbergs, 1962; Chao et al., 1962a, Kilmer and Nerrpass, 1960; McClung et al., 1959.

### **6.3. Sampling programme**

To investigate the secondary geochemical dispersion haloes in non-residual sand, a total of 102 samples were taken from the surface at the Kantienpan and Areachap deposits.

The sampling programme involved three regolith traverses from Kantienpan (18 samples from KP5, 16 samples from KP8 and 19 samples from KP12) and three regolith traverses from Areachap (20 samples from T1, 21 samples from T2 and 8 samples from T3). The location of the regolith traverses from Kantienpan and Areachap are shown in Figures 6.2 and 6.3. Sample intervals are 10 m near the projected position of the mineralized zone and increase to 20, 50 and 100 m further away from this zone.

The calcrete layer that may act as a potential geochemical barrier to the dispersion of the elements of interest and which also forms part of secondary environment was also

investigated. For this, a total of 14 samples of approximately 3 kg each were collected from the calcrete layer in the two areas under investigation. Six calcrete samples were collected from the surface near the gossan zone at Kantienpan (Fig. 6.2), together with two calcrete samples (outside the Kantienpan geology map) further away from the ore zone. All of the samples collected from directly above the ore zones contained inclusions of gossan materials. The latter are used for comparisons. Six calcrete samples were collected in two depth profiles from an old excavation at Areachap (Fig. 6.3), each profile includes three samples. A Frantz isodynamic magnetic separator was used to separate the magnetic part of calcrete samples by varying the electric current flowing through the electromagnet (Appendix D). Mineralogical phases in the magnetic and non-magnetic parts of one sample (KP12/4) were determined by x-ray diffractometry (XRD) and element concentrations in the magnetic, non-magnetic and original sample were analyzed by XRF.

#### **6.4. Selection of the most appropriate extraction reagent**

To generate results and identify a method that would be commercially viable in a general exploration application, it was decided to use the standard reagents freely available and not to use expensive spectroscopically pure reagents, nor to engage in stringent cleaning procedures for the reagents. In the current research, the extractants selected from the tables (Tables 6.2 and 6.3) included ammonium nitrate ( $\text{NH}_4\text{NO}_3$ ) (Table 6.3), ammonium acetate ( $\text{NH}_4\text{OAC}$ ) (Table 6.3), ethylene diamine tetraacetic acid ( $\text{NH}_4\text{EDTA}$ ) (Tables 6.2 and 6.3) and calcium hydro-phosphate ( $\text{Ca}(\text{H}_2\text{PO}_4)_2$ ) (Table 6.3) were all tested to find the best extracting solution for the mobile metal ions from the sand samples. The results obtained (see Appendix D) show that the  $\text{NH}_4\text{EDTA}$  solution provide the most reliable results and that this reagent could be used to extract the mobile metal ions such as Cu, Zn, Pb, Mn and Fe with an optimum shaking time of 180-minutes.  $\text{Ca}(\text{H}_2\text{PO}_4)_2$  solution represent a successful reagent that may be used to extract the S in the samples with an optimum shaking time of 120-minutes.

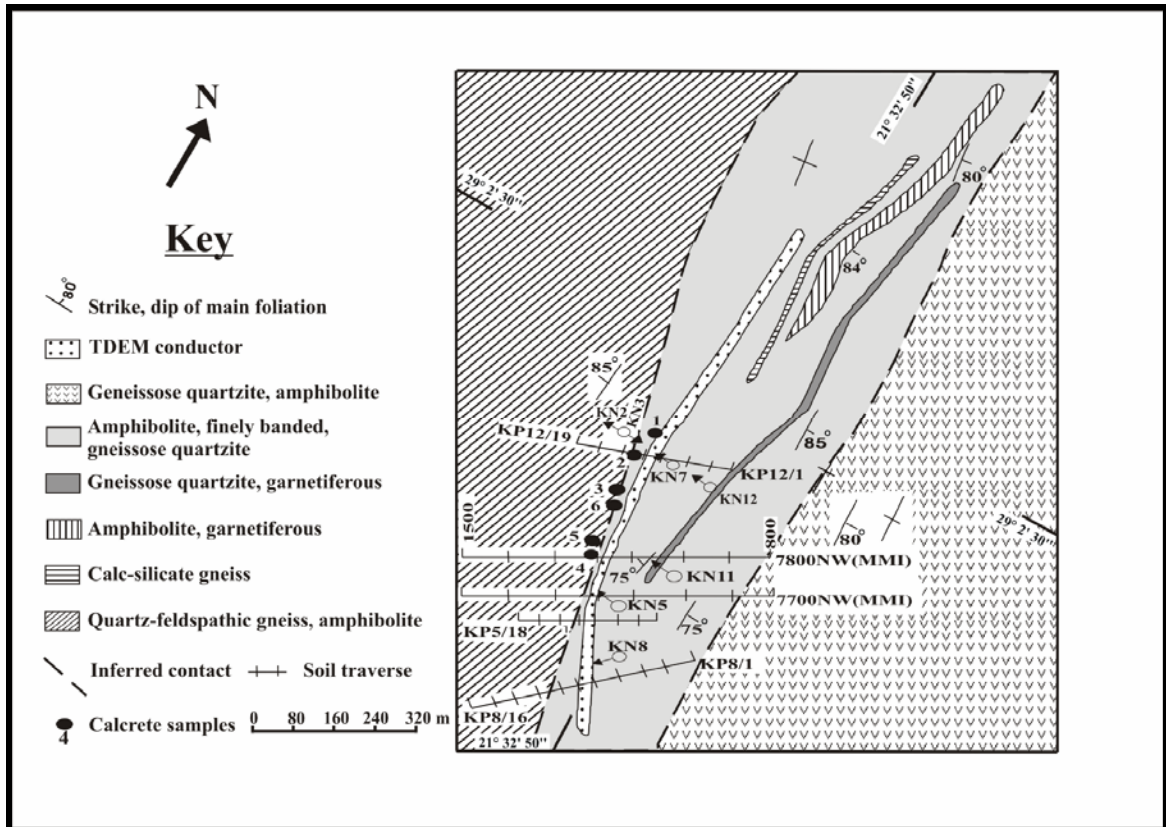


Figure 6.2: Regolith traverses and geology map of the Kantienpan area (after Rossouw, 2003)

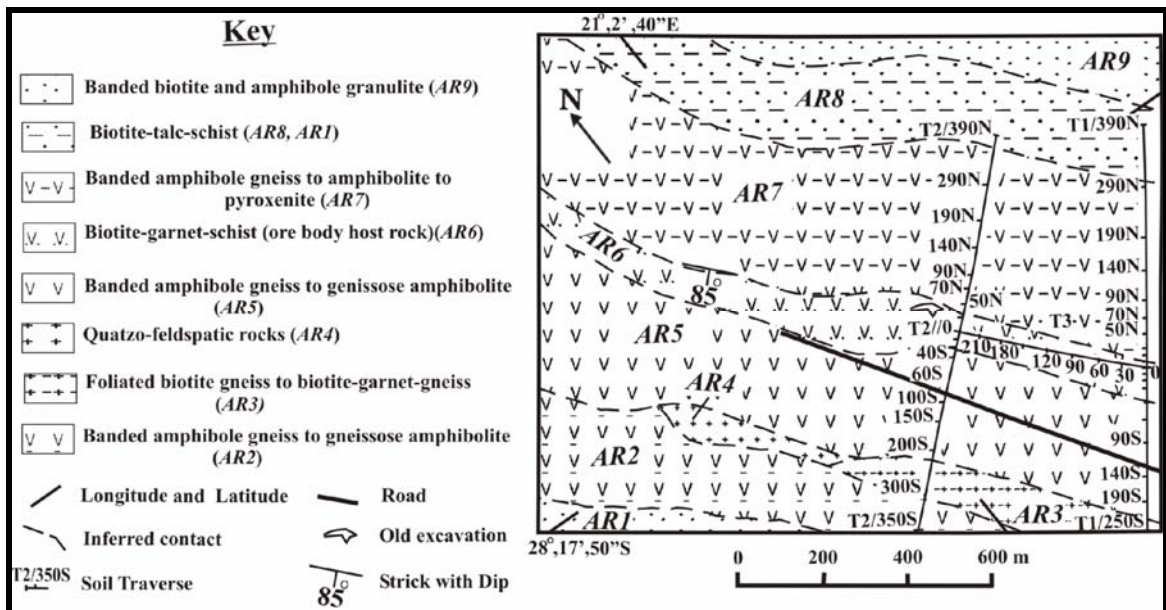


Figure 6.3: Regolith traverses and geology map of the Areachap area (after Voet and King, 1986)

## **6.5. Calculation of the threshold value for the anomalous population**

To discriminate and define the dispersion zone related to a concealed ore deposit, the threshold value for the anomalous samples has to be determined. For this purpose, the type of statistical distribution and the number of populations (polimodality) has to be investigated before the calculation of the threshold values could be attempted.

SAS software (SAS<sup>®</sup> version 8.2) was used to test the normality of the population. The null hypothesis for this test is that the input data values are a random sample from a normal distribution (SAS<sup>®</sup> version 8.2). For sample sizes greater than six, the Shapiro and Wilk (1965) value (W) is computed. If the W statistic is very small, then the normality hypothesis is rejected (Shapiro and Wilk, 1965). By definition, a normal distribution should have the same mean, median and mode, and both the skewness and kurtosis should be equal to zero (SAS<sup>®</sup> version 8.2).

If the results of the test and probability plot of the data shows a single normal or lognormal population, then the mean plus one and/or two standard deviations may be used as the threshold value. Where the results show more than one population, the Probplot software application of Sinclair (1976) is used to separate the anomalous sub-population and to calculate the lower threshold value for this sub-population.

In the following sections, the threshold value calculation is explained for different partial extractions and total analyses results.

### **6.5.1. The threshold value for NH<sub>4</sub>EDTA extraction**

The NH<sub>4</sub>EDTA solution was used to extract the mobile metal ions in 52 sand samples from Kantienpan. The extracts were analyzed by ICP-MS and the results are listed in Appendix D, Tables D.12-D.14. To arrive at a statistically valid interpretation, a data set that includes all the analytical results is used to perform the test for normality.

Based on Table 6.4, all the elements have a lognormal population (the log values have the highest W value). The mean, median and mode of the log values are nearly the same, and their skewness and kurtosis in most of elements are very close to zero, confirming that the samples display a lognormal distribution.

**Table 6.4:** Results of the normality test for the data from Kantienpan (ICP-MS method, n = 52)

Element	Shapiro-Wilk		Mean	Median	Mode	Skewness	Kurtosis
	W	Pr<W					
Pb	0.2918	<0.0001	7.5	3.5	3	6	39
Log Pb	0.7359	<0.0001	1.4	1.2	1.1	2.4	69
Zn	0.9113	0.0009	5144.5	4925.5	5654	1.19	2.31
Log Zn	0.9655	0.1350	5.3	5.4	4.4	-0.27	-0.77
Cu	0.8625	<0.0001	4297.4	3914	0	1.65	3.57
Log Cu	0.9663	0.1469	8.3	8.3	0	0.55	0.77
Mn	0.9427	0.0144	217.7	211.5	80	0.63	-0.27
Log Mn	0.9655	0.1350	5.3	5.4	4.4	-0.27	-0.77
Ba	0.8866	0.0001	23.9	22	22	1.48	2.98
Log Ba	0.9608	0.0850	3.1	3.1	3.1	0.71	0.72

The probability plots of the log values for each element are shown in Figure 6.4. A linear trend in the plots for each element may be used as proof for a single lognormal distribution.

Results indicate an effective detection limit of 2 ppm Pb, probably reflecting the background concentration in the reagents used. To obtain a more amicable distribution of the population, it was decided to substitute the value, for samples returning concentrations equal to the effective detection limit, with zero.

The single lognormal distribution of elements may be related to the ore forming process and indicate that the elements investigated may be regarded as derived from an exogenic source. All samples returning concentrations higher than the threshold value (Mean  $\pm$  standard deviation or Mean  $\pm$  two times the standard deviation) is regarded as anomalous. The statistical calculations for the mean, standard deviation, and threshold values for each element are summarized in Table 6.5. The mean and standard deviation of untransformed data is used. Blank values reported reflect the concentration of the elements in the NH<sub>4</sub>EDTA reagent solution.

**Table 6.5:** The threshold values of elements in the Kantienpan data set (ICP-MS method, n=52 samples).

Element	Mean (M)	Standard deviation (SD)	Blank value	Threshold values	
				M + SD	M + 2*SD
Cu (ppb)	4297	1470	400	5768	7238
Zn (ppb)	5145	2044	1742	7189	9233
Pb (ppm)	7	17	163 (ppb)	24	41
Mn (ppm)	218	109	2	327	436
Ba (ppm)	24	6	410 (ppb)	30	36

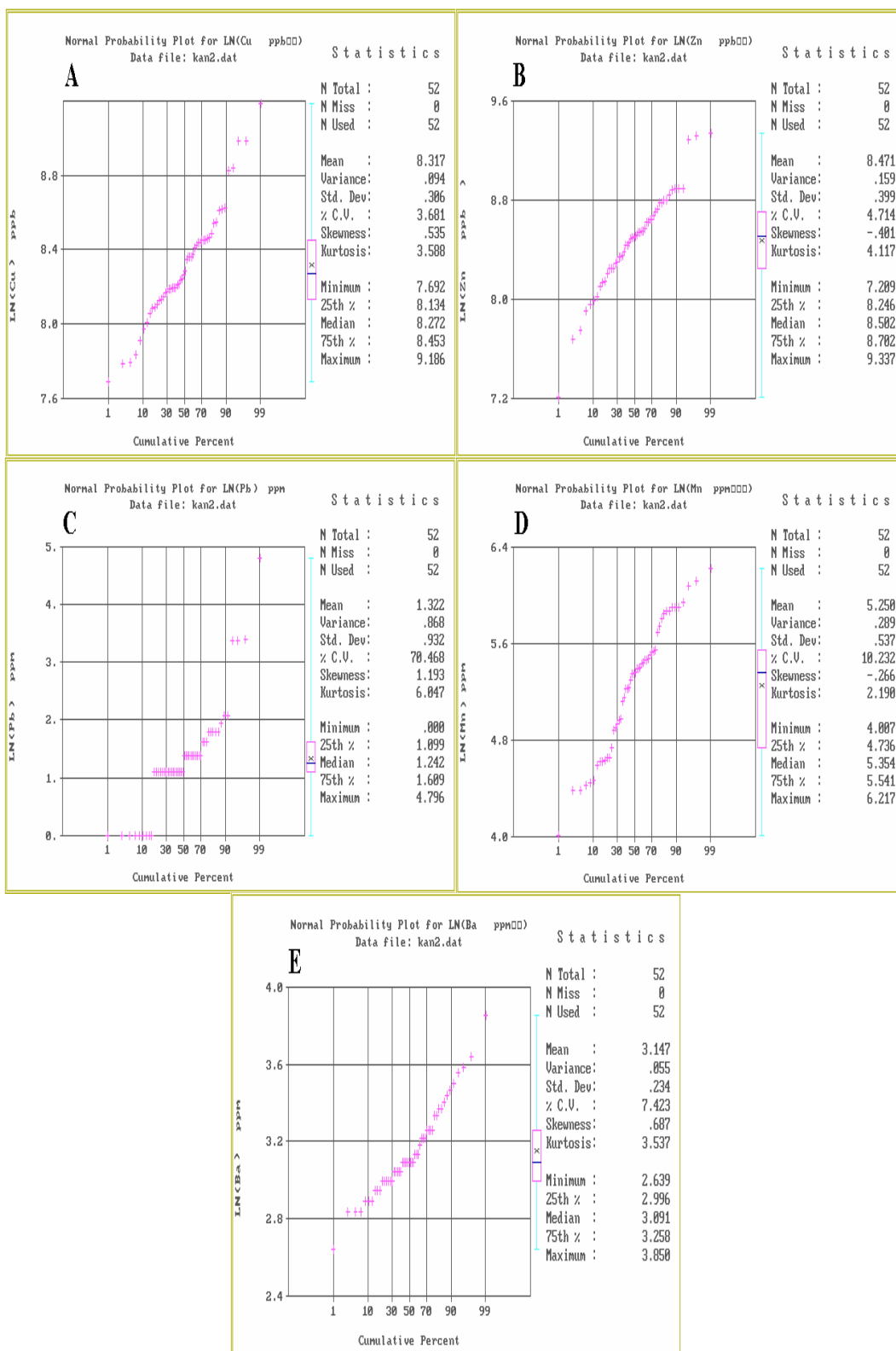


Figure 6.4: Probability plot of the log values for Cu (A), Zn (B), Pb (C), Mn (D) and Ba (E), whole Kantiempen regolith data set (ICP-MS method, n=52 samples).

The NH<sub>4</sub>EDTA solution was also used to extract the mobile metal ions in 61 sand samples from Areachap. The extracts were analyzed by ICP-MS (Appendix D, Tables D.16 to D.18), and a regolith data set including these analytical results was used for the normality test, by using the univariate procedure (Table 6.6). Based on the normality test, all elements have lognormal distribution, as the log values have the highest W value. This is also supported by the mean, median and mode of the log values which are nearly the same, and the skewness and kurtosis for most elements that are very close to zero.

**Table 6.6:** The results of the normality test for the data set from Kantienpan (ICP-MS method, n = 52)

Element	Shapiro-Wilk		Mean	Median	Mode	Skewness	Kurtosis
	W	Pr<W					
Cu (ppb)	0.5869	<0.0001	4928	2420	0	3.2	11.1
Log Cu	0.9128	0.0004	8	7.8	0	0.9	0.5
Zn (ppb)	0.7390	<0.0001	7577	5180	0	2.4	6.5
Log Zn	0.9527	0.0194	8.7	8.6	0	0.5	-0.3
Pb (ppb)	0.8083	<0.0001	2572	2119	0	1.9	3.9
Log Pb	0.9435	0.0072	7.8	7.7	0	0.8	0.2
Mn (ppm)	0.8848	<0.0001	112	106	44	1.5	3.8
Log Mn	0.9719	0.1737	4.6	4.7	3.8	-0.02	-0.4
Fe (ppm)	0.8457	<0.0001	79	74	64	1.8	3.7
Log Fe	0.9401	0.0050	4.3	4.3	4.2	1	1

The probability plots of the log values for each element are shown in Figure 6.5. The linear trend of the data for each element may be interpreted as proof of a single lognormal distribution. The low values in the Cu probability plot may be due to the background effect i.e., the concentration in the reagent solution.

The single lognormal distribution of elements may be related to the ore forming process and indicate that the element investigated may be regarded as derived from an exogenic source. Statistical calculations for the mean, standard deviation, and threshold values are summarized in Table 6.7.

**Table 6.7:** The threshold values for whole Areachap data set (NH<sub>4</sub>EDTA method, n=61).

Element	Mean (M)	Standard deviation (SD)	Blank values	Threshold values	
				M + SD	M + 2*SD
Cu (ppb)	4928	3411	47-74	8339	11750
Zn (ppb)	7577	6314	670-819	13891	20205
Pb (ppb)	2572	1290	<1-17	3862	5152
Mn (ppm)	112	59	≈1	171	230
Fe (ppm)	79	22	2-61	101	123

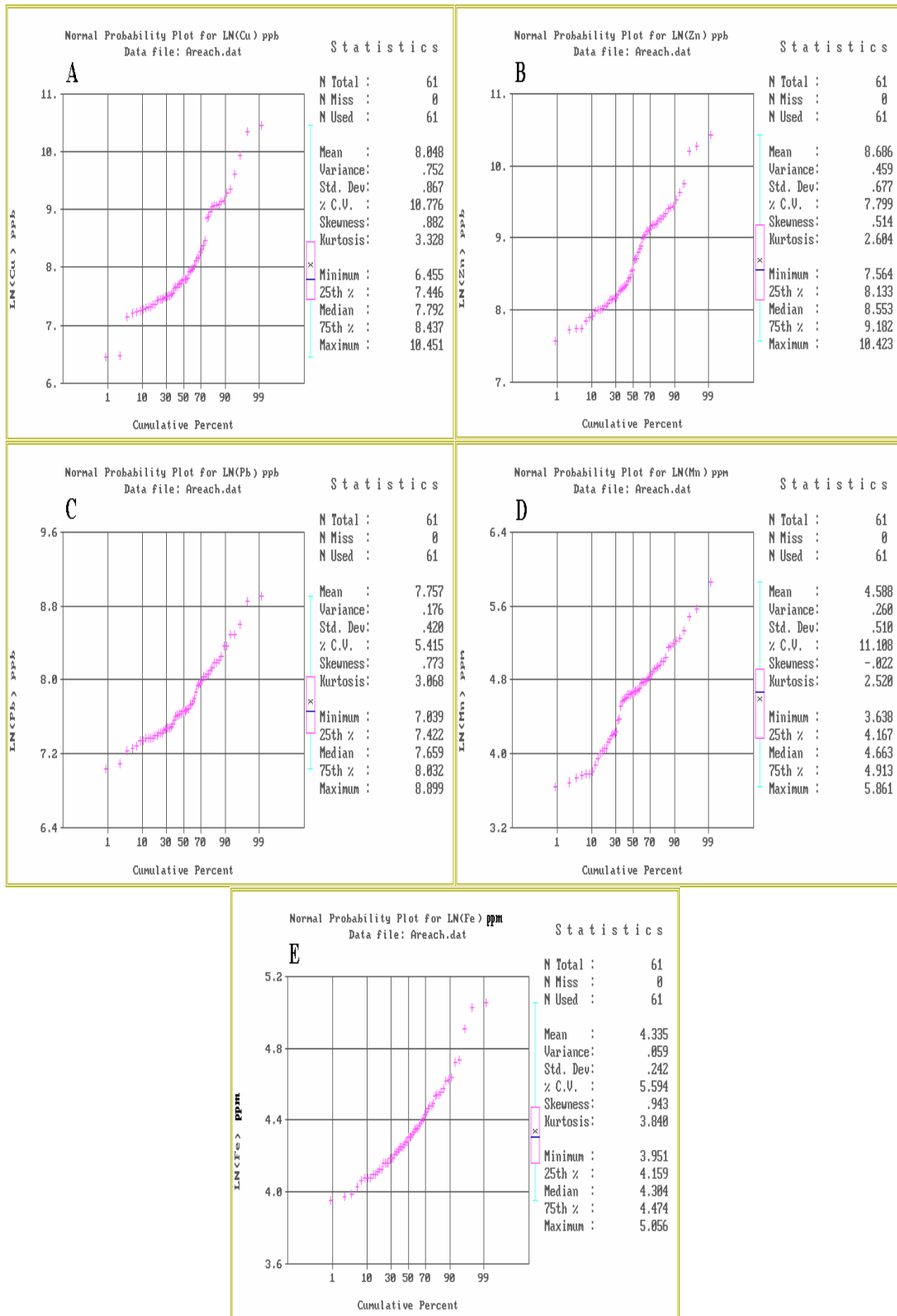


**Figure 6.5:** Probability plot of the log values for Cu (A), Zn(B), Pb(C), Mn (D) and Fe (E), whole Areachap regolith data set (ICP-MS method, n=61 samples).

### 6.5.2. The threshold value for $\text{Ca}(\text{H}_2\text{PO}_4)_2$ extraction

$\text{Ca}(\text{H}_2\text{PO}_4)_2$  solution was used to extract S from 33 sand samples from Kantienpan. The extracts were analyzed by ICP-MS and the results are given in Appendix D,

Tables D.7, D.9 and D.12. A regolith data set of these analyses is used for the normality test. The results of the statistical test for normality are given in Table 6.8. S has lognormal distribution, as the log values have high W value, and the mean, median and mode of the log vales are nearly the same.

**Table 6.8:** The normality test of distribution of S in Kantienganpan data set (ICP-MS method, n = 33 samples)

Element	Shapiro-Wilk		Mean	Median	Mode	Skewness	Kurtosis
	W	Pr<W					
S (ppm)	0.4387	<0.0001	21	10	8	3.8	16.1
Log S	0.7033	<0.0001	2.6	2.3	2.1	2.1	3.9

The probability plot of the log values for S is shown in Figure 6.6. Two linear trends are present, one for low and the other for high values of S. This indicates an effective detection limit of 7-8 ppm S, probably reflecting the background concentration in the reagents used (Table 6.9). To obtain a more amicable distribution of the population, it was decided to substitute the value, for samples returning concentrations equal to the effective detection limit, with zero. The distribution of the rest of the samples approach a single lognormal distribution.

**Table 6.9:** S values for samples within and outside the halo and blank sample, Kantienganpan and Areachap.

S (ICP-MS results, ppm)				
Blank sample	Outside the halo		Within the halo	
	Kantienganpan	Areachap	Kantienganpan	Areachap
5-6	9-10	7-10	90-180	12-20

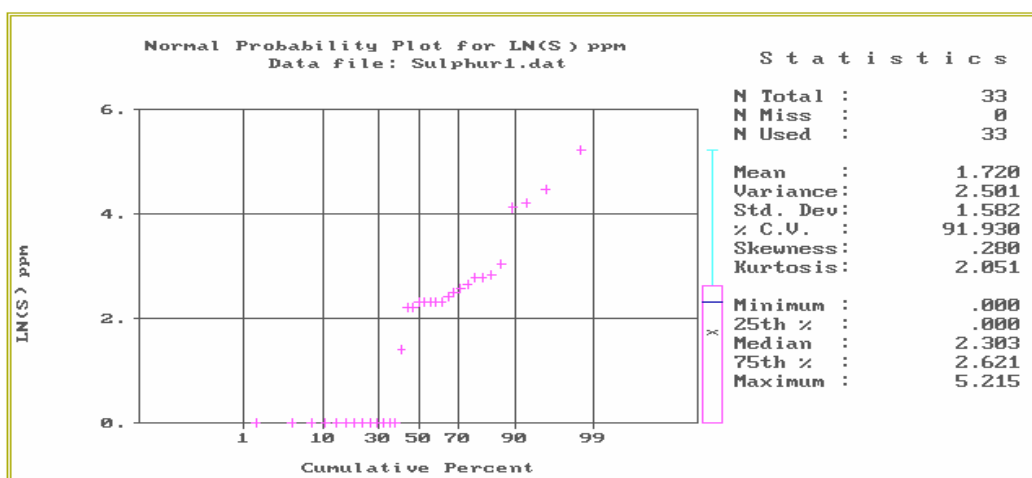


**Figure 6.6:** Probability plot of S, Kantienganpan (Ca (H<sub>2</sub>PO<sub>4</sub>)<sub>2</sub>, shaking time of 120-minutes, ICP-MS method)

The statistical calculations of the mean, standard deviation, and threshold values for S are summarized in Table 6.10.

**Table 6.10:** The threshold values of S for the Kantienpan data set (ICP-MS method, n=33 samples).

Element	Mean (M)	Standard deviation (SD)	Blank value	Threshold values	
				M + SD	M + 2*SD
S (ppm)	18	36	5-6	54	90

Ca(H<sub>2</sub>PO<sub>4</sub>)<sub>2</sub> solution was also used to extract S from 21 sand samples from Areachap. The extracts were analyzed by ICP-MS and the results are listed in Appendix D, Table D.18. Descriptive statistics of the data set and the results of the normality test are given in Table 6.11. The log values for S have a high W value suggesting that it has a lognormal population. This is confirmed by the similar values for the mean, median and mode of the log vales. The straight line distribution on the probability plot (Fig. 6.7) confirms this interpretation.

**Table 6.11:** The normality test for the distribution of S in the Areachap data set (ICP-MS method, n = 21 samples)

Element	Shapiro-Wilk		Mean	Median	Mode	Skewness	Kurtosis
	W	Pr<W					
S (ppm)	0.9448	0.2703	12	11	14	0.7	0.2
Log S	0.9708	0.7504	2.4	2.4	2.6	0	-0.4

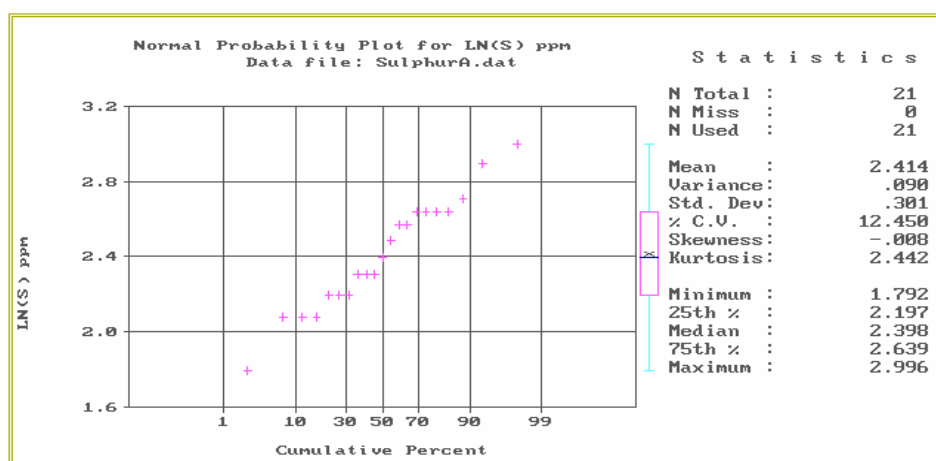


**Figure 6.7:** Probability plot of S, Areachap (Ca (H<sub>2</sub>PO<sub>4</sub>)<sub>2</sub>, shaking time 120-minutes, ICP-MS method).

Table 6.12 summarizes the statistical parameters and threshold values for S at Areachap.

**Table 6.12:** The threshold values of S for the Areachap data set (ICP-MS method, n=21 samples).

Element	Mean (M)	Standard deviation (SD)	Threshold values	
			M + SD	M + 2*SD
S (ppm)	12	4	16	20

### 6.5.3. The threshold value for MMI-A analyses results

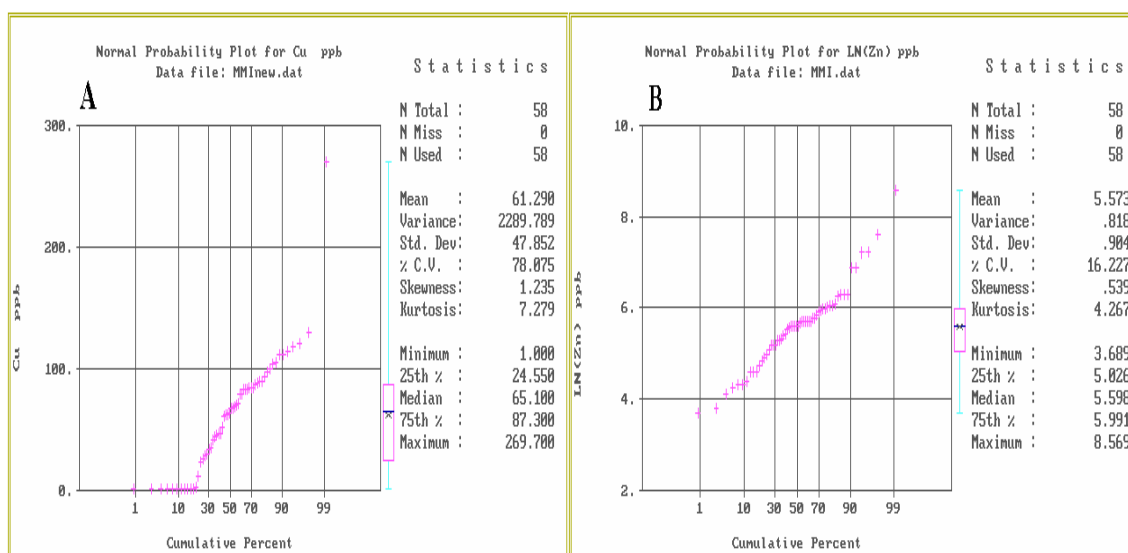
Rossouw (2003) sampled two traverses in the Kantienpan area, and submitted them for Cu and Zn analyses using the patented MMI-A method (Appendix D, Table D.15, and Table 6.1). The data is considered here in order to compare the results of the MMI-A results with the other methods, which were applied in the current research.

Table 6.13 summarizes the results of statistical tests for normality on the normal and log values of Cu and Zn. Cu has a normal and Zn has a lognormal distribution, which is confirmed by the calculated statistical parameters listed in this table.

**Table 6.13:** Results of the normality test (MMI method, n = 58 samples).

Element	Shapiro-Wilk		Mean	Median	Mode	Skewness	Kurtosis
	W	Pr<W					
Cu (ppb)	0.8740	<0.0001	61.5	65.1	1.9	1.3	4.9
Log Cu	0.7483	<0.0001	3.5	4.2	0.6	-1.1	-0.3
Zn (ppb)	0.4192	<0.0001	435	270	270	5.4	34.1
Log Zn	0.9590	0.0480	5.6	5.6	5.6	0.6	1.5

The probability plot of the normal (Cu) and log values (Zn) of the elements are plotted in Figure 6.8 A and B. The lowest values in the Cu probability plot (Fig. 6.8 A), may be due to the detection limit of the method. This may also explain the high kurtosis of Cu in Table 6.13. Based on these results, Cu has a single normal distribution and Zn has a single lognormal distribution.



**Figure 6.8:** Probability plot of the normal and log values for Cu (A) and Zn (B) (MMI method, n=58 samples).

The statistical calculations of the mean, standard deviation, and threshold values for Cu and Zn determined with the MMI-A method are summarized in Table 6.14.

**Table 6.14:** The threshold values of Cu and Zn (MMI method, n=58 samples).

Element	Mean (M)	Standard deviation (SD)	Threshold values	
			M + SD	M + 2*SD
Cu (ppb)	61	48	109	157
Zn (ppb)	435	733	1168	1901

#### 6.5.4. The threshold value for total analyses (XRF method)

To compare the results of the partial extraction analyses ( $\text{NH}_4\text{EDTA}$  and  $\text{Ca}(\text{H}_2\text{PO}_4)_2$  solutions) with the total (XRF) analyses, samples of one regolith traverse from Kantienpan (KP12) and one from Areachap (T2) were also analyzed by XRF. (Appendix D, Table D.10 and D.11). The outcome of the normality test and other statistics for Cu, Zn, Pb, MnO and S obtained from XRF analyses of the Kantienpan samples are summarized in Table 6.15. Based on these results, Cu, Pb and MnO show normal distributions, whereas Zn and S display lognormal distributions.

The probability graphs of the normal and log values of the elements are given in Figure 6.9. Based on these it may be concluded that, Cu, Pb and MnO have single normal distributions and S has a single lognormal distribution. The results indicate an effective lower detection limit of 16 ppm S, probably reflecting the detection limit of the XRF method. To obtain a more amicable distribution of the population, it was

**Table 6.15:** Results of the normality test for regolith traverse of KP12 (XRF method, n = 19).

Element	Shapiro-Wilk		Mean	Median	Mode	Skewness	Kurtosis
	W	Pr<W					
Cu	0.9623	<0.6175	25	25	22	-0.64	1.1
Log Cu	0.8912	<0.0338	3.2	3.2	3.1	-1.46	3.77
Zn	0.8827	0.0239	108	102	94	0.62	-1.2
Log Zn	0.9016	0.0520	4.7	4.6	4.5	0.49	-1.25
Pb	0.9338	<0.2037	16	15	15	0.30	0.08
Log Pb	0.9322	0.1899	2.8	2.71	2.71	-0.43	1.19
MnO	0.892	0.0356	0.1	0.09	0.09	0.34	0.11
Log MnO	0.900	0.0492	-2.3	-2.4	-2.4	-0.08	0.5
S	0.5933	<0.0001	41	16	16	2.4	6.1
Log S	0.6694	<0.0001	3.3	2.8	2.8	1.35	0.52

decided to substitute the value, for samples returning concentrations equal to this detection limit, with zero. Statistics such as the mean, standard deviation, and threshold values for Cu, Pb, MnO and S are summarized in Table 6.16.

**Table 6.16:** Threshold values for regolith traverse KP12 (XRF method, n=19).

Element	Mean (M)	Standard deviation (SD)	Threshold values	
			M + SD	M + 2*SD
Cu (ppm)	25	5	30	35
Pb (ppm)	16	3	19	23
MnO (%)	0.10	0.01	0.11	0.12
S (ppm)	30	56	86	142

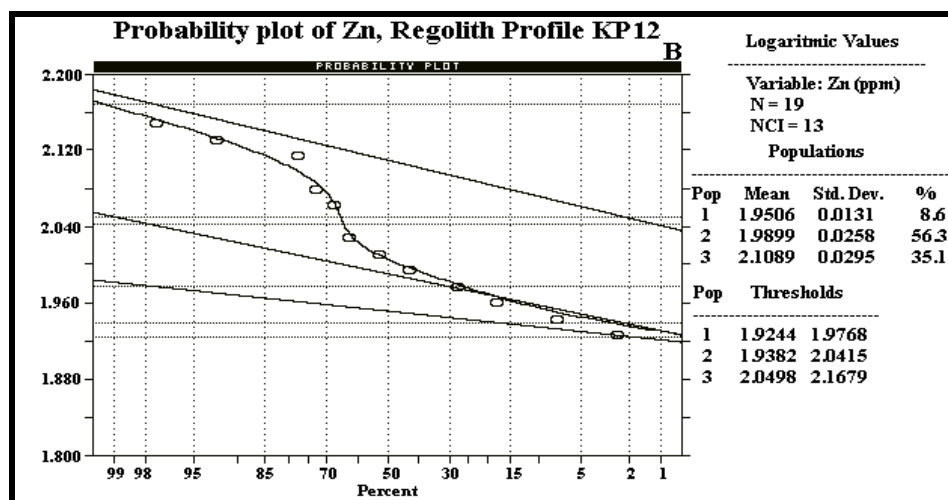
Zn shows a bimodal distribution (Fig. 6.9 B). The probplot software was used to separate these populations (Fig. 6.10). The observed distribution of Zn (Fig. 6.10) may be ascribed to three sub-populations. The first represents less than 8.6% of the sample population, the second between 8.6% and 64.9% and the third represents 35.1%. The second sub-population is regarded to represent a mixture of the first and third populations. Whereas the first population may reflect the geochemical background, the third population is directly related to the concealed massive sulphide ore zone. The anomalous sub-population of Zn has a threshold value of 112 ppm (Table 6.17).

The outcome of the normality test and the other statistics for Cu, Zn, Pb, MnO, Fe<sub>2</sub>O<sub>3</sub> and S concentrations obtained from XRF for regolith traverse T2 in Areachap are summarized in Table 6.18. Based on these results, MnO and Fe<sub>2</sub>O<sub>3</sub> display normal distributions, whereas Cu, Zn, Pb and S show lognormal distributions.

**Table 6.17:** The threshold value of Zn for regolith traverse KP12 (XRF analysis, n=19 samples).

Element	No. of popul.	Means (M)	Std. Dev. (SD)	%	Threshold values
Zn (ppm)	1	89	-86.6	8.7	84
			+92		95
	2	98	-92.1	56.3	87
			+103.7		110
	3	129	-120	35	112
			+137.5		147

Note: No. of popul.: Number of population, SD: Standard deviation


**Figure 6.10:** Probability plot of Zn based on the regolith traverse KP12 data, Kantienpan, XRF method.

**Table 6.18:** Results of the normality test for regolith traverse of T2 (XRF method, n = 25).

Element	Shapiro-Wilk		Mean	Median	Mode	Skewness	Kurtosis
	W	Pr<W					
Cu (ppm)	0.7747	<0.0001	38	29	29	1.7	2.5
Log Cu	0.8769	0.0060	3.6	3.4	3.4	1	0.2
Zn (ppm)	0.8030	0.0003	97	84	79	1.3	0.3
Log Zn	0.8689	0.0041	4.5	4.4	4.4	0.9	-0.3
Pb (ppm)	0.6937	<0.0001	25	22	21	2.4	5.6
Log Pb	0.8138	0.0004	3.2	3.1	3	1.7	3
MnO (%)	0.9037	0.0221	0.08	0.08	0.08	0.8	0.8
Log MnO	0.9174	0.0447	-2.6	-2.5	-2.5	0.3	-0.3
Fe <sub>2</sub> O <sub>3</sub> (%)	0.9488	0.2350	5.7	5.6	5.6	0.6	-0.02
Log Fe <sub>2</sub> O <sub>3</sub>	0.9602	0.4193	1.7	1.7	1.7	0.4	-0.2
S (ppm)	0.5758	<0.0001	329	124	69	2.7	7.1
Log S	0.9556	0.3345	5.1	4.8	4.2	0.5	0

The probability graphs of the normal and log values of the elements are given in Figure 6.11. MnO and Fe<sub>2</sub>O<sub>3</sub> have single normal distributions and Cu, Pb and S have single lognormal distributions. The statistics including the mean, standard deviation,

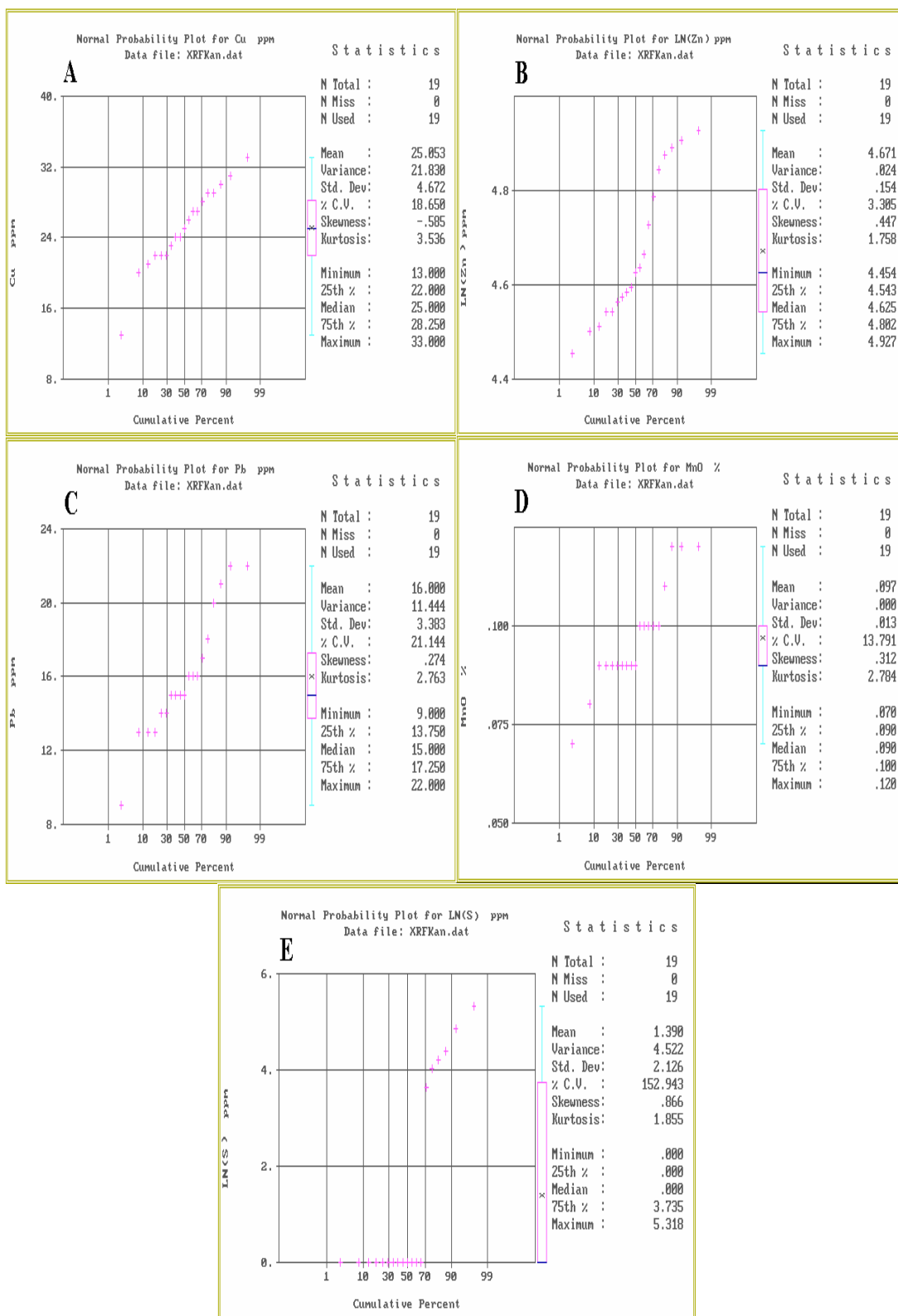


Figure 6.9: Probability plot of the normal and log values for Cu (A), Zn (B), Pb (C), MnO (D) and S (E), regolith traverse KP12, Kantienpan (XRF method, n=19 samples).

and threshold of these elements are summarized in Table 6.19.

**Table 6.19:** Threshold values for regolith traverse T2 (XRF method, n=25).

Element	Mean (M)	Standard deviation (SD)	Threshold values	
			M + SD	M + 2*SD
Cu (ppm)	38	18	56	74
Pb (ppm)	25	7	32	39
MnO (%)	0.08	0.02	0.1	0.12
Fe <sub>2</sub> O <sub>3</sub> (%)	5.69	0.48	6.2	6.7
S (ppm)	329	496	825	1321

Zn shows a bimodal distribution (Figure 6.11 B) and the probplot software was used to separate these populations (Fig. 6.12). The observed distribution of Zn may be considered to be composed of three sub-populations. The first represents less than 66.2% of the sample population, the second between 66.2% and 80.3% and the third represents 19.7%. The second sub-population probably represents a mixture of the first and third. The anomalous sub-population of Zn has a threshold value of 135 ppm (Table 6.20).

**Table 6.20:** Threshold values for Zn, regolith traverse T2 (XRF method, n=25 samples).

Element	No. of popul.	Means (M)	Std. Dev. (SD)	%	Threshold values
Zn (ppm)	1	77	-68.3	66.2	60
			+87.5		99
	2	101	-86.3	14.1	74
			+117.4		137
	3	159	-146.8	19.7	135
			+172.6		187

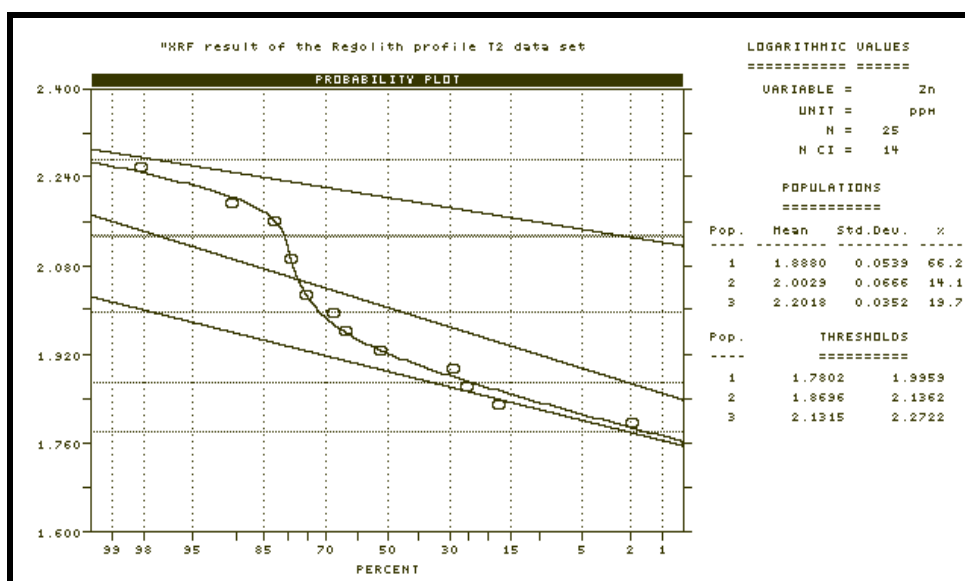


**Figure 6.12:** Probability plot of Zn, regolith traverse T2 (XRF method, n=25 samples).

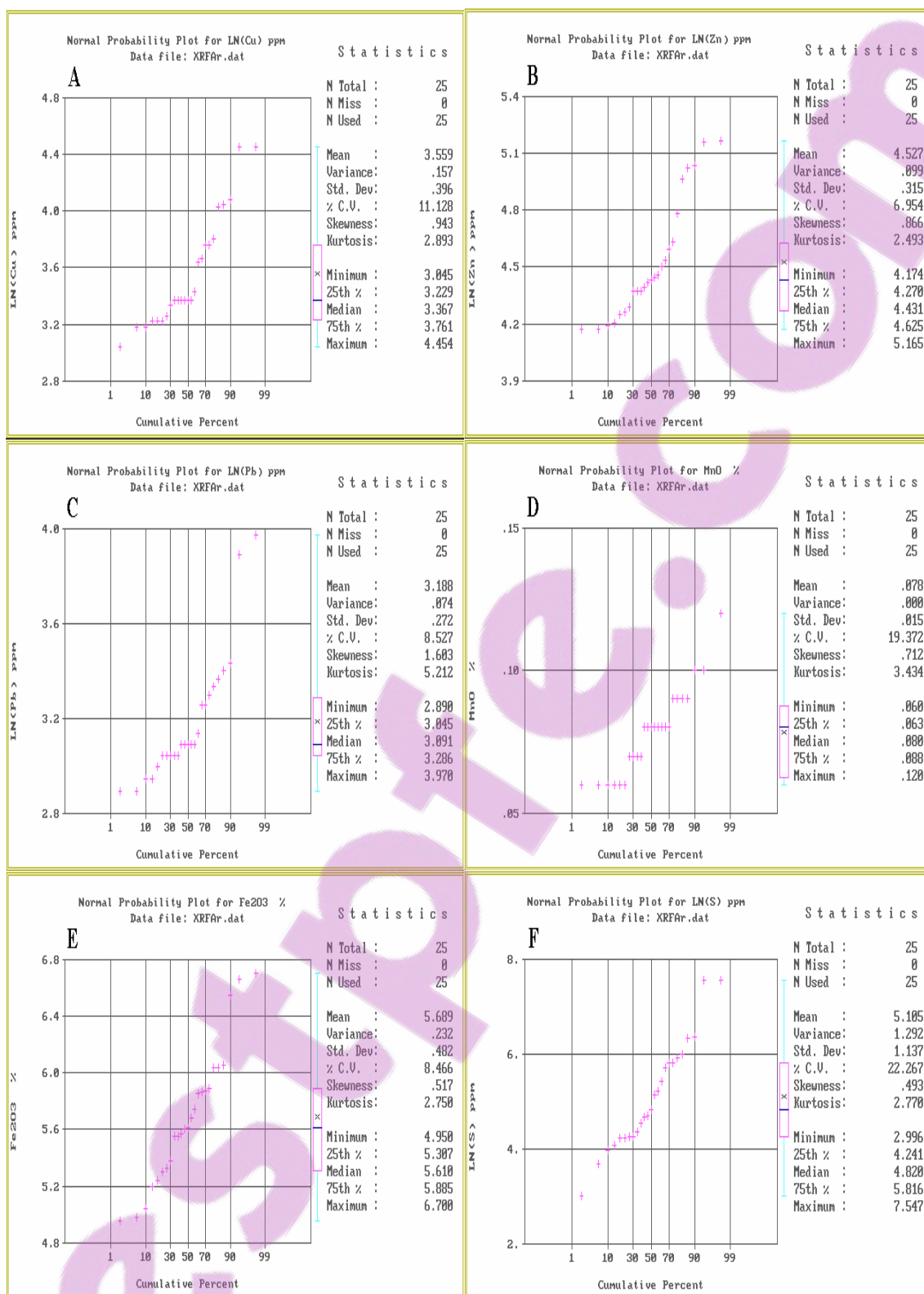


**Figure 6.11:** Probability plot of the normal and log values for Cu (A), Zn (B), Pb (C), MnO (D), Fe<sub>2</sub>O<sub>3</sub> (E) and S (F), regolith traverse T2, Areachap (XRF method, n=21 samples).

## **6.6. Discrimination of concealed ore zones in the surface samples**

The anomalous samples in the regolith traverses in the Kantienpan and Areachap may be identified relative to the threshold values calculated for Cu, Zn, Pb, Mn, MnO and S as analyzed by ICP-MS (for NH<sub>4</sub>EDTA and Ca(H<sub>2</sub>PO<sub>4</sub>)<sub>2</sub> solutions) and XRF methods. The threshold values and the traverse background may then be used to determine the width of the secondary dispersion haloes in the studied areas.

### **6.6.1. Comparison of partial extraction techniques with total analysis method**

#### **Traverse KP12 (Kantienpan)**

In Figures 6.13 to 6.17 the results of ICP-MS and XRF analyses for each element and oxide are plotted for regolith traverse KP12 at Kantienpan. A cross section which includes the location of regolith samples and the approximate projection of the ore body is also provided. There are two massive sulphide lenses in this cross-section and their projection positions at surface are from 150 to 170 (from sample 9 to 11) and 200 to 220-m (from sample 14 to 16). The grade of the ore zones are given in the cross sections (Fig. 6.13 to 6.17).

The ICP-MS results for EDTA soluble Cu (threshold value 5768 ppb, Fig. 6.13 A) are not diagnostic of the underlying mineralization, but there is an increasing trend between 180 and 240 and a peak at 150-m distance. The values are lower than the threshold value, but higher than the traverse background (Fig. 6.13 A). Another peak higher than the traverse background occurs at 0-m, which is located above the quartzo-feldspathic gneiss rocks which have a Cu content of 7 ppm (unit 5 in the cross section, under the calcrete and sand cover). On the other hand, XRF analyses of this element (Fig. 6.13 B) show three anomalous peaks (threshold value 30 ppm) at 150, 180 and 240-m distances. Cu values between 200 and 250-m distance are higher than the traverse background, but lower than the threshold value. Between 80 and 120-m distance, located above the amphibolite rocks (unit 6 in the cross section), there is a peak which is higher than the traverse background (Fig. 6.13 B). The amphibolite contains 4 to 359 ppm Cu.

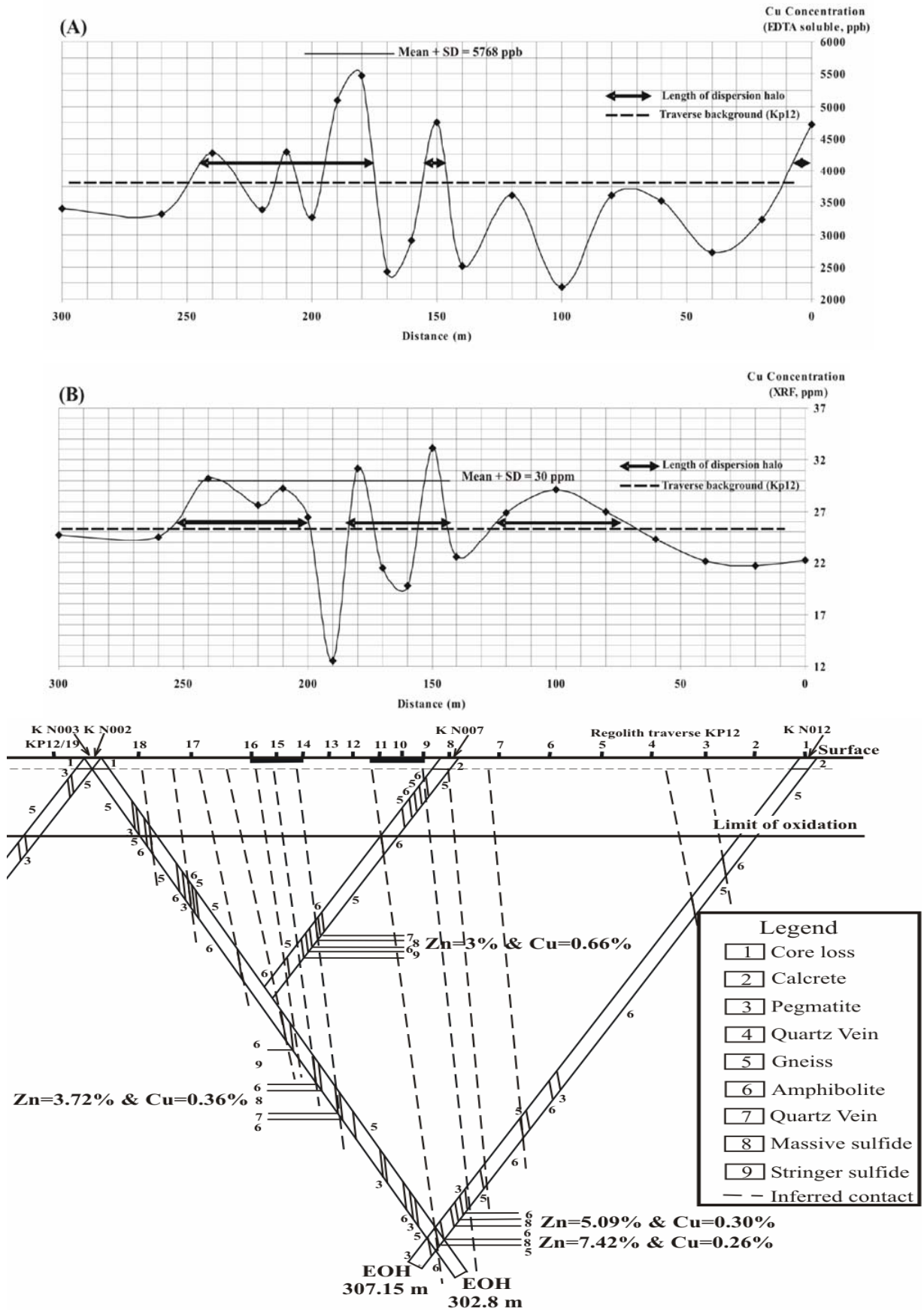
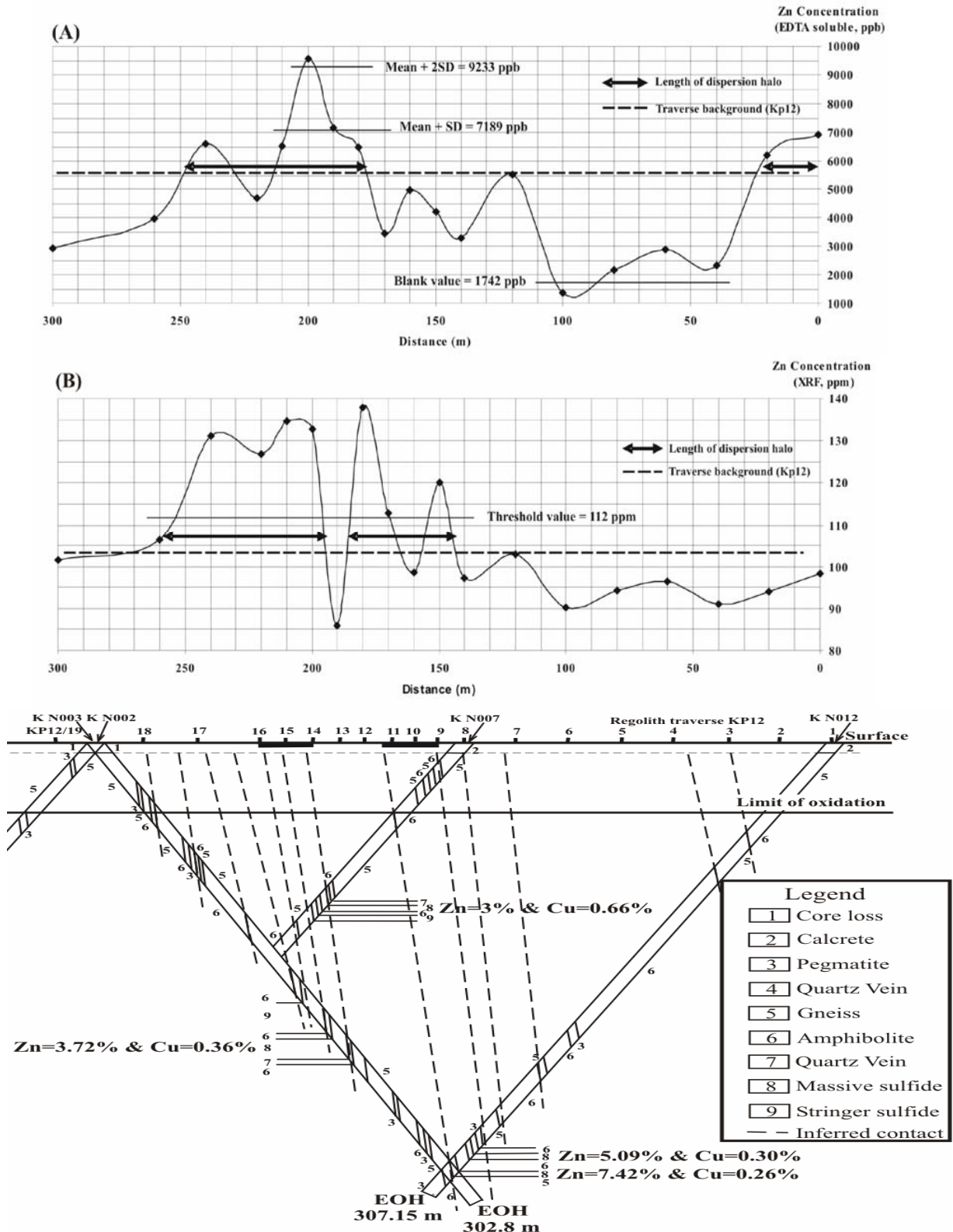


Figure 6.13: Variation of Cu in regolith traverse KP12 based on ICP-MS (A, by using  $\text{NH}_4\text{EDTA}$  and 180-minutes shaking times) and XRF analyses (B).

BestPre.COM  
List of research project topics and materials



**Figure 6.14:** Variation of Zn in regolith traverse KP12 based on ICP-MS (A, by using  $\text{NH}_4\text{EDTA}$  and 180-minutes shaking times) and XRF analyses (B).

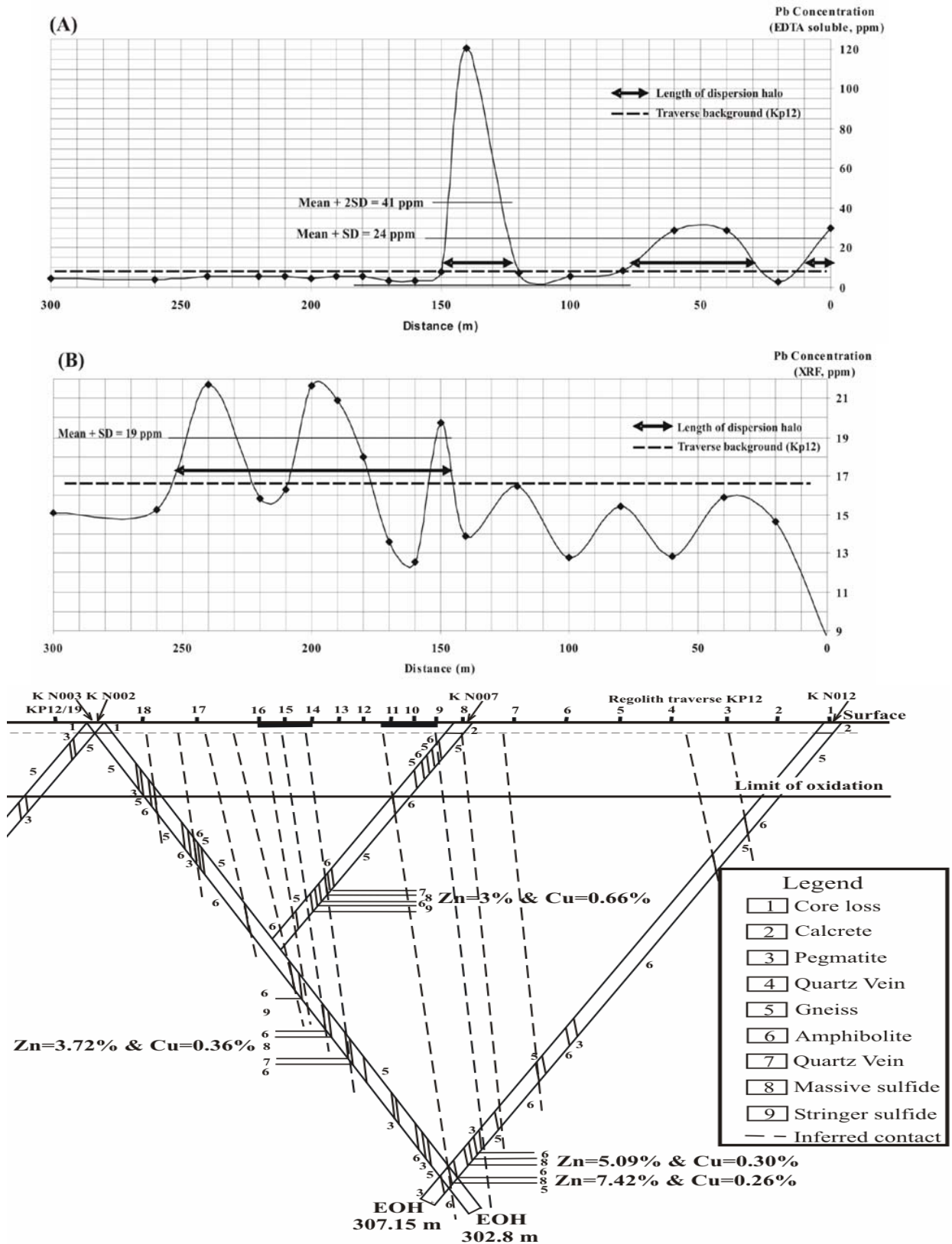
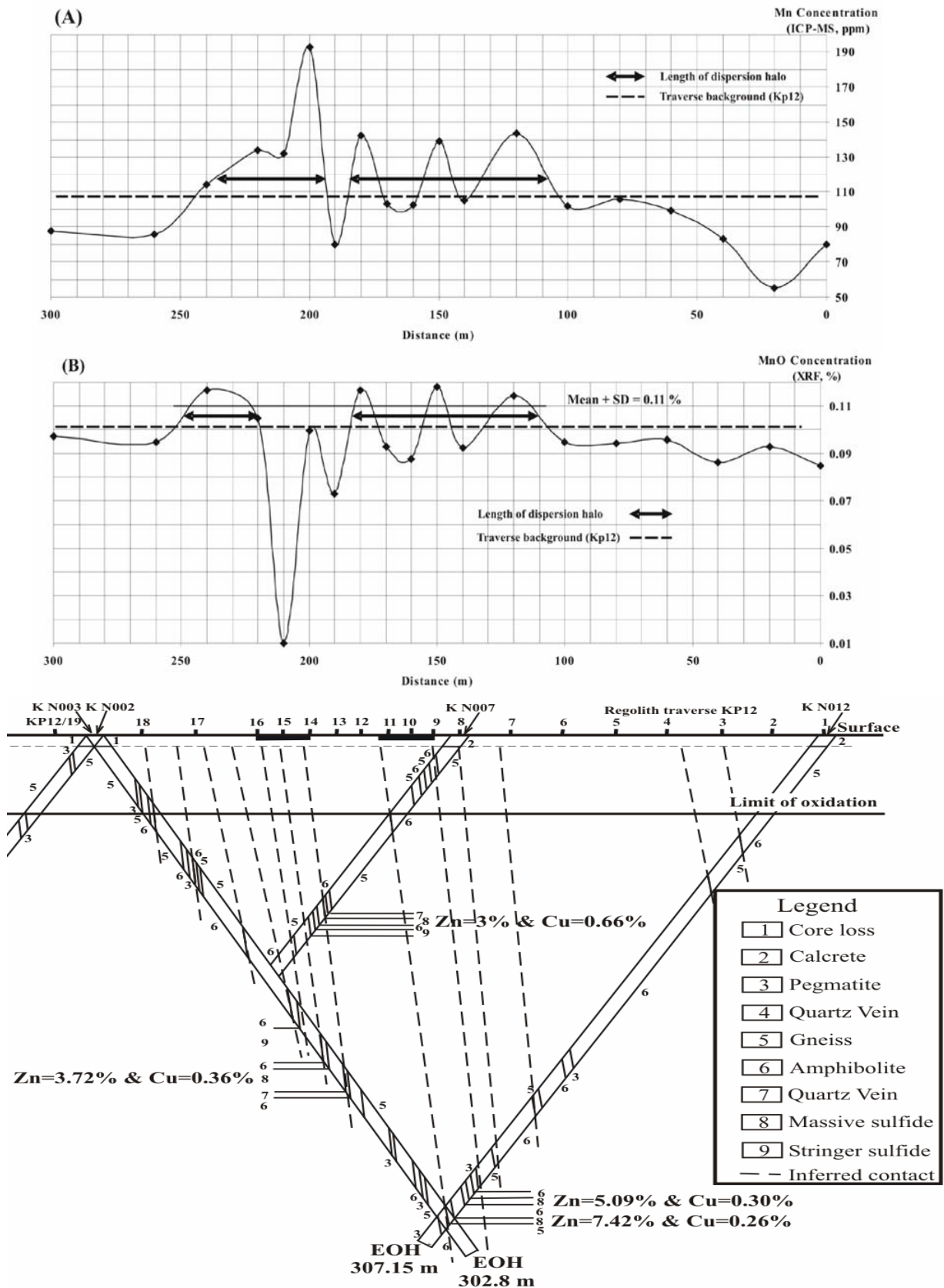
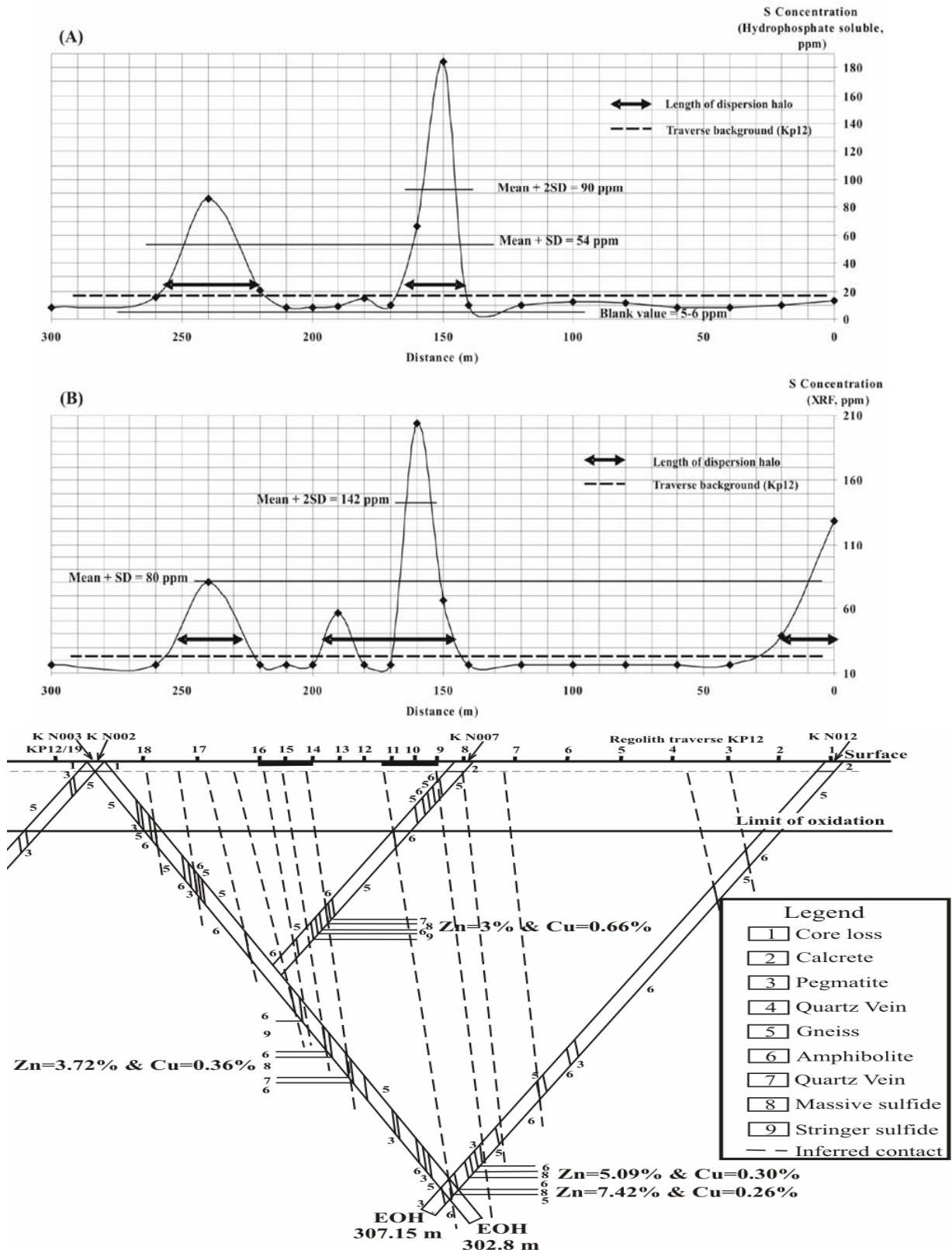


Figure 6.15: Variation of Pb in regolith traverse KP12 based on ICP-MS (A, by using  $\text{NH}_4\text{EDTA}$  and 180-minutes shaking times) and XRF analyses (B).



**Figure 6.16:** Variation of Mn in regolith traverse KP12 based on ICP-MS (A, by using  $\text{NH}_4\text{EDTA}$  and 180-minutes shaking times) and XRF analyses (B).



**Figure 6.17:** Variation of S in regolith traverse KP12 based on ICP-MS (A, by using NH<sub>4</sub>EDTA and 180-minutes shaking times) and XRF analyses (B).

The variation of Cu in both methods confirms the existence of two lenses of concealed ore. XRF results show two clear peak areas above the concealed ore, but

the EDTA extraction method shows a narrow sharp peak for one and shows both elevated and low values dispersed over a larger area for the second ore zone. In general, the EDTA extraction and XRF methods display Cu dispersion haloes that have approximately the same width.

Figure 6.14A and 6.14B shows the variation of Zn analysed by ICP-MS and XRF. Based on the threshold value of Zn as determined by ICP-MS (7189 ppb), there is an anomalous peak between 180 and 210-m distance. However, based on the traverse background, ICP-MS results show a peak area from 180 to 250 and a peak between 0 to 20-m distances. Again, the last peak is located above the quartzo-feldspathic rocks (unit 5) where the Zn content is 98 ppm. XRF results (threshold value 112 ppm) also show an anomalous area between 200 and 250 m, and two anomalous peaks at 180 and 150-m distance. If the traverse background is considered for XRF results, then Zn shows two peaks, one from 150 to 180 and the other from 200 to 260-m distance.

The partial extraction method shows only one anomalous area whereas the XRF results show two which are located above the two concealed ore lenses. XRF also shows a wider dispersion halo for Zn in comparison to partial (EDTA) extraction.

Pb (Fig. 6.15 A) displays two anomalous peaks at 0 and 140 m (unit 5), an anomalous area from 40 to 60-m (unit 5 and 6) based on the ICP-MS results (threshold 24 ppm) and traverse background. However, XRF analysis (Fig. 6.15 B, threshold value 19 ppm), display an anomaly between 190 and 200 m and two anomalous peaks at 150 and 240-m distance. Based on the traverse background, there is peak area from 150 to 250-m.

The partial (EDTA) extraction method only shows one narrow peak near one of the ore lenses when projected on surface. The XRF results also show a narrow peak at one of the locations and wider dispersion haloes and thus better identification of the concealed ore lenses than the partial (EDTA) extraction.

Mn analyzed by ICP-MS does not show anomalous values (Fig. 6.16, threshold value 327 ppm). Mn shows a peak area from 110 to 240-m. Four anomalous peaks can be identified based on XRF results of Mn (Fig. 6.16 B) i.e., at 120, 150, 180 and 240-m

distance. Based on the traverse background and threshold value of Mn for XRF results, there are two peak areas, i.e., from 210 to 240 and from 110 to 180-m distance.

Partial (EDTA) extraction and total analyses (XRF) results show the same dispersion halo span for Mn. The XRF results show two separate anomalies for the two concealed ore lenses, but the partial extraction shows an approximately continuous halo based on the traverse background.

S shows anomalous areas for both ICP-MS (threshold value 54 and 90 ppm) and XRF (80 and 142 ppm) analyses between 150 and 160 and at 240-m distances (Fig. 6.17 A and Fig. 6.17 B). XRF results (Fig. 6.17 B) show a third anomalous peak at 0 (unit 5, where the S content is 81 ppm). Based on the traverse background for XRF results, one of the peak areas is from 150 to 200-m.

The sulphur concentration shows anomalous peaks above the concealed ore lenses that are projected to surface, but these haloes are narrower than for the other elements. The XRF results show a slightly wider halo when compared to that of partial (EDTA) extraction for one of the locations.

Based on these observations, Cu, Mn and especially Zn may be used to locate the (residual) anomalous area in the regolith traverse.

Later, for the two other traverses in the Kantienpan (KP5 and KP8), the variation of Cu, Zn and Mn will be discussed based on analytical results from the ICP-MS method.

### **Traverse T2 (Areachap)**

Figures 6.18 to 6.23 show the results of ICP-MS and XRF analyses for Cu, Zn, Pb, Fe<sub>2</sub>O<sub>3</sub>, MnO and S at Areachap in regolith traverse T2, which crosses over the ore deposit and its host rocks. Also shown in the figures is a cross section showing the location of the regolith samples and the surface projection of the ore zone (from sample 30 to -40 m). In Figure 6.18, the variation of Cu, determined by ICP-MS and XRF, is shown. Based on the threshold value of the ICP-MS for Cu (8339 ppb, Fig.

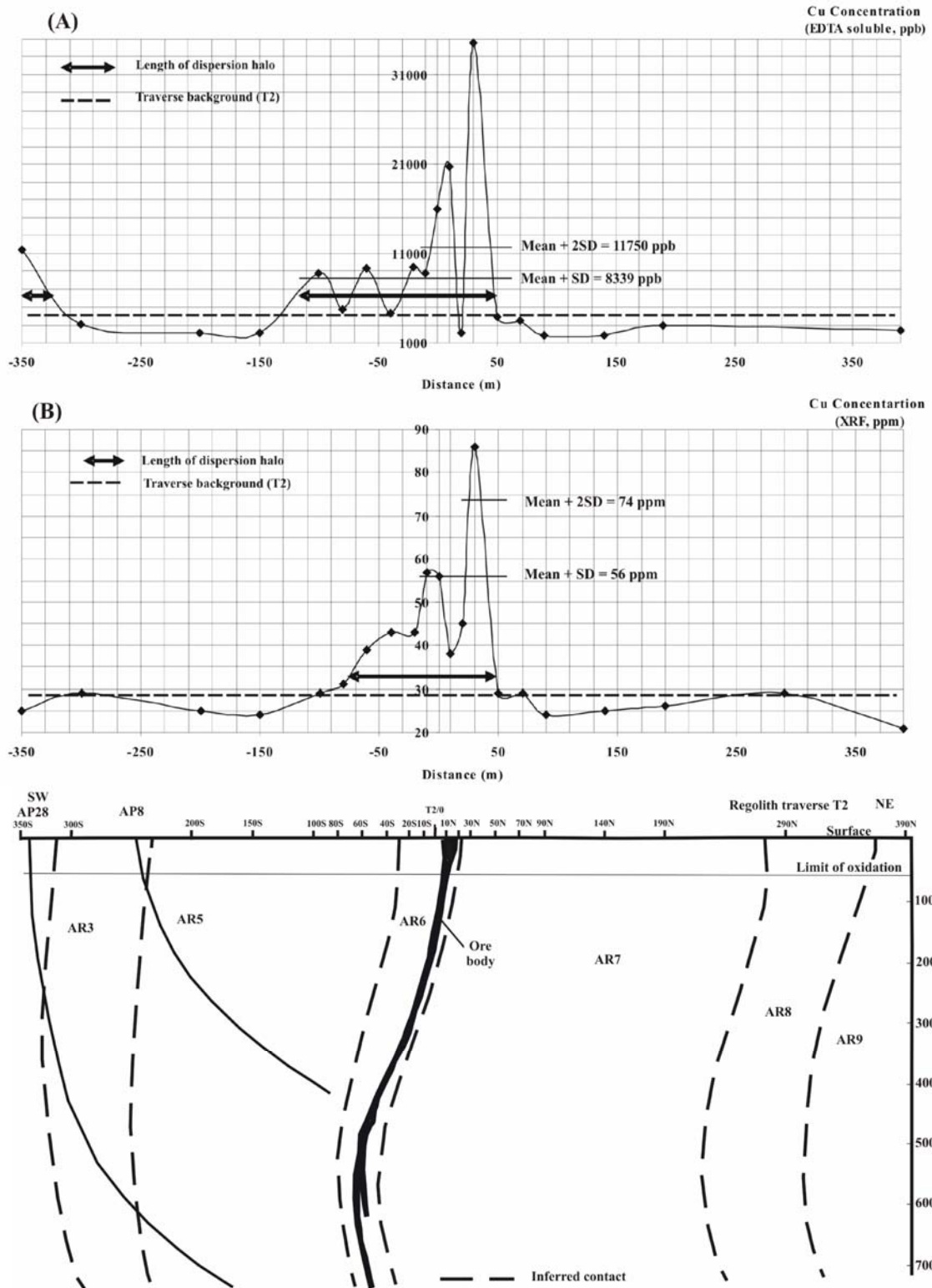


**Figure 6.18:** Variation of Cu in the regolith traverse T2 based on ICP-MS (A) ( $\text{NH}_4\text{EDTA}$ , 180-minutes shaking times) and XRF (B) analysis.

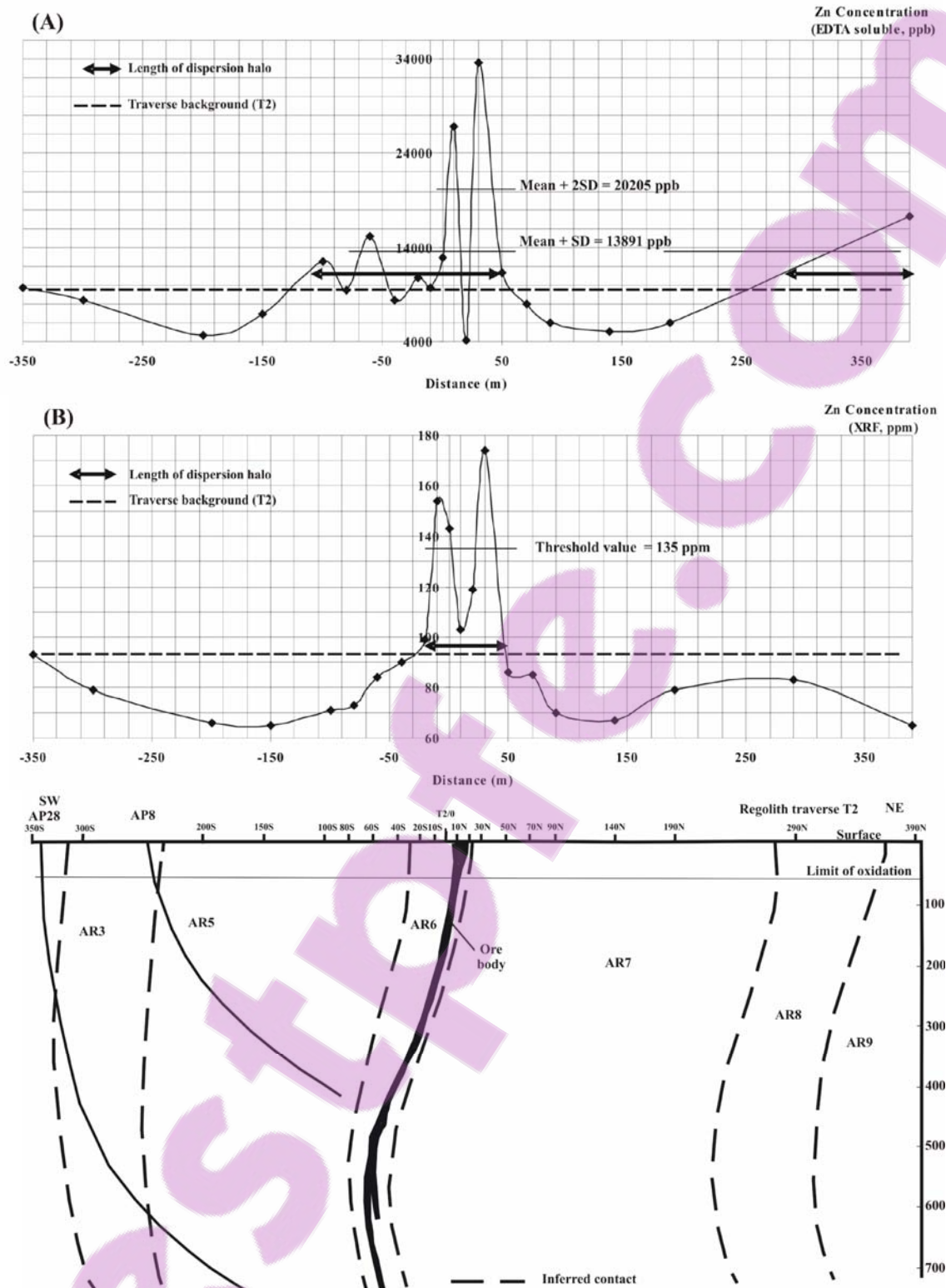


**Figure 6.19:** Variation of Zn in the regolith traverse T2 based on ICP-MS (A) ( $\text{NH}_4\text{EDTA}$ , 180-minutes shaking times) and XRF (B) analysis.

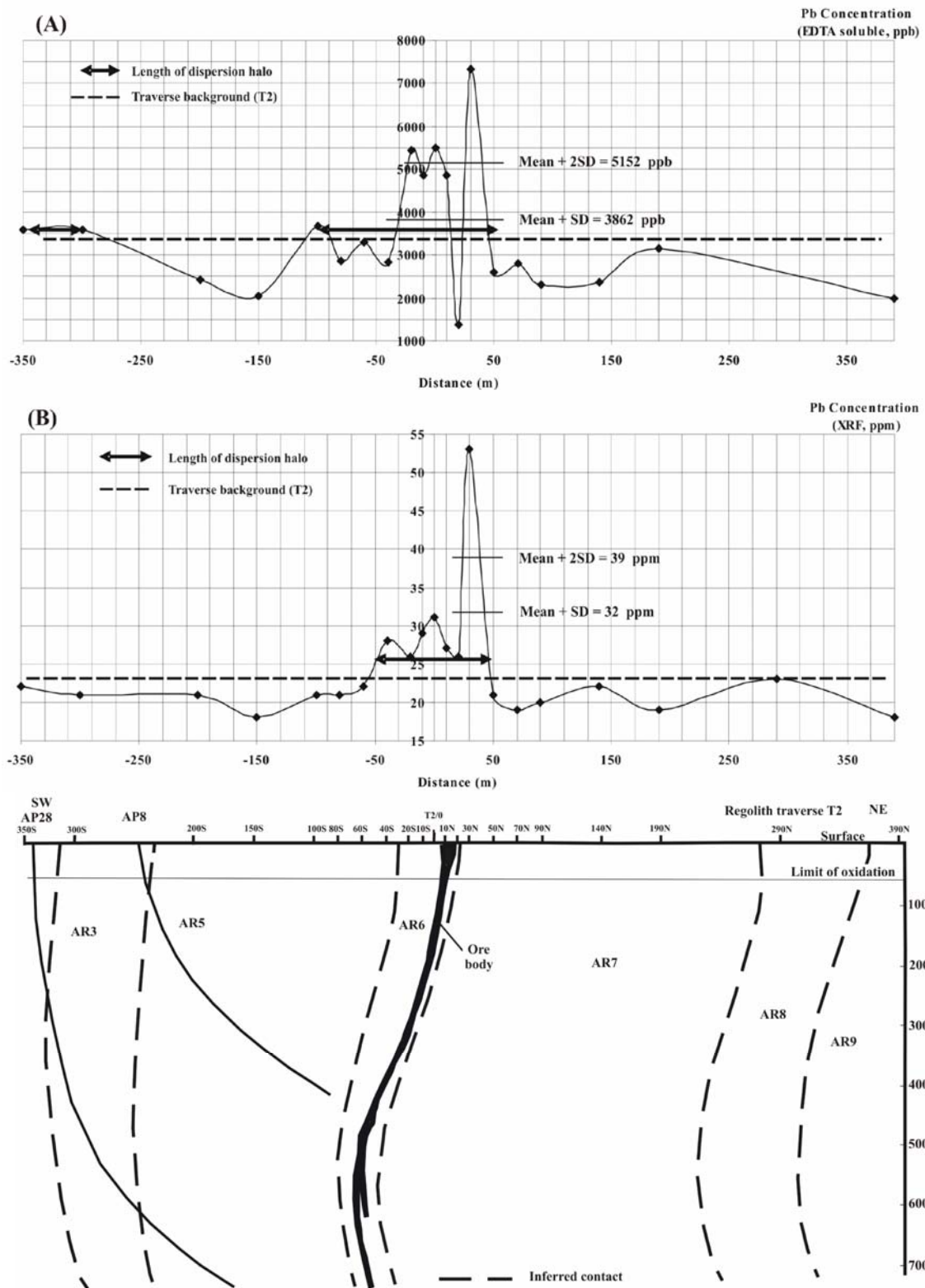


**Figure 6.20:** Variation of Pb in the regolith traverse T2 based on ICP-MS (A) ( $\text{NH}_4\text{EDTA}$ , 180-minutes shaking times) and XRF (B) analysis.

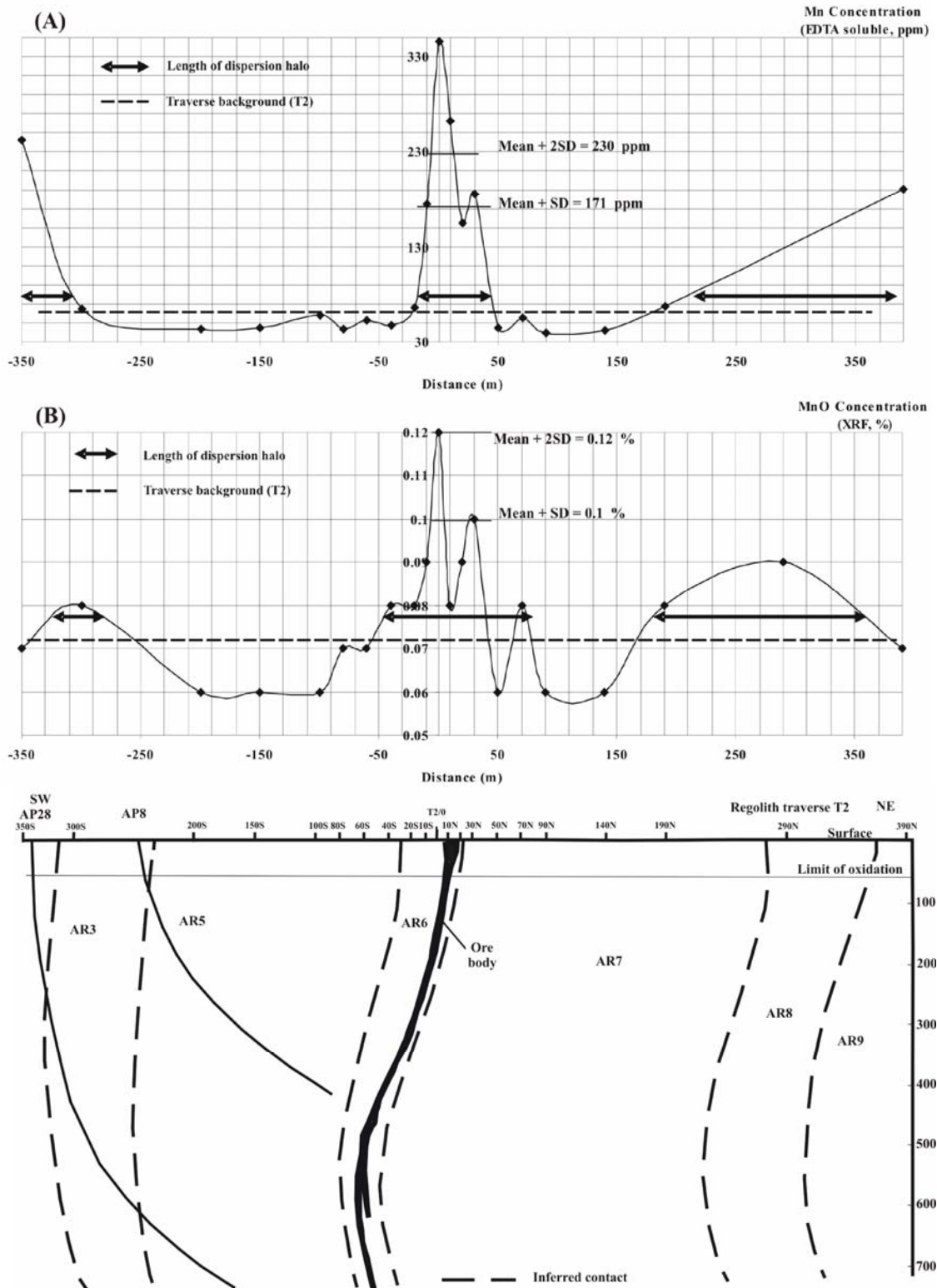


**Figure 6.21:** Variation of Mn in the regolith traverse T2 based on ICP-MS (A) ( $\text{NH}_4\text{EDTA}$ , 180-minutes shaking times) and XRF (B) analysis.

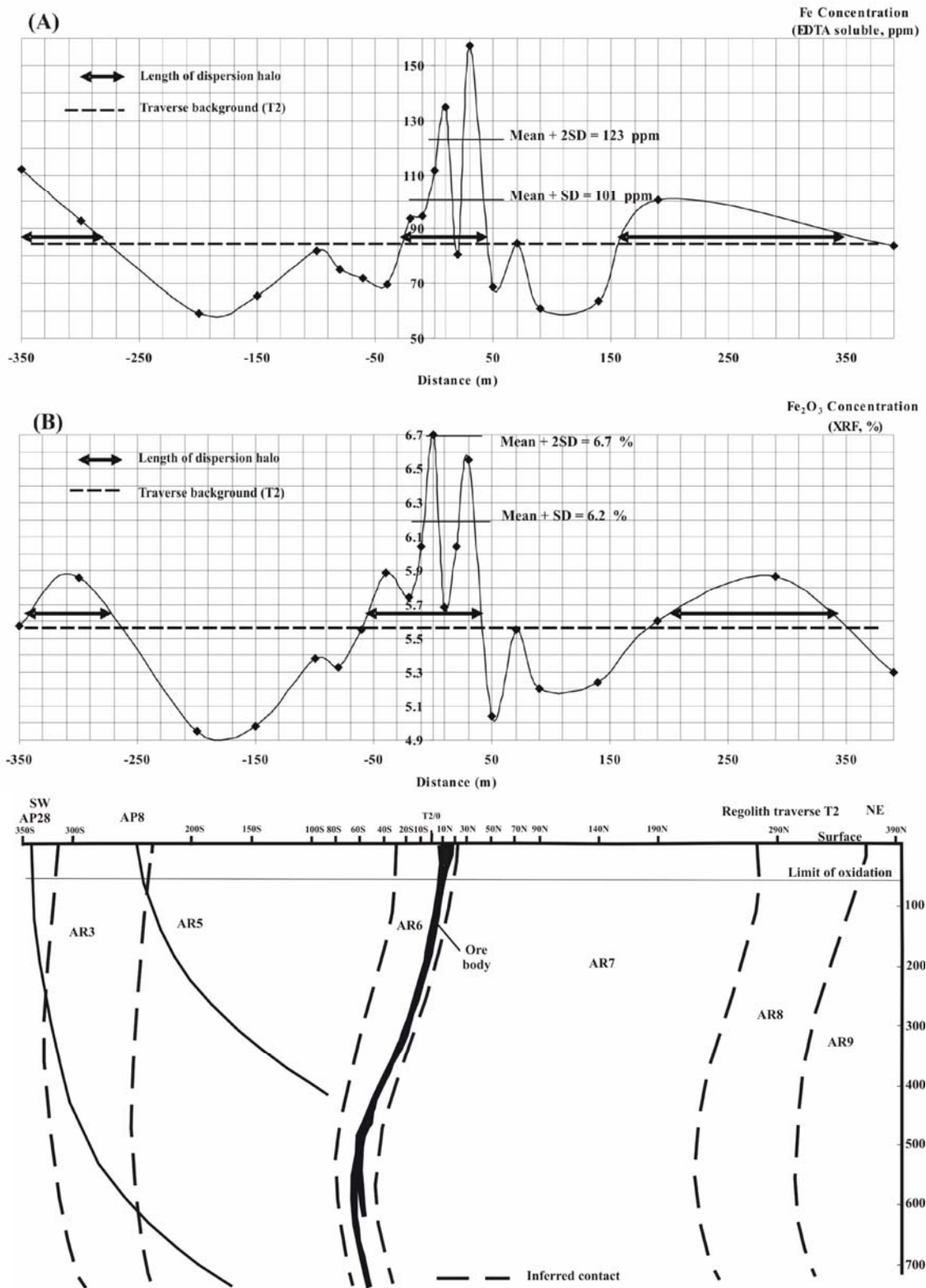


**Figure 6.22:** Variation of Fe in the regolith traverse T2 based on ICP-MS (A) (NH<sub>4</sub>EDTA, 180-minutes shaking times) and XRF (B) analysis.

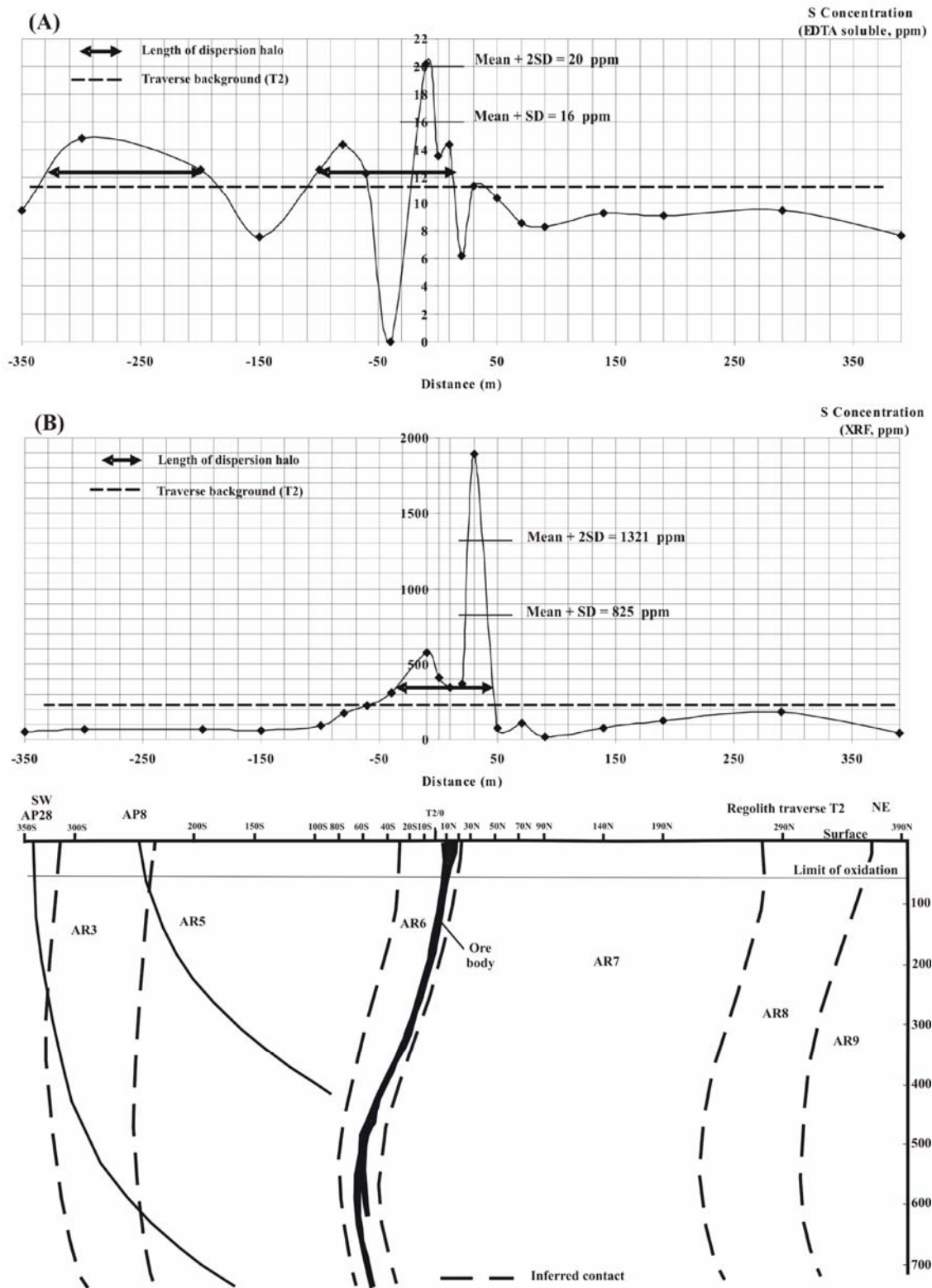


**Figure 6.23:** Variation of S in the regolith traverse T2 based on ICP-MS (A) ( $\text{NH}_4\text{EDTA}$ , 180-minutes shaking times) and XRF (B) analysis.

6.18 A), there is an anomalous zone from -110 to 50 m. XRF results for Cu (threshold value 56 ppm, Fig. 6.18 B) show an anomalous zone from -10 to 40 m, coinciding

with the expected locations of the ore body host rocks (AR6 symbol in the cross section) under the calcrete and sand cover. Based on the traverse background, peaks occur from -120 to 50 and -70 to 50-m distance for ICP-MS and XRF results, respectively.

The partial (EDTA) extraction of Cu shows wider dispersion haloes when compared to the XRF analyses.

The variation of Zn for ICP-MS and XRF results is shown in Figure 6.19. Based on the Zn threshold value as determined by ICP-MS (13891 ppb), there are two anomalous peaks at 0 and 30 m, which are located directly above the mineralized rocks and a third at 390 m, located at the right end of this traverse. The latter peak is related to the banded pelitic gneiss (unit AR8 in the cross section). This unit may be a metasedimentary rock with a higher Zn background content. The ICP-MS results show another anomalous peak at -60 m, which may be assumed to be part of the mineralized zone. XRF results of Zn show two anomalous peaks (135 ppm) from -10 to 0 and at 30 m, nearly at the same location as the ICP-MS results. Based on traverse background, peak values in T2 occur from -110 to 50 and -20 to 50 m for ICP-MS and XRF results, respectively.

The partial (EDTA) extraction of Zn shows a wider dispersion halo when compared to that of the total analyses (XRF), a trend similar to that shown by Cu.

Figure 6.20 shows the variations of Pb as determined by ICP-MS and XRF results. With a threshold value of 3862 ppb for Pb (Fig. 6.20 A), an anomalous zone from -30 to nearly 50 m has been identified. The XRF results of Pb only show a peak at 30 m. Based on traverse background of T2, peaks occur from -110 to 50 and -50 to 50 m distance for ICP-MS and XRF results, respectively.

The partial (EDTA) extraction of Pb shows wider dispersion haloes in comparison to the total analyses (XRF), as noted in the Cu and Zn dispersion haloes.

The variation of Mn for ICP-MS and XRF results is shown in Figure 6.21. Based on the threshold value of Mn from ICP-MS (171 ppm, Fig. 6.21 A), there is an anomalous area from -10 to 30 m above the host rock. Samples at either end of this

traverse also show anomalous values for ICP-MS analyses. Samples on the left end side of this traverse occur above the banded garnet-biotite-gneiss (unit AR3 in the cross section) whereas those on the right end of the traverse occur above the biotite-hornblende-gneiss rock (unit AR7), and banded pelitic gneiss rocks (unit AR8, as explained). The gneisses may be sedimentary in origin, possibly explaining the higher Mn background values. XRF results of Mn (threshold value of 0.1%, Fig. 6.21B) show an anomalous area from -10 to 30 m distance. Based on the background values for traverse T2, peaks occur from -20 to 50 and -50 to 40 m for ICP-MS and XRF results, respectively.

The total analyses (XRF) of Mn show a wider dispersion halo when compared to that of the partial (EDTA) extraction.

Figure 6.22 shows the variation in the Fe contents as determined by ICP-MS and XRF results. Based on the threshold value of Fe (ICP-MS data; 101 ppm, Fig. 6.22 A), there is an anomalous zone from -10 to 40 m. Samples at both ends of this traverse (at -350 and 190 m) also show anomalous values for ICP-MS analyses which may be explained as above. XRF results of Fe (threshold value 6.2 %, Fig. 6.22 B) show a small anomalous zone between 0 and 30 m above the ore zone. Based on the traverse background for XRF results, there are two peaks at -350 and 190 m, which are confirming the ICP-MS analyses. In traverse T2, peaks occur from -30 to 50 and -50 to 50 m distance for ICP-MS and XRF results, respectively, based on the background values.

The total analysis (XRF) of Fe shows a wider dispersion halo when compared to that of partial (EDTA) extraction, which is the same as for Mn dispersion haloes.

In Figure 6.23, the variation in S is shown for ICP-MS and XRF results. The threshold value of the S concentrations determined by ICP-MS is 16 ppm (Fig. 6.23 A). An anomalous peak is present at -10 m. The XRF results have a threshold value 825 ppm (Fig. 6.23 B) and show an anomalous peak at 30 m. Based on traverse background values in traverse T2, there are peaks from -90 to 10 m for ICP-MS and from -30 to 50 m distance for XRF results. There is another peak area from -200 to -300 for ICP-MS analyses located above unit AR3.

The partial (EDTA) extraction of S shows wider dispersion haloes when compared to those of the total analyses (XRF), as seen in the Cu, Zn and Pb dispersion haloes.

Elements such as Cu, Zn and Pb show a wider secondary dispersion halo in the ICP-MS results, with Cu and Zn giving the widest halo. Mn and Fe show a slightly wider halo for elements analyzed by XRF and the span of dispersion halo for S analyzed by ICP-MS method is slightly wider than XRF results. Mn, Cu, Zn and Pb variations are also investigated in other traverses (T1 and T3) in the Areachap area.

### **6.6.2. Discrimination of the secondary dispersion haloes in other traverses**

The potentially mobile metal ions of interest (Cu, Zn and Mn) in samples from regolith traverse KP5 were extracted by NH<sub>4</sub>EDTA solution and analyzed by ICP-MS. The variation in the concentration of these elements along the traverse is shown in Figures 6.24 and 6.25. The cross section of this traverse, which includes the location of samples and projection of the ore zone on the surface (from 70 to 90 m) are also provided. Based on the calculated threshold values (Cu=5768 ppb, Zn=7189 and 9233 ppb and Mn=327 ppm), all elements show an anomalous peak in concentration at 80 m distance (i.e., from sample 5 to 7). Mn shows additional anomalous peak at 220 m distance. Based on the traverse background (dash line), all elements show an anomaly at 220 or after 200 m, above the amphibolite rocks (unit 6 in the cross section, below the calcrete). This rock contains 4 to 359 ppm Cu, 73 to 112 ppm Zn and 0.09 to 0.24 % MnO contents. Cu contents are only slightly higher than the traverse background at 0 m above unit 3 (pegmatite).

Anomalous concentrations of Cu, Zn and Mn may be used to locate the ore zone. The secondary dispersion haloes of Cu and Zn around the ore zone are wider than that of Mn in this regolith traverse.

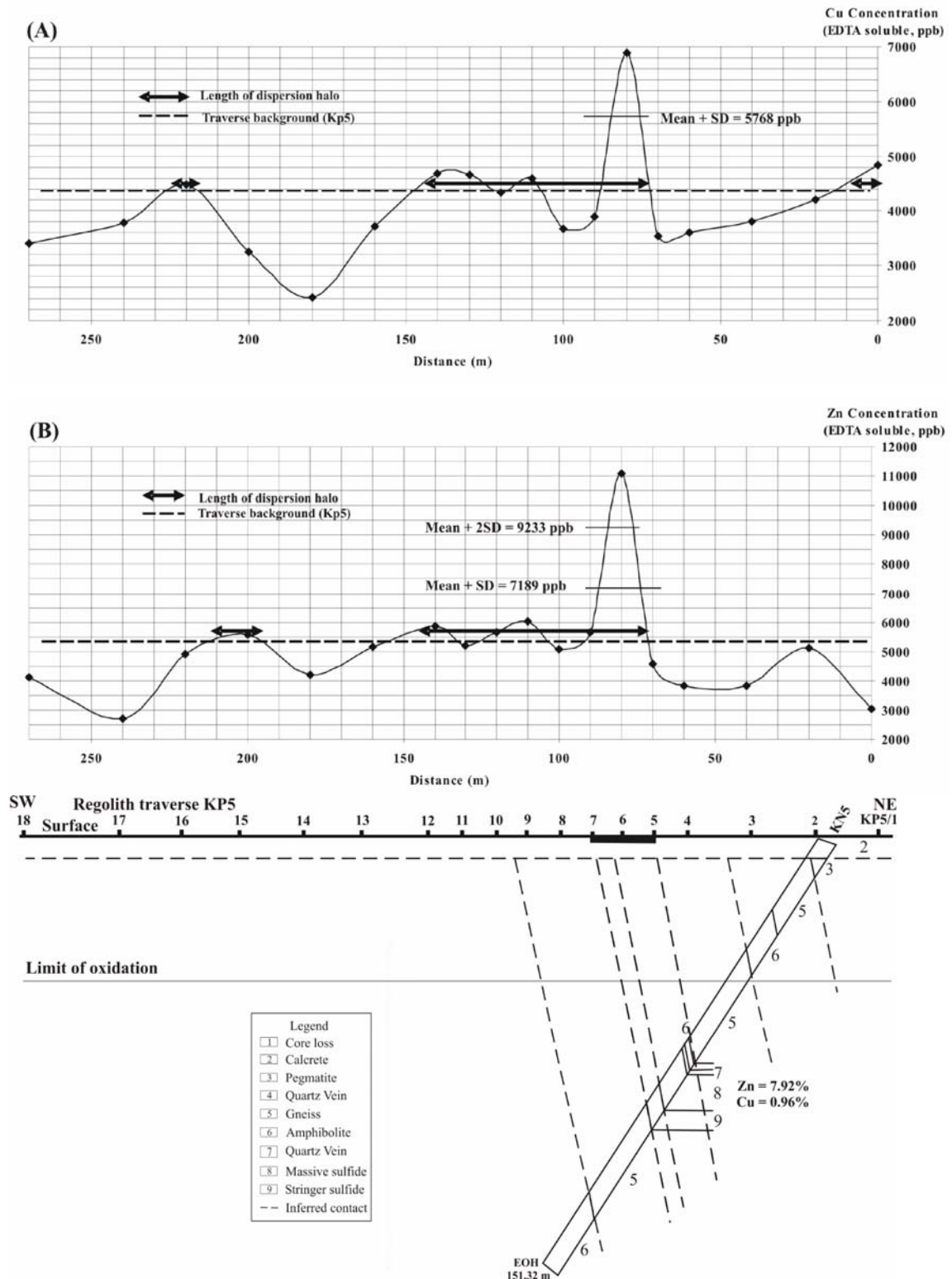


**Figure 6.24:** Variation of Cu (A) and Zn (B) in the regolith traverse KP5 (Kantienpan) based on ICP-MS analysis (using  $\text{NH}_4\text{EDTA}$  and 180-minutes shaking times).

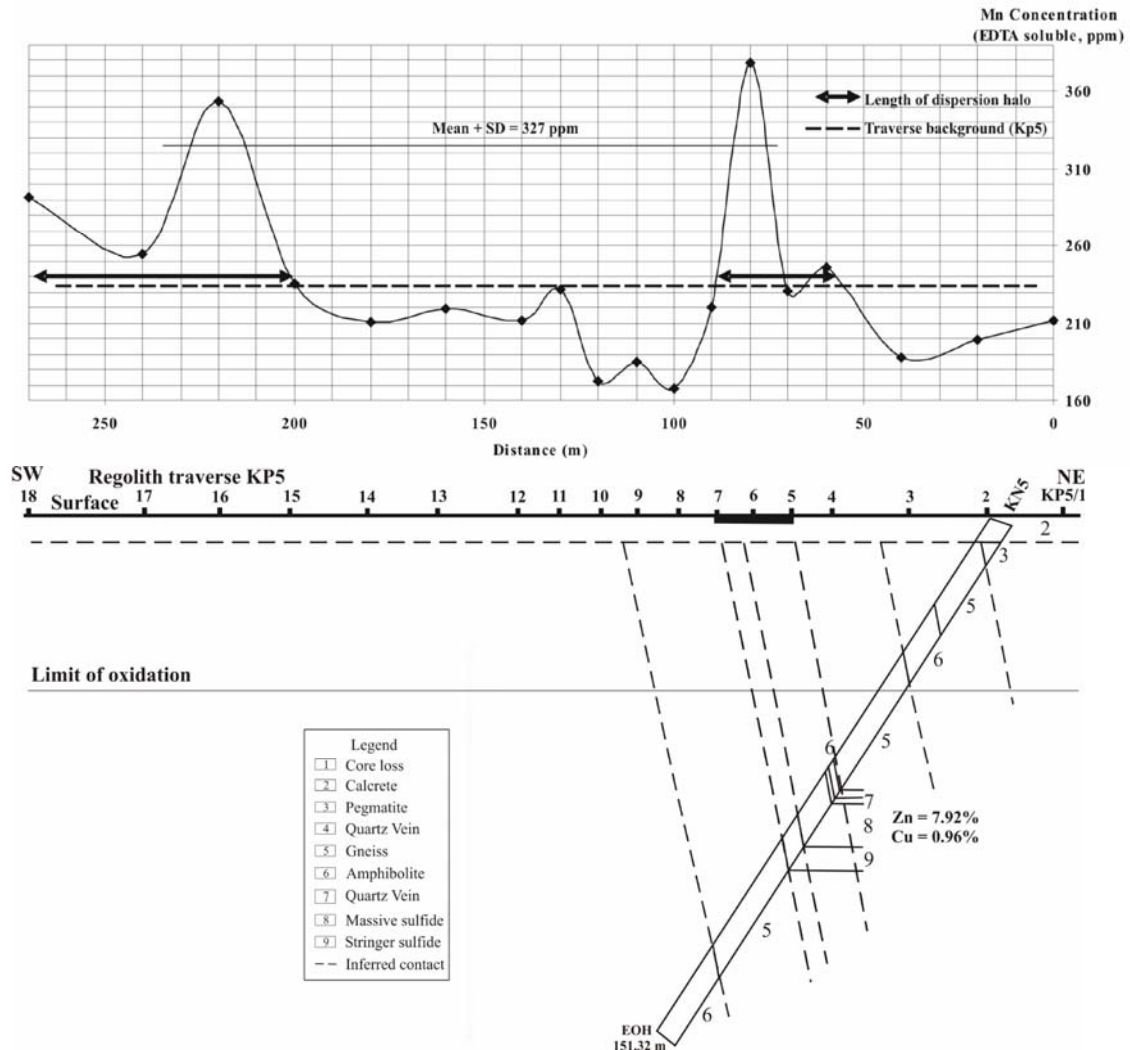


**Figure 6.25:** Variation of Mn in the regolith traverse KP5 (Kantienpan) based on ICP-MS analysis (using  $\text{NH}_4\text{EDTA}$  and 180-minutes shaking times).

The variations of the mobile metal ions Cu, Zn and Mn, extracted with a  $\text{NH}_4\text{EDTA}$  solution and analyzed by ICP-MS, from traverse KP8 are shown in Figures 6.26 and 6.27. The figure also shows the sample locations, projection of ore zone at surface (at 80, 120 and 170-180 m) and a cross section of the traverse. Based on the calculated threshold values, an anomalous area have been detected from 30 to 140 m that corresponds with the projection of the ore zone. Mn shows another anomalous area from 190 to 270 m, above the weathered amphibolite rocks with Mn contents from 0.09 to 0.24 % (unit 6 in the cross section). Based on the traverse background, the dispersion haloes are slightly wider.

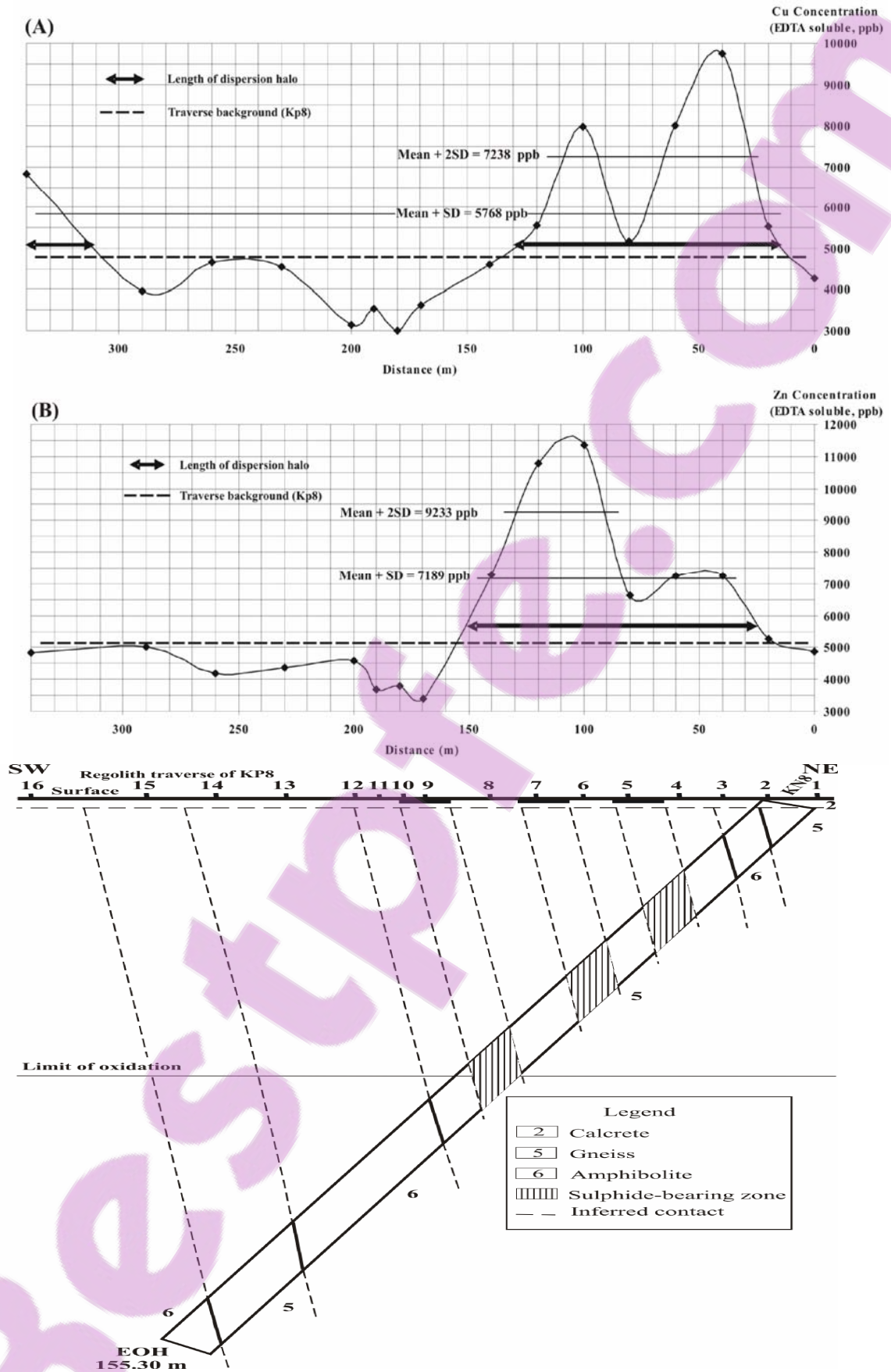
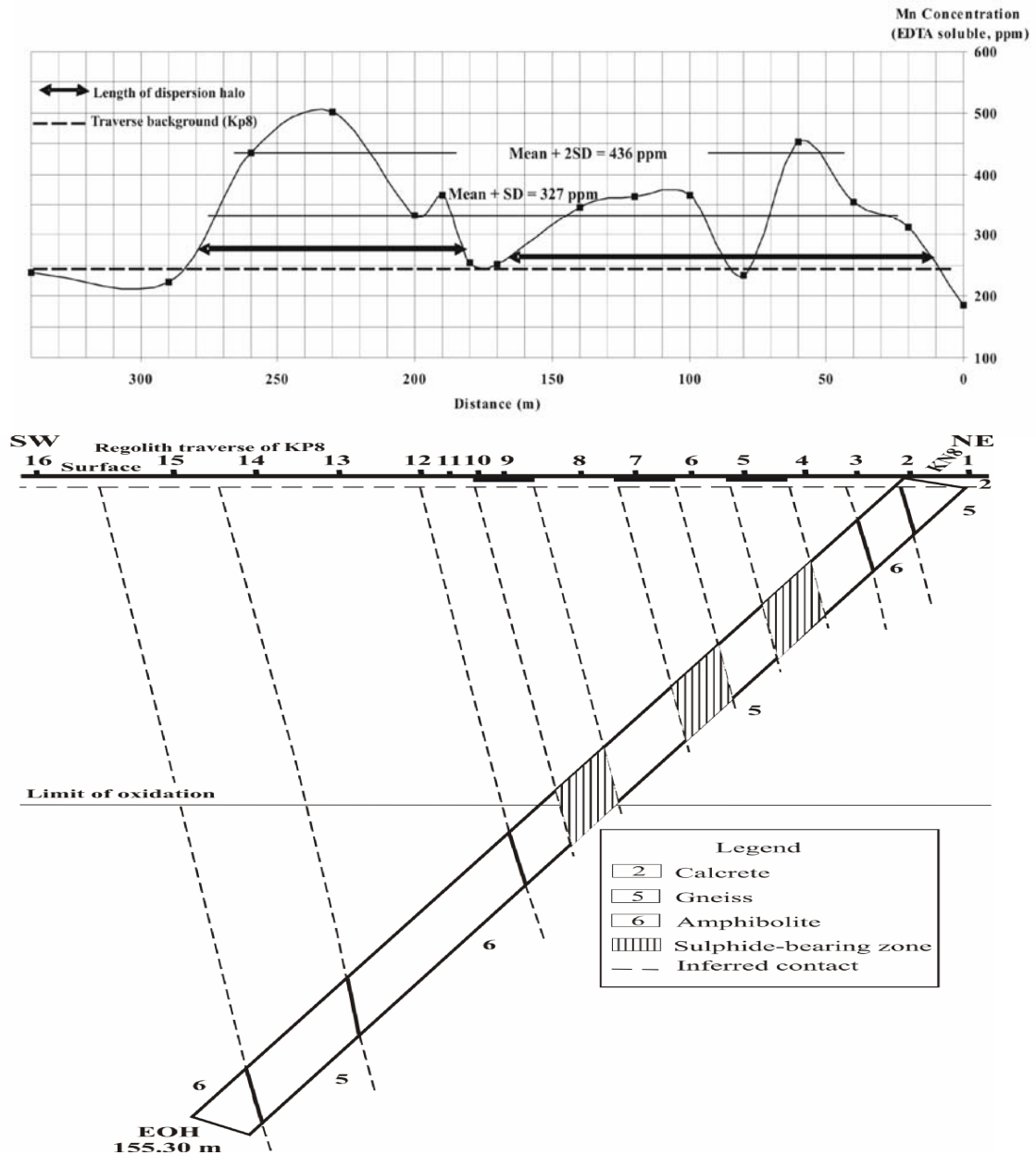


Figure 6.26: Variation of Cu (A) and Zn (B) in the regolith traverse KP8 based on ICP-MS analysis (using  $\text{NH}_4\text{EDTA}$  solutions and 180-minutes shaking times).



**Figure 6.27:** Variation of Mn in the regolith traverse KP8 based on ICP-MS analysis (using  $\text{NH}_4\text{EDTA}$  solutions and 180-minutes shaking times).

The ore zone's location at surface is clearly defined by the Cu, Zn and Mn concentrations determined from the  $\text{NH}_4\text{EDTA}$  solution by ICP-MS analyses.

Results of ICP-MS analyses of the extractable Cu, Zn, Pb and Mn concentrations in the regolith traverse T1 at Areachap, located slightly further away from the ore zone, are shown in Figures 6.28 and 6.29. The cross section shows the location of regolith samples and the nature of the underlying geology. Based on the calculated threshold value for Cu (8339 ppb, Figure 6.28 A), there are no anomalous samples, but based

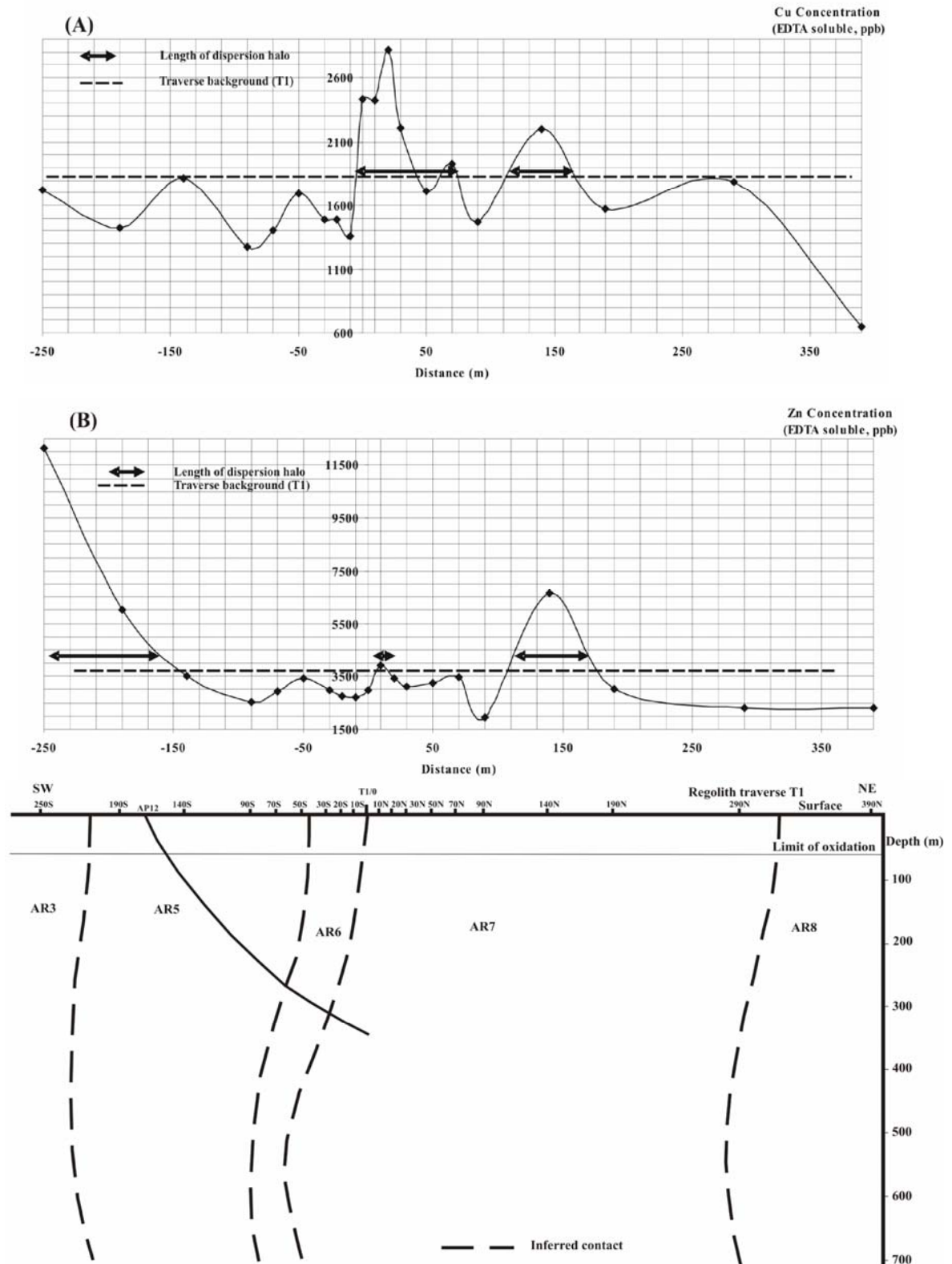


**Figure 6.28:** Variation of Cu (A) and Zn (B) in the regolith traverse T1 based on ICP-MS analysis ( $\text{NH}_4\text{EDTA}$ , 180-minutes shaking times).

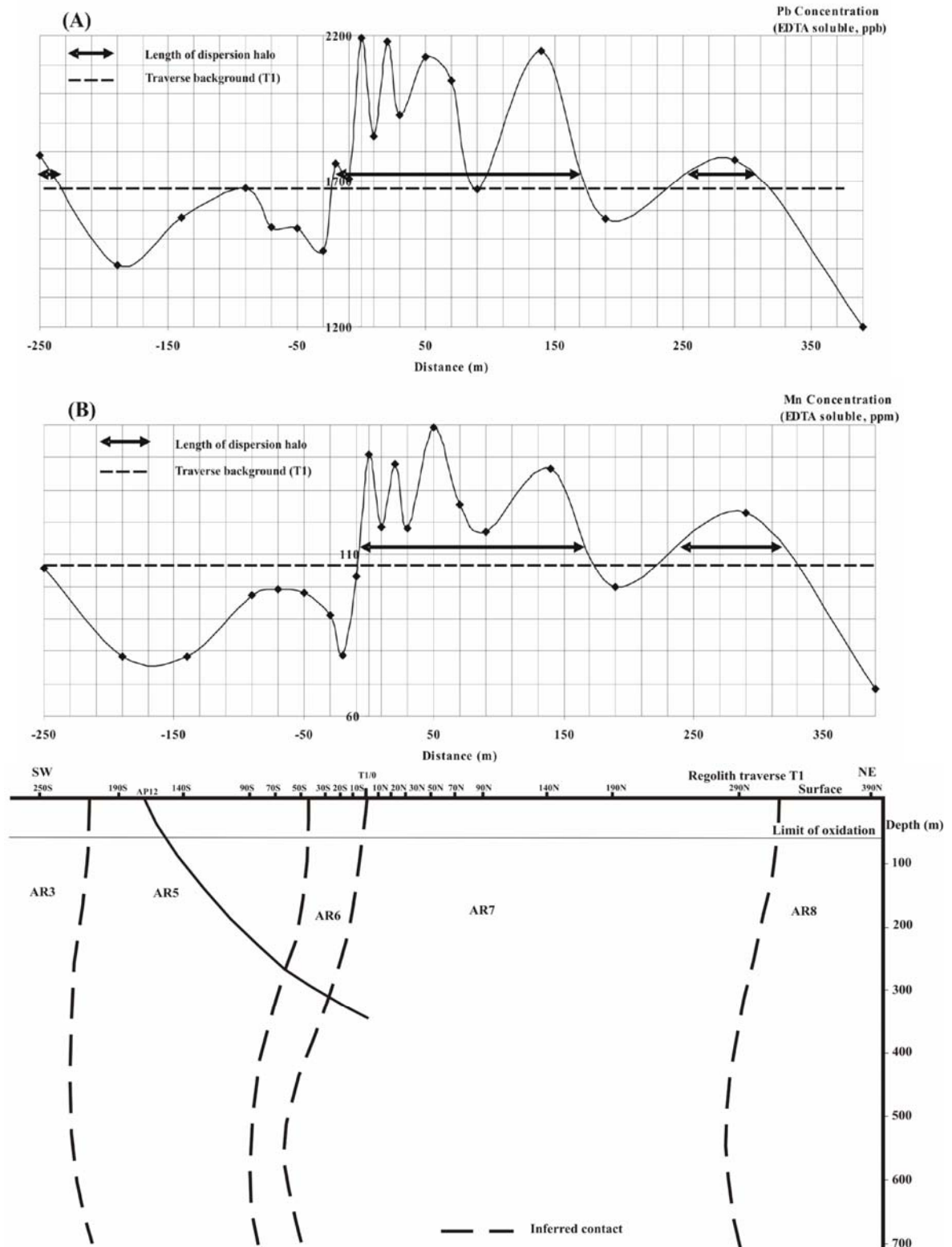


**Figure 6.29:** Variation of Pb (A) and Mn (B) in the regolith traverse T1 based on ICP-MS analysis ( $\text{NH}_4\text{EDTA}$ , 180-minutes shaking times).

on the traverse background values there is a peak from 0 to 70 m distance above the host rocks. Another peak occurs at 140 m, above the biotite-hornblende-gneiss which has a whole rock Cu concentration of 779 ppm (unit AR7; Theart, 1985).

In Figure 6.28 B, the variation of Zn is shown, with a calculated threshold value of 13891 ppb. No anomaly could be identified above the ore zone (AR6). Zn contents increase from 2000 to 6000 ppb at 140 m (unit AR7 with Zn contents from 5 to 446 ppm), and to 12134 ppb at -250 m (unit AR3, with Zn content 76 ppm).

The variation of Pb is shown in Figure 6.29 A. The calculated threshold value is 3862 ppb Pb. No anomalous sample was identified. Based on the traverse background value, two peaks occur from -20 to 170 and at 290 m, located above the biotite-hornblende-gneiss rock with a whole rock Pb concentration varying from 8 to 47 ppm (unit AR7; Theart, 1985).

Figure 6.29 B shows the variation in Mn with a calculated threshold value of 171 ppm. No anomalous samples were identified. Based on the traverse background value, Mn contents show two peaks, one from -10 to 170 and the other at 290 m distance. These are peaks above the biotite-hornblende-gneiss rock (unit AR7) that may be a metasedimentary rock.

Based on the information available (Voet and King, 1986), this traverse was designed to sample the regolith above the host rock unit (AR6), away from the ore zone in a NE-SW direction. The element concentrations are lower than the anomalous values, and they only show an increasing trend above the stratigraphic extension of the host rock lithology.

Figure 6.30 and 6.31 show variation in the results of ICP-MS determinations of the following elements Cu, Zn, Pb and Mn from the regolith traverse T3, located between traverses T1 and T2. Sample 0 is T1/0 and sample 240 is T2/0 and the traverse overlies the host rock unit (AR6). Borehole AP8 cuts through the ore zone and the projection of the ore zone at the surface is located near the end of this traverse. The locations of regolith samples are also indicated on the cross section. In Figure 6.30, the variation in the concentration of Cu and Zn are shown for ICP-MS results. Based on the calculated threshold value of Cu (8339 ppb, Fig. 6.30 A) there are an anomalous area from 180 to 240 m. Based on the local background for Zn (5000 ppb) in traverse T3 (Fig. 6.30 B) there is an increasing trend in the Zn concentration from 160-m to the end of the traverse.

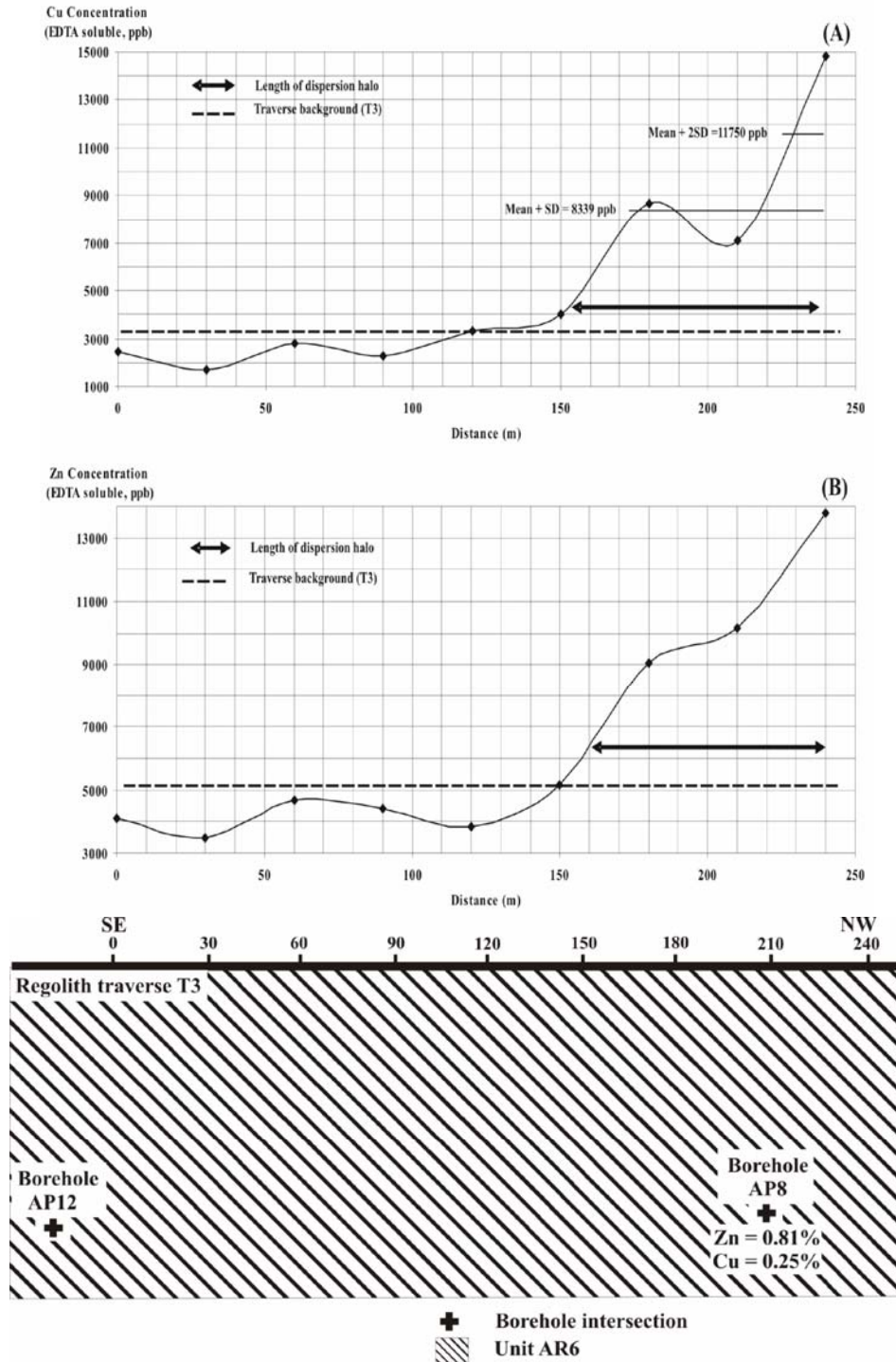


**Figure 6.30:** Variation of Cu (A) and Zn (B) in the regolith traverse T3 based on ICP-MS analysis (NH<sub>4</sub>EDTA, 180-minutes shaking times).

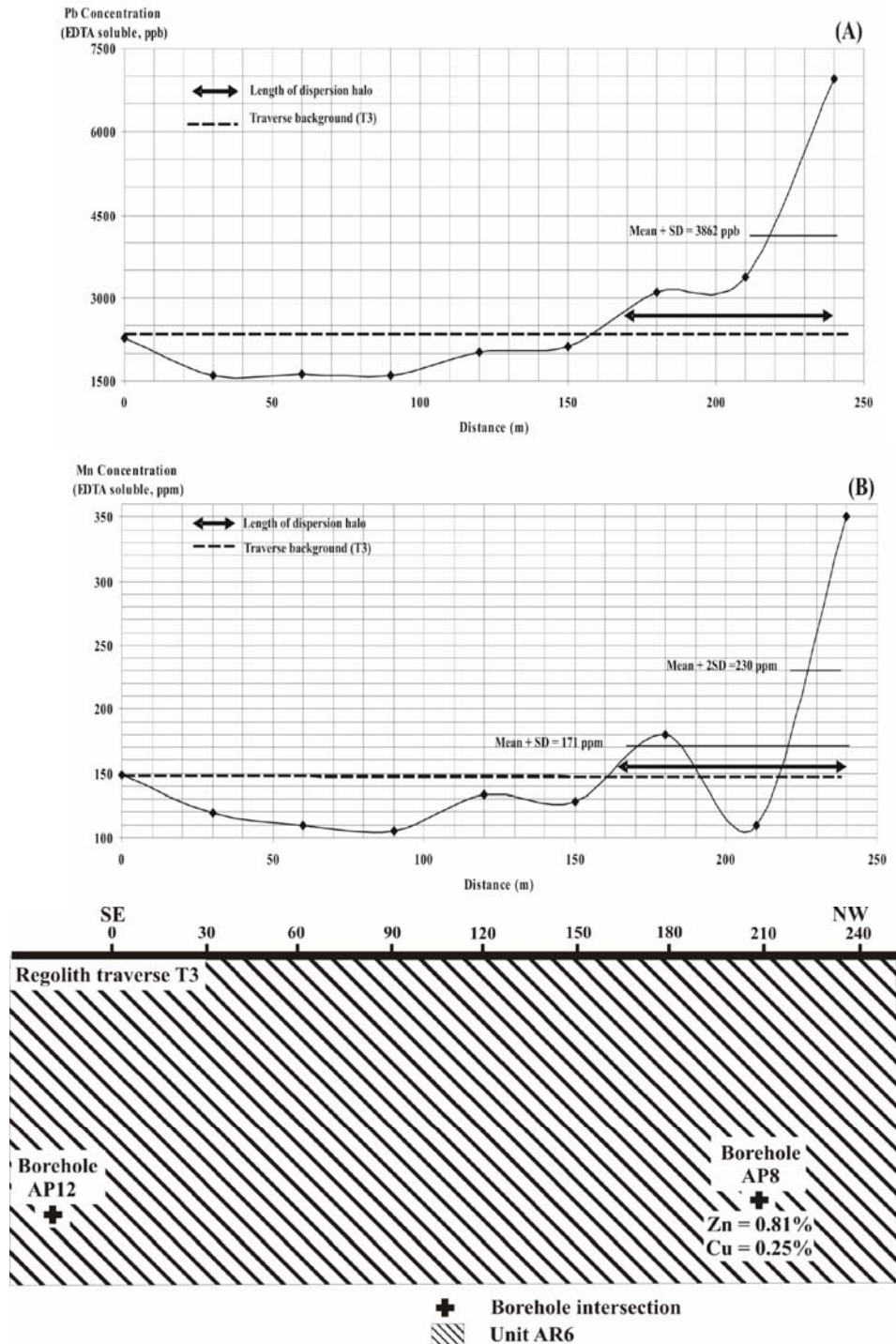


**Figure 6.31:** Variation of Pb (A) and Mn (B) in the regolith traverse T3 based on ICP-MS analysis (NH<sub>4</sub>EDTA, 180-minutes shaking times).

Pb contents are anomalous in samples from 220 to 240 m (calculated threshold value 3862 ppb, Fig. 6.31 A) and Mn contents (calculated threshold value 171 ppm, Fig. 6.31 B) from 170 to 240 m. Based on the traverse background, the peak area extends from 160 to the ore zone at 240 m for both Pb and Mn.

Variations of all elements show an increasing trend and anomalous values towards the ore zone at the end of the traverse. This corresponds to a dispersion halo in this direction of approximately 70 m.

### **6.6.3. Discrimination of the secondary dispersion haloes (MMI results, Kantienpan)**

The variations in the concentration of Cu and Zn in samples from the regolith traverse 7800NW are plotted in Figure 6.32. As this regolith traverse is close to the cross section of KN11 (Fig. 6.3), the profile derived from this drill hole will be used for the interpretation. Cu shows anomalous values from 1200 to 1225 m. Zn values are anomalous from 1100 to 1250 m. Based on the traverse background, this anomaly starts from 1300 m.

The secondary dispersion haloes of these two elements are coincident. Zn shows a wider halo when compared to Cu, as could be expected because of the higher known mobility of Zn in the secondary environment.

Figure 6.33 shows the variation of Cu and Zn concentrations of samples from the regolith traverse 7700NW. Due to the proximity of this regolith traverse to drill hole KN5 (Fig. 6.3), the profile derived from this drill hole will be used for the interpretation. It can be seen that Cu shows five anomalous peaks at 1100 m, 1175 m, 1250 m, 1300 m and 1425 m. Zn shows a very sharp anomalous peak at 1225 m. Based on the traverse background, elevated values start from 1225 and ends at 1350 m. There is another small peak in the Zn concentrations towards the left end of this traverse, located above the weathered amphibolite rocks with 4 to 359 ppm Cu in the whole rock samples (unit 6 in the cross section).

The sinuous nature of the variation in Cu concentrations makes it difficult to distinguish the exact location of the anomaly. Zn variation defines a better anomalous zone above the assumed projection of the ore deposit.

Taking these results into account the variation in Zn concentration is better suited for the identification of the location of the ore zone than that of Cu. The results of the MMI method will be compared to the other partial extraction and total analyses

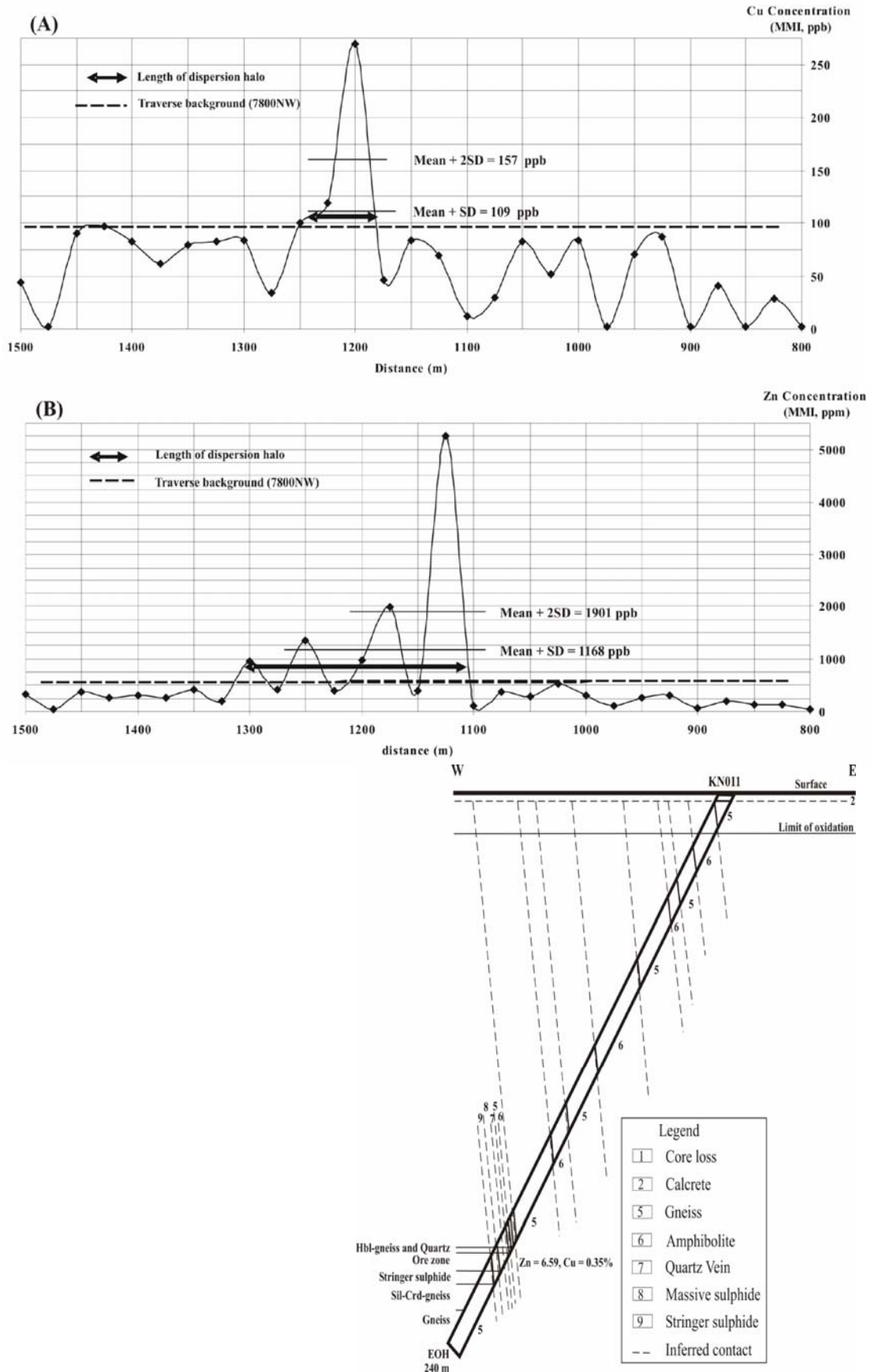


**Figure 6.32:** Variation of Cu (A) and Zn (B) in the regolith traverse 7800NW, MMI method (Sil: sillimanite; Crd: cordierite and Hbl: hornblende)

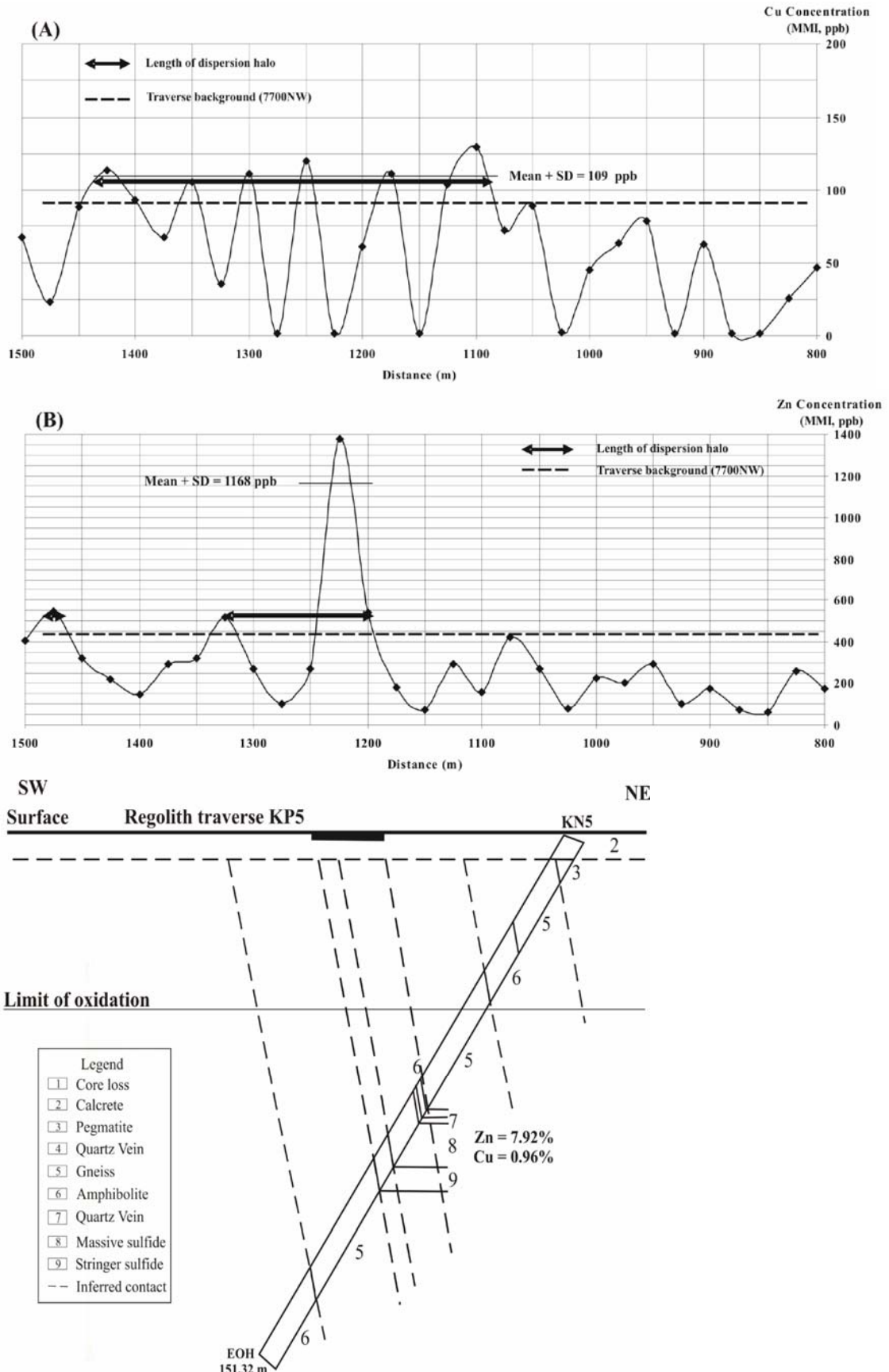


Figure 6.33: Variation of Cu (A) and Zn (B) in the regolith traverse 7700NW, MMI method.

techniques in the next section.

#### 6.6.4. Comparison of NH<sub>4</sub>EDTA, MMI and XRF methods

Different analytical methods such as total analysis by XRF and partial analyses using the MMI technique and NH<sub>4</sub>EDTA extractions analyzed by ICP-MS were used in previous sections to identify anomalous sand samples located above buried sulphide mineralization. To compare the results, the peak to background ratio is calculated for comparison in Table 6.21, where the background value is estimated for the individual length of the traverse. The dispersion halo for Zn as determined from the MMI results shows a larger span, followed by ICP-MS and finally XRF. For the Cu halo, the NH<sub>4</sub>EDTA method exhibits the largest span then XRF and then MMI. The largest span for Mn is shown by NH<sub>4</sub>EDTA (ICP-MS) method followed by XRF. The XRF method shows the largest span for Pb and S in comparison to NH<sub>4</sub>EDTA (ICP-MS).

In some cases the peak to background ratio is high (KP12, NH<sub>4</sub>EDTA for Pb, etc), but the length of the dispersion halo is small. In reconnaissance exploration, the size of the dispersion haloes is more important than the peak to background ratio. Cu and Zn show the widest dispersion haloes when compared to those of other elements and oxides.

**Table 6.21:** Anomaly to background ratio of different analytical methods for Cu, Zn, Pb, Mn and S

Analytical Method	Regolith Traverse	Element (unit)	Background Value	Peak Value	P/B ratio <sup>1</sup>	Length of dispersion halo (m)
XRF	KP12	Cu (ppm)	25	33	1.32	50
		Zn (ppm)	104	138	1.33	110
		Pb (ppm)	17	22	1.29	110
		MnO (%)	0.1	0.12	1.20	75
		S (ppm)	22	205	9.32	110
	T2	Cu (ppm)	28	86	3.07	130
		Zn (ppm)	93	174	1.87	70
		Pb (ppm)	23	53	2.30	100
		MnO (%)	0.07	0.12	1.71	80
		S (ppm)	220	1900	8.64	80
NH <sub>4</sub> EDTA (ICP-MS)	KP12	Cu (ppb)	3750	5500	1.47	70
		Zn (ppb)	5500	9552	1.74	70
		Pb (ppb)	8	120	15	25
		Mn (ppm)	109	191	1.75	110
		S (ppm)	20	182	9.10	25
	T2	Cu (ppb)	4500	34590	7.69	170
		Zn (ppb)	9600	33638	3.50	160
		Pb (ppb)	3400	7327	2.16	150
		Mn (ppm)	62	346	5.58	70
		S (ppm)	11	20	1.82	110
MMI	7700NW	Zn (ppb)	445	1380	3.10	125
	7800NW	Zn (ppb)	650	5265	8.10	200
		Cu (ppb)	90	270	3	50

Note: 1: peak to background ratio; Background = traverse background value

This study came to different conclusions regarding the size of the dispersion halo that can be detected at the two investigated deposits. At Kantienpan were the sand cover is

very shallow to absent, dispersion appears to be related to the secondary redistributions of gossaniferous clasts rather than dispersion of mobile metal ions on the surface of sand particles. The total analytical approach (XRF method) shows a wider dispersion halo than methods based on partial extraction. Whereas, at Areachap, where relatively thick sand (approximately one meter) covers the calcrete layer, partial extraction (based on a  $\text{NH}_4\text{EDTA}$  solution) results in a larger, recognizable, dispersion halo than that, that could be detected by total analysis (XRF).

### **6.7. Dispersion of the elements of interest in the calcrete environment**

Vermaak (1984) studied the calcrete in the Areachap, Copperton, Jacomynspan and Hartebeestpan areas and the following conclusions were derived from his findings:

- Calcretes associated with the gossan above the ore zone display anomalous ore-related element concentrations (Cu, Zn and Pb).
- Dispersion of the ore-related elements is largely restricted to the calcrete directly overlying the ore zone.
- The concentration of the ore-related elements increase with depth above the ore zone.
- Calcrete with gossan inclusions, where the gossan was removed by hand picking, shows elevated concentrations of the ore-related elements.
- That the ore related elements are weakly dispersed in the calcite, but are concentrated in the other constituents of the calcrete as confirmed by comparing XRF analyses with the analyses of the HCl soluble component by atomic absorption.
- EDTA extractions does not effectively discriminate between samples with a high total Cu, Zn and Pb contents based on XRF analyses.

The current investigation intends to the further study of the calcretes by establishing the actual host of the elements of interest such as Cu, Zn, Pb and S in the calcrete environment. The question asked is if these elements are dispersed into the calcrete itself, or if they are confined to the distribution of gossan inclusions. Should the former be the case, calcrete may have to be sampled in future geochemical exploration programmes. On the other hand, the identification of gossan material may be regarded as an alternative to indication of the presence of concealed mineralization. In this regard it is important to

refer to the study of McQueen et al. (1999) where it was found that Au could be found in the low Mg-calcite of calcrete from southeastern Australia.

The calcrete of this area is mainly composed of a calcite (low Mg), and quartz as determined by XRD (Table 6.23). The calcite is expected to buffer surface water at relatively high pH conditions and therefore lower the solubility of base metals, limiting the mobility of these elements (Cu, Zn and Pb). In their experiment Mann et al. (1995) and Mann et al. (1997) have shown that varying quantities of calcium carbonate placed artificially as a single layer on top of sand does not prevent the solution from transmitting a base metal anomaly from the underlying material to the overlying sand. In the current study, this finding is tested under natural conditions where the anomaly related to the weathered massive sulphide deposit is separated from overlying eolian sand by a calcrete layer of substantial thickness.

The objective of sampling the calcrete is to investigate if these metals may remain sufficiently mobile in the groundwater of the secondary environment to be transported to surface under these high pH conditions. For this the variations in the concentration of the elements of interest in the calcrete layer are investigated with depth.

### **6.7.1. Kantienpan calcrete samples**

To investigate the mobility of the elements of interest in the calcrete, it is important to discriminate between the base metals contained in gossan clasts in the calcrete and those dispersed in the calcrete itself. Two possible ways by which the calcrete and gossan fragments could be investigated separately were considered here, namely selective dissolution as done by Vermaak (1984) and physical separation using magnetic properties. Because of the potential contamination of the chemical solutions by these elements contained in materials displaying variable solubility under different physical condition that effect the solution, it was decided to investigate the dispersion of the ore related elements in the calcite part of the calcrete. It is unpractical to determine the concentrations of elements of which the abundances are in the parts per million range by microprobe analysis. It was therefore decided to analyze the calcrete by XRF after the physical separation of the calcite rich portion from the gossan rich material. For this purpose, the magnetic component of the calcrete sample was separated first by hand sorting and then by using a hand magnet followed by a Frantz

isodinamic magnetic separator (see Appendix D for detail). The results of the XRF analysis on the magnetic and non-magnetic parts of sample KP12/4 are given in Table D.19 (Appendix D). Assuming that most of the Ca and Mg present in the sample would be in a carbonate form and the Ca and Mg contents (normally expressed as oxides) were recalculated as carbonates.

**Table 6.22:** The comparison of major and trace elements of interest in visually cleaned, magnetic and non-magnetic parts of calcrite sample KP12/4, Kantienpan (A: ampere)

Major (%)	Visually clean KPR 12/4	Non-magnetic part of sample			Magnetic part of sample				
		Completely clean		Clean <sup>1</sup>	Hand magnet	0.1A	0.3A	0.5-0.9A	1.1-1.7A
		Non-Mag1	Non-Mag2	Non-Mag3	Mag1	Mag2	Mag3	Mag4	Mag5
CaCO <sub>3</sub> *	70.25	71.09	75.00	71.36	75.75	71.29	72.80	72.73	72.46
SiO <sub>2</sub> *	18.43	16.84	13.84	15.56	12.67	12.71	12.42	13.79	14.69
TiO <sub>2</sub> *	0.22	0.09	0.1	0.15	0.21	0.51	1.1	0.98	0.53
Fe <sub>2</sub> O <sub>3</sub> *	1.52	0.74	0.74	1	1.61	9.99	3.2	3.3	2.14
MgCO <sub>3</sub> *	5.35	5.04	4.90	5.26	5.09	5.64	5.14	5.62	5.83
Al <sub>2</sub> O <sub>3</sub> *	2.54	1.99	1.91	2.05	1.91	1.92	1.94	2.35	2.66
Na <sub>2</sub> O*	0.23	0.24	0.24	0.23	0.23	0.27	0.27	0.28	0.28
K <sub>2</sub> O*	0.71	0.66	0.58	0.64	0.57	0.41	0.44	0.49	0.56
<b>TOTAL</b>	<b>99.25</b>	<b>96.69</b>	<b>97.31</b>	<b>96.25</b>	<b>98.04</b>	<b>102.74</b>	<b>97.31</b>	<b>99.54</b>	<b>99.15</b>
<b>Trace elements (ppm)</b>									
Cu	20	12	8	12	5	6	11	14	13
Pb	4	3	3	6	3	16	3	4	3
Zn	45	42	39	52	42	70	86	68	62
S*	513	578	363	1142	446	289	300	299	329
V	35	16	18	19	37	305	72	63	46

Note: KPR12/4 is the original sample, \*: semi-quantitative analysis, 1: Cleaned by hand magnet

The fact that the recalculated total sum of major elements shown in Table 6.22 is much closer to the ideal 100% shows that this is a valid assumption. These samples contain 70.25 to 75.75% CaCO<sub>3</sub>, 12.4 to 18.4% SiO<sub>2</sub>, 0.74 to 10% Fe<sub>2</sub>O<sub>3</sub>, 5.04 to 5.83% MgCO<sub>3</sub> and 1.9 to 2.7% Al<sub>2</sub>O<sub>3</sub> as based on semi-quantitative major element XRF powder analyses. In terms of trace elements, non-magnetic parts (sample Non-Mag1 and 3) have the highest concentration of S (Table 6.22). However, in some of the other samples higher S contents were observed in the magnetic fractions (KP12/2 and KP12/3, Table 6.24) and it must be concluded that the results on the S distribution remains inconclusive. The magnetic separate has higher Zn, Cu, Pb and V contents when compared to the original and non-magnetic samples (Table 6.22). Based on the results of this table, the Frantz isodinamic magnetic separator did not give a significant improvement on the purity of the calcite rich material separated visually. The sample cleaned with the Frantz separator (Non-Mag 1 and 2) does not result in a marked improvement when comparing its composition with the visually cleaned sample (KP12/4, after hand separation). It was decided to use only visually

cleaned calcrete material for further investigation, since these results would also be easy to reproduce and cost efficient during an exploration campaign.

To identify the mineralogy of the calcrete sample in the magnetic and non-magnetic parts, and to also identify the host mineral of the elements of interest, XRD analyses were done on both magnetic and non-magnetic parts of the separate and the results are listed in Appendix E. The different minerals present in the magnetic and non-magnetic parts of a calcrete sample KPR12/4 as determined by quantitative XRD are given in Table 6.23.

**Table 6.23:** The different minerals in the visually cleaned, magnetic and non-magnetic parts of a calcrete sample (KPR12/4, Kantienpan) as determined by quantitative XRD.

Sample	Cal	Q	Mc	Ab	Ms	Ilm	Hem	Mgt	Act	Reference
<b>KPR12/4</b>	77.09	13.10	2.84	4.20	2.78	-	-	-	-	Original Sample
<b>Non-Mag 1</b>	75.59	12.17	5.51	4.96	1.77	-	-	-	-	Reza2
<b>Non-Mag 2</b>	75.15	11.69	6.45	4.39	2.32	-	-	-	-	Reza12
<b>Non-Mag 3</b>	73.21	13.91	6.05	4.72	2.11	-	-	-	-	Reza1
<b>Mag 1</b>	77.24	10.36	5.61	4.89	1.55	-	-	0.35	-	Reza13
<b>Mag 2</b>	78.04	9.75	4.85	1.88	0.87	-	1.73	2.56	-	Reza3
<b>Mag 3</b>	77.92	9.24	3.93	5.05	2.09	0.9	-	-	0.44	Reza4
<b>Mag 4</b>	78.89	7.52	3.75	5.93	1.88	0.87	-	-	1.17	Reza5
<b>Mag 5</b>	75.65	8.70	5.78	6.46	2.89	0.23	0.29	-	-	Reza6

Cal: calcite, Q: quartz, Mc: microcline, Ab: albite, Ms: muscovite, Ilm: Ilmenite, Hem: hematite, Mgt: magnetite, and Act: Actinolite

The non-magnetic part of the sample contains calcite, quartz and alkali feldspars, whereas the magnetic part of sample comprises calcite and some quartz and alkali feldspars together with the hematite and magnetite minerals (Table 6.23). This is most probably due to the difficulty of liberating the different minerals in the calcrete material. Table 6.23 demonstrates that albite and microcline are concentrated in the non-magnetic fractions. Calcite is present in both the magnetic and non-magnetic fractions of the sample. Quartz, relative to calcite, is more abundant in the nonmagnetic fraction. Magnetite and hematite, presumably related to the gossan component of the sample, are extracted in the first and second magnetic separates. Ilmenite and actinolite are present in the higher current magnetic fractions of the calcrete sample in very low concentrations. Cu is associated with the iron oxides, but

seems to be dispersed in the rest of the sample as well. This conclusion is substantiated by the results of the other samples (Table 6.23), showing that Cu may be concentrated in the hematite/magnetite (iron rich) components of the samples. Distribution of Zn appears to be more strongly related to the distribution of magnetite, although some of the Zn may also be dispersed in the other iron-bearing fractions of the sample. Pb may be directly associated with the distribution of magnetite in Table 6.22. But the abundance of Pb is low in the other samples (Table 6.24) and no significant conclusion could be reached. Finally, the distribution of V appears to be strongly related to the distribution of magnetite (Tables 6.22 and 6.24).

The variation of major oxides and trace elements for the visually cleaned calcrete samples taken from the surface at Kantienpan are given in Table 6.24.

**Table 6.24:** The comparison of major oxides and trace elements of interest in visually cleaned parts of calcrete samples in the Kantienpan (A: ampere and \*: semi-quantitative analyses)

Major elements(%)	Visually clean calcrete samples					
	Major oxides (%)					
	KPR12/1	KPR12/2	KPR12/3	KPR 12/4	KPR12/5	KPR12/6
CaCO <sub>3</sub> *	77.32	78.88	83.27	70.25	70.93	79.20
SiO <sub>2</sub> *	14	11.79	9.44	18.43	16.59	11.34
TiO <sub>2</sub> *	0.1	0.15	0.12	0.22	0.19	0.16
Fe <sub>2</sub> O <sub>3</sub> *	0.79	1.48	1.54	1.52	2.31	3.05
MgCO <sub>3</sub> *	6.02	6.07	4.15	5.35	5.95	4.15
Al <sub>2</sub> O <sub>3</sub> *	1.22	1.68	1.23	2.54	2.42	2.01
Na <sub>2</sub> O *	0.18	0.19	0.19	0.23	0.24	0.2
K <sub>2</sub> O *	0.33	0.51	0.29	0.71	0.72	0.45
<b>TOTAL</b>	99.96	100.75	100.23	99.25	99.35	100.56
Trace elements (ppm)						
Cu	9	19	32	20	17	49
Pb	3	5	9	4	7	4
Zn	40	95	117	45	62	210
S*	532	488	601	513	469	495
V	26	28	28	35	37	60

These samples contain 70.25 to 83.27 % of CaCO<sub>3</sub>, 9.4 to 18.43 % SiO<sub>2</sub>, 1.22 to 2.54 % Al<sub>2</sub>O<sub>3</sub>, 4.15 to 6.07 % MgCO<sub>3</sub> and 0.79 to 2.31 % Fe<sub>2</sub>O<sub>3</sub> contents based on semi-quantitative XRF powder analyses. Samples KP12/3 and KP12/6 are from the gossan-bearing zone, and shown the highest Cu, Zn, S and V contents as determined by quantitative (Cu, Zn and V) and semi-quantitative (S) XRF analyses.

### 6.7.2. Areachap calcrete samples

To investigate the variation of selected trace elements in the calcrete layer, two profiles were sampled (grab samples) in the calcrete layer as exposed in an old

excavation at the Areachap deposit (Fig. 6.34 A and B). A gossan zone with malachite-filled veinlets occurs at the bottom of this layer (Fig 6.34 C). The gossan zone at Areachap display fractures filled with what appears to be Dwyka tillite. If this is the case it would imply that the gossan formed before the denudation as result of the glaciation at the onset of the Karoo sedimentation. Following the erosion of the Karoo sediments the entire area was covered with a thick layer (three to six meters) of calcrete, which in turn is overlain by wind blown Kalahari sand deposits. Within the calcrete layer, there are blocks and fragments of the silicified gossan material, distributed from the bottom of the layer to surface. The sampling profiles were positioned so as to avoid the larger gossan fragments.

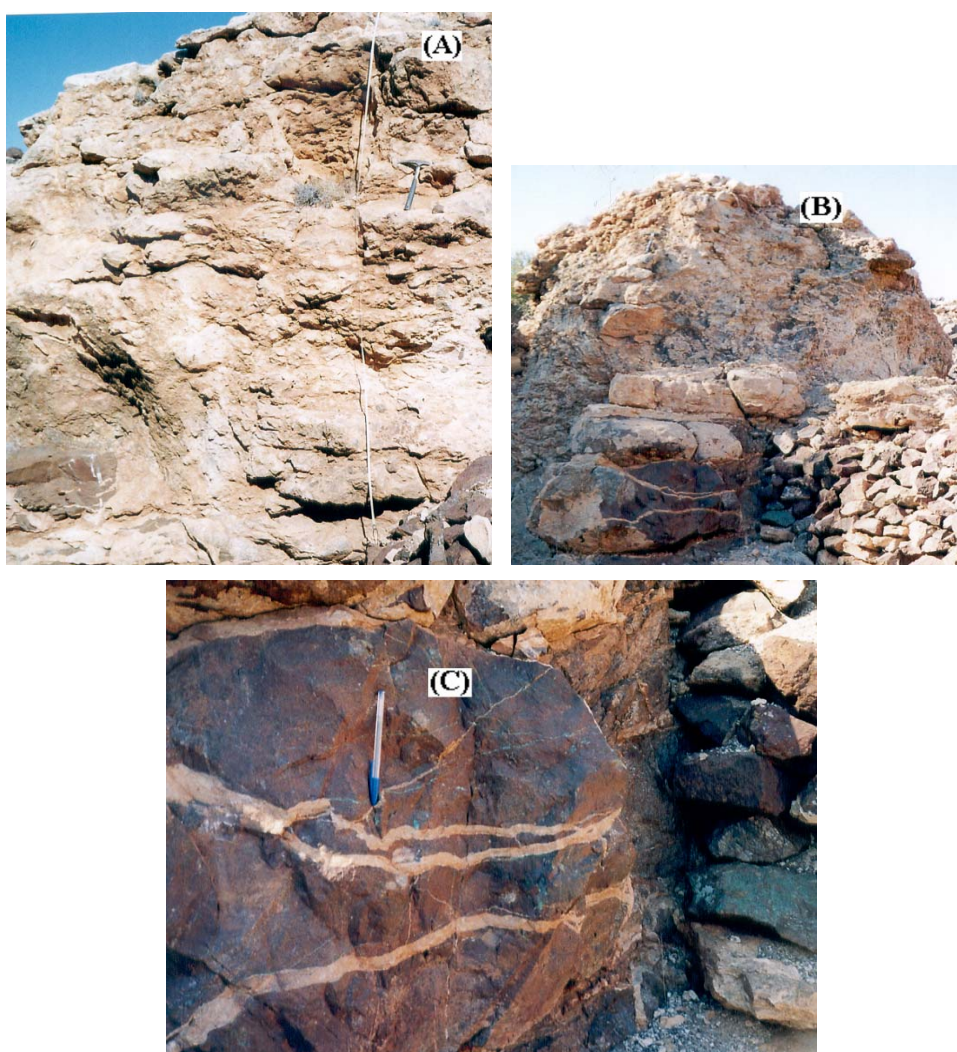


**Figure 6.34:** The calcrete layer in an old excavation at Areachap. Calcrete profile Calc1 (A), Calc2 (B) and a gossan rock with malachite and calcrete-filled veinlets at the bottom of calcrete layer (C).

XRF results of the original and magnetic separates of one of these profiles (Calc1) are given in Table D.22 (Appendix D). In Figure 6.35, the variation of major oxides versus depth is shown for the non-magnetic parts of the original samples (visually clean calcrite). They are composed of 54.98 to 83.34 %  $\text{CaCO}_3$ , 10 to 26.52 %  $\text{SiO}_2$ , 1.43 to 6.24 %  $\text{Al}_2\text{O}_3$ , 3.36 to 5.69 %  $\text{MgCO}_3$  and 0.91 to 4.77 %  $\text{Fe}_2\text{O}_3$  based on semi-quantitative XRF powder analyses.

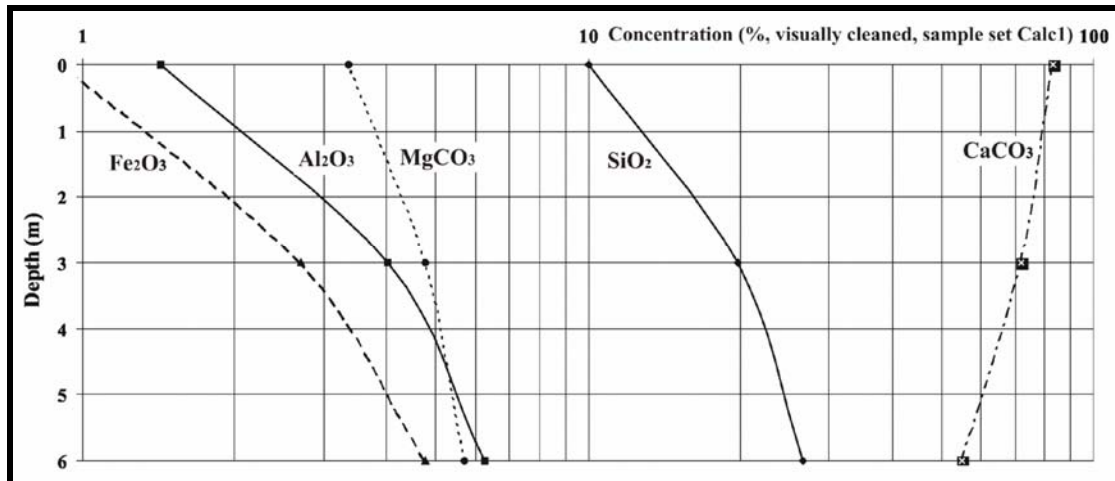


**Figure 6.35:** Major oxides variation versus depth in the Areachap calcrite layer (visually cleaned samples referred to as Calc1).

The variations of Cu, Zn, Pb and S as determined by quantitative (Cu, Zn and Pb) and semi-quantitative (S) XRF analyses versus depth in original calcrite samples (visually clean calcrite) for the same sample profile (Calc1) are shown in Figure 6.36. Based on this figure, Cu, Zn and Pb contents increase with depth. The concentrations of these elements are therefore much lower at surface than deeper down the calcrite profile. It may be concluded that the peak to background ratio of anomalies in surface samples would depend on the thickness of the underlying calcrite layer. S does not show the same trend as Cu, Zn and Pb. This may be explained by the presence of different types of sulphur phases in the sample, i.e., sulphates as a result of ground water compositions and the evaporation processes and sulphates as remnants of the oxidized primary sulphide minerals. It should also be considered that sulphates may accumulate in the surface environment due to the interaction of rain water, groundwater and evaporation processes such as seen in pan formation. This may result in false S anomalies not related to underlying sulphide mineralization.

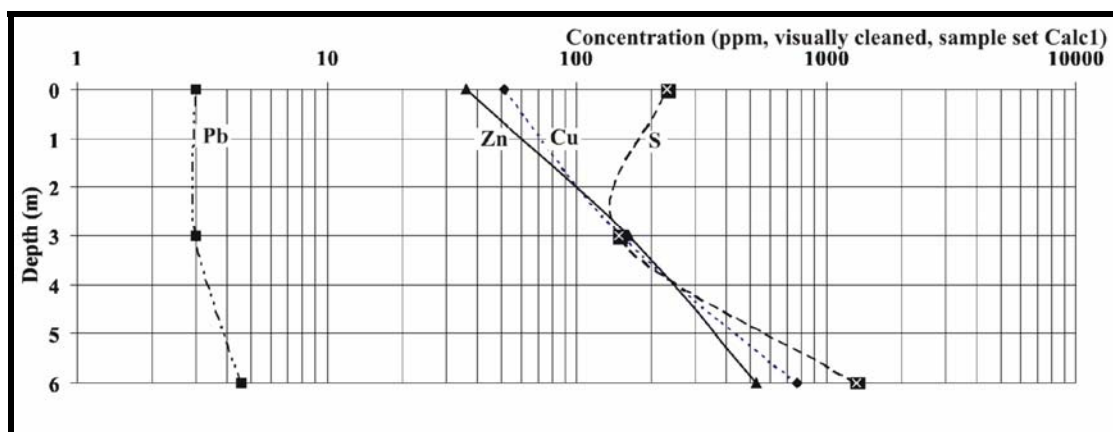


**Figure 6.36:** Variation of Cu, Zn, Pb and S versus depth in the Areachap calcrete layer, (visually cleaned samples referred to as Calc1).

Figure 6.35 and 6.36 display an increasing trend of trace elements (Cu, Zn and Pb) and major oxides such as  $\text{Al}_2\text{O}_3$ ,  $\text{MgCO}_3$ ,  $\text{SiO}_2$  and  $\text{Fe}_2\text{O}_3$  with depth. This may be seen as evidence that the calcrete formation was superimposed on a weathered soil profile and that the calcrete does not merely represent calcretized Kalahari sand. This interpretation is also supported by the observation that gossan clasts are enclosed directly above the ore zone in the calcrete over the entire thickness of the calcrete layer. It is expected that the primary mineral phases present would be the same as determined for Kantienpan namely calcite, quartz, albite and microcline.

The chemical composition of calcrete in sample set Calc2 in the Areachap area are given in Table D.23 (Appendix D). In Figure 6.37, the variation of major oxides versus depth in this area is shown (original samples). They contain 48.89 to 63.89 %  $\text{CaCO}_3$ , 8.12 to 25.8 %  $\text{SiO}_2$ , 1.41 to 11.36 %  $\text{Fe}_2\text{O}_3$ , 1.68 to 7.3 %  $\text{Al}_2\text{O}_3$  and 3.22 to 6.55 %  $\text{MgCO}_3$  contents based on semi-quantitative XRF powder analyses.

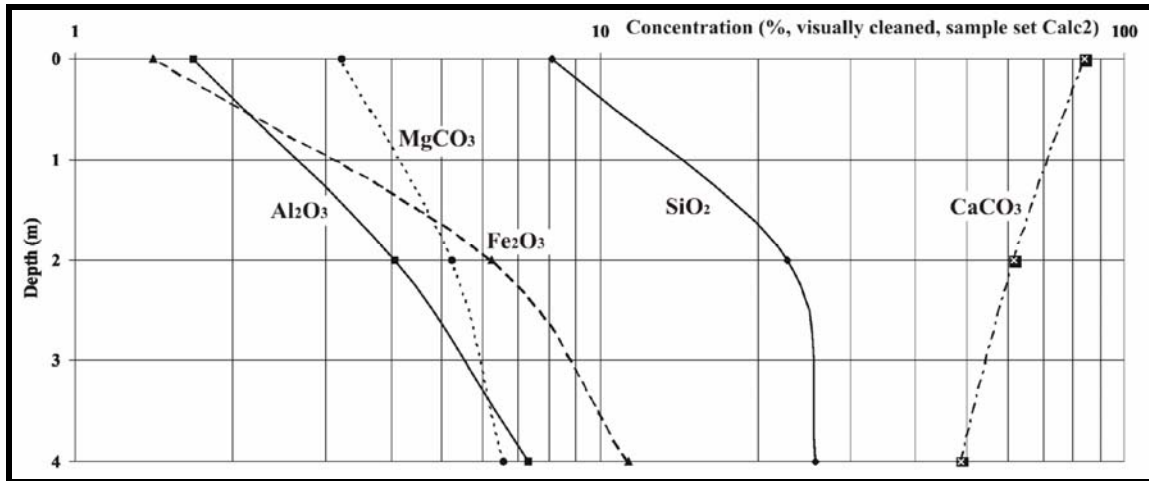


**Figure 6.37:** Major oxides variation versus depth (visually cleaned samples referred to as Calc2) in the Areachap.

The variations of trace elements in the original samples are demonstrated in Figure 6.38 (for sample set Calc2) as determined by quantitative (Cu, Zn and Pb) and semi-quantitative (S) XRF analyses. Based on this figure, Zn and Pb contents increase with depth, but Cu and S contents decrease. The highest content of S occurs at the surface and the lowest content at a depth of 4 m. Trace elements, such as Pb and Zn, and major oxides, i.e.  $\text{Al}_2\text{O}_3$ ,  $\text{MgCO}_3$ ,  $\text{SiO}_2$  and  $\text{Fe}_2\text{O}_3$  show the same trend.

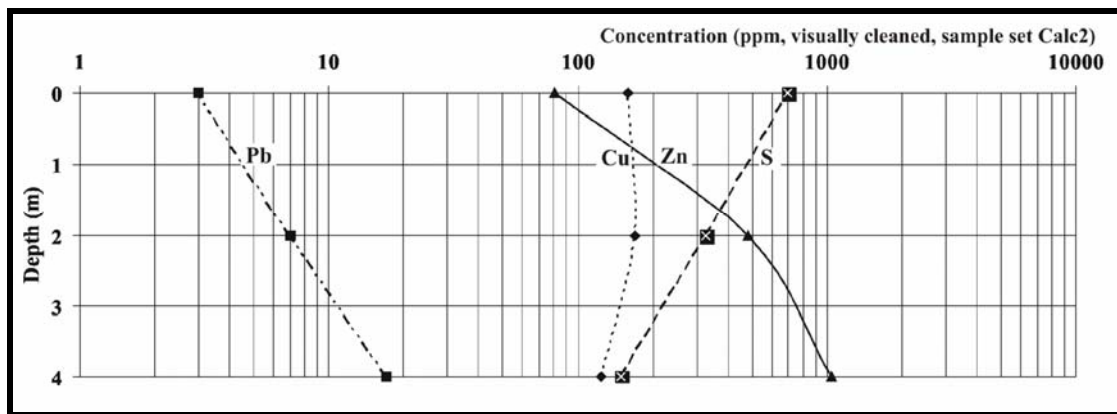


**Figure 6.38:** Variation of Cu, Zn, Pb and S versus depth in the calcrete layer, Areachap (visually cleaned samples referred to as Calc2).

The concentration of trace elements in calcrete samples at the surface therefore depends on the thickness of the calcrete layer in the area.

### 6.7.3. Comparison of calcretes close to the ore zone and further away

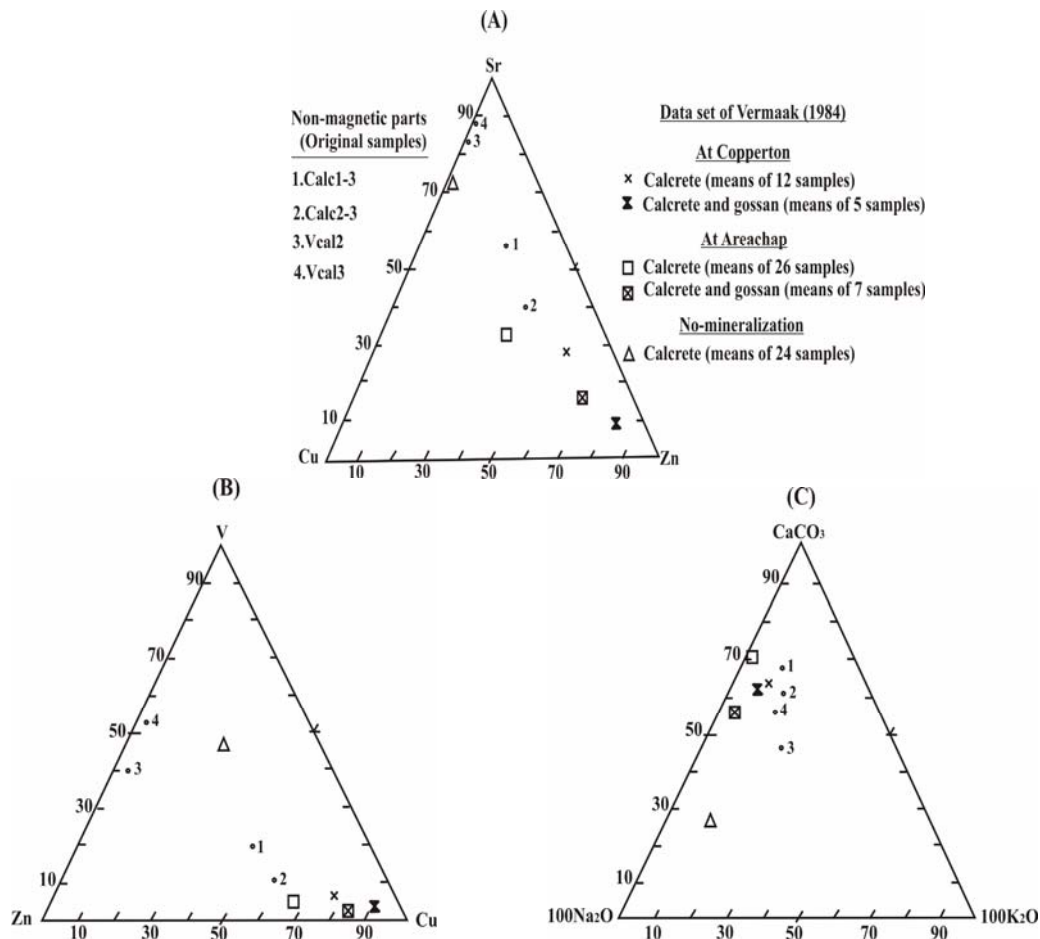
In this section the composition of calcrete samples collected from above the ore zone (anomalous samples, Calc1-3 and Calc2-3) are compared to samples (Vcal2 and Vcal3) that were collected away from any known mineralization (background samples). XRF results of these samples are given in Tables D.24 and D.25 (Appendix D). Some of the calcrete samples (Table D.26) provided by Vermaak (1984) from Areachap and Copperton Cu-Zn Mine and further away from the known mineralization are also used here. These samples include of the calcrete and complex calcrete, which are calcrete samples that contain gossan particles. The average values of the elements and oxides for these samples are used for plotting in the three angular diagrams.

In Table 6.25 the chemical composition of the original calcrete samples near the ore zone in the study area is compared to calcrete samples further away from the ore zone. In Figure 6.39, the chemical composition of original calcretes above the ore zone and data set of Vermaak (1984) is compared to that of those samples collected further away from the known mineralization. Based on this figure, the calcrete samples near the ore zone are enriched in  $\text{CaCO}_3$ , Cu and Zn and samples collected further away from the known mineralization are enriched in V and Sr. The latter samples have higher  $\text{Na}_2\text{O}$  and  $\text{K}_2\text{O}$  contents when compared to the calcrete samples close to the ore zone. Calcretes directly related to massive sulphide mineralization may be discriminated from those developed in areas away from the mineralization by plotting the V-Cu-Zn and Sr-Cu-Zn contents in triangular diagrams as presented in Figure 6.39, A and B.

**Table 6.25:** Chemical composition of visually cleaned calcretes near the ore zone (Calc1-3 and Calc2-3 at Areachap) and further away from the mineralized zone (Vcal2 and Vcal3)

Major oxides (%)	Original	Original	Original	Original
	calc1-3	Calc2-3	Vcal2	Vcal3
SiO <sub>2</sub> *	10.01	8.12	18.2	12.9
MgCO <sub>3</sub> *	3.36	3.22	7.44	7.44
CaCO <sub>3</sub> *	83.34	83.89	69.64	76.25
Na <sub>2</sub> O *	0.14	0.19	0.3	0.2
K <sub>2</sub> O *	0.25	0.33	0.5	0.4
Trace elements (ppm)				
Cu	52	159	2	2
Pb	3	3	3	3
Sr	114	158	149	236
Zn	36	81	29	30
S *	229	699	294	231
Sc	1	1	<1	<1
V	19	28	24	41
Depth	Surface	Surface	Surface	Surface

\*: Semi-quantitative analysis


**Figure 6.39:** Variation of trace elements (A and B) and major components (C) of calcrete samples close to ore deposit and further away from the mineralized zone.

It is concluded that the trace elements contents in soil or sand samples directly overlying the calcrete would depend to the thickness of the calcrete layer above the ore deposit. A very thick layer of calcrete may not allow for much dispersion of the elements of interest in trace elements in the surface sands. These elements may be concentrated in non-magnetic and magnetic part of calcrete. Based on this research, mineralogical composition of the non-magnetic part of the calcrete contains of calcite, quartz and microcline and the magnetic part comprises of magnetite, hematite, calcite and albite (at Kantienpan).

It could therefore be demonstrated that calcrete samples close to the ore zone have higher contents of Cu, Zn and  $\text{CaCO}_3$  when compared to the calcrete samples further away from the ore zone and lithochemical exploration programme based on the visually cleaned calcrete samples may therefore lead to the successful identification of underlying mineralization, but the dispersion of the elements of interest may be severely restricted.

It is however evident that these elements are available at the calcrete-sand interface and that these elements of interest could then be dispersed in the sand by ground and rain water as in the case of mobile metal ions.

## Chapter 7

### Discussions and Conclusion

During the course of this research, different applied geochemical techniques were employed to investigate and confirm the location of the Areachap and Kantienpan concealed ore deposits by analyzing rock and regolith samples. In the following sections these aspects would be addressed under:

- 1) The recognition of evidence for hydrothermal alteration in the footwall and hangingwall rocks related to VHMS ore deposits, and the use of this in regional lithogeochemical exploration.
- 2) The recognition of secondary geochemical dispersion within a non-residual, wind blown sand cover above a massive sulphide ore body.
- 3) The suitability of the geochemistry of the near surface calcrete layer in detecting the signature of mineralization.

Lastly, an integrated geochemical approach would be recommended for the identification of undiscovered concealed mineralization in this and similar environments.

#### **7.1. Lithogeochemical characteristics of the hydrothermal alteration zones in VHMS deposits and vectors for further exploration**

Various lithogeochemical and mineralogical methods were used to identify, characterise and investigate the lithogeochemical characteristics of the footwall alteration zones of VHMS deposits in upper amphibolite to granulite-grade

metamorphic rocks. Whereas a hydrothermal alteration zone has been identified in the past at the Prieska Cu-Zn deposit at Copperton (Theart, 1985), this study has now confirmed the presence of similar zones at Kantienpan and Areachap. The metamorphic minerals that characterize the alteration zones at these latter two VHMS deposits include plagioclase, almandine, pyrope, enstatite, clinoenstatite, cummingtonite, gedrite, cordierite, sillimanite, and retrograde chlorite, chamosite and pinite. Some of these minerals display characteristic mineral chemical variations relative to their respective positions in the alteration system, such as;

- a) Plagioclase is more Ca-rich (anorthite rich) close to the ore zone and more Na-rich (albite rich) further away from the ore zone.
- b) Pyroxene adjacent to the ore zone in KN11 has the highest relative Mg contents ( $Mg^* \text{ ratio} = Mg/(Mg+Fe+Ca)$ ) and this value decreases in the stringer footwall zone and also in the hangingwall zone. The Mn and Fe content of pyroxene near the ore zone and alteration zones are lower than those in pyroxene further away from these zones.
- c) The Mg number ( $Mg \text{ number} = 100 * Mg/(Mg+Fe)$ ) in cordierite is the highest in the ore zone and this decreases away from the ore zone into the host rocks. The Mn content of cordierite in the ore zone is higher than that in the footwall alteration zone.
- d) The almandine and pyrope components calculated for garnet are high in the alteration zones, whereas the spessartine and grossular components are low. Garnet in the ore zone has high Ca contents, but low Mg contents when compared to garnets in footwall and hangingwall.
- e) Based on the Mg and Fe values in mica, the Mg-rich variety, phlogopite is more common adjacent to the ore zone.
- f) The peraluminous nature of the footwall alteration zone is reflected by the presence of spinel (gahnite type close to the ore zone).

g) Retrograde chlorites of the ore zone are characterised by the highest Mg# ( $Mg\# = Mg / (Mg + Fe)$ ) when compared to those in the footwall and hangingwall succession. This suggests that the system behaved relatively closed during the retrograde stages of its evolution as the chlorite reflects the precursor bulk rock composition.

The abovementioned mineralogical characteristics together with the PER analyses of the compositions of cordierite, pyroxene and garnet may be used to constrain the proximity to sulphide mineralization when conducted on drill core during exploration.

Geochemically, the peraluminous ratio ( $Al_2O_3 / (Na_2O + K_2O + CaO)$ ) is high for samples adjacent to the ore zone in Areachap and Kantienpan VHMS ore deposits. Mineralogically and lithologically these samples represent to the garnet-sillimanite-cordierite-gneiss, identified as the rock type representing metamorphic equivalent of the originally formed in the hydrothermal footwall alteration zone. However, in borehole AP5, the high peraluminous ratios occur structurally above the ore zone suggesting that the original sequence have been inverted.

Based on the variation of the major oxides variation, the borehole sampling intervals with low CaO and Na<sub>2</sub>O and high MgO and K<sub>2</sub>O represent the alteration zone in the original footwall rocks of the deposit. This interpretation requires that the ore body in borehole AP5 were structurally overturned in acquiring its present habit confirming the conclusion based on the interpretation of the peraluminous ratio.

Isocon studies have shown that the alteration zones at the Areachap and Kantienpan deposits are enriched in Mg, Fe (total), S, Zn, Si, Co and F and depleted in Na, Ca, Sr, Ni, V and La. Ba is enriched in the footwall alteration zone at the Areachap, but depleted at the Kantienpan deposit. Elements that behaved relatively immobile include Zr, Ti, P, Mn, Al, Y, and U. Theart (1989) reported that the alteration zone at the Prieska Cu-Zn Mine is similarly enriched in Mg, K, V, Sc, Ni, Ba, Cu and Zn, and depleted in Ca, Na, Sr and Si.

The lithogeochemical and mineralogical characteristics of these alteration zones may now be used in exploration in this and similar terranes to identify concealed VHMS

mineralization. The box plot suggested by Large et al. (2001) and modified for metamorphic rocks here, is shown to be an effective method in identifying those rocks that were affected by hydrothermal alteration processes at the time of ore formation. In this case, the combination of the highest AI (Alteration Index) and CCPI (Chlorite-Carbonate-Pyrite Index) values ( $CCPI > 70$  and  $AI > 70$ ) correspond to the footwall alteration zone. Based on the investigation of the regional data set provided by Kumba Resources Limited, the location of peraluminous samples with extremely high Mg ( $MgO \gg K_2O$ ,  $AI > 90\%$  and  $CCPI > 98\%$ ) may be categorized as highly prioritized anomalous areas, those with high Mg ( $MgO > K_2O$ ,  $AI > 64\%$  and  $CCPI > 93\%$ ) as moderate to highly prioritized anomalous areas, and the samples with high K ( $K_2O > MgO$ ,  $AI > 64\%$  and  $55\% < CCPI < 93\%$ ) as lower priority anomalous areas in an lithogeochemical exploration programme.

A statistical analysis of whole rock analyses has shown that, the rocks in the footwall alteration zone of VHMS metamorphic deposits are peraluminous and that the peraluminous factor has the highest values. This zone may be further recognized by MgO contents that are higher (to extremely high) than  $K_2O$  contents, or display the highest alteration factor values.

The statistical analyses of the regional data set shows that the variations in the scores for the altered rock factor (FAR) versus the peraluminous factor (FPer) and the pelitic factor (FPR) may be used to differentiate the originally altered samples from the metapelitic samples. Altered samples are characterised by high scores for the FAR ( $FAR > 23$ ), low scores for the peraluminous factor ( $FPer < 15.7$ ) and pelitic factor ( $FPR < 7$ ). The peraluminous samples may be separated from the amphibolite samples by introducing a lower cut off value of three for the peraluminous factor and a very low scores for the ortho-amphibolite1 factor ( $Forth-Amp1 < 8$ ). In order to distinguish the peraluminous samples from the hornblende-gneiss samples, lower cut off value of three may also be used for the scores of the peraluminous factor; where samples returning a score of greater than three samples belong to the peraluminous variety of hornblende gneisses indicating rocks of intermediate composition that could have been affected by hydrothermal alteration prior to metamorphism. Applying these principals now to a regional lithogeochemical data set (the Kumba data set), it is

possible to identify samples from specific areas where no previously discovered VHMS deposits are known and such areas are prioritized as highly prospective.

## **7.2. The appropriateness of regolith geochemical survey in this region**

The concealed mineralization at Kantienpan and Areachap were effectively defined in samples of the wind blown Kalahari sand cover. Indicating the transfer of anomalous concentrations of the ore related elements to the sand in the relatively short period since its deposition. These anomalies were detectable by both the total analytical method (XRF) and partial extraction methods followed by ICP-MS.

In regolith geochemical surveys, the size of the dispersion haloes is more important than the peak to background ratio, because this will increase the possibility of detecting mineralization where samples are spaced relatively far apart. This study came to different conclusions regarding the size of dispersion halo that can be detected at the two investigated deposits. At Kantienpan where the sand cover is very shallow to absent, dispersion appears to be more related to the secondary redistribution of gossaniferous clasts, than dispersion of mobile metal ions on the surface of sand particles. In this area, the total analytical approach (XRF method) shows up a wider dispersion halo than methods based on partial extraction. Whereas, at Areachap, where relatively thick sand (approximately one metre) covers the calcrete layer, partial extraction (based on a  $\text{NH}_4\text{EDTA}$  solution) results in a larger, recognizable, dispersion halo than that which could be detected by total analysis (XRF). Based on the results of the three methods ( $\text{NH}_4\text{EDTA}$ , MMI and XRF), MMI results shows a larger span for Zn (about two times that of extraction by  $\text{NH}_4\text{EDTA}$ ), followed by  $\text{NH}_4\text{EDTA}$  and finally XRF, and for the Cu, the  $\text{NH}_4\text{EDTA}$  method exhibits the largest span (about one and half times that of XRF analyses) followed by XRF and then MMI.

Cu, Zn and Pb show high values when extracted by partial extraction methods whereas Mn and Fe, in some cases, show high values when analysed by the XRF method. This may suggest that Cu, Zn and Pb are derived from the ore minerals related to the mineral deposits or also referred to as an exogenic source, and Mn and

Fe are derived from both primary minerals, which are not directly related to the mineralization (an endogenic source), and from ore related minerals.

### **7.3. Signature of the mineralization in the calcrete regolith**

Even though it could be expected that the calcrete layer forms an effective geochemical barrier to the secondary dispersion of ore related trace elements. The current study confirmed the presence of elevated contents of these elements in samples collected from above the mineralization.

The calcrete from the studied areas consists of a gossan bearing magnetic and calcite rich non-magnetic part. Based on quantitative XRD analyses of these two parts it is concluded that magnetite and hematite are concentrated in the magnetic fractions, calcite, albite, microcline and quartz are more abundant in the non-magnetic fractions. Calcite is present in both the magnetic and non-magnetic fractions of the sample due to poor liberation during grinding. The distribution of trace elements, especially Cu and Zn, are strongly related to the distribution of magnetite (the magnetic part of the sample) although some of the Cu and Zn are also dispersed in the non-magnetic “cleaned “ fractions of the sample. Pb and V are directly associated with the distribution of magnetite.

The variation of the elements of interest in the visually cleaned calcrete shows that the concentrations of Cu, Zn and Pb are much lower at, and near surface than deeper down within the calcrete profiles. The concentrations of these elements that could be expected in calcrete at the surface and the peak to background ratio of anomalies at surface will therefore depend on the thickness of the underlying calcrete layer in the area.

S, as a trace element, does not show the same trend as Cu, Zn and Pb. This may be explained by the presence of different types of sulphur-bearing phases in the sample, i.e., sulphates that form as a result of the ground water compositions and evaporation processes, or sulphates that form as remnants after the oxidized primary sulphide

minerals. The former may result in false S anomalies not related to underlying sulphide mineralization.

The calcrete layer shows the signature of mineralization even though the size of the halo is only restricted to the ore zone. Calcretes directly related to massive sulphide mineralization may be discriminated from those developed in areas away from the mineralization by plotting the Sr-Cu-Zn and V-Cu-Zn contents in triangular diagrams. The original calcrete samples near the ore zone are enriched in  $\text{CaCO}_3$ , Cu and Zn. Those samples collected further away from the known mineralization are enriched in V, Sr and  $\text{MgCO}_3$  and have higher  $\text{Na}_2\text{O}$ ,  $\text{K}_2\text{O}$  and  $\text{SiO}_2$  contents.

#### **7.4. An integrated approach to geochemical exploration of arid areas**

The VHMS deposit at Areachap, Kantienpan and the defunct Prieska Cu-Zn Mine are hosted by a volcano sedimentary succession known as the Areachap Group, in the eastern part of Namaqua Metamorphic Province, South Africa. A collisional event affected the mineralization and host rocks and the secession was metamorphosed to upper amphibolite-granulite grade ( $M_1$ ) metamorphic conditions (Theart, 1985; Humphreys et al., 1988). This was followed by widespread intrusion of syntectonic granitic melts in the form of granite intrusion in a large part of the Namaqua Metamorphic Province resulting in high-grade  $M_2$  upper amphibolite grade metamorphic imprint (Theart, 1985; Theart et al., 1989; Cornell et al., 1992). Following uplift and subsequent deformation a metamorphic overprint developed in the form of grain boundary textures ( $M_3$ ) (Theart, 1985). After the intrusion and deformation, the steady state geotherm was re-established (Cornell et al., 1992) and retrogressive metamorphism ( $M_4$ ) was caused by ascending hydrothermal fluids (Theart et al., 1989). The rocks were exposed at the surface and were later covered by a thick layer of old sediments of the Karoo Supergroup (Catuneanu et al., 2005). After the erosion of the most of the Karoo sediments the area was again exposed to surface weathering conditions. This was followed by the deposition of the basal Kalahari Group sediments. The semi-arid environment during the onset of Kalahari Group (Netterberg, 1970; Malherbe, 1984) sedimentation led to the calcretization. Sand

covered the whole area during the subsequent arid period (Malherbe, 1984) that still persists.

As demonstrated above the study area suffered various events throughout geological time which complicate the applicability and results of routine exploration methods. Notwithstanding this a number of VHMS style massive sulphide deposits were discovered. As it is believed that there is strong probability for further discoveries, more advanced geochemical techniques were tested and developed to aid future exploration.

It was founded that massive sulphide mineralization concealed by a calcrete layer could be detected by chemical analyses of surface calcrete samples (chapter 6, section 6.7). The detection of anomalous zones could be enhanced by analyzing both calcrete material and magnetic inclusions found within this material. It has been demonstrated that the calcrete layer behaves as a geochemical barrier, which limits the secondary dispersion of the elements of interest above the massive sulphide zone. In profile, the concentration of the ore metal increase with depth (chapter 6, section 6.7.2). The peak to background ratio may therefore be expected to reduce as the thickness of the calcrete increase. Triangular discrimination graphs have been designed to distinguish between calcretes directly related to underlying sulphide mineralization and those from further away (chapter 6, section 6.7.3).

It was also demonstrated in this study that concealed sulphide mineralization can also be detected in non-residual sand (chapter 6, section 6.6), covering the calcrete layer, by the presence and abundance of the ore metals adsorbed onto the sand particles. Different reagents were used to extract these elements. The most successful reagent for anomaly detection was found to be  $\text{NH}_4\text{EDTA}$  solution (Appendix D, section D.1). This method works particularly well where the sand cover is thicker (one to two meters).

In the absence of a calcrete cover, lithogeochemical samples may be collected directly at surface (chapter 2, section 2.4). Utilizing sophisticated lithogeochemical techniques the whole rock analyses could be studied to identify areas affected by primary ore forming alteration processes. The box plot, which gives the variation of AI versus

CCPI, is one of the useful lithogeochemical methods based on whole rock XRF results. This diagram may be used to identify the proximity to the footwall alteration and ore zone, and also to prioritize the anomalous areas for further exploration programmes. In addition, the peraluminous ratio may also be used to distinguish the proximity to the footwall alteration and ore zone. The variation of this ratio, the AI and CCPI versus depth may confirm and clarify the location of the footwall alteration and ore zone.

The exploration methodology developed and tested here is not restricted in its application to this area alone, but would also be applicable to exploration in other similar high grade metamorphic terranes, currently experiencing arid to semi-arid climate conditions.

## References

- Adriano, D.C. (1986). Trace elements in the terrestrial environment. *Springer-Verlag, New York*.
- Aftabi, A.; Ghodrati, Z. and Maclean, W.H. (in proof). Metamorphic textures and geochemistry of the Cyprus-type massive sulfide lenses at Zurabad, Khoy, Iran. *Journal of Asian earth sciences XX*, 1-11.
- Alymore, L.A.G.; Karim, M. and Quirk, J.P. (1967). Adsorption and desorption of sulphate ions by soil constituents. *Soil Science*, **103**, 10-15.
- Attridge, R.L. (1986). The Jacomynspan copper-nickel occurrence, Kenhardt District in Mineral Deposits of Southern Africa, II. In: C.R., Anhaeusser and S., Maske (Editors) *Geological Society of South Africa, Johannesburg*, 1539-1546.
- Badham, J.P.N. (1981). Shale- hosted Pb-Zn deposits: products of exhalation of formation waters? *Institution of Mining and Metallurgy, Transactions*, **90**, B71-B76.
- Bardshaw, P.M.D.; Thomson, I.; Smee, B.W. and Larsson, J.O. (1974). The application of different analytical extractions and soil profile sampling in exploration geochemistry. *Journal of Geochemical Exploration*, **3**, 209-225.
- Barton, E.S. and Burger, A.J. (1983). Reconnaissance isotopic investigation of the marginal zone of the Proterozoic Namaqua mobile belt, Upington Geotraverse. *Geological Society of South Africa, Special Publication*, **10**, 173-192.
- Beus, A.A. and Grigorian, S.V. (1977). Geochemical exploration methods for mineral deposits. *Applied Publishing LTD., U.S.A.*, 286 pp.
- Bonnet AL.; Corriveau L. and La Fleche MR. (2005). Chemical imprint of highly metamorphosed volcanic-hosted hydrothermal alterations in the La Romaine Supercrustal Belt, eastern Grenville Province, Quebec. *Canadian Journal of Earth Sciences*, **42**, 1783-1814.
- Bowers, T.S.; Von Damm, K.L. and Edmond, J.M. (1985). Chemical evolution of mid-ocean ridge hot springs. *Geochimica et Cosmochimica Acta*, **49**, 2239-2252.
- Bradshaw, P.M.D.; Thomson, I.; Smee, B.W. and Larsson, J.O. (1974). The application of different analytical extractions and soil traverse sampling exploration geochemistry. *Journal of Geochemical Exploration*, **3**, 209-225.

- Brauhart, C.W.; Huston, D.L. and Andrew, A.S. (2000). Oxygen isotope mapping in the Panorama VMS district, Pilbara Craton, Western Australia: applications to estimating temperatures of alteration and to exploration. *Mineralium Deposita*, **35**, 727-740.
- Bruker Advanced X-Ray Solutions. (2003). DIFFRAC<sup>plus</sup>, EVA version 9.0, Karlsruhe, Germany.
- Cahen, L.; Snelling, N.J.; Delhal, J. and Vail, J.R. (1984). The geochronology and evolution of Africa. *Clarendon Press, Oxford*, 512 pp.
- Cameron, E.M.; Hamilton, S.M.; Leybourne, M.I. and Hall, G.E.M. (2004). Finding deeply buried deposits using geochemistry. *Geochemistry: Exploration, Environment, Analysis*, **4**, 7-32.
- Cameron, E.M. and Hattori, K. (1987). Archean sulphur cycle: Evidence from sulphate minerals and isotopically fractionated sulphides in superior province, Canada. *Chemical Geology, Isotope Geoscience section*, **65**, 341-358.
- Campbell, I.H.; Franklin, J.M.; Gorton, M.P.; Hart, T.R. and Scott, S.D. (1981). The role of subvolcanic sills in the generation of massive sulphide deposits. *Economic Geology*, **76**, 2248-2253.
- Canet, C.; Alfonso, P.; Melgarejo, J.C. and Belyatsky, B.V. (2004). Geochemical evidences of sedimentary-exhalative origin of the shale-hosted PGE-Ag-Au-Zn-Cu occurrences of the Prades Mountains (Catalonia, Spain): trace-element abundances and Sm-Nd isotopes. *Journal of Geochemical Exploration*, **82**, 17-33.
- Carlisle, D. (1980). Possible variations on the calcrete-gypcrete uranium model. *United State Department of Energy, open file Report GJBX 53(80), Subcontract 76-022-E, Bendix Field Engng. Corp. and University of California.*, Los Angeles, 38 pp.
- Cathles, L.M. (1983). An analysis of the hydrothermal system responsible for massive sulphide deposition in the Hokuroku basin of Japan. *In: H. Ohmoto, and B.J. Skinner, (Editors) Kuroko and related volcanogenic massive sulphide deposits. Economic Geology, Monograph 5*, 439-487.
- Chao, T.T. (1984). Use of partial dissolution techniques in geochemical exploration. *Journal of Geochemical Exploration*, **20**, 101-135.
- Chao, T.T.; Harward, M.E. and Fang, S.C. (1962a). Movement of <sup>35</sup>S tagged sulfate through soil columns. *Soil Science Society of America proceedings*, **26**, 27-32.

- Cilliers, F.H. (1987). Isotope characteristics of the sulphide-bearing sequence of the Areachap Group in the Bokspits area, Northwest Cape. *Unpublished M.Sc. thesis, University of Orange Free State, Bloemfontein*, 171 pp.
- Clark, J.R. (1997). Concepts and models for the interpretation of enzyme leach data for mineral and petroleum exploration. *In: Enzyme leach: Model, Sampling Protocol and Case histories. Activation Laboratories, Ontario*, 1-62.
- Clark, J.R. and Russ, G.P. (1991). A new enzyme partial leach enhances anomalies in pediment soils near buried gold deposits. *15th international Geochemical Exploration Symposium, Association of exploration Geochemists Reno, NV, 29 April-1 May 1991*.
- Cogley, J.G. (1985). Hypsometry of the continents. *Zeitschrift für Geomorphologie, Supplementbände*, **53**, 48 pp.
- Conradie, J.A. and Schoch, A.E. (1986). Petrological characteristics of the Koperberg Suite, South Africa: An analogy to massif-type anorthosites? *Precambrian Research*, **31**, 1570-188.
- Cornell, D.H.; Kroner, A.; Humphreys, H. and Griffin, G. (1990a). Age of origin of the polymetamorphosed Copperton Formation, Namaqua-Natal Province, by single grain zircon Pb-Pb dating. *South African Journal of Geology*, **93**, 709-714.
- Cornell, D.H.; Humphreys, H.C.; Theart, H.F.J. and Scheepers, D.J. (1992). A collision-related pressure-temperature-time path for Prieska copper mine, Namaqua-Natal tectonic Province, South Africa. *Precambrian Research*, **59**, 43-71.
- Cornell, D.H.; Theart, H.F.J. and Humphreys, H.C. (1990b). Dating a collision-related metamorphic cycle at Prieska copper mines, South Africa. *In: P.G. Spry, & T. Bryndzia (Editor) Regional metamorphism of ore deposits and genetic implications, VSP, Utrecht*, **11**, 97-116.
- Dawood YH.; Saleh GM. and EI-Naby HHA. (2005). Effects of hydrothermal alteration on geochemical characteristic of the EI Sakkari granite, Central eastern desert, Egypt. *International Geology Review*, **47**, 1316-1329.
- De Wit, M.J.; Roering, C.; Hart, R.J.; Armstrong, R.A.; De Ronde, R.E.J.; Green R.W.E.; et al. (1992). Formation of an Archaean continent. *Nature*, **357**, 553-562.
- Dhir, R.P.; Tandon, S.K.; Sareen, B.K.; Ramesh, R.; Rao, T.K.G.; Kailath, A.J. and Sharma, N. (2004). Calcretes in the Thar desert: genesis, chronology and palaeoenvironment.

- Proceedings of the Indian Academy of Sciences-Earth and Planetary Sciences*, **113**, 473-515.
- Dingle, R.V.; Siesser, W.G. and Newton, A.R. (1983). Mesozoic and Tertiary geology of Southern Africa. *A.A. Balkema, Rotterdam*, 375 pp.
- Fox, R.L.; Olson, R.A. and Rhoades, H.F. (1964). Evaluating the sulfur status of soils by plants and soil test. *Soil Science Society of America Proceedings*, **28**, 243-246.
- Francheteau, J.; Needham, H.D.; Choukroune, P.; Juteau, T.; Seguret, M.; Ballard, R.D.; Fox, P.J.; Normark, W.; Carranza, A.; Cordoba, D.; Guerrero, J.; Rangin, C.; Bougault, H.; Cambon, P. and Hekinian, R. (1979). Massive deep-sea sulphide ore deposits discovered on the East Pacific Rise. *Nature*, **227**, 523-528.
- Franklin, J.M.; Lydon, J.W. and Sangster, D.F. (1981). Volcanic associated massive sulphide deposits. *Economic Geology, 75<sup>th</sup> Anniversary Volume*, 485-627.
- Gaal, G. (1990). Tectonic styles of early Proterozoic ore deposition in the Fennoscandian Shield. *Precambrian Research*, **46**, 83-114.
- Genalysis Laboratory Services Pty Ltd. (© 2002, Cited 2005, Jan, 20). Terra leach<sup>TM</sup> Partial digest geochemistry (internat), TerraV6-0.doc, <http://www.genalysis.com.au>
- Geriner, G.J.; Botha, B.J.V.; Pretorius, J.J. and Ludick, D.J. (1987). Calc-alkaline volcanism along the eastern margin of the Namaqua mobile belt, South Africa-A possible middle proterozoic volcanic arc. *Precambrian Research*, **33**, 139-170.
- Geriner, G.J.; Humpherys, H.C. and Scheepers, D.J. (1994). Lithostratigraphy, protolithology, and tectonic setting of the Areachap group along the eastern margin of the Namaqua mobile belt, South Africa. *South African Journal of Geology*, **97**, 78-100.
- Geringer, G.J. and Ludick, D.J. (1990). Middle Proterozoic calc-alkaline, shoshonitic volcanism along the eastern margin of the Namaqua Mobile Belt, South Africa-implications for tectonic evolution in the area. *South African Journal of Geology*, **93**, 389-399.
- Geweke, J.F. and Singleton, K.J. (1980). Interpreting the likelihood ratio statistic in factor models when sample size is small. *Journal of the American Statistical Association*, **75**, 133-137.

- Goldberg, I.S. (1998). Vertical migration of elements from mineral deposits. *Journal of Geochemical Exploration*, **61**, 191-202.
- Goldfarb, M.S.; Converse, D.R.; Holland, H.D. and Edmond, J.M. (1983). The genesis of hot spring deposits on the East Pacific Rise, 210N. *In: H. Ohmoto, and B.J. Skinner (Editors) Kuroko and related volcanogenic massive sulphide deposits. Economic Geology, Monograph 5*, 184-197.
- Goodfellow, W.D.; Lydon, J.W. and Turner, R.J.W. (1993). Geology and genesis of stratiform sediment-hosted (SEDEX) zinc-lead-silver sulphide deposits. *In: R.V., Kirkham, W.D., Sinclair, R.I., Thorpe, J.M.S., Duke (Editors) Mineral Deposit Modeling. Special Paper, Geological Association of Canada*, **40**, 201-251.
- Gorton, R.K. (1981). The petrology of the Kielder sulphide bodies and their wall rocks: District of Prieska, N. Cape, South Africa. *Unpublished M.Sc. thesis, University of Cape Town*, 153 pp.
- Grant, J.A. (1986). The isocon diagram-A simple solution to Gresens' equation for metasomatic alteration. *Economic Geology*, **81**, 1976-1982.
- Gray, D.J.; Wildman, J.E. and Longman, G.D. (1999). Selective and partial extraction analyses of transported overburden for gold exploration in the Yilgarn Craton, Western Australia. *Journal of Geochemical Exploration*, **67**, 51-66.
- Gresens, R.L. (1967). Composition- volume relationships of metasomatism. *Chemical Geology*, **2**, 47-55.
- Hajash, A. (1975). Hydrothermal processes along mid-ocean ridges: an experimental investigation. *Contributions to Mineralogy and Petrology*, **53**, 205-226.
- Hall, G.E.M.; Maclaurin, A.I. and Garrett, R.G. (1998). Assessment of the 1 M NH<sub>4</sub>NO<sub>3</sub> extraction protocol to identify mobile forms of Cd in soils. *Journal of Geochemical Exploration*, **64**, 153-159.
- Harman, H.H. (1976). Modern factor analysis. 3<sup>rd</sup> Edition, Chicago, University of Chicago press.
- Hartnady, C.J.H.; Joubert, P. and Stowe, C.W. (1985). Proterozoic crustal evolution in southwestern Africa. *Episodes*, **8**, 36-44.
- Haymon, R.M. (1983). Growth history of hydrothermal black smoker chimneys. *Nature*, **301**, 695-698.

- Haymon, R.M. and Kastner, M. (1981). Hot spring deposits on the East Pacific Rise at  $21^{\circ}\text{N}$ : preliminary description of mineralogy and genesis. *Earth and Planetary Science Letters*, **53**, 363-381.
- Hodgson, C.J. and Lydon, J.W. (1977). Geological setting of volcanogenic massive sulphide deposits and active hydrothermal systems: some implications for exploration. *Canadian Institution of Mining and Metallurgy, Bulletin*, **70**, 95-106.
- Hughes, C.J. (1972). Spilites, keratophyes and igneous spectrum. *Geological Magazine*, **109**, 513-527.
- Humphreys, H.C. (1993). Metamorphic evolution of amphibolite-bearing aluminous gneisses from the Eastern Namaqua Province, South Africa. *American Mineralogist*, **78**, 1041-1055.
- Humphreys, H.C.; Van Bever Donker, J.M.; Scott, W.D. and Van Schalkwyk, L. (1988a). The early deformational history of the eastern Namaqua Province: new evidence from Prieska copper mines. *South African Journal of Geology*, **91**, 174-183.
- Humphreys, H.C; Van Schalwyk, L. and Scott, W.D. (1988b). A geological and structural map of the Areachap Group succession at Prieska Copper Mines. *South African Journal of Geology*, **91**, 373-380.
- Hutchinson, R.W. (1973). Volcanogenic sulfide deposits and their metallogenic significance. *Economic Geology*, **68**, 1223-1246.
- Ishikawa, Y.; Sawaguchi, T.; Iwaya, S. and Horiuchi, M. (1976). Delineation of prospecting targets for Kuroko deposits based on modes of volcanism of underlying dacite and alteration halos. *Mining Geology (in Japan with English abstract)*, **26**, 105-117.
- Iyengar, S.S.; Martens, D.C. and Miller, W.P. (1981). Distribution and plant availability of soil zinc fractions. *Soil Science Society of America Journal*, **45**, 735-739.
- Jacobs, J. and Weber, K. (1993). Accretion and indentation tectonics at the southern edge of the Kaapvaal craton during the Kibaran (Grenville) orogeny. *Geology*, **21**, 203-206.
- Janecky, D.R. and Seyfried, W.E., Jr. (1984). Formation of massive sulphide deposits on oceanic ridge crest: Incremental reaction models for mixing between hydrothermal solutions and seawater. *Geochimica et Cosmochimica Acta*, **48**, 2723-2738.

- Jenner, G.A. (1996). Trace element geochemistry of igneous rocks: geochemical nomenclature and analytical geochemistry. *In: D.A. Wyman (Editors) Trace element geochemistry of volcanic rocks: Applications for massive sulphide exploration, Geological Association of Canada, Short course notes volume 12*, 51-77.
- Jiang, SY. (2000). Controls on the mobility of high field strength elements (HFSE), U, and Th in an ancient submarine hydrothermal system of the Proterozoic Sullivan Pb-Zn-Ag deposit, British Columbia, Canada. *Geochemical Journal* , **34**, 341-348.
- Jimenez-Espinosa R. and Jimenez-Millan J. (2003). Calcrete development in Mediterranean colluvial carbonate systems from SE Spain. *Journal of Arid Environments*, **53**, 479-489.
- Kalogeropoulos, S.I. and Scott, S.D. (1983). Mineralogy and geochemistry of tuffaceous exhalites (tetsusekiei) of the Fukazawa mine. *In: H., Ohmoto and B.J. Skinner (Editors) Kuroko and related volcanogenic massive sulphide deposits. Economic Geology, Monograph 5*, 412-432.
- Kataba-Pendias, A. and Pendias, H. (1991). Trace elements in soil and plants. *2<sup>nd</sup> Edition, CRC Press, Inc., Boca Raton, Fl.*
- Kawakami, T. (2001). Tourmaline breakdown in the migmatite zone of the Ryoke metamorphic belt, SW Japan. *Journal of Metamorphic Geology*, **19**, 61-75.
- Khadkikar A.S.; Chemyal L.S. and Ramesh R. (2000). The character and genesis of calcrete in Late Quaternary alluvial deposits, Gujarat, western India, and its bearing on the interpretation of ancient climates. *Palaeogeography, Palaeoclimateology, Palaeoecology*, **162**, 239-261.
- Khadkikar A.S.; Merh S.S.; Malik J.N. and Chamyal L.S. (1998). Calcretes in semi-arid alluvial systems: formative pathways and sinks. *Sedimentary Geology*, **116**, 251-260.
- Kilmer, V.J. and Nerpass, D.C. (1960). The determination of available sulfur in soils. *Soil Science Society of America proceedings*, **24**, 337-340.
- Klau, W. and Large, D.E. (1980). Submarine exhalative Cu-Pb-Zn deposits- a discussion of their classification and metallogenesis. *Geologisches Jahrbuch*, **40**, 13-58.
- Kowalik, J.; Rye, R. and Sawkins, F.J. (1981). Stable isotope study of the Buchans polymetallic sulphide deposits. *In: E.A., Swanson, D.F., Strong and J.G., Thurlow*

- (Editors) The Buchans orebodies: Fifty years of geology and mining. *Geological Association of Canada, Special Paper*, **22**, 229-254.
- Kshirsagar, A.M. (1972). Multivariate analysis. *New York, Marcel Dekker, Inc.*
- Kunckey, M.J. (1975). Geology of the Millenbach copper-zinc deposit, Noranda, Quebec, Canada. *Society of economic geologists-American institute of mining and metallurgical engineers, Annual general meeting*, Feb. 1975.
- Large, R.R. (1977). Chemical evolution and zonation of massive sulphide deposits in volcanic terrains. *Economic Geology*, **72**, 549-572.
- Large, R.; Doyle, M.; Raymond, O.; Cooke, D.; Jones, A. and Heasman, L. (1996). Evaluation of the role of Cambrian granites in the genesis of world class VHMS deposits in Tasmania. *Ore Geology Reviews*, **10**, 215-230.
- Large, R.; Gemmell, J.B.; Paulick, H. and Huston, D.L. (2001). The alteration box plot: A simple approach to understanding the relationship between alteration mineralogy and litho geochemistry associated with volcanic-hosted massive sulphide deposits. *Economic Geology*, **96**, 957-971.
- Leake, B.E. (1964). The chemical distinction between ortho-amphibolite and para-amphibolites. *Journal of Petrology*, **5**, 238-254.
- Leinz, R.A. and Hoover, D.B. (1993). The Russian CHIM method electrically or diffusion driven collection of ions. *Explore*, **79**, 1-9.
- Levinson, A.A. (1974). Introduction to exploration geochemistry. *Applied publishing Ltd., Illinois, U.S.A.*, 924 pp.
- Liang, J.; Strwart, J.W.B. and Karamanos, R.E. (1991). Distribution and plant availability of soil copper fractions in Saskatchewan. *Canadian Journal of Soil Science*, **71**, 89-99.
- Lindsay, W.L. and Norvell, W.A. (1987). Development of a DTPA test for zinc, iron, manganese, and copper. *Soil Science Society of America Journal*, **42**, 421-428.
- Lombaard, A.F. and Schreuder, F.J.G. (1978). Distribution pattern and general geological features of steep structures, mega-breccias and basic rocks in the Okiep Copper district. In: W.J., Verwoerd (Editors) Mineralization in metamorphic terranes. *Geological Society of South Africa, Special Publication*, **4**, 269-295.

- Lott, D.A. (1999). Sedimentary exhalative nickel-molybdenum ores in south China. *Economic geology and bulletin of the society of economic geologists*, **94**, 1051-1066.
- Lowell, R.P. and Rona, P.A. (1985). Hydrothermal models for the generation of massive sulphide ore deposits. *Journal of Geophysical Research*, **90**, 8769-8783.
- Ludick, D.J. (1987). Die stratigrafie en tektoniese verwantskappe van die Areachap groep in die Upington-omgewing. *Unpublished M.Sc. thesis, University of Orange Free State, Bloemfontein*, 143 pp.
- Luoma, S.N. and Jenne, E.A. (1976). Estimating bio-availability of sediment-bound trace metals with chemical extractants. *Trace Substances in Environmental Health-X*, **10**, 343-351.
- Lydon, J.W. (1983). Chemical parameters controlling the origin and deposition of sediment-hosted stratiform lead-zinc deposits. *In: D.F., Sangster (Editors) Sediment-hosted stratiform lead-zinc deposits, Mineralogical Association of Canada, Short course handbook*, **9**, 175-250.
- Lydon, J.W. (1986). Models for the generation of metalliferous hydrothermal systems within sedimentary rocks and their applicability to the Irish Carboniferous Zn-Pb deposits. *In: C.J., Andrew, R.W.A., Crowe, S., Finlay, W.M., Pennell and J.F., Pyne (Editors) Geology and genesis of mineral deposits in Ireland, Irish Association for Economic Geology, Dublin*, 555-577.
- Lydon, J.W. (1998a). Volcanogenic massive sulphide deposit, part1: A descriptive model. *In: R.G, Roberts and P.A., Sheahan (Editors) Ore deposit models, Geoscience Canada*, 145-153.
- Lydon, J.W. (1998b). Volcanogenic massive sulphide deposit, part2: Genetic models. *In: R.G, Roberts and P.A., Sheahan (Editors) Ore deposit models, Geoscience Canada*, 155-181.
- Lydon, J.W. and Galley, A. (1986). Chemical and mineralogical zonation of the Mathiati alteration pipe, Cyprus, and its genetic significance. *In: M.J., Gallagher, R.A., Ixer, C.R., Neary and H.M., Prichard (Editors) Metallogeny of basic and ultrabasic rocks, Institution of Mining and Metallurgy, London*, 49-68.

- Maes, A.; Vanthuyne, M.; Cauwenberg, P. and Engels, B. (2003). Metal partitioning in a sulfidic canal sediment: metal solubility as a function of pH combined with EDTA extraction in anoxic conditions. *The Science of the Total Environment*, **312**, 181-193.
- Malherbe, S.J. (1984). The geology of the Kalahari Gemsbok National Park. *Proceedings of a Symposium on the Kalahari Ecosystem*, 33-44.
- Mann, A.W.; Birrell, R.D.; Fedikow, M.A.F. and De Souza, H.A.F. (2005). Vertical ionic migration: mechanisms, soil anomalies, and sampling depth for mineral exploration. *Geochemistry: Exploration, Environment, Analysis*, **5**, 201-210.
- Mann, A.W.; Birrell, R.D.; Mann, A.T.; Humphreys D.B. and Perdrix, J.L. (1998). Application of the mobile metal ion technique to routine geochemical exploration. *Journal of Geochemical Exploration*, **61**, 87-102.
- Mann, A.W.; Birrell, R.D.; Perdrix, J.L.; Mann, A.T.; Humphreys, D.B. and Gry, L.M. (1995). Project M219: Mechanism of formation of mobile metal ion anomalies. *Meriwa report No. 153, Perth, W.A.*, 407 pp.
- Mann, A.W.; Mann, A.T.; Humphreys, D.B.; Dowling, S.E.; Staltari, S. and Myers, L. (1997). Soil geochemical anomalies-their dynamic nature and interpretation. *Meriwa report No. 184, Perth.*, 132 pp.
- Mardia, K.V.; Kent, J.T. and Biddy, J.M. (1979). Multivariate analysis. *London, Academic press, Inc.*
- McClung, A.C.; DeFreitas, L.M. and Lott, W.L. (1959). Analyses of several Brazilian soils in relation to plant responses to sulfur. *Soil Science Society of America proceedings*, **23**, 221-224.
- McQueen, K.G.; Hill, S.M. and Foster, K.A. (1999). The nature and distribution of regolith carbonate accumulations in southeastern Australia and their potential as a sampling medium in geochemical exploration. *Journal of Geochemical Exploration*, **67**, 67-82.
- Mehlich, A. (1984). Mehlich 3 soil test extractant: A modification of Mehlich 2 extractant. *Communications in Soil Science Plant Analysis*, **15**, 1409-1416.
- Middleton, R.C. (1976). The geology of the Prieska copper mines (Pty) Ltd. *Economic Geology*, **71**, 328-350.

- Miller, W.P.; Martens, D.C.; Zelazny, L.W. and Kornegay, E.T. (1986). Forms of solid phase copper in copper-enriched swine manure. *Journal of Environmental Quality*, **15**, 69-72.
- Miller, W.P. and McFee, W.W. (1983). Distribution of Cd, Zn, Cu and Pb in soils of industrial north western Indiana. *Journal of Environmental Quality*, **12**, 29-33.
- Miyashiro, A. (1994). Metamorphic petrology. *UCL press*, 404 pp.
- Morrison, D.F. (1976). Multivariate statistical methods. 2<sup>nd</sup> edition, New York, McGraw-Hill book Co.
- Moen, H.F.G. (1988). 2820 Upington 1:250000 Geological Series. *Council for Geoscience, Pretoria, South Africa*.
- Moen, H.F.G. (1999). The Kheis tectonic subprovince, South Africa: A lithostratigraphic perspective. *South African Journal of Geology*, **102**, 27-42.
- Moore, J.M.; Reid, D.L. and Watkeys, M.K. (1990). The regional setting of the Aggenys/Gamsberg base metal deposits, Namaqualand, South Africa, *In: P.G. Spry, & L.T. Bryndzia, (Editors) Regional metamorphism of ore deposits*, 77-95.
- Moore, AE. (1999). A reappraisal of epirogenic flexure axes in southern Africa. *South African Journal of Geology*, **102**, 363-376.
- Mottl, M.J. and Holland, H.D. (1978). Chemical exchange during hydrothermal alteration of basalt by seawater: I. Experimental results for major and minor components of seawater and basalt. *Geochimica et Cosmochimica Acta*, **42**, 1103-1116.
- Nash, D.J. and McLaren, S.J. (2003). Kalahari valley calcretes: their nature, origins, and environmental significance. *Quaternary International*, **111**, 3-22.
- Nelisen, D.; Hoyt, P.B. and Mackenzi, A.F. (1986). Distribution of soil Zn fractions in British Columbia interior orchard soils. *Canadian Journal of Soil Science*, **66**, 445-454.
- Netterberg, F. (1970). Ages of calcretes in Southern African. *South African Archaeological Bulletin*, **24**, 88-92.
- Ohlander B.; Land M.; Ingri J. and Widerlund A. (1996). Mobility of rare earth elements during weathering of till in northern Sweden. *Applied Geochemistry*, **11**, 93-99.
- Ohmoto, H. and Rye, R.O. (1974). Hydrogen and oxygen isotopic compositions of fluid inclusions in the Kuroko deposits, Japan. *Economic Geology*, **69**, 947-953.

- Ohmoto, H. and Skinner, B.J. (1983). The Kuroko and related volcanogenic massive sulfide deposits. *Economic Geology, Monograph 5*, 604 pp.
- Oudin, E. (1981). Etudes mineralogique et geochemique des depots sulfures sous-marins actuels de la ridge est-pacifique (21<sup>0</sup>N). *Documents du BRGM 25*, 241 pp.
- Oudin, E. (1983). Hydrothermal sulphide deposits of the East Pacific Rise (210N) Part 1: Descriptive mineralogy. *Marine Mining*, **4**, 39-72.
- Pan, Y. and Fleet, M.E. (1995). Geochemistry and origin of cordierite-orthoamphibole gneiss and associated rocks at an Archaean volcanogenic massive sulphide camp: Manitouwadge, Ontario, Canada. *Precambrian Research*, **74**, 73-89.
- Partridge, T.C. and Maud, R.R. (1987). Geomorphic evolution of Southern Africa since the Mesozoic, *South African Journal of Geology*, **90**, 179-208.
- Piercey, S.J.; Pardis, S.; Murphy, D.C. and Mortensen, J.K. (2001). Geochemistry and Paleotectonic setting of felsic volcanic rocks in the Finlayson Lake volcanic-hosted massive sulphide District, Yukon, Canada. *Economic Geology*, **96**, 1877-1905.
- Pottorf, R.J. and Barnes, H.J. (1983). Mineralogy, geochemistry, and ore genesis of hydrothermal sediments from the Atlantis II deep, Red Sea. *In: H., Ohmoto and B.J., Skinner (Editors) Kuroko and related volcanogenic massive sulphide deposits. Economic Geology, Monograph 5*, 198-223.
- Pupin, J.P. (1980). Zircon and granite petrology. *Contributions to Mineralogy and Petrology*, **73**, 207-220.
- Rao, C.R. (1964). The use and interpretation of principal component analysis in applied research. *Sankhy A*, **26**, 329-358.
- Reed, M.H. (1983). Seawater-basalt reaction and the origin of greenstones and related ore deposits. *Economic Geology*, **78**, 446-485.
- Richards, H.G. and Boyle, J.F. (1986). Origin, alteration and mineralization of inter-lava metalliferous sediments of the Troodos ophiolite, Cyprus. *In: M.J., Gallagher, R.A., Ixer, C.R., Neary and H.M., Prichard (Editors) Metallogeny of basic and ultrabasic rocks, Institute of Mining and Metallurgy, London*, 21-31.
- Ringrose S.; Downey B.; Genecke D.; Sefe F. and Vink B. (1999). Nature of sedimentary deposits in the Western Makgadikgadi basin, Botswana. *Journal of Arid Environments*, **43**, 375-397.

- Rossouw, D. (2003). A technical risk evaluation of the Kantienpan volcanic-hosted massive sulphide deposit and its financial viability. *Unpublished M.Sc. thesis, University of Pretoria*, 118 pp.
- Ruiz, C.; Arribas, A. and Arribas Jr., A. (2002). Mineralogy and geochemistry of the Masa Valverde blind massive sulphide deposit, Iberian Pyrite Belt (Spain). *Ore Geology Reviews*, **19**, 1-22.
- Ryan, P.J.; Lawrence, R.D.; Lipson, R.D.; Moore, J.M.; Paterson, A.; Stedman, D. P. and Van Zyl, D. (1986). The Aggeneys base metal sulphide deposits, Namaqualand District, Mineral Deposits of Southern Africa. In: C.R., Anhaeusser and S., Maske (Editors) *Geological Society of South Africa, Johannesburg*, 1447-1473.
- Salomons, W. and Forstner, U. (1984). Metals in the hydrocycle. *Springer-Verlag, Berlin*.
- Sangster, D.F. (2002). The role of dense brines in the formation of vent distal sedimentary-exhalative (SEDEX) lead-zinc deposits: field and laboratory evidence. *Mineralium Deposita*, **37**, 149-157.
- Sanchez-Espana, J.; Velasco, F. and Yusta, I. (2000). Hydrothermal alteration of felsic volcanic rocks associated with massive sulphide deposition in the northern Iberian Pyrite Belt (SW Spain). *Applied Geochemistry*, **15**, 1265-1290.
- Sangster, D.F. (1972). Precambrian volcanogenic massive sulphide deposits in Canada: A review. *Geological Survey of Canada, paper 72-22*, 44 pp.
- Sangster, D.F. and Scott, S.D. (1976). Precambrian, strata-bound, massive Cu-Zn-Pb sulphide ores of North America. In: K.H., Wolf (Editors) *Handbook of stratabound and stratiform ore deposits. Elsevier Scientific Publishing Co., Amsterdam*, **6**, 130-221.
- SAS<sup>®</sup> V 8.2 (2003). Integrated system of software providing control of data management, analysis, and presentation. *SAS Institute, Cary, North Carolina, USA*.
- Sawkins, F.J. (1976). Massive sulphide deposits in relation to geotectonics. In: D.F., Strong (Editors) *Metallogeny and plate tectonics. Geological Association of Canada, Special Paper 14*, 221-240.
- Sawkins, F.J. (1984). Ore genesis by episodic dewatering of sedimentary basins: Application to giant Proterozoic lead-zinc deposits. *Geology*, **5**, 451-454.

- Schade, J.; Cornell, D.H. and Theart, H.F.J. (1989). Rare earth element and isotopic evidence for the genesis of the Prieska massive sulphide deposit, South Africa. *Economic Geology*, **84**, 49-63.
- Schnitzer, M. (1978). Humic substances: Chemistry and reactions. In: M. Schnitzer and S.U. Khan (Editors) Soil organic matter. *Elsevier, Amsterdam*, 1-64
- Seyfried, W.E., Jr. and Bischoff, J.L. (1979). Low temperature basalt alteration by seawater: an experimental study at 70<sup>0</sup>C and 150<sup>0</sup>C. *Geochimica et Cosmochimica Acta*, **43**, 1937-1947.
- Shapiro, S.S. and Wilk, M.B. (1965). An analysis of variance test for normality (complete samples). *Biometrika*, **52**, 591-611.
- Shpak, A.P.; Kalinichenko, A.M.; Bagmut, N.N.; Kalinichenko, Y.A.; Karbivs'ky, V.L. and Trashchan, Y.A. (2003). Influencing of isomorphic replacements on electron distribution in point defects of oxygen-phosphorous compounds of calcium and strontium. *Metallofizika I Noveishie TeknologII*, **25**, 699-712.
- Shuman, L.M. (1983). Sodium hypochlorite methods for extracting microelements associated with soil organic matter. *Soil Science Society of America Journal*, **47**, 656-660.
- Sibson, R.H.; Moore, J.Mc.M. and Rankin, A.H. (1975). Seismic pumping- a hydrothermal fluid transport mechanism. *Journal of the Geological Society of London*, **131**, 653-659.
- Sillitoe, R.H. (1973). Environments of formation of volcanogenic massive sulphide deposits. *Economic Geology*, **68**, 1321-1325.
- Sinclair, A.J. (1976). Applications of probability graphs in mineral exploration. *The association of exploration geochemists, Special volume No. 4, Richmond printers LTD*.
- Smmerfield, M.A. (1985). Plate tectonics and landscape development on the African continent, In: M. Morisawa, & J.J. Hack (Editors) Tectonic Geomorphology. *Allen and Unwin, Boston*, 390 pp.
- Solomon, M. (1976). Volcanic massive sulphide deposits and their host rocks- a review and an explanation. In: K.H., Wolf (Editors) Handbook of stratabound and stratiform ore deposits. *Elsevier, Amesterdam*, **2**, 21-50.

- Soltanpour, P.N. (1991). Determination of nutrient availability and elemental toxicity by AB-DTPA soil test and ICPS. *Advances in Soil Science*, **16**, 165-190.
- Soltanpur, P.N.; Jones, J.B., Jr. and Workman, S.M. (1982). Optical emission spectrometry. In: A.L., Page et al., (Editors). *Methods of soil analysis, part 2*, 2nd Ed, *Agron. Monogr. 9. ASA and SSSA, Madison, WI*.
- Speiss, F.N.; Macdonald, K.C.; Atwater, T.; Ballard, R.; Carranza, A.; Cordoba, D.; Cox, C.; Diaz Garcia, V.M.; Francheteau, J.; Guerrero, J.; Hawhins, J.; Haymon, R.; Hessler, R.; Juteau, T.; Kastner, M.; Larson, R.; Luyendyke, B.; Macdougall, J.D.; Miller, S.; Normark, W.; Orcutt, J. and Rangin, C. (1980). East Pacific Rise; hot springs and geophysical experiments. *Science*, **207**, 1421-1433.
- Spooner, E.T.C. (1977). Hydrodynamic model for the origin of the ophiolite cupriferous pyrite ore deposits of Cyprus, in volcanic processes in ore genesis. *Geological Society of London, Special Publication 7*, 58-71.
- Stanford, J.O. and Lancaster, J.D. (1962). Biological and chemical evaluation of the readily available sulfur status of Mississippi soils. *Soil Science Society of America Proceedings*, **26**, 63-65.
- Stover, R.C.; Sommers, L.E. and Silviera, D.J. (1976). Evaluation of metals in wastewater sludge. *Journal of Water. Pollution Control Federation* **48**, 2165-2175.
- Stowe, C.W. (1983). The Upington geotraverse and its implications for Craton margin tectonics. In: Botha, B.J.V. (ED.), Namaqualand metamorphic complex. *Geological Society of South Africa, Special Publication*, **10**, 147-171.
- Sundblad, K. (1991). Lead isotopic evidence for the origin of 1.8-1.4 Ga ores and granitoids in the southeastern part of the Fennoscandian Shield. *Precambrian Research*, **51**, 265-281.
- Tabatabai, M.A. and Lafen, J.M. (1976a). Nitrogen and sulfur content and pH of precipitation in Iowa. *Journal of Environmental Quality*, **5**, 108-112.
- Tauson, V.L. (1999). Isomorphism and endocrypty: Novel approaches in studies of behavior of microelements in mineral systems. *Geologyia I Geofizika*, **40**, 1488-1494.
- Tessier, A.; Campbell, P.G.C. and Bisson, M. (1979). Sequential extraction procedure for the speciation of particular trace metals. *Analytical Chemistry*, **51**, 844-851.

- Theart, H.F.J. (1985). Copperton-Areachap Cu-Zn mineralization, *Unpublished Ph.D. thesis, University of Stellenbosch*, 329 pp.
- Theart, H.F.J.; Cornell, D.H. and Schade, J. (1989). Geochemistry and metamorphism of the Prieska Zn-Cu deposit, South Africa. *Economic Geology*, **84**, 34-49.
- Thomas, M.A. (1981). The geology of the Kalahari in the northern Cape Province (Areas 2620 and 2720). *Unpublished M.Sc. thesis, University of the Orange Free State, Bloemfontein*.
- Thomas, R.J.; Agenbacht, A.L.D.; Cornell, D.H. and Moore, J.M. (1994b). The Kibaran of Southern Africa: Tectonic evolution and metallogeny. *Ore Geology Reviews*, **9**, 131-160.
- Thomas, R.J.; Cornell, D.H.; Moore, M.J. and Jacobs, J. (1994a). Crustal evolution of the Namaqua-Natal metamorphic Province, Southern Africa. *South African Journal of Geology*, **97**, 8-14.
- Tivey, M.K. and Delaney, J.R. (1986). Growth of large sulphide structures on the Endeavour segment of the Juan de Fuca Ridge. *Earth and Planetary Science Letters*, **77**, 303-317.
- Tornos, F. (2006). Environment of formation and styles of volcanogenic massive sulphides: The Iberian Pyrite Belt. *Ore Geology Reviews*, **28**, 259-307.
- Ulrich, T.; Golding, S.D.; Kamber, B.S.; Zam, K. and Taube, A. (2002). Different mineralization styles in a volcanic-hosted ore deposit: the fluid and isotopic signatures of the Mt Morgan Au-Cu deposit, Australia. *Ore Geology Reviews*, **22**, 61-90.
- Van Niekerk, H.S.; Beukes, N.J. and Gutzmer, J. (1999). Post-Gondwana pedogenic ferromanganese deposits, ancient soil profiles, African land surfaces and palaeoclimatic change on the Highveld of South Africa. *Journal of African Earth Sciences*, **26**, 761-781.
- Van Zyl, C.Z. (1981). Structural and metamorphic evolution in the transitional zone between craton and mobile belt, Upington geotraverse. *Chamber of mines Precambrian research unit, Bulletin 31, University of Cape Town*.

- Vermaak, J. J. (1984). Aspects of the secondary dispersion of ore-related elements in calcrete-environments of the Northern Cape Province. *Unpublished M.Sc. thesis, University of the Orange Free State, Bloemfontein*, 549.1145 VER.
- Voet, H.W. and King, B.H. (1986). The Areachap copper-zinc deposit, Gordonia district., *In: S. Maske (Editors) Mineral Deposits of southern Africa, Geological Society of South Africa*, **2**, 1529 pp.
- Vokes, F.M. (1969). A review of metamorphism of sulphide deposits. *Earth Science Review*, **5**, 99-143.
- Wagener, J.H.F. and Van Schalkwyk, L. (1986). The Prieska zinc-copper deposit, north-western Cape Province, Mineral Deposits of Southern Africa, II . *In: C.R., Anhaeusser and S., Maske (Editors). Geological Society of South Africa, Johannesburg*, 1503-1527.
- Walker, R.N.; Logan, R.G. and Binnekamp, J.G. (1977). Recent geological advances concerning the H.Y.C and associated deposits, Mearthur River, N.T. *Journal of the Geological Society of Australia*, **24**, 365-380.
- Wang, X. (1998). Leaching of mobile forms of metals in overburden: development and application. *Journal of Geochemical Exploration*, **61**, 39-55.
- Ward, J.D., Seely, M.K. and Lancaster, I.N. (1983). On the antiquity of the Namib. *South African Journal of Science*, **79**, 175-183.
- Wear, J.I. and Evans, C.E. (1968). Relationship of zinc uptake by corn and sorghum to soil zinc measured by three extractants. *Soil Science Society of America Proceedings*, **32**, 543-546
- Watanabe, M. and Sakai, H. (1983). Stable isotope geochemistry of sulfates from the Neogene ore deposits in the Green Tuff region, Japan. *In: H., Ohmoto and B.J., Skinner (Editors) Kuroko and related volcanogenic massive sulphide deposits. Economic Geology, Monograph 5*, 282-291.
- Whitbread, M.A. and Moore, C.L. (2004). Two lithochemical approaches to the identification of alteration patterns at the Elura Zn-Pb-Ag deposit, Cobar, New South Wales, Australia: use of Pearce Element Ratio analysis and isocon analysis. *Geochemistry: Exploration, Environment, Analysis*, **4**, 129-141.

- Williams, C.H. and Steinbergs, A. (1962). The valuation of plant-available sulphur in soils: I. The chemical nature of sulphates in some Australian soils. *Plant Soil* **17**, 279-294.
- Wilson, M.G.C. and Anhaeusser, C.R. (1998). The mineral resources of South Africa. *Handbook 16, Sixth edition, Council for Geosciences*.
- Young, R.A. (1996). The Rietveld method, IUCr Monographs on Crystallography, 5. *International Union of Crystallography, Oxford Science Publications*, 298 pp.
- Xueqiu, W. (1998). Leaching of mobile forms of metals in overburden: development and application. *Journal of Geochemical Exploration* , **61**, 39-55.

## **Appendix A**

### **Cross sections and extra figure**

Bestpofe.com

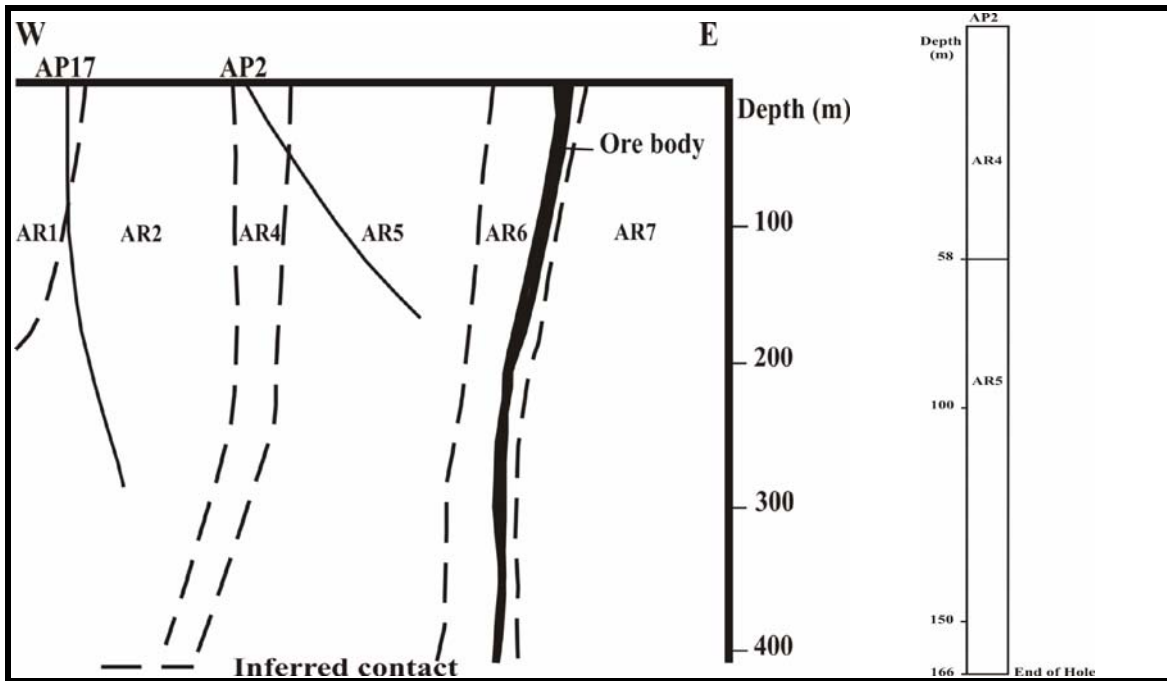


Figure A.1: Cross section includes borehole AP2 and sample locations

Table A.1: Depth of samples in drill hole AP2, Areachap

Sample No.	Depth (m)	Sample No.	Depth (m)	Sample No.	Depth (m)
AP2/1	62.2	AP2/9	92.5	AP2/18	112.4
AP2/2	71.2	AP2/14	92.6	AP2/16	113.2
AP2/3	74.4	AP2/12	97.8	AP2/15	118.0
AP2/4	81.2	AP2/10	105.7	AP2/22	120.1
AP2/5	82.5	AP2/11	106.3	AP2/24	122.1
AP2/6	87.1	AP2/21	107.5	AP2/23	124.1
AP2/7	91.1	AP2/20	108.7	AP2/25	141.1
AP2/13	91.1	AP2/19	111.7	AP2/26	153.7
AP2/8	92.2	AP2/17	112.2	AP2/27	165.0

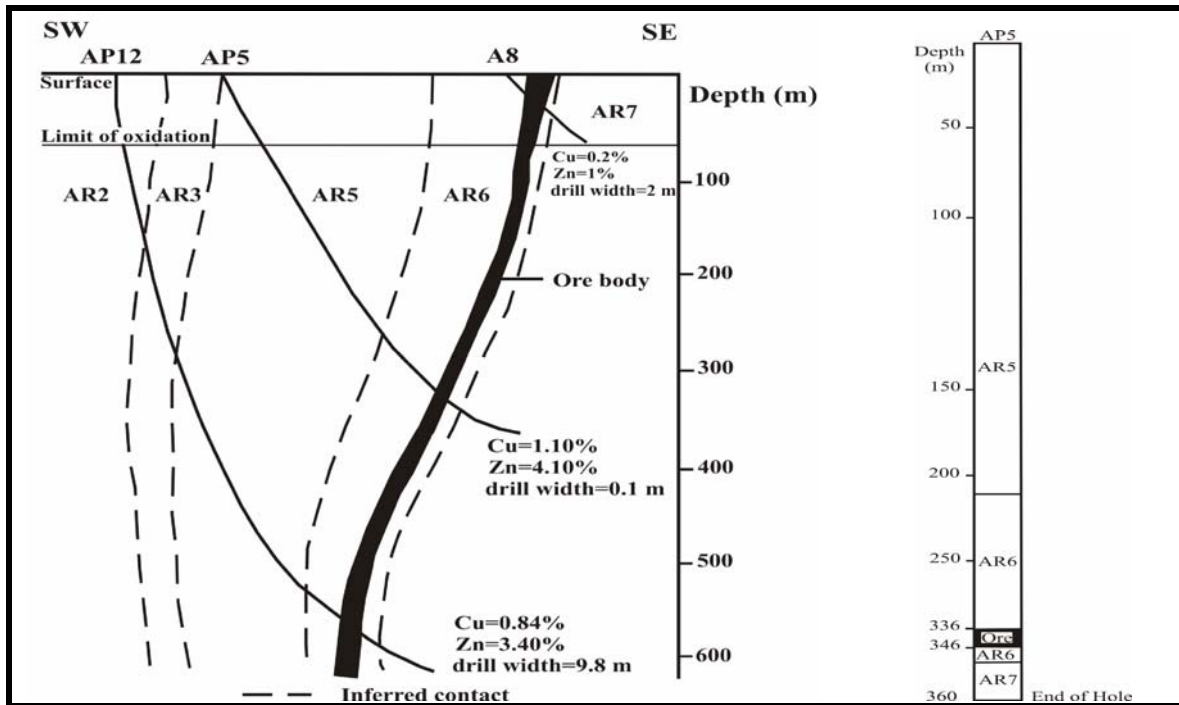


Figure A.2: Cross section includes borehole AP5 and sample locations.

Table A.2: Depth of samples in drill hole AP5, Areachap

Sample No.	Depth (m)						
AP5/2	29.7	AP5/11	177.9	AP5/25	298.5	AP5/34	335.7
AP5/3	33.5	AP5/14	188.1	AP5/27	306.1	AP5/33	336.8
AP5/4	46.2	AP5/15	196.6	AP5/26	311.5	AP5/40	338.0
AP5/5	60.8	AP5/16	206.9	AP5/29	317.4	AP5/39	339.0
AP5/1	79.2	AP5/17	219.3	AP5/28	318.8	AP5/41	341.4
AP5/6	84.8	AP5/18	228.0	AP5/30	318.9	AP5/42	343.7
AP5/7	108.6	AP5/19	243.2	AP5/31	322.7	AP5/43	344.7
AP5/8	120.8	AP5/20	253.4	AP5/32	326.8	AP5/44	349.0
AP5/9	145.8	AP5/21	269.9	AP5/38	327.4	AP5/45	354.8
AP5/10	154.6	AP5/23	277.6	AP5/37	328.4	AP5/46	360.1
AP5/12	176.2	AP5/24	281.4	AP5/36	331.3		
AP5/13	176.5	AP5/22	282.7	AP5/35	334.2		

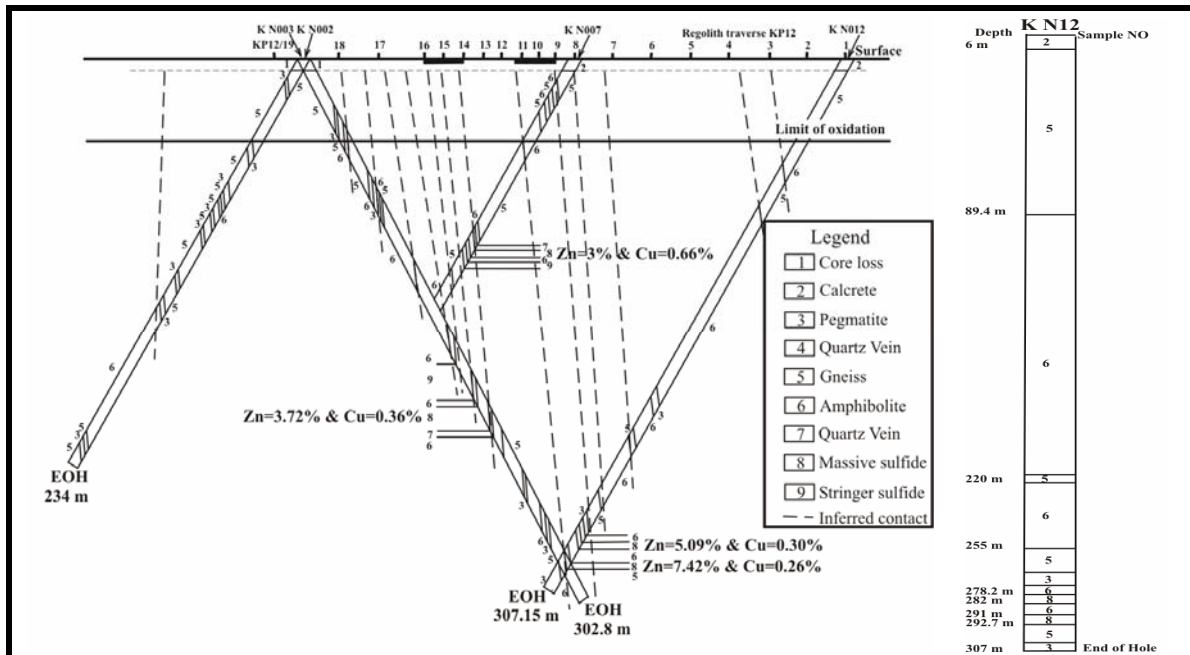


Figure A.3: Cross section includes borehole KN12 and sample locations.

Table A.3: Depth of samples in drill hole KN12, Kantiengan

Sample No.	Depth (m)						
KN12/1	175.68	KN12/11	233.67	KN12/22	278.5	KN12/33	291.29
KN12/2	179.78	KN12/12	239.8	KN12/19	278.7	KN12/32	292
KN12/3	188.27	KN12/14	250.62	KN12/23	279.41	KN12/34	292.65
KN12/4	190.12	KN12/13	253.95	KN12/24	280.28	KN12/35	293.03
KN12/5	194.67	KN12/15	255.82	KN12/25	280.74	KN12/36	293.8
KN12/6	203.23	KN12/16	262.1	KN12/26	281.8	KN12/37	295.1
KN12/7	209.93	KN12/17	266.8	KN12/28	283.32	KN12/38	297.2
KN12/8	216.76	KN12/18	274.8	KN12/29	285.32	KN12/39	299.1
KN12/9	221.15	KN12/20	276.5	KN12/30	287.25		
KN12/10	228.83	KN12/21	277.97	KN12/31	290.8		

Note: KN12/27: missing sample

**Table A. 4:** Lithological description of borehole KN12 (Rossouw, 2003)

Depth (m)	Lithological description of borehole KN12
0.00-6.00	Calcrete
6.00-89.40	Light grey-beige, weathered to 17.80 m, medium-grained, and granular to weakly banded quartzo-feldspathic gneiss with intercalated bands of feldspathic amphibolite
89.40-219.60	Dark-grey, fine-grained and weakly foliated feldspathic amphibolite
219.60-222.40	Light grey-beige, very weathered, medium-grained, granular to weakly banded quartzo-feldspathic gneiss
222.40-255.23	Dark-grey, fine-grained and weakly foliated feldspathic amphibolite
225.23-267.52	Pale-grey, strongly banded feldspar-quartz-amphibole gneiss with a quartzo-feldspathic gneiss maker and a garnetiferous layer at the bottom
267.52-274.73	Pegmatite
274.73-278.24	Dark-grey, fine-grained and weakly foliated feldspathic amphibolite
278.24-278.34	Chert
278.34-282.04	Massive sulphides (80%) and wall-rock clasts (20% - gneiss and quartz). Bronze coloured and medium- to coarse-grained. Sulphides: pyrrhotite ( $\pm 30\%$ ), sphalerite ( $\pm 7\%$ ), pyrite ( $\pm 60\%$ ) and chalcopyrite ( $\pm 3\%$ ). Two barren zones of gneiss with disseminated pyrite (3%) start at 280.12 and 280.62 m with varying thickness of 7 and 19 cm respectively. Thin chert topping (10 cm).
282.04-290.82	Grey, fine-grained, weakly banded feldspathic amphibolite. Spotty alteration and weakly defined foliation and a gradational bottom contact with massive sulphide
290.82-292.70	Massive sulphides (30%) and wall-rock clasts (80% - chlorite and quartz). Bronze coloured and medium- to coarse-grained. Sulphides: pyrrhotite ( $\pm 20\%$ ), sphalerite ( $\pm 2\%$ ), pyrite ( $\pm 80\%$ ) and chalcopyrite ( $\pm 1\%$ )
292.70-300.07	Grey, polymict medium- to coarse-grained, moderately banded quartzo-feldspathic gneiss. Few fractured and a gradational bottom contact with pegmatite
300.07-307.15	Pegmatite
307.15	End of Hole

**Table A. 5:** Lithological description of borehole KN7 (Rossouw, 2003)

Depth (m)	Lithological description of borehole KN7
0.00-5.89	Calcrete
5.89-12.91	Pegmatite
12.91-39.50	Light grey-beige, weathered to a depth of 25.26m, medium-grained, and granular to weakly banded quartzofeldspathic gneiss with intercalated bands of feldspathic amphibolite
39.50-54.70	Dark-grey, slightly weathered fine-grained feldspathic amphibolite
54.70-83.82	Dark-grey, medium-grained feldspar-quartz-amphibole gneiss
83.82-98.89	Pale-grey, strongly banded feldspar-quartz-amphibole gneiss. Weakly defined foliation with $\pm 2\%$ pyrrhotite and pyrite
98.89-104.52	Quartzofeldspathic gneiss maker with a garnetiferous layer
104.52-105.86	Dark-grey, fine-grained and weakly foliated feldspathic amphibolite with a 1m mineralised brecciated zone at the top
105.86-105.96	Chert
105.96-111.35	Massive sulphides (70%) and wall-rock clasts (30% - chlorite, epidote and quartz). Sulphides: Pyrrhotite ( $\pm 60\%$ ), sphalerite ( $\pm 10\%$ ), pyrite ( $\pm 30\%$ ) and chalcopyrite ( $\pm 2\%$ )
111.35-112.96	Grey, fine-grained, weakly banded feldspathic amphibolite. Spotty alteration, garnetiferous and weakly defined foliation with disseminated sulphides ( $\pm 3\%$ pyrite)
112.96-113.55	Massive sulphides (70%) and wall-rock clasts (30% - chlorite, epidote and quartz). Sulphides: Pyrrhotite ( $\pm 60\%$ ), sphalerite ( $\pm 10\%$ ), pyrite ( $\pm 30\%$ ) and chalcopyrite ( $\pm 2\%$ )
113.55-116.54	Stinger sulphides in medium-grained garnet-cordierite-feldspathic amphibolite. Spotty alteration, moderately banded and weakly defined foliation with disseminated sulphides ( $\pm 5\%$ pyrite). A carbon shale layer occurs between 114.82-116.54m with $\pm 10\%$ disseminated sulphides (pyrite)
116.54-126.64	Grey, polymict medium- to coarse-grained, moderately banded quartzofeldspathic gneiss
126.64-140.00	Dark-grey, fine-grained, weakly banded biotite with some intercalated thin metaquartzites and a garnet marker
140.00	End of Hole

**Table A. 6:** Lithological description of borehole KN3 (Rossouw, 2003)

Depth (m)	Lithological description of borehole KN3
0.00-4.67	Core loss
4.67-5.47	Calcrete
5.47-49.70	Light-grey, moderately banded medium-grained quartzofeldspathic gneiss. Weathered to a depth of 41.80m
49.70-57.77	Dark-grey, fine-grained, weakly banded feldspathic amphibolite with a pink pegmatite vein
57.77-76.15	Light-grey, moderately banded coarse-grained quartzofeldspathic gneiss
76.15-120.45	Dark-green, fine-grained, weakly banded biotite amphibolite with intercalated bands of gneiss, a sugary metaquartzite vein and pegmatite veins
120.45-163.35	Grey, coarse-grained, moderately banded quartzofeldspathic gneiss
163.35-169.01	Dark-grey, medium-grained feldspathic amphibolite
169.01-189.91	Stringer sulphides in a medium-grained feldspathic amphibolite. Spotty alteration and moderately banded. Gradational bottom contact with massive sulphides
189.91-190.75	Massive sulphides ( $\pm 70\%$ ) and wall-rock clasts (30% - chlorite, epidote and quartz). Sulphides: Pyrrhotite 60%, pyrite 40%, sphalerite 1% and chalcopyrite 1% (pyrite crystals in a matrix of pyrrhotite)
190.75-192.27	Light-green and fine-grained amphibolite. Sharp bottom contact with massive sulphides
192.27-204.60	Massive sulphides (80%) and wall-rock clasts (20% - chlorite, epidote and quartz). Bronze coloured and unweathered. Blebs of chalcopyrite are more frequent at the bottom 2m of the zone. Sulphides: Pyrrhotite ( $\pm 50\%$ ), sphalerite ( $\pm 15\%$ ), pyrite ( $\pm 30\%$ ) and chalcopyrite ( $\pm 3\%$ ). Sphalerite matrix to pyrrhotite and pebbly and coarse blebby pyrite replaces both
204.60-206.15	Chert
206.15-219.85	Dark-grey, fine-grained and weakly foliated feldspathic amphibolite. Gradational bottom contact with gneiss
219.85-230.60	Grey medium-grained quartzofeldspathic gneiss maker with garnetiferous layer (220-226m)
230.60-236.38	Pale-grey, strongly banded feldspar-quartz-amphibole gneiss. Weakly defined foliation
236.38-285.44	Dark-grey, medium-grained feldspar-quartz-amphibole gneiss
285.44-302.80	Dark-grey, slightly weathered fine-grained feldspathic amphibolite. A weakly defined foliation
302.80	End of Hole

**Table A. 7:** Lithological description of borehole KN2 (Rossouw, 2003)

Depth (m)	Lithological description of borehole KN2
0.00-5.50	Core loss
5.50-6.00	Calcrete
6.00-18.65	Light-grey, moderately banded, weathered, medium- to coarse-grained quartzofeldspathic gneiss. Moderately defined foliation with a gradational bottom contact with the pegmatite
18.65-21.22	Pegmatite
21.22-78.98	Pale-grey, moderately banded, medium- to coarse-grained quartzofeldspathic gneiss. Weathered to a depth of 39.83m Moderately defined foliation with pink pegmatite veins. Few fractures and a gradational bottom contact with pegmatite
78.98-83.33	Pegmatite
83.33-86.56	Pale-grey, moderately banded, medium-grained quartzofeldspathic gneiss. Weakly defined foliation with disseminated sulphides (<1%). Few fractures and a gradational bottom contact with amphibolite
86.56-88.42	Dark grey and fine grained. A sharp bottom contact with grey gneiss
88.42-146.09	Pale-grey, moderately banded, medium-grained quartzofeldspathic gneiss. Weakly defined foliation with pink pegmatite veins with a gradational bottom contact with pink pegmatite
146.09-148.12	Pegmatite
148.12-223.60	Dark-grey, fine-grained, moderately banded feldspathic amphibolite. Pink pegmatite veins with a gradational bottom contact with gneiss
223.60-234.03	Pale-grey, moderately banded, medium-grained quartzofeldspathic gneiss. Weakly defined foliation with a pink pegmatite vein
234.03	End of Hole

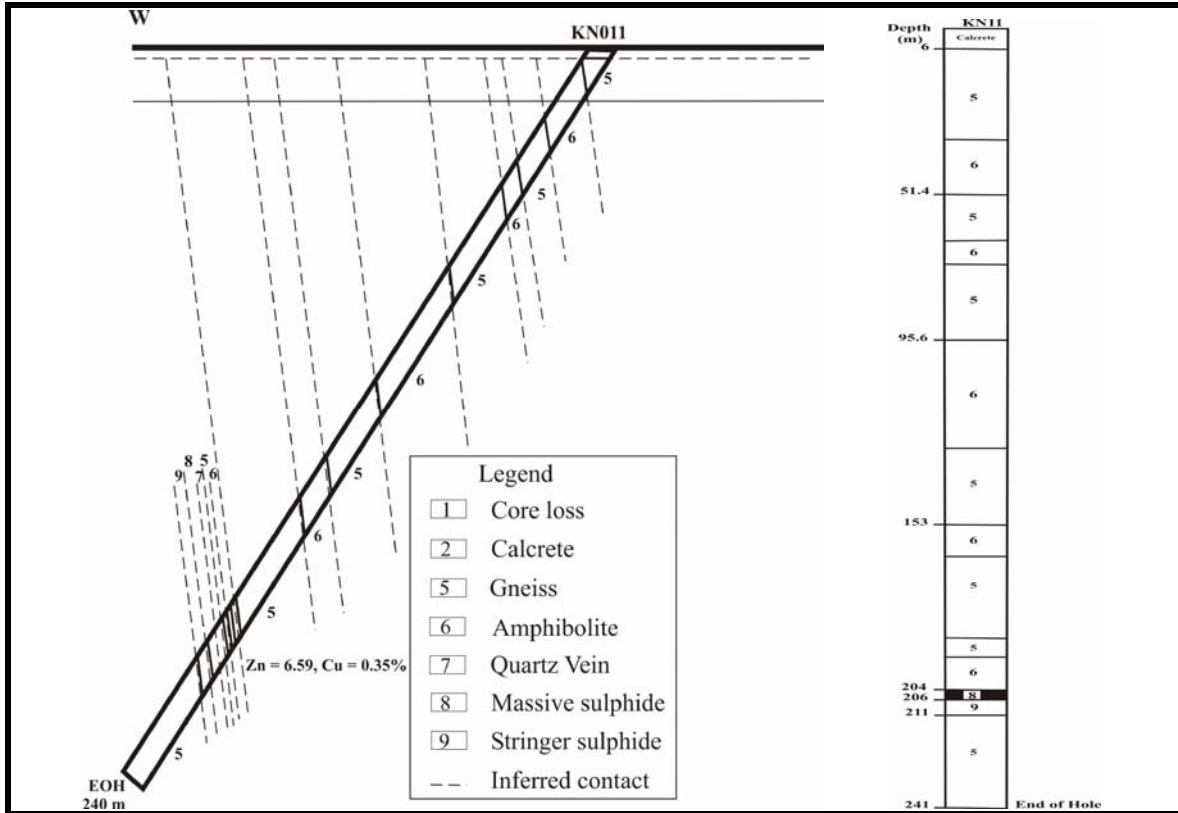


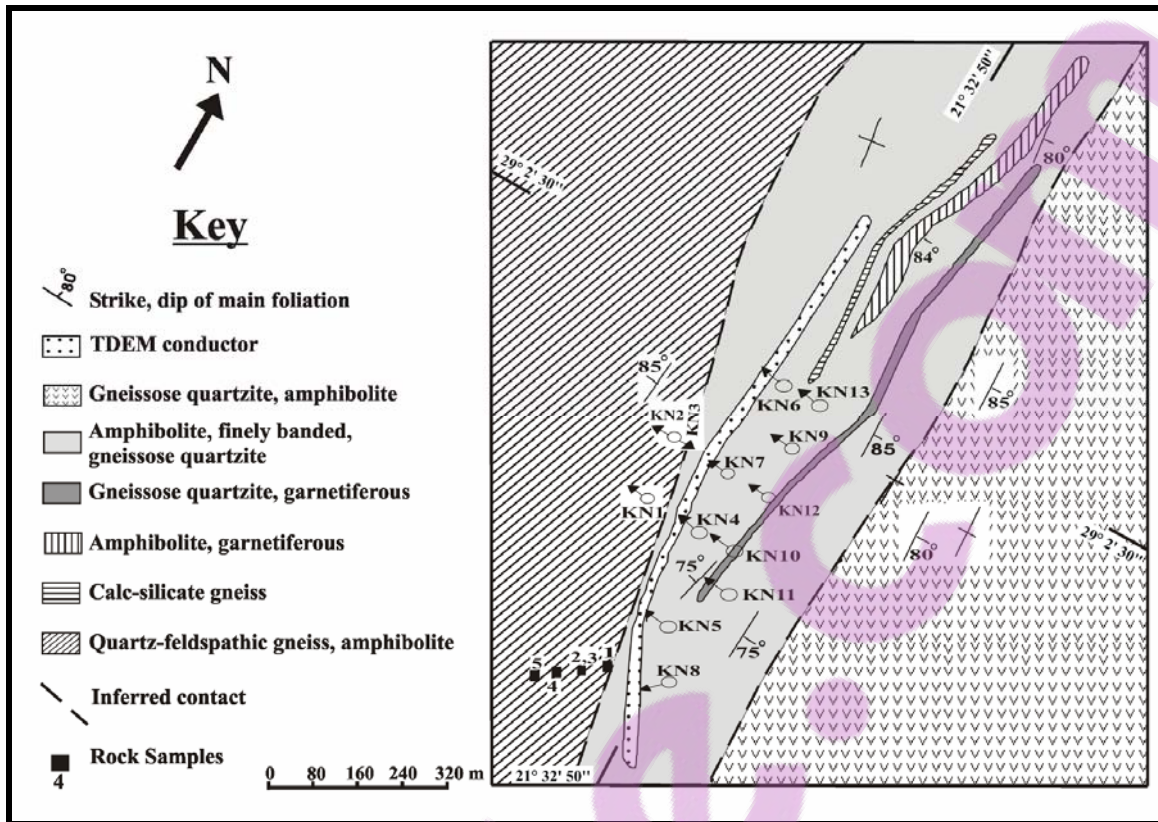
Figure A.4: Cross section of KN11 and location of samples.

Table A.8: Depth of samples in drill hole KN11, Areachap

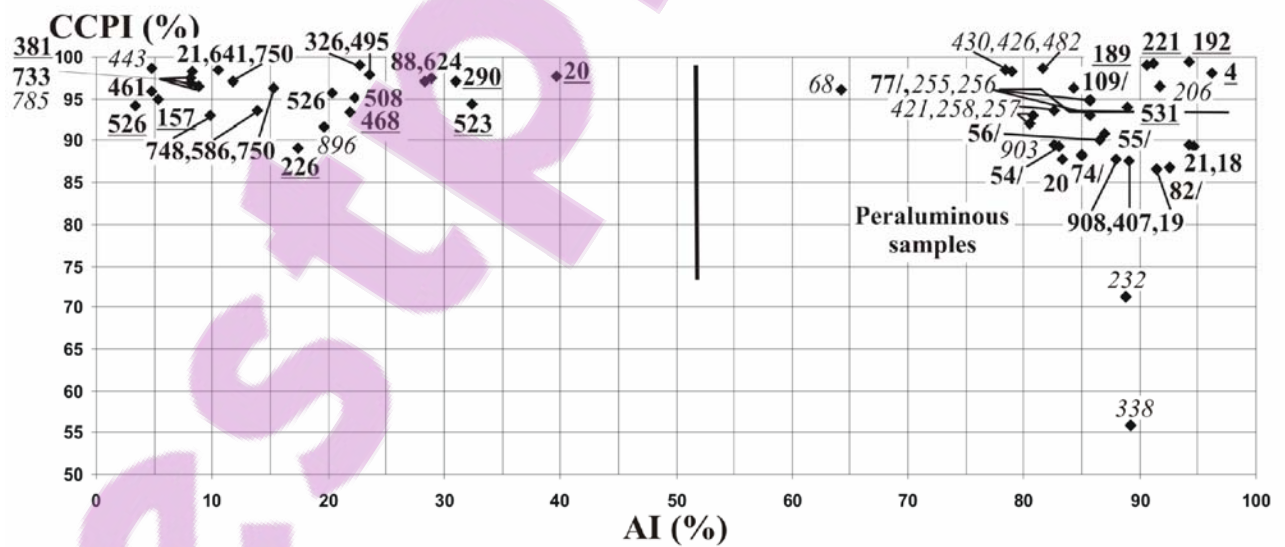
Sample No.	Depth (m)						
KN11/2	22.1	KN11/14	101.3	KN11/26	172.2	KN11/38	210.7
KN11/1	24.2	KN11/15	108.3	KN11/27	175.8	KN11/39	212.2
KN11/3	27.2	KN11/16	112.5	KN11/28	182.4	KN11/40	216.2
KN11/4	42.0	KN11/17	120.1	KN11/29	188.3	KN11/41	217.7
KN11/6	42.8	KN11/18	126.1	KN11/30	195.4	KN11/42	217.8
KN11/5	48.9	KN11/19	130.2	KN11/31	196.8	KN11/43	218.2
KN11/7	60.5	KN11/20	136.8	KN11/32	198.8	KN11/45	224.1
KN11/8	68.4	KN11/21	142.7	KN11/33	205.0	KN11/44	226.7
KN11/9	72.0	KN11/22	149.6	KN11/34	206.6	KN11/47	229.3
KN11/10	78.1	KN11/23	154.4	KN11/35	207.0	KN11/46	231.2
KN11/11	84.7	KN11/24	159.6	KN11/36	208.3	KN11/48	237.7
KN11/12	90.0	KN11/25	165.7	KN11/37	209.2	KN11/49	239.3
KN11/13	97.7						

**Table A. 9:** Lithological description of borehole KN11 (Rossouw, 2003)

Depth (m)	Lithological description of borehole KN11
0.00-6.00	Calcrete
6.00-33.70	Light grey-beige, weathered to 33.70m, medium-grained, and granular to weakly banded quartzofeldspathic gneiss with pegmatite veins. Weakly defined foliation with a 25° angle to the core axis. Feldspar
33.70-51.14	Dark-grey, fine-grained feldspathic amphibolite. Disseminated sulphide of pyrite and pyrrhotite ( $\pm 2\%$ ). A few fractures occur with a gradational bottom contact with the gneiss
51.14-65.26	Grey and medium grained quartzofeldspathic gneiss. Weakly defined foliation with a few fractures and a gradational bottom contact with amphibolite
65.26-72.17	Dark-grey, fine-grained feldspathic amphibolite. Garnetiferous and $\pm 3\%$ disseminated sulphide of pyrite and pyrrhotite at the bottom $\pm 1.5\text{m}$ of this section
72.17-95.58	Light grey-beige, very weathered, medium-grained, granular to weakly banded quartzofeldspathic gneiss
95.58-129.56	Dark-grey, fine-grained feldspathic amphibolite
129.56-153.00	Light grey-beige, very weathered, medium-grained, granular to weakly banded quartzofeldspathic gneiss with intercalated bands of feldspathic amphibolite. Few fractures with a sharp bottom contact with the amphibolite
153.00-163.17	Dark-grey, weakly foliated fine-grained feldspathic amphibolite
163.17-188.35	Pale-grey, medium-grained strongly banded feldspar-quartz-amphibole gneiss. Disseminated sulphide of pyrite ( $\pm 2\%$ )
188.35-193.05	Quartzofeldspathic gneiss maker with garnetiferous layer (192.00-193.05m)
193.05-204.07	Dark-grey, fine-grained and weakly foliated feldspathic amphibolite
204.07-206.70	Massive sulphides (80%) and wall-rock clasts (20% - chlorite and quartz). Bronze coloured. Sulphides: Pyrrhotite ( $\pm 55\%$ ), sphalerite ( $\pm 7\%$ ), pyrite ( $\pm 35\%$ ) and chalcopyrite ( $\pm 3\%$ ). Thin chert topping (10cm)
206.70-211.02	Stinger sulphides in medium-grained garnet-cordierite-feldspathic amphibolite. Spotty alteration and moderately banded with disseminated sulphides of pyrite ( $\pm 10\%$ ). A 14cm carbon shale layer occurs at 207.28m
211.02-239.52	Grey, polymict medium- to coarse-grained, moderately banded quartzofeldspathic gneiss. Weakly defined foliation with occasional garnet porphyroblasts and $\pm 1\%$ disseminated sulphide of pyrite
239.52	End of Hole



**Extra Figures**



Note 4: Kantienpan (Boks); 19: Bokspuit (Kant); 68: south of Upington (BeUp) and 82/: north of Upington (UpUp).

Figure A.6: Box plot of final results of regional data set (Figure 5.18).

## **Appendix B**

### **Microprobe Analyses**

Microprobe analyses here were done by using a energy dispersion spectrometer (EDS), or a wavelength dispersion spectrometer (WDS). EDS was used as a qualitative method for fast determination of mineral composition, whereas WDS was used for quantitative mineral analyses.

A CAMECA EPMA- SX 100 was used to analyse minerals such as biotite, feldspars, chlorite, pyroxenes, amphiboles, cordierite (pinitite), and garnets. The analytical results for selected samples from boreholes KN11 and KN12 from the Kantienpan and AP2 and AP5 from the Areachap deposit are summarized in tables B.1 to B.7.

**Table B.1:** Chemical composition of feldspar grains adjacent to the ore zone (Areachap and Kantienpan)

	Sample No.	SiO <sub>2</sub>	Al <sub>2</sub> O <sub>3</sub>	MgO	FeO	MnO	CaO	K <sub>2</sub> O	Na <sub>2</sub> O	F	Cl	Total	TiO <sub>2</sub>	ZnO	Cr <sub>2</sub> O <sub>3</sub>	NiO
<i>Areachap</i>																
FW	AP5_22A_P2_Plag	62.58	22.50	0.00	0.02	0.00	3.83	0.05	9.05	0.00	0.00	98.11	0.00	0.00	0.00	0.01
FW	AP5_22A_P2_alt_Plag	63.42	22.58	0.22	0.48	0.00	0.75	2.10	8.91	0.01	0.02	98.53	0.00	0.00	0.00	0.00
HW	AP5_44_P4_alt_Plag	69.23	19.41	0.00	0.03	0.00	0.10	0.06	11.20	0.03	0.00	100.07	0.00	0.00	0.01	0.00
HW	AP5_44_P3_UN	64.79	18.24	0.00	0.13	0.02	0.00	15.57	0.19	0.00	0.00	98.96	0.00	0.00	0.00	0.00
<i>Kantienpan</i>																
HW	KN11_20_P2_Plag	62.73	23.49	0.07	0.00	0.01	4.88	0.44	8.34	0.06	0.00	100.04	0.02	0.00	0.01	0.00
HW	KN11_27B_P1_Plag	59.29	25.33	0.06	0.00	0.00	7.13	0.17	7.42	0.00	0.00	99.50	0.03	0.00	0.01	0.00
HW	KN11_27B_P3_Plag	60.38	25.10	0.08	0.00	0.00	6.83	0.24	7.39	0.00	0.01	100.07	0.01	0.00	0.00	0.00
HW	KN11_28_P2_Plag	63.20	22.27	0.00	0.02	0.01	3.88	0.49	8.80	0.02	0.01	98.78	0.02	0.00	0.01	0.00
HW*	KN11_32_P2_Plag	54.15	29.12	0.00	0.17	0.01	10.96	0.12	4.84	0.01	0.00	99.44	0.02	0.00	0.00	0.00
HW*	KN11_33_2_P5_Plag	57.82	26.45	0.03	0.31	0.02	8.17	0.05	6.62	0.00	0.00	99.53	0.00	0.00	0.00	0.00
FW	KN11_40_P6_Plag	48.81	32.35	0.20	0.00	0.02	15.72	0.08	2.46	0.04	0.01	99.76	0.02	0.00	0.02	0.00
FW	KN11_44_P1_Plag	58.15	26.50	0.00	0.07	0.00	8.36	0.13	6.54	-0.02	0.01	99.82	0.02	0.01	0.00	0.00

Note: HW\*: Amphibolite, HW: Gneiss and HW: hangingwall

**Table B.2:** Chemical composition of pyroxene grains near the ore zone (Areachap and Kantienpan)

	Sample No.	SiO <sub>2</sub>	Al <sub>2</sub> O <sub>3</sub>	MgO	FeO	MnO	CaO	K <sub>2</sub> O	Na <sub>2</sub> O	F	Cl	Total	TiO <sub>2</sub>	ZnO	Cr <sub>2</sub> O <sub>3</sub>	NiO
<i>Areachap</i>																
FW	AP5_38A_P2_OPX	53.65	1.16	16.95	22.51	1.01	1.24	0.01	0.10	0.07	0.00	96.82	0.04	0.07	0.00	0.00
<i>Kantienpan</i>																
HW	KN11_20_P4_Opx	50.06	1.16	12.82	33.26	1.63	0.22	0.00	0.02	0.00	0.00	99.37	0.11	0.07	0.00	0.01
HW	KN11_27B_P3_Opx	51.17	4.04	21.78	19.62	2.65	0.15	0.00	0.02	0.00	0.00	99.68	0.15	0.07	0.00	0.01
HW	KN11_27B_P4_Opx	52.11	2.90	22.21	19.17	2.66	0.16	0.00	0.02	0.09	0.00	99.56	0.09	0.13	0.02	0.00
HW*	KN11_32_P2_Cpx	53.34	1.40	13.91	8.11	0.71	20.97	0.01	0.31	0.07	0.01	99.02	0.14	0.00	0.00	0.00
Ore	KN12_35A_P2_mica	55.69	2.82	24.10	13.73	1.34	0.15	0.44	0.23	0.42	0.00	99.21	0.01	0.28	0.00	0.00
Stringer	KN11_38_P2_opx	48.92	4.77	16.29	26.87	1.78	0.19	0.00	0.01	0.03	0.00	98.97	0.02	0.07	0.02	0.01
FW	KN11_39_P3_opx	50.51	3.89	19.32	25.10	0.78	0.11	0.00	0.02	0.00	0.00	99.82	0.03	0.05	0.00	0.00
FW	KN11_40_P1_Opx	49.53	3.96	16.07	28.62	1.13	0.20	0.01	0.00	0.00	0.00	99.83	0.03	0.24	0.00	0.00
FW	KN11_40_P4_Ch1?	52.60	3.94	16.77	20.80	1.52	0.23	0.05	0.30	0.28	0.01	96.58	0.01	0.07	0.00	0.00
FW	KN11_40_P5_Opx	49.74	3.47	27.93	16.64	1.12	0.20	0.00	0.02	0.03	0.00	99.40	0.03	0.20	0.01	0.00
FW	KN11_40_P6_Opx	49.34	4.16	27.91	16.42	1.10	0.22	0.00	0.03	0.03	0.00	99.48	0.02	0.22	0.00	0.00
FW	KN11_44_P3_Opx	51.45	3.41	20.79	22.10	1.57	0.20	0.01	0.01	0.03	0.00	99.70	0.04	0.08	0.00	0.00

Note: HW\*: Amphibolite, HW: Gneiss and HW: hangingwall

**Table B.3:** Chemical composition of cordierite grains close to the ore zone (Areachap and Kantienpan)

	Sample No.	SiO <sub>2</sub>	Al <sub>2</sub> O <sub>3</sub>	MgO	FeO	MnO	CaO	K <sub>2</sub> O	Na <sub>2</sub> O	F	Cl	Total	TiO <sub>2</sub>	ZnO	Cr <sub>2</sub> O <sub>3</sub>	NiO
<i>Areachap</i>																
FW	AP5_23_Cord	48.92	32.71	8.64	7.34	0.34	0.00	0.01	0.19	0.02	0.00	98.21	0.00	0.01	0.00	0.00
FW	AP5_25_P5_(Bio-Cord,alt)	40.17	32.80	5.24	9.81	0.10	0.14	0.78	0.10	0.10	0.02	89.30	0.00	0.02	0.01	0.00
FW	AP5_29A_P3_Bio	42.45	31.27	4.76	6.94	0.13	0.15	1.61	0.09	0.10	0.00	87.55	0.02	0.02	0.00	0.00
FW	AP5_32_P1_Cord	49.32	32.98	9.93	5.09	0.42	0.01	0.00	0.18	0.00	0.01	98.00	0.02	0.01	0.00	0.00
FW	AP5_32_P1_alt Cord?	38.93	29.65	5.20	12.70	0.20	0.13	2.54	0.06	0.10	0.01	89.55	0.01	0.02	0.00	0.00
FW	AP5_23_P6_Sill	36.98	61.63	0.05	0.53	0.01	0.00	0.01	0.01	0.13	0.00	99.36	0.00	0.00	0.00	0.00
<i>Kantienpan</i>																
HW	KN11_27B_P5_Cord	49.69	33.15	10.57	4.01	0.57	0.02	0.07	0.13	0.00	0.00	98.26	0.00	0.00	0.00	0.00
HW*	KN11_33_2_P4_Cord	50.09	33.41	11.06	3.56	0.54	0.01	0.00	0.19	0.01	0.01	98.99	0.00	0.09	0.00	0.00
Ore	KN11_34B_P3_Cord	50.05	33.48	11.60	2.44	0.73	0.01	0.00	0.10	0.09	0.01	98.59	0.00	0.05	0.01	0.00
Stringer	KN11_38_P4_cord	49.23	33.07	9.25	6.68	0.33	0.02	0.01	0.08	0.01	0.00	98.71	0.00	0.02	0.01	0.00
FW	KN11_39_P4_Cord	49.91	33.41	10.36	4.84	0.28	0.03	0.00	0.11	0.00	0.00	98.98	0.01	0.00	0.00	0.00
FW	KN11_40_P3_cord	49.56	33.07	9.26	6.64	0.28	0.00	0.01	0.11	0.00	0.01	99.00	0.00	0.04	0.01	0.00
FW	KN11_41_P3_Cord	48.62	32.62	8.39	7.64	0.31	0.01	0.00	0.37	0.03	0.00	98.06	0.02	0.00	0.02	0.00
FW	KN11_42_P3_Cor	49.07	32.89	8.57	7.07	0.44	0.01	0.01	0.17	0.00	0.00	98.31	0.00	0.06	0.00	0.00
FW	KN11_43_P2_Cord	49.35	33.06	9.32	6.13	0.42	0.05	0.00	0.19	0.00	0.00	98.59	0.01	0.04	0.00	0.00

Note: HW\*: Amphibolite, HW: Gneiss and HW: hangingwall

**Table B.4:** Chemical composition of garnet grains adjacent to the ore zone (Areachap)

	Sample No.	SiO <sub>2</sub>	Al <sub>2</sub> O <sub>3</sub>	MgO	FeO	MnO	CaO	K <sub>2</sub> O	Na <sub>2</sub> O	F	Cl	Total	TiO <sub>2</sub>	ZnO	Cr <sub>2</sub> O <sub>3</sub>	NiO
	AP5_20_P2_Garn	37.68	20.86	3.96	24.66	12.52	0.25	0.00	0.01	0.00	0.01	100.00	0.02	0.00	0.00	0.00
FW	AP5_22A_P3_Gar	37.26	20.44	2.67	33.08	5.41	0.87	0.00	0.03	0.05	0.00	99.85	0.02	0.00	0.00	0.00
FW	AP5_23_P1_Gar?	35.36	23.48	3.30	30.88	6.21	0.78	0.01	0.01	0.00	0.01	100.23	0.01	0.12	0.00	0.00
FW	AP5_23_P4_Gar	37.09	23.55	3.26	30.04	5.90	0.72	0.00	0.01	0.02	0.00	100.69	0.00	0.02	0.01	0.00
FW	AP5_25_P1_Gar	37.23	20.87	2.63	35.85	2.43	0.52	0.00	0.02	0.00	0.00	99.62	0.00	0.00	0.02	0.00
FW	AP5_28_B_P4_Garn	37.78	20.91	3.28	36.58	0.90	0.60	0.00	0.03	0.00	0.00	100.15	0.02	0.01	0.00	0.00
FW*	AP5_38A_P7_Garn	37.62	21.30	4.40	34.56	1.38	0.56	0.00	0.02	0.00	0.01	99.84	0.01	0.00	0.01	0.00
HW	AP5_42_P1_Gar	37.00	19.89	1.14	24.20	13.24	3.52	0.00	0.04	0.00	0.00	99.11	0.02	0.00	0.01	0.00
HW	AP5_43_P3_Garn	37.21	19.99	1.27	24.99	11.60	4.32	0.00	0.03	0.01	0.00	99.49	0.02	0.02	0.01	0.00

FW\*: Unaltered footwall, FW: Altered footwall

**Table B.5:** Chemical composition of biotite grains near the ore zone (Areachap and Kantienpan)

	Sample No.	SiO <sub>2</sub>	Al <sub>2</sub> O <sub>3</sub>	MgO	FeO	MnO	CaO	K <sub>2</sub> O	Na <sub>2</sub> O	F	Cl	Total	TiO <sub>2</sub>	ZnO	Cr <sub>2</sub> O <sub>3</sub>	NiO
<i>Areachap</i>																
FW	AP5_23_P3_Bio	36.19	18.09	12.29	16.74	0.10	0.00	7.87	0.63	0.55	0.02	93.94	1.46	0.00	0.00	0.00
FW	AP5_22A_P3_Bio	36.32	18.42	11.07	18.27	0.06	0.00	8.07	0.41	0.51	0.00	94.73	1.56	0.02	0.00	0.00
FW	AP5_30B_P2_bio	38.32	17.94	15.34	12.42	0.13	0.01	8.21	0.42	0.74	0.02	95.10	1.48	0.06	0.00	0.02
FW	AP5_32_P4_Bio	37.33	18.53	15.57	13.46	0.21	0.00	7.04	0.44	0.53	0.01	93.55	0.39	0.04	0.00	0.00
FW*	AP5_35_P8_Bio	35.23	15.45	6.12	25.00	0.83	0.01	8.76	0.13	0.12	0.05	94.21	2.40	0.09	0.00	0.00
<i>Kantienpan</i>																
HW	KN11_20_P5_Bio	35.07	14.93	21.90	9.07	0.14	0.05	8.49	0.05	0.24	0.01	94.18	4.20	0.02	0.00	0.00
HW	KN11_27B_P2_Bio	37.97	16.85	11.56	15.68	0.35	0.00	9.56	0.05	1.00	0.02	95.85	2.79	0.02	0.00	0.00
HW	KN11_28_P4_Bio	35.79	17.48	14.88	12.74	0.49	0.00	8.51	0.09	0.27	0.10	93.12	2.76	0.00	0.00	0.00
FW	KN11_38_P3_bio	36.86	17.86	14.40	13.78	0.15	0.00	8.82	0.15	1.45	0.02	94.63	1.17	0.00	0.01	0.00
FW	KN11_39_P2_Bi	38.12	16.41	10.39	18.39	0.09	0.00	8.45	0.25	2.00	0.01	94.40	0.25	0.03	0.00	0.01
FW	KN11_41_P2_Bio	36.94	19.10	15.49	12.96	0.12	0.01	8.47	0.31	0.92	0.05	95.44	1.02	0.04	0.00	0.01
FW	KN11_43_P2_Bio	36.76	18.68	14.67	13.34	0.20	0.02	7.95	0.31	1.11	0.06	94.19	1.06	0.04	0.00	0.00
FW	KN11_44_P1_Bio	37.83	15.93	11.32	17.10	0.21	0.00	8.84	0.14	1.27	0.03	95.15	2.43	0.04	0.00	0.00

FW: Altered footwall and FW\*: Unaltered footwall

**Table B.6:** Chemical composition of gahnite (spinel group) grains close the ore zone (Kantienpan)

	Sample No.	SiO <sub>2</sub>	Al <sub>2</sub> O <sub>3</sub>	FeO	MgO	MnO	CaO	K <sub>2</sub> O	Na <sub>2</sub> O	F	Cl	Total	TiO <sub>2</sub>	ZnO	Cr <sub>2</sub> O <sub>3</sub>	NiO
Ore Zone	KN11_34B_P5_Spin	0.03	59.02	5.39	6.26	0.46	0.00	0.00	0.66	0.00	0.01	101.27	0.00	29.39	0.01	0.00
FW	KN11_42_P1_Spin	0.21	56.12	13.71	2.30	0.23	0.00	0.01	0.63	0.06	0.00	99.73	0.01	26.43	0.01	0.00
FW	KN11_43_P4_Spin	0.23	56.31	12.04	2.47	0.23	0.00	0.00	0.69	0.00	0.00	100.71	0.01	28.69	0.01	0.00
Ore Zone	KN12_32_P2_Gah	0.42	56.39	9.50	4.28	0.22	0.00	0.00	0.63	0.02	0.00	99.42	0.00	27.94	0.01	0.00
Ore Zone	KN12_35A_P3_SP	0.01	59.94	16.60	8.56	0.39	0.00	0.01	0.31	0.00	0.01	99.97	0.02	14.10	0.00	0.00

FW: Altered footwall

**Table B.7:** Chemical composition of chlorite grains near the ore zone (Areachap and Kantienpan)

	Sample No.	SiO <sub>2</sub>	Al <sub>2</sub> O <sub>3</sub>	MgO	FeO	MnO	CaO	K <sub>2</sub> O	Na <sub>2</sub> O	F	Cl	Total	TiO <sub>2</sub>	ZnO	Cr <sub>2</sub> O <sub>3</sub>	NiO
<i>Areachap</i>																
HW	AP5_40_P3_Bio	29.07	16.90	12.57	27.94	0.42	0.04	0.89	0.05	0.13	0.02	88.48	0.39	0.04	0.00	0.01
HW	AP5_42_P3_Bio	27.00	17.01	6.68	34.06	0.88	0.14	1.04	0.04	0.00	0.00	87.72	0.79	0.07	0.00	0.00
HW	AP5_44_P2_Ch1	26.21	18.46	9.48	33.31	0.68	0.02	0.02	0.01	0.05	0.00	88.31	0.04	0.01	0.00	0.00
HW	AP5_45_P4_Bio	26.55	18.23	12.41	28.71	1.05	0.09	0.08	0.01	0.05	0.00	87.45	0.17	0.06	0.00	0.00
<i>Kantienpan</i>																
Ore	KN11_36_P2_alt(chl or pin)	30.22	12.57	38.05	4.94	0.76	0.13	0.08	0.02	0.00	0.01	86.82	0.00	0.02	0.00	0.02
FW	KN11_41_P4_Amp	25.43	23.09	16.71	21.01	0.31	0.01	0.02	0.01	0.12	0.01	86.81	0.03	0.03	0.01	0.01

FW: Altered footwall and HW: Hangingwall

The calculated mineral formulae from the analyses of plagioclase, pyroxene, cordierite and garnet grains are given in Table B.8 to B. 11.

**Table B.8:** Chemical composition and unit formulae of plagioclase grains close to the ore zone (Areachap and Kantienpan).

Sample No.	Plagioclase Analyses									
	AP5_22A [P2_Plug (FW)]	AP5_22A [P2_alt_Plug (FW)]	AP5_44 [P4_alt_Plug (HW)]	KN11_27B [P1_Plug (HW)]	KN11_27B [P3_Plug (HW)]	KN11_28 [P2_Plug (HW)]	KN11_32 [P2_Plug (HW*)]	KN11_33 [2_P5_Plug (Ore Zone)]	KN11_40 [P6_Plug (FW)]	KN11_44 [P1-Plug (FW)]
Mineral	Oligoclase	Albite	Albite	Andesine	Andesine	Oligoclase	Labradorite	Andesine	Bytownite	Andesine
SiO <sub>2</sub>	62.58	63.42	69.23	59.29	60.38	63.20	54.15	57.82	48.81	58.15
Al <sub>2</sub> O <sub>3</sub>	22.50	22.58	19.41	25.33	25.10	22.27	29.12	26.45	32.35	26.50
FeO	0.02	0.48	0.03	0.00	0.00	0.02	0.17	0.31	0.00	0.07
TiO <sub>2</sub>	0.00	0.00	0.00	0.03	0.01	0.02	0.02	0.00	0.02	0.02
MgO	0.00	0.22	0.00	0.06	0.08	0.00	0.00	0.03	0.20	0.00
CaO	3.83	0.75	0.10	7.13	6.83	3.88	10.96	8.17	15.72	8.36
Na <sub>2</sub> O	9.05	8.91	11.20	7.42	7.39	8.80	4.84	6.62	2.46	6.54
K <sub>2</sub> O	0.05	2.10	0.06	0.17	0.24	0.49	0.12	0.05	0.08	0.13
MnO	0.00	0.00	0.00	0.00	0.00	0.01	0.01	0.02	0.02	0.00
FeO	0.00	0.01	0.03	0.00	0.00	0.02	0.01	0.00	0.04	0.00
<b>Total</b>	98.11	98.53	100.07	99.50	100.07	98.78	99.44	99.53	99.76	99.82
<b>Based on 32(O)</b>										
Si	11.26	11.38	12.06	10.63	10.74	11.31	9.82	10.40	8.96	10.42
Al	4.77	4.78	3.98	5.35	5.26	4.70	6.22	5.61	6.99	5.60
Fe <sup>+2</sup>	0.00	0.07	0.00	0.00	0.00	0.00	0.03	0.05	0.00	0.01
Ti	0.00	0.00	0.00	0.00	0.00	0.00	0.00	0.00	0.00	0.00
Mg	0.00	0.06	0.00	0.02	0.02	0.00	0.00	0.01	0.05	0.00
Ca	0.74	0.14	0.02	1.37	1.30	0.74	2.13	1.57	3.09	1.60
Na	3.16	3.10	3.78	2.58	2.55	3.05	1.70	2.31	0.88	2.27
K	0.01	0.48	0.01	0.04	0.05	0.11	0.03	0.01	0.02	0.03
Ca+Na+K	3.91	3.73	3.81	3.99	3.90	3.91	3.86	3.89	3.98	3.91
Ab	80.81	83.22	99.16	64.68	65.27	78.11	44.10	59.28	21.97	58.16
An	18.90	3.87	0.49	34.35	33.34	19.03	55.18	40.43	77.56	41.08
Or	0.29	12.91	0.35	0.98	1.39	2.86	0.72	0.29	0.47	0.76

Note: HW\*: amphibolite, HW: gneiss, HW: hangingwall, FW: footwall, Plug: plagioclase, and AP5\_22A [P2\_Plug (FW)] means borehole AP5\_ sample No. 22A\_[analysis point No\_ in plagioclase (from the footwall zone)].

**Table B.9:** Chemical composition and unit formulae of pyroxene grains close to the ore zone (Areachap and Kantienpan).

Sample No.	Pyroxene Analyses												
	AP5_38A [P2_OPX (FW)]	KN11_20 [P4_Opx (HW)]	KN11_27B [P3_Opx (HW)]	KN11_27B [P4_Opx (HW)]	KN11_32 [P2_Cpx (Ore)]	KN12_35A [P2_mica (Ore)]	KN11_38 [P2_opx (Stringer)]	KN11_39 [P3_opx (FW)]	KN11_40 [P1_Opx (FW)]	KN11_40 [P4_Ch!? (FW)]	KN11_40 [P5_Opx (FW)]	KN11_40 [P6_Opx (FW)]	KN11_44 [P3_Opx (FW)]
Mineral	Clino- Enstatite	Clino- Ferrosilite	Clino- Enstatite	Clino- Enstatite	Augite	Clino- Enstatite	Clino- Enstatite	Clino- Enstatite	Pigeonite	Clinoenstaite- Ferrosilite	Clino- Enstatite	Clino- Enstatite	Clino- Enstatite
<b>SiO<sub>2</sub></b>	53.65	50.06	51.17	52.11	53.34	55.69	48.92	50.51	49.53	52.60	49.74	49.34	51.45
<b>Al<sub>2</sub>O<sub>3</sub></b>	1.16	1.16	4.04	2.90	1.40	2.82	4.77	3.89	3.96	3.94	3.47	4.16	3.41
<b>TiO<sub>2</sub></b>	0.04	0.11	0.15	0.09	0.14	0.01	0.02	0.03	0.03	0.01	0.03	0.02	0.04
<b>FeO</b>	22.51	33.26	19.62	19.17	8.11	13.73	26.87	25.10	28.62	20.80	16.64	16.42	22.10
<b>MgO</b>	16.95	12.82	21.78	22.21	13.91	24.10	16.29	19.32	16.07	16.77	27.93	27.91	20.79
<b>MnO</b>	1.01	1.63	2.65	2.66	0.71	1.34	1.78	0.78	1.13	1.52	1.12	1.10	1.57
<b>CaO</b>	1.24	0.22	0.15	0.16	20.97	0.15	0.19	0.11	0.20	0.23	0.20	0.22	0.20
<b>Na<sub>2</sub>O</b>	0.10	0.02	0.02	0.02	0.31	0.23	0.01	0.02	0.00	0.30	0.02	0.03	0.01
<b>K<sub>2</sub>O</b>	0.01	0.00	0.00	0.00	0.01	0.44	0.00	0.00	0.01	0.05	0.00	0.00	0.01
<b>Cr<sub>2</sub>O<sub>3</sub></b>	0.00	0.00	0.00	0.02	0.00	0.00	0.02	0.00	0.00	0.00	0.01	0.00	0.00
<b>NiO</b>	0.00	0.01	0.01	0.00	0.00	0.00	0.01	0.00	0.00	0.00	0.00	0.00	0.00
<b>F</b>	0.07	0.00	0.00	0.09	0.07	0.42	0.03	0.00	0.00	0.28	0.03	0.03	0.03
<b>Total</b>	96.82	99.37	99.68	99.56	99.02	99.21	98.97	99.82	99.83	96.58	99.40	99.48	99.70

Note: Mg\*=100Mg/(Mg+Fe+Mn), Opx: ortho-pyroxene, chl: Chlorite, FW: footwall, HW: hangingwall and AP5\_38A [P2\_OPX (FW)] means borehole AP5\_ sample No. 38A\_[analysis point No\_ in orthopyroxene( from the footwall zone)].

Table B.9: Continued

Pyroxene Analyses													
Sample No.	AP5_38A [P2_OPX (FW)]	KN11_20 [P4_Opx (HW)]	KN11_27B [P3_Opx (HW)]	KN11_27B [P4_Opx (HW)]	KN11_32 [P2_Cpx (Ore)]	KN12_35A [P2_mica (Ore)]	KN11_38 [P2_opx (Stringer)]	KN11_39 [P3_opx (FW)]	KN11_40 [P1_Opx (FW)]	KN11_40 [P4_Ch!? (FW)]	KN11_40 [P5_Opx (FW)]	KN11_40 [P6_Opx (FW)]	KN11_44 [P3_Opx (FW)]
Mineral	Clino- Enstatite	Clino- Ferrosilite	Clino- Enstatite	Clino- Enstatite	Augite	Clino- Enstatite	Clino- Enstatite	Clino- Enstatite	Pigeonite	Clinoenstaite- Ferrosilite	Clino- Enstatite	Clino- Enstatite	Clino- Enstatite
Based on 6(O)													
Si	2.07	1.99	1.91	1.94	2.00	2.02	1.90	1.91	1.92	2.02	1.84	1.82	1.93
Al	0.00	0.01	0.09	0.06	0.00	0.00	0.10	0.09	0.08	0.00	0.15	0.18	0.07
Al	0.05	0.04	0.09	0.07	0.06	0.12	0.12	0.08	0.10	0.18	0.00	0.00	0.08
Ti	0.00	0.00	0.00	0.00	0.00	0.00	0.00	0.00	0.00	0.00	0.00	0.00	0.00
Fe <sup>+2</sup>	0.73	1.11	0.61	0.60	0.25	0.42	0.87	0.79	0.93	0.67	0.51	0.51	0.69
Cr	0.00	0.00	0.00	0.00	0.00	0.00	0.00	0.00	0.00	0.00	0.00	0.00	0.00
Mn	0.03	0.05	0.08	0.08	0.02	0.04	0.06	0.03	0.04	0.05	0.04	0.03	0.05
Ni	0.00	0.00	0.00	0.00	0.00	0.00	0.00	0.00	0.00	0.00	0.00	0.00	0.00
Mg	0.97	0.76	1.21	1.23	0.78	1.30	0.94	1.09	0.93	0.96	1.54	1.54	1.16
Ca	0.05	0.01	0.01	0.01	0.84	0.01	0.01	0.00	0.01	0.01	0.01	0.01	0.01
Na	0.01	0.00	0.00	0.00	0.02	0.02	0.00	0.00	0.00	0.02	0.00	0.00	0.00
K	0.00	0.00	0.00	0.00	0.00	0.02	0.00	0.00	0.00	0.00	0.00	0.00	0.00
Atomic Percentages													
Mg+Fe+Ca	1.75	1.87	1.83	1.84	1.87	1.72	1.82	1.89	1.86	1.64	2.06	2.05	1.86
Mg	55.63	40.52	66.21	67.14	41.48	75.52	51.71	57.70	49.80	58.63	74.66	74.87	62.37
Fe <sup>+2</sup>	41.45	58.98	33.46	32.51	13.57	24.14	47.85	42.06	49.76	40.80	24.96	24.71	37.20
Ca	2.93	0.50	0.33	0.35	44.95	0.34	0.43	0.24	0.45	0.58	0.38	0.42	0.43
Mg*	56.21	39.56	63.51	64.42	73.74	74.01	50.31	57.08	49.04	57.23	73.69	73.94	61.00

Note: Mg\*=100Mg/(Mg+Fe+Mn), Opx: ortho-pyroxene, chl: Chlorite, FW: footwall, HW: hangingwall and AP5\_38A [P2\_OPX (FW)] means borehole AP5\_ sample No. 38A\_[analysis point No\_ in orthopyroxene( from the footwall zone)].

**Table B.10:** Chemical composition and unit formulae of cordierite grains near the ore zone (Areachap and Kantienpan).

Sample No.	Cordierite Analyses													
	AP5_23 [Cord (FW)]	AP5_25 [P5_(Bio- alt Cord.) (FW)]	AP5_29A [P3_Bio (FW)]	AP5_32 [P1_Cord (FW)]	AP5_32 [P1_alt Cord? (FW)]	KN11_27 B [P5_Cord (HW)]	KN11_33 _2 [P4_Cord (HW*)]	KN11_34 B [P3_Cord (Ore)]	KN11_38 [P4_cord (Stringer)]	KN11_39 [P4_Cord (FW)]	KN11_40 [P3_cord (FW)]	KN11_41 [P3_Cord (FW)]	KN11_42 [P3_Cord (FW)]	KN11_43 [P2_Cord (FW)]
Mineral	Cordierite	Cordierite	Cordierite	Cordierite	Cordierite	Cordierite	Cordierite	Cordierite	Cordierite	Cordierite	Cordierite	Cordierite	Cordierite	Cordierite
SiO <sub>2</sub>	48.92	40.17	42.45	49.32	38.93	49.69	50.09	50.05	49.23	49.91	49.56	48.62	49.07	49.35
Al <sub>2</sub> O <sub>3</sub>	32.71	32.80	31.27	32.98	29.65	33.15	33.41	33.48	33.07	33.41	33.07	32.62	32.89	33.06
TiO <sub>2</sub>	0.00	0.00	0.02	0.02	0.01	0.00	0.00	0.00	0.00	0.01	0.00	0.02	0.00	0.01
FeO	7.34	9.81	6.94	5.09	12.70	4.01	3.56	2.44	6.68	4.84	6.64	7.64	7.07	6.13
MgO	8.64	5.24	4.76	9.93	5.20	10.57	11.06	11.60	9.25	10.36	9.26	8.39	8.57	9.32
MnO	0.34	0.10	0.13	0.42	0.20	0.57	0.54	0.73	0.33	0.28	0.28	0.31	0.44	0.42
Na <sub>2</sub> O	0.19	0.10	0.09	0.18	0.06	0.13	0.19	0.10	0.08	0.11	0.11	0.37	0.17	0.19
CaO	0.00	0.14	0.15	0.01	0.13	0.02	0.01	0.01	0.02	0.03	0.00	0.01	0.01	0.05
K <sub>2</sub> O	0.01	0.78	1.61	0.00	2.54	0.07	0.00	0.00	0.01	0.00	0.01	0.00	0.01	0.00
F	0.02	0.10	0.10	0.00	0.10	0.00	0.01	0.09	0.01	0.00	0.00	0.03	0.00	0.00
Cl	0.00	0.02	0.00	0.01	0.01	0.00	0.01	0.01	0.00	0.00	0.01	0.00	0.00	0.00
Total	98.21	89.30	87.55	98.00	89.55	98.26	98.99	98.59	98.71	98.98	99.00	98.06	98.31	98.59
Based on 18(O)														
Si	5.03	4.66	4.95	5.03	4.65	5.03	5.03	5.02	5.02	5.03	5.03	5.02	5.03	5.03
Al	0.97	1.34	1.05	0.97	1.35	0.97	0.97	0.98	0.98	0.97	0.97	0.97	0.97	0.97
Al	2.99	3.14	3.24	2.99	2.83	2.99	2.98	2.98	2.99	2.99	2.99	3.00	3.01	3.01
Ti	0.00	0.00	0.00	0.00	0.00	0.00	0.00	0.00	0.00	0.00	0.00	0.00	0.00	0.00
Fe <sup>+2</sup>	0.63	0.95	0.68	0.43	1.27	0.34	0.30	0.20	0.57	0.41	0.56	0.66	0.61	0.52
Mg	1.32	0.91	0.83	1.51	0.93	1.60	1.65	1.74	1.40	1.55	1.40	1.29	1.31	1.41
Mn	0.03	0.01	0.01	0.04	0.02	0.05	0.05	0.06	0.03	0.02	0.02	0.03	0.04	0.04
Na	0.04	0.02	0.02	0.04	0.01	0.03	0.04	0.02	0.02	0.02	0.02	0.07	0.03	0.04
Ca	0.00	0.02	0.02	0.00	0.02	0.00	0.00	0.00	0.00	0.00	0.00	0.00	0.00	0.01
K	0.00	0.12	0.24	0.00	0.39	0.01	0.00	0.00	0.00	0.00	0.00	0.00	0.00	0.00
Mg#	67.72	48.77	55.01	77.67	42.19	82.45	84.70	89.44	71.17	79.23	71.31	66.19	68.36	73.05

Note: HW\*: amphibolite, HW: gneiss, HW: hangingwall, FW: footwall, Mg# = 100\*Mg/(Mg+Fe), Bio: biotite, Cord: cordierite, alt: altered and AP5\_25 [P5\_(Bio- alt Cord.) (FW)] means borehole AP5\_ sample No. 25 [analysis point No\_ in biotite or altered cordierite (from the footwall zone)].

**Table B.11:** Chemical composition and unit formulae of garnet grains near the ore zone (Areachap).

Sample No.	Garnet Analyses								
	AP5_20 [P2_Garn]	AP5_22A [P3_Gar n (FW)]	AP5_23 [P1_Garn? (FW)]	AP5_23 [P4_Garn (FW)]	AP5_25 [P1_Garn (FW)]	AP5_28_B [P4_Garn (FW)]	AP5_38A [P7_Garn (FW*)]	AP5_42 [P1_Garn (HW)]	AP5_43 [P3_Garn (HW)]
<b>Mineral</b>	Almandine	Almandine	Almandine	Almandine	Almandine	Almandine	Almandine	Almandine	Almandine
<b>SiO<sub>2</sub></b>	37.68	37.26	35.36	37.09	37.23	37.78	37.62	37.00	37.21
<b>Al<sub>2</sub>O<sub>3</sub></b>	20.86	20.44	23.48	23.55	20.87	20.91	21.30	19.89	19.99
<b>Cr<sub>2</sub>O<sub>3</sub></b>	0.00	0.00	0.00	0.01	0.02	0.00	0.01	0.01	0.01
<b>FeO</b>	24.66	33.08	30.88	30.04	35.85	36.58	34.56	24.20	24.99
<b>TiO<sub>2</sub></b>	0.02	0.02	0.01	0.00	0.00	0.02	0.01	0.02	0.02
<b>MgO</b>	3.96	2.67	3.30	3.26	2.63	3.28	4.40	1.14	1.27
<b>MnO</b>	12.52	5.41	6.21	5.90	2.43	0.90	1.38	13.24	11.60
<b>CaO</b>	0.25	0.87	0.78	0.72	0.52	0.60	0.56	3.52	4.32
<b>K<sub>2</sub>O</b>	0.00	0.00	0.01	0.00	0.00	0.00	0.00	0.00	0.00
<b>Na<sub>2</sub>O</b>	0.01	0.03	0.01	0.01	0.02	0.03	0.02	0.04	0.03
<b>F</b>	0.00	0.05	0.00	0.02	0.00	0.00	0.00	0.00	0.01
<b>Total</b>	100.00	99.85	100.23	100.69	99.62	100.15	99.84	99.11	99.49
<b>Based on 24(O)</b>									
<b>Si</b>	6.04	6.05	5.69	5.87	6.04	6.07	6.01	6.08	6.07
<b>Al</b>	3.94	3.91	0.31	0.13	3.99	3.96	4.01	3.85	3.85
<b>Al</b>	0.00	0.00	4.15	4.26	0.00	0.00	0.00	0.00	0.00
<b>Cr</b>	0.00	0.00	0.00	0.00	0.00	0.00	0.00	0.00	0.00
<b>Fe<sup>+2</sup></b>	3.31	4.49	4.16	3.98	4.86	4.91	4.62	3.32	3.41
<b>Ti</b>	0.00	0.00	0.00	0.00	0.00	0.00	0.00	0.00	0.00
<b>Mg</b>	0.95	0.65	0.79	0.77	0.64	0.79	1.05	0.28	0.31
<b>Mn</b>	1.70	0.74	0.85	0.79	0.33	0.12	0.19	1.84	1.60
<b>Ca</b>	0.04	0.15	0.13	0.12	0.09	0.10	0.10	0.62	0.76
<b>Mol per cent end-members</b>									
<b>Mg+Fe+Mn+Ca</b>	6.00	6.03	5.93	5.66	5.93	5.92	5.95	6.06	6.08
<b>Pyrope</b>	15.78	10.71	13.35	13.59	10.74	13.26	17.62	4.60	5.08
<b>Almandine</b>	55.14	74.45	70.10	70.27	82.10	82.94	77.63	54.81	56.11
<b>Spessartine</b>	28.36	12.33	14.28	13.98	5.64	2.07	3.14	30.37	26.38
<b>Grossular</b>	0.72	2.51	2.27	2.16	1.53	1.74	1.61	10.21	12.43

Note: FW\*: Unaltered footwall; FW: Altered footwall; Garn: garnet; Mol: molciular and **AP5\_22A** [P3\_Gar n (FW)] means borehole **AP5\_** sample No. **22A\_**[analysis point No\_ in garnet (from the footwall zone)].

**Table B.12:** Chemical composition and unit formulae of biotite grains near the ore zone (Areachap and Kantienpan)

Sample No.	Biotite Analyses												
	AP5_23 [P3_Bio (FW)]	AP5_22A [P3_Bio (FW)]	AP5_30B [P2_Bio (FW)]	AP5_32 [P4_Bio (FW)]	AP5_35 [P8_Bio (FW*)]	KN11_20 [P5_Bio (HW)]	KN11_27B [P2_Bio (HW)]	KN11_28 [P4_Bio (HW)]	KN11_38 [P3_Bio (Ore Zone)]	KN11_39 [P2_Bio (FW)]	KN11_41 [P2_Bio (FW)]	KN11_43 [P2_Bio (FW)]	KN11_44 [P1_Bio (FW)]
Mineral	Biotite	Biotite	Phlogopite	Phlogopite	Annite	Phlogopite	Biotite	Phlogopite	Phlogopite	Biotite	Phlogopite	Phlogopite	Biotite
SiO <sub>2</sub>	36.19	36.32	38.32	37.33	35.23	35.07	37.97	35.79	36.86	38.12	36.94	36.76	37.83
TiO <sub>2</sub>	1.46	1.56	1.48	0.39	2.40	4.20	2.79	2.76	1.17	0.25	1.02	1.06	2.43
Al <sub>2</sub> O <sub>3</sub>	18.09	18.42	17.94	18.53	15.45	14.93	16.85	17.48	17.86	16.41	19.10	18.68	15.93
FeO	16.74	18.27	12.42	13.46	25.00	9.07	15.68	12.74	13.78	18.39	12.96	13.34	17.10
MgO	12.29	11.07	15.34	15.57	6.12	21.90	11.56	14.88	14.40	10.39	15.49	14.67	11.32
MnO	0.10	0.06	0.13	0.21	0.83	0.14	0.35	0.49	0.15	0.09	0.12	0.20	0.21
CaO	0.00	0.00	0.01	0.00	0.01	0.05	0.00	0.00	0.00	0.00	0.01	0.02	0.00
K <sub>2</sub> O	7.87	8.07	8.21	7.04	8.76	8.49	9.56	8.51	8.82	8.45	8.47	7.95	8.84
Na <sub>2</sub> O	0.63	0.41	0.42	0.44	0.13	0.05	0.05	0.09	0.15	0.25	0.31	0.31	0.14
F	0.55	0.51	0.74	0.53	0.12	0.24	1.00	0.27	1.45	2.00	0.92	1.11	1.27
<b>Total</b>	93.94	94.73	95.10	93.55	94.21	94.18	95.85	93.12	94.63	94.40	95.44	94.19	95.15
<b>Based on 22(O)</b>													
Si	5.51	5.51	5.64	5.57	5.62	5.19	5.69	5.42	5.56	5.90	5.46	5.51	5.76
Al	2.49	2.49	2.36	2.43	2.38	2.81	2.31	2.58	2.44	2.10	2.54	2.49	2.24
Al	0.75	0.81	0.74	0.82	0.53	-0.21	0.67	0.53	0.73	0.89	0.78	0.81	0.61
Ti	0.17	0.18	0.16	0.04	0.29	0.47	0.31	0.31	0.13	0.03	0.11	0.12	0.28
Fe <sup>+2</sup>	2.13	2.32	1.53	1.68	3.34	1.12	1.97	1.61	1.74	2.38	1.60	1.67	2.18
Mg	2.79	2.50	3.36	3.46	1.46	4.83	2.58	3.36	3.24	2.40	3.41	3.28	2.57
Mn	0.01	0.01	0.02	0.03	0.11	0.02	0.04	0.06	0.02	0.01	0.02	0.03	0.03
Ca	0.00	0.00	0.00	0.00	0.00	0.01	0.00	0.00	0.00	0.00	0.00	0.00	0.00
K	1.53	1.56	1.54	1.34	1.78	1.60	1.83	1.64	1.70	1.67	1.60	1.52	1.72
Na	0.37	0.24	0.24	0.25	0.08	0.03	0.03	0.05	0.09	0.15	0.18	0.18	0.08
Mg/Fe	1.31	1.08	2.2	2.06	0.44	4.3	1.31	2.08	1.86	1.01	2.13	1.96	1.18

FW: Altered footwall, FW\*: Unaltered footwall, HW: hanging wall and AP5\_22A [P3\_Bio (FW)] means borehole AP5\_ sample No 22A\_[analysis point No\_ in biotite (from the footwall zone)].

## Appendix C

### Sample preparation and whole rock analysis

#### C.1. Sample preparation for XRF Analysis

The remainder of quarter-core samples after making thin sections was crushed in a jaw crusher before being milled in a carbon-steel mill. The samples were milled to a particle size of <63 micron. To minimize possible cross contamination, the mill was cleaned after every sample by milling clean quartz, washing the mill pots, and drying with acetone, followed by pre contaminating the mill with the sample to be milled.

3 grams of each sample powder were weighed and dried at 100°C overnight before being roasted at 1000°C overnight to determine the absorbed ( $H_2O^-$ ) and the percentage loss on ignition ( $H_2O^+$ ), respectively.

Major elements were determined on fused beads, prepared following the standard method used in the analytical laboratory of the Department of Geology, University of Pretoria, as adapted from Bennett and Oliver (1992). One gram of pre-roasted sample powder and 6 grams of flux (Lithium tetra-borate) mixed in a Pt crucible is fused at 1050°C for 15

minutes in a muffle furnace with occasional swirling. The fused mixture is poured into a pre-heated Pt/Au mould and left to cool at room temperature in a desiccator. The bottom surface of the glass disk is analysed by x-ray fluorescence spectroscopy (XRF) using an ARL 9400XP+ wavelength dispersive XRF Spectrometer.

Trace elements were determined on pressed powder briquettes prepared following the method of Watson (1996). Approximately 16-20ml of sample powder is mixed with less than 1 volume % of a liquid binder (Mowiol: polyvinyl alcohol). This mixture is loaded into aluminium cups to increase the stability and strength before being pressed at  $\pm 7$  tons/in<sup>2</sup>.

#### **C.1.1. CALIBRATION**

The XRF Spectrometer was calibrated with certified reference materials. The NBSGSC fundamental parameter program was used for matrix correction of major elements as well as for Cl, Co, Cr, V, Sc and S. The Rh Compton peak ratio method was used for the other trace elements.

### **C.3. XRF analytical precision and accuracy**

Standard deviations and detection limits are listed in Table C.1.

### **C.4. Results of XRF analyses**

The results of XRF analysis are given below in Tables C.2 to C.6. The word “Fused” in the table refers to fused bead analysis and “Powder” to pressed powder briquette analysis. The first three columns in Table C.2 (LIT, GSN, and NIMN) are standard reference samples.

The sulphide samples were analysed as pressed powder briquettes using the UNIQUANT software, a fundamental parameter based programme, calibrated with pure metals and oxides (Samples KN12/22 to KN12/25 and KN11/34 to KN11/37). This software

analyses samples by specifying a sulphide matrix. In this case S is analysed at a different peak position and Fe, Mn, Cu, Ni, Zn and Pb expressed as elements.

**Table C.1:** Standard deviation and detection limit of XRF analysis

wt %	Standard deviation (%)	LOD
SiO <sub>2</sub>	0.4	0.02
TiO <sub>2</sub>	0.03	0.0032
Al <sub>2</sub> O <sub>3</sub>	0.3	0.01
Fe <sub>2</sub> O <sub>3</sub>	0.3	0.0097
MnO	0.0065	0.0013
MgO	0.1	0.0118
CaO	0.07	0.01
Na <sub>2</sub> O	0.11	0.0265
K <sub>2</sub> O	0.06	0.005
P <sub>2</sub> O <sub>5</sub>	0.08	0.01
ppm	Standard deviation (%)	LOD
Cl*	100	11
Co	6	3
Cr	40	15
F*	500	400
S*	300	40
Sc	5	1
V	10	1
As*	10	3
Cu	3	2
Ga	2	2
Mo	1	1
Nb	3	2
Ni	6	3
Pb	3	3
Rb	4	2
Sr	4	3
Th	2	3
U	2	3
W*	10	6
Y	4	3
Zn	4	4
Zr	6	10
Ba	14	5
La	24	5
Ce	14	6

Values for elements indicated with an \*should be considered semi-quantitative

**Table C.2:** XRF analytical results for samples from borehole AP5 (Areachap)

Fused	LIT	GSN	NIMN	AP5/1	AP5/2	AP5/3	AP5/4	AP5/5	AP5/6	AP5/7	AP5/8	AP5/9	AP5/10	AP5/11	AP5/12	AP5/13
<b>Depth (m)</b>	-	-	-	79.2	29.7	33.5	46.2	60.8	84.8	108.6	120.8	145.8	154.6	177.9	176.2	176.5
<b>Rock Name</b>	Standard	Standard	Standard	Bt-Hbl Gn	Hbl- Gn	Bt-Hbl Gn	Amph.	Amph.	Hbl- Bt-Gn	Amph.	Garnet- Bt-Gn	Hbl- Gn	Garnet- Bt-Gn	Chl- Schist	Granite rock	Granite rock
<b>SiO<sub>2</sub> (wt%)</b>	0.01	65.87	52.5	64.68	52.11	56.69	47.74	54.18	66.1	52.04	75.36	53.54	71.27	70.71	75.84	69.16
<b>TiO<sub>2</sub></b>	n.d.	0.65	0.19	0.68	1.1	0.74	0.77	0.89	0.42	0.88	0.26	0.92	0.34	0.41	0.21	0.53
<b>Al<sub>2</sub>O<sub>3</sub></b>	0.01	14.85	16.71	14.6	17.43	16.51	19.69	16.73	15.09	14.58	12.29	14.56	12.16	13.92	11.73	14.39
<b>Fe<sub>2</sub>O<sub>3</sub></b>	n.d.	3.67	9.01	7.65	11.23	10.41	10.84	10.52	5.97	12.14	4.52	11.7	5.37	4.44	2.68	3.69
<b>MnO</b>	0.01	0.05	0.18	0.2	0.18	0.19	0.19	0.22	0.16	0.13	0.16	0.26	0.14	0.05	0.02	0.06
<b>MgO</b>	n.d.	2.22	7.63	1.53	3.82	3.64	4.78	3.28	1.48	6.78	0.57	5.2	1.04	1.21	0.22	1.79
<b>CaO</b>	n.d.	2.69	11.38	5.42	9.31	3.71	10.43	7.55	4.01	7.76	1.21	9.28	1.69	0.57	0.63	0.75
<b>Na<sub>2</sub>O</b>	0.23	3.83	2.63	3.08	2.89	4.02	2.2	3.17	3.41	3.59	4.84	2.96	3.96	6.7	6.5	6.83
<b>K<sub>2</sub>O</b>	n.d.	4.74	0.24	0.87	1.24	1.45	1.29	1.32	1.98	0.68	1.31	0.74	1.8	0.54	0.35	0.58
<b>P<sub>2</sub>O<sub>5</sub></b>	0.01	0.3	0.03	0.23	0.43	0.19	0.2	0.28	0.15	0.12	0.07	0.2	0.09	0.16	0.07	0.18
<b>LOI</b>	n.d.	1.29	0.00	0.52	0.83	2.48	1.36	0.92	0.58	0.89	0.3	0.78	0.58	1.19	0.91	1.63
<b>Total:</b>		100.16	100.28	99.45	100.57	100.03	99.49	99.04	99.37	99.56	100.89	100.14	98.44	99.90	99.16	99.59

Hbl: hornblende, Bt: biotite, Gn: gneiss, Chl: chlorite, Amph.: amphibolite and n.d.: Not detected.

Table C.2: Continued

Powder	SIO2	GSN	NIMN	AP5/1	AP5/2	AP5/3	AP5/4	AP5/5	AP5/6	AP5/7	AP5/8	AP5/9	AP5/10	AP5/11	AP5/12	AP5/13
Cl* (ppm)	90	536	57	12	84	41	56	9	91	110	29	217	8	40	26	71
Co	2	39	49	42	47	41	49	43	33	51	28	51	30	28	32	32
Cr	16	51	36	10	40	27	62	27	11	34	10	62	10	10	10	10
F*	584	4789	100	100	100	100	100	100	528	100	551	100	1218	191	288	190
S*	16	108	16	350	132	16	16	45	16	16	16	454	16	16	16	16
Sc	1	5	20	14	15	31	9	20	11	33	8	28	10	14	4	10
V	3	55	200	57	247	169	210	185	76	339	5	322	1	37	36	46
As	3	9	3	3	3	3	3	3	3	3	4	3	3	3	3	3
Cu	2	23	11	46	186	3	44	35	26	4	19	40	4	7	2	5
Ga	2	20	17	16	16	16	16	17	14	16	18	16	16	14	10	13
Mo	1	1	1	1	2	1	1	1	1	1	1	1	2	1	1	1
Nb	2	22	2	5	6	3	3	4	4	2	8	3	8	5	2	10
Ni	3	36	109	6	19	10	43	9	6	24	6	32	5	6	4	6
Pb	3	55	3	8	7	4	6	7	8	5	8	4	15	4	3	3
Rb	2	181	5	21	27	64	54	38	56	21	26	17	109	20	22	18
Sr	3	583	264	309	417	309	431	401	427	190	86	331	167	77	24	35
Th	3	43	3	5	3	3	4	3	6	3	4	3	5	10	4	3
U	3	13	3	3	3	3	3	3	3	3	3	3	4	5	3	3
W*	6	452	6	316	112	100	95	118	228	85	325	146	299	281	463	369
Y	4	18	6	33	27	24	16	25	19	24	87	23	65	23	14	28
Zn	11	54	59	92	89	103	76	92	70	30	126	90	100	36	11	41
Zr	10	213	12	105	96	58	42	67	79	44	265	55	217	139	159	220
Ba	5	1443	81	506	573	351	378	400	1009	123	231	269	703	131	47	133
La	5	49	19	31	47	32	31	42	15	43	32	55	23	18	29	13
Ce	28	122	10	44	45	25	18	24	42	6	54	35	46	27	52	37

\*: Semi-quantitative analysis.

Table C.2: Continued

Fused	AP5/14	AP5/15	AP5/16	AP5/17	AP5/18	AP5/19	AP5/20	AP5/21	AP5/22	AP5/23	AP5/24	AP5/25	AP5/26	AP5/27	AP5/28	AP5/29
Depth (m)	188.1	196.6	206.9	219.3	228	243.2	253.4	269.9	282.7	277.6	281.4	298.5	311.5	306.1	318.8	317.4
Rock Name	Amph.	Hbl-Gn	Amph.	Hbl-Gn	Hbl-Gn	Sil-Crd-Bt-Gn	Bt-Gn	Sil-Crd-Bt-Gn	Garnet-Sil-Crd-Bt-Gn	Sil-Crd-Bt-Gn	Sil-Crd-Bt-Gn	Sil-Crd-Bt-Gn	Garnet-Crd-Gn	Garnet-Sil-Crd-Bt-Gn	Garnet-Sil-Crd-Bt-Gn	Sil-Crd-Bt-Gn
SiO <sub>2</sub> (wt%)	47.51	58.37	48.51	55.14	53.54	65.7	66.89	65.25	70.51	67.44	75.03	72.59	64.25	56.41	70.12	78.07
TiO <sub>2</sub>	0.47	0.76	1.07	1.16	0.95	0.8	0.4	0.37	0.47	0.3	0.25	0.25	0.56	0.55	0.27	0.25
Al <sub>2</sub> O <sub>3</sub>	15.21	15.35	14.52	14.06	14.67	13.75	13.91	13.23	11.85	10.89	11.6	11.63	14.9	14.11	15.02	9.2
Fe <sub>2</sub> O <sub>3</sub>	8.96	7.64	12.85	13.42	12.62	9.26	6.62	9.61	7.01	13.55	4.51	7.32	7.69	12.61	9.91	4.5
MnO	0.16	0.14	0.33	0.43	0.33	0.19	0.14	0.1	0.08	0.08	0.05	0.13	0.11	0.17	0.13	0.06
MgO	8.94	4.25	7.06	5.51	4.66	2.67	2.55	5.98	4.21	3.86	3.24	2.34	4.68	7.27	3.12	2.65
CaO	12.99	6.11	5.14	3.66	5.71	2.31	0.56	0.05	0.34	n.d.	0.23	0.01	0.76	0.56	0.02	0.07
Na <sub>2</sub> O	1.55	3.79	3.91	3	5.03	3.56	5.47	0.32	0.82	0.23	1.42	0.38	2.23	1.51	0.1	1.03
K <sub>2</sub> O	1.28	1.34	0.36	0.87	0.68	0.79	0.32	2.65	2.15	1.54	1.42	1.57	1.47	1.25	0.91	1.34
P <sub>2</sub> O <sub>5</sub>	0.09	0.21	0.15	0.17	0.15	0.27	0.13	0.12	0.18	0.04	0.06	0.04	0.21	0.07	0.06	0.05
LOI	1.78	1.58	6.08	2.43	1.08	0.96	2.18	2.26	2.47	2.59	2.14	1.79	3.37	1.25	0.24	1.61
<b>Total:</b>	98.96	99.55	99.97	99.87	99.43	100.26	99.20	99.93	100.11	100.52	99.94	98.05	100.23	95.78	99.91	98.84

Hbl: hornblende, Bt: biotite, Gn: gneiss, Sil: sillimanite, Crd: cordierite, Amph.: amphibolite and n.d.: Not detected.

Table C.2: Continued

Powder	AP5/14	AP5/15	AP5/16	AP5/17	AP5/18	AP5/19	AP5/20	AP5/21	AP5/22	AP5/23	AP5/24	AP5/25	AP5/26	AP5/27	AP5/28	AP5/29
Cl* (ppm)	130	131	13	15	78	8	8	15	18	8	8	8	8	8	8	17
Co	47	39	58	50	49	42	28	39	33	50	27	39	33	54	48	38
Cr	323	58	25	15	19	10	10	10	10	10	10	10	10	16	10	16
F*	100	100	100	100	567	100	1032	1438	945	1615	913	887	231	467	281	733
S*	16	404	16	16	16	381	637	1139	16	27647	16	16	92	247	16	16
Sc	41	11	41	34	36	19	11	18	16	13	9	13	18	23	12	12
V	241	136	279	325	343	6	1	31	12	1	6	1	27	174	1	1
As	3	3	5	3	3	3	3	4	3	3	3	3	3	3	4	4
Cu	5	28	2	8	2	22	9	57	3	137	2	3	3	16	2	2
Ga	11	15	25	19	17	17	16	14	14	19	12	16	15	24	21	10
Mo	1	1	1	1	1	1	1	21	3	1	1	2	1	1	1	1
Nb	2	7	2	4	2	5	6	6	8	5	6	5	5	6	4	3
Ni	106	39	24	6	15	5	3	3	3	3	3	3	4	7	3	9
Pb	8	6	13	31	5	6	49	3	3	3	3	3	29	3	3	15
Rb	74	61	29	52	30	25	70	63	46	31	31	36	37	24	17	43
Sr	264	477	56	142	132	158	28	9	29	9	48	8	66	52	6	30
Th	5	3	5	3	3	3	3	3	3	3	3	6	3	7	6	3
U	4	3	19	3	3	3	3	3	3	3	3	6	3	3	5	3
W*	75	133	32	116	116	339	279	184	213	362	210	355	147	237	500	377
Y	9	20	31	34	27	40	51	34	60	56	67	67	25	21	89	43
Zn	63	72	184	144	156	68	257	49	49	38	32	53	48	109	34	51
Zr	22	81	53	71	48	144	209	150	197	195	241	161	107	175	225	150
Ba	511	633	26	292	130	336	656	1423	1328	1474	881	1008	967	623	1115	659
La	28	34	35	33	39	29	8	5	7	14	6	13	17	28	14	5
Ce	11	35	23	18	12	28	37	39	39	25	46	29	22	62	54	40

\*: Semi-quantitative analysis.

Table C.2: Continued

Fused	AP5/30	AP5/31	AP5/32	AP5/33	AP5/34	AP5/35	AP5/36	AP5/37	AP5/38	AP5/39	AP5/40	AP5/41	AP5/42	AP5/43	AP5/44	AP5/45	AP5/46
Depth (m)	318.9	322.7	326.8	336.8	335.7	334.2	331.3	328.4	327.4	339	338	341.4	343.7	344.7	349	354.8	360.1
Rock Name	Sil-Crd-Bt-Gn	Hbl-Schist	Sil-Crd-Gn	Amph.	Bt-Hbl-Gn	Bt-Gn	Gneiss	Sil-Crd-Schist	Garnet-Hbl-Schist	Amph.	Bt-Hbl-Gneiss	Hbl-Gneiss	Garnet-Bt-Gn	Hbl-Garnet-Bt-Gneiss	Hbl-Gn	Hbl-Bt-Gn	Amph.
SiO <sub>2</sub> (wt%)	73.05	53.1	71.03	51.14	60.7	68.26	74.38	66.37	55.85	49.57	51.69	56.38	73.83	59.51	70.5	69.61	46.85
TiO <sub>2</sub>	0.29	1.3	0.25	0.89	0.96	0.31	0.29	0.49	0.51	1.04	0.89	1.2	0.23	0.46	0.32	0.44	1.9
Al <sub>2</sub> O <sub>3</sub>	11.64	13.92	11.84	14.62	14.12	13.05	11.23	12.74	15.31	14.56	14.63	13.8	12.32	12.43	12.12	12.67	13.44
Fe <sub>2</sub> O <sub>3</sub>	6.36	18.78	7.69	14.64	11.88	6.28	4.92	8.91	10.59	15.08	14.09	13.34	4.23	10.17	5.86	6.47	17.02
MnO	0.09	0.23	0.11	0.29	0.36	0.15	0.11	0.16	0.22	0.34	0.4	0.33	0.17	0.24	0.14	0.16	0.26
Mg	3.99	8.86	4.7	4.65	1.39	1.92	0.5	4.88	5.89	4.54	4.55	2.4	0.41	2.39	0.91	1.26	7.1
CaO	n.d.	1.01	0.03	7.94	4.22	3.26	1.09	n.d.	4.99	8.2	7.37	6.12	1.73	7.09	2.22	3.66	10.12
Na <sub>2</sub> O	0.49	0.9	0.35	4.22	4.56	4.36	5.52	0.33	2.92	3.87	3.9	4.31	4.83	2.54	4.15	3.12	1.82
K <sub>2</sub> O	1.48	0.37	1.55	1.35	1.11	1.13	0.41	2.32	1.32	1.65	0.99	1.21	0.64	2.22	0.96	1.42	0.77
P <sub>2</sub> O <sub>5</sub>	0.05	0.27	0.05	0.13	0.48	0.08	0.06	0.06	0.1	0.14	0.13	0.6	0.07	0.13	0.08	0.06	0.24
LOI	2.41	1.34	2.14	0.47	0.62	0.78	0.55	3.32	1.76	0.65	0.85	0.46	0.48	0.85	0.94	0.91	0.79
Total:	99.85	100.07	99.73	100.34	100.42	99.58	99.07	99.58	99.46	99.54	99.49	100.14	98.96	98.06	98.20	99.78	100.31

Hbl: hornblende, Bt: biotite, Gn: gneiss, Sil: sillimanite, Crd: cordierite, Amph.: amphibolite and n.d.: Not detected.

Table C.2: Continued

Powder	AP5/30	AP5/31	AP5/32	AP5/33	AP5/34	AP5/35	AP5/36	AP5/37	AP5/38	AP5/39	AP5/40	AP5/41	AP5/42	AP5/43	AP5/44	AP5/45	AP5/46
Cl* (ppm)	8	8	8	50	26	23	8	8	8	108	40	29	13	33	16	182	36
Co	40	60	38	61	43	35	34	35	46	60	57	45	30	44	36	39	68
Cr	10	15	10	19	10	18	10	10	52	23	18	10	10	17	10	12	143
F*	717	100	784	100	100	551	100	100	100	100	100	100	384	100	136	281	100
S*	1542	16	74	16	56	16	140	497	400	452	203	69	180	16	16	34	780
Sc	14	35	13	29	23	14	9	21	37	33	30	32	7	20	14	11	36
V	2	260	1	378	1	49	12	11	198	384	301	30	1	103	34	58	390
As	3	26	4	3	3	3	3	3	3	3	3	3	3	3	6	3	4
Cu	37	2	11	28	14	11	20	25	23	72	51	18	20	3	8	16	75
Ga	17	19	15	16	21	16	18	17	15	16	18	18	15	16	17	17	17
Mo	1	1	3	1	1	1	1	1	1	1	1	1	1	1	1	1	1
Nb	4	3	5	2	3	6	7	5	3	2	4	3	7	3	7	6	2
Ni	3	11	6	9	4	12	5	3	27	16	13	3	4	10	4	9	62
Pb	22	39	21	9	6	6	4	130	6	4	14	4	11	3	3	9	7
Rb	38	13	45	40	36	36	15	81	54	59	24	52	37	79	40	34	46
Sr	12	23	15	171	167	153	71	13	95	136	174	151	169	337	177	190	86
Th	5	3	3	3	3	5	3	4	3	3	5	3	5	3	3	4	3
U	3	3	3	3	3	4	3	3	3	3	3	3	3	3	3	3	3
W*	408	162	281	111	253	238	389	165	114	95	119	154	329	190	362	300	94
Y	61	29	49	22	45	55	82	46	27	25	40	36	53	35	57	65	36
Zn	101	96	92	99	151	95	54	181	111	105	129	114	99	96	90	125	170
Zr	187	80	203	43	80	232	241	201	71	47	68	55	167	76	180	200	72
Ba	751	237	705	325	535	604	157	959	1496	456	327	302	376	490	381	482	90
La	23	44	18	47	33	34	25	26	5	41	34	42	13	44	17	32	31
Ce	48	8	42	6	26	45	45	41	15	15	19	19	46	33	40	44	10

\*: Semi-quantitative analysis.

**Table C.3:** XRF analytical results for samples from borehole AP2 (Areachap)

Fused	AP2/1	AP2/2	AP2/3	AP2/4	AP2/5	AP2/6	AP2/7	AP2/8	AP2/9	AP2/10	AP2/11	AP2/12	AP2/13	AP2/14	AP2/15	AP2/16	AP2/17
Depth (m)	62.2	71.2	74.4	81.2	82.5	87.1	91.1	92.2	92.5	105.7	106.3	97.8	91.1	92.6	118	113.2	112.2
Rock Name	Garnet-Schist	Amph.	Garnet-mica-Gn	Bt-Hbl-Gn	Bt-Gn	Hbl-Gn	Hbl-Gn	Highly altered rock	Highly altered rock	Gossan Zone	Gossan Zone	Gossan Zone	Granite(?)	Granite(?)	Hbl-Bt-Gn	Gneiss	Gossan Zone
SiO <sub>2</sub> (wt%)	62.72	33.98	54.41	62.63	76.33	46.63	53.46	45.83	48.82	72.14	73.63	49.75	54.31	77.66	53.15	53.22	39.43
TiO <sub>2</sub>	0.61	0.62	0.97	0.63	0.05	1.07	0.96	0.53	0.64	0.25	0.05	0.04	0.04	0.03	2.05	1.49	1.64
Al <sub>2</sub> O <sub>3</sub>	15.52	12.3	16.75	15.84	13.38	17.31	15.58	17.91	20.45	11.63	12.89	10.03	9.07	12.87	14.37	12.27	14.25
Fe <sub>2</sub> O <sub>3</sub>	7.65	9.93	11.57	7.2	0.93	10.23	12.06	15.63	11.84	4.97	3.49	26.32	0.53	0.66	13.64	13.69	26.51
MnO	0.18	0.19	0.25	0.18	0.01	0.26	0.22	0.21	0.21	0.19	0.03	0.11	n.d.	0.01	0.24	0.3	0.33
MgO	2.86	3.77	4.11	2.82	0.08	7.51	4.13	6.93	5.85	3.51	1.07	2.29	n.d.	n.d.	4.83	5.71	6.34
CaO	1.28	6.29	3.1	1.03	0.59	4.37	5.69	0.7	0.95	0.29	n.d.	n.d.	0.02	n.d.	5.6	7.26	0.98
Na <sub>2</sub> O	5.71	2.49	4.18	5.63	3.66	5.03	3.47	4.97	5.22	1.6	6.75	1.01	3.79	7.6	4.06	2.91	1.06
K <sub>2</sub> O	0.8	0.77	1.53	1.06	4.92	0.76	1.22	0.73	1.33	2.43	0.03	4.98	2.26	0.12	0.54	0.57	2.87
P <sub>2</sub> O <sub>5</sub>	0.23	0.12	0.24	0.17	0.04	0.31	0.23	0.09	0.08	0.06	0.03	0.05	0.02	0.05	0.83	0.16	0.18
LOI	2.31	29.65	3.14	2.28	0.45	6.74	1.72	5.22	4.45	2.61	1.42	4.44	29.65	0.42	0.89	1.81	5.89
<b>Total:</b>	99.84	100.10	100.24	99.46	100.45	100.24	98.2	98.75	99.83	99.70	99.41	99.01	99.71	99.41	100.22	99.40	99.48

Hbl: hornblende, Bt: biotite, Gn: gneiss, Amph.: amphibolite and n.d.: Not detected.

Table C.3: Continued

Powder	AP2/1	AP2/2	AP2/3	AP2/4	AP2/5	AP2/6	AP2/7	AP2/8	AP2/9	AP2/10	AP2/11	AP2/12	AP2/13	AP2/14	AP2/15	AP2/16	AP2/17
Cl* (ppm)	36	8	40	45	27	8	8	8	40	33	47	39	30	41	50	38	8
Co	44	58	46	36	28	46	48	63	54	38	41	81	36	43	46	56	96
Cr	11	19	17	14	10	24	26	24	49	10	10	11	10	10	12	96	164
F*	100	100	100	100	432	100	100	100	100	100	462	108	485	431	100	100	100
S*	16	16	351	16	16	16	16	16	16	16	16	16	16	16	44	16	16
Sc	22	26	29	30	1	34	28	18	25	14	1	6	2	1	29	38	65
V	87	341	182	105	3	222	221	141	164	54	11	121	5	6	155	317	395
As	3	6	3	3	3	3	3	7	5	3	3	4	3	3	3	3	3
Cu	45	11	56	12	2	3	53	175	83	80	64	572	7	5	11	87	4
Ga	15	17	17	15	11	19	18	16	15	12	10	14	9	8	17	15	23
Mo	1	1	1	1	1	1	1	1	1	1	1	25	1	1	1	3	1
Nb	5	4	4	4	2	4	4	3	3	4	4	3	4	2	4	4	5
Ni	7	6	9	4	3	15	16	15	19	5	4	4	3	3	9	38	75
Pb	21	6	34	8	41	9	38	10	8	3	3	35	22	3	4	9	31
Rb	23	34	53	21	122	21	45	34	84	15	2	114	76	6	20	13	161
Sr	111	295	179	73	96	88	223	125	205	100	27	57	62	34	167	77	93
Th	8	3	3	3	43	6	3	20	3	5	28	17	25	48	3	3	3
U	5	3	3	12	5	9	3	10	8	8	4	23	3	7	3	3	40
W*	298	122	135	141	397	22	116	19	12	234	489	110	544	615	168	92	25
Y	23	18	30	15	47	15	26	39	8	13	17	24	13	49	43	36	45
Zn	236	109	165	280	211	247	83	5414	2409	2404	1558	5761	275	267	111	346	3026
Zr	85	39	88	60	14	51	64	78	23	72	58	11	10	86	84	98	84
Ba	339	357	857	354	234	194	588	273	242	34	5	694	272	5	155	96	538
La	22	19	24	11	13	18	39	52	30	14	10	18	5	5	47	46	66
Ce	37	25	38	28	55	31	28	41	17	39	10	10	18	30	33	25	88

\*: Semi-quantitative analysis.

Table C.3: Continued

Fused	AP2/18	AP2/19	AP2/20	AP2/21	AP2/22	AP2/23	AP2/24	AP2/25	AP2/26	AP2/27
Depth (m)	112.4	111.7	108.7	107.5	120.1	124.1	122.1	141.1	153.7	165
Rock Name	Amph.	Hbl-Gn	Amph.	Amph.	Bt-Hbl-Gn	Bt-Gn	Hbl-Gn	Bt-Schist	Hbl-Gn	Amph.
SiO <sub>2</sub> (wt%)	52.01	46.95	47.62	47.07	69.81	70.85	53.67	62.46	56.44	50.27
TiO <sub>2</sub>	1.34	1.85	1.01	0.85	0.44	0.42	1.05	0.83	0.57	0.81
Al <sub>2</sub> O <sub>3</sub>	13.56	14.02	17.42	18	11.88	12.32	15.22	12.47	14.99	14.64
Fe <sub>2</sub> O <sub>3</sub>	15.68	16.39	14.84	12.59	6.81	6.76	12.48	9.51	8.23	11.38
MnO	0.3	0.28	0.25	0.24	0.14	0.19	0.21	0.15	0.18	0.21
MgO	6.44	7.02	5.33	5.67	1.48	1.31	4.41	5.67	4.38	6.54
CaO	3.19	6.51	5.17	8.59	4.18	1.86	8.5	1.14	7.45	10.83
Na <sub>2</sub> O	2.55	3.41	4.54	3.46	3.17	4.37	3.32	2.25	3.39	2.56
K <sub>2</sub> O	0.8	0.9	1.07	1	0.56	0.95	0.63	3.63	1.67	0.78
P <sub>2</sub> O <sub>5</sub>	0.16	0.2	0.16	0.14	0.09	0.07	0.18	0.24	0.14	0.2
LOI	3.67	2.29	2.82	3.02	0.42	1.12	0.48	1.39	1.32	1.16
<b>Total:</b>	99.70	99.83	100.21	100.61	98.97	100.22	100.17	99.74	98.73	99.40

Hbl: hornblende, Bt: biotite, Gn: gneiss, Amph.: amphibolite and n.d.: Not detected.

Table C.3: Continued

Powder	AP2/18	AP2/19	AP2/20	AP2/21	AP2/22	AP2/23	AP2/24	AP2/25	AP2/26	AP2/27
Cl* (ppm)	8	30	15	42	8	8	8	14	77	70
Co	68	63	57	54	39	30	54	38	43	54
Cr	120	108	38	37	10	10	19	10	69	150
F*	100	100	100	100	110	1388	100	1196	100	1238
S*	16	16	16	16	216	16	43	16	132	313
Sc	48	51	38	28	9	18	27	30	19	27
V	266	379	313	299	82	42	311	95	201	300
As	3	4	3	4	4	3	3	3	7	3
Cu	10	5	5	6	17	2	25	4	21	44
Ga	17	19	15	16	14	18	17	18	14	15
Mo	1	1	1	1	1	1	1	3	1	1
Nb	6	5	3	3	3	6	2	7	5	3
Ni	55	55	24	25	3	6	8	5	28	50
Pb	13	8	6	3	7	9	4	7	6	3
Rb	34	32	50	52	22	30	15	314	93	24
Sr	77	97	186	194	145	68	157	45	252	257
Th	4	3	4	3	8	4	3	3	7	3
U	8	5	4	3	4	3	3	3	3	3
W*	64	55	45	44	311	205	173	82	188	173
Y	29	36	19	16	52	64	27	56	23	18
Zn	1228	622	293	229	99	155	90	133	65	86
Zr	100	96	29	28	168	230	66	157	55	39
Ba	224	209	196	140	146	368	72	288	432	122
La	41	53	37	41	18	25	19	32	19	22
Ce	35	18	17	20	45	40	20	54	33	26

\*: Semi-quantitative analysis.

**Table C.4:** XRF analytical results from surface (Kantienpan).

<b>Fused</b>	<b>KPR5/1</b>	<b>KPR5/2</b>	<b>KPR5/3</b>	<b>KPR5/4</b>	<b>KPR5/5</b>
<b>Depth (m)</b>	Surface	Surface	Surface	Surface	Surface
<b>Rock Name</b>	Amph.	Bt-Crd-Gn	Crd-Sil-Bt-Gn	Amph.	Hbl-Gn to Amph.
<b>SiO<sub>2</sub> (wt%)</b>	46.05	48.31	73.26	47.15	53
<b>TiO<sub>2</sub></b>	0.7	0.82	0.21	0.66	0.53
<b>Al<sub>2</sub>O<sub>3</sub></b>	14.27	20.56	12.89	12.81	14.45
<b>Fe<sub>2</sub>O<sub>3</sub></b>	10.66	10.56	4	8.62	7.56
<b>MnO</b>	0.19	0.19	0.13	0.24	0.22
<b>MgO</b>	6.54	3.78	5.14	8.3	3.95
<b>CaO</b>	19.99	10.39	n.d.	20.51	17.72
<b>Na<sub>2</sub>O</b>	1.32	3.33	0.34	0.96	1.97
<b>K<sub>2</sub>O</b>	0.11	1.04	3.03	0.25	0.6
<b>P<sub>2</sub>O<sub>5</sub></b>	0.09	0.24	0.04	0.09	0.13
<b>LOI</b>	0.61	1.21	1.02	0.56	0.56
<b>Total:</b>	100.54	100.42	100.06	100.16	100.70

Bt: biotite, Gn: gneiss, Sil: sillimanite, Crd: cordierite, Amph.: amphibolite and n.d.: Not detected.

**Table C.4:** Continued

<b>Powder</b>	<b>KPR5/1</b>	<b>KPR5/2</b>	<b>KPR5/3</b>	<b>KPR5/4</b>	<b>KPR5/5</b>
<b>Cl* (ppm)</b>	8	23	8	8	8
<b>Co</b>	47	35	30	45	39
<b>Cr</b>	273	10	10	614	173
<b>F*</b>	100	968	4094	100	100
<b>S*</b>	16	16	16	26	159
<b>Sc</b>	6	5	9	9	1
<b>V</b>	250	1	3	191	150
<b>As</b>	3	3	3	3	11
<b>Cu</b>	190	2	2	35	13
<b>Ga</b>	13	16	19	13	16
<b>Mo</b>	1	1	1	1	1
<b>Nb</b>	2	16	20	8	4
<b>Ni</b>	81	4	7	136	139
<b>Pb</b>	5	5	6	3	3
<b>Rb</b>	6	56	63	16	21
<b>Sr</b>	291	34	18	242	228
<b>Th</b>	4	13	11	3	3
<b>U</b>	3	3	3	3	3
<b>W*</b>	99	372	314	88	124
<b>Y</b>	12	14	27	34	18
<b>Zn</b>	77	69	140	69	82
<b>Zr</b>	24	302	297	35	61
<b>Ba</b>	350	1366	993	226	384
<b>La</b>	41	14	31	43	37
<b>Ce</b>	12	87	75	18	25

\*: Semi-quantitative analysis.

**Table C.5:** XRF analytical results for samples from borehole KN12 (Kantienpan)

Fused	KN12/1	KN12/2	KN12/3	KN12/4	KN12/5	KN12/6	KN12/7	KN12/8	KN12/9	KN12/10	KN12/11	KN12/12	KN12/13	KN12/14
<b>Depth (m)</b>	175.68	179.78	188.27	190.12	194.67	203.23	209.93	216.76	221.15	228.83	233.67	239.8	253.95	250.62
<b>Rock Name</b>	Bt-Hbl-Gn	Amph.	Bt-Hbl-Gn	Amph.	Amph.	Amph.	Bt-Gn	Bt-Gn	Amph.	Amph.	Bt-Hbl-Gn	Bt-Gn	Amph.	Amph.
<b>SiO<sub>2</sub> (wt%)</b>	76.08	45.72	48.2	47.25	48.54	49.75	49.29	69.69	48.91	49.46	48.97	65.01	50.39	48.42
<b>TiO<sub>2</sub></b>	0.19	0.89	0.78	0.77	0.79	0.98	0.97	0.45	1.02	1.31	1.02	0.59	0.84	1.43
<b>Al<sub>2</sub>O<sub>3</sub></b>	11.54	20.16	19.91	19.69	18.04	17.79	19.62	14.39	18.82	15.83	18.14	14.18	18.97	15
<b>Fe<sub>2</sub>O<sub>3</sub></b>	5.04	11.4	11.37	12.61	11.42	12.38	10.65	5.12	13.05	14.59	12.3	7.15	10.12	16.24
<b>MnO</b>	0.09	0.24	0.18	0.18	0.18	0.16	0.21	0.1	0.27	0.28	0.19	0.23	0.2	0.36
<b>MgO</b>	2.47	3.44	4.62	3.75	5.51	4.39	4.01	0.64	3.96	5.08	5.61	1.75	4.47	4.98
<b>CaO</b>	0.01	14.17	9.09	10.61	8.17	7.41	8.3	3.71	6.67	8.67	4.92	3.43	8.45	8.2
<b>Na<sub>2</sub>O</b>	0.57	2.01	3.66	3.37	3.92	3.91	4.06	3.82	3.68	3.88	4.52	4.68	4.6	3.23
<b>K<sub>2</sub>O</b>	3.57	1.26	1.06	0.66	1.53	1.58	1.69	1.38	1.55	1.11	3	1.02	0.77	1.26
<b>P<sub>2</sub>O<sub>5</sub></b>	0.04	0.27	0.27	0.21	0.24	0.33	0.29	0.14	0.26	0.45	0.23	0.21	0.22	0.34
<b>LOI</b>	0.27	0.4	1.34	0.36	0.51	1.07	0.46	0.38	0.00	0.00	0.75	0.1	0.23	0.58
<b>Total:</b>	99.86	99.95	100.46	99.47	98.87	99.76	99.56	99.83	97.94	100.64	99.65	98.37	99.26	100.03

Hbl: hornblende, Bt: biotite, Gn: gneiss, Amph.: amphibolite and n.d.: Not detected.

Table C.5: Continued

Powder	KN12/1	KN12/2	KN12/3	KN12/4	KN12/5	KN12/6	KN12/7	KN12/8	KN12/9	KN12/10	KN12/11	KN12/12	KN12/13	KN12/14
Cl* (ppm)	48	18	76	55	44	59	27	21	38	50	57	8	16	8
Co	49	44	49	48	49	49	45	29	49	52	50	31	56	41
Cr	28	32	41	41	55	34	27	10	24	30	27	10	21	26
F*	100	100	100	100	100	2867	994	1217	1415	100	100	100	398	100
S*	51	136	267	1380	72	733	76	535	81	645	391	282	236	42
Sc	13	8	22	16	23	26	20	15	26	30	27	18	37	23
V	251	264	253	227	247	279	292	19	301	420	348	27	430	267
As	3	5	4	4	3	3	3	3	3	3	3	3	4	3
Cu	47	42	54	359	3	59	7	71	7	69	3	6	66	2
Ga	19	20	18	19	15	20	20	16	23	21	17	16	20	16
Mo	1	1	1	1	1	1	2	1	1	1	1	1	1	1
Nb	4	3	4	4	5	5	6	6	4	4	3	4	5	3
Ni	18	21	23	26	29	18	19	3	16	11	15	3	6	15
Pb	6	8	5	7	6	11	11	7	7	19	4	8	6	14
Rb	23	30	27	12	37	63	61	36	55	22	82	9	51	18
Sr	586	400	560	567	444	213	324	161	133	366	284	191	359	327
Th	3	3	3	3	3	3	4	4	3	3	3	3	3	7
U	3	3	3	3	3	5	3	3	3	3	3	3	3	3
W*	152	118	80	120	90	78	81	285	108	81	71	242	81	93
Y	21	20	20	22	20	32	26	34	26	30	22	28	31	22
Zn	76	93	83	82	73	112	99	73	98	76	59	100	184	59
Zr	58	37	50	52	51	63	73	156	56	58	45	110	59	46
Ba	501	496	320	260	508	533	610	481	723	235	602	639	815	326
La	38	24	45	35	28	16	40	23	38	42	37	17	37	36
Ce	28	33	28	29	31	45	38	45	22	41	28	32	34	30

\*: Semi-quantitative analysis.

Table C.5: Continued

Fused	KN12/15	KN12/16	KN12/17	KN12/18	KN12/19	KN12/20	KN12/21	KN12/22	KN12/23	KN12/24	KN12/25	KN12/28
Depth (m)	255.82	262.1	266.8	274.8	278.7	276.5	277.97	278.5	279.41	280.28	280.74	281.8
Rock Name	Garnet-Bt-Crd-Gn	Sil-Crd-Bt-Gn	Sil-Crd-Bt-Gn	Bt-Hbl-Gn	Crd-Bt-Gn	Hbl-Gn	Bt-Hbl-Gn	Ore Zone	Ore Zone	Ore Zone	Ore Zone	Bt-Crd-Gn
SiO <sub>2</sub> (wt%)	63.98	66.5	68.6	53.79	60.77	55.33	51.45	41.27	24.86	15.47	23.46	35.6
TiO <sub>2</sub>	0.38	0.37	0.45	0.95	0.88	1.06	1.29	0.11	0.0642	132	340	0.16
Al <sub>2</sub> O <sub>3</sub>	14.95	13.62	13.86	16.54	15.9	14.84	15.16	3.74	5.83	1.36	3.43	10.37
Fe <sub>2</sub> O <sub>3</sub>	5.45	5.71	5.3	11.96	9.26	13.41	15.21	24.04	37.98	45.82	36.40	29.09
MnO	0.06	0.13	0.11	0.31	0.14	0.26	0.29	0.14	0.18	0.13	0.18	0.42
MgO	4.06	2.17	1.41	4.52	2.97	2.97	3.7	1.46	2.61	1.86	2.60	6.4
CaO	1.29	2.11	2.34	8.01	4.56	7.17	8.02	0.43	0.93	0.98	0.28	1.04
Na <sub>2</sub> O	1.92	2.45	4.19	2.42	3.8	3.03	2.83	<10 ppm	<10 ppm	<10 ppm	<10 ppm	0.72
K <sub>2</sub> O	3.28	3.48	1.52	0.77	0.91	0.39	0.42	663	0.20	154	680	1.31
P <sub>2</sub> O <sub>5</sub>	0.07	0.08	0.06	0.28	0.23	0.37	0.47	247	675	370	413	0.09
LOI	3.46	1.75	0.98	0.73	0.64	n.d.	0.09	n.a.	n.a.	n.a.	n.a.	9.84
Total:	98.91	98	98.83	100.30	100.08	98.84	98.92	94.19 **	96.10**	92.96**	91.20**	95.06

n.a.: not applicable, Hbl: hornblende; Bt: biotite; Gn: gneiss; Sil: sillimanite; Crd: cordierite, n.d.: Not detected and \*\*: recalculated total for sulphide riched samples (S, Cu, Zn and Pb) based on the powder disc analysis.

Table C.5: Continued

Powder	KN12/15	KN12/16	KN12/17	KN12/18	KN12/19	KN12/20	KN12/21	KN12/22	KN12/23	KN12/24	KN12/25	KN12/27
Cl* (ppm)	8	8	8	14	8	48	45	8	8	8	8	13
Co	25	28	33	51	42	51	55	63	76	111	85	60
Cr	10	10	10	10	15	10	12	10	10	22	16	10
F*	2233	1074	1225	1699	932	539	319	3227	3604	3915	3061	3199
S*	14913	10252	4014	720	1048	643	1121	127976	145676	181278	158576	90645
Sc	19	19	17	19	24	25	26	2	1	1	2	7
V	8	26	4	158	159	157	228	17	9	5	5	15
As	3	3	3	3	3	3	3	3	3	3	7	6
Cu	142	11	18	26	13	91	483	3425	4319	5442	4749	15955
Ga	17	14	15	20	19	18	20	3	5	2	2	35
Mo	2	1	1	1	1	1	1	16	25	27	57	22
Nb	7	5	4	6	3	6	4	4	6	2	2	7
Ni	3	3	4	6	8	5	5	15	14	25	22	9
Pb	12	18	12	24	39	10	45	341	532	406	589	1079
Rb	76	66	26	23	35	7	12	4	12	3	3	60
Sr	130	141	228	218	247	357	351	7	22	21	4	57
Th	7	6	6	4	3	3	3	3	9	5	5	14
U	4	3	3	3	3	3	3	3	7	8	3	3
W*	220	222	346	330	273	340	272	322	168	279	242	1 47
Y	44	37	35	46	23	43	32	4	18	6	5	78
Zn	111	86	81	126	168	160	183	97306	83299	85577	90797	2 3213
Zr	168	142	139	120	121	91	65	58	41	10	25	136
Ba	578	1115	529	332	434	382	528	117	926	2175	235	4542
La	30	5	26	51	39	37	34	64	43	11	72	5
Ce	56	50	43	48	39	40	40	9	33	10	10	105

\*: Semi-quantitative analysis

Table C.5: Continued

Fused	KN12/28	KN12/29	KN12/30	KN12/31	KN12/32	KN12/33	KN12/34	KN12/35	KN12/36	KN12/37	KN12/38	KN12/39
Depth (m)	283.32	285.32	287.25	290.80	292	291.29	292.65	293.03	293.80	295.10	297.20	299.10
Rock Name	Bt-Crd-Gn	Crd-Bt-Gn	Bt-garnet-Crd-Gn	Bt-Crd-Gn	Ore Zone	Ore Zone	Bt-Crd-Gn	Ore Zone	Crd-Bt-Gn	Garnet-Bt-Crd-Gn	Bt-Gn	Crd-Bt-Gn
SiO <sub>2</sub> (wt%)	78.31	78.49	79.18	68.86	34.92	56.65	73.74	33.38	62.6	71	70.64	69.07
TiO <sub>2</sub>	0.07	0.09	0.09	0.08	0.15	0.12	0.11	0.37	0.3	0.37	0.41	0.37
Al <sub>2</sub> O <sub>3</sub>	8.03	8.09	7.34	14.26	8.51	7.17	10.37	16.8	11.89	13.26	13.89	13.3
Fe <sub>2</sub> O <sub>3</sub>	6.53	8.12	7.67	7.85	30.65	20.22	6.46	24.14	12.69	5.74	4.7	5.77
MnO	0.09	0.04	0.12	0.04	0.09	0.07	0.04	0.17	0.19	0.18	0.13	0.22
MgO	3.48	3.15	2.28	2.17	5.48	4.97	1.65	10.59	5.15	1.29	1.14	1.11
CaO	0.08	n.d.	0.08	0.64	0.26	0.09	1.64	0.64	2.63	2.55	4.11	3.27
Na <sub>2</sub> O	0.13	0.1	0.12	1.57	0.13	0.13	1.63	0.21	1.48	3.54	3.54	3.32
K <sub>2</sub> O	0.52	0.63	0.41	1.61	1.64	1.38	1.17	2.54	1.81	1.2	0.49	1.09
P <sub>2</sub> O <sub>5</sub>	0.02	0.02	0.02	0.02	0.01	0.02	0.03	0.03	0.05	0.06	0.12	0.09
LOI	2.01	0.99	0.92	2.75	16.77	8.81	2.8	9.43	1.01	0.51	0.37	0.75
Total:	99.27	99.73	98.25	99.85	98.63	99.66	99.63	98.31	99.80	99.68	99.54	98

Hbl: hornblende, Bt: biotite, Gn: gneiss, Crd: cordierite and n.d.: Not detected.

Table C.5: Continued

Powder	KN12/28	KN12/29	KN12/30	KN12/31	KN12/32	KN12/33	KN12/34	KN12/35	KN12/36	KN12/37	KN12/38	KN12/39
Cl* (ppm)	9	8	8	8	8	8	8	11	8	8	8	20
Co	43	45	52	40	74	69	44	55	48	38	34	41
Cr	10	10	10	10	10	10	10	34	11	10	10	10
F*	2011	2210	1175	1113	4573	4265	1339	5063	2657	524	497	212
S*	9667	1689	4873	20996	108778	51831	12360	47767	6250	450	153	1975
Sc	2	5	5	1	8	6	2	18	12	10	10	7
V	2	1	2	8	9	6	8	64	76	23	40	29
As	3	3	3	3	3	3	5	3	3	3	3	3
Cu	315	38	165	1849	4707	1529	626	2352	184	6	3	70
Ga	19	15	12	22	39	32	14	37	18	14	14	14
Mo	1	1	1	2	19	19	10	10	1	1	1	1
Nb	4	4	3	3	7	5	3	8	7	7	3	4
Ni	5	4	4	4	12	4	5	5	13	5	4	3
Pb	91	11	16	91	17	12	53	19	13	13	8	13
Rb	20	21	19	37	61	71	40	109	86	25	12	21
Sr	12	8	11	57	5	7	115	73	167	183	334	244
Th	3	4	5	3	3	3	4	12	6	5	6	9
U	3	3	3	3	3	3	3	7	3	3	3	3
W*	438	480	571	360	413	444	545	109	338	418	368	4 39
Y	13	23	44	7	6	15	31	50	36	37	19	32
Zn	280	113	87	322	1238	971	247	2586	211	230	67	99
Zr	124	133	117	211	137	130	201	336	143	157	152	146
Ba	1011	458	389	806	482	420	312	1166	585	585	516	727
La	5	24	26	7	42	37	19	47	41	19	28	18
Ce	23	22	24	24	6	6	37	66	49	65	45	47

\*: Semi-quantitative analysis.

**Table C.6:** XRF analytical results for samples from borehole KN11 (Kantienpan).

Fused	KN11/1	KN11/2	KN11/3	KN11/4	KN11/5	KN11/6	KN11/7	KN11/8	KN11/9	KN11/10	KN11/11	KN11/12	KN11/13	KN11/14
Depth (m)	24.20	22.10	27.20	42.00	48.90	42.80	60.54	68.40	72.00	78.13	84.66	90.00	97.65	101.28
Rock Name	Granite	Bt-Crd-Gn	Bt-Crd-Gn	Amph.	Amph.	Gneiss	Crd-Bt-Gn	Amph.	Amph.	Amph.	Bt-Gn	Spotty Gneiss	Amph.	Amph.
SiO <sub>2</sub> (wt%)	67.12	65.88	68.06	48.44	49.03	72.2	71.24	50.23	46.57	51.74	63.04	61.18	50.2	51.6
TiO <sub>2</sub>	0.46	0.37	0.31	1.05	1.01	0.43	0.4	1.21	1.18	1.13	1.02	1.02	1.19	1.27
Al <sub>2</sub> O <sub>3</sub>	14.96	13.51	13.91	17.27	16.95	12.43	13.48	17.09	16.86	15.72	15.01	15.05	15.97	15.36
Fe <sub>2</sub> O <sub>3</sub>	5.31	6.48	6.42	12.94	12.59	4.76	4.41	13.48	15.95	12.92	8.59	8.63	13.42	11.75
MnO	0.14	0.11	0.13	0.2	0.21	0.11	0.11	0.43	0.52	0.33	0.23	0.27	0.34	0.38
MgO	2.52	1.87	2.18	4.97	4.37	0.66	0.67	4.07	4.61	3.1	1.91	1.76	3.9	3.46
CaO	1.77	1.62	1.89	8.95	6.72	2.08	1.2	5.44	4.32	5.7	3.72	3.39	8.49	8.15
Na <sub>2</sub> O	2.55	2.92	2.87	4.03	4.56	4.76	4.68	4.54	3.95	4.01	4.35	3.58	4.32	4.86
K <sub>2</sub> O	3.55	3.87	2.3	0.9	1.96	1.06	3.33	1.41	2.55	1.06	1.75	3.79	1.02	0.72
P <sub>2</sub> O <sub>5</sub>	0.08	0.07	0.06	0.26	0.3	0.09	0.1	0.54	0.52	0.46	0.38	0.39	0.58	0.6
LOI	0.82	2.35	1.19	0.23	0.73	0.1	0.17	0.13	0.41	0.00	0.00	0.15	0.00	0.00
<b>Total:</b>	99.29	99.06	99.32	99.24	98.42	98.68	99.80	98.58	97.45	96.17	99.98	99.19	99.37	97.94

Hbl: hornblende, Bt: biotite, Gn: gneiss, Crd: cordierite, Amph.: amphibolite and n.d.: Not detected.

Table C.6: Continued

Powder	KN11/1	KN11/2	KN11/3	KN11/4	KN11/5	KN11/6	KN11/7	KN11/8	KN11/9	KN11/10	KN11/11	KN11/12	KN11/13	KN11/14
Cl* (ppm)	8	13	8	21	16	8	8	29	8	60	10	8	15	8
Co	37	31	34	52	47	37	36	46	50	46	34	36	46	44
Cr	10	10	10	45	40	10	10	10	11	10	10	10	15	17
F*	504	626	1316	100	906	100	223	695	1738	787	249	274	296	100
S*	3121	8500	12305	107	200	545	365	163	5243	1368	838	4615	25	2160
Sc	17	20	12	22	17	11	12	26	30	27	18	19	17	22
V	19	26	21	329	304	1	1	149	197	134	42	33	252	248
As	3	3	3	3	3	3	3	3	3	3	3	3	4	3
Cu	5	64	14	84	28	159	24	24	1114	94	33	98	2	99
Ga	15	15	16	17	17	14	14	22	21	21	17	18	19	20
Mo	1	2	1	1	1	1	6	2	7	10	1	1	1	1
Nb	5	5	4	4	5	5	4	4	4	5	6	6	3	6
Ni	4	4	5	23	23	3	5	4	5	3	4	4	5	6
Pb	6	36	16	3	3	3	5	22	72	9	12	26	7	9
Rb	49	65	37	10	43	4	35	33	65	26	20	43	16	4
Sr	125	168	122	245	289	231	132	303	170	150	149	146	175	249
Th	4	11	8	3	3	6	6	3	4	3	4	3	3	3
U	3	4	4	4	3	3	3	3	4	3	3	3	3	3
W*	396	224	284	115	68	447	470	123	66	134	199	221	109	1 47
Y	37	41	39	23	22	27	50	38	31	36	38	24	35	42
Zn	75	103	108	81	70	54	46	370	472	297	202	149	140	208
Zr	143	154	158	46	49	175	183	85	77	81	158	141	61	23
Ba	1106	1079	954	315	630	373	960	730	775	882	842	1574	427	291
La	5	15	5	40	35	21	11	37	37	22	35	5	34	46
Ce	44	52	50	35	30	43	61	38	34	28	50	33	38	32

\*: Semi-quantitative analysis.

Table C.6: Continued

Fused	KN11/15	KN11/16	KN11/17	KN11/18	KN11/19	KN11/20	KN11/21	KN11/22	KN11/23	KN11/24	KN11/25	KN11/26
Depth (m)	108.25	112.48	120.05	126.10	130.20	136.80	142.70	149.55	154.43	159.60	165.66	172.20
Rock Name	Gneiss	Amph.	Amph.	Bt-Hbl-Gn	Spotty Gneiss	Bt-Gn	Bt-Gn	Bt-Gn	Bt-Hbl-Gn	Bt-Hbl-Gn	Sil-Crd-Bt-Gn	Crd-Gn
SiO <sub>2</sub> (wt%)	69.47	50.32	47.7	49.42	72.92	73.2	72.5	72.24	47.61	49.88	64.71	68.22
TiO <sub>2</sub>	0.73	0.8	1	0.76	0.33	0.47	0.47	0.21	0.81	0.71	0.46	0.35
Al <sub>2</sub> O <sub>3</sub>	12.48	19.47	17.4	18.74	12.69	12.72	13.97	12.8	17.9	18.14	14.15	14.29
Fe <sub>2</sub> O <sub>3</sub>	6.56	10.22	13.11	10.63	4.07	4.59	2.91	1.78	11.83	11.2	5.53	5.92
MnO	0.2	0.32	0.37	0.27	0.1	0.12	0.07	0.04	0.29	0.21	0.05	0.18
MgO	1.56	3.89	5.4	4.04	0.63	0.83	0.67	0.33	6.08	5.11	1.4	1.69
CaO	4.22	7.48	6.66	7.42	1.07	2.46	1.53	1.33	7.45	8.62	1.14	1.65
Na <sub>2</sub> O	3.61	4.49	4.05	4.78	4.75	4.35	4.49	3.12	3.53	4.29	2.37	2.24
K <sub>2</sub> O	0.62	1.91	1.93	1.46	2.59	0.91	2.7	5.45	2.08	0.94	3.01	2.75
P <sub>2</sub> O <sub>5</sub>	0.28	0.2	0.25	0.15	0.03	0.11	0.05	0.07	0.21	0.18	0.05	0.06
LOI	0.26	0.48	0.51	0.54	0.21	0.23	0.26	0.7	1.15	0.61	3.15	1.85
Total:	99.98	99.59	98.37	98.22	99.42	100.01	99.64	98.08	98.94	99.90	96.04	99.18

Hbl: hornblende, Bt: biotite, Gn: gneiss, Sil: sillimanite, Crd: cordierite, Amph.: amphibolite and n.d.: Not detected.

Table C.6: Continued

Powder	KN11/15	KN11/16	KN11/17	KN11/18	KN11/19	KN11/20	KN11/21	KN11/22	KN11/23	KN11/24	KN11/25	KN11/26
<b>Cl* (ppm)</b>	18	31	36	16	8	9	8	55	159	98	8	8
<b>Co</b>	37	43	50	43	31	37	27	27	50	48	29	36
<b>Cr</b>	10	28	30	34	10	10	10	10	52	46	10	10
<b>F*</b>	100	380	100	100	100	100	1086	579	100	100	305	359
<b>S*</b>	1591	24	1239	831	292	140	16	16	173	140	18678	13916
<b>Sc</b>	9	19	28	21	13	11	11	1	22	22	9	10
<b>V</b>	47	261	287	269	7	7	2	18	287	278	3	22
<b>As</b>	3	3	3	3	3	3	3	3	3	3	3	3
<b>Cu</b>	70	2	152	124	11	45	4	2	161	197	9	17
<b>Ga</b>	13	19	18	18	13	14	13	12	18	17	17	14
<b>Mo</b>	1	1	1	1	18	1	1	1	1	1	1	2
<b>Nb</b>	4	3	4	3	5	6	6	7	5	3	7	7
<b>Ni</b>	4	14	12	15	3	4	4	4	25	23	5	4
<b>Pb</b>	14	73	86	30	9	5	12	32	13	11	25	26
<b>Rb</b>	10	39	51	33	24	9	45	137	53	17	46	37
<b>Sr</b>	146	219	271	335	107	232	140	144	314	202	128	119
<b>Th</b>	5	3	3	4	7	5	7	20	3	3	6	4
<b>U</b>	3	3	3	3	3	3	3	6	3	3	3	3
<b>W*</b>	348	91	66	78	397	456	300	312	77	99	302	325
<b>Y</b>	23	19	23	19	43	31	33	25	18	15	41	40
<b>Zn</b>	115	296	223	126	51	60	41	40	115	77	92	100
<b>Zr</b>	108	46	54	47	195	165	189	152	44	38	163	145
<b>Ba</b>	495	956	769	700	706	485	676	1113	633	256	569	1044
<b>La</b>	20	23	37	43	21	16	22	20	43	43	22	23
<b>Ce</b>	28	24	33	21	61	46	66	83	37	22	56	49

\*: Semi-quantitative analysis.

Table C.6: Continued

Fused	KN11/27	KN11/28	KN11/29	KN11/30	KN11/31	KN11/32	KN11/33	KN11/34	KN11/35	KN11/36
<b>Depth (m)</b>	175.80	182.40	188.32	195.35	196.84	198.80	205	206.57	206.95	208.25
<b>Rock Name</b>	Crd-Bt-Gn	Crd-Bt-Gn	Bt-Gn	Bt-Hbl-Gn	Bt-Hbl-Gn	Hbl-Gn to Amph.	Bt-Sil-Crd-Gn	Bt-Garnet-Crd-Gn	Ore Zone	Ore Zone
<b>SiO<sub>2</sub> (wt%)</b>	67.84	66.73	61.96	51.34	45.23	48.81	85.96	59.71	14.00	13.15
<b>TiO<sub>2</sub></b>	0.37	0.44	0.5	0.81	1.24	1.45	0.08	0.05	0.03	0.01
<b>Al<sub>2</sub>O<sub>3</sub></b>	14.24	14.19	16.5	18.43	17.05	14.95	3.91	12.01	4.38	1.30
<b>Fe<sub>2</sub>O<sub>3</sub></b>	5.77	6.12	8.37	9.87	15.35	16.32	3.95	9.87	35.67	43.24
<b>MnO</b>	0.16	0.1	0.21	0.25	0.28	0.28	0.06	0.13	0.28	0.19
<b>MgO</b>	2.74	1.48	1.94	3.75	5.26	4.34	1.72	1.99	3.18	2.82
<b>CaO</b>	2.02	1.4	5.65	8.39	11.94	9.31	0.05	3.26	2.98	0.90
<b>Na<sub>2</sub>O</b>	2.52	3.21	2.61	3.91	2.01	2.81	0.17	0.78	n.d.	n.d.
<b>K<sub>2</sub>O</b>	3.07	2.8	1.35	0.82	0.39	0.36	0.4	0.64	0.28	0.10
<b>P<sub>2</sub>O<sub>5</sub></b>	0.08	0.09	0.14	0.24	0.22	0.31	0.03	0.062	0.04	0.04
<b>LOI</b>	1.25	2.46	0.7	1.69	0.65	0.55	1.87	n.a.	n.a.	n.a.
<b>Total:</b>	100.04	99.03	99.93	99.51	99.64	99.47	98.23	94.73 **	92.50 **	89.95 **

n.a.: not applicable; Hbl: hornblende; Bt: biotite; Gn: gneiss; Sil: sillimanite; Crd: cordierite, n.d.: Not detected, \*\*: recalculated total for sulfide riched samples (S, Cu, Zn and Pb) based on the powder disc analysis and Amph.: amphibolite.

Table C.6: Continued

Powder	KN11/27	KN11/28	KN11/29	KN11/30	KN11/31	KN11/32	KN11/33	KN11/34	KN11/35	KN11/36
<b>Cl* (ppm)</b>	19	68	96	89	53	64	14	8	8	9
<b>Co</b>	33	29	39	39	56	54	41	64	93	97
<b>Cr</b>	10	10	19	40	41	26	10	10	17	10
<b>F*</b>	1047	393	1500	2049	100	272	1214	524	2506	4081
<b>S*</b>	8408	10108	1140	4602	1076	733	8384	52269	163606	159185
<b>Sc</b>	17	18	23	30	25	33	2	1	1	1
<b>V</b>	27	8	125	284	490	458	2	1	7	5
<b>As</b>	7	3	3	6	3	10	3	3	3	3
<b>Cu</b>	8	12	22	72	284	185	235	1461	9470	6724
<b>Ga</b>	15	15	17	21	20	19	10	34	2	2
<b>Mo</b>	1	1	1	1	1	1	1	1	13	62
<b>Nb</b>	5	5	5	8	3	3	2	4	3	3
<b>Ni</b>	5	3	11	14	16	8	3	7	27	21
<b>Pb</b>	20	31	23	182	27	12	233	1509	447	673
<b>Rb</b>	53	38	55	24	20	9	13	12	17	11
<b>Sr</b>	136	194	90	345	479	414	23	119	40	56
<b>Th</b>	7	3	6	5	3	3	3	13	11	3
<b>U</b>	3	3	4	6	3	3	3	3	8	5
<b>W*</b>	307	253	233	135	158	133	519	327	195	163
<b>Y</b>	37	45	29	32	19	26	23	40	13	6
<b>Zn</b>	113	82	128	262	200	189	214	7023	143196	113388
<b>Zr</b>	137	156	81	49	35	50	51	107	44	12
<b>Ba</b>	902	887	512	312	117	221	2260	3859	1328	2311
<b>La</b>	14	15	24	27	33	51	5	5	37	6
<b>Ce</b>	47	58	43	31	24	25	33	37	17	6

\*: Semi-quantitative analysis.

Table C.6: Continued

Fused	KN11/37	KN11/38	KN11/39	KN11/40	KN11/41	KN11/42	KN11/43	KN11/44	KN11/45	KN11/46	KN11/47	KN11/48	KN11/49
Depth (m)	209.2	210.66	212.16	216.23	217.73	217.8	218.19	226.69	224.06	231.18	229.29	237.65	239.33
Rock Name	Ore Zone	Garnet-Bt-Crd-Gn	Bt-Crd-Gn	Bt-Crd-Gn	Sil-Bt-Crd-Gn	Sil-Crd-Bt-Gn	Sil-Bt-Crd-Gn	Sil-Bt-Gn	Amph.	Bt-Gn	Gneiss to granulite	Bt-Gn	Bt-Gn
SiO <sub>2</sub> (wt%)	13.66	78.43	76.69	75.12	75.22	75.86	79.52	68.55	44.7	70.72	67.15	56.57	65
TiO <sub>2</sub>	0.02	0.09	0.09	0.12	0.13	0.13	0.09	0.36	0.86	0.36	0.57	0.55	0.47
Al <sub>2</sub> O <sub>3</sub>	1.42	8.85	9.33	9.67	10.77	10.56	7.47	11.19	19.15	12.94	15.1	16.42	13.47
Fe <sub>2</sub> O <sub>3</sub>	40.56	7.86	7.85	8.26	8.04	7.77	7.62	7.34	12.94	4.76	5.7	8.15	10.78
MnO	0.18	0.1	0.06	0.12	0.06	0.09	0.08	0.21	0.32	0.12	0.13	0.14	0.19
MgO	2.00	2.81	3.6	4.11	2.97	2.83	2.72	4.25	5.64	0.98	1.44	3.87	1.51
CaO	0.27	n.d.	n.d.	0.04	n.d.	n.d.	0.02	2.84	11.62	3.19	3.95	9.32	2.51
Na <sub>2</sub> O	n.d.	0.13	0.13	0.16	0.18	0.26	0.23	2.16	2.16	3.62	3.66	2.78	3.36
K <sub>2</sub> O	0.07	0.58	0.8	1.16	1.17	1.17	0.85	1.39	0.21	0.64	1.28	0.41	1.68
P <sub>2</sub> O <sub>5</sub>	0.03	0.02	0.02	0.03	0.02	0.03	0.02	0.05	0.24	0.08	0.15	0.19	0.07
LOI	n.a.	0.75	0.99	1.34	0.87	1.19	1.2	0.47	0.43	0.86	0.38	0.27	0.37
Total:	90.03 **	99.62	99.60	100.11	99.44	99.89	99.84	98.83	98.29	98.28	99.53	98.68	99.42

n.a.: not applicable; Hbl: hornblende; Bt: biotite; Gn: gneiss; Sil: sillimanite; Crd: cordierite, n.d.: Not detected, \*\*: recalculated total for sulfide riched samples (S, Cu, Zn and Pb) based on the powder disc analysis and Amph.: amphibolite

Table C.6: Continued

Powder	KN11/37	KN11/38	KN11/39	KN11/40	KN11/41	KN11/42	KN11/43	KN11/44	KN11/45	KN11/46	KN11/47	KN11/48	KN11/49
Cl* (ppm)	8	214	279	247	254	416	286	296	247	257	408	135	211
Co	99	52	46	45	43	46	44	41	49	33	34	40	43
Cr	10	10	10	10	10	10	10	10	54	10	10	31	10
F*	3488	928	2131	3209	2001	1990	1687	2228	832	460	1465	401	354
S*	165953	3476	4959	4853	1272	6230	9094	430	1146	383	427	16	811
Sc	1	7	4	5	6	5	4	12	22	13	16	17	10
V	6	1	1	1	1	1	1	57	280	25	23	155	43
As	3	3	4	3	3	3	3	3	3	3	3	3	3
Cu	6885	192	54	71	39	141	274	10	45	15	19	8	21
Ga	2	17	17	16	16	16	14	15	19	12	16	15	15
Mo	54	1	1	1	1	1	1	1	1	1	1	1	1
Nb	4	4	4	5	4	4	3	17	3	4	5	2	4
Ni	15	3	4	4	3	4	3	9	27	4	4	19	4
Pb	634	3	12	3	8	10	11	5	13	8	11	7	5
Rb	5	16	24	35	28	31	23	38	9	14	30	5	23
Sr	4	10	13	13	13	11	18	142	428	274	226	365	259
Th	3	3	4	3	4	5	7	16	3	5	5	3	7
U	3	3	3	3	3	3	3	3	3	3	3	3	3
W*	157	585	486	398	388	435	421	308	143	307	275	184	318
Y	4	52	18	30	18	23	17	34	22	31	38	18	29
Zn	144803	111	85	263	133	903	111	125	226	51	74	50	118
Zr	15	143	135	161	173	169	118	185	35	147	134	63	175
Ba	31	1036	2940	494	714	944	1037	1048	86	291	884	255	1232
La	55	9	5	24	16	10	5	35	50	26	13	37	36
Ce	6	12	15	22	26	30	21	115	25	26	45	24	53

\*: Semi-quantitative analysis.

## Appendix D

### Analytical methods and results of regolith analyses

#### D.1. Regolith samples

These samples were collected from the sand cover that was deposited by the wind, commonly referred to as the Kalahari sand. The sand samples were sieved to identify the best size fraction with the highest element content. For this, a few samples from within and outside of the assumed secondary dispersion haloes of the deposit were selected and sieved into five fractions:

- 1) -710 to +180 micron.
- 2) -180 to +125 micron.
- 3) -125 to +75 micron.
- 4) -75 to +45 micron; and
- 5) -45 micron.

Different extractions were prepared using ammonium nitrate ( $\text{NH}_4\text{NO}_3$ ), ammonium acetate ( $\text{NH}_4\text{OAC}$ ), ethylene diamine tetraacetic acid ( $\text{NH}_4\text{EDTA}$ ) and calcium hydro phosphate ( $\text{Ca}(\text{H}_2\text{PO}_4)_2$ ) before analyzing the solutions by Inductively Coupled Plasma Mass Spectrometry (ICP-MS) for the elements of interest including Cu, Zn, Pb, Cd, Mn, Fe, Ba and S.

### **D.1.1. $\text{NH}_4\text{NO}_3$ extraction**

A 0.2 M  $\text{NH}_4\text{NO}_3$  solution is used to remove weakly bound elements of interest from the sand particles. 50 ml of this solution is added to a small plastic container (100 ml), with 5 grams of the sand sample. The container is shaken for 30-minutes in a mechanical shaker. Two blank samples, comprising a plastic container with 50 ml of the 0.2 M  $\text{NH}_4\text{NO}_3$  solution, were also shaken for 30-minutes. The blank samples are analyzed to determine the abundance of the elements of interest in the reagents.

The suspension was then poured into a centrifuging tube to separate the solid part of the sample. The solution is for analysis. The results of the ICP-MS analysis of these samples are given in Table D.1. Duplicate samples were also analyzed and later used for statistical analysis. Based on this table, most of the elements, except Ba and Mn, have very high blank contents. The finest sample fraction analyzed ( $-75\mu$ ) shows the highest contents of the elements of interest. The  $-45\mu$  size fraction was analyzed for a limited number of samples, but as inadequate quantities of this fraction was available for most of the samples, it was decided to base the interpretation of the data on the  $-75\mu$  grain size fraction. When the samples from within (KP12/13) and outside (KP12/2) the assumed geochemical halo are compared to each other, samples from within the halo returned higher concentrations of the elements of interest.

The results of statistical validation exercises (regression and correlation procedures) for duplicated samples are summarized in Table D.2. The slope of the regression line between the duplicate analyses is close to one for only Ba and Mn where the null hypothesis ( $H_0=0$ ) that the slope is equal to null may be rejected (probability values  $< 0.0001$ ). Inaccuracy in the intercept is probably caused by the small number of duplicate pairs. However, inspection of the data reveals that the repeatability of both high and low concentrations is poor. In general, this is confirmed by the strong correlation coefficients determined for Ba and Mn. The results of Cu, Zn, Pb, Cd and Fe are rejected due to the high blank values for these elements and the poor repeatability of the determinations.

**Table D.1:** ICP-MS analytical results of wind blown sand samples (5 gram sample + 50 ml of 0.2 M NH<sub>4</sub>NO<sub>3</sub> solution, 30minute shacking times)

Location	Sample No	Fraction (μ)	Cu (ppb)	Zn (ppb)	Pb (ppb)	Ba (ppb)	Mn (ppb)	Fe (ppb)	Cd (ppb)	T (°C) <sup>1</sup> Extraxt.	PH <sup>1</sup> Extract.	T (°C) <sup>2</sup> solution	PH <sup>2</sup> solution
Outside the halo	<b>T2/290N</b> From Areachap	-710 to +180	180 161	609 676	203 163	5518 5971	1291 1600	800 900	66 126	21.9 23.8	4.63 4.91	22.3 24.7	5.2 5
		-180 to +125	165 155	626 690	195 166	7638 10705	1283 2040	700 900	63 98	22 23.8	5.2 4.91	22.3 24.7	5 5.1
		-125 to +75	162 160	552 679	173 159	9861 7536	1637 1741	700 550	65 102	22 23.8	5.2 4.91	22.3 24.8	5.33 5.1
		-75 to +45	183 184	643 904	171 170	14897 16036	2642 3081	700 900	82 102	22 23.8	5.2 4.91	22.3 24.6	5.38 5.1
		-45	251 183	1085 651	186 169	21077 21646	7194 8453	740 800	91 128	22 23.8	5.2 4.91	22.3 24.7	5.27 5.2
		-710 to +180	158 141	401 519	174 177	5212 4913	1100 884	700 700	87 141	21.9 23.8	4.6 4.9	22 22.4	6.1 6.2
		-180 to +125	189 132	602 282	165 164	6766 6616	723 697	700 700	70 115	21.9 23.8	4.6 4.9	22 24.7	6.1 6.2
		-125 to +75	144 136	501 569	167 159	9019 9457	996 948	800 700	88 136	22 23.8	5.2 4.9	22.4 24.6	6.4 6.3
		-75 to +45	125 156	379 869	167 161	12903 13606	925 1071	700 120	75 108	22 23.8	5.2 4.9	22.5 24.6	6.7 6.5
		-45	130 144	221 286	163 173	15885 17683	1276 1452	700 700	82 131	22 23.8	5.2 4.9	22.7 24.7	7 6.9
Inside the halo	<b>KP12/13</b> From Kantienpan	-710 to +180	231 166	1127 547	202 168	8075 8741	2274 1213	900 700	92 160	22 23.8	5.2 4.9	23.5 24.6	5.8 5.9
		-180 to +125	245 136	1282 447	202 166	11045 11561	2219 90.30	900 600	114 133	22 23.8	5.2 4.9	23.5 24.6	5.9 5.9
		-125 to +75	296 143	1629 424	201 168	14083 15050	2557 1089	1000 700	101 162	22 23.8	5.2 4.9	23.5 24.7	6 6
		-75 to +45	188 368	939 1838	172 218	17346 17907	1649 3709	700 900	84 120	24.1 23.8	5 4.9	24.4 24.5	6.1 5.3
		-45	159 149	702 524	168 174	22252 24030	3576 3105	700 700	104 127	24.1 23.8	5 4.9	24.1 24.7	6 6.3
		Background	<b>Blank</b>		183 117	922 501	173 176	215 296	507 311	600 700	135 110	23.8 23.8	4.91 4.91

1. The temperature and pH of NH<sub>4</sub>NO<sub>3</sub>

2. The temperature and pH of the solution at the end of shacking time

**Table D.2:** Results of statistical analysis on duplicate samples and the null hypothesis (0.2 M NH<sub>4</sub>NO<sub>3</sub> solution, 30 min shacking time, n=16)

Elements	Slope	H <sub>0</sub> =0 (Pr>   t  )	Intercept	H <sub>0</sub> =0 (Pr>   t  )	Correlation coefficient
<b>Cu</b>	0.02	0.9278	747	0.0025	0.05
<b>Zn</b>	0.04	0.8630	180	0.0003	0.02
<b>Pb</b>	-0.19	0.5236	213	0.0008	-0.17
<b>Ba</b>	0.92	<0.0001	363	0.5316	0.99
<b>Mn</b>	0.73	<0.0001	513	0.0823	0.89
<b>Fe</b>	-0.01	0.7858	1281	0.0476	-0.07
<b>Cd</b>	0.34	0.2045	45	0.1766	0.34

### D.1.2. NH<sub>4</sub>OAC extraction

The second solution tested for its ability to remove weakly-bound cations of the elements of interest from the sand, is 1 M NH<sub>4</sub>OAC solution. For this, 45 ml of this solution is added to a plastic container with 2.5 grams of the sand sample. This container is shaken for 30, 60 and 120-minutes. Two blank samples, contain only the reagents, were also shaken for 120-minutes as references samples.

The results of ICP-MS analyses of these samples and their duplicates are given in Table D.3. Again, Ba and Mn are concentration show the lowest contents in the reagents. The finest sample fraction (-75μ) returned the highest contents, and samples from within the halo have higher element concentrations.

The statistical validation for duplicate samples is summarized in Table D.4. The slope of the regression line between the duplicate analyses is close to one for Ba and Mn. Inaccuracy in the intercept is probably caused by the small number of duplicate pairs. The null hypothesis (H<sub>0</sub>=0) that the slope equal to null is only rejected for Ba and Mn, (probability values < 0.0001). This is confirmed by the high correlation coefficients determined for Ba and Mn.

Inspection of the data reveals that the repeatability of both low and high concentrations is poor.

**Table D.3:** ICP-MS analytical results of sand samples (2.5 gram sample + 45 ml of 1 M NH<sub>4</sub>OAC solution, different shacking times)

<b>&lt;75-45μ fraction</b>											
Location	Sample No	Shacking Time	Cu (ppb)	Zn (ppb)	Pb (ppb)	Ba (ppb)	Mn (ppb)	PH <sup>1</sup> of Extract.	T (°C) <sup>1</sup> Extract.	PH <sup>2</sup> of Solution	T (°C) <sup>2</sup> Solution
Outside the halo	T2/290N	30	351	752	56	19721	2912	7.2	22.3	7.2	22
			313	787	74	20772	3395	7.2	22.3	7.2	22
		60	304	590	54	21181	3470	7.2	22.3	7.2	22.1
			517	1264	63	21807	4750	7.2	22.3	7.1	22.3
		120	308	479	77	24457	3517	7.2	22.3	7.2	22.4
			297	760	31	21058	3710	7.2	22.3	7.3	22.3
Inside the halo	KP12/14	30	320	846	50	39704	3474	7.2	22.3	7.2	21.6
			329	1008	76	38954	4140	7.2	22.3	7.2	21.9
		68	356	972	68	40115	4262	7.2	22.3	7.21	21.9
			342	630	68	41584	4349	7.2	22.3	7.21	21.8
		125	432	1494	97	41260	4106	7.2	22.3	7.1	22.2
			326	792	13	40099	4455	7.2	22.3	7.2	21.7
<b>&lt;710-180 μ fraction</b>											
Outside the halo	T2/290N	30	265	918	65	6991	1546	7.2	22.3	7	21.9
			257	504	45	8383	1624	7.2	22.3	7.2	21.9
		60	236	486	22	6228	1562	7.2	22.3	7.2	21.8
			245	612	65	6561	1823	7.2	22.3	7.1	22.1
		120	241	342	70	6926	1991	7.2	22.3	7.2	22.2
			265	1044	38	6755	1867	7.2	22.3	7.1	22.3
Inside the halo	KP12/14	30	241	378	94	11844	1472	7.2	22.3	7.2	21.5
			254	774	79	12033	1561	7.2	22.3	7.2	21.7
		68	263	594	112	13057	3706	7.2	22.3	7.2	21.7
			319	1602	97	12524	3274	7.2	22.3	7.2	21.7
		125	277	810	135	12874	2106	7.2	22.3	7.2	21.9
			274	522	83	11930	1908	7.2	22.3	7.2	22.9
Background	Blank	120	265	918	65	6991	1546	7.2	22.3	7	21.9
			257	504	45	8383	1624	7.2	22.3	7.2	21.9

1. The temperature and pH of NH<sub>4</sub>OAC

2. The temperature and pH of the solution at the end of shacking time

**Table D.4:** Results of statistical analysis on duplicate samples and null hypothesis (1 M NH<sub>4</sub>OAC solution, different shaking time, n=13)

Elements	Slope	H <sub>0</sub> =0 (Pr>   t  )	Intercept	H <sub>0</sub> =0 (Pr>   t  )	Correlation coefficient
<b>Cu</b>	0.32	0.1754	198	0.0159	-0.30
<b>Zn</b>	-0.29	0.3221	975	0.0022	0.40
<b>Pb</b>	0.20	0.6006	62	0.0215	0.16
<b>Ba</b>	1.01	<0.0001	-267	0.7167	0.99
<b>Mn</b>	0.80	<0.0001	362	0.2102	0.94

Using different shaking times for extracting the cations of interest did not result in any meaningful improvement of the results.

### D.1.3. NH<sub>4</sub>EDTA extraction

A 0.02 M NH<sub>4</sub>EDTA solution may also be used to remove weakly bound cations of the elements of interest from the finest parts of sand (here -75 $\mu$ ). 50 ml of this solution was added to a plastic container, with 2 grams of the sand sample. These different duplicates were shaken for 30, 60, 120 and 240-minutes. Two blank samples, with 50 ml of 0.02 M NH<sub>4</sub>EDTA solution, were also shaken for 240-minutes.

The solution was analyzed by ICP-MS (Table D.5). The blank 0.02 M NH<sub>4</sub>EDTA solution contains low contents of Cu, Zn, Pb, Mn and Ba (see the blank sample contents in Table D.5). Samples from within the halo (KP12/13) have significantly higher element contents than the samples from outside the halo (KP12/2).

The results of the statistical validation are summarized in Table D.6. The slopes of the regression lines between duplicate analyses are in all cases close to one. The hypothesis that there is no correlation can be rejected with probability values of less than 0.0005. This is confirmed by the high correlation coefficients. Inaccuracy in the intercept is probably caused by the small number of duplicate pairs. Inspection of the data reveals that the repeatability of high concentrations is poorer than that of lower concentrations. The numbers of duplicate pairs are too small to infer anything from the differences between the elements.

**Table D.5:** ICP-MS analytical results of sand samples (2 gram sample + 50 ml of 0.02 M NH<sub>4</sub>EDTA solution, different shacking times)

<b>&lt;75-45u fraction</b>											
Location	Sample No	Shacking Time	Cu	Zn	Pb	Ba	Mn	PH <sup>1</sup>	T (°C) <sup>1</sup>	PH <sup>2</sup>	T (°C) <sup>2</sup>
			(ppb)	(ppb)	(ppb)	(ppb)	(ppb)	Extract.	Extract.	Solution	Solution
Outside the halo	KP12/2	30	2270	3858	1770	19840	65913	4.49	22.4	4.14	22.6
			2833	4200	1965	18535	58348	4.49	22.4	4.16	24.3
		75	2570	3748	1843	21578	66305	4.49	22.4	4.16	22.9
			2690	4675	2450	19495	54878	4.49	22.4	4.12	24.4
		125	2955	4588	2530	24248	71298	4.49	22.4	4.16	22.8
			2848	4468	2350	20380	55583	4.49	22.4	4.18	24.6
		240	3145	4845	2908	23175	54425	4.49	22.4	4.2	23
			3230	6180	2863	21970	55153	4.49	22.4	4.24	24.5
Inside the halo	KP12/13	30	3853	6023	3923	32665	68833	4.5	24	4.11	24.4
			4553	6160	4505	34830	79068	4.5	24	4.13	24.8
		60	4103	6225	4805	34370	74235	4.5	24	4.11	24.6
			4703	6395	5135	34420	79970	4.5	24	4.15	24.5
		120	5390	8563	4813	34355	86328	4.5	24	4.11	24.9
			4825	7625	5355	34900	81153	4.5	24	4.11	24.9
		180	6758	8743	7255	43313	97883	4.5	24	4.17	24.4
			5100	7175	5735	36488	79765	4.5	24	4.18	24.3
Background	Blank	240	439	1645	175	618	2148	4.49	22.4	4.5	24.9
			361	1839	163	410	1046	4.49	22.4	4.5	25.1

 1. The temperature and pH of NH<sub>4</sub>EDTA

2. The temperature and pH of the solution at the end of shacking time

**Table D.6:** Results of statistical analysis on duplicate samples and null hypothesis (1 M NH<sub>4</sub>EDTA solution, different shacking time, n=9)

Elements	Slope	H <sub>0</sub> =0 (Pr>   t  )	Intercept	H <sub>0</sub> =0 (Pr>   t  )	Correlation coefficient
<b>Cu</b>	1.12	0.0004	-366	0.5971	0.94
<b>Zn</b>	1.20	0.0002	-1150	0.2674	0.92
<b>Pb</b>	1.07	<0.0001	-280	0.5906	0.95
<b>Ba</b>	1.01	0.0002	1200	0.6151	0.98
<b>Mn</b>	0.99	<0.0001	5504	0.5709	0.93

In Figure D.1, variations in the concentrations of Zn, Cu and Pb following different shacking times are shown. Zn (Fig. D.1, A and C) shows an optimum time of 180 minutes for both samples from within and outside of the halo. Cu (Fig. D.1B) and Pb (Fig. D.1 E) shows the same optimum times for samples outside the halo. For samples from within the halo, Cu (Fig. D.1 D) shows an increasing trend, whereas Pb (Fig. D.1 F) shows two increases, one from 30 to 60 and the other from 120 minutes. The latter may suggest that after this shaking time, another phase hosting Pb may begin to be leached. Based on Figures D.1, NH<sub>4</sub>EDTA could be used as a solution for the extraction of mobile metal ions with a shaking time of 180-minutes.

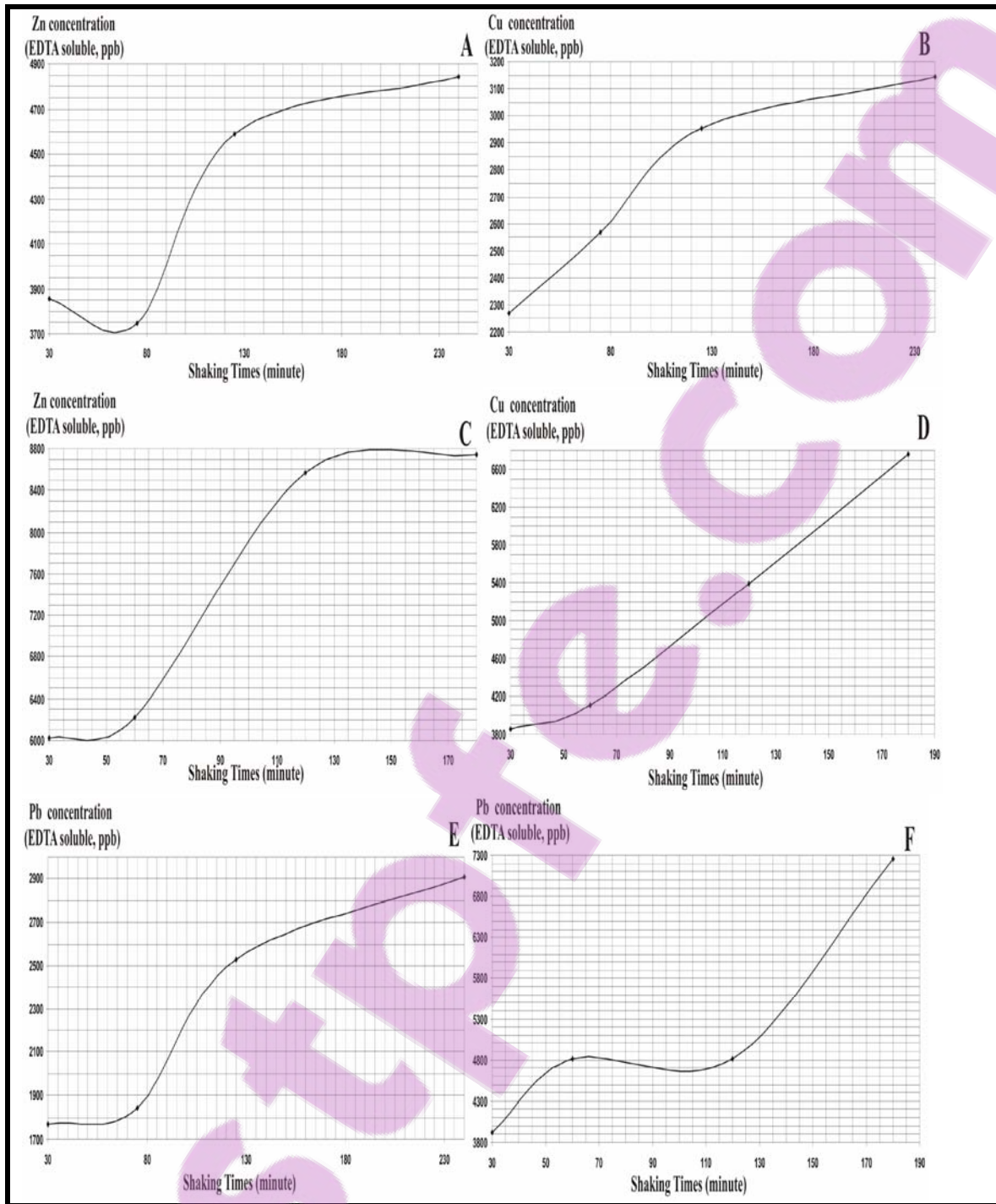


**Figure D.1:** Optimization of the shaking times and concentrations for Zn (A and C), Cu (B and D) and Pb (E and F) within and outside of the halo, NH<sub>4</sub>EDTA method

#### **D.1.4. Ca (H<sub>2</sub>PO<sub>4</sub>)<sub>2</sub> extraction**

A 0.02 M Ca (H<sub>2</sub>PO<sub>4</sub>)<sub>2</sub> solution is used to remove S that is weakly bound to the sand. 50 ml of this solution was added to a plastic container (100 ml), with 5 grams of the -75 μ of the sand sample. The container is shaken for 120-minutes. Two blank samples were also shaken for 120-minutes.

The solution together with the blank samples was analyzed by ICP-MS (Table D.7). The S content in the reagents is lower than that of the sample solutions. Based on this table, samples within the halo show high contents of S when compared to the rest of the samples.

The results of the statistical calculations of duplicate samples are summarized in Table D.8. The slope of the regression lines between duplicate analyses is close to the ideal slope of one. The hypothesis that there is no correlation is rejected, with probability values of < 0.0001. This is confirmed by the good correlation coefficients determined. Inaccuracy in the intercept is probably caused by the small number of duplicate pairs. Inspection of the data reveals that the repeatability of high concentrations is poorer than that of lower values.

**Table D.7:** ICP-MS analytical results of sand samples for sulphur (5 grams sample + 50 ml of 0.02 M Ca (H<sub>2</sub>PO<sub>4</sub>)<sub>2</sub> solution, 120-minute shaking times)

<b>&lt;75µ fraction</b>							
Location	Sample No	Sulphur (mg/l)	S (ppb)	PH <sup>1</sup> Extract.	T (°C) <sup>1</sup> Extract.	PH <sup>2</sup> Solution	T (°C) <sup>2</sup> Solution
Outside the halo	KP12/3	0.84	8400	3.3	25		
		1.44	14400	3.3	25		
Inside the halo	KP12/12	0.87	8700	3.3	25	4.6	25
		0.8	8000	3.3	25	4.6	25
Inside the halo	KP12/13	0.84	8400	3.3	25		
		0.95	9500	3.3	25		
Inside the halo	KP12/14	0.82	8200	3.3	25		
		1.04	10400	3.3	25		
Inside the halo	KP12/15	0.78	7800	3.3	25	4.2	25
		0.83	8300	3.3	25	4.2	25
Outside the halo	KP12/19	0.78	7800	3.3	25	3.9	25
		0.98	9800	3.3	25	3.9	25
Background	Blank	0.59	5900	3.4	25.9	3.1	25.1
		0.571	5710	3.4	25.9	2.9	24.7
Inside the halo	KP12/1	1.291	12910				
		1.564	15640				
Inside the halo	KP12/7	1.016	10160				
		1.137	11370				
Inside the halo	KP12/10	6.085	60850				
		6.636	66360				
Inside the halo	KP12/18	1.581	15810				
		1.658	16580				
Background	Blank	0.699	6990				
		0.680	6800				

1. The temperature and pH of Ca (H<sub>2</sub>PO<sub>4</sub>)<sub>2</sub>
2. The temperature and pH of the solution at the end of shaking time

**Table D.8:** Results of statistical analysis on duplicate samples and null hypothesis (0.02 M Ca (H<sub>2</sub>PO<sub>4</sub>)<sub>2</sub> solution, different shaking times, n=12)

Elements	Slope	H <sub>0</sub> =0 (Pr>   t  )	Intercept	H <sub>0</sub> =0 (Pr>   t  )	Correlation coefficient
S	0.92	<0.0001	-460	0.52	0.99

To optimize the shaking times, one sample within the halo at Kantienpan (KP12/13) was analyzed at different shaking times (Table D.9) and the variation of S versus shaking times shown in Figure D.2. S contents increase until it reaches a peak (~

12400 ppb) after 60-minutes of shaking, then decreases to 11300 ppb for a shaking time of 120-minute. The error calculated for duplicate pairs of sulphur analyses amounts to 6.7%. The difference observed between a shaking period of 60 minutes and 120 minutes approximates the same amount and it was decided to use a 120 minutes period for the routine sample preparation.

**Table D.9:** ICP-MS analytical results of sand samples for S for different shacking times (5 gram sample + 50 ml of 0.02 M Ca (H<sub>2</sub>PO<sub>4</sub>)<sub>2</sub> solution)

Location	Sample No	Shaking Time (Minute)	S (ppb)
Inside of the halo	KP12/13/1	20	8721
		20	12880
	KP12/13/2	40	11143
		40	12368
	KP12/13/3	60	12344
		60	9545
	KP12/13/4	120	11316
		120	11173
Blank	Background	120	5888
		120	5706

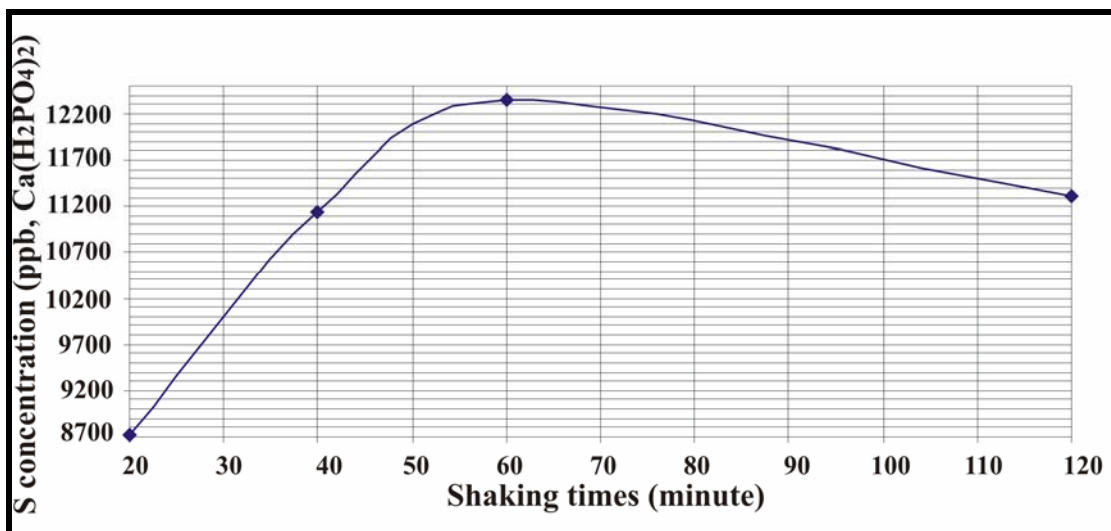


**Figure D.2:** Optimization of the shacking times and concentrations of S for sample from inside of the halo, Ca (H<sub>2</sub>PO<sub>4</sub>)<sub>2</sub> method.

### D.1.5. XRF total analyses

The samples collected from two regolith sampling traverses, one from Kantienpan (KP12) and the other from Areachap (T2), were analyzed by x-ray fluorescence spectroscopy (XRF) to compare the results with those from the partial extraction methods. The same sample preparation and analytical method (XRF) as the one used for whole rock sample analyses was used for the analyses of regolith samples except that only pressed powder pellets were analyzed. The analytical results are presented in Tables D. 10 and D.11. Note that the major element concentrations in these samples are semi-quantitative in nature.

**Table D.10:** XRF analytical results of regolith sampling traverse KP12 for the <75  $\mu$  size fraction

Sample No.	% MnO	ppm																			
	Cu	Zn	Pb	S	Rb	Sr	Cl	Co	Sc	V	As	Ga	Mo	Nb	Ni	Th	U	Y	Zr	Cr	
KP 12/1	0.08	22	98	9	128	90	124	67	24	17	106	7	14	1	18	29	18	3	41	986	48
KP 12/2	0.09	22	94	15	38	97	116	244	27	20	126	11	14	1	19	32	22	3	43	989	70
KP 12/3	0.09	22	91	16	16	101	112	12	26	20	113	4	14	1	18	32	20	3	43	876	48
KP 12/4	0.10	24	96	13	16	102	109	8	30	24	117	11	16	1	18	34	19	3	44	851	64
KP 12/5	0.09	27	94	15	16	101	115	74	28	23	116	12	14	1	17	31	20	3	43	920	47
KP 12/6	0.09	29	90	13	16	101	109	55	27	22	116	8	15	1	19	32	20	3	46	929	55
KP 12/7	0.11	27	103	17	16	109	102	43	32	24	122	11	16	1	19	35	19	3	45	833	71
KP 12/8	0.09	23	97	14	16	99	111	8	28	21	115	9	14	1	19	32	21	3	46	1044	55
KP 12/9	0.12	33	120	20	66	124	89	183	38	28	130	10	17	1	17	44	22	3	45	564	75
KP 12/10	0.09	20	99	13	204	95	118	115	25	19	114	11	13	1	18	29	21	3	42	1036	35
KP 12/11	0.09	21	113	14	16	97	114	21	28	20	117	10	14	1	19	30	22	3	46	1113	57
KP 12/12	0.12	31	138	18	16	111	103	50	35	26	128	9	18	1	19	37	21	3	46	783	68
KP 12/13	0.07	13	86	21	56	96	89	182	31	89	98	12	9	1	12	20	11	3	19	274	10
KP 12/14	0.10	26	133	22	16	103	103	104	28	22	121	10	14	1	19	33	17	3	44	895	68
KP 12/15	0.10	29	135	16	16	109	103	39	32	25	127	9	17	1	20	36	20	3	49	969	76
KP 12/16	0.10	28	127	16	16	110	101	23	32	26	122	9	16	1	20	35	23	3	44	804	59
KP 12/17	0.12	30	131	22	81	111	100	142	34	25	122	9	17	1	19	38	22	3	43	837	66
KP 12/18	0.09	24	106	15	16	102	105	85	30	23	120	13	15	1	21	37	20	3	49	1047	80
KP 12/19	0.10	25	102	15	16	111	101	8	30	26	118	13	16	1	19	35	22	3	44	819	66

**Table D.11:** XRF analytical results of regolith sampling traverse T2 for the <75 µ finest size fraction

Sample No.	%	ppm																				
	MnO	Cu	Zn	Pb	Fe <sub>2</sub> O <sub>3</sub>	S	Rb	Sr	Cl	Co	Sc	V	As	Ga	Mo	Nb	Ni	Th	U	Y	Zr	Cr
T2/390N	0.07	21	65	18	5.30	40	86	124	8	16	13	111	8	12	1	23	23	16	5	55	1413	137
T2/290N	0.09	29	83	23	5.87	185	97	113	8	21	17	108	3	14	1	21	30	12	4	45	976	138
T2/190N	0.08	26	79	19	5.60	124	89	121	8	18	14	111	8	14	1	23	27	16	4	53	1318	135
T2/140N	0.06	25	67	22	5.24	71	82	123	8	15	13	109	7	14	1	24	24	18	5	54	1494	128
T2/90NB	0.06	24	70	20	5.20	20	82	124	8	14	11	106	3	13	1	24	22	17	5	53	1539	134
T2/90NA	0.08	29	85	19	5.55	109	86	120	40	18	14	110	16	15	1	24	24	17	4	53	1387	130
T2/50N	0.06	29	86	21	5.04	78	82	122	8	14	13	100	3	13	1	23	21	15	3	51	1345	122
T2/30N	0.10	86	174	53	6.55	1895	93	114	8	24	17	114	12	16	1	20	29	15	3	49	1038	142
T2/20N	0.09	45	119	26	6.04	369	88	121	8	21	16	117	6	15	1	23	27	17	5	54	1300	138
T2/10N	0.08	38	103	27	5.68	337	84	123	8	20	13	112	3	14	1	24	25	18	5	58	1551	136
T2/0 (T3/240)	0.12	56	143	31	6.70	403	98	120	8	26	17	119	3	17	1	18	34	11	3	43	711	135
T2/10S	0.09	57	154	29	6.04	569	90	118	8	22	16	108	3	15	1	21	28	15	3	49	1092	144
T2/20S	0.08	43	99	26	5.74	332	88	117	8	18	16	112	3	14	1	23	26	16	4	51	1339	136
T2/40S	0.08	43	90	28	5.89	304	85	122	8	20	15	117	6	13	1	25	25	19	5	57	1560	149
T2/60S	0.07	39	84	22	5.55	228	84	121	8	17	13	112	16	13	1	25	25	18	6	57	1662	142
T2/80S	0.07	31	73	21	5.33	172	85	123	8	16	13	107	8	12	1	24	23	18	4	53	1496	131
T2/100S	0.06	29	71	21	5.38	93	86	125	8	16	12	110	3	14	1	24	22	17	5	57	1549	134
T2/150S	0.06	24	65	18	4.98	59	82	122	8	15	11	102	8	12	1	23	22	15	4	54	1438	114
T2/200S	0.06	25	66	21	4.95	69	82	125	8	14	12	104	3	12	1	22	22	14	4	52	1364	116
T2/300S	0.08	29	79	21	5.86	69	90	123	8	19	14	119	8	15	1	24	27	17	5	56	1393	139
T2/350S	0.07	25	93	22	5.57	53	89	122	8	17	13	117	8	13	1	24	26	17	5	57	1468	137
T2/190N	0.08	28	81	22	5.61	106	89	120	8	20	14	112	3	14	1	23	27	15	3	50	1235	129
T2/30N	0.10	86	175	49	6.66	1885	94	115	8	25	17	113	8	16	1	20	29	14	3	47	1017	138
T2/10S	0.09	59	152	30	6.05	576	87	117	8	22	15	109	5	15	1	21	29	13	4	48	1057	130
T2/300S	0.08	29	79	22	5.85	71	93	125	8	20	15	120	3	16	1	24	27	17	4	55	1381	134

**D.1.6. Regolith data set of the Kantienpan traverses**

**Table D.12:** ICP-MS results of regolith sampling traverse KP12 (0.02 M Ca (H<sub>2</sub>PO<sub>4</sub>)<sub>2</sub> solutions for S, shaking time: 120-minutes, and 0.02 M NH<sub>4</sub>EDTA solutions for the rest of the elements shaking time 180-minutes)

Sample No.	Sample interval (m)	Cu (ppb)	Zn (ppb)	Pb (ppb)	Ba (ppb)	Mn (ppb)	S (mg/l) (Duplicate)	S (mg S/Kg soil) (ppm)
KP12/1	0	4712	6931	29984	20101	79674	1.291	13
		4267	6245	3024	19272	66012	1.564	16
KP12/2	20	3230	6181	2861	21967	55153	0.972	10
KP12/3	40	2716	2329	28720	22064	83073	0.84	8
KP12/4	60	3517	2866	28905	21923	98921	0.832	8
KP12/5	80	3609	2151	8424	26216	105322	1.186	12
		3449	2176	3578	23697	80709	-	-
KP12/6	100	2190	1351	5416	18605	101596	1.24	12
KP12/7	120	3611	5527	7474	27026	143786	1.016(1.137)	10(11)
KP12/8	140	2519	3294	120681	22117	104948	0.963	10
KP12/9	150	4754	4216	7807	29775	138939	18.43	184
KP12/10	160	2910	4959	3431	22779	102246	6.085	61
		2699	3592	2785	20010	69948	6.636	66
KP12/11	170	2421	3448	3656	26426	102942	1.018	10
KP12/12	180	5477	6486	5761	46845	142653	1.44	14
KP12/13	190	5100	7175	5736	36488	79764	0.87	9
KP12/14	200	3258	9552	4240	23363	193172	0.8	8
KP12/15	210	4282	6501	5862	38136	132096	0.84	8
		4443	6864	4931	32897	93406	-	-
KP12/16	220	3382	4693	5660	34671	133881	2.067	21
KP12/17	240	4274	6606	5831	33177	113758	8.594	86
KP12/18	260	3309	3962	3995	28089	85337	1.581(1.658)	16(17)
KP12/19	300	3409	2938	4290	31478	87442	0.78	78
Blank		68	218	84	266	2144	0.699(0.68)	7(7)

**Table D.13:** ICP-MS results of regolith sampling traverse KP5 (0.02 M NH<sub>4</sub>EDTA solutions for Cu, Zn, Pb, Ba, Mn and Fe, shaking time: 180-minutes)

Sample No.	Sample interval (m)	Cu	Zn	Pb	Ba	Mn	Fe
		(ppb)	(ppb)	(ppb)	(ppb)	(ppb)	(ppb)
KP5/1	0	4838	3030	2089	16784	211	132
		4072	2419	2593	16518	213	136
KP5/2	20	4201	5121	2140	19209	199	88
KP5/3	40	3805	3812	1727	17006	187	86
KP5/4	60	3594	3820	2503	21121	246	155
KP5/5	70	3526	4581	2942	20802	231	123
		3591	4584	1898	21063	229	121
KP5/6	80	6897	11078	3075	28241	379	150
KP5/7	90	3880	5654	2270	21546	220	96
KP5/8	100	3658	5086	2351	20143	167	107
KP5/9	110	4603	6014	2275	20320	185	102
KP5/10	120	4342	5654	2602	18084	173	103
		4169	5798	2669	17521	177	103
KP5/11	130	4672	5177	2886	19588	232	112
KP5/12	140	4688	5858	2851	21543	212	114
KP5/13	160	3703	5153	2935	20782	219	127
KP5/14	180	2413	4200	2667	17849	211	112
KP5/15	200	3253	5549	3532	22430	236	142
		3318	5710	3185	21832	233	138
KP5/16	220	4487	4892	3413	23608	354	147
KP5/17	240	3784	2709	3594	21388	255	133
KP5/18	270	3409	4096	3274	20775	292	160
		3458	4007	3015	20499	297	153

**Table D.14:** ICP-MS results of regolith traverse KP8 (0.02 M NH<sub>4</sub>EDTA solutions for Cu, Zn, Pb, Ba, Mn and Fe, shaking time: 180-minutes)

Sample No.	Sample interval (m)	Cu (ppb)	Zn (ppb)	Pb (ppb)	Ba (ppb)	Mn (ppb)	Fe (ppb)
KP8/1	0	4268	4875	1961	14271	185	84
		4178	5195	1720	12916	177	79
KP8/2	20	5535	5263	3221	25316	312	145
KP8/3	40	9756	7233	4217	25787	354	92
KP8/4	60	7991	7233	3678	29336	453	149
KP8/5	80	5159	6633	2042	22664	235	75
		5313	8413	1941	20902	231	72
KP8/6	100	7990	11349	3503	29159	366	132
KP8/7	120	5562	10792	4164	31777	364	149
KP8/8	140	4608	7280	3400	25945	345	171
KP8/9	170	3620	3391	2652	20683	252	115
		3679	4379	2594	20002	260	105
KP8/10	180	3004	3804	2783	17849	254	139
		3060	3622	2468	16795	263	133
KP8/11	190	3548	3677	3595	21887	366	192
KP8/12	200	3152	4592	3654	20060	332	182
KP8/13	230	4552	4355	4575	22798	501	254
KP8/14	260	4665	4191	4541	25041	435	164
KP8/15	290	3948	5009	2593	19193	222	110
		3887	4894	2536	19148	221	112
KP8/16	340	6815	4830	2661	16571	239	142

**Table D.15:** MMI results of regolith traverses 7700NW and 7800NW for Cu and Zn (Rossouw, 2003)

Regolith Traverse 7700NW					Regolith Traverse 7800NW				
Sample No.	Zn (ppb)	R/R <sup>1</sup> (B=98)	Cu (ppb)	R/R <sup>2</sup> (B=16)	Sample No.	Zn (ppb)	R/R <sup>1</sup> (B=98)	Cu (ppb)	R/R <sup>2</sup> (B=16)
800	175	1.8	46.5	2.9	800	45	0.5	1.9	0.1
825	260	2.7	25.9	1.6	825	135	1.4	28.6	1.8
850	60	0.6	1.9	0.1	850	125	1.3	1.9	0.1
875	75	0.8	1.9	0.1	875	200	2.0	41.1	2.6
900	175	1.8	62.4	3.9	900	70	0.7	1.9	0.1
925	100	1.0	1.9	0.1	925	300	3.1	86.5	5.4
950	295	3.0	78.7	4.9	950	255	2.6	70.4	4.4
975	205	2.1	62.9	3.9	975	115	1.2	1.9	0.1
1000	225	2.3	45.2	2.8	1000	300	3.1	83.6	5.2
1025	80	0.8	2.1	0.1	1025	540	5.5	51.5	3.2
1050	270	2.8	89.1	5.6	1050	295	3.0	83	5.2
1075	420	4.3	71.7	4.5	1075	370	3.8	30.2	1.9
1100	160	1.6	130	8.1	1100	100	1.0	12	0.8
1125	295	3.0	104.1	6.5	1125	5265	53.7	69	4.3
1150	75	0.8	1.9	0.1	1150	400	4.1	83.9	5.2
1175	180	1.8	111.5	7.0	1175	1980	20.2	46.2	2.9
1200	540	5.5	60.6	3.8	1200	980	10.0	269.7	16.9
1225	1380	14.1	1.9	0.1	1225	400	4.1	118.3	7.4
1250	270	2.8	120	7.5	1250	1345	13.7	99.6	6.2
1275	100	1.0	1.9	0.1	1275	430	4.4	33.9	2.1
1300	270	2.8	111.2	7.0	1300	955	9.7	83.7	5.2
1325	520	5.3	35.3	2.2	1325	200	2.0	82.8	5.2
1350	320	3.3	105.4	6.6	1350	420	4.3	78.7	4.9
1375	290	3.0	67.6	4.2	1375	270	2.8	61.7	3.9
1400	145	1.5	93.2	5.8	1400	300	3.1	82.9	5.2
1425	220	2.2	113.7	7.1	1425	270	2.8	96.8	6.1
1450	320	3.3	88.1	5.5	1450	385	3.9	89.9	5.6
1475	545	5.6	23.2	1.5	1475	40	0.4	1.9	0.1
1500	405	4.1	67.3	4.2	1500	340	3.5	44.1	2.8

Note: R/R<sup>1</sup>=[(peak/background) <sub>Zn</sub>, Background= 98 ppb]; R/R<sup>2</sup>=[(peak/background) <sub>Cu</sub>, Background= 16 ppb]

## D.1.7. Regolith data set of the Areachap traverses

Table D.16: ICP-MS results of regolith sampling traverse T1 (0.02 M NH<sub>4</sub>EDTA solutions for Cu, Zn, Pb, Ba, Mn and Fe, shaking time: 180-minutes; <75 $\mu$  size fraction)

Sample No.	Sample interval (m)	Cu (ppb)	Zn (ppb)	Pb (ppb)	Ba (ppb)	Mn (ppb)	Fe (ppm)
T1/390N	390	647	2294	1199	8586	68531	58
		636	2251	1140	8359	68084	52
T1/290N	290	1785	2312	1773	15534	122906	77
T1/190N	190	1572	3027	1572	11950	99999	64
T1/140N	140	2203	6664	2147	14419	136571	88
T1/90N	90	1471	1928	1671	10876	117036	71
T1/70N	70	1925	3465	2046	15040	125658	72
T1/50N	50	1710	3231	2127	9957	149248	94
T1/30N	30	2209	3130	1928	12460	118183	70
T1/20N	20	2813	3402	2180	12840	137797	74
T1/10N	10	2420	3907	1853	11626	118671	70
T1/0	0	2430	2987	2191	13908	140861	89
		2350	3991	2108	13059	142242	88
		2480	4112	2261	13725	148332	87
T1/10S	-10	1360	2706	1708	9393	102775	68
		1388	3132	1666	9633	105520	68
		1566	3689	1750	10548	108189	74
T1/20S	-20	1492	2745	1762	9438	103259	64
T1/30S	-30	1490	2996	1461	8589	78532	56
T1/50S	-50	1693	3420	1537	8526	90973	54
T1/70S	-70	1405	2937	1541	10606	97924	60
T1/90S	-90	1270	2544	1675	10283	99216	74
T1/140S	-140	1812	3530	1574	9974	97244	59
T1/190S	-190	1425	6016	1412	9894	78391	59
T1/250S		1720	12134	1790	8321	105853	76
T1/250S	-250	1736	12269	1764	8260	104247	78
Blank		74	819	17	478	1345	61
		47	670	<1	392	308	2

**Table D.17:** ICP-MS results of regolith sampling traverse T3 (0.02M NH<sub>4</sub>EDTA solutions for Cu, Zn, Pb, Ba, Mn and Fe, shaking time: 180-minutes; <75 $\mu$  size fraction)

Sample No.	Sample interval	Cu (ppb)	Zn (ppb)	Pb (ppb)	Ba (ppb)	Mn (ppb)	Fe (ppm)
<b>T3/0 (T1/0)</b>	0	2480	4112	2261	13725	148332	87
<b>T3/30</b>	30	1704	3496	1590	10825	119164	67
<b>T3/60</b>	60	2772	4679	1635	9908	109543	64
<b>T3/90</b>	90	2270	4424	1592	9992	105432	62
<b>T3/120</b>	120	3315	3845	2030	12362	133356	53
<b>T3/150</b>	150	4038	5180	2119	12549	128565	79
<b>T3/180</b>	180	8667	9054	3082	14858	180343	102
<b>T3/210</b>	210	7120	10174	3378	12520	109333	62
<b>T3/240</b>	240	14821	13789	6963	19647	351	114

**Table D.18:** ICP-MS results of regolith sampling traverse T2 (0.02M NH<sub>4</sub>EDTA solutions for Cu, Zn, Pb, Ba, Mn and Fe, shaking time: 180-minutes; <75μ size fraction)

Sample No.	Sample interval (m)	Cu (ppb)	Zn (ppb)	Pb (ppb)	Ba (ppb)	Mn (ppb)	Fe (ppm)	S (mg/l)	S (ppm)
<b>T2/0 (T3/240)</b>	0	14821	13789	6963	19647	350500	114	1.35	14
		15870	12899	5494	21585	345750	112		
<b>T2/10N</b>	10	20715	26877	4849	21348	261750	135	1.43	14
		19484	25012	4918	20328	264000	135		
<b>T2/20N</b>	20	2141	4197	1384	13790	154500	81	0.62	6
		1626	3638	1443	13370	145750	76		
<b>T2/30N</b>	30	30810	28977	4281	11201	207007	152	1.13	11
		34590	33638	7327	13084	185374	157		
<b>T2/50N</b>	50	3864	11272	2590	7208	44475	69	1.04	10
<b>T2/70N</b>	70	3472	7955	2809	10078	54697	85	0.86	9
<b>T2/90N</b>	90	1851	6010	2315	7558	39784	61	0.83	8
<b>T2/140N</b>	140	1821	5069	2360	7237	42203	64	0.93	9
<b>T2/190N</b>	190	2888	6051	3159	10992	66796	101	0.91	9
<b>T2/290N</b>	<b>There was no enough sample left</b>							0.95	10
<b>T2/390N</b>	390	2440	17236	1997	16876	191250	84	0.77	8
		2399	17294	1873	16996	188750	83		
<b>T2/10S</b>	-10	8781	9691	4853	18491	175000	95	2.02	20
		9038	9744	3765	18627	173000	92		
<b>T2/20S</b>	-20	9475	10836	5434	10796	65924	94	1.75	18
		10808	10603	4297	11020	57963	97		
<b>T2/40S</b>	-40	3518	8900	2062	7548	38009	60	1.22	12
		4342	8393	2817	8251	47603	70		
<b>T2/60S</b>	-60	9226	15092	3301	10788	52391	72	1.43	14
<b>T2/80S</b>	-80	4710	9477	2864	6505	43577	75	1.25	13
<b>T2/100S</b>	-100	8727	12469	3677	10351	57630	82	0.76	8
		7849	10468	3864	9293	55527	80		
<b>T2/150S</b>	-150	2087	6954	2034	6893	45026	66	1.25	13
<b>T2/200S</b>	-200	2107	4611	2422	6650	42958	59	1.48	15
<b>T2/300S</b>	-300	2966	7176	2967	9865	62205	78	0.95	10
		3086	8326	3575	9253	63899	93		
<b>T2/350S</b>	-350	11414	9726	3580	22563	242250	112	1.36	14
		11400	9511	3334	21940	240500	112		

## **D.2. Calcrete samples**

Calcrete material collected from the cover above the ore deposits contains pieces of gossan. To distinguish the source of the elements of interest in the calcrete samples analyzed by XRF, the magnetic component was separated by using a hand magnet followed by a Frantz isodinamic magnetic separator (a procedure explained in Fig. D.3). For this purpose, the whole procedure was done on sample (KP12/4), a calcrete sample collected from above the ore zone in the Kantienpan area. Both the magnetic and non-magnetic parts of the sample were analyzed. The sample numbers given in brackets in this figure indicate those fractions that were analyzed by XRF. The results of XRF analysis on the magnetic and non-magnetic parts of the samples are given in Table D.18.

For the other calcrete samples, the magnetic part was removed and the original and magnetic parts were analyzed by XRF (Tables D.19 and D.23).

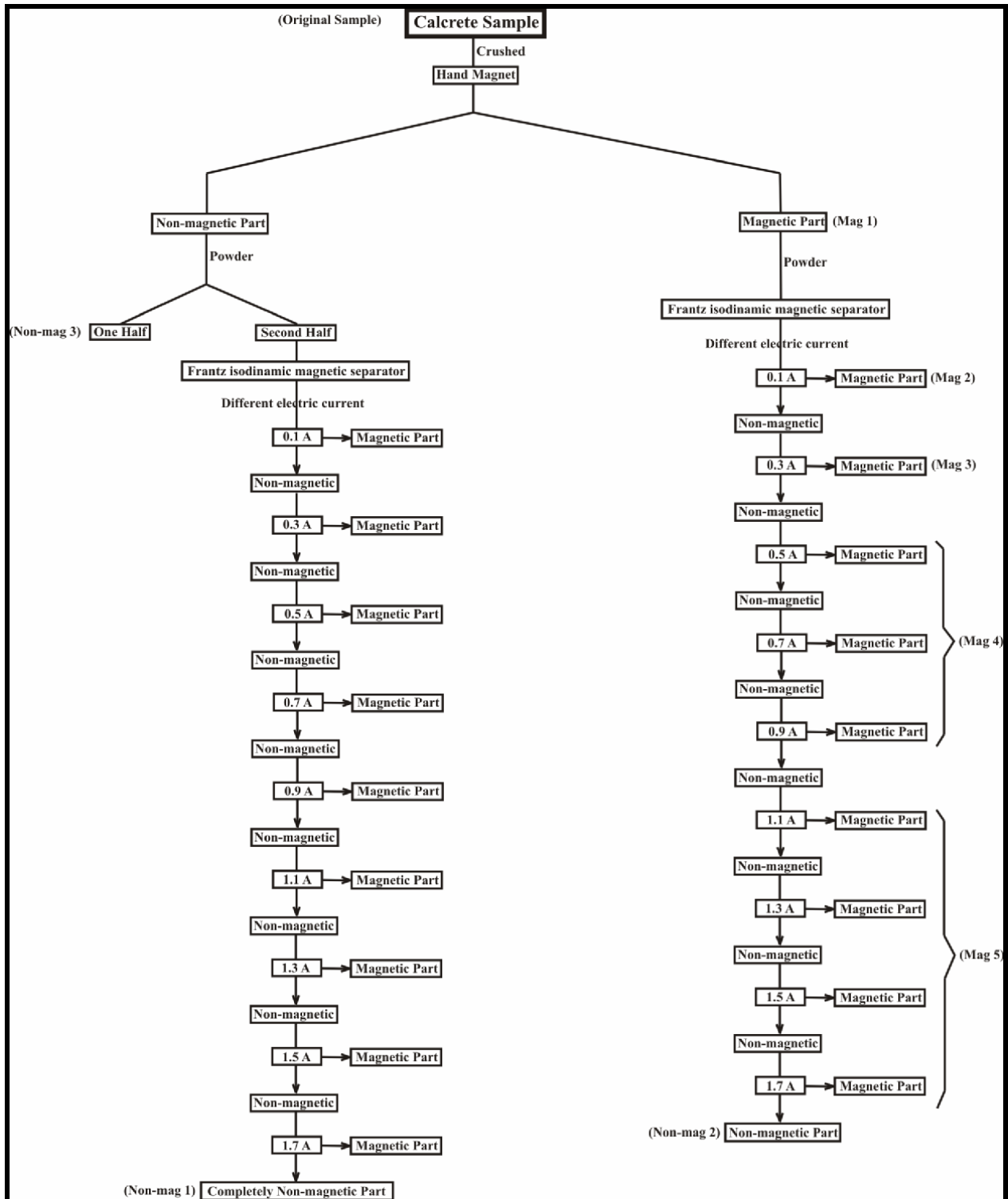


Figure D.3: Flow chart of the separation of magnetic and non-magnetic parts of calcrete samples [(in bracket): sample number for XRF analysis, A: ampere].

**Table D.19:** XRF results of the magnetic, non-magnetic and visually cleaned parts of the calcrete sample KPR12/4, Kantienpan (major elements: wt. %)

%	KPR 12/4	Non-Mag1	Non-Mag2	Non-Mag3	Mag1	Mag2	Mag3	Mag4	Mag5
<b>SiO<sub>2</sub></b> *	18.43	16.84	13.84	15.56	12.67	12.71	12.42	13.79	14.69
<b>TiO<sub>2</sub></b> *	0.22	0.09	0.1	0.15	0.21	0.51	1.1	0.98	0.53
<b>Al<sub>2</sub>O<sub>3</sub></b> *	2.54	1.99	1.91	2.05	1.91	1.92	1.94	2.35	2.66
<b>Fe<sub>2</sub>O<sub>3</sub></b> *	1.52	0.74	0.74	1	1.61	9.99	3.2	3.3	2.14
<b>MnO</b> *	0.05	0.04	0.04	0.05	0.04	0.06	0.08	0.08	0.06
<b>MgO</b> *	2.23	2.10	2.04	2.19	2.12	2.35	2.14	2.34	2.43
<b>CaO</b> *	39.34	39.81	42.0	39.96	42.42	39.92	40.77	40.73	40.58
<b>Na<sub>2</sub>O</b> *	0.23	0.24	0.24	0.23	0.23	0.27	0.27	0.28	0.28
<b>K<sub>2</sub>O</b> *	0.71	0.66	0.58	0.64	0.57	0.41	0.44	0.49	0.56
<b>P<sub>2</sub>O<sub>5</sub></b> *	0.17	0.21	0.11	0.22	0.11	0.09	0.09	0.12	0.17
<b>TOTAL</b>	65.44	62.72	61.57	62.04	61.90	68.23	62.46	64.45	64.10

Note: KPR12/4 is the original sample, Non-Mag: non-magnetic part of sample; Mag: magnetic part of samples.

\*: Semi-quantitative XRF powder analyses

Table D.19: Continued

Trace elements (ppm)	KPR 12/4	Non-Mag1	Non-Mag2	Non-Mag3	Mag1	Mag2	Mag3	Mag4	Mag5
As	9	12	8	5	6	16	8	11	6
Cu	20	12	8	12	5	6	11	14	13
Ga	2	2	2	2	2	3	2	2	2
Mo	1	1	1	1	1	1	1	1	1
Nb	4	2	3	3	5	6	13	10	7
Ni	6	4	4	5	4	9	5	8	9
Pb	4	3	3	6	3	16	3	4	3
Rb	24	20	19	20	19	16	18	18	22
Sr	180	218	242	219	240	233	233	237	238
Th	4	4	3	6	5	4	3	6	6
U	3	3	3	3	3	3	3	3	3
W *	82	156	104	68	54	6	11	19	22
Y	10	8	8	9	8	9	10	16	16
Zn	45	42	39	52	42	70	86	68	62
Zr	85	69	73	87	76	65	94	90	92
Cl *	552	528	287	486	441	172	197	174	197
Co	9	9	4	2	2	31	3	5	3
Cr	10	10	10	10	10	10	10	10	10
F *	268	491	274	471	419	100	1452	560	651
S *	513	578	363	1142	446	289	300	299	329
Sc	1	1	1	1	1	1	1	1	1
V	35	16	18	19	37	305	72	63	46

Note: KPR12/4 is the original sample, Non-Mag: non-magnetic part of sample; Mag: magnetic part of samples.

\*: Semi-quantitative analyses

**Table D.20:** XRF results of calcrete samples and magnetic parts, Kantienpan (major elements: wt. %, A: ampere)

	Original	0.1A	0.3 - 0.9A	Original	0.1- 0.3A	0.5- 0.9A	Original	0.1 - 0.3A	0.5 - 0.9A
%	KPR12/1	KPR12/1	KPR12/1	KPR12/2	KPR12/2	KPR12/2	KPR12/3	KPR12/3	KPR12/3
SiO <sub>2</sub> *	14	16.78	17.82	11.79	13.58	13.06	9.44	9.81	12.08
TiO <sub>2</sub> *	0.1	0.47	0.97	0.15	0.88	0.83	0.12	0.77	0.77
Al <sub>2</sub> O <sub>3</sub> *	1.22	2.11	2.26	1.68	2.36	2.23	1.23	1.7	2.28
Fe <sub>2</sub> O <sub>3</sub> *	0.79	8.08	3.14	1.48	10.72	4.22	1.54	12.23	5.77
MnO *	0.05	0.04	0.06	0.05	0.08	0.14	0.04	0.07	0.07
MgO *	2.51	1.95	1.96	2.53	2.48	2.28	1.73	1.85	1.69
CaO *	43.30	37.20	39.70	44.17	39.11	39.37	46.63	37.60	40.75
Na <sub>2</sub> O *	0.18	0.45	0.4	0.19	0.44	0.35	0.19	0.23	0.4
K <sub>2</sub> O *	0.33	0.38	0.45	0.51	0.4	0.47	0.29	0.24	0.27
P <sub>2</sub> O <sub>5</sub> *	0.11	0.11	0.12	0.18	0.16	0.16	0.08	0.07	0.06
<b>TOTAL</b>	62.59	67.56	66.87	62.72	70.20	63.12	61.28	64.56	64.15

Note: \*: Semi-quantitative XRF powder analyses

**Table D.20:** Continued

	Original	0.1 - 0.2A	0.35- 0.8A	Original	0.1- 0.2A	0.4 - 0.85A
%	KPR12/5	KPR12/5	KPR12/5	KPR12/6	KPR12/6	KPR12/6
SiO <sub>2</sub> *	16.59	14.18	15.81	11.34	14.01	13.51
TiO <sub>2</sub> *	0.19	0.95	0.88	0.16	0.98	1.54
Al <sub>2</sub> O <sub>3</sub> *	2.42	2.36	2.86	2.01	2.75	2.87
Fe <sub>2</sub> O <sub>3</sub> *	2.31	8.36	5.46	3.05	11.91	10.54
MnO *	0.05	0.08	0.1	0.06	0.09	0.15
MgO *	2.48	2.62	2.73	1.73	1.98	1.88
CaO *	39.72	35.85	35.81	44.35	37.23	34.84
Na <sub>2</sub> O *	0.24	0.23	0.24	0.2	0.26	0.26
K <sub>2</sub> O *	0.72	0.43	0.55	0.45	0.45	0.47
P <sub>2</sub> O <sub>5</sub> *	0.12	0.1	0.14	0.18	0.17	0.19
<b>TOTAL</b>	64.84	65.15	64.58	63.52	69.82	66.25

Note: \*: Semi-quantitative XRF powder analyses

Table D.20: Continued

	Original	0.1A	0.3- 0.9A	Original	0.1 - 0.3A	0.5 - 0.9A	Original	0.1 - 0.3A	0.5 - 0.9A
ppm	KPR12/1	KPR12/1	KPR12/1	KPR12/2	KPR12/2	KPR12/2	KPR12/3	KPR12/3	KPR12/3
As	12	6	6	7	6	3	6	14	3
Cu	9	15	15	19	30	27	32	35	42
Ga	2	5	3	2	6	2	2	3	2
Mo	1	1	1	1	6	1	2	1	1
Nb	3	8	10	3	17	2	2	7	2
Ni	3	3	3	6	11	3	3	7	3
Pb	3	4	7	5	7	7	9	8	22
Rb	14	18	13	17	25	2	12	14	2
Sr	154	138	134	158	182	86	207	225	123
Th	7	5	3	3	15	3	3	3	3
U	3	5	3	3	13	3	3	3	3
W*	6	14	16	13	10	17	6	6	20
Y	5	7	7	7	16	3	4	6	3
Zn	40	31	36	95	118	124	117	156	107
Zr	33	61	77	47	67	68	35	58	59
Cl*	485	8	8	8	8	8	8	260	8
Co	2	20	2	2	34	10	2	42	14
Cr	10	75	44	10	118	73	10	10	52
F*	635	1069	3358	290	219	2573	276	100	2184
S*	532	412	418	488	555	453	601	654	849
Sc	1	1	1	1	1	1	1	1	1
V	26	203	51	28	282	61	28	395	94

Note: \*: Semi-quantitative analyses

Table D.20: Continued

	Original	0.1 - 0.2A	0.35 - 0.8A	Original	0.1- 0.2A	0.4 - 0.85A
ppm	KPR12/5	KPR12/5	KPR12/5	KPR12/6	KPR12/6	KPR12/6
As	8	9	14	9	10	15
Cu	17	14	42	49	37	106
Ga	2	2	3	2	4	2
Mo	1	1	1	2	1	2
Nb	4	12	11	4	8	16
Ni	6	7	12	4	9	13
Pb	7	4	12	4	6	19
Rb	23	19	22	16	18	18
Sr	251	241	234	187	170	181
Th	4	7	6	3	6	6
U	3	3	3	3	3	3
W*	32	15	9	8	11	33
Y	12	14	24	10	11	22
Zn	62	100	124	210	191	409
Zr	76	109	102	46	101	105
Cl*	238	11	26	8	8	8
Co	2	28	18	2	42	46
Cr	10	10	10	10	171	10
F*	256	100	189	182	100	100
S*	469	398	330	495	428	702
Sc	1	1	1	1	1	1
V	37	234	98	60	370	201

Note: \*: Semi-quantitative analyses

**Table D.21:** XRF results of calcrete samples and magnetic parts, Kantienpan (major elements: wt. %, A: ampere)

	Original	0.1 - 0.3A	0.5 - 0.9A	Original	0.1A	0.3-0.9A
%	Vcal2	Vcal2	Vcal2	Vcal3	Vcal3	Vcal3
<b>SiO<sub>2</sub></b> *	18.19	17.47	15.04	12.87	22.26	19.11
<b>TiO<sub>2</sub></b> *	0.16	0.88	0.62	0.17	0.8	0.98
<b>Al<sub>2</sub>O<sub>3</sub></b> *	2.52	2.57	2.33	1.82	5.19	3.48
<b>Fe<sub>2</sub>O<sub>3</sub></b> *	1.14	10.21	2.5	1.42	15.44	4.9
<b>MnO</b> *	0.04	0.08	0.04	0.05	0.16	0.16
<b>MgO</b> *	3.13	3.43	2.51	3.13	4.36	4.37
<b>CaO</b> *	38.99	36.53	37.06	42.66	27.71	34.09
<b>Na<sub>2</sub>O</b> *	0.32	0.32	0.45	0.18	0.79	0.45
<b>K<sub>2</sub>O</b> *	0.54	0.39	0.37	0.39	0.51	0.49
<b>P<sub>2</sub>O<sub>5</sub></b> *	0.14	0.1	0.07	0.13	0.33	0.29
<b>TOTAL</b>	65.17	71.99	60.99	62.82	77.56	68.33

Note: \*: Semi-quantitative XRF powder analyses

Table D.21: Continued

	Original	0.1 - 0.3A	0.5 - 0.9A	Original	0.1A	0.3-0.9A
ppm	Vcal2	Vcal2	Vcal2	Vcal3	Vcal3	Vcal3
As	9	7	4	6	22	5
Cu	2	2	12	2	7	10
Ga	2	4	3	2	8	4
Mo	1	1	1	1	2	1
Nb	3	8	2	4	5	9
Ni	6	10	3	6	21	15
Pb	3	3	4	3	4	3
Rb	18	17	2	16	31	25
Sr	149	144	96	236	366	364
Th	3	7	3	4	5	3
U	3	3	3	3	3	3
W *	44	14	25	9	12	14
Y	8	10	3	8	27	22
Zn	29	43	26	30	101	76
Zr	66	93	62	41	71	85
Cl *	102	8	8	8	363	305
Co	2	35	2	2	73	28
Cr	10	10	37	10	17	10
F *	100	100	3110	366	100	340
S *	294	258	200	231	359	338
Sc	1	1	1	1	1	1
V	24	275	20	41	502	103

Note: \*: Semi-quantitative analyses

**Table D.22:** XRF results of calcrete samples and magnetic parts, Areachap (major elements: wt. %, A: ampere, Sample set Calc1)

	Original	<0.9 A	>0.9A
%	Calc1-1	Calc1-1	Calc1-1
<b>Depth of sample: 6 m</b>			
SiO <sub>2</sub> *	26.52	47.61	35.41
TiO <sub>2</sub> *	0.26	0.60	0.46
Al <sub>2</sub> O <sub>3</sub> *	6.24	16.57	9.31
Fe <sub>2</sub> O <sub>3</sub> *	4.77	16.60	6.78
MnO *	0.12	0.23	0.17
MgO *	2.37	4.42	3.62
CaO *	30.79	12.26	25.39
Na <sub>2</sub> O *	0.11	0.05	0.05
K <sub>2</sub> O *	1.00	1.93	1.52
P <sub>2</sub> O <sub>5</sub> *	0.06	0.05	0.05
<b>TOTAL</b>	72.23	100.31	82.75

Original	0.1 – 1.7A
Calc1-2	Calc1-2
<b>Depth of sample: 3 m</b>	
19.83	30.80
0.17	0.38
4.01	7.62
2.70	8.18
0.05	0.07
1.99	2.54
40.31	28.54
0.09	0.05
0.62	1.13
0.03	0.03
69.80	79.34

Original	0.1 – 1.7A
Calc1-3	Calc1-3
<b>Depth of sample: surface</b>	
10.01	20.11
0.15	1.22
1.43	4.24
0.91	6.44
0.05	0.10
1.40	2.13
46.67	36.68
0.14	0.37
0.25	0.56
0.03	0.06
61.05	71.92

Note: \*: Semi-quantitative XRF powder analyses

Table D.22: Continued

	Original	<0.9 A	>0.9A
%	Calc1-1	Calc1-1	Calc1-1
<b>Depth of sample: 6 m</b>			
As	11	9	4
Cu	761	1998	1148
Ga	8	31	14
Mo	1	6	2
Nb	4	9	9
Ni	7	22	13
Pb	5	37	21
Rb	30	58	50
Sr	118	83	122
Th	3	7	6
U	3	3	3
W*	19	9	6
Y	18	37	23
Zn	527	1117	570
Zr	98	147	121
Cl*	648	157	202
Co	16	85	28
Cr	10	111	77
F*	301	100	1849
S*	1332	141	231
Sc	1	1	1
V	85	264	110

Original	0.1 – 1.7A
Calc1-2	Calc1-2
<b>Depth of sample: 3 m</b>	
10	5
152	439
2	12
1	1
3	2
4	6
3	12
20	28
55	38
3	3
3	3
12	25
8	18
163	400
45	93
144	8
2	35
10	90
508	846
148	81
1	1
46	94

Original	0.1 – 1.7A
calc1-3	Calc1-3
<b>Depth of sample: surface</b>	
5	6
52	88
2	2
1	1
2	2
3	8
3	5
14	2
114	43
4	3
3	3
14	6
10	3
36	59
70	92
8	8
2	21
10	199
177	1738
229	386
1	1
19	114

Note: \*: Semi-quantitative analyses

**Table D.23:** XRF results of calcrete samples and magnetic parts, Areachap (major elements: wt. %, A: ampere, Sample set Calc2)

	Original	0.1 – 1.7 A	Original	<0.9 A	>0.9 A	Original
%	Calc2-1	Calc2-1	Calc2-2	Calc2-2	Calc2-2	Calc2-3
<b>Depth of sample: 4 m</b>			<b>Depth of sample: 2 m</b>			<b>Depth of sample: surface</b>
SiO <sub>2</sub> *	25.80	24.01	22.83	28.90	20.83	8.12
TiO <sub>2</sub> *	0.07	1.09	0.11	0.23	0.09	0.19
Al <sub>2</sub> O <sub>3</sub> *	7.29	5.59	4.06	8.72	4.29	1.68
Fe <sub>2</sub> O <sub>3</sub> *	11.36	12.40	6.24	18.45	6.05	1.41
MnO *	0.08	0.08	0.07	0.08	0.07	0.05
MgO *	2.73	2.54	2.17	3.12	2.23	1.34
CaO *	27.38	31.80	34.47	25.82	36.11	46.98
Na <sub>2</sub> O *	0.05	0.21	0.10	0.05	0.10	0.19
K <sub>2</sub> O *	0.58	0.49	0.48	0.64	0.52	0.33
P <sub>2</sub> O <sub>5</sub>	0.05	0.05	0.04	0.03	0.04	0.09
<b>TOTAL</b>	75.38	78.25	70.57	86.04	70.35	60.37

Note: \*: Semi-quantitative XRF powder analyses

**Table D.23:** Continued

	Original	0.1 – 1.7 A	Original	<0.9 A	>0.9 A	Original
ppm	Calc2-1	Calc2-1	Calc2-2	Calc2-2	Calc2-2	Calc2-3
<b>Depth of sample: 4 m</b>			<b>Depth of sample: 2 m</b>			<b>Depth of sample: surface</b>
As	12	4	11	5	12	11
Cu	125	61	169	335	191	159
Ga	14	3	5	23	6	2
Mo	2	1	1	5	1	1
Nb	5	2	4	15	5	3
Ni	3	3	3	13	5	3
Pb	17	3	7	33	9	3
Rb	22	2	18	31	20	14
Sr	98	19	141	116	144	158
Th	14	3	10	23	12	4
U	3	3	3	12	3	3
W *	57	6	28	56	32	6
Y	14	3	11	26	12	9
Zn	1047	176	480	1204	504	81
Zr	68	65	85	73	81	145
Cl *	8	8	8	8	349	40
Co	78	59	33	122	33	2
Cr	10	118	10	37	10	10
F *	100	100	173	100	300	310
S *	149	236	327	358	330	699
Sc	1	1	1	1	1	1
V	116	268	85	186	84	28

Note: \*: Semi-quantitative analyses

**Table D.24:** Chemical composition of calcretes near the ore zone (Calc1-3 and Calc2-3) and further away from ore zone (Vcal2 and Vcal3)

	Original	Original	Original	Original
%	Calc1-3	Calc2-3	Vcal2	Vcal3
SiO <sub>2</sub> *	10.01	8.12	18.20	12.90
TiO <sub>2</sub> *	0.15	0.19	0.20	0.20
Al <sub>2</sub> O <sub>3</sub> *	1.43	1.68	2.50	1.80
Fe <sub>2</sub> O <sub>3</sub> *	0.91	1.41	1.10	1.40
MnO *	0.05	0.05	0.00	0.00
MgCO <sub>3</sub> *	3.36	3.22	7.44	7.44
CaCO <sub>3</sub> *	83.34	83.89	69.64	76.25
Na <sub>2</sub> O *	0.14	0.19	0.30	0.20
K <sub>2</sub> O *	0.25	0.33	0.50	0.40
P <sub>2</sub> O <sub>5</sub> *	0.03	0.09	0.10	0.10
<b>TOTAL</b>	99.67	99.17	99.98	100.69

Note: \*: Semi-quantitative XRF powder analyses

Table D.24: Continued

	Original	Original	Original	Original
ppm	calc1-3	Calc2-3	Vcal2	Vcal3
As	5	11	9	6
Cu	52	159	2	2
Ga	2	2	2	2
Mo	1	1	1	1
Nb	2	3	3	3.7
Ni	3	3	6	6
Pb	3	3	3	3
Rb	14	14	18	16
Sr	114	158	149	236
Th	4	4	3	3.5
U	3	3	3	3
W *	14	6	44	9
Y	10	9	8	8
Zn	36	81	29	30
Zr	70	145	66	41
Cl *	8	40	102	8
Co	2	2	2	2
Cr	10	10	10	10
F *	177	310	100	366
S *	229	699	294	231
Sc	1	1	<1	<1
V	19	28	24	41

Note: \*: Semi-quantitative analyses

**Table D.25:** Chemical composition of magnetic parts of calcretes near the ore zone (Calc1-3) and further away from ore zone (Vcal2 and Vcal3) (A: ampere in)

	0.1 – 1.7A	0.1– 0.3A	0.5 – 0.9A	0.1A	0.3– 0.9A
%	Calc1-3	Vcal2	Vcal2	Vcal3	Vcal3
SiO <sub>2</sub> *	20.11	17.50	15.00	22.30	19.10
TiO <sub>2</sub> *	1.22	0.90	0.60	0.80	1.00
Al <sub>2</sub> O <sub>3</sub> *	4.24	2.60	2.30	5.20	3.50
Fe <sub>2</sub> O <sub>3</sub> *	6.44	10.20	2.50	15.40	4.90
MnO *	0.10	0.10	0.00	0.20	0.20
MgCO <sub>3</sub> *	5.11	8.16	6.00	10.56	10.56
CaCO <sub>3</sub> *	65.50	65.18	66.25	49.46	60.89
Na <sub>2</sub> O *	0.37	0.30	0.50	0.80	0.40
K <sub>2</sub> O *	0.56	0.40	0.40	0.50	0.50
P <sub>2</sub> O <sub>5</sub> *	0.06	0.10	0.10	0.30	0.30
<b>TOTAL</b>	103.71	105.44	93.65	105.52	101.35
<b>Depth</b>	surface	Surface	Surface	Surface	Surface

Note: \*: Semi-quantitative XRF powder analyses

Table D.25: Continued

	0.1 – 1.7A	0.1– 0.3A	0.5 – 0.9A	0.1A	0.3– 0.9A
ppm	Calc1-3	Vcal2	Vcal2	Vcal3	Vcal3
As	6	7	4	22	5
Cu	88	2	12	7	10
Ga	2	4	3	8	4
Mo	1	1	1	2	1
Nb	2	8	2	5	9
Ni	8	10	3	21	16
Pb	5	3	4	4	3
Rb	2	17	2	31	25
Sr	43	144	96	366	364
Th	3	7	3	5	3
U	3	3	3	3	3
W*	6	14	25	12	14
Y	3	10	3	27	22
Zn	59	43	26	101	76
Zr	92	93	62	71	85
Cl*	8	8	8	363	305
Co	21	35	2	73	28
Cr	199	10	37	17	10
F*	1738	100	3109.7	100	340.3
S*	386	258	200	359	338
Sc	1	<1	<1	<1	<1
V	114	275	20	502	103
Depth	surface	Surface	Surface	Surface	Surface

Note: \*: Semi-quantitative analyses

**Table D.26:** Chemical composition of calcretes near and further away from ore zone analyzed by the XRF method (Vermaak, 1984).

Vermaak Data set (1984)					
Major Oxides (%)	Copperton Cu-Zn deposit		Areachap Cu-Zn deposit		No Mineralization
	Calcrete	Complex samples	Calcrete	Complex samples	Average
<b>No. of Samples</b>	12	5	26	7	24
<b>SiO<sub>2</sub></b>	21.18	29.24	20.00	24.71	28.94
<b>Fe<sub>2</sub>O<sub>3</sub></b>	2.75	11.35	1.29	12.89	1.82
<b>MgCO<sub>3</sub></b>	8.81	7.20	4.83	3.35	6.06
<b>CaCO<sub>3</sub></b>	61.46	52.09	67.72	52.80	53.43
<b>Na<sub>2</sub>O</b>	0.03	0.06	0.00	0.03	0.25
<b>K<sub>2</sub>O</b>	0.25	0.27	0.29	0.39	1.30
<b>Trace elements (ppm)</b>					
<b>Sr</b>	344	378	195	173	242
<b>V</b>	151	628	13	101	22
<b>Cu</b>	1850	20883	325	5945	14
<b>Zn</b>	372	1792	140	1018	13

## Appendix E

### Quantitative X-Ray Diffractometry (XRD) analyses results

Samples for quantitative x-ray diffractometry analyses are milled in a carbon-steel mill and then analyzed in a Siemens D-501 instrument (Table E.1). Utilizing Bruker AXS GmbH (Bruker AXS, 2003), the different mineral phases present are identified. This is followed by a calculation of the quantitative abundance of these minerals using the Rietveld method (Young, 1996).

**TABLE E.1:** Instrument and data collection parameters

Instrument	Siemens D-501
Radiation	Cu $K$ (1.5418 $\Delta$ )
Temperature	25EC
Specimen	flat-plate, rotating (30 RPM)
Power Setting	40 kV, 40 mA
Soller slits	2E (diffracted beam side)
Divergence slits	1E
Receiving slits	0.05E
Monochromator	secondary, graphite
Detector	scintillation counter
Range of $2\theta$	5-70E $2\theta$ ?
Step width	0.04E $2\theta$
Time per step	1.5s

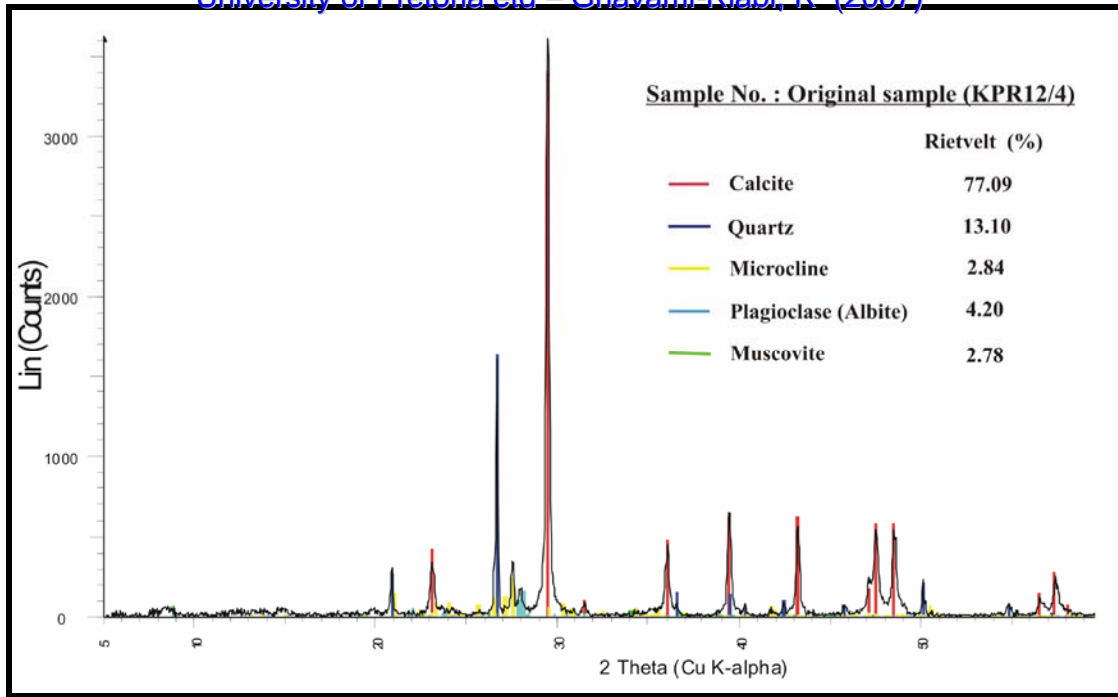


Figure E.1: XRD result for original sample KPR12/4

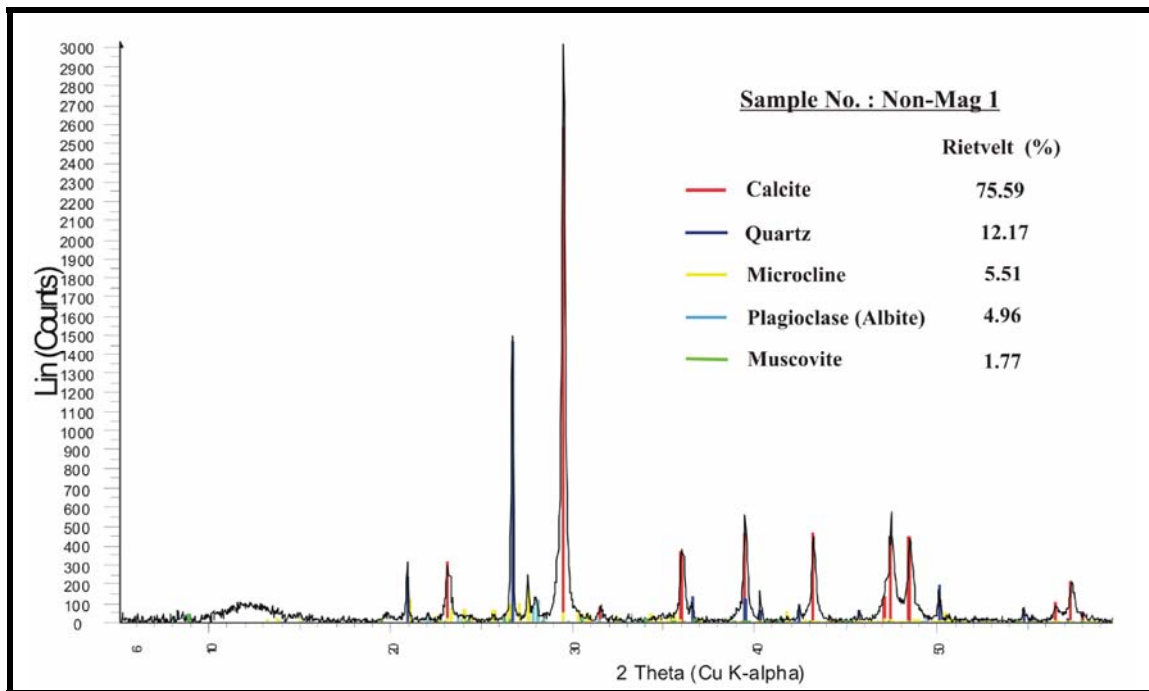


Figure E.2: XRD result for sample Non-Mag 1

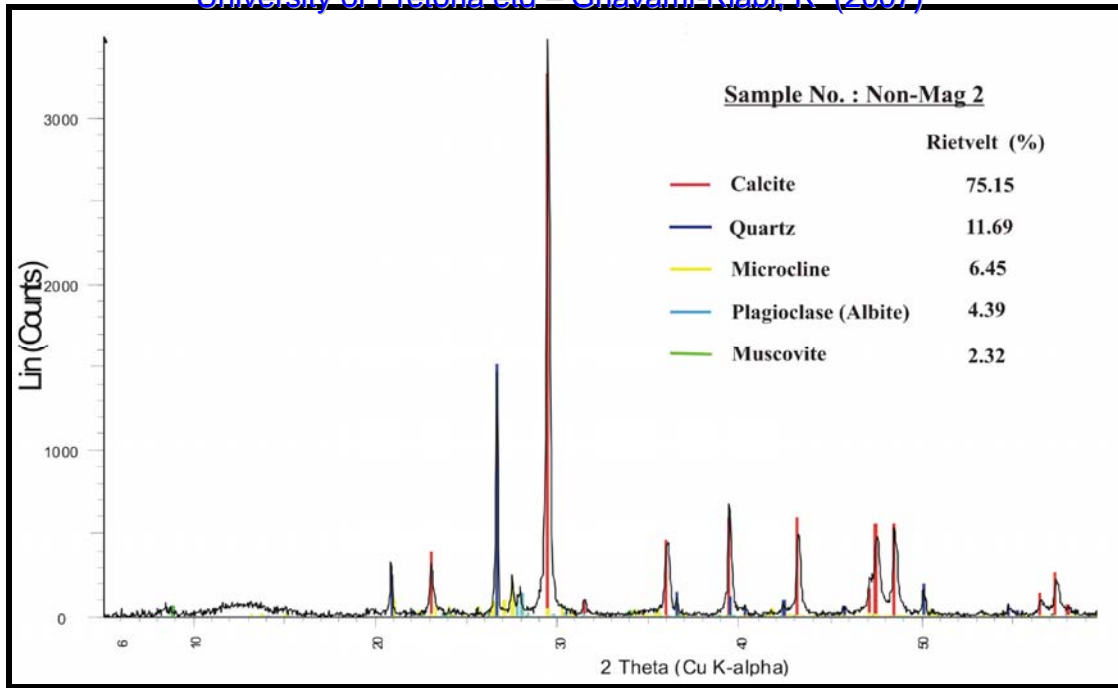


Figure E.3: XRD result for sample Non-Mag 2

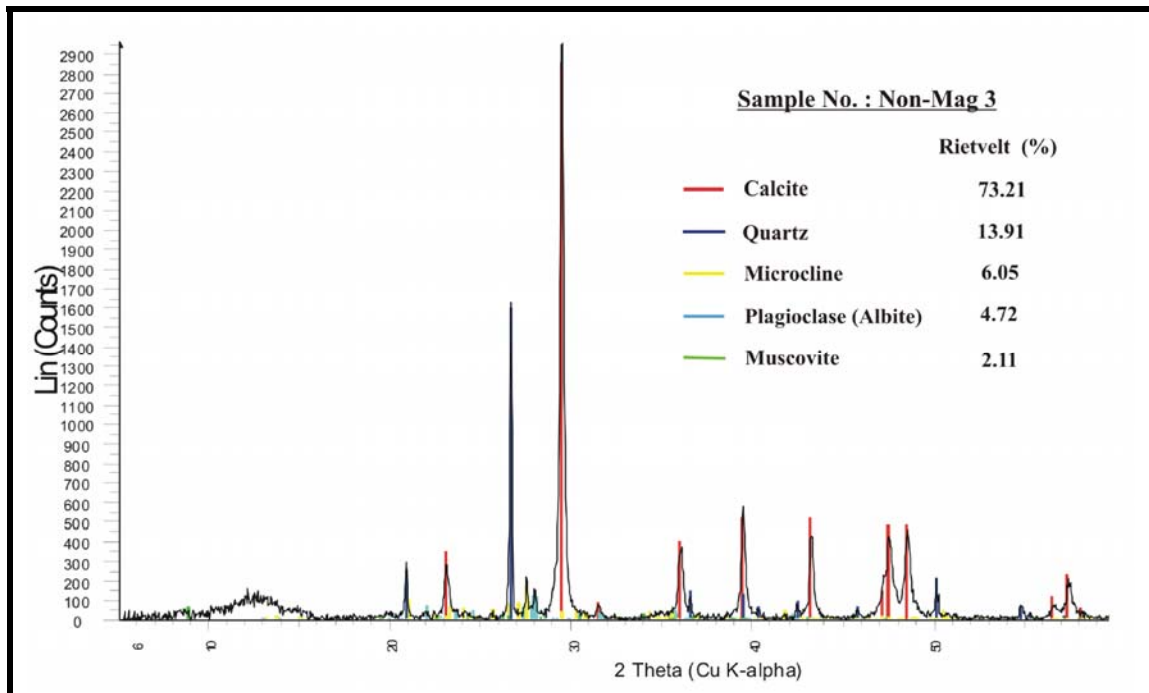


Figure E.4: XRD result for sample Non-Mag 3

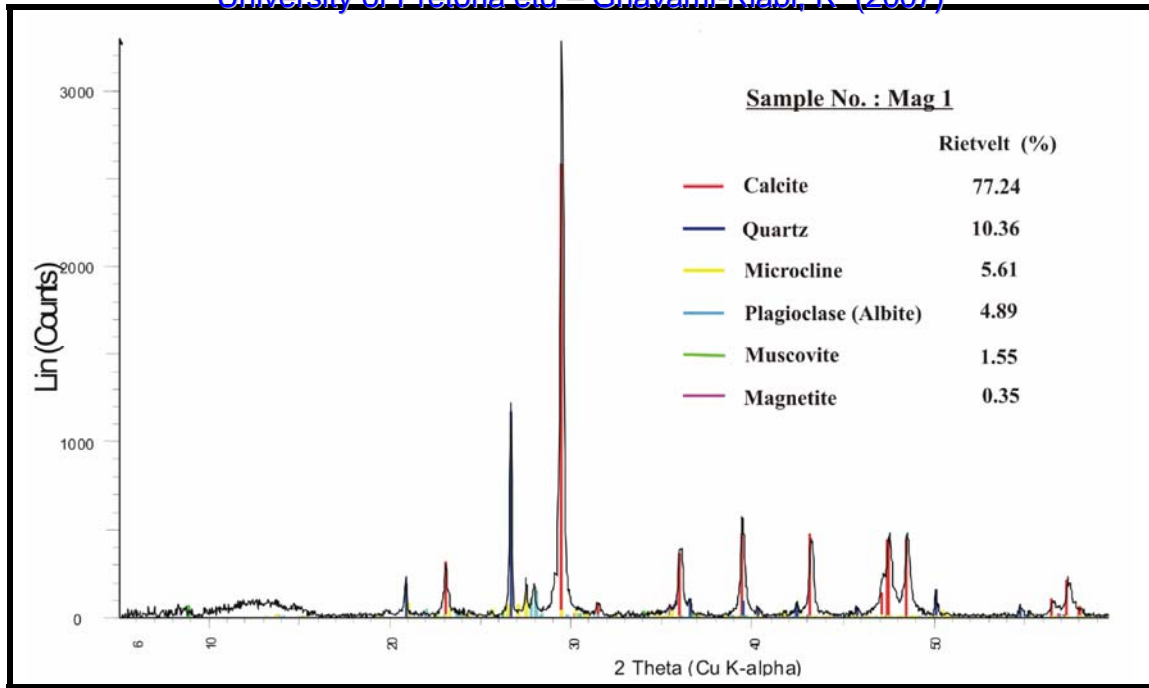


Figure E.5: XRD result for sample Mag 1

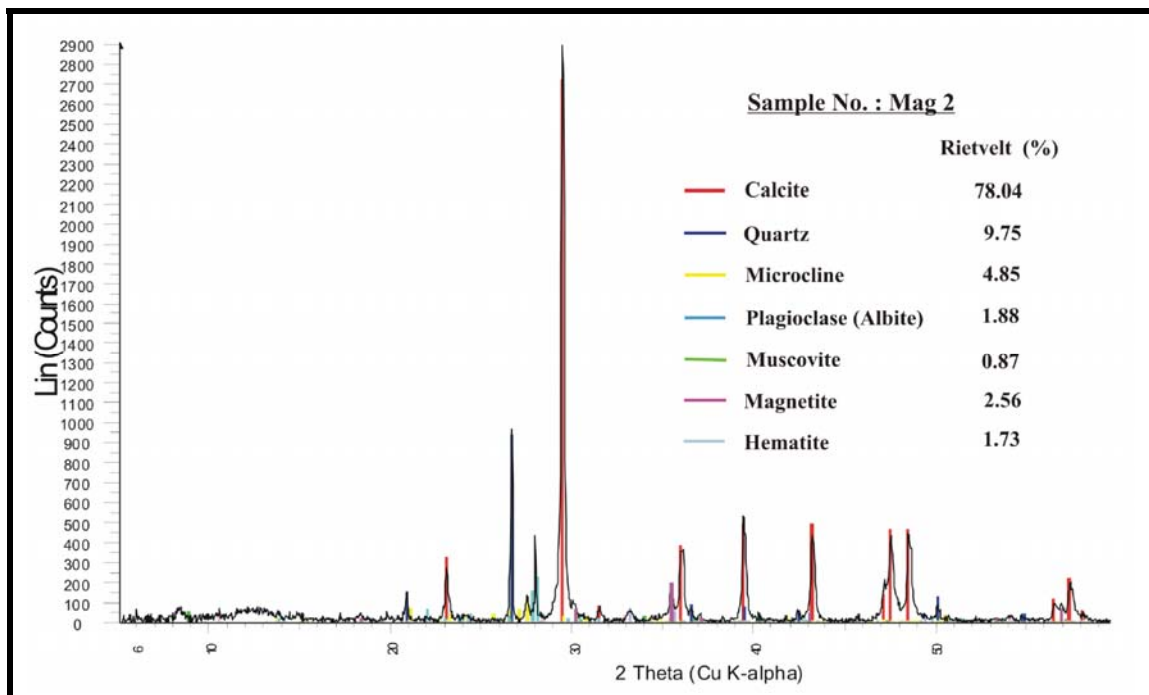


Figure E.6: XRD result for sample Mag 2

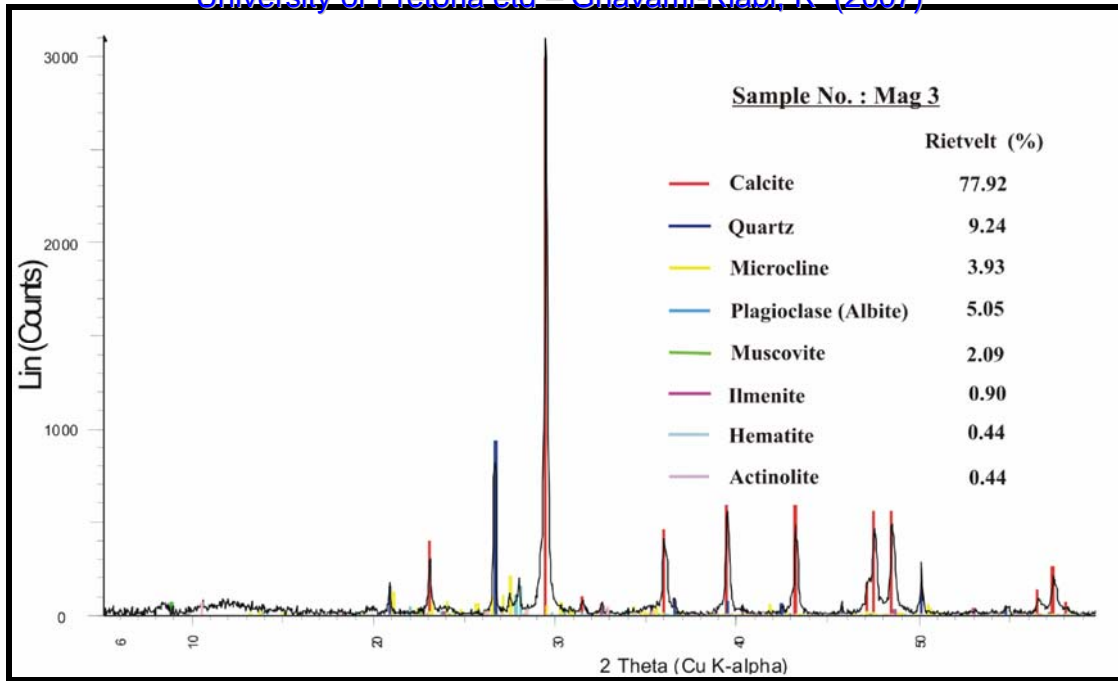


Figure E.7: XRD result for sample Mag 3

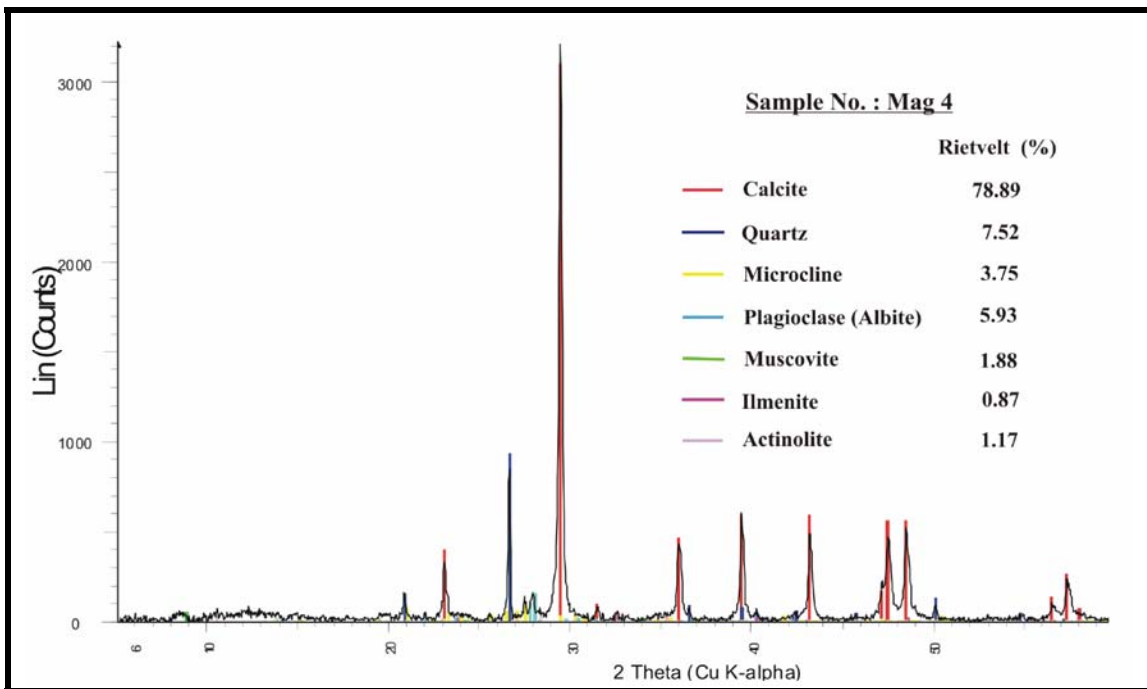


Figure E.8: XRD result for sample Mag 4

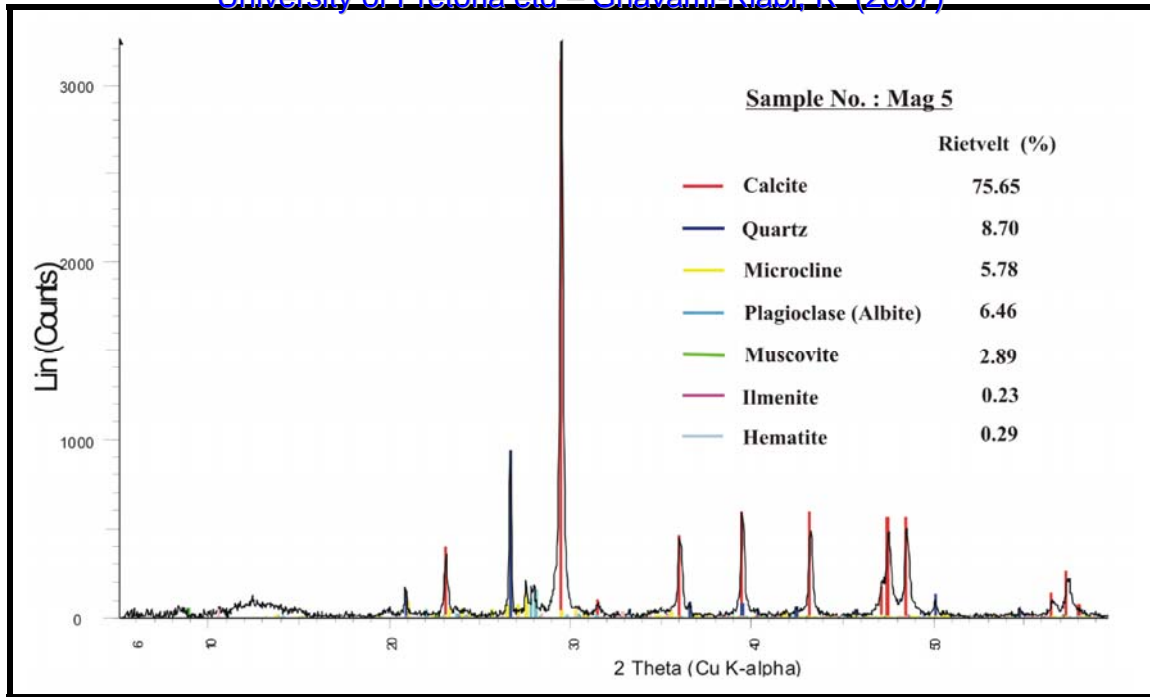
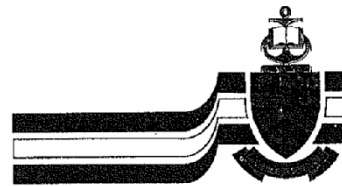


Figure E.9: XRD result for sample Mag 5

## Appendix F

# Confidentiality agreement with Kumba Resources Limit



Universiteit van Pretoria

Pretoria 0002 Republiek van Suid-Afrika Tel 012-420-2454  
Faks 012-362-5219 <http://www.up.ac.za>

Fakulteit Natuur- en  
Landbouwetenskappe

**Prof Hennie Theart**  
Department of Geology  
Pretoria, 0002  
Tel. 012 420 3613  
Fax 012 362 5219  
e-mail: [htheart@postino.up.ac.za](mailto:htheart@postino.up.ac.za)

20<sup>th</sup> June 2003

Mr H J van den Berg  
General Manager Geology  
Kumba Resources Limited  
P O Box 9229  
Pretoria, 0001

Dear Mr van den Berg,

*Department of Geology, University of Pretoria, Namaqua Project: Mr Reza Ghavami-Riabi*

Following our discussion on Thursday 19 June 2003, I wish to confirm the following:

- 1) Kumba Resources Limited (the Company) gave Mr Ghavami-Riabi permission to utilize the results of a lithochemical survey the company conducted between Areachap and Copperton in his research towards his PhD degree. The Company would also permit him to sample the core from boreholes drilled on the farms Kantienpan and Areachap, which is kept at a storage facility on the farm Areachap.
- 2) In return Mr Ghavami-riabi undertakes to inform the company of his findings with regard this material and not to publish or publicly present these findings or the supplied information, until two years after the completion of this research project without prior permission from the Company's General Manager Geology. He and his Supervisor would treat the Company's information as confidential during this period.

Please accept our sincere appreciation for the Company's support of Mr Ghavami-Riabi's studies in this way.

Yours truly,

  
Mr Reza Ghavami-Riabi

  
Supervisor: Prof Hennie Theart